

AD-A030 394

RIA-76-U559

Vol. I

AD-A030 394

TECHNICAL  
LIBRARY



# Army Science Conference Proceedings

22 – 25 June 1976

Volume I

Principal Authors A thru G

This document has been approved for public  
release and sale; its distribution is unlimited.

Deputy Chief of Staff for Research, Development, & Acquisition  
Department of the Army

**RIA-70-U804**

**Office, Chief of Research and Development  
Department of the Army**

**ARMY SCIENCE CONFERENCE PROCEEDINGS - 16-19 June 1970**

**Volume I - Principal Authors - A thru G**

**Volume II- Principal Authors - H thru L**

**Volume III-Principal Authors - M thru Z**





DEPARTMENT OF THE ARMY  
OFFICE OF THE ADJUTANT GENERAL AND THE ADJUTANT GENERAL CENTER  
WASHINGTON, D.C. 20314

HQDA Ltr 70-76-4

DAAG-PAP-A (M) (18 Aug) DRCDE-E

31 August 76

Expires 31 August 77

SUBJECT: 1976 Army Science Conference, Volume I

SEE DISTRIBUTION

1. Inclosed for your information and use is Volume I of the 1976 Army Science Conference Proceedings. This volume contains the unclassified papers by principal authors A through G which were presented at the conference, 22-25 June 1976, U. S. Military Academy, West Point, New York.
2. Volumes II, III and IV of the Proceedings are being distributed separately.
3. Chiefs of Army Staff Agencies, major commanders, and heads of laboratories on the distribution list will insure that copies of the documents are placed in Technical Libraries where they will be available for reference.

BY ORDER OF THE SECRETARY OF THE ARMY:

PAUL T. SMITH  
Major General, United States Army  
The Adjutant General

1 Incl  
Vol I, 1976 Army Science  
Conference Proceedings



SUBJECT: 1976 Army Science Conference, Volume I

DISTRIBUTION:

The Surgeon General

Chief of Engineers, ATTN: DAEN-RDZ-A

Chief of Engineers, ATTN: DAEN-FEP

Chief of Engineers, ATTN: DAEN-MCZ-S

Chief of Engineers, ATTN: DAEN-CWM-R

The Army Library, ATTN: ANRAL-RS

Commander:

US Army Materiel Development and Readiness Command

US Army Missile Command

US Army Electronics Command

US Army Armament Command

US Army Test and Evaluation Command

US Army Aviation Systems Command

US Army Tank-Automotive Research and Development Command

US Army Troop Support Command

US Army Concepts Analysis Agency

US Army Research Institute for the Behavioral & Social Sciences

US Army Training and Doctrine Command

US Army Forces Command

US Army Medical Research and Development Command

US Army Security Agency

US Army Communications Command

US Army Computer Systems Command

US Army Avionics Laboratory

US Army Electronic Warfare Laboratory

US Army Mobility Equipment Research and Development Command

US Army Natick Research and Development Command

US Army Materials and Mechanics Research Center

US Army Materials Systems Analysis Activity

US Army Satellite Communications Agency

US Army Aberdeen Proving Ground

US Army Dugway Proving Ground

US Army Yuma Proving Ground

US Army Electronic Proving Ground

US Army Foreign Science and Technology Center

US Army Tropic Test Center

US Army White Sands Missile Range

US Army Research Office

US Army Research and Standardization Group (Europe)

Rock Island Arsenal

Watervliet Arsenal

Edgewood Arsenal

Frankford Arsenal

Picatinny Arsenal



31 August 76

SUBJECT: 1976 Army Science Conference, Volume I

Electronics Technology and Devices Laboratory  
Atmospheric Sciences Laboratory  
Combat Surveillance and Target Laboratory  
Communication/Automatic Data Processing Laboratory  
Harry Diamond Laboratories  
US Army Coastal Engineering Research Center  
US Army Construction Engineering Research Laboratory  
US Army Cold Regions Research and Engineering Laboratory  
US Army Engineer Topographic Laboratories  
US Army Engineer Waterways Experiment Station  
US Army Facilities Engineering Support Agency  
US Army Institute of Surgical Research  
US Army Aeromedical Research Laboratory  
US Army Research Institute of Environmental Medicine  
US Army Environmental Hygiene Agency  
US Army Medical Research Institute of Infectious Diseases  
US Army Tripler Medical Center  
US Army Institute of Dental Research  
Dwight D. Eisenhower Army Medical Center  
Brooke Army Medical Center  
Fitzsimons Army Medical Center  
Armed Forces Institute of Pathology  
Madigan Army Medical Center  
Health Services Command

Director:

US Army Ballistic Missile Defense Program Office  
US Army Air Mobility Research and Development Laboratory  
US Army Ballistic Research Laboratories  
US Army Human Engineering Laboratory  
Thomas J. Rodman Laboratory  
Ames Directorate, US Army Air Mobility Research & Development Laboratory  
Feltman Research Laboratory  
Eustis Directorate, US Army Air Mobility Research & Development Laboratory  
Langley Directorate, US Army Air Mobility Research & Development Laboratory  
Lewis Directorate, US Army Air Mobility Research & Development Laboratory  
Night Vision Laboratory  
The Hydrologic Engineering Center  
US Army Engineer Institute for Water Resources  
Biomedical Laboratory

Project Manager:

MALOR, Fort Monmouth  
REMBASS, Fort Monmouth

Superintendent:

US Military Academy, ATTN: Technical Laboratory  
US Military Academy, ATTN: Acquisition Branch

SUBJECT: 1976 Army Science Conference, Volume I

Copies Furnished:

- Director of Defense Research and Engineering
- Director, US Naval Research Laboratories
- Director, Air University Library
- Director, Defense Communications Agency
- Director, Research, Development, Test and Evaluation, US Navy
- Director, Weapons Systems Evaluation Group
- Director, Energy Research and Development Administration
- National Aeronautics and Space Agency
- National Institutes of Health
- National Science Foundation
- National Academy of Sciences
- Defense Advanced Research Projects Agency
- Assistant Chief of Staff for Intelligence
- Chief of Naval Research
- Chairman, Defense Science Board

Commander:

- Air Force Systems Command
- Air Force Office of Scientific Research
- US Coast Guard Research and Development Center

Commandant:

- National War College
- Industrial College of the Armed Forces
- Academy of Health Sciences
- National Defense University

HQDA (DAAG-TCZ-B)

US Army Reserve Components Personnel & Administration Center

PROCEEDINGS  
OF THE  
1976 ARMY SCIENCE CONFERENCE  
UNITED STATES MILITARY ACADEMY, WEST POINT, N.Y.  
22 - 25 JUNE 1976

VOLUME I

Principal Authors A through G



All experiments involving live animals that are reported in the Proceedings were performed in accordance with the principles of laboratory animal care as promulgated by the National Society of Medical Research

TABLE OF CONTENTS

PROCEEDINGS OF THE 1976 ARMY SCIENCE CONFERENCE

<u>Author</u>	<u>Title</u>	<u>Vol</u>	<u>Page</u>
Adams, A. A.	See Walker, G. W.	3	345
Addison, H. J.	See Schillinger, D. E.	3	187
Agar, K. H. Davenport, O. A.	Methodology of Vulnerability Analysis in Electronic Warfare	4	1
Agee, F. J. Roberts, H. A.	The Invention and Development of PLACER	1	1
Aitken, G. W. Swinzow, G. K. Farrell, D. R.	Projectile and Fragment Pene- tration in Snow and Frozen Soil	1	17
Alesi, A. L.	See Prifti, J. J.	3	91
Allen, R. G. Irwin, G. R.	Antibody to Hepatitis B Core Antigen	1	31
Amoruso, M. J. Babiak, S. T. Van Damme, G. E.	Target Discrimination with an Infrared Reticle Seeker	4	11
Anderson, D. H.	See Carlon, H. R.	1	187
AuCoin, T. R.	See Schwartz, A.	3	203
Ayers, O. E. Murfree, J. A. Martignoni, P. Chew, W. M.	Solid Propellants for Hydrogen Gas Generators	1	41
Babiak, S. T.	See Amoruso, M. J.	4	11
Bensinger, T. A. Zuck, T. F.	Optional Additive Systems as an Effective Strategy for Blood Storage in Military Blood Banking	1	53
Berkowitz, H. L.	See Kronenberg, S.	2	347
Bernard, R. S.	A Projectile Penetration Theory for Layered Targets	1	63

<u>Author</u>	<u>Title</u>	<u>Vol</u>	<u>Page</u>
Bondurant, A. J.	A New Photogrammetric Comparator Design	1	77
Bosco, C. D.	See Zeto, R. J.	3	413
Bottone, A. G.	Remote Portable Solar Powered Microwave System	1	89
Boxwell, D. A. Schmitz, F. H.	In-Flight Far-Field Measurement of Helicopter Impulsive Noise	1	99
Boyle, V.	See Howe, P. M.	4	71
Bradley, L. M.	An Adaptive Prediction Filter Algorithm for Optimizing Servo System Performance	1	115
Brady, J. M.	See Cutright, D. E.	1	235
Breckenridge, J. R.	See Goldman, R. F.	1	447
Brooke, R. H.	A Procedure for the Statistical Analysis of Vehicular Noise Emission Spectra for Limited Samples	1	131
Brown, T. J. Farassat, F.	A New Capability for Predicting Helicopter Rotor Noise in Hover and in Flight	1	143
Bruce, C. W.	See White, K. O.	3	359
Buser, R. G.	See Fishbein, W.	4	23
Butler, D. K.	High-Velocity Fragment Penetration into Sand: A Comparison of Experimental Results with Theoretical Predictions	1	157
Callendar, R. E. Flannery, R. E.	The Development of Thin Film Photodetectors for the 8-14 Micrometer Atmospheric Window	1	173
Carlson, H. R. Anderson, D. H.	Aerosol Spectroscopy in the Infrared	1	187
Chew, W. M.	See Ayers, O. E.	1	41
Choi, C. S.	See Iqbal, Z.	2	183



<u>Author</u>	<u>Title</u>	<u>Vol</u>	<u>Page</u>
Chrepta, M. M.	See Jacobs, H.	2	231
Christenson, C. R. Smith, J. L. Martin, T. A. Griffin, J. R.	Optical Measurement of Missile Wing Deformations in High Velocity Tests	1	203
Christianson, C.	See Yeager, G.	4	177
Christoe, C. W.	See Iqbal, Z.	2	183
Chu, S. C.	See Toal, J. J.	3	303
Church, E. L. Jenkinson, H. A. Esposito, R. J.	Plastic Piezoids for Fuze Applications	1	219
Claus, W. D.	See McManus, L. R.	2	421
Cox, J. T.	See Petito, F. C.	3	59
Cress, D. H.	See Link, L. E.	2	389
Cutright, D. E. Brady, J. M. Getter, L. Miller, R. A.	Lactic Acid Derived Biode- gradable Implant Materials	1	235
Cutright, D. E.	See Huget, E. F. and Levin, M. P.	2 2	159 359
Dammann, J. F.	A Method for Analyzing Air Target Fuzes	1	249
Davenport, O. A.	See Agar, K. H.	4	1
Davidson, T. E. Kendall, D. P. Homan, C. G. Frankel, J. Rich, F. J.	Unique Materials and Properties in the New High Pressure- Temperature Regime Above 250 Kbars	1	265
Davis, L. K.	Effects of Low-Yield Nuclear Warheads on Airfield Runways	1	279
Davis, R.	See Tyroler, J. F.	3	331
DeLuca, E.	See Prifti, J. J.	3	91

<u>Author</u>	<u>Title</u>	<u>Vol</u>	<u>Page</u>
Denniston, J. C. Ramos, M. U. Jackson, R. E.	Incidence of Coronary Risk Factors and Evidence of Ischemic Heart Disease in a Selected Military Population	1	291
de Simon, L. B.	See Huget, E. F.	2	159
DeVenuto, F. Zegna, A. Moores, W. Y. Zuck, T. F.	Transfusions with Hemoglobin Prepared by Crystallization	1	307
Doherty, R. W.	See Holst, G. C.	4	55
Doremus, L. W.	See Nicolaides, R. V.	3	1
Downs, D. S.	See Gora, T.	1	455
Duncan, L. D.	SATFAL - The Application of Meteorological Satellite Data to Nuclear Fallout Prediction	1	321
Durand, P. E.	See McManus, L. R.	2	421
Eisenberg, G. H. G. Osterman, J. V.	Experimental Scrub Typhus Immunogens	1	335
Emigh, C.	See Yeager, G.	4	177
Esposito, R. J.	See Church, E. L.	1	219
Farassat, F.	See Brown, T. J.	1	143
Farr, M. K.	See Iqbal, Z.	2	183
Farrell, D. R.	See Aitken, G. W.	1	17
Fine, B. J. Kobrick, J. L.	Effects of High Altitude and Heat on Simulated Artillery Fire Direction Center Tasks	1	345
Fishbein, W. Buser, R. G. Rittenbach, O. Rohde, R. S.	Combined Radar - Electro/Optic Sensor	4	23
Flannery, R. E.	See Callendar, R. E.	1	173
Foiani, D.	See Yeager, G.	4	177

<u>Author</u>	<u>Title</u>	<u>Vol</u>	<u>Page</u>
Forsyth, A. C.	See Iqbal, Z.	2	183
Frankel, J.	See Davidson, T. E.	1	265
Frey, R. B.	See Howe, P. M.	4	71
Gardner, H. B.	Chemotherapeutic Agents in Ocular Metallosis	1	361
Garrett, W. L.	See Gora, T.	1	455
Gazza, G. E.	Silicon Nitride/Yttria: A Potential Gas Turbine Material	1	377
Gerber, B. V. Stuempfle, A. K.	A New Experimental Technique for Studying the Explosive Comminution of Liquids	1	389
Gerhart, G. R.	The Measurement of the Third- Order Elastic Constants in a Slightly Anisotropic Solid Using Ultrasonic Surface Waves	1	405
Getter, L.	See Cutright, D. E. and Levin, M. P.	1 2	235 359
Glass, C. M. Greenhut, V. A. Kingman, P. W.	Porosity and Spall Fracture of Shock Loaded Metals	1	415
Gleason, T. J. Sword, M. E.	Laser Terminal Homing Engage- ment Simulator (Eye-Safe)	1	431
Goble, G. W.	See Moore, R. L.	2	465
Goes, M. J.	See Masly, J. R.	4	135
Goldman, R. F. Breckenridge, J. R.	Current Approaches to Resolving the Physiological Heat Stress Problems Imposed by Chemical Protective Clothing Systems	1	447
Gonano, J. R.	Comparison of Nuclear Resonance Techniques for Detection of Concealed Explosives	4	39
Gora, T. Sharma, J. Wiegand, D. A. Garrett, W. L. Downs, D. S.	Contact and Surface Effects in the Electric Field Initiation of Explosives	1	455



<u>Author</u>	<u>Title</u>	<u>Vol</u>	<u>Page</u>
Gora, T.	See Tyroler, J. F.	3	331
Graft, R. D.	Photoelectron Noise Limitations in High Performance Imaging Sensors	1	469
Greendale, J. H.	See McManus, L. R.	2	421
Greenhut, V. A.	See Glass, C. M.	1	415
Griffin, J. R.	See Christensen, C. R.	1	203
Gualtieri, J. G.	See Schwartz, A.	3	203
Hafner, E. Schodowski, S. S. Vig, J. R. Mazurczyk, H.	Gunhardened Crystal Oscillators for Remotely Monitored Battle- field Sensor Systems	2	1
Haggerty, R. F.	See Hussain, M. A.	2	167
Halliday, J. W.	See Taub, I. A.	3	289
Hammond, C. E. Weller, W. H.	Wind-Tunnel Testing of Aero- elastically Scaled Helicopter Rotor Models	2	17
Harvey, J. T.	See Wright, H. L.	3	391
Haskell, R. W. Imam, A. R.	Chemically Vapor Deposited Tungsten Coatings for Erosion Protection	2	33
Hawley, E. F.	Shoreline Reaction to an Impermeable Groin	2	49
Heberlein, D. C.	Chemical Neutralization of Tri- nitrotoluene	2	63
Hertert, R. S.	See Huget, E. F.	2	159
Hill, N.	See Houle, M. J.	2	123
Hittle, D. C. Walton, G. N. Holshouser, D. F.	Method for Estimating Solar Heating and Cooling System Performance	2	79
Hodge, D. C.	See Price, G. R.	3	75
Hoff, G. C.	A New Cement for Cold Weather Construction	2	93
Holmes, L. G.	See Taub, I. A.	3	289
Holshouser, D. F.	See Hittle, D. C.	2	79

<u>Author</u>	<u>Title</u>	<u>Vol</u>	<u>Page</u>
Holst, G. C. Doherty, R. W. Stuebing, E. W.	Infrared Effectiveness of Tactical Screening Smokes	4	55
Homan, C. G.	See Davidson, T. E.	1	265
Honig, E. M.	RFI Shielding Effectiveness of Steel Sheets with Partly Welded Seams	2	107
Houle, M. J. Hill, N. LeGrand, R. Janroga, S.	The Fate of Isopropyl Methyl- phosphonofluoridate in Growing Plants	2	123
Howard, J. D.	Analysis of Multivariate Sensor Responses in a Surveillance Environment	2	137
Howe, P. M. Frey, R. B. Boyle, V. Taylor, B.	Physics of the Response of Explosives to Shock Loading	4	71
Hryckowian, E.	See Zeto, R. J.	3	413
Huddleston, R. L.	Diagnostic Significance of Macro- and Microscopic Features of Catastrophic Gun-Tube Failures	2	149
Huget, E. F. Hertert, R. S. Cutright, D. E. de Simon, L. B.	Electroanesthesia	2	159
Hussain, M. A. Haggerty, R. F. Pu, S. L. Noble, B.	Exterior Collocation for Three Dimensional Surface Flaws	2	167
Imam, A. R.	See Haskell, R. W.	2	33
Iqbal, Z. Choi, C. S. Christoe, C. W. Farr, M. K. Forsyth, A. C. Prask, H. J. Trevino, S. F.	Advances in Techniques for Structural and Dynamical Studies of Stability in Energetic Materials and Applications to Diverse End-Item Problems	2	183
Irwin, G. R.	See Allen, R. G.	1	31

<u>Author</u>	<u>Title</u>	<u>Vol</u>	<u>Page</u>
Iskandar, I. K. Leggett, D. C.	Reclamation of Wastewater by Application on Land	2	199
Jackson, R. E.	See Denniston, J. C.	1	291
Jackson, R. K. Weingart, R. C.	Detonation Properties of the Insensitive Explosive TATB	2	215
Jacobs, H. Chrepta, M. M.	Mechanisms of Dielectric Resonant Oscillators for Micro- wave and Millimeter-Wave Integrated Circuits	2	231
Janroga, S.	See Houle, M. J.	2	123
Jenkinson, H. A.	See Church, E. L.	1	219
Joebstl, J. A.	Surface Research for Develop- ment of New Electrocatalysts for Acid Electrolyte Fuel Cells	2	247
Jones, R. A.	Methodology for Forecasting Soviet Weapon Trends	4	87
Jones, R. D. Kaminski, W. J.	Maximizing User Acceptance - A Systems Approach	2	263
Kaminski, W. J.	See Jones, R. D.	2	263
Kapsalis, J. G.	See Rahman, A.	3	113
Kayser, L. D.	See Sturek, W. B.	3	273
Kemmey, P.	See Tyroler, J. F.	3	331
Kendall, D. P.	See Davidson, T. E.	1	265
Keown, M. P. Stoll, J. K.	Automated Procedure for Airfield Site Evaluation	2	279
Kern, P. J.	See Korohey, O. B.	2	331
Killoran, J. J.	Irradiation of Multilayered Materials to Improve Performance for Packaging of Thermoprocessed Foods	2	293
Kingman, P. W.	See Glass, C. M.	1	415

<u>Author</u>	<u>Title</u>	<u>Vol</u>	<u>Page</u>
Kinzer, N. S.	Historical and Cross-Cultural Perspectives on Women in Combat	2	303
Kitchen, J. H. Malseed, D. T.	Evaluation of Gamma-Ray Techniques for Nondestructive Measurement of Vegetative Biomass	2	317
Kobrick, J. L.	See Fine, B. J.	1	345
Koropey, O. B. Kern, P. J.	Effects of a Thermal Reactor on the Energy Efficiency of a Turbocharged, Stratified Charge Engine	2	331
Kowalick, J. F.	See Puchalski, W. J.	3	107
Kraybill, W.	See Tribble, H.	3	319
Kronenberg, S. Lux, R. A. Pfeffer, R. Berkowitz, H. L. Nilson, K.	Charge Transport Tactical Dosimeter	2	347
Lawrence, R. V.	See Walker, G. W.	3	345
Leggett, D. C.	See Iskandar, I. K.	2	199
LeGrand, R.	See Houle, M. J.	2	123
Levin, A.	A Criterion for Swim-Capable Combat Vehicles: Analyses and Evaluations	4	103
Levin, M. P. Getter, L. Cutright, D. E.	The Use of Biodegradable Ceramic as a Bone Implant Material	2	359
Lindberg, A. W. Mayer, M. S.	Laboratory Testing Techniques for High-Noise Environment Communications Systems	2	373
Link, L. E. Cress, D. H.	Application of Remote Sensing to Environmental Management at Military Facilities	2	389

<u>Author</u>	<u>Title</u>	<u>Vol</u>	<u>Page</u>
Lux, R. A.	See Kronenberg, S.	2	347
Malseed, D. T.	See Kitchen, J. H.	2	317
Mapes, C. A. Sobocinski, P. Z.	Multiple Leukocytic Factors That Induce Reactions Characteristic of the Inflammatory Response	2	405
Martignoni, P.	See Ayers, O. E.	1	41
Martin, T. A.	See Christensen, C. R.	1	203
Masaitis, C.	Stochastic Combat Model	4	119
Masly, J. R. Goes, M. J.	Fluidic Security Systems for Bunkers and Storage Areas	4	135
Mayer, M. S.	See Lindberg, A. W.	2	373
Mazurczyk, H.	See Hafner, E.	2	1
McManus, L. R. Durand, P. E. Claus, W. D. Greendale, J. H.	Development of a New Infantry Helmet	2	421
McSherry, L. K.	Ionospheric Scintillations at SHF	2	437
Meason, J. L.	See Wright, H. L.	3	391
Mescall, J. F. Riffin, P. V. Polley, C. J.	New Wave-Shaping Concepts in Fragmentation Munitions	2	451
Miller, R. A.	See Cutright, D. E.	1	235
Moore, R. L. Goble, G. W.	Combustion Instability in a 175mm Gun Firing Chamber	2	465
Moores, W. Y.	See DeVenuto, F.	1	307
Mumford, S.	See Tribble, H.	3	319
Murfree, J. A.	See Ayers, O. E.	1	41
Nemarich, J.	See Sattler, J. P.	3	159
Nicolaides, R. V. Doremus, L. W.	A New Development in Radiation Hardening of Military Electronic Circuitry	3	1

<u>Author</u>	<u>Title</u>	<u>Vol</u>	<u>Page</u>
Nida, A. V. Stewart, G. S.	Dual Purpose Nuclear Power Plants for Military Installations	3	15
Nilson, K.	See Kronenberg, S.	2	347
Noble, B.	See Hussain, M. A.	2	167
Opalka, K. O.	See Sturek, W. B.	3	273
Osterman, J. V.	See Eisenberg, G. H. G.	1	335
Patton, J. F. Vogel, J. A.	An Evaluation of Physical Fitness in the "Pro-Life" Program, 2d Infantry Division, Korea	3	29
Peekna, A.	Development of the Brinell Sandwich Passive Transducer	3	43
Petito, F. C. Cox, J. T.	High Performance Pyroelectric Vidicon	3	59
Pfeffer, R.	See Kronenberg, S.	2	347
Pital, A.	See Tribble, H.	3	319
Polley, C. J.	See Mescall, J. F.	2	451
Prask, H. J.	See Iqbal, Z.	2	183
Price, G. R. Hodge, D. C.	Detection of Combat Sounds by the Human Ear	3	75
Prifti, J. J. DeLuca, E. Alesi, A. L.	Hardened Tuned-Wall Plastic Radomes for Military Radars	3	91
Pu, S. L.	See Hussain, M. A.	2	167
Puchalski, W. J. Kowalick, J. F.	Wake Region Perturbation for Base Drag Reduction	3	107
Rahman, A. R. Shipman, J. W. Wallner, S. J. Westcott, D. E. Segars, R. A. Kapsalis, J. G.	Novel Techniques for the Preservation of Crispness and Tissue Integrity of Salad Vegetables	3	113
Ramos, M. U.	See Denniston, J. C.	1	291



<u>Author</u>	<u>Title</u>	<u>Vol</u>	<u>Page</u>
Randolph, D. I. Stuck, B. E.	Sensitivity of the Rhesus Monkey Cornea and Surrounding Tissues to Heat Produced by CO <sub>2</sub> Laser Radiation	3	129
Redwinski, R. J.	Improved Hawk Survivability Study	4	149
Reed, H. L.	Fundamental Limitations on Fire Control Predictions	3	145
Reklis, R. P.	See Sturek, W. B.	3	273
Ricca, J. J.	See Shuford, R. J.	3	217
Rich, F. J.	See Davidson, T. E.	1	265
Riffin, P. V.	See Mescall, J. F.	2	451
Rittenbach, O.	See Fishbein, W.	4	23
Roberts, H. A.	See Agee, F. J.	1	1
Robbins, F. M.	See Taub, I. A.	3	289
Rohde, R. S.	See Fishbein, W.	4	23
Sattler, J. P. Weber, B. A. Nemarich, J.	Tunable Mercury Cadmium Telluride Infrared Lasers	3	159
Scheder, R. A.	A Self-Adapting Target State Estimator	3	173
Schillinger, D. E. Addison, H. J.	"Fused On" Rotating Bands for Small Caliber Ammunition	3	187
Schmitz, F. H.	See Boxwell, D. A.	1	99
Schodowski, S. S.	See Hafner, E.	2	1
Schroyer, F. K.	See Tyroler, J. F.	3	331
Schwartz, A. Wade, M. J. AuCoin, T. R. Gualtieri, J. G.	High Efficiency Pentaphosphates for Miniaturized Laser Appli- cations	3	203
Segars, R. A.	See Rahman, A. R.	3	113
Shaffer, R.	See Tribble, H.	3	319

<u>Author</u>	<u>Title</u>	<u>Vol</u>	<u>Page</u>
Sharma, J.	See Gora, T.	1	455
Shepel, M.	See Tribble, H.	3	319
Shipman, J. W.	See Rahman, A. R.	3	113
Shuford, R. J. Wilde, A. F. Ricca, J. J. Thomas, G. R.	Piezoelectric Polymer Films for Application in Monitoring Devices	3	217
Sletten, R. S. Uiga, A.	Wastewater Treatment in Cold Climates	3	231
Smith, J. L.	See Christensen, C. R.	1	203
Sobocinski, P. Z.	See Mapes, C. A.	2	405
Soicher, H.	Ionospheric and Plasmaspheric Effects in Satellite Navigation Systems	3	247
Stephen, E. L.	First Successful Use of a Chemical Compound for the Prophylaxis and Treatment of a Lethal, Systemic, Viral Infec- tion Common to Man and Subhuman Primates	3	263
Stewart, G. S.	See Nida, A. V.	3	15
Stoll, J. K.	See Keown, M. P.	2	279
Stuck, B. E.	See Randolph, D. I.	3	129
Stuebing, E. W.	See Holst, G. C.	4	55
Stuempfle, A. K.	See Gerber, B. V.	1	389
Sturek, W. B. Reklis, R. P. Kayser, L. D. Opalka, K. O.	Three Dimensional Boundary Layer Studies as Applied to the Magnus Effect on Spinning Projectiles	3	273
Swinzow, G. K.	See Aitken, G. W.	1	17
Sword, M. E.	See Gleason, T. J.	1	431
Taub, I. A. Halliday, J. W. Holmes, L. G. Walker, J. E. Robbins, F. M.	Chemical Effect of Irradiating Frozen, Hydrated Muscle Proteins: Myosin and Actomyosin	3	289

<u>Author</u>	<u>Title</u>	<u>Vol</u>	<u>Page</u>
Taylor, B.	See Howe, P. M.	4	71
Thomas, G. R.	See Shuford, R. J.	3	217
Thornton, C. G.	See Zeto, R. J.	3	413
Toal, J. J. Chu, S. C.	A More Rational Approach for Analyzing and Designing the Steel Cartridge and Chamber Interface	3	303
Trevino, S. F.	See Iqbal, Z.	2	183
Tribble, H. Shaffer, R. Shepel, M. Kraybill, W. Pital, A. Mumford, S.	Discrimination of Microbio- logical Organisms by the Luminol Chemiluminescent Reaction	3	319
Tyroler, J. F. Kemney, P. Gora, T. Davis, R. Schroyer, F. K.	Development of a Methodology for Design of Optimum - Illumination Flare Systems	3	331
Uiga, A.	See Sletten, R. S.	3	231
Van Damme, G. E.	See Amoruso, M. J.	4	11
Vig, J. R.	See Hafner, E.	2	1
Vogel, J. A.	See Patton, J. F.	3	29
Wade, M. J.	See Schwartz, A.	3	203
Wagner, R. J.	Radar Vulnerability Reduction: Evaluation of XP-Polymer Material for Antenna Radomes	4	163
Walker, G. W. Lawrence, R. V. Adams, A. A.	An Improved Electrolyte for Direct Oxidation Fuel Cells	3	345
Walker, J. E.	See Taub, I. A.	3	289
Wallner, S. J.	See Rahman, A. R.	3	113
Walton, G. N.	See Hittle, D. C.	2	79

<u>Author</u>	<u>Title</u>	<u>Vol</u>	<u>Page</u>
Watkins, W. R.	See White, K. O.	3	359
Weber, B. A.	See Sattler, J. P.	3	159
Weingart, R. C.	See Jackson, R. K.	2	215
Weller, W. H.	See Hammond, C. E.	2	17
Westcott, D. E.	See Rahman, A. R.	3	113
White, K. O. Watkins, W. R. Bruce, C. W.	Water Vapor Absorption Measurements Using a Line Tunable Deuterium Fluoride Laser	3	359
Wiegand, D. A.	See Gora, T.	1	455
Wilburn, J. B.	Estimates of Climatic Changes Following Volcanic Eruptions from Tree Growth Records	3	375
Wilde, A. F.	See Shuford, R. J.	3	217
Wright, H. L. Meason, J. L. Harvey, J. T.	Neutron Spectrum Measurements at the White Sands Missile Range Fast Burst Reactor (FBR)	3	391
Yeager, G. Emigh, C. Christianson, C. Foiani, D.	Automatic Height Correction Technique for Use with Weapon Location Radars	4	177
Zarwyn, B.	New Concept of Survivability Enhancement with Self-Organizing Electronic Circuits	3	397
Zegna, A.	See DeVenuto, F.	1	307
Zeto, R. J. Thornton, C. G. Hryckowian, E. Bosco, C. D.	Low Temperature Pressure - Oxidation of Silicon for Integrated Circuit Technology	3	413
Zuck, T. F.	See Bensinger, T. A. and DeVenuto, F.	1 1	53 307

## THE INVENTION AND DEVELOPMENT OF PLACER

FORREST J. AGEE, Ph.D  
HUEY A. ROBERTS, Ph.D  
HARRY DIAMOND LABORATORIES  
ADELPHI, MD 20783

INTRODUCTION.--The importance of hardening the SAFEGUARD System to EMP was established in the turbulent arguments of complexity and potential vulnerability of any ABM system during the deployment debates of the late 1960s. During the course of the considerable effort to achieve the operational Grand Forks Tactical Site, a unique problem was posed by the over 40 miles of buried conduits which formed part of the shielding for the control and power cables connected to each missile cell. Since these conduits were buried less than a skin depth deep, they constituted major receiving antennas for EMP and lightning. It was recognized that a nondestructive test technique was needed that would permit verification of the shielding provided by the conduits, initially to verify adequacy of construction, and periodically through the system life to insure that rust, freezing, or ground movement had not degraded the conduit system in such a way as to compromise the protection afforded by it. The Harry Diamond Laboratories was tasked by the SAFEGUARD Systems Command to develop such a technique. A survey of methods used by oil companies, power companies, and other users of pipelines and conduits disclosed that no technique was available which would be suitable for an EMP threat-relatable assessment. A program was initiated to proceed through several phases to identify possible approaches, to experimentally evaluate the most promising ones, and to develop and field the one most suited for inclusion in the SAFEGUARD Protection Integrity Maintenance Program (PIM). Shortly after the PIM Program began, water was discovered pouring out of some of the power and communications conduits during cable pulling at the missile fields, and a sense of urgency and increased visibility were added to the effort.

Technically, the problem was to test the shielding provided by 2- and 4-in. steel conduits containing power or control cables buried at depths from 6 to 12 ft and to determine how to measure the effects of single and multiple flaws in the conduits when exposed to EMP from a high-altitude nuclear burst. The conduits were laid in a network of conduit banks of varying cross section with as many as 35 conduits near terminal structures and eventually as few as one or two conduits at the entry points to missile launch stations. The conduits were located at five missile sites with typical conduit lengths varying from 100 to 500 ft between shielded structures (manholes, terminal structures, control buildings, and missile cells). As the conduit banks proceeded from power or control cable distribution points out into the missile fields, groups of conduits were directed away from the main conduit runs at manhole structures or at branch points in the missile fields. This situation posed a complexity in terms of conduit current sharing which had to be resolved to conduct a threat analysis. Since the conduits were buried in earth in close proximity (compared to a skin depth for wavelengths of interest for EMP) in the conduit banks, it was clear that there should be some current sharing, with outer conduits probably carrying more of the current than inner ones. What was not clear was how the sharing would go and how to account for it in relating any kind of test data to the EMP threat, which had been formulated analytically in terms of the current which would be induced on a single conductor, taking into account soil conductivity, depth of burial, and other relevant parameters. Little was known about what kind of flaws might exist in conduit systems which would be important from an EM shielding standpoint. It was apparent that a detailed knowledge of classes of probable types of flaws would be required since it was improbable that a technique would be developed which would exactly duplicate an EMP excitation. Hence, supporting analysis would require a knowledge of characteristics of flaws as a function of frequency and amplitude. To this end, a program of field and laboratory tests on conduits and types of possible flaws was undertaken at the Woodbridge Research Facility. The program began with studies of a single buried conduit and laboratory transmission-line measurements on single flaws and progressed in stages to more complicated field test models. Since the conduits were constructed by joining 10-ft lengths of steel pipe together with threaded couplings and unions, several joint-type flaws were possible, including rusted threads and loose and misaligned unions, as well as cracked, fractured, rusted, or improperly assembled conduit sections and flex-joints.



It was decided to concentrate the HDL resources on EM techniques, since these appeared to offer the greatest potential for achieving a threat-relatable assessment. Another factor was that other organizations were conducting visual inspections of the interior of the conduits by use of miniature television cameras and doing air-leak testing. Altogether, five EM techniques were tried out on the single and five conduit test models, which contained various flaws (broken conduit, rusted couplings, and the like). Two CW techniques (1,2) were evaluated through contractor efforts and three time-domain techniques were tried using HDL developed simulation equipment which was tailored to suit the conduit application. CW techniques were found to be inferior to the pulsed techniques in testing at the conduit test models, especially when multiple flaws were present in a conduit.

THE INVENTION OF PLACER.--Figure 1 shows a dual-loop version of Pulsed Loop Antenna Conduit Electromagnetic Radiator (PLACER) used during the preliminary experiments to excite a buried conduit. The loops were driven in parallel by discharging a storage capacitor across a spark gap in series with each loop terminated in 40 ohms. Thus PLACER was simply a pulse-driven series LRC circuit. The initial experiments were conducted using a test model which consisted of a 2-1/2-in. ID conduit, 100 ft long, which was buried at a depth of 3 ft. One end of the conduit was secured to a shielded instrumentation box, while the other end was sealed with a threaded end cap. Both ends of the conduit were grounded using 4-ft-long ground rods driven into the earth. Conduit current was measured by using a clamp-on type of current probe. Inside the conduit, a cable (sense wire) extended the entire length of the conduit and was terminated in the characteristic impedance of the conduit-sense-wire transmission line. Current which was coupled onto the sense-wire at the conduit flaw was monitored inside the shielded enclosure by using an oscilloscope and a camera. The oscilloscope was powered by a storage battery and inverter.

In order to couple current onto the conduit, PLACER was positioned about 1 ft aboveground and parallel to the ground. When the center of the loop was directly over the buried conduit, the conduit current was zero, and the current was observed to reverse polarity as the loop was moved in a perpendicular direction across the conduit. In this manner, it was possible to locate the buried conduit very precisely by observing the nulling effect in the conduit current or in the sense-wire current when a conduit flaw was present. The optimum range for coupling the maximum current onto the conduit was 5 ft between the center of the loop and the point

directly above the conduit opposite PLACER. Figure 2 shows the waveform of the conduit current which was measured opposite PLACER when it was positioned 5 ft from the conduit. The breakdown voltage was 85 kV.

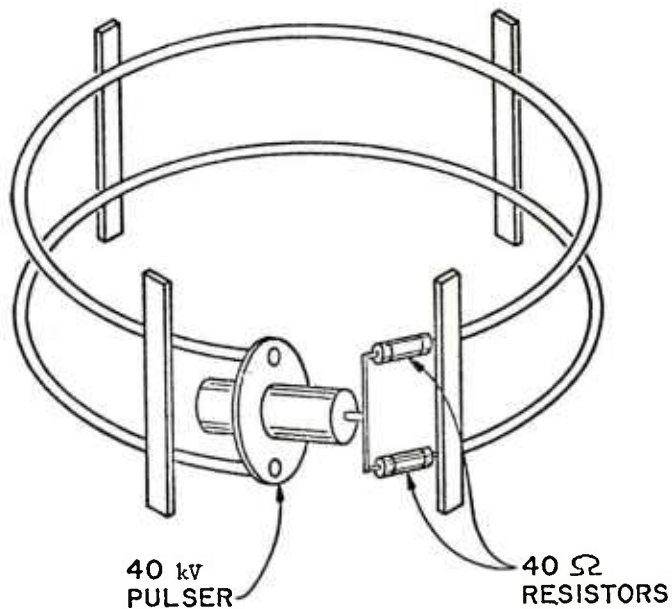


Figure 1. Experimental Dual-Loop Version of PLACER.

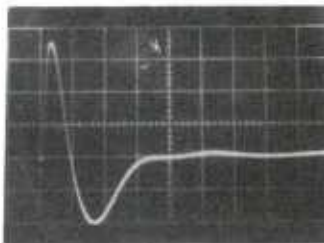


Figure 2. Conduit Current Waveform, 26.6 A/div, 500 ns/div.

During the course of the preliminary experiments, several spark gap pulsers were used to drive the 9-ft-diameter, two-turn parallel loop antenna. The pulser breakdown voltage and storage capacitance were varied to determine their influence on the current coupled onto the buried conduit. The peak conduit current increased linearly as the breakdown voltage was varied from 20 to 100 kV; however, the conduit current waveform was not significantly different for a storage capacitance of 5nF, 0.3  $\mu$ F or 1 $\mu$ F. Hence, the waveform was determined primarily by the loop diameter and the combined 20-ohm load resistance used throughout the experiments.

Figure 3 shows a cutaway view of the experimental arrangement for the preliminary evaluation of the PLACER technique for locating conduit flaws, using the single buried conduit. The conduit fault was a 5-in. transverse slot introduced into the conduit. The sense wire was lying inside the 2-1/2-in. ID conduit opposite the upward turned slot. The variation of the peak conduit current with perpendicular range from the conduit is shown in figure 4. With PLACER positioned at the optimum distance of 5 ft from the conduit, PLACER was moved parallel to the conduit. The peak conduit current for the parallel sweep along the conduit is shown in figure 5. A similar plot of the peak sense-wire current resulting from the transverse slot is shown in figure 6. The strong peaking effect shown in figures 5 and 6 resulted from the combined effects of the localized excitation from the loop antenna and the attenuation of the current pulses as they propagated down the conduit, which was surrounded by the lossy earth medium. The more pronounced peaking effect in the sense-wire current resulted from the fact that the slot preferentially coupled higher frequency current onto the sense wire. When a rusted coupling was introduced as the conduit flaw, the peaking effect and the waveform of conduit and sense-wire currents were similar (data not shown).

SAFEGUARD SYSTEM DEVELOPMENTAL TESTING.--In October 1973 a significant opportunity was exploited to test the feasibility of the three best approaches at one of the Sprint Launch Sites (RSL 1) as an added effort in an EMP test. This test also provided a vehicle to resolve the current sharing problem. In support of a Corps of Engineers program to evaluate the hardening provided by the site construction, HDL developed a portable 250 kV biconic-dipole repetitively pulsed simulator (fig. 7) which could be suspended from a crane. The test plan was expanded to include digging two shafts so that conduit current measurements could be made during the EMP testing on a bank containing 20 conduits. In addition, it was possible to arrange for clamp-around current probes to be attached to conduits at the Missile Site Radar (MSR)

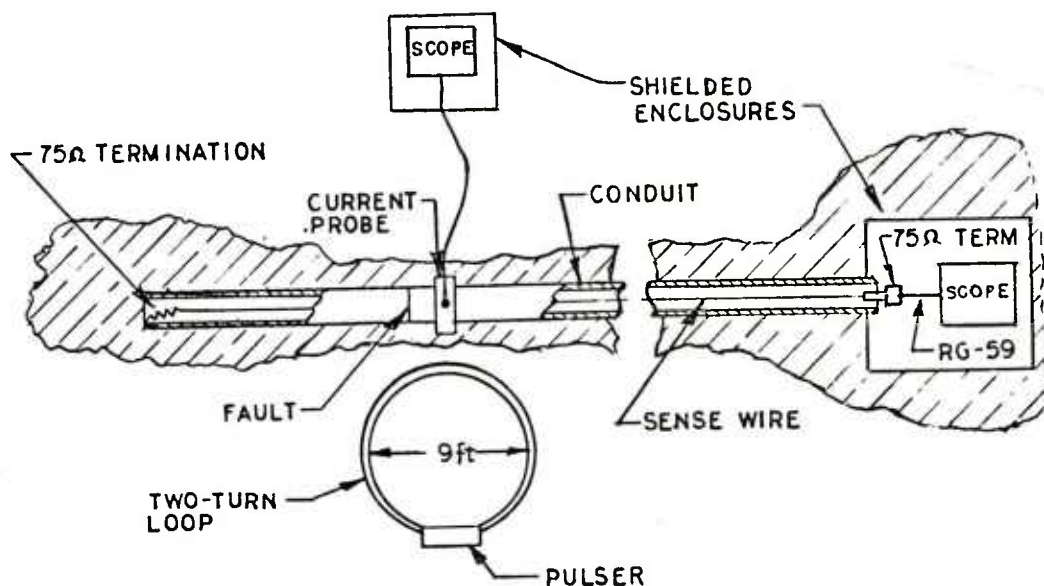


Figure 3. Cutaway View of Single Buried Conduit Test Model.

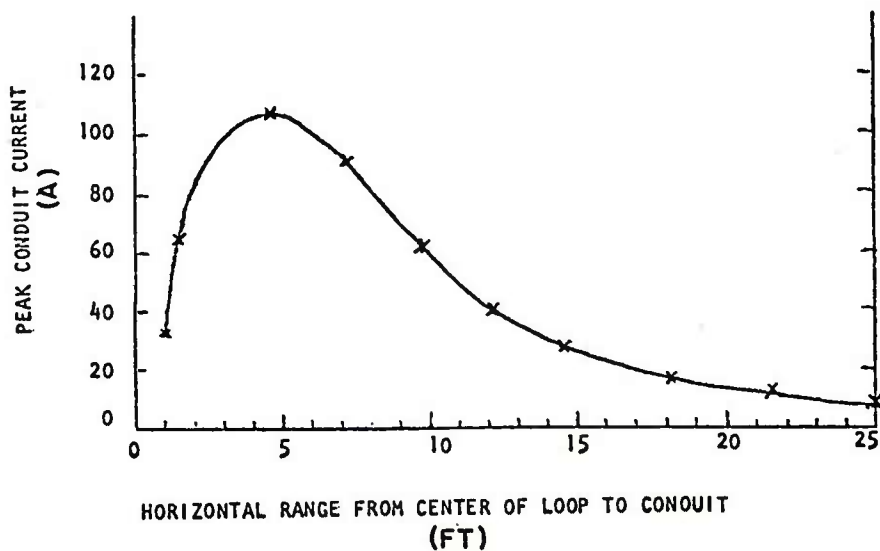


Figure 4. Peak Conduit Current Variation With Range from 85-kV PLACER.

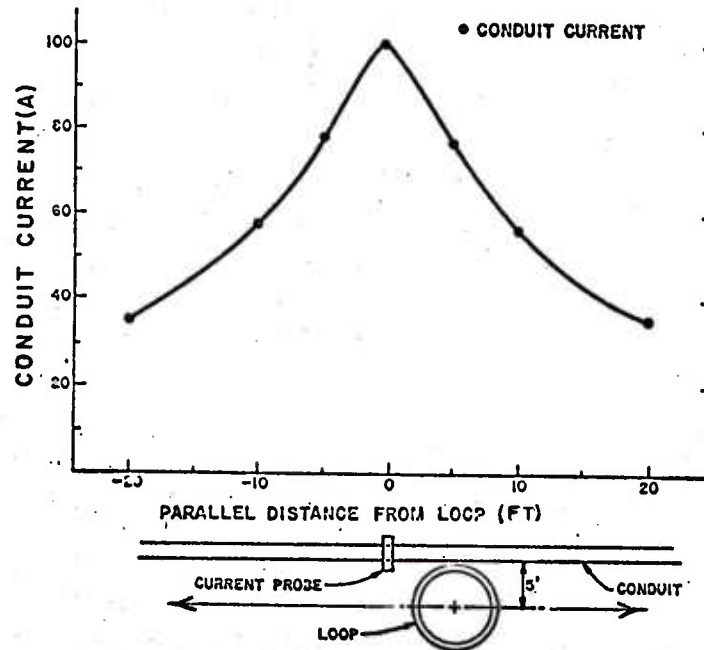


Figure 5. Peak Conduit Current for Parallel Sweep at Range of 5 ft.

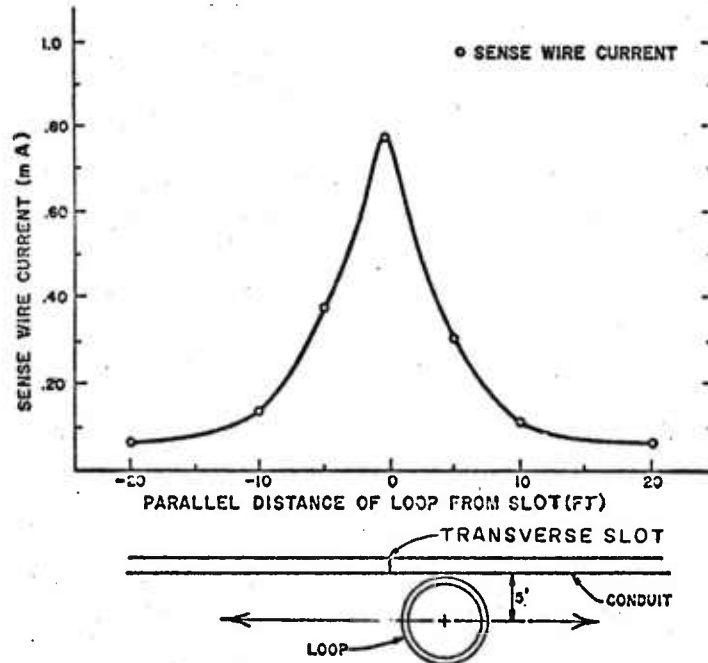


Figure 6. Peak Sense Wire Current for Parallel Sweep at Range of 5 ft.



Collocated Missile Field so that PIM experimentation and calibration could be conducted there as well as at the RSL 1 test site. The tests were made possible by the expedited development of 5-in. window Stoddart current probes which were sized to fit in the conduit banks.

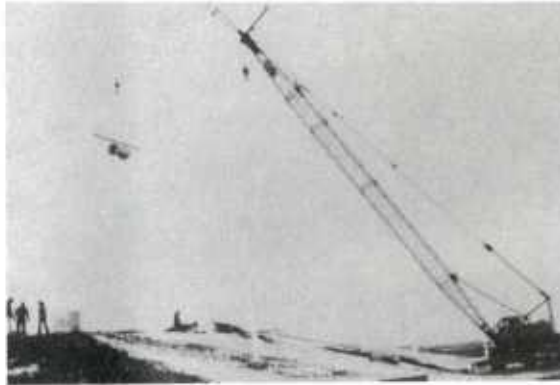


Figure 7. 250-kV Bicone-Dipole EMP Simulator at RSL 1.

The conduit testing at RSL 1 consisted of conduit current measurements with the conduits excited by the bicone-dipole simulator (fig. 7) and by the 85-kV version of PLACER (fig. 1). The conduit current measurements indicated that both the EMP simulator and the pulsed loop exhibited similar conduit current distributions among the conduits in the bank and that the greatest current in both cases appeared on corner conduits, with outer conduits having the effect of shielding inner ones, as expected. Subsequent measurements on a single buried conduit in the vicinity of a missile cell showed that the current on a top corner conduit in a bank was 25 percent of that induced on a single buried conduit. These data provided the scaling needed to relate test calibration data taken on a top corner conduit to the single buried conduit analytical threat current, as well as providing a direct accounting for conduit current sharing. The testing at RSL 1 also provided a bonus which was to be significant to the program. The conduit illumination by the EMP simulator was being monitored by measurements of current induced on Launch Enable and Status Order (LE and SO) cables inside the Remote Launch Operations Buildings (RLOB). It was discovered that relatively large currents were coupled onto the cables inside the conduit leading to Sprint Cell 8. This discovery did not correlate with the results of earlier air-leak



testing, which had not identified a major air leak in this conduit but had indicated only a minor one near the RLOB. This provided an opportunity to demonstrate PLACER flaw location technique in situ in a missile field; however, there were several difficulties which had to be overcome.

The construction and equipment installation activities underway at the time precluded EMP test operations except at night at RSL 1. The PIM activities constituted therefore an added effort to an already time-constrained test schedule, and the presence of additional current and field pulses from the loop could conceivably interfere with the principal test objectives. Consequently, the PLACER testing had to be conducted on a noninterference basis with the EMP test. The early experimental version of PLACER was then configured so that it had to be taken apart to be moved. This problem was overcome by constructing a crude sled of plywood and two-by-fours and by tying the pulser and antennas to the sled. The weather during the testing was seasonal for October and November in North Dakota. The 20-knot winds and near zero temperatures combined with the snow had been a hindrance up until this point. However, the snow and ice made it somewhat easier to drag the sled alongside the locus of the conduit bank. The major flaw was located very near the missile cell, and a minor flaw was also located near the RLOB. The PLACER technique described earlier caused a current nulling when the antenna was directly over a conduit and a reversal when it was moved to the opposite side of the conduit. This property was used to verify that the flaw was in the conduit itself rather than a shielding deficiency in the missile cell.

The supplementary testing at the MSR Collocated Missile Field verified that three pulsed techniques (the pulsed transmission line, the pulsed dipole (3) and PLACER) were capable of driving adequate currents on conduits for testing and further verified the test calibration approach which was adopted. The unique ability of PLACER to locate flaws as well as to indicate their presence and magnitude led to further development of PLACER as the test technique for both the initial assessment and subsequent PIM testing of the missile field conduits.

THREAT ANALYSIS.--While the PLACER technique is adequate for detecting and locating conduit flaws, it does not simulate a nuclear EMP environment. The frequency content of PLACER induced conduit current is limited by the loop dimension, while the current amplitude is determined by the breakdown voltage of the spark gap. Therefore, a threat-relatable conduit assessment using the PLACER

requires additional and complementary information concerning the characteristics of conduit flaws and propagation of currents within the conduit system.

The current induced on an interior cable at the site of a conduit flaw can be described in terms of a flaw impedance ( a characteristic of the flaw), the current on the outer surface of the conduit, and the characteristic impedance of the conduit-cable transmission line. In the frequency domain, these quantities are related by

$$(1) \quad I_O(w) = \frac{I_C(w) Z_F(w)}{2Z_O + Z_F(w)}$$

where  $w$  is the angular frequency,  $I_O(w)$  is the induced current,  $I_C(w)$  is the conduit current,  $Z_F(w)$  is the flaw impedance, and  $Z_O$  is the characteristic impedance of the conduit-cable line. The total cable current at any point  $y$  in the conduit system can then be expressed as

$$(2) \quad I_S(w,y) = I_O(w) H(w,y)$$

where  $H(w,y)$  is the Fourier transform of the system response to a unit impulse current. The system function  $H(w,y)$  is completely determined by the transmission-line characteristics and load impedance of the conduit-cable line. For most cable configurations at SAFEGUARD,  $H(w,y)$  is derivable from simple transmission-line considerations. In other cases of interest, the impulse response can be determined by observing the PLACER induced cable current at selected points along the cable route. Considering the length of the cables (500 to 1500 ft), the PLACER induced conduit current (and hence induced cable current) approximates an impulse (4).

Equation (2) can be readily transformed to express the total cable current as a function of time. The calculated cable current can then be compared with the current levels which cause upset or damage to the system. These current levels have been determined by the weapons system contractors (5,6).

In most cases,  $Z_F$  is much less than  $Z_O$ . When it is not, the cable current becomes comparable to the conduit current, in which case the conduit should be repaired. For the special case of a completely broken conduit,  $Z_F$  is infinite, and equation (1) becomes  $I_O(w) = I_C(w)$ .

Equation (1) can be rewritten for the case  $I_o \ll I_c$  (small flaws):

$$(3) \quad Z_F(w) = \frac{2Z_o I_o(w)}{I_c(w)}, \text{ or } \frac{Z_F(w)}{2Z_o} = \frac{I_o(w)}{I_c(w)}.$$

Therefore, in order to characterize each type of conduit flaw, it is sufficient to measure  $I_o(w)/I_c(w)$  over the appropriate frequency range. A study of the conduit flow characteristics was conducted in the laboratory (4). These experiments used current injection techniques to couple current onto the outer surface of a short section of conduit into which flaws were introduced one at a time. The conduit contained a sense wire terminated at both ends in the characteristic impedance (100 ohms) of the conduit-sense-wire transmission line. The ratio of the sense-wire current to conduit current was monitored as a function of both time and frequency to measure the transfer characteristics of apertures, rusted couplings and unions, and thin flexible sections of conduit (flex-joints). The coupling through apertures was observed by first increasing the length of a 0.040-in.-wide transverse slot in the conduit from 1 to 5 in. and then increasing the slot width from 0.040 to 2 in. The coupling through rusted connectors was investigated at currents both below and above the threshold currents required to produce arcing across the rusted surfaces. It was considered necessary to investigate nonlinear effects, such as arcing, because the field tests using PLACER are conducted at currents far below the threat-level currents which could cause arcing.

Based on the laboratory studies, the following general statements can be made concerning the coupling of EMP induced currents through conduit flaws:

1) Below 10KHz, the thin-wall flex-joints provide roughly 100 dB of shielding and with increasing frequency the shielding improves considerably. The low frequency shielding is directly proportioned to the wall thickness of the flex-joint.

2) Coupling through apertures increases linearly with frequency. The magnitude of the coupled current (although quite small in the EMP frequency range) is proportional to the third power of the circumferential length and to the first power of the longitudinal length.

3) A properly installed clean coupling or union provides more than 140 dB of shielding. However, if the joint is rusted or dirty so that no metal-to-metal contact is provided, and if arcing does not occur, then the resulting flaw impedance (which can be very

large in the case of rust) is predominantly resistive. In this case, the induced sense-wire current waveform is nearly identical to the exciting conduit waveform. When the conduit current is sufficient to induce arcing, the ratio of the sense-wire current to conduit current is reduced, although the two current waveforms in this case are quite dissimilar. Thus, the onset of arcing functions as a protecting mechanism by reducing the flaw impedance. Although most of the rusted joints studied were observed to arc, the experimental results indicate that it ~~is~~ not possible to predict a threshold conduit current at which arcing will begin.

4) In performing a threat-related analysis using PLACER test data, the visual inspection of the data identifies the flaw as being either an aperture flaw or a joint-type flaw, and the amplitude of the PLACER data fixes its magnitude over the frequency range of the PLACER test data. This amplitude coupled with the frequency dependence common to the class of flaw provides the frequency-dependent flaw impedance for a convolution integration with the threat conduit current. For a joint-type flaw, this frequency dependence is

$$(4) \quad Z_F = \text{Constant}$$

For an aperture flaw, the frequency dependence is

$$(5) \quad Z_F = k i w ,$$

where  $k$  is a constant and  $i$  is  $\sqrt{-1}$ . The frequency dependence of a flex-joint is also known (4). However, the likelihood of detecting one exhibiting the referenced frequency dependence is remote, even in the extreme case of corrosion, since apertures would appear long before the wall thickness would become thin enough to produce a measurable flaw. Corroded flex-joints would therefore first appear as aperture flaws. The conclusion of the testing of the various types of flaws was that only circumferential joint-type flaws were important (e.g. broken conduit, rusted couplings, or other flaws which introduce a significant flaw impedance into a conduit), and for these, the flaw impedance is a constant over the frequency range of interest.

THE FIELDIED PIM TEST USING PLACER.--The testing was conducted in two phases using PLACER in a 30kV cart-mounted single-loop configuration with an on-board power supply powered by a small 12-V battery. In the first phase, the PLACER unit (fig. 8) was pulled along both sides of the conduit bank at a range of 9 ft between the center of the loop and the center of the conduit bank. The cables inside each conduit (power or LE and SO) were monitored using a



clamp-around current probe at the cable entry point to the RLOB or at a manhole. A current probe was connected to a voltage pulse level detector. The level detector was adjusted to give an alarm if current pulses above a predetermined sure-safe level were induced on the cable as PLACER was moved along the conduit bank. When a signal was detected above the threshold level, the location was noted and marked for subsequent flaw location. The second phase of testing consisted of precision flaw location in which PLACER was moved in a prescribed fashion (7) in the vicinity of the location where the flaw was detected, and measurements were made as a function of loop position by using an oscilloscope (fig. 9). Following the testing of all of the conduits at the missile fields (8), a threat analysis was performed (4), and those flaws which posed a potential threat to the system were excavated and repaired. The PLACER was then used again during repair operations (fig. 10) to verify adequate repair.



Figure 8. (Left)  
PLACER Flaw Detection  
at RSL Site.

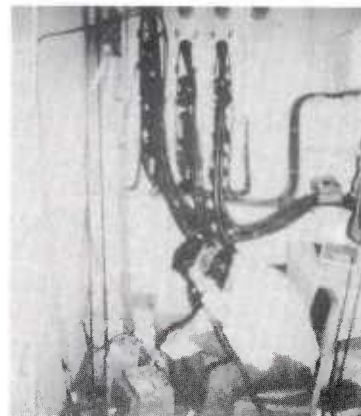


Figure 9. (Right)  
Instrumentation for Flaw  
Location at RSL Site.



Figure 10. PLACER Conduit Repair Verification at MSR Site.

CONCLUSIONS.--The development of PLACER has provided the Army with a means for testing the shielding of buried conduits in hardened facilities for ABM or other systems. In the broader sense, the experience gained during the construction of the buried test models at Woodbridge and in the repairs at Grand Forks has provided an experiential base for constructing better conduit systems in future applications.

It was learned that it is relatively easy to join 2-in. conduits which were used for most of the power conduits in the SAFEGUARD site; consequently, there were relatively few problems in the power conduit system. One notable exception was a severe flaw which was the result of not joining the conduit at all at a point where a field-constructed nipple proved shorter than a gap which was simply taped over, rather than cutting a section that would fit to join the two sections together. The 4-in. conduits were a different matter. It was observed at Woodbridge that joining the sections together to a prescribed torque did not in itself insure that many threads would be engaged, unless someone relieved the moment by supporting the end of the conduit sections while they were being torqued tightly. Professional electricians employed by the contractor to assemble the 16-conduit test model did not achieve tight joints until they were coached in proper assembly. The explosive type of unions used in the construction of the conduits leaked water even when installed properly, but these unions were not necessarily any more likely than a coupling to induce an EM flaw.



The data developed during air-leak testing and conduit interior TV inspections were not correlatable with EM flaws. The latter proved to be of some aid as a supplement to PLACER testing to give precise locations of joints along the conduit run; however, it was not possible to detect shielding flaws by inspection.

The flaw characterization studies indicated that it would be best to weld the conduits to the couplings and unions in at least one spot to preclude possible joint-type flaws. A repair technique for joint-type flaws consisted of a sheet-metal clamshell formed to fit over a union or coupling. This repair was found to work well in eliminating shielding flaws when clamped to the bare conduit on each side with a liberal coating of conductive paste to insure good contact. Based upon the lessons learned and the PLACER technique, it is now possible to insure adequate conduit shielding effectiveness in mission critical conduits.

Although PLACER was developed for an EMP application, it should provide a solution to a wider class of shielding and nondestructive test applications for which shielding of buried conductors is desirable for reasons of security or protection from other EM threats.

#### REFERENCES

1. "CW Flaw Detection in Buried Conduits," EG&G Report AL-1020 (7 December 1973).
2. "Conduit Electrical Leak Detection Feasibility Test," McDonnell Douglas Report MDC G5061 (December 1973).
3. H. A. Roberts, E. Seijo, F. J. Agee, "EMP Testing of Buried Conduits, the Pulsed Dipole and Pulsed Transmission Line," Harry Diamond Laboratories TM-75-12 (September 1975).
4. H. A. Roberts, J. Capobianco, and F. J. Agee, "SAFEGUARD Buried Conduit Studies," Harry Diamond Laboratories TR (To be published).
5. "Ground Electromagnetic Pulse Effects, Phase IV Program Summary," Martin Marietta Report OR 316, Vol. I and II (April 1974).
6. "Spartan Launch Preparation Equipment Set Electromagnetic Pulse Susceptibility Analysis and Test Report, Phase IV," McDonnell Douglas Report MDC G5114 (February 1974).
7. "SAFEGUARD Protection Integrity Maintenance (PIM) Test Procedures for Buried Conduits," Harry Diamond Laboratories SR-75-1 through SR-75-5 (February 1975).
8. "SAFEGUARD Protection Integrity Maintenance (PIM) Conduit Test Data," Harry Diamond Laboratories BDM/W-75-258-TR (29 August 1975).



## PROJECTILE AND FRAGMENT PENETRATION IN SNOW AND FROZEN SOIL

George W. Aitken, George K. Swinzow, Ph.D. and Dennis R. Farrell  
U.S. Army Cold Regions Research and Engineering Laboratory  
Hanover, N.H. 03755

INTRODUCTION: The work described herein was accomplished as part of an investigation of terminal ballistics in snow, ice and frozen soil conducted for the Field Engineering Division, Directorate of Facilities Engineering, OCE. The objectives of this investigation are to develop design criteria for effective utilization of indigenous cold regions materials in field fortifications, to develop methods for estimating the terminal effectiveness of remotely emplaced munitions and sensor systems, and to evaluate foreign expertise in these areas. To accomplish these objectives, a number of laboratory and field investigations have been conducted to quantify the effectiveness of various projectiles fired into snow, ice and frozen soil targets. The performance of fragment-simulating projectiles (FSP's) that simulate typical fragments from mortar and rocket rounds have also been studied. Penetration data from these tests were analyzed using a theory developed for use with unfrozen soil targets and were found to be in reasonable agreement with predicted penetrations in both snow and frozen soil.

BALLISTIC TEST LABORATORY: The laboratory penetration tests were conducted in the CRREL ballistics laboratory in Hanover, N.H. The laboratory was constructed to permit investigation of terminal ballistics in snow, ice and frozen soil. It consists of a 16 x 28-ft wood frame building containing a controlled temperature target room, a weapons room, and instrumentation and projectile preparation areas (Fig. 1). A detailed description of this facility was presented by Farrell (1975).

TEST SOIL DESCRIPTION: Four different soils were used in the laboratory tests: a sand, a sandy clay, a marine clay and a silt. The first three matched, as closely as practicable, unfrozen soils tested by the U. S. Army Engineer Waterways Experiment Station (USAEWES). Because the strengths of these frozen soils were estimated, only an approximate correlation between measured and predicted penetrations was obtained. The silt soil was added to the program because a relatively large quantity of soil was needed to develop the comprehensive data package necessary to correlate measured with predicted penetrations and this soil was available locally in sufficient amounts.

TARGET PREPARATION: The soil samples were molded in 12-in.-square, 12-in.-high boxes constructed of 3/4-in.-thick plywood. The boxes were lined with polyethylene to minimize loss of moisture. The samples were compacted in 1-in.-thick layers using approximately 40 blows from a 10-lb hammer with an 18-in. drop height. The soil was tempered overnight at 40°F prior to molding. After each layer was molded, the sample was placed in a coldroom at -5°F for freezing. This one-layer-at-a-time preparation method minimized moisture migration during freezing of the test specimens.

The snow targets were prepared by sifting snow through a no. 4 sieve into 20-in.-square, 12-in.-high plywood boxes. The snow sintered in these boxes quite quickly, allowing the ends of the boxes to be removed and a sufficient number of boxes aligned to assure projectile retention in the snow.

PROJECTILES: Two different projectiles were used to obtain laboratory data: 5.56-mm cubes and 7.62-mm NATO ball ammunition (Fig. 2). The cubes were designed as fragment-simulating projectiles, as described by Kakel (1971), while the 7.62-mm round represents approximately the mid-energy level for small arms projectiles.

PENETRATION TEST RESULTS: Impact velocity vs penetration data for the 5.56-mm steel FSP's fired into Hanover silt are given in Figure 3. These data show that penetration into the frozen silt was roughly half that into the unfrozen soil. Small temperature changes of the frozen soil had a relatively small influence on penetration; but reducing the temperature from -3 to -25°C noticeably reduced penetration.

At velocities above about 700 m/sec deformation of the FSP's was noted in both the frozen and unfrozen silt (Fig. 4). The decrease in penetration obtained in the frozen soil at the higher velocities is attributed to the increase in frontal area of the projectile that resulted from this deformation. The magnitude of this area change is shown by the data in Figure 5 where a coefficient of deformation,  $C_D$

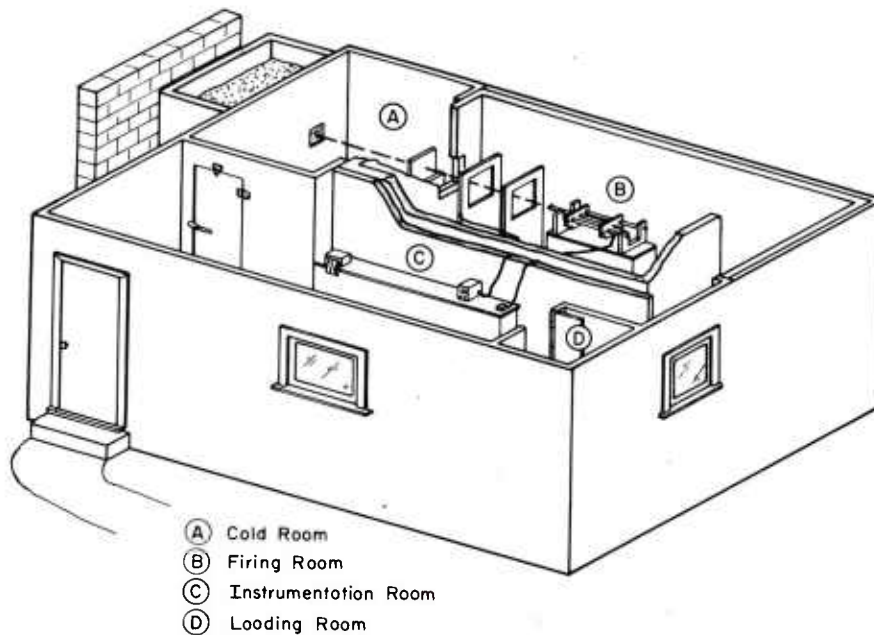
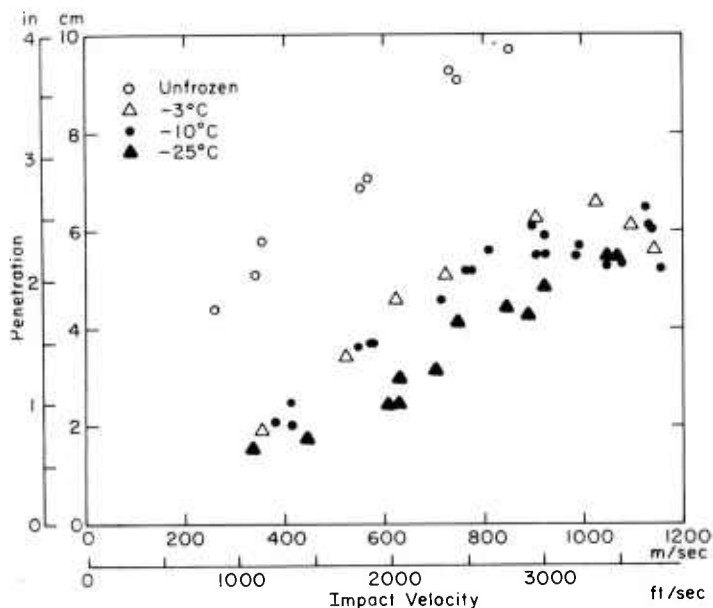


Figure 1. CRREL terminal ballistics facility (TBF).



Figure 2. Projectiles used in ballistic test program.



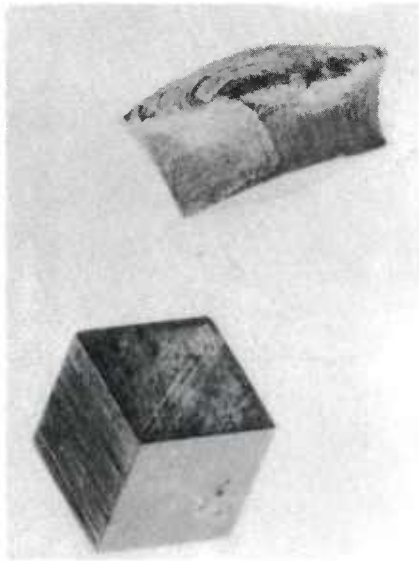


Figure 4. Deformed 5.56-mm steel cube.

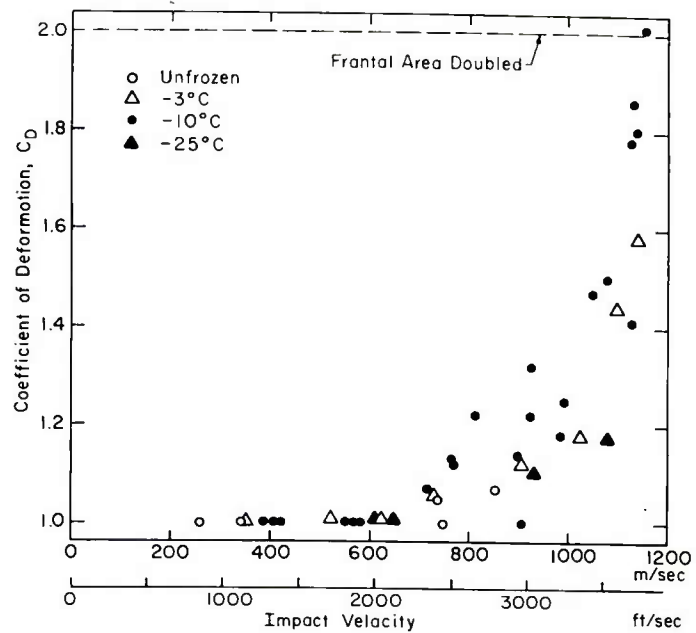


Figure 5. Deformation coefficient vs impact velocity for 5.56-mm steel cube fragment simulating projectiles in Hanover silt.

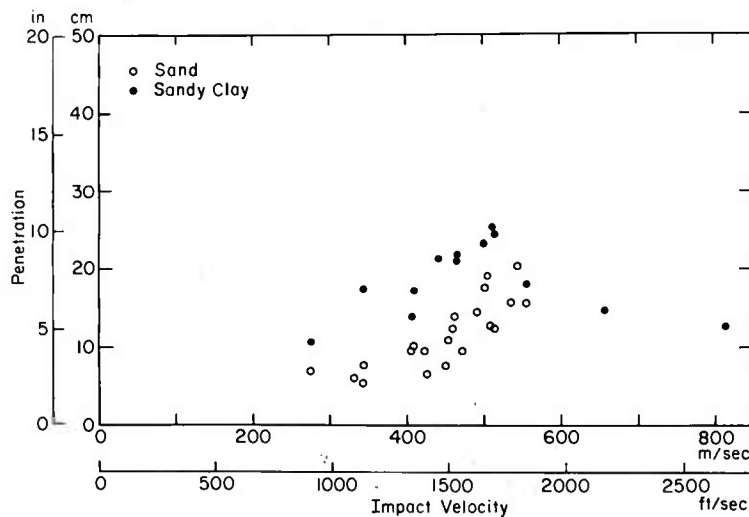


Figure 6. Impact velocity vs penetration for 7.62-mm NATO ball ammunition fired into frozen soil targets at  $-10^{\circ}\text{C}$ .



(deformed FSP frontal area divided by original area), is plotted versus impact velocity. For a given impact velocity, the temperature of the frozen soil appears to have a strong influence on the magnitude of projectile deformation.

Figure 6 contains velocity vs penetration data for 7.62-mm NATO ball ammunition fired into frozen sand and sandy clay soils. These tests, conducted at a temperature of  $-10^{\circ}\text{C}$  and for a given impact velocity, show significantly higher penetrations for this projectile than were previously observed for the FSP's into frozen silt. It is suggested that this increased penetration results from the higher energy of the 7.62-mm projectile due to its increased mass, rather than a difference in soil target properties. At velocities higher than about 600 m/sec the jackets of many 7.62-mm projectiles failed. Several of these rounds were also observed to tumble at impact velocities between 570 and 730 m/sec. This tumbling resulted in significantly reduced penetrations as shown in Figure 7.

Typical impact velocity vs penetration data for FSP's into snow are given in Figure 8. Compared to similar data in frozen silt (Fig. 3) penetration of these FSP's in snow appears to be relatively insensitive to impact velocity. The data also indicate that snow temperature does not affect projectile penetration. As with soil, projectile deformation is suggested as a factor influencing penetration into snow at velocities above about 800 m/sec.

PENETRATION PREDICTION TECHNIQUES: There are two methods frequently used to analyze projectile penetration data. One of the most widely accepted, described by Young (1972), utilizes penetration test results to prepare empirical equations relating impact velocity to penetration depth. Young's equations contain a projectile nose-shape factor and represent target properties with a soil constant ranging from 0.2 to 50. These equations have been verified for projectile weights from 0.9 to 2613 kg and impact velocities from 33 to 843 m/sec. Equation 1 was proposed by Young for impact velocities greater than 66 m/sec and produces a linear relationship between penetration and impact velocity:

$$D = 0.0117 \text{ KSN } \sqrt{W/A} \quad (V-30.5) \quad (1)$$

where

D = depth of penetration, m

K = mass scaling factor, dimensionless

S = soil constant, dimensionless (1 to 2 for frozen silt or clay)

N = nose performance coefficient, dimensionless (0.56 for flat nose)

W = projectile weight, kg

A = projectile area, cm<sup>2</sup>

V = velocity, m/sec

This approach has the advantages of relative mathematical simplicity together with the inclusion of a projectile nose-shape factor. It has also been adapted for predicting penetrations through layered materials. Its primary disadvantages are that penetration tests must be conducted on all target materials of interest to develop appropriate material constants and that a mass scaling factor must be determined for projectiles weighing less than 27 kg.

Another common approach to penetration analysis is to develop a mathematical model for predicting penetration that considers pertinent projectile characteristics and target strength properties.

One such model, based on dynamic cavity expansion theory, was developed by Ross and Hanagud (1969). It was used by Rohani (1973) to analyze penetration data from unfrozen soils. This model, equation 2, describes a spherical nose projectile penetrating a homogeneous isotropic material. The projectile is further characterized by its weight and radius. The target material is idealized as a locked-elastic, locked-plastic medium (Fig. 9) and described in terms of its mass density, yield strength, plastic and elastic moduli and compressibility.

$$P = \frac{3W}{4Ag \rho_P B_2} + \frac{B_1 R}{2 B_2} \ln \left( 1 + \frac{2B_2 \rho_P V^2}{3B_3} \right) \quad (2)$$

where

V = velocity, ft/sec

P = penetration, ft

W = projectile weight, lb

A = projectile area, ft<sup>2</sup>

g = acceleration of gravity, ft/sec<sup>2</sup>

R = projectile radius, ft

$\rho_P$  = locked plastic density of target material, slugs/ft<sup>3</sup>

and

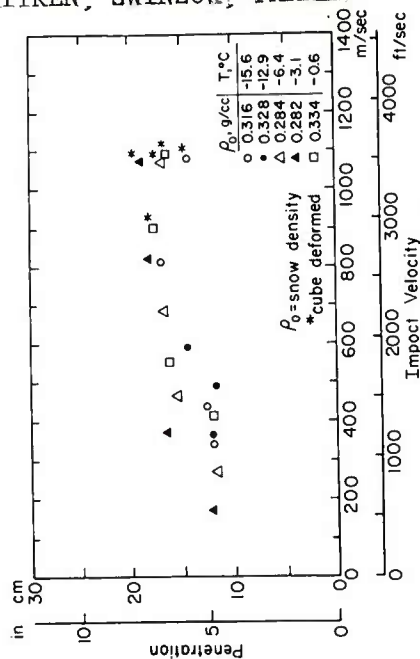


Figure 8. Impact velocity vs penetration for 5.56-mm aluminum cubes fired into snow.

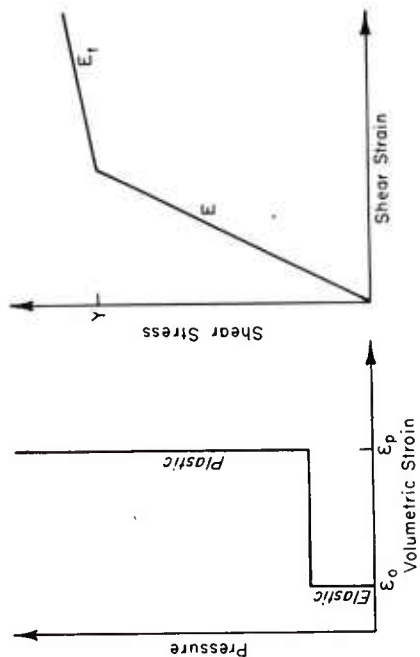


Figure 9. Idealized stress strain curves.



Figure 7. 7.62-mm projectile penetration into sandy clay at  $-8^{\circ}\text{C}$  and 16% water content. Impact velocity of top projectile that tumbled was 621 m/sec, penetration was 21.5 cm. Velocity of bottom projectile was 380 m/sec, penetration was 27.5 cm.

$$\rho_P = \rho_0 \exp(\Sigma_P) \quad (3)$$

where

$\rho_0$  = initial density of target material, slugs/ft<sup>3</sup>

$\Sigma_P$  = plastic volumetric strain, %

and

$$B = \frac{y}{2E} - \frac{\Sigma_i}{3} \quad (4)$$

where

y = yield strength of target material, psf

E = Young's modulus of target material, psf

$\Sigma_i$  = elastic volumetric strain, %

$$\alpha_P = 1 - \frac{\rho_0}{\rho_P} \quad (5)$$

$$\delta = \alpha_P \exp(-3B) \quad (6)$$

$$B_1 = 1 - \delta^{1/3} \quad (7)$$

$$B_2 = 3/2 - (1 + \alpha_P) \delta^{1/3} + 1/2 \delta^{4/3} \quad (8)$$

$$B_3 = 4/9E (1 - \exp(-3B) - 2/3 y \ln \delta + 2/27 \pi^2 E_t - 4/9 E_t \eta) \quad (9)$$

where

$E_t$  = plastic modulus of deformation, psf

and

$$\eta = \sum_{n=1}^{\infty} \frac{\delta^n}{n^2} \quad (10)$$

The advantage of this method is that it does not require any empirical constants. Its disadvantages are: that the target yield strength is assumed to be independent of projectile velocity and penetration depth; projectile mass and/or caliber area change during penetration are not accounted for; and it is strictly applicable only to projectiles with a spherical nose-shape. Rigorous use of this approach also requires that the constitutive properties of the target material be obtained at

strain rates equal to those occurring under actual projectile penetration.

TARGET STRENGTH DATA: Frozen soil strength data were obtained from unconfined compression tests. These tests were conducted at a strain rate of 4444%/min on 1.4-in.-diam, 4.5-in.-high cylindrical samples. The samples were compacted in 1-in. layers using 60 blows of a Harvard miniature compactor per layer (40-lb spring with 1/2-in.-diam compaction head). After compaction the specimens were tempered at 33°F for one week to assure uniform moisture distribution and then placed in a 5°F cold chamber for freezing. Ends of the samples were squared by lapping prior to testing.

Typical stress/strain curves from these tests are shown in Figure 10. The yield strength, elastic and plastic moduli were obtained by fitting idealized curves (dashed lines on Fig. 10) of the form shown in Figure 9 to these stress/strain curves. The compressibility was estimated by assuming that the volumetric strain  $\epsilon_p$  is equivalent to the volume of air in the soil sample. Data obtained from the compression tests on Hanover silt are summarized below.

<u>Temp, °C</u>	<u><math>\rho_o</math>, slugs/ft<sup>3</sup></u>	<u>E, psf</u>	<u>Y, psf</u>
-3	3.7	17.6x10 <sup>6</sup>	29.8x10 <sup>4</sup>
-10	3.7	30.9x10 <sup>6</sup>	46.3x10 <sup>4</sup>
-25	3.7	57.6x10 <sup>6</sup>	86.4x10 <sup>4</sup>

Snow strength properties were obtained by relating the snow targets' density to yield strength, compressibility and elastic modulus using information presented by Mellor (1964). Typical values are tabulated below.

<u><math>\rho_o</math>, slugs/ft<sup>3</sup> (g/cc)</u>	<u>E, psf</u>	<u>Y, psf</u>
0.58 (0.3)	4.3x10 <sup>6</sup>	0.14x10 <sup>4</sup>
0.78 (0.4)	13.2x10 <sup>6</sup>	0.22x10 <sup>4</sup>
0.97 (0.5)	20.7x10 <sup>6</sup>	2.16x10 <sup>4</sup>

COMPARISON OF MEASURED WITH PREDICTED PENETRATION: Predicted penetration of the 5.56-mm FSP's into frozen silt, computed using Equation 2, is compared with test results in Figure 11. There appears to be a tendency to underpredict penetration at velocities between 600 and 1000 m/sec. This could have resulted, in part, from differences in soil properties between the ballistic targets and the unconfined compression test specimens. The average dry unit weight of the soil

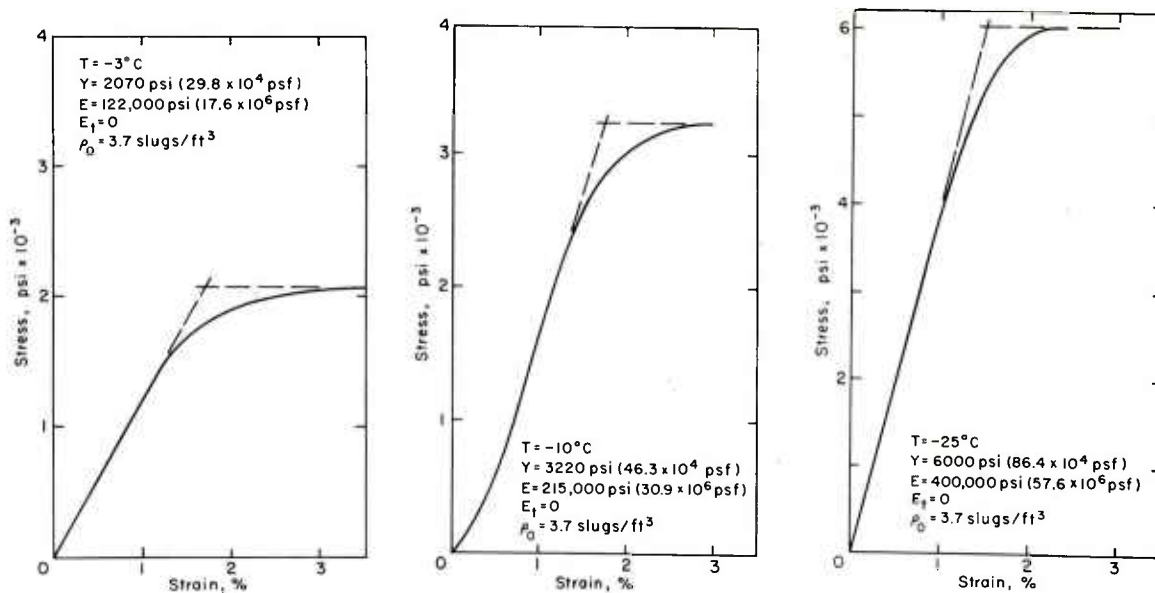


Figure 10. Stress vs strain curves from unconfined uniaxial compression tests on frozen Hanover silt.

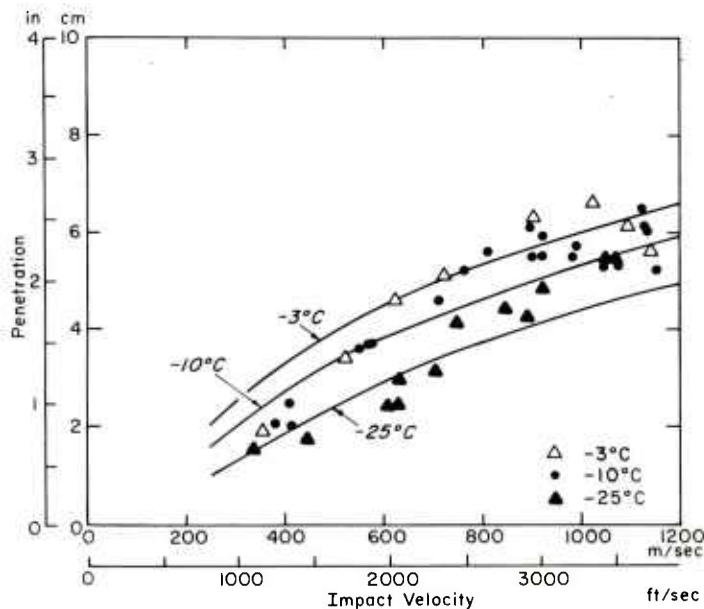


Figure 11. Comparison of test data with predicted penetration curves for 5.56-mm steel cubes into Hanover silt.



targets was about  $10 \text{ lb/ft}^3$  ( $0.31 \text{ slug/ft}^3$ ) less than that of the unconfined test samples. This lower soil target density resulted because the size and shape of available soil compaction equipment was not compatible with the size and shape of the target samples. The penetration computations were thus made using parameters biased on the high strength/low penetration side which should result in measured penetrations being somewhat larger than predicted.

A similar comparison between measured and predicted penetration in snow is presented in Figure 12. These computed penetrations are in excellent agreement with the test data. These data are of particular importance because they show the effect of projectile mass and verify that mass is correctly represented in Equation 2.

FIELD TEST PROGRAM: A field test program was conducted in Alaska to expand the scope of the laboratory experiments. A complete description of this program was presented by Johnson (1975). The program included extensive tests to evaluate the ability of snow structures to resist penetration by 5.56-mm, 7.62-mm and 50-cal ammunition. Projectile penetration vs snow density data obtained during these tests are given in Figure 13. As expected, the smallest and lightest projectile (5.56-mm) had the least penetration. The small increase in penetration of the 50-cal round relative to the 7.62-mm was not expected. It had been estimated, using the Ross Hanagud equation, that the 50-cal round would penetrate about twice as deep as the 7.62-mm. The relatively low observed penetration of the 50-cal round is attributed to increased resistance generated by case rupture and deformation (Fig. 14).

Data from these tests and the laboratory experiments, which emphasized the influence of snow density on penetration, suggested the concept of a hardened snow trench for hasty expedient protection of troops against small arms fire. A trench in the snow can be excavated very rapidly. Even when the snow is so light that it appears it would offer little or no resistance to small arms fire, tests have shown that such a trench (Fig. 15a) offers a surprising amount of protection. An important reason for the effectiveness of this trench is that fire against it normally strikes the snow at a shallow angle, resulting in ricocheting and broaching of the rounds. Increasing the density of the snow ahead of the trench by rodding and packing (Fig. 15b) greatly increases the probability for ricocheting as well as reducing penetration of bullets that do not ricochet or broach. In tests where approximately one hundred 5.56- and 7.62-mm rounds were fired at these trenches from close range, only two 5.56-mm and three 7.62-mm bullets came through the snow into the simple trench and no penetrations were observed into the hardened trench. Forty rounds of

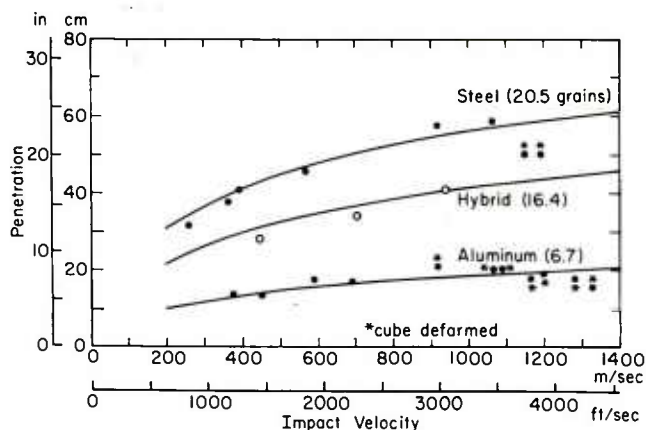


Figure 12. Comparison of test data with predicted penetration curves for 5.56-mm cubes in snow. Snow temperature  $-13^{\circ}\text{C}$ , density 0.8 slug/ft<sup>3</sup> (0.41 g/cc).

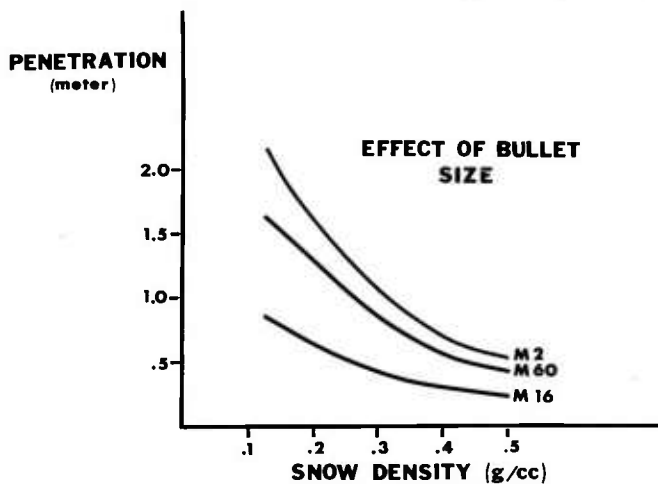


Figure 13. Bullet penetration vs snow density for 5.56-mm, 7.62-mm and 50-cal ammunition.

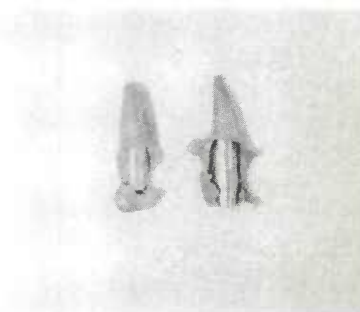


Figure 14. 50-cal projectile after impact into snow, illustrating magnitude of case damage.

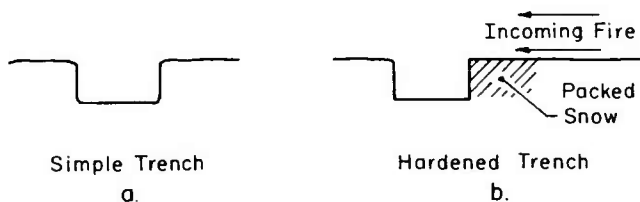


Figure 15. Snow trenches for personnel protection.

50-cal ammunition were also fired against the hardened trench and, again, no penetrations were observed.

CONCLUSIONS: Based on these test data, projectile penetrations into frozen soil are significantly lower than in unfrozen soil. For the 5.56-mm steel FSP's, penetration was reduced by about a factor of 2 in frozen Hanover silt. Temperature of the frozen soil influenced projectile penetration, with penetration decreasing at lower temperatures. But for Hanover silt, temperature changes in excess of 10°C were required to obtain significant changes in penetration.

For a projectile at a given impact velocity, penetration is a function of target properties with yield strength, density and compressibility probably being the most important. A theoretical technique based on dynamic cavity expansion in a locked-elastic, locked-plastic medium can be used to calculate projectile penetration in both frozen soil and snow with reasonable accuracy.

There are some critical impact velocities above which damage to projectiles occurred not only in frozen soil, but also in snow. In frozen soil the 5.56-mm steel FSP's deformed at velocities above about 800 m/sec and 7.62-mm NATO rounds started to tumble and/or strip their jackets above a velocity of about 600 m/sec. In snow, the aluminum FSP's started to deform at impact velocities above 900 m/sec and steel cubes above 1000 m/sec.

Snow can be used as a construction material for expedient defensive positions and affords protection against small arms fire up to 50 cal. In part this protection was achieved by designing the position to cause ricocheting and breaching of the rounds fired at it.

LITERATURE CITED

1. Farrell, D., 1975 Terminal Ballistics Testing Procedures, USACRREL Technical Note, June.
2. Johnson, P.R., 1975 Design and Effectiveness of Snow Fortifications in the Subarctic, USACRREL Technical Note, June.
3. Kakel, W.W., 1971 Fragment Defeating Capabilities of Plastic Armor, WES, TR N-71-10, June.
4. Mellor, M., 1964 Properties of Snow, USACRREL Monograph III-A1, Dec.
5. Rohani, B., 1973 Fragment and Projectile Penetration Resistance of Soils. Rpt. 2, High Velocity Fragment Penetration into Laboratory-Prepared Soil Targets, WES, MP S-71-12, June.
6. Ross, B. and Hanagud, S., 1969 Penetration Studies of Ice with Application to Arctic and Subarctic Warfare, Rpt. prepared for ONR by Stanford Research Institute, RPT. NWRC 7000-452-4.
7. Young, C.W., 1972 Empirical Equations for Predicting Penetration Performance in Layered Earth Materials for Complex Penetrator Configurations, Sandia Laboratories Rpt. SC-DR-72 0523, Dec.

## ANTIBODY TO HEPATITIS B CORE ANTIGEN

RICHARD G. ALLEN, CPT MSC  
GILBERT R. IRWIN, MAJ MC  
WALTER REED ARMY INSTITUTE OF RESEARCH  
WASHINGTON, D. C. 20012

Type B hepatitis, formerly called serum hepatitis, represents a serious health problem. In the United States there are approximately 150,000 clinical cases of type B hepatitis occurring each year (based on 1973 statistics). An increasing proportion of these cases in recent years is associated with the use of illicit drugs in the young adult population (the 14-24 age group).

Over the last 10 years (Table 1) there have been significant outbreaks of hepatitis B in the military. Overall peak attack rates for hepatitis B virus (HBV) in combat units in CONUS as well as USAREUR have ranged from 19-27/1000 clinical cases of hepatitis per year. Specific battalion-sized units in these areas have had rates of 100-300/1000/year. The economic impact alone (Table 2), when one considers length of hospitalization, convalescent leave following hospitalization, and the effect of loss of manpower to the military unit, are significant. The average length of hospitalization at Fort Hood was 22 days for the acute hepatitis B patient, followed by 30-60 days of convalescent leave. In addition, approximately 9% of the patients with acute hepatitis have been readmitted for recurrence of hepatitis associated with abnormal liver function tests.

Because of the magnitude of hepatitis B in the military, an effort to define the most efficient way to serologically diagnose both clinical and subclinical hepatitis B infection is needed. In a typical patient, as seen in Figure 1, hepatitis B surface antigen (HB<sub>s</sub>Ag) appears in the serum several weeks after exposure to HBV and is followed by the onset of clinical symptoms. Following closely the appearance of the surface antigen is the presence of antibody to the

hepatitis B core antigen (HB<sub>C</sub>Ag). This antibody remains present throughout the convalescent period. Antibody to the surface antigen (anti-HB<sub>S</sub>) appears from 1-6 months after the circulating HB<sub>S</sub>Ag has disappeared, and gradually rises during convalescence.

Of interest is this period of time between the clearing of the HB<sub>S</sub>Ag and the appearance of the surface antibody, for at this time the disease is only detectable by the presence of antibody to hepatitis B core antigen. This hiatus between clearing of antigen and development of surface antibody (in which detection of the disease can be made) is the time at which anti-HB<sub>C</sub> is the only potential marker of HBV infection. In fact, approximately 50% of clinical cases present with having already cleared their HB<sub>S</sub>Ag at the onset of symptoms of fatigue and jaundice. Thus, the serological diagnosis of HBV infection is frequently missed because HB<sub>S</sub>Ag is absent, and anti-HB<sub>S</sub> has not yet appeared. It is in this situation that the presence of anti-HB<sub>C</sub> is most important because it confirms the etiology of the acute hepatitis.

A second and very important future use of the core antibody test is in the monitoring, for HBV infection, of field units who have been immunized with HBV vaccine. Anti-HB<sub>C</sub> appears to be a marker of recent HBV infectivity. In that context, a primary antibody response to hepatitis B virus infection may result in the production of both anti-HB<sub>C</sub> and anti-HB<sub>S</sub>. Immunization with a killed HB<sub>S</sub>Ag vaccine would result in only the production of anti-HB<sub>S</sub>. The work presented in this paper describes the production of HB<sub>C</sub>Ag in chimpanzees, the development of a sensitive radioimmune test for anti-HB<sub>C</sub>, and the application of the test to the diagnosis and ultimately, to the prevention of HBV in the military.

#### METHOD

Hepatitis B core antigen is a very scarce reagent. For our work, two male chimpanzees, weighing 50 and 55 pounds, were isolated and started on a course of immunosuppression, using the drug cyclophosphamide in a dosage of 15 mg/kgm. This drug was administered 2-3 times/week throughout the course of the experiment. Twenty-six days after initiation of cyclophosphamide, both animals received 1 ml of a 1:10 dilution of infectious human plasma containing HB<sub>S</sub>Ag. (The plasma samples were kindly provided by Dr. Hoofnagle of Division of Biologics, FDA, Bethesda, Maryland).

At 32 days after inoculation with HBV, HB<sub>S</sub>Ag was detected by RIA in both chimpanzees. Liver biopsies were performed on



each animal biweekly during this period of HB<sub>s</sub> antigenemia. The presence of core antigen in the liver tissue was tested for by complement fixation, using anti-HB<sub>c</sub> sera derived from a human and chimpanzee source. When it was recognized that the HB<sub>c</sub>Ag titers in homogenates of serial liver biopsies were not increasing, the animals were sacrificed and the livers removed and frozen at -70°C. The titer HB<sub>c</sub>Ag in the liver homogenate was 1:8, and 1:16, respectively, for chimps 682 and 683.

The harvested chimpanzee liver was used as a source of antigen for developing the radioimmune inhibition test for anti-HB<sub>c</sub>. A 20% liver suspension was prepared in a hypotonic phosphate buffered saline. After homogenization, the liver suspension was clarified by centrifugation and the supernatant was used as a source of antigen.

IgG was labeled by the method of Purcell et al (1). The following reagents were added, in order, to a test tube: 20 uliters of 0.2 M phosphate buffer, pH 7.4; 200 uCi of high-specific activity <sup>125</sup>I (in 5 uliters); 10 ug of the protein to be labeled (in 1 to 10 uliters); 15 uliters of a solution of chloramine T (3.5 ug/uliter); 20 uliters of a solution of sodium metabisulfite (4.8 ug/uliter); and 20 uliters of a solution of sucrose (22.5%), potassium iodide (2 mg/ml). After the addition of chloramine T, the reaction was allowed to proceed for 15 s before being terminated by the addition of sodium metabisulfite. The mixture was applied to the top of a column (0.9 by 15 cm) packed with Sephadex G-200, and equilibrated with phosphate-buffered saline, pH 7.4 with 0.1% sodium azide. The protein was eluted with the same buffer; fractions containing the first peak of radioactivity were pooled and diluted with an equal volume of 1% bovine serum albumin. This stock mixture was stored at 4°C and diluted 1:2 with 1% bovine serum albumin just before use.

The micro-solid-phase radioimmunoassay was a modification of the method of Purcell et al (2). The wells of polyvinyl microtiter plates were coated with diluted anti-HB<sub>c</sub> in phosphate buffered saline for 4 hr at 37°C. After washing with saline, the sensitized wells received 200 ul of 1% bovine serum albumin in saline, followed by incubation overnight at 4°C. After washing, the wells were inoculated with 50 ul of HB<sub>c</sub>Ag and the plates were incubated at 4°C for 24-48 hrs. Following washing, 50 ul of each patient's serum was added to duplicate wells. Each plate contained four wells of anti-HB<sub>c</sub> negative serum as a control for plate variation. The plates were incubated at 4°C for 24 hr, then washed and 50 ul of radiolabeled anti-HB<sub>c</sub> globulin was added to each well and incubated at 37°C for 4-6 hrs or at 4°C overnight.

The plates were given a final wash and the wells were cut with scissors and transferred to gamma counting tubes and counted in a Nuclear Chicago gamma spectrometer for 1 min. Marked reduction in radioactivity with unlabeled anti-HB<sub>C</sub> antibody but not with normal serum was indicative of the specificity of the reaction (Table 3).

## RESULTS AND DISCUSSION

With the aid of the radioimmune assay inhibition test (RIAI), a variety of military populations have been examined for the presence of anti-HB<sub>C</sub>. In Table 4, anti-HB<sub>C</sub> is routinely detected in 100% of soldiers with acute HB<sub>S</sub>Ag<sup>+</sup> hepatitis. Of importance, however, is the observation that 34 sera from 85 acutely ill HB<sub>S</sub>Ag negative individuals with jaundice had anti-HB<sub>C</sub>, thus confirming the etiology of their infection. Likewise, the presence of anti-HB<sub>C</sub> is crucial to the detection and timing of subclinical HB infection as shown in Table 5. Since most HBV infection is subclinical, it is important to detect individuals in this category. Of 2,333 soldiers followed at Fort Hood, Texas, with a blood sample drawn at time of arrival, 4, 8, and 12 months later (from March 1974 to April 1975), 48 developed anti-HB<sub>S</sub> over the course of one year of observation. It is important to note, however, that 18 of these soldiers had anti-HB<sub>C</sub> without other evidence of HBV infection in their first blood sample. The presence of anti-HB<sub>C</sub> upon entering Fort Hood indicates that their exposure to HBV was prior to arrival at Fort Hood and not due to acquisition of HBV while there. Individuals who are in the process of losing anti-HB<sub>S</sub> also have a lower prevalence of anti-HB<sub>C</sub> as compared to soldiers who maintain anti-HB<sub>S</sub> over one year. Why some individuals lack anti-HB<sub>C</sub> in the presence of anti-HB<sub>S</sub> may be due to previous exposure to HBV many years ago and a subsequent recent secondary exposure, resulting only in boost in anti-HB<sub>S</sub> without replication of HBV, as measured by anti-HB<sub>C</sub>.

Of critical importance to the understanding of HBV epidemiology is the observation that 23 of 216 soldiers without other evidence of HBV infection had anti-HB<sub>C</sub>. Fifteen of these cases represent soldiers acquiring subclinical HBV while at Fort Hood. If one extrapolates from the 216 soldiers randomly tested for anti-HB<sub>C</sub> to the entire population of 2333 individuals, it would appear that 7% of the troops per year have subclinical HBV infection. Thus, for every clinical case of HBV, there are 10-15 subclinical cases. This observation is even more awesome if you recall the data concerning clinical attack rates/1000 of HBV in various troop populations listed in Table 1. Thus, overall HBV infection rates in Germany (if subclinical infection is included) would be at least 270/1000/year instead of

27/1000/yr (clinical cases only). Table 6 depicts the prevalence of HB<sub>s</sub>Ag, anti-HB<sub>s</sub>, and anti-HB<sub>c</sub> detected in platoons of soldiers at Fort Hood, Texas, in 1973 during an outbreak of HBV. With the aid of anti-HB<sub>c</sub> test, an additional 20 soldiers were identified who had evidence of HBV infection.

From these initial epidemiological surveys in U. S. Army soldiers, it is apparent that the detection of anti-HB<sub>c</sub> is of value in the serologic diagnosis of both acute clinical and subclinical disease. The RIAI test for anti-HB<sub>c</sub> has allowed investigators to obtain a better estimate of the total experience of any population with HBV.. The detection of anti-HB<sub>c</sub> not only defines exposure to HBV, but when taken with serial blood specimens, it allows one to estimate the timing when the exposure occurred.

The RIAI test is currently used for serological diagnosis of patients with clinical HB<sub>s</sub>Ag negative hepatitis and for epidemiological research in military populations. In addition, the radio-immune assay test can be modified to detect core antigen (HB<sub>c</sub>Ag) by simply eliminating the inhibitor anti-HB<sub>c</sub>. The application of this test to basic research on HB<sub>c</sub>Ag is important to the isolation of purified HB<sub>c</sub>Ag from ultracentrifuge gradients, and the characterization of HB<sub>c</sub>Ag, etc. Perhaps the most important future need for the anti-HB<sub>c</sub> test will come shortly when efficacy trials of the hepatitis B vaccine are started. The presence of anti-HB<sub>c</sub> in recipients of the HB<sub>s</sub>Ag vaccine (who will make only anti-HB<sub>s</sub>) will provide an indication as to whether candidate HBV vaccines are protective or not in the field.

#### REFERENCES

1. Purcell, R. H., Wong, D. C., Alter, H. J., and Holland, P. V., 1973. Microtiter solid-phase radioimmunoassay for hepatitis B antigen. *Applied Microbiology* 26: 478-484.
2. Purcell, R. H., Gerin, J. L., Almeida, J. B., and Holland, P. V., 1973/74. Radioimmunoassay for the detection of the core of the Dane particle and antibody to it. *Intervirology* 2: 231-243.

---

\*In conducting the research described in this report, the investigators adhered to the "Guide for Laboratory Animals Facilities and Care," as promulgated by the Committee on the Guide for Laboratory Animal Facilities and Care of the Institute of Laboratory Animal Resources, National Academy of Sciences - National Research Council.

Table 1. Recent epidemics of hepatitis B in the military

Locale	Year	Clinical attack rate
Fort Bragg, North Carolina	1970	20/1000*
Fort Hood, Texas	1972	19/1000
Fort Riley, Kansas	1973	10/1000*
Germany (USAREUR)	1973	26/1000
Camp Zama, Japan	1974	123/1000
Viet Nam	1972	9.9/1000
Korea	1971	9.1/1000

\*Approximation

Table 2. Economic impact of hepatitis B infection in troops at Fort Hood, Texas

Average length of hospitalization	20 days (30-60)
Convalescent leave	30 days
Assume attack rate of 10/1000 men (40,000 troops at Fort Hood)	400 cases/year
Work days lost by acute hepatitis B at Fort Hood	20,000
Dollar estimate of loss to US Army in Germany/year (LaVoie, 1974)	\$20,000,000
(Based on 3,975 hospitalized cases of hepatitis in 1973)	

Table 3. Sensitivity and Specificity of Radioimmune Assay Test for anti-HB<sub>C</sub>

---

1.	In comparison with complement fixation, RIAI is 10-50 times more sensitive.
2.	Labeled anti-HB <sub>C</sub> (I <sup>125</sup> ) used as the indicator system in this test does not cross react with: <ul style="list-style-type: none"> <li>a. human liver</li> <li>b. chimpanzee liver</li> </ul>
3.	Labeled anti-HB <sub>C</sub> (I <sup>125</sup> ) is not inhibited by sera containing anti-HB <sub>S</sub> only.

---

Table 4. Detection of anti-HB<sub>C</sub> by radioimmune assay inhibition in military populations (acute hepatitis)

---

	Number tested	Number anti HB <sub>C</sub> (%) positive
Acute hepatitis:		
HB <sub>S</sub> Ag positive	75	75 (100%)
HB <sub>S</sub> Ag negative	85	34 ( 39%)

---

Table 5. Detection of anti-HB<sub>C</sub> by radioimmune assay inhibition  
in military populations  
(Subclinical hepatitis B)

2333 soldiers followed 1 year*	Total observed	Total anti-HB <sub>C</sub> positive	Number initially anti-HB <sub>C</sub> positive	Number developing anti-HB <sub>C</sub>
Seroconversion to anti-HB <sub>S</sub> :				
Negative to positive	48	22	18	4
Positive to negative	37	17	17	0
Remain positive for 12 months	38	35	35	0
Never positive for anti-HB <sub>S</sub>	216	23	8	15

\* Blood drawn every 4 months

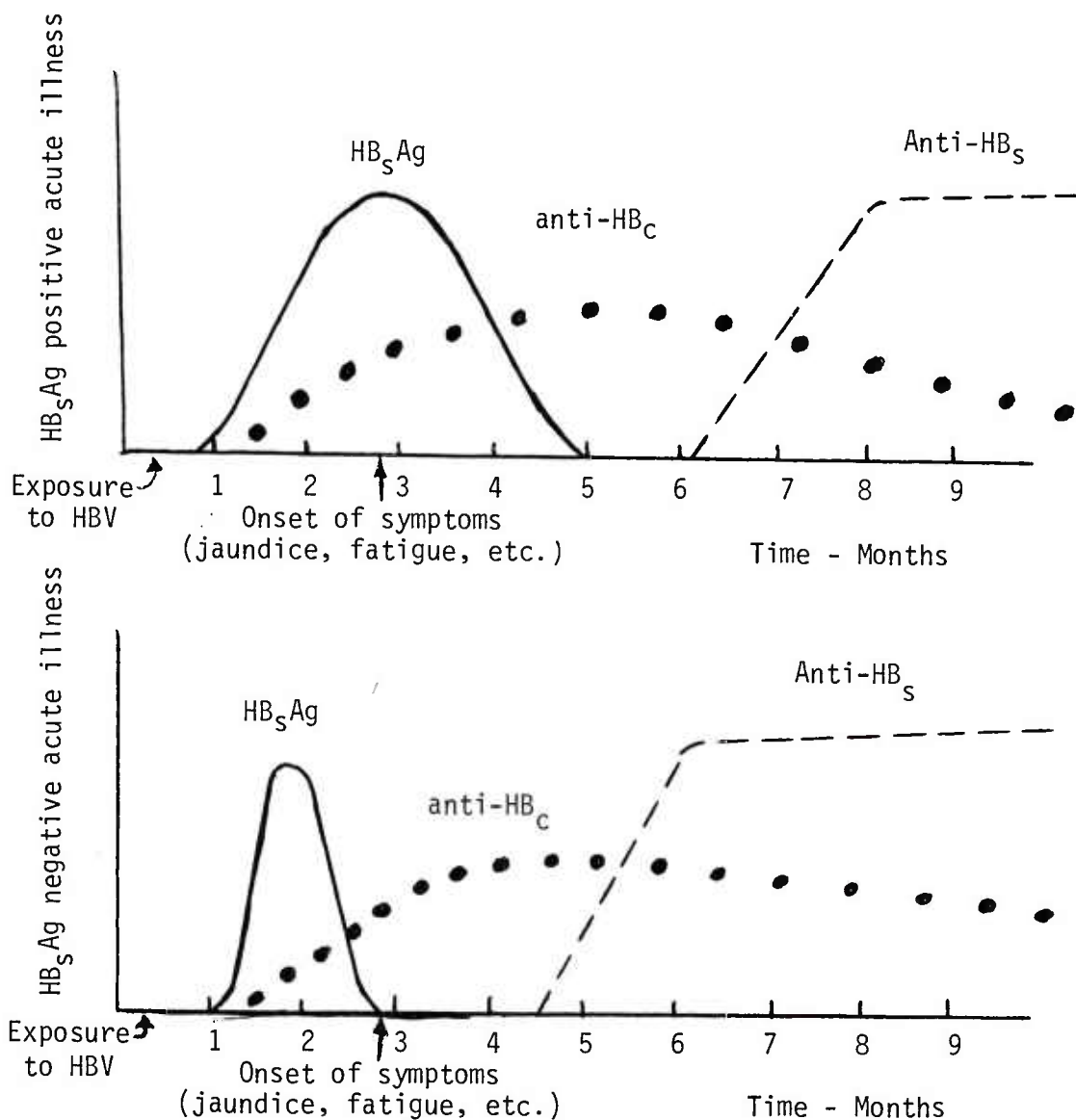
Table 6. Detection of anti-HB<sub>C</sub> in index and control units  
of soldiers at Fort Hood, Texas  
(during outbreak of hepatitis B)

	Total	HB <sub>S</sub> Ag	Anti-HB <sub>S</sub>	Anti-HB <sub>C</sub>	Anti-HB <sub>C</sub> only
Index Units	377	5	53	46	13*
Control Units	520	5	70	57	7*

\* 20 additional soldiers had evidence of HBV without the presence  
of HB<sub>S</sub>Ag or anti-HB<sub>S</sub>



Figure 1. Immune response in acute hepatitis B infection





AYERS, MURFREE, MARTIGNONI,  
and CHEW

AD A025974

## SOLID PROPELLANTS FOR HYDROGEN GAS GENERATORS (U)

ORVAL E. AYERS, Ph.D., JAMES A. MURFREE, Ph.D.,  
PASQUALE MARTIGNONI, Ph.D., AND WILLIAM M. CHEW, Ph.D.  
US ARMY MISSILE COMMAND  
REDSTONE ARSENAL, ALABAMA 35809

### INTRODUCTION

In the past few years, considerable effort has been expended to develop hydrogen fluoride/deuterium fluoride (HF/DF) chemical lasers. These lasers depend on the use of high pressure gaseous or cryogenic liquid reactants and diluents. The replacement of cryogenic or high pressure gaseous materials by storable reactant and diluent sources in the condensed phase is highly desirable for Army field use of the chemical laser.

Thus, long-term storable reactants are needed for advanced chemical laser systems for improvement of system handling, packaging, and safety. Preliminary efforts have been initiated to verify the feasibility of solid storable hydrogen sources for use in HF/DF chemical lasers. The development of storable sources of hydrogen for high energy chemical laser applications was the objective of this investigation.

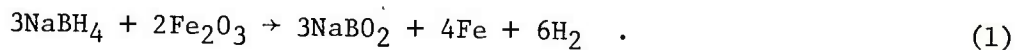
Storable sources of hydrogen and deuterium, in a compact form, are needed for the HF/DF chemical laser system. The system must be storable in a standby operational mode for long periods of time under the environmental conditions required by the Army. Storage life and environmental conditions should be similar to those required of missile propellants. An important consideration in the future application of HF/DF chemical lasers is the safety associated with the use of various reactants. Storage, transportation, and handling procedures prior to use and the hazards associated with gas generation as part of the laser operation are aspects of particular importance to the Army where the laser operation is in close proximity to operating personnel.

AYERS, MURFREE, MARTIGNONI,  
and CHEW

Both storability and safety restrict the use of cryogenic liquid hydrogen and deuterium in an operational chemical laser. Also, safety and weight considerations make high pressure bottled gas sources appear unattractive for application in Army chemical laser systems. Since there is no significant difference in chemical properties between hydrogen and deuterium gas generators, these  $H_2/D_2$  combinations will be referred to as hydrogen throughout this paper. The primary objective of the work described in this paper is to avoid the storage and handling hazards associated with high pressure or liquid hydrogen by developing an all-solid propellant composition which, upon ignition, can supply the hydrogen gas for the laser. These solid propellant gas generators will provide a completely storable hydrogen gas source that combines instant readiness with excellent handling behavior and compact storage.

#### EXPERIMENTAL

A solid propellant has been developed and evaluated as a hydrogen gas generator for use in the HF/DF chemical laser. This generator is based on the reaction of sodium borohydride ( $NaBH_4$ ) with ferric oxide ( $Fe_2O_3$ ) to produce hydrogen gas according to the following equation:



The thermochemical reaction takes place at a 3/2 molar ratio or a weight ratio of 26/74. Sodium borodeuteride ( $NaBD_4$ ) can be used in place of the  $NaBH_4$  in the above equation to give a solid composition that generates deuterium gas ( $D_2$ ). A weight ratio of  $NaBD_4/Fe_2O_3$  of 28.2/71.8 is used in the deuterium formulation.

Solid propellant grains were prepared by the following general procedure: Moisture free  $Fe_2O_3$  was obtained by drying the material in a furnace at 823 to 873°K for 4 hours to remove any adsorbed moisture or water of hydration. Stoichiometric ratios of  $NaBH_4$  and dry  $Fe_2O_3$  were uniformly mixed in a blending mill or by shaking in a closed container taking precautions to minimize exposure to moisture. The mixed propellant was then pressed into pellets or metal canisters using a remote hydraulic press at a total load of 907.2 kg (2000 lb) for approximately 5 minutes.

AYERS, MURFREE, MARTIGNONI,  
and CHEW

Pellets and canisters can be made in various diameters and lengths to produce small or large volumes of hydrogen gas depending on the demand. The rate of hydrogen generation may be varied by varying the diameter of the grain. Grains of the  $\text{NaBH}_4/\text{Fe}_2\text{O}_3$  formulation have been pressed into canisters with a diameter of 25.4 mm and up to 101.6 mm in length. Propellants weighing up to 0.08 kg have been prepared by the above procedure and evaluated in an operating HF/DF chemical laser.

Grains pressed at 907.2 kg total load had a burning rate of 4.06 mm/sec under an inert nitrogen pressure of 13.8 MPa (2000 psi). Density measurements were made on the solid propellant by pressing small pellets at 907.2 kg total load, weighing and determining the volume by displacement of an inert liquid such as n-heptane. The theoretical density of the stoichiometric formulation based on the densities of the ingredients is  $2.61 \text{ Mg/m}^3$  (g/cc) as compared with an experimental value of  $2.50 \text{ Mg/m}^3$  (g/cc).

Ignition of propellant grains was by use of a hot nichrome wire. Ten volts at approximately 10 amperes were required to produce enough heat in the nichrome wire to initiate the self-sustaining thermochemical reaction in the solid propellant. The reaction went easily to completion and produced hydrogen gas with a purity greater than 99 mole % as indicated by mass spectrometric analysis. A solid "clinker" residue remained after combustion and gas production.

The solid grain hydrogen generator based on  $\text{NaBH}_4/\text{Fe}_2\text{O}_3$  was evaluated in a small scale HF/DF chemical laser device as a laser cavity fuel and as a combustor fuel, and the results were compared to those obtained from bottled hydrogen gas. A schematic of the apparatus used for evaluating the solid propellant on a chemical laser device is shown in Figure 1. It consisted of a solid grain combustor with an accumulator tank and a HF/DF chemical laser device consisting of a precombustor injector, variable length precombustor, secondary nozzle, laser cavity and associated feed systems, and exhaust system. A cross-sectional drawing of the secondary nozzle is shown in Figure 2. This is a parallel flow slit nozzle in which fluorine atoms from the precombustor are flowed through the center of the nozzle and mixed with deuterium or hydrogen from the top and bottom slits in the laser cavity. The nozzle is 9.5 mm high and 101.6 mm long and is water cooled.

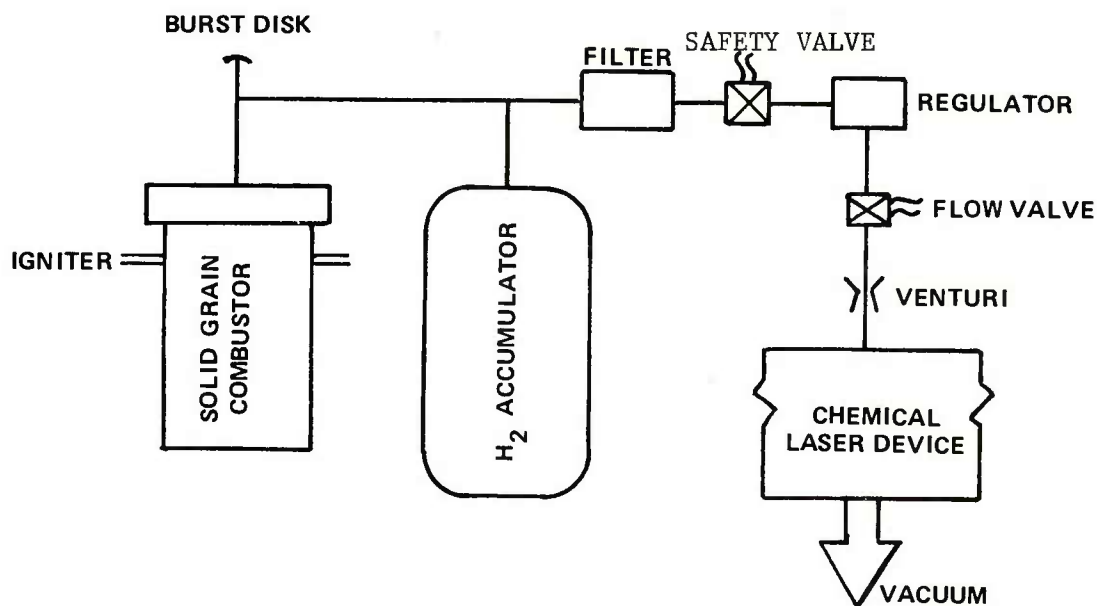


Figure 1. Apparatus for Firing Solid Propellant Grain as Hydrogen Generator for Chemical Laser.

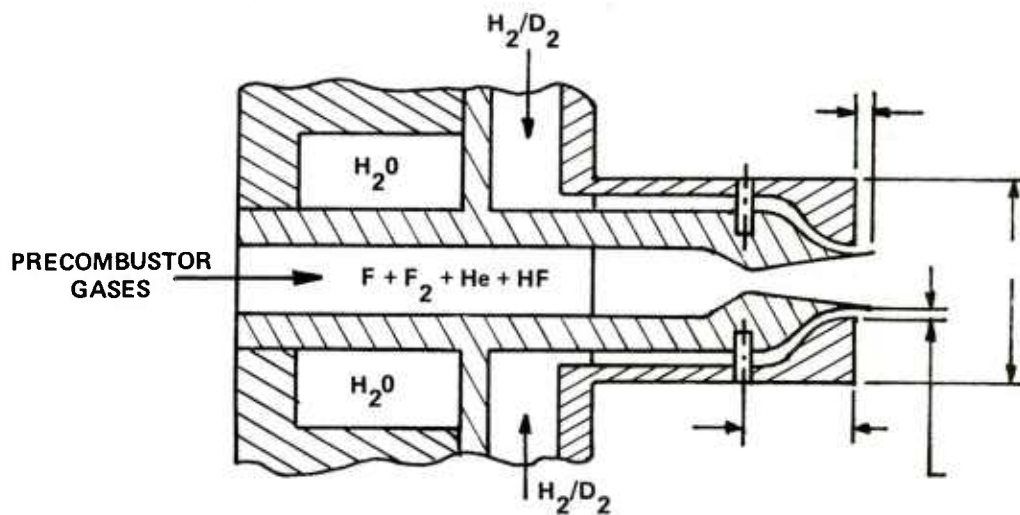


Figure 2. Typical Nozzle (Scale = 5/1).



AYERS, MURFREE, MARTIGNONI,  
and CHEW

Calcium fluoride windows were used on each side of the laser cavity to permit power extraction. These windows were mounted at Brewster's angle on adapter plates with 2-in. diameter openings in conjunction with external mirrors. The optical cavity was plano-concave, consisting of a 5 m radius of curvature gold coated mirror and a plane, partially transmitting germanium output mirror coated for 5% transmittance.

Cylindrical grains measuring 25.4 mm in diameter and up to 101.6 mm long have been fired in the apparatus using a hot nichrome wire to initiate combustion. The hydrogen gas generator was used to pressurize an evacuated 1.0 liter accumulator tank with  $H_2$  to approximately 2.45 MPa (350 psi).

## RESULTS AND DISCUSSION

The major effort of this investigation has been concentrated on solid propellant compositions containing  $NaBH_4$ . Experimental studies with this metallic hydride have confirmed the feasibility of this approach to a solid hydrogen gas generator. Several solid formulations have been prepared that show reliable ignition and combustion behavior with good retention of the solid products and production of gas free of particulate matter. Hydrogen gas produced by the most promising  $NaBH_4/Fe_2O_3$  composition showed gas purity equivalent to or exceeding that of commercial tank hydrogen. This gas generator formulation containing  $NaBH_4/Fe_2O_3$  in a 26/74 weight ratio was found to be very stable with no sensitivity to impact or friction and to have a high autoignition temperature. In addition,  $NaBH_4$ , in contrast to many other hydrides, can be handled in the open in the presence of atmospheric moisture for a limited time and requires no special handling procedures.

A limited amount of experimental data have been obtained on solid compositions containing  $LiAlH_4$ . This hydride has a low autoignition temperature (423°K) and exhibits a greater sensitivity to impact and friction than  $NaBH_4$  in solid propellants. Also,  $LiAlH_4$  reacts violently with water, and formulations containing this material have to be processed and stored under very dry conditions to avoid accidental ignition or deterioration of the solid grain. Other hydrides such as  $AlH_3$ ,  $LiBH_4$ , and  $NaAlH_4$  have been briefly investigated in solid propellant compositions.

AYERS, MURFREE, MARTIGNONI,  
and CHEW

In solid hydrogen gas generators based on formulations such as  $\text{NaBH}_4/\text{Fe}_2\text{O}_3$  or  $\text{LiAlH}_4/\text{NH}_4\text{Cl}/\text{Fe}_2\text{O}_3$ , the weight of available hydrogen is a small percentage of the total weight of the formulation. In the  $\text{NaBH}_4/\text{Fe}_2\text{O}_3$  propellant, approximately 3 weight % hydrogen gas is produced with a purity of 99 mole % or better. However, this gas generator gives a favorable volumetric efficiency that is equivalent to that of liquid hydrogen. For example,  $1 \text{ cm}^3$  (cc) of this solid propellant will theoretically produce  $804 \text{ cm}^3$  (cc) of hydrogen gas at standard temperature and pressure (STP) as compared to  $1.0 \text{ cm}^3$  (cc) of liquid hydrogen producing  $778 \text{ cm}^3$  (cc) of hydrogen at STP. Samples of the  $\text{NaBH}_4/\text{Fe}_2\text{O}_3$  propellant have been fired that produced experimental volumetric efficiencies equivalent to that of liquid hydrogen. Table I summarizes the theoretical volumetric efficiencies of several solid propellants containing various metal hydrides. From Table I, it may be seen that compositions 2-4 have higher volumetric efficiencies for  $\text{H}_2$  release than the  $\text{NaBH}_4/\text{Fe}_2\text{O}_3$  formulation. However, composition 2 with  $\text{LiBH}_4$  and composition 4 with  $\text{LiAlH}_4$  are more sensitive to moisture, friction, impact, and heat than composition 1. Thus, the ease of handling of  $\text{NaBH}_4$  and the  $\text{NaBH}_4/\text{Fe}_2\text{O}_3$  formulation compensates for its less efficient production of  $\text{H}_2$ .

The  $\text{NaBH}_4/(\text{NH}_4)_2\text{SO}_4$  composition (composition 3 in Table I) appears to be one of the more promising solid hydrogen gas generator formulations from volumetric and weight yield considerations. An optimum  $\text{NaBH}_4/(\text{NH}_4)_2\text{SO}_4$  formulation should produce mainly hydrogen with a small amount of nitrogen which can serve as inert diluent in the HF/DF chemical laser. Preliminary experimental work on the  $\text{NaBH}_4/(\text{NH}_4)_2\text{SO}_4$  composition shows that a gas mixture containing approximately 90%  $\text{H}_2$ , 4%  $\text{N}_2$ , 5%  $\text{NH}_3$ , and traces of other gaseous products is produced from grain combustion.

Tests have been performed on a small screening HF/DF chemical laser to determine the effects of  $\text{NH}_3$  in  $\text{D}_2$  on the DF laser. As shown in Figure 3, 2%  $\text{NH}_3$  in the  $\text{D}_2$  will decrease the power output to approximately 1/2 its original value when compared to pure  $\text{D}_2$  as the cavity fuel. Therefore, the production of  $\text{NH}_3$  by the  $\text{NaBH}_4/(\text{NH}_4)_2\text{SO}_4$  formulation is undesirable. Some of the  $\text{NH}_3$  formation may occur during the slow thermal decomposition of the grain as a result of the ignition delay encountered when using the nichrome wire to ignite the solid grain. Additional work is being performed on the

TABLE I. Comparison of Efficiency of Hydrogen Gas Generators

	Composition 1	Composition 2	Composition 3	Composition 4	Liquid H <sub>2</sub>
Ingredients	NaBH <sub>4</sub> /Fe <sub>2</sub> O <sub>3</sub>	LiBH <sub>4</sub> /Fe <sub>2</sub> O <sub>3</sub>	NaBH <sub>4</sub> /(NH <sub>4</sub> ) <sub>2</sub> SO <sub>4</sub>	LiAlH <sub>4</sub> /NH <sub>4</sub> Cl/Fe <sub>2</sub> O <sub>3</sub>	H <sub>2</sub>
Composition (wt %)	26/74	17/83	53.4/46.6	61.2/28.8/10.0	100
Density (Mg/m <sup>3</sup> )	2.61	2.41	1.32	1.14	0.07
H <sub>2</sub> at STP/cm <sup>3</sup> Propellant	804	842	1247	940	778
Temperature (°K)	918		923		
H <sub>2</sub> Yield (wt %)	2.8	3.15	8.5	7.59	100

AYERS, MURFREE, MARTIGNONI,  
and CHEW

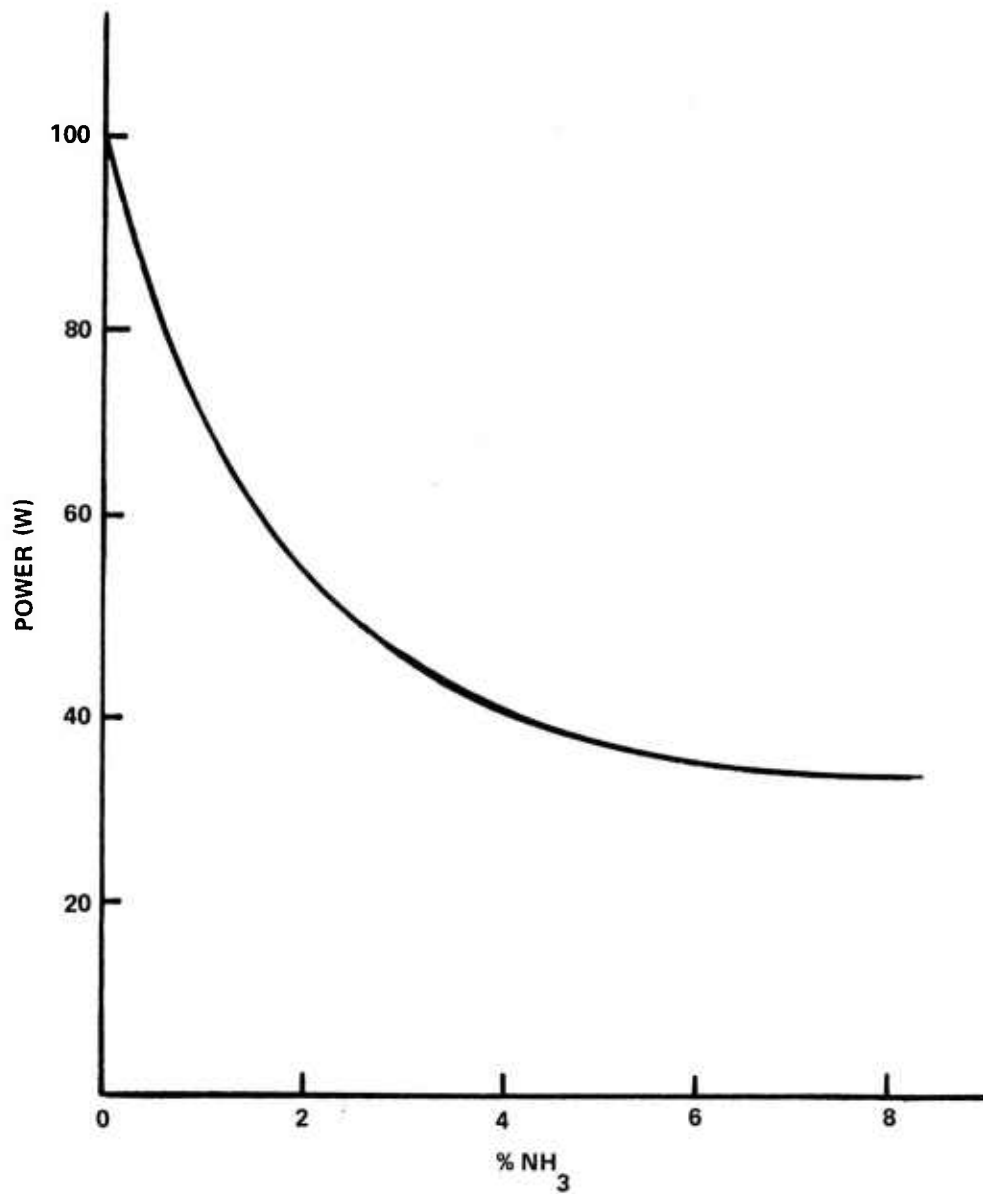


Figure 3. Effects of  $\text{NH}_3$  in  $\text{D}_2$  on DF Laser.

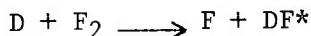
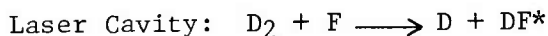
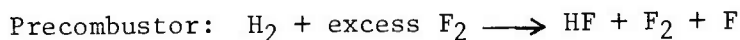
AYERS, MURFREE, MARTIGNONI,  
and CHEW

$\text{NaBH}_4/(\text{NH}_4)_2\text{SO}_4$  composition to improve the experimental hydrogen yield and eliminate the  $\text{NH}_3$  from the gaseous products.

Composition 4 produces a larger volume of  $\text{H}_2$  per unit weight of formulation and a higher weight % yield of hydrogen than compositions 1 and 2. However, the composition containing  $\text{LiAlH}_4$  is more hazardous to handle and process than the borohydride compositions due to the fact that  $\text{LiAlH}_4$  is more sensitive to impact, friction, heat, and moisture. Also, the  $\text{LiAlH}_4$  composition leaves a reactive "clinker" residue containing  $\text{LiH}$  after combustion. Tests have shown that this solid clinker material will spontaneously ignite upon contact with water.

The solid grain hydrogen generator based on  $\text{NaBH}_4/\text{Fe}_2\text{O}_3$ , composition 1 in Table I, was evaluated in a small scale HF/DF chemical laser device as a laser cavity fuel and as a precombustor fuel. Initial lasing runs were made in both DF and HF laser output modes using commercial bottled hydrogen and deuterium to obtain baseline data. These data were compared with those obtained using the solid propellant gas generator as the hydrogen source. The data for each laser run are summarized in Table II. All the runs were at a total flow rate ranging from 1874 to 2010  $\text{cm}^3/\text{sec}$  or approximately 0.001 kg/sec. Each experimental run lasted for a total duration of 10 sec. Hydrogen produced by the solid gas generator was run as a precombustor fuel in the DF laser and as the laser cavity fuel in the HF laser. The following equations show the reactions that are taking place in the HF/DF chemical laser using  $\text{H}_2/\text{D}_2$  and  $\text{F}_2$  as the reactants:

#### DF Laser



#### HF Laser

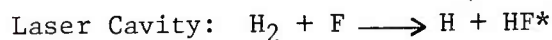
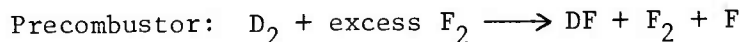
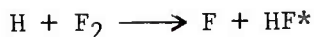


TABLE II. Summary of Laser Runs

Laser Species	Flow Rates (cm <sup>3</sup> /sec)						Power (W)
	F <sub>2</sub>	Cylinder H <sub>2</sub>	Generator H <sub>2</sub>	D <sub>2</sub>	He	Total	
DF	379	202	---	566	745	1892	50.9
	380	202	---	571	734	1887	43.5
	380	202	---	571	734	1887	45.9
	379	---	190	566	739	1874	46.4
	380	---	202	566	739	1887	45.9
	380	---	202	566	739	1887	46.6
	380	---	202	566	734	1882	45.9
	380	---	---	---	---	---	---
HF	380	594	---	196	728	1898	6.0
	381	594	---	196	756	1927	5.0
	381	594	---	196	756	1927	5.9
	381	---	661	196	750	1988	5.5
	381	---	683	196	750	2010	6.0





The experimental data obtained in the evaluation of the solid hydrogen gas generator on the small HF/DF chemical laser are shown in Table II. The various experimental runs give a direct comparison of bottled hydrogen with the hydrogen produced by the solid propellant gas generator. In the DF laser, both bottled hydrogen and  $\text{H}_2$  from the solid gas generator were run as precombustor fuels. Both sources of hydrogen gave approximately the same average power output in the DF mode. Thus, experimental data confirm that hydrogen produced from a solid propellant grain is as good as commercial hydrogen for use as a fuel in the precombustor of the HF/DF chemical laser.

In the HF laser, hydrogen from the solid gas generator gave comparable experimental results to that of bottled hydrogen. In this mode, the hydrogen, either commercial bottle or solid generator, was the laser cavity fuel. Again, the two sources of hydrogen are equivalent. For all the lasing runs reported in Table II, the chemical laser device was optimized in the DF mode. Thus, the low power output in the HF mode was attributed to this optimization of the laser in the DF mode.

Based on the experimental results obtained from the  $\text{NaBH}_4/\text{Fe}_2\text{O}_3$  solid hydrogen gas generator, it is apparent that a solid gas generator of this type is feasible and practical as a storable source of hydrogen or deuterium for use in the operation of HF/DF chemical lasers. Compositions that contain  $\text{NaBH}_4/(\text{NH}_4)_2\text{SO}_4$  or  $\text{NaBH}_4/(\text{NH}_4)_2\text{Cr}_2\text{O}_7$  have a much larger theoretical volumetric efficiency and weight % yield of hydrogen than  $\text{NaBH}_4/\text{Fe}_2\text{O}_3$  and, therefore, are potentially attractive as solid hydrogen gas generators. Work is in progress on the preparation and evaluation of solid propellant grains containing these ammonium salts and  $\text{NaBH}_4$ . Only preliminary data have been obtained on the use of  $(\text{NH}_4)_2\text{Cr}_2\text{O}_7$  in a solid formulation, but work is continuing on the development of this formulation.

## CONCLUSIONS

Solid propellants have been developed and evaluated in a hydrogen gas generator as potential sources of hydrogen for the HF/DF chemical laser. Formulations based on the reaction of  $\text{NaBH}_4$  with  $\text{Fe}_2\text{O}_3$  to produce high purity hydrogen and the reaction of  $\text{NaBH}_4$  with

AYERS, MURFREE, MARTIGNONI,  
and CHEW

$(\text{NH}_4)_2\text{SO}_4$  to produce a mixture of hydrogen and nitrogen have been investigated. When deuterated compounds are used in place of the hydrogen-containing compounds, deuterium ( $\text{D}_2$ ) is generated in place of hydrogen ( $\text{H}_2$ ). Propellant grains of  $\text{NaBH}_4/\text{Fe}_2\text{O}_3$  weighing approximately 0.08 kg have been prepared and used to generate high purity hydrogen gas for use as a laser cavity fuel and precombustor fuel in a small HF/DF chemical laser device. The propellant formulations that contain  $\text{NaBH}_4$  are very stable to moisture, exhibit no sensitivity to impact or friction, and have autoignition temperatures above 773°K. These propellants or similar type solid propellants are potential storable  $\text{H}_2/\text{D}_2$  gas sources that combine instant readiness with excellent handling characteristics and compact storage. The volumetric efficiency of these solid propellants is equivalent to or greater than that of liquid hydrogen as a source of gaseous hydrogen. Experimental data from the HF/DF chemical laser tests confirm that hydrogen produced from a solid propellant grain is equivalent to commercial hydrogen for use as a cavity or precombustor fuel in the HF/DF chemical laser.

OPTIONAL ADDITIVE SYSTEMS AS AN EFFECTIVE STRATEGY  
FOR BLOOD STORAGE IN MILITARY BLOOD BANKING (U)

THOMAS A. BENSINGER, MAJ, MC  
THOMAS F. ZUCK, LTC, MC  
LETTERMAN ARMY INSTITUTE OF RESEARCH  
PRESIDIO OF SAN FRANCISCO, CA 94129

INTRODUCTION

Blood transfusions are necessary for resuscitation of many severely injured soldiers. The 21 day limit of the effectiveness of presently licensed red cell liquid storage preservation solutions results in severe logistic difficulties in insuring adequate blood supplies during wartime. Because of this three-week limit, blood wastage from outdating has been high in remote areas outside the continental United States. Modified preservative solutions which would safely extend useful shelf-life of liquid stored red cells would yield significant military benefit.

Many experimental studies (1,2) as well as recent clinical blood banking experience in Germany (3) and Sweden (4), have demonstrated conclusively that red cell liquid storage can safely be extended to 35 days by supplementing currently available preservative solutions with adenine. In these reports, the adenine has been incorporated within the preservative solution into which the whole blood is drawn at the time of donation. This technique exposes all militarily important non-red cell components, principally plasma fractions and platelets, to adenine, yet these components do not benefit from adenine supplementation. Similarly, red cells transfused within the first two weeks of liquid storage do not show improved survivability when drawn into adenine supplemented preservative solutions. The beneficial effects of adenine are manifest principally during prolonged red cell liquid storage.

Although most clinical reports (3,4) document the safety of adenine, the potential kidney toxicity of one of its metabolites (2,8-dihydroxyadenine) remains of concern, particularly in soldiers suffering from severe hemorrhagic shock. These patients may require massive replacement of blood stored less than five days, and non-red cell component infusions. Thus, they are subjected to the potential toxicity of adenine from blood transfusion products not known to benefit by adenine supplementation. Further, it also would be desirable to reduce, if possible, the amount of adenine required to effectively prolong red cell liquid storage.

To attack the problem associated with the exposure of all blood products to adenine, and to determine whether a lower adenine concentration would be effective, a new storage strategy has been developed. In this system, which may be termed an optional additive system (OAS) (5,6), blood is collected, processed, and initially stored in currently available preservative solutions. After 7 or 14 days of refrigerated storage, adenine and glucose are added from a sterile integral pouch. The efficacy of this strategy in preserving red cell biochemical energy levels for 35 days is the subject of this report.

#### METHODS

Although the concentrations, composition, and day of addition varied, the general construct of all studies was identical. Blood was drawn from a total of 9 normal healthy adult volunteer donors who had been free from clinical illness for at least three months prior to phlebotomy and were taking no medications. Within one hour after phlebotomy, all units were centrifuged at  $4500 \times g$  for five minutes at  $4^{\circ}\text{C}$  in a Sorvall RC-3 centrifuge with the horizontal swinging bucket rotor. The plasma was pressed off to obtain the desired hematocrit (7). The unit was then equally subdivided into three transfer packs and subsequently stored at  $4^{\circ}\text{C}$  in a monitored blood bank refrigerator. Thus, each unit yielded one control subunit and two subunits in which the effects of delayed supplementation were observed. All additions were 15 ml, and the adenine and glucose were suspended in 154 mM saline solution. The concentrations of adenine and glucose were calculated and expressed as molarity in relation to the red cell mass following packing. Additions were performed by injection into the subunits through a sterile port. The injection syringes were fitted with  $0.22 \mu$  filters to sterilize the supplemental solutions.

Group One: Four units were packed to an hematocrit of 90% and subdivided as above. On day zero, 15 ml of 154 mM saline were added to the control subunits. The other subunits were supplemented at either days 7 or 14 with adenine and glucose to yield final concentrations of 0.25 mM and 71.0 mM, respectively.

Group Two: Five units were packed to an hematocrit of 70%, and subdivided as above. On days 0, 7, and 14 each of the subunits was supplemented with adenine and glucose to yield final concentrations of 0.125 mM and 71.0 mM, respectively.

In both groups, subunits were agitated thoroughly once weekly just prior to blood sampling and at the time of addition of the supplemental storage media. Hematocrits were measured by a standard micro technique. Erythrocyte adenosine triphosphate (ATP) and glucose concentrations were determined by the hexokinase method in which hexokinase is used to phosphorylate glucose, the reaction being coupled with Glucose-6-Phosphate Dehydrogenase to reduce NADP to NADPH (8). The concentration of 2,3 diphosphoglycerate (2,3-DPG) was measured by a modification of the technique of Krimsky (9). The pH was measured by a technique which allowed anaerobic determination at 0° - 4°C (10). Bacteriological culturing was performed weekly. All statistical results are reported as the mean plus or minus the standard error of the mean.

## RESULTS

Group One: The results are illustrated in Figure 1A and B. The control subunits showed a mean fall in red cell ATP concentration to  $1.00 \pm 0.25$   $\mu$ moles/g of Hb (25.6% of the day zero level) at 35 days of storage. Subunits supplemented with glucose and adenine on days 7 and 14 showed a fall of red cell ATP concentration to  $2.49 \pm 0.17$   $\mu$ moles/g of Hb (63.8% of the initial level), and  $2.68 \pm 0.27$   $\mu$ moles/g of Hb (68.7% of the initial level), respectively, at 35 days. The glucose concentration in control subunits fell to 25 mg/dl at storage day 35, but were 100 mg/dl in the supplemented subunits.

Group Two: The data from group two units are illustrated in Figures 2A and B. The control subunits supplemented with adenine and glucose on day zero showed a mean fall in red cell ATP concentration to  $2.47 \pm 0.32$   $\mu$ moles/g of Hb (60.2% of the initial storage level) at 35 days of storage. Subunits supplemented on days 7 and 14 showed a fall in red cell ATP concentration to  $2.92 \pm 0.23$   $\mu$ moles/g of Hb (71.2% of the initial day zero level), and to  $2.13 \pm 0.23$



$\mu$ moles/g of Hb (52.1% of day zero level), respectively at 35 days of storage. The glucose levels in all subunits remained above 120 mg/dl throughout storage.

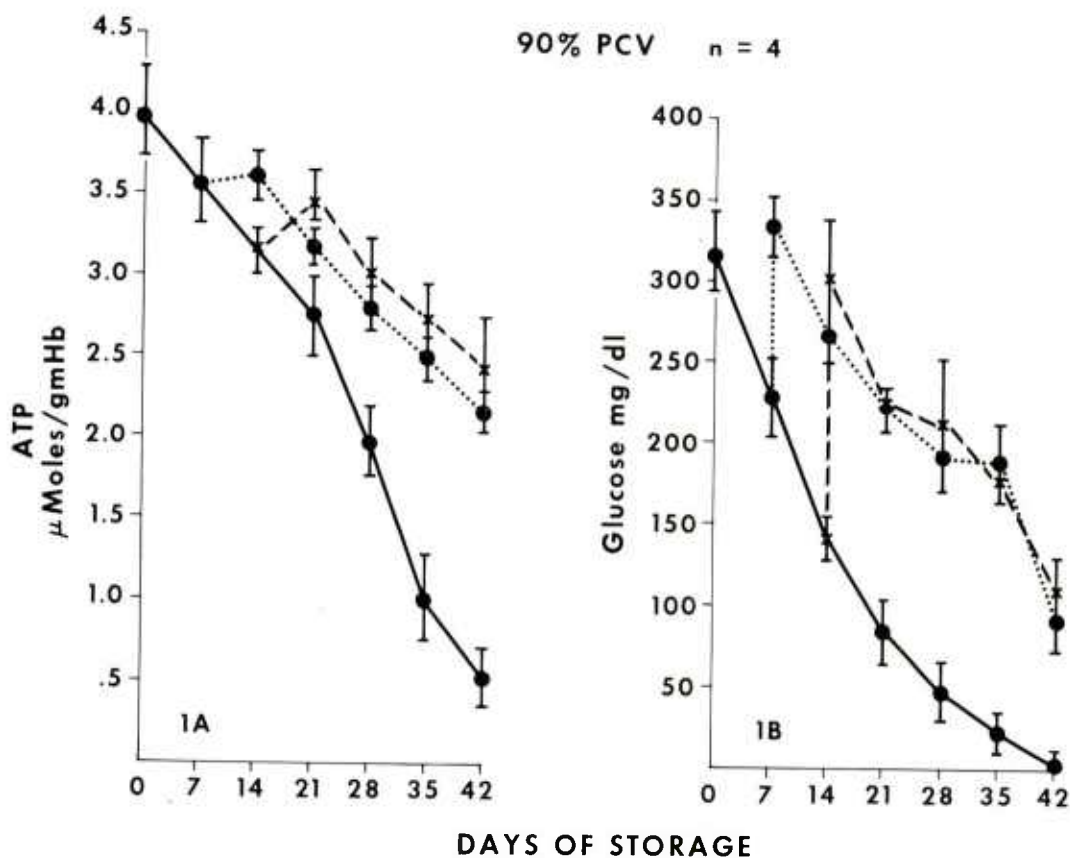


Figure 1A and B: Adenosine triphosphate (ATP) and glucose levels are plotted against days of storage. The units of blood were subdivided as described in the Methods section. The solid line (—) represents the subunit supplemented on day zero with 15 ml of 0.9% NaCl. The dotted line (....) represents subunits supplemented on day 7 with 15 ml of 0.9% NaCl containing 0.25 mM adenine (final concentration) and 71.0 mM glucose (final concentration). The dotted X line (X---X) represents subunits supplemented on day 14 with the same material as day 7. As can be seen, ATP levels are well maintained in units supplemented on day 7 or 14.



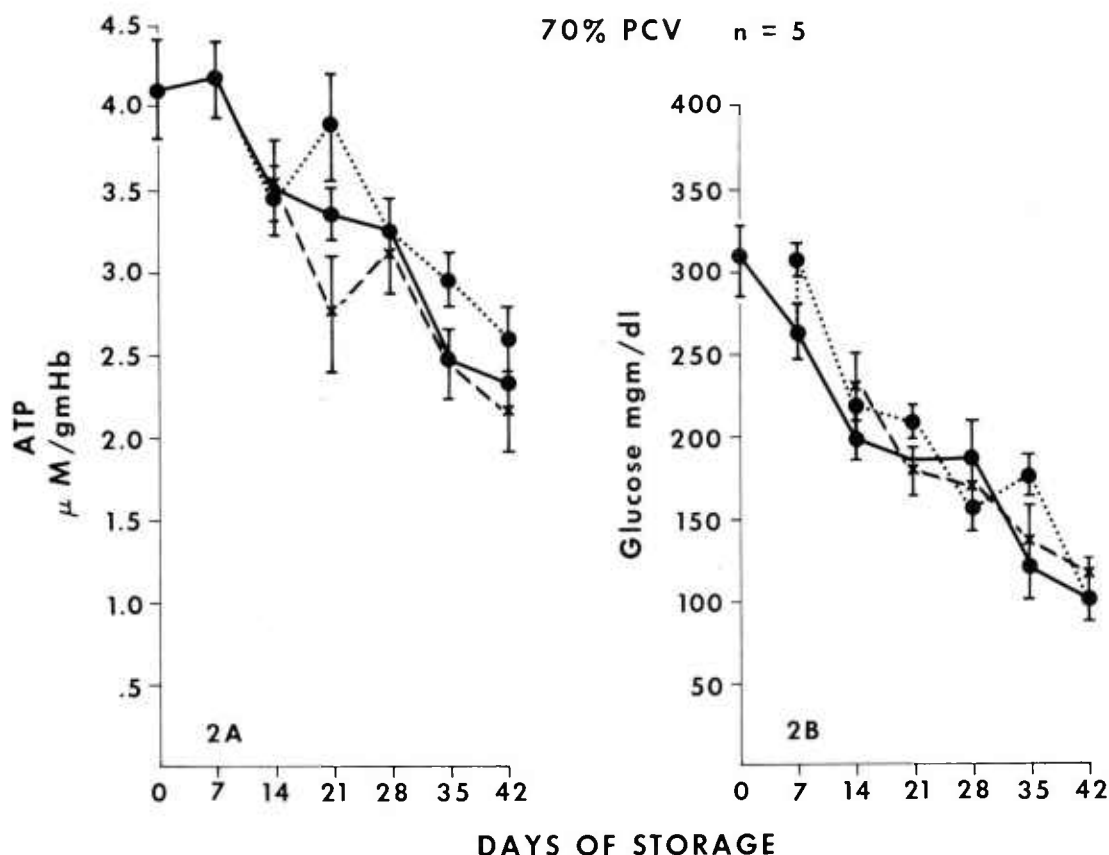


Figure 2A and B: Adenosine triphosphate (ATP) and glucose levels are plotted against days of storage. The units were packed and subdivided as described in the Methods section. The subunits were supplemented on day 0 (—), day 7 (····), or day 14 (X---X) with 15 ml of 0.9% NaCl containing 0.125 mM adenine (final concentration) and glucose 71.0 mM (final concentration). ATP is apparently adequately maintained in all three subgroups and sufficient glucose is available throughout storage.

In both groups, most subunits showed a rapid increase in red cell ATP concentration at the time of delayed supplementation. This occurred between the time of supplementation and drawing the test samples, usually less than one hour. Among the various subunits of both groups there was no significant difference between the 2,3-diphosphoglycerate, pH and hematocrit measurements. All units remained sterile throughout storage.

## DISCUSSION

The OAS described possesses those preservation solution characteristics which are desirable: red cell liquid storage can be extended to 35 days, toxicity potential is minimal, and virtually all of the available plasma may be harvested.

The maintenance of high levels of red cell ATP during storage with these OAS studies suggest that postinfusion red cell survivability will be acceptable following 35 days of storage. Dern, et al. (11) have shown that if at the end of storage a red cell ATP concentration was 48% of the original level, greater than 70% of the cells infused would survive at least 24 hours. Although adequate red cell ATP levels do not, of themselves, insure acceptable postinfusion survivability (12), red cell ATP remains the most appropriate in vitro parameter to assess the potential value of a storage strategy.

From previous studies it would be anticipated that the OAS would be effective in maintaining red cell ATP. Strumia et al. (13,14) found delayed addition of inosine, together with adenine at a higher concentration than reported here, to be as effective in preserving red cell ATP as their addition on day zero. It is also known that red cells will undergo biochemical "rejuvenation" if incubated with various nutrient mixtures containing inosine following 21 days of storage (15). The difficulty of these previous systems is the content of inosine, which must be removed by washing prior to infusion.

The OAS system reported sharply reduces the potential toxicity risks of adenine in two ways. First, the final concentration of 0.125 mM is 75% less than currently used clinically in Europe, and the toxicity risks are thus reduced concomitantly. Second, recipients of either red cells stored for less than two weeks or all non-red cell components are spared exposure to adenine. This second advantage is best illustrated by exploring how the system would be employed in clinical practice.

An initial design of the bag configuration is illustrated in Figure 3. At the donor center, whole blood is drawn into the primary bag containing only CPD as currently licensed. If plasma and/or platelets for specific component therapy are to be harvested, separation must be done within four hours of phlebotomy. The satellite bags containing these components are then separated and stored separately from the packed red cells. The latter are placed under

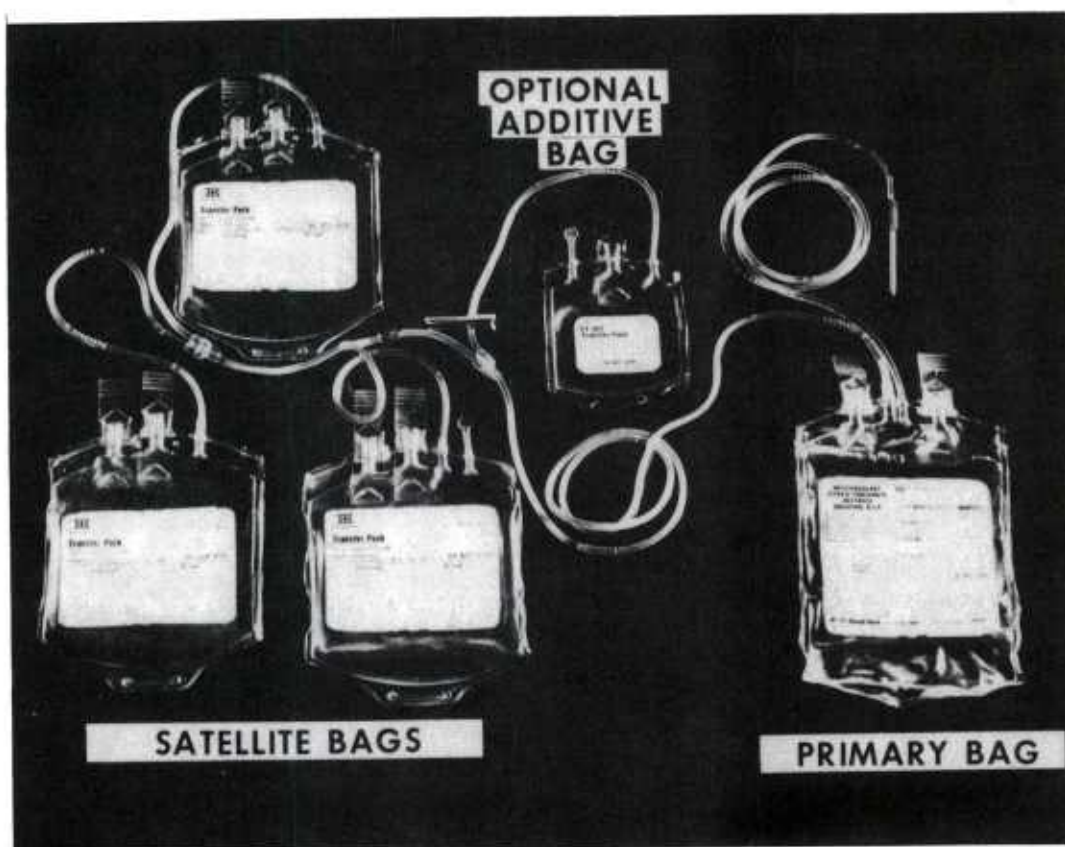


Figure 3: Initial design of the blood bag configuration with the optional additive bag

refrigeration with the integral pouch containing adenine and glucose still attached. Only if the blood had not been infused by day 7 to 14 would the adenine and glucose be added to the red cells. Under current practice the original inlet tube into the primary bag is dielectrically sealed into segments as a source of cells for performing crossmatches. In the OAS system, these segments would be discarded at the time of supplementation and the tube between the optional additive pouch and the primary bag segmented to provide cells for crossmatching. The red cells used for crossmatching must be preserved in a manner identical to the infused cells. Military logistics might not always permit supplement precisely on day 7 or 14. The studies suggest that optimal addition any time during the second storage week would yield similar red cell ATP levels.

It requires approximately two minutes of technician time to supplement a unit of red cells and seal the transfer tubing into new crossmatch segments. Although exact costs of the new bag configuration can only be estimated, it should not yield a negative cost-benefit ratio. We have determined that the additive as described will tolerate autoclaving. The system is fully compatible with current CPD, and thus with current civilian blood bank practice.

Not only will all non-red cell components be spared exposure to adenine, but maximum plasma harvest is possible. When a unit is packed to an hematocrit of 90%, less nutrients are available to support red cell storage. The proposed additive has been designed to permit storage of tightly packed red cells without an undue loss of red cell ATP.

The OAS advocated has the desired characteristics of a preservative solution, and affords an approach to red cell storage designed to fulfill the unique military requirements.

The authors wish to acknowledge the technical assistance of SP5 Victor Cheong.

#### REFERENCES

1. Simon ER, Chapman RG, Finch CA: Adenine in red cell preservation. J Clin Invest 41:351-359, 1962.
2. Shields CE, Bunn HF, Litwim SD, et al: Clinical evaluation of transfused blood after long term storage in ACD with adenine. Transfusion 9:246-250, 1969.
3. Spielmann W, Seidl S: Summary of clinical experience in Germany with preservative-anticoagulant solutions with newer additives, in Greenwalt TJ, Jamieson GA (eds): The Human Red Cell In Vitro, New York, Grune & Stratton, 1974, pp 255-275.
4. Hogman CF, Akerblom O, Arturson G, et al: Experience with new preservatives: summary of the experiences in Sweden, in Greenwalt TJ, Jamieson GA (eds): The Human Red Cell In Vitro, New York, Grune & Stratton, 1974, pp 217-254.
5. Zuck TF, Bensinger TA: Implications of sterile docking devices. Transfusion 15:399-401, 1975.

6. Zuck TF, Bensinger TA: Beneficial effects on red cell adenosine triphosphate (ATP) of delayed addition of glucose and adenine. Transfusion 15:517, 1975.
7. Bensinger TA, Zuck TF: Additional studies concerning the metabolism of packed erythrocytes in CPD adenine. Transfusion, In press.
8. Bensinger TA, Metro J, Beutler E: In vitro metabolism of packed erythrocytes stored in CPD-adenine. Transfusion 15:135-139, 1975.
9. Beutler E: Red Cell Metabolism: A Manual of Biochemical Methods, ed 2, New York, Grune & Stratton, 1975.
10. Bensinger TA, Metro J, Beutler E: Redesigned apparatus for anaerobic measurement of blood pH at low temperatures. Amer J Clin Path 63:264-268, 1975.
11. Dern JR, Brewer CJ, Wiorkowski JJ: Studies on the preservation of human blood. II. The relationship of erythrocyte adenosine triphosphate levels and other in vitro measures to red cell storage ability. J Lab Clin Med 69:968-978, 1967.
12. Wood L, Beutler E: The viability of human blood stored in phosphate adenine media. Transfusion 7:401-408, 1967.
13. Strumia MM, Strumia PV: Conditions affecting the maintenance of adenosine triphosphate, 2,3 diphosphoglycerate and oxygen dissociation by addition of adenine and inosine to blood stored at 1C. Transfusion 12:68-74, 1972.
14. Strumia MM, Strumia PV, Eusebi AJ: The preservation of blood for transfusion. VII. Effect of adenine and inosine on the adenosine triphosphate and viability of red cells when added to blood stored from zero to seventy days at 1C. J Lab Clin Med 75:244-249, 1970.
15. Valeri CR, Zargoulis CG: Rejuvenation and freezing of outdated stored human red cells. NEJM 287: 1307-1313, 1972.





A PROJECTILE PENETRATION THEORY  
FOR LAYERED TARGETS

ROBERT S. BERNARD  
U. S. ARMY ENGINEER WATERWAYS EXPERIMENT STATION  
VICKSBURG, MISSISSIPPI 39180

INTRODUCTION

Projectile penetration has been studied by military engineers since ancient times, but the analytical investigation of this phenomenon was not undertaken until the eighteenth century. Robins (1), Euler (2), and Poncelet (3) developed the first empirical equations describing the axial force which opposes the motion of a rigid projectile as it passes through a deformable solid target. Experimental data consisting of impact velocity and final depth of penetration were used to estimate the coefficients in the relation between axial force and projectile velocity. However, these coefficients were not specified in terms of standard material properties, and so they were applicable only for the particular targets for which they were determined.

Since the mid-twentieth century, the availability of high-speed digital computers has made it possible to analyze the projectile/target interaction by means of two-dimensional finite-difference techniques. The constitutive relations for both the target and the projectile can be accurately specified, and many of the details in the penetration process can be realistically simulated. Analyses of this kind are valuable because of the detailed information which they provide, but they are usually too costly and cumbersome for large scale parameter studies.

In recent years, significant progress has been made toward the development of a simple relation between penetration resistance and fundamental target properties such as density and compressive

strength. Bishop, Hill, and Mott (4) analyzed the quasistatic expansion of spherical and cylindrical cavities in metals and observed a correlation between the resistance to cavity expansion and the resistance to indentation by a rigid static punch. Goodier (5) used an analogy with the dynamic expansion of spherical cavities in metals to develop a penetration theory for rigid spherical projectiles. In the present work, the quasistatic expansion of a spherical cavity in a concentrically layered medium will be analyzed in order to obtain an approximation for the radial stress at the surface of a slowly expanding spherical cavity in a vertically layered medium with a plane interface. This approximation will then be used to construct a simple equation of motion for a rigid cylindrical projectile (with a conical or ogival nose shape) which penetrates a layered target.

#### SPHERICAL CAVITY EXPANSION IN A CONCENTRICALLY LAYERED MEDIUM

Consider a slowly expanding spherical cavity surrounded by an infinite medium composed of two distinct concentric layers (Figure 1). The materials surrounding the cavity exhibit elastic-

plastic behavior without volume change (Figure 2). The geometry is spherically symmetric and the material equation of equilibrium is

$$\frac{d\sigma_r}{dr} + \frac{2}{r} (\sigma_r - \sigma_\theta) = 0 \quad (1)$$

where  $r$  is the radial coordinate and  $\sigma_r$  and  $\sigma_\theta$  are respectively the radial and circumferential components of stress. (Compressive stress and strain are taken to be positive.) The stress-strain relation for the material in the elastic state is

$$\sigma_r - \sigma_\theta = \frac{2}{3} E(\epsilon_r - \epsilon_\theta) \quad (2)$$

and in the plastic state it is

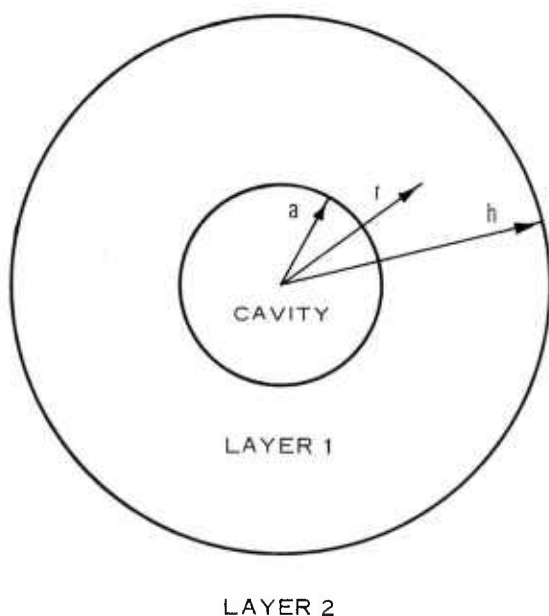


Figure 1. Slowly expanding spherical cavity in a concentrically layered medium

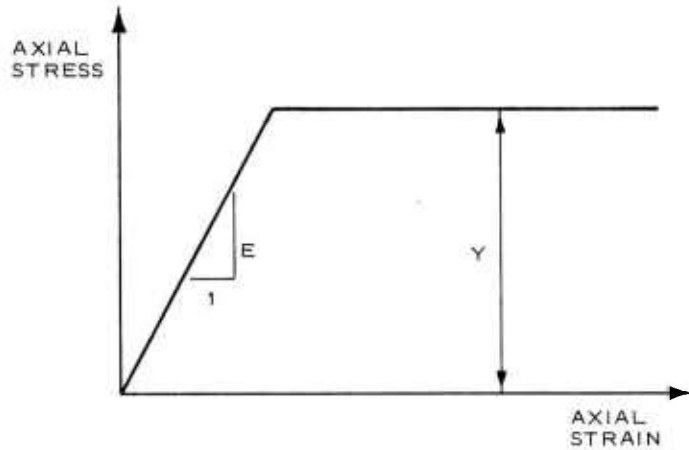


Figure 2. Material response to uniaxial stress

$$\sigma_r - \sigma_\theta = Y \quad (3)$$

where  $E$  is the elastic modulus,  $Y$  is the compressive strength, and  $\epsilon_r$  and  $\epsilon_\theta$  are respectively the radial and circumferential strains. Both materials are incompressible, and the relation between  $\epsilon_r$  and  $\epsilon_\theta$  is

$$\epsilon_r + 2\epsilon_\theta = 0 \quad (4)$$

Equations 2 and 4 are now combined so that the stress-strain relation in the elastic state becomes

$$\sigma_r - \sigma_\theta = -2E\epsilon_\theta \quad (5)$$

The circumferential strain at any radial position is given by

$$\epsilon_\theta = -\ln \frac{r}{r_0} \quad (6)$$

where  $r_0$  is the initial radial position of a material particle which has been displaced to position  $r$ . Assuming that the spherical cavity expands from a small initial radius  $a_0$  to an instantaneous radius  $a \gg a_0$ , the principle of conservation of mass requires that

$$r^3 - r_0^3 = a^3 - a_0^3 \approx a^3 \quad (7)$$

When Equation 7 is rearranged, it follows that

$$\frac{r^3}{r_o^3} \approx \left(1 - \frac{a^3}{r^3}\right)^{-1} \quad (8)$$

and the expression for the circumferential strain becomes

$$\epsilon_\theta \approx \frac{1}{3} \ln \left(1 - \frac{a^3}{r^3}\right) \quad (9)$$

Restricting attention to small strains in the elastic state, Equation 9 is further approximated by

$$\epsilon_\theta \approx -\frac{1}{3} \frac{a^3}{r^3} \quad (10)$$

and the stress-strain relation in the elastic state now becomes

$$\sigma_r - \sigma_\theta \approx \frac{2}{3} E \frac{a^3}{r^3} \quad (11)$$

Combining Equation 1 alternately with Equations 3 and 11, the material equation of equilibrium in the plastic state is

$$\frac{d\sigma_r}{dr} = -\frac{2}{r} Y \quad (12)$$

and in the elastic state it is

$$\frac{d\sigma_r}{dr} = -\frac{4}{3} E \frac{a^3}{r^4} \quad (13)$$

Each material layer may contain distinct elastic and plastic regions (Figure 3) which are separated by spherical plastic "fronts" located at  $r = b$  and  $r = k$  in layers 1 and 2, respectively. It is obvious from Figure 3 that  $b \leq h$  since the plastic region in layer 1 cannot extend beyond the location of the layer interface at  $r = h$ . Similarly, it follows that  $k \geq h$  in layer 2. Evaluating Equations 12 and 13 at  $r = b$  and  $r = k$  and equating the right-hand sides at each of these locations, then it is found that

$$b = a \left( \frac{2E_1}{3Y_1} \right)^{1/3}, \quad \frac{2E_1}{3Y_1} \leq \frac{h^3}{a^3} \quad (14)$$

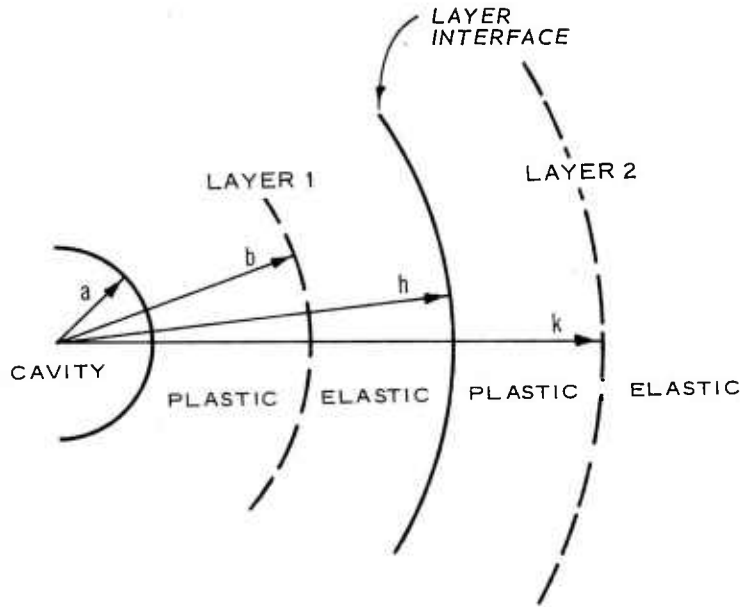


Figure 3. Location of concentric elastic and plastic regions surrounding cavity

$$b = h, \quad \frac{2E_1}{3Y_1} \geq \frac{h^3}{a^3} \quad (15)$$

and that

$$k = h, \quad \frac{2E_2}{3Y_2} \leq \frac{h^3}{a^3} \quad (16)$$

$$k = a \left( \frac{2E_2}{3Y_2} \right)^{1/3}, \quad \frac{2E_2}{3Y_2} \geq \frac{h^3}{a^3} \quad (17)$$

where the subscripts 1 and 2 indicate the evaluation of quantities in layers 1 and 2, respectively. Denoting the initial radial position of the layer interface by  $h_0$  and evaluating Equation 7 at  $r = h$ , the relation between the cavity radius and the position of the layer interface becomes

$$h^3 \approx h_0^3 + a^3 \quad (18)$$

The positions of the layer interface and the plastic

fronts are now completely specified in terms of the cavity radius, and Equations 12 and 13 can be integrated to determine the radial stress  $\sigma$  at the cavity surface:

$$\sigma = \int_{\infty}^a \frac{d\sigma_r}{dr} dr = -\frac{4}{3} E_2 a^3 \int_{\infty}^k \frac{dr}{r^4} - 2Y_2 \int_k^h \frac{dr}{r} - \frac{4}{3} E_1 a^3 \int_h^b \frac{dr}{r^4} - 2Y_1 \int_b^a \frac{dr}{r} \quad (19)$$

It is assumed that  $\sigma_r \rightarrow 0$  as  $r \rightarrow \infty$ , and, upon evaluation of the integrals, Equation 19 reduces to

$$\sigma = 2Y_1 \ln \frac{b}{a} + \frac{4}{9} E_1 \left( \frac{a^3}{b^3} - \frac{a^3}{h^3} \right) + 2Y_2 \ln \frac{k}{h} + \frac{4}{9} E_2 \frac{a^3}{k^3} \quad (20)$$

#### SPHERICAL CAVITY EXPANSION IN A VERTICALLY LAYERED MEDIUM

Consider an infinite medium composed of two distinct vertical layers separated by a plane interface (Figure 4). A slowly

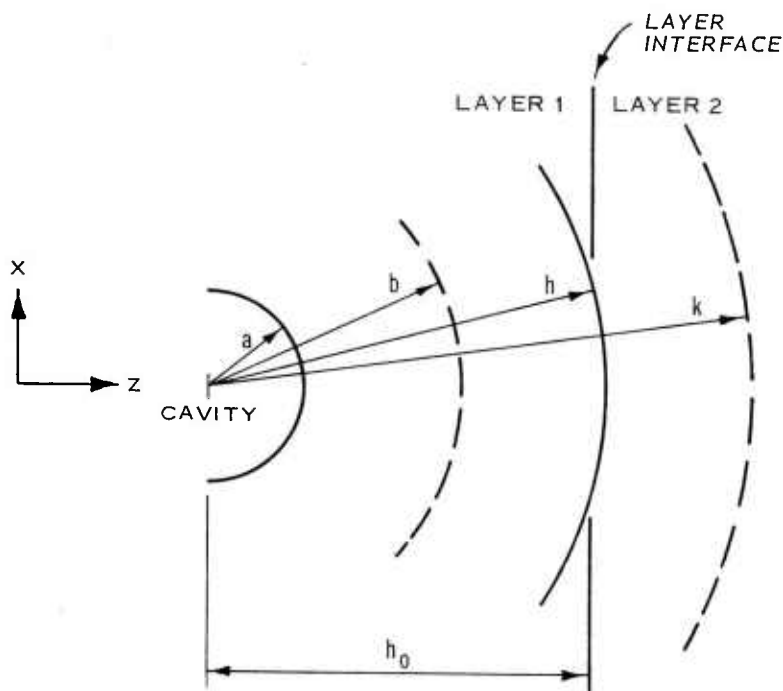


Figure 4. Slowly expanding spherical cavity in a vertically layered medium



expanding spherical cavity is centered on the  $z$ -axis at a distance  $h_0$  from the left side of the layer interface. A first-order approximation for the radial stress  $\sigma$  on the right hemisphere of the cavity surface can be obtained by regarding the vertical layers as quasi-concentric layers with the initial position of the layer interface located at a radial distance  $r = h_0$  from the center of the cavity. The effective radial position of the layer interface is then given by Equation 18, and the first-order approximation for  $\sigma$  is given by Equation 20.

#### PROJECTILE EQUATION OF MOTION IN A VERTICALLY LAYERED MEDIUM

Projectile penetration and spherical cavity expansion represent geometrically dissimilar processes. Nevertheless it has been observed that the axial force which opposes penetration is more or less proportional to  $\sigma$  at low velocities in materials which are composed of a single semi-infinite layer (4,5). It has been further observed that the relation between final depth and impact velocity is approximately linear for deep penetration (5), which implies a possible linear relation between the axial resisting force and the projectile velocity.

These observations will now be used as guidelines in the formulation of an ad hoc expression for the effective stress normal to the frontal surface of a penetrating projectile.

Consider a rigid axisymmetric projectile which penetrates a semi-infinite target composed of two distinct vertical layers (Figures 5 and 6). The projectile axis of symmetry coincides with the direction of motion, which is normal to the target surface. The quantity  $\sigma$  contains the pertinent dimensions and material properties of the target

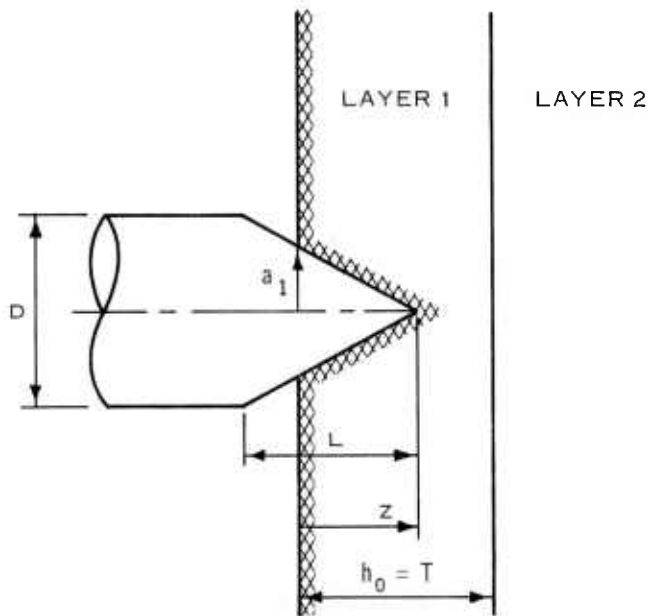


Figure 5. Projectile with frontal surface partially embedded in a two-layer target

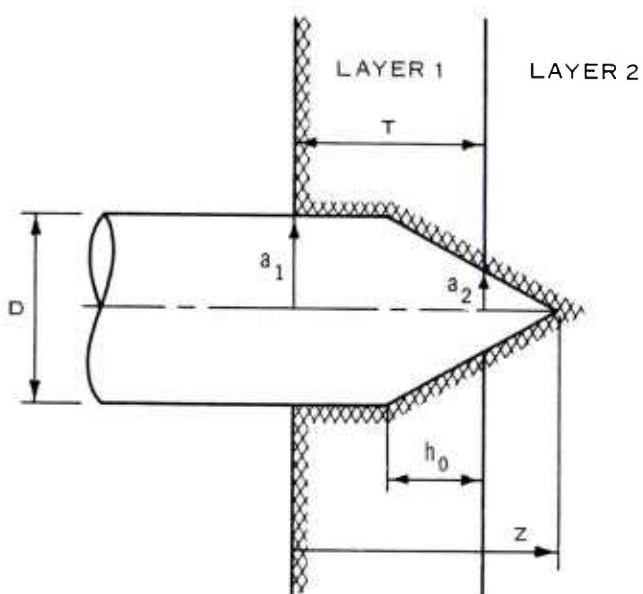


Figure 6. Projectile with frontal surface in contact with both target layers at the same time

as they relate to spherical cavity expansion, and this quantity will be used as a scaling function in the determination of the axial force which opposes the motion of the projectile.

Denoting the projectile velocity by  $v$  and the target density by  $\rho$ , the following ad hoc expression is proposed for the effective stress  $\sigma_n(1)$  normal to any portion of the projectile frontal surface which is in contact with layer 1:

$$\sigma_n(1) = (1 + \sin \alpha) \sigma_1 + v \sqrt{\rho_1 \sigma_1} \quad (21)$$

The subscripts 1 and 2 are used to designate the evaluation of quantities in layers 1 and 2, respectively. For conical nose shapes, the quantity  $\alpha$  represents the cone half-angle, which is related to the nose length  $L$  and the base diameter  $D$  by

$$\sin \alpha = \left( \frac{4L^2}{D^2} + 1 \right)^{-1/2} \quad (22)$$

For ogival nose shapes,  $\alpha$  represents the cone half-angle at the nose tip, which is related to the ogive caliber radius (CRH) and to  $L$  and  $D$  by

$$\sin \alpha = \frac{(4\text{CRH} - 1)^{1/2}}{2\text{CRH}} = \frac{4L/D}{4L^2/D^2 + 1} \quad (23)$$

The evaluation of  $\sigma_1$  by equation 20 is the same as the evaluation of  $\sigma$  for an equivalent spherical cavity with a radius equal to the maximum radius of contact  $a_1$  between the projectile and layer 1 (Figure 5). When the frontal surface is only partially embedded in

the target, the equivalent spherical cavity is centered at the target surface, i.e.

$$h_0 = T, \quad z \leq L \quad (24)$$

where  $T$  is the thickness of layer 1 and  $z$  is the penetration depth. When the frontal surface is fully embedded in the target, the equivalent spherical cavity is centered at the base of the nose, i.e.

$$h_0 = T - z + L, \quad L \leq z \leq T + L \quad (25)$$

The evaluation of  $b$ ,  $k$ , and  $h$  is the same as in Equations 14-18 with  $a = a_1$ .

In accordance with Equation 21, the effective stress  $\sigma_n(2)$  normal to any portion of the frontal surface which is in contact with layer 2 is

$$\sigma_n(2) = (1 + \sin \alpha) \sigma_2 + v \sqrt{\rho_2 \sigma_2} \quad (26)$$

The evaluation of  $\sigma_2$  is the same as the evaluation of  $\sigma$  for an equivalent spherical cavity with a radius equal to the maximum radius of contact  $a_2$  between the projectile and layer 2 (Figure 6). This equivalent cavity is centered at the layer interface ( $h_0 = 0$ ), and Equation 20 reduces to

$$\sigma_2 = \frac{2}{3} Y_2 \left( 1 + \ln \frac{2E_2}{3Y_2} \right) \quad (27)$$

Tangential stresses are neglected, and the axial component of the effective normal stress is integrated over the embedded portion of the frontal surface. The projectile equation of motion then becomes:

$$m \frac{dv}{dt} = -\pi a_1^2 \sigma_n(1), \quad z \leq T \quad (28)$$

$$m \frac{dv}{dt} = -\pi (a_1^2 - a_2^2) \sigma_n(1) - \pi a_2^2 \sigma_n(2), \quad T \leq z \leq T + L \quad (29)$$

$$m \frac{dv}{dt} = -\pi a_2^2 \sigma_n(2), \quad z \geq T + L \quad (30)$$

where  $m$  is the projectile mass and  $t$  is time. The right-hand side of the equation of motion represents the total axial force

exerted on the projectile by the target.

Whenever the condition  $\sigma_n(2) \geq \sigma_n(1)$  is satisfied, the material in layer 1 undergoes contained plastic flow, and Equation 21 represents a reasonable approximation for  $\sigma_n(1)$ . However, if this condition is not satisfied, then the containment provided by layer 2 may be insufficient to prevent a loss of cohesion in layer 1, and Equation 21 then represents an upper bound for the value of  $\sigma_n(1)$ . In this event, a lower bound can be obtained for  $\sigma_n(1)$  by introducing the following "plastic interface criterion:"

If  $\sigma_n(2) < \sigma_n(1)$  when  $b = h$  (i.e. when the spherical plastic front located at  $r = b$  reaches the effective layer interface located at  $r = h$ ), then Equation 21 is replaced by

$$\sigma_n(1) \approx \sigma_n(2) = (1 + \sin \alpha)\sigma_2 + v\sqrt{\rho_2\sigma_2} \quad (31)$$

#### PENETRATION AND PERFORATION OF CONCRETE SLABS

Canfield and Clator (6) have investigated the high speed penetration of steel projectiles into thick slabs of 5000-psi reinforced concrete, and their experimental results are shown in Figure 7. The projectile characteristics are  $m = 5.9$  kg,  $D = 76.2$  mm, and  $CRH = 1.5$  (ogival nose shape,  $L/D = 1.12$ ). The target properties are  $\rho = 2.31$  gm/cm<sup>3</sup>,  $E = 240$  kbar, and  $Y = 0.347$  kbar. The projectile equation of motion developed in the present work is integrated to obtain the theoretical relation between final depth and impact velocity (Figure 7), based on the assumption of a single semi-infinite layer of homogeneous concrete. The empirical results shown in Figure 7 are obtained from a penetration nomogram for concrete developed by the National Research Council (NRC) committee on passive protection against bombing (7). The NRC nomogram is allegedly accurate to within 15 percent, and the agreement achieved among the empirical, experimental, and theoretical results is typical for cohesive targets in which the distance from the nose tip to the back face of the target is large in comparison with the projectile diameter ( $T - z \gg D$ ).

The results shown in Figure 7 provide partial verification of the applicability of the theory for cohesive targets composed of a single semi-infinite layer. Now, in order to make an assessment of the applicability for targets composed of distinct layers, the theory is used to calculate the penetration and perforation of a concrete slab of finite thickness. This represents an example of a

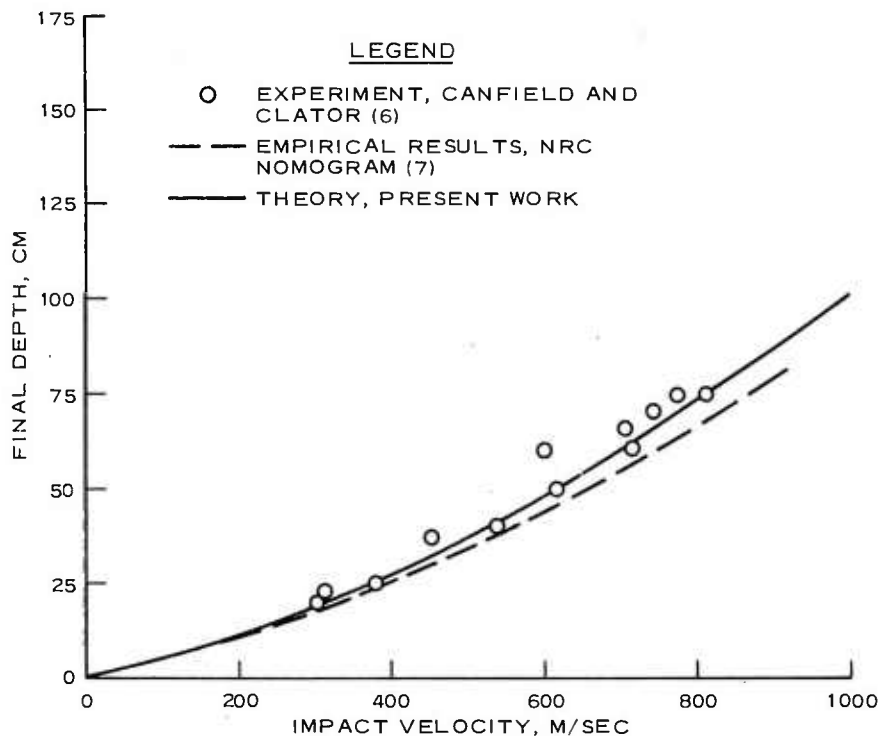


Figure 7. Penetration performance of 76-mm steel projectile in a semi-infinite slab of 5000-psi concrete

two-layer configuration in which the first layer (concrete) has a finite strength and density while the second layer (air or vacuum) has a negligible strength and density. The concrete properties and the projectile characteristics are identical with those used in the foregoing calculation for a semi-infinite concrete slab, but in the present calculation the projectile equation of motion is integrated numerically to determine the minimum impact velocity required for complete perforation\* of a slab with a given finite thickness. The theoretical results are compared with empirical results in Figure 8. The empirical results are obtained from an NRC perforation nomogram for concrete slabs (7) which is allegedly accurate to within 15 percent.

Two sets of theoretical results are presented in Figure 8,

---

\* Complete perforation means that the projectile frontal surface passes completely through the slab, achieving a penetration depth  $z \geq T + L$  (Figures 5 and 6).

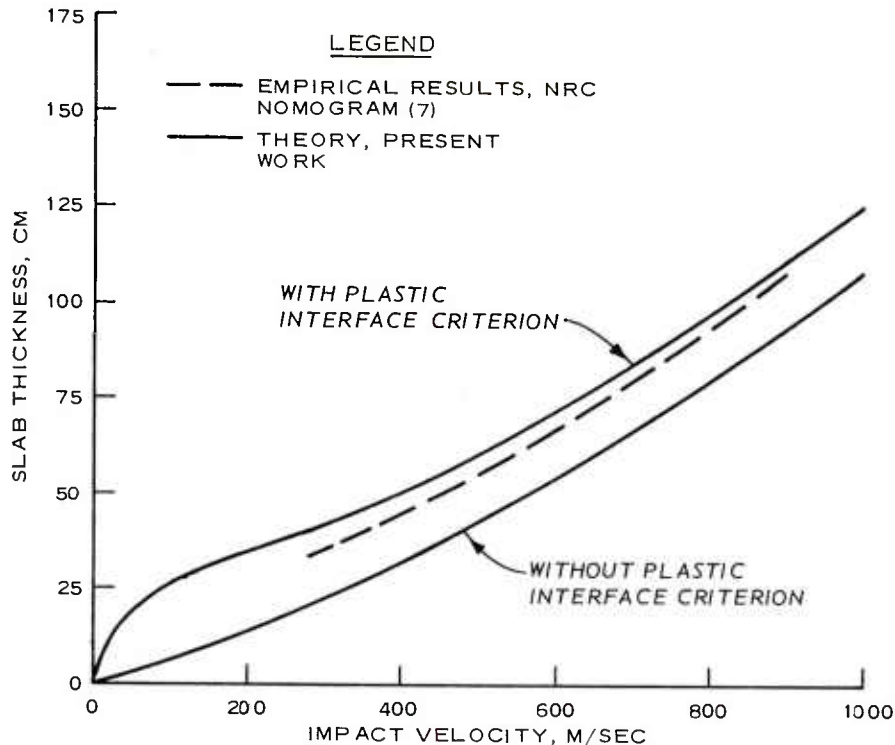


Figure 8. Minimum thickness of 5000-psi concrete required to prevent complete perforation by a 76-mm steel projectile

corresponding to calculations made with and without the plastic interface criterion (Equation 31). The theoretical results form a fairly tight band about the empirical results, but the calculations made with the plastic interface criterion produce the best agreement with the NRC nomogram. The end points of the empirical curve coincide with the ranges of impact velocity and slab thickness for which the nomogram is applicable.

#### CONCLUSION

The projectile equation of motion which has been developed herein appears to be applicable for cohesive slabs and layered targets in which the thickness of a given slab or layer is greater than the projectile base diameter by at least a factor of five. The spherical cavity expansion analysis, which is used as the basis of the penetration theory, is inappropriate when the diameter of the projectile is comparable with the dimensions of the target. The analysis of the penetration of thin target layers ( $T \lesssim D$ ) requires



a different conceptual approach which lies beyond the scope of the present work. The theory can be used to calculate the instantaneous deceleration, velocity, and position of a rigid cylindrical projectile (with conical or ogival nose shape) when the direction of motion is coincident with the projectile axis of symmetry and normal to the target surface. The details of the target motion are not predicted by the theory, which relies on a highly idealized model of the projectile/target interaction. Two-dimensional finite-difference solutions represent the only means presently available for assessing the details of the target behavior during the penetration process.

## REFERENCES

1. B. Robins, New Principles of Gunnery, London, 1742.
2. L. Euler, Neue Grundsätze der Artillerie, Berlin; reprinted as Euler's Opera Omnia, Druck und Verlag von B. G. Teubner, Berlin, 1922, first edition, p. 450.
3. J. V. Poncelet, Cours de Mecanique Industrielle, 1829, first edition.
4. R. F. Bishop, R. Hill, and N. F. Mott, "The Theory of Indentation and Hardness Tests," Proceedings, London Physical Society, Vol 57, 1945, pp. 147-159.
5. J. N. Goodier, "On the Mechanics of Indentation and Cratering in Solid Targets of Strain-Hardening Metal by Impact of Hard and Soft Spheres," Proceedings, Seventh Hypervelocity Impact Symposium, Vol III, Tampa, Fla., Feb 1965, pp. 215-260.
6. J. A. Canfield and I. G. Clator, "Development of a Scaling Law and Techniques to Investigate Penetration in Concrete," NWL Report No. 2057, U. S. Naval Weapons Laboratory, Dahlgren, Va., Aug 1966.
7. "Terminal Ballistics and Explosive Effects," National Research Council, Committee on Passive Protection against Bombing, Washington, D. C., Oct 1943.

BERNARD

#### ACKNOWLEDGMENTS

This work was sponsored by the Defense Nuclear Agency under Subtask SB211, Work Unit 09, "Earth Penetrator Calculation Studies and Comparative Analysis with Field Measurements." The application of the cavity expansion analysis to the projectile penetration problem for layered targets was originally suggested by Professor S. V. Hanagud, Georgia Institute of Technology, Atlanta, Georgia.

## A NEW PHOTOGRAMMETRIC COMPARATOR DESIGN (U)

ANDREW J. BONDURANT, JR.  
US ARMY ENGINEER TOPOGRAPHIC LABORATORIES  
FORT BELVOIR, VIRGINIA 22060

## INTRODUCTION

During the early 1970's, the US Army Engineer Topographic Laboratories (ETL) was tasked to develop a target location system for use with the Lance Missile. This effort resulted in the development of the Analytical Photogrammetric Positioning System or APPS which was subsequently type classified and fielded. As the name implies, the system employs analytical photogrammetric techniques to derive three-dimensional target coordinates.

Because of the success of the APPS and their more stringent positioning requirements, the Defense Mapping Agency Aeronautical Center requested ETL to develop an improved version of the APPS. It was first attempted to contract this development to some commercial firm; however, due to a lack of responsive bidders and the high cost of those bids received, it was decided to develop the system in-house. This paper describes the comparator component of the improved APPS.

A photogrammetric comparator is an instrument for making precision X-Y measurements on a photograph, usually an aerial photograph. The primary components of a comparator consist of a set of optics for observing the image point of interest, a photocarriage (X-Y stage) for positioning the photograph so that the point of interest coincides with the measuring reference, and a system for measuring rectilinear coordinates. A stereocomparator, such as the one under discussion, consists of two of each of these components so that corresponding images on overlapping pairs of photographs can be stereoscopically viewed and simultaneously measured.

Precision photogrammetric comparators are characteristically large and expensive, and require skilled operators as well as a laboratory environment. The comparator being described minimizes some of these objections, and at the same time provides improved capabilities.

#### DESCRIPTION

The design of the comparator was influenced by factors other than the classical design criteria. In addition to requirements for accuracy, size, and format accommodation, the schedule for project completion was very short, dictating that the more complex components be readily available. Based upon this consideration, the search for components that could be readily integrated into an operable system began. The following is a description of the three primary subassemblies and the more important reasons for their selection.

Mensuration System. A survey of the market resulted in the selection of a laser transducer manufactured by the Hewlett-Packard Company, possibly the first time a laser has been used in a photogrammetric comparator. Besides providing a measuring scale with extremely high resolution (low least count reading), the laser transducer does not need a direct mechanical connection to the object being measured. This feature makes it ideally suited for monitoring the motion of X-Y stages, as is the case with the photogrammetric comparator. When all the comparator components are optimally positioned, measurements are immune to pitch and yaw of the moving stages.

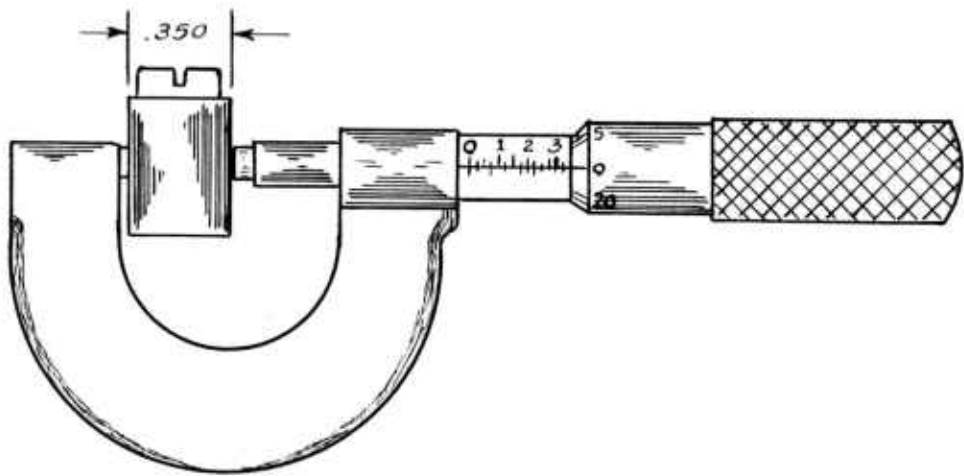
Many years ago a European scientist, Ernst Abbe, postulated two very fundamental design principles to be considered in the construction of a precision mensuration device. They were essentially:

(1) "to base exclusively the measurements in all cases on a longitudinal graduation with which the distance to be measured is directly compared," and

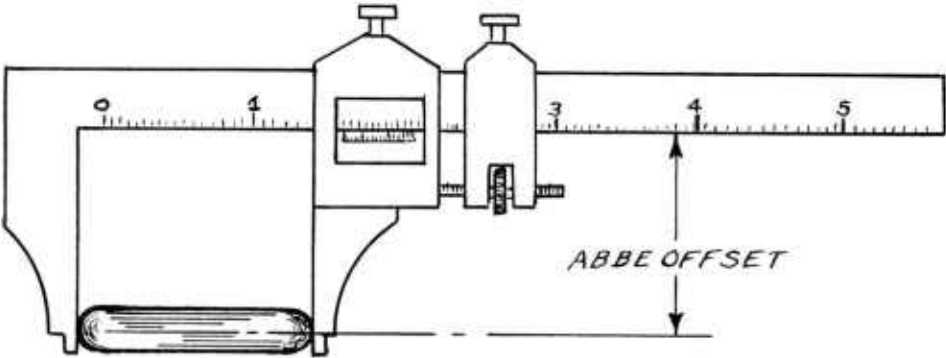
(2) "to design always the measuring apparatus in such a way that the distance to be measured will be the rectilinear extension of the graduation used as a scale."

An excellent example of a very simple device that fulfills these two criteria is the engineer's screw micrometer shown in figure 1. An example of an instrument that satisfies the first principle but not the second is the slide rule caliper shown in figure 2.

In general, Abbe's second principle is not adhered to in instrument design because the measuring device is usually a rotating lead screw or interferometric scale which cannot be physically positioned in rectilinear extension of the object being measured.



MICROMETER  
FIGURE 1



VERNIER CALIPER  
FIGURE 2

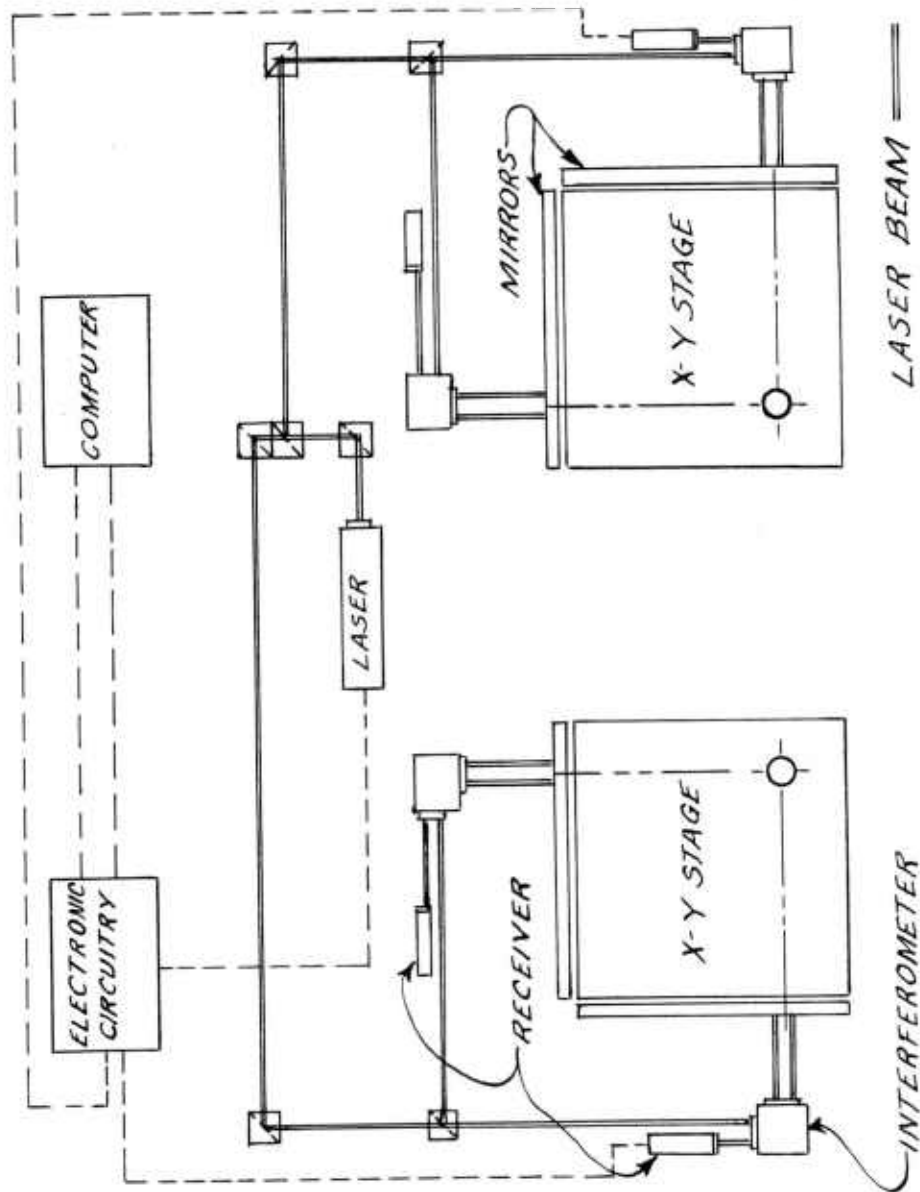
An examination of figure 2 illustrates why such precision components are required when deviating from the rectilinear extension principle. If the right caliper in figure 2 becomes worn so that it rotates about an axis orthogonal to the plane of the paper at the reference mark on the vernier, the measuring error introduced by the rotation is the product of the ABBE-OFFSET and some function ( $\text{Error} = K \cdot \text{OFFSET} \cdot f\phi$ ) of the rotation angle ( $\phi$ ). As the ABBE-OFFSET is minimized, so is the measuring error. With the micrometer shown in figure 1, the ABBE-OFFSET has been reduced to essentially zero and any resulting error can be attributed primarily to inaccuracies of the threaded lead screw.

The placement of the components of the comparator mensuration system is illustrated in figure 3. The two photocarriages freely move in the plane of the paper while the laser interferometers are rigidly positioned at the rear and outside edges of the carriages. Two plane mirrors are attached to each of the photocarriages. Not shown is the stereoscopic viewer used to observe the photographs that would normally be placed on the photocarriages. The operator views a small image area at the position of the circled reticles. To observe a different point, he shifts the photocarriages until the new image appears at the reticle.

The beam of light generated by the laser is split and directed to the four interferometers and to the four mirrors along the sides of the photocarriages. The mirrors reflect the beams back into the interferometers. The phase relationships of the return beams are compared with the outgoing beam by the receiver to detect and measure any change in the path-length between the mirror and the interferometers. The receivers and associated electronic circuitry count the phase reversals which occur at every  $1/2$  wavelength (approximately 0.08 micrometer) of carriage travel. This is the least count reading or resolution of the mensuration system.

In figure 3 if the laser beams emanating from the interferometers were extended beyond the plane mirrors, they would intersect at the measuring reference (reticles). This complies with Abbe's design criteria (rule 2) and minimizes errors resulting from mechanical imperfections in the photocarriages. This is of the utmost significance because it means that the instrument can be built without the massive mechanical components usually required for rigidity and stability. This, plus the fact that it and its associated electronic circuitry and computer interface were readily available, made the laser interferometer a logical choice for use as the mensuration component of the comparator.





SCHEMATIC OF LASER MEASURING SYSTEM  
FIGURE 3

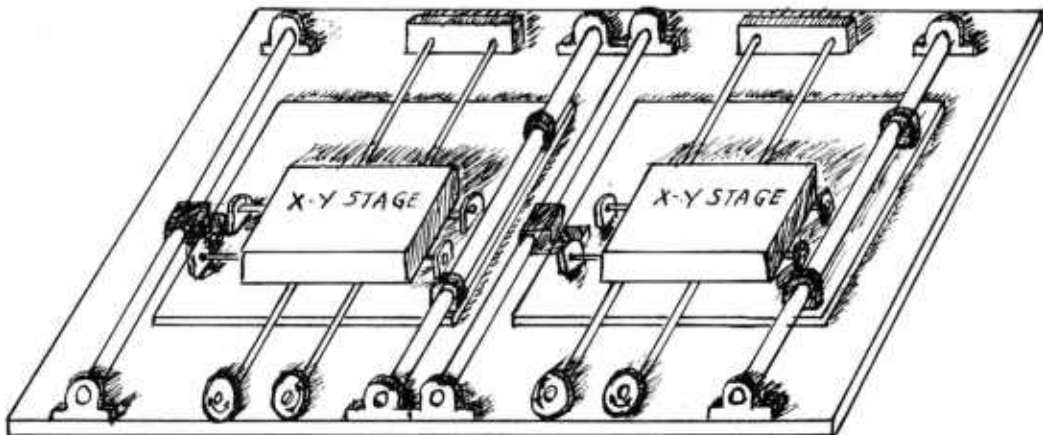
Stereoscopic Viewer. The stereoscopic viewer contains the optics required for viewing the photographic imagery and the photo-carriages which position the desired image points to the measuring reference mark in the center of the optical field of view. The essential detailed requirements for the stereoscopic viewer are as follows:

- a. Must provide a capability for independently varying the magnification ratio of the two optical trains from 6 to 30X.
- b. Must provide  $\pm 180^\circ$  of image rotation in each of the optical trains.
- c. Must be capable of positioning any corresponding image points, regardless of position in the format area, to the measuring reference points.
- d. Must provide measuring reference (reticles).

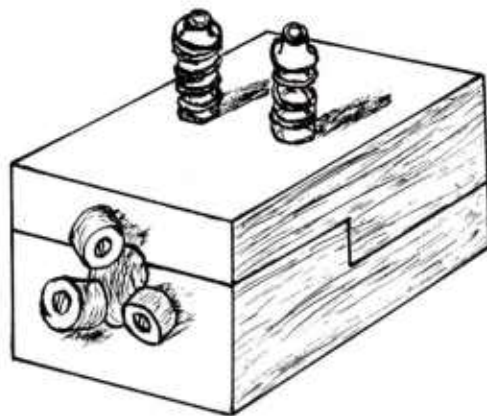
Under contract to ETL, the Bausch and Lomb Company had previously designed and built an instrument with a stereoscopic viewing capability meeting these requirements. It was subsequently produced and sold commercially under the trade name "Micromark." The purpose of the instrument was to view and mark corresponding image points on stereopairs of photographs. Since there was no requirement for a marking capability, the marking component was removed. The photo-carriages were also removed because they used pneumatic support bearings and had other deficiencies which made them unsuitable for comparator use.

The replacement photocarriages were designed and built in-house. Since the laser transducer decreases the dependency of accuracy upon precision mechanical components, components normally used in the construction of machine tools and other similar applications could be used. The supporting and guiding elements of the photocarriages consisted of commercial-grade round shafting and linear ball bushing. Figure 5 is a simplified diagram showing these components.

The X-Y drive (positioning) mechanisms for the carriages were of the threadless lead screw type. Here again, commercial-grade round shafting was used with linear actuators (illustrated in figure 5) manufactured by the Barry Company to make up the drive system. All of the components were relatively inexpensive but achieved the desired result. The threadless lead screw (shaft) simplified the drive system substantially because it eliminated the need for a separate fine- and coarse-positioning mechanism. Coarse positioning is achieved by



*X-Y CARRIAGE  
FIGURE 4*



*LINEAR ACTUATOR  
FIGURE 5*

overriding the friction of the rollers on the shaft by pushing the carriage by hand. The pitch of the rollers on the actuators, which is analogous to the thread pitch on a conventional lead screw, was selected to provide the degree of fine positioning needed.

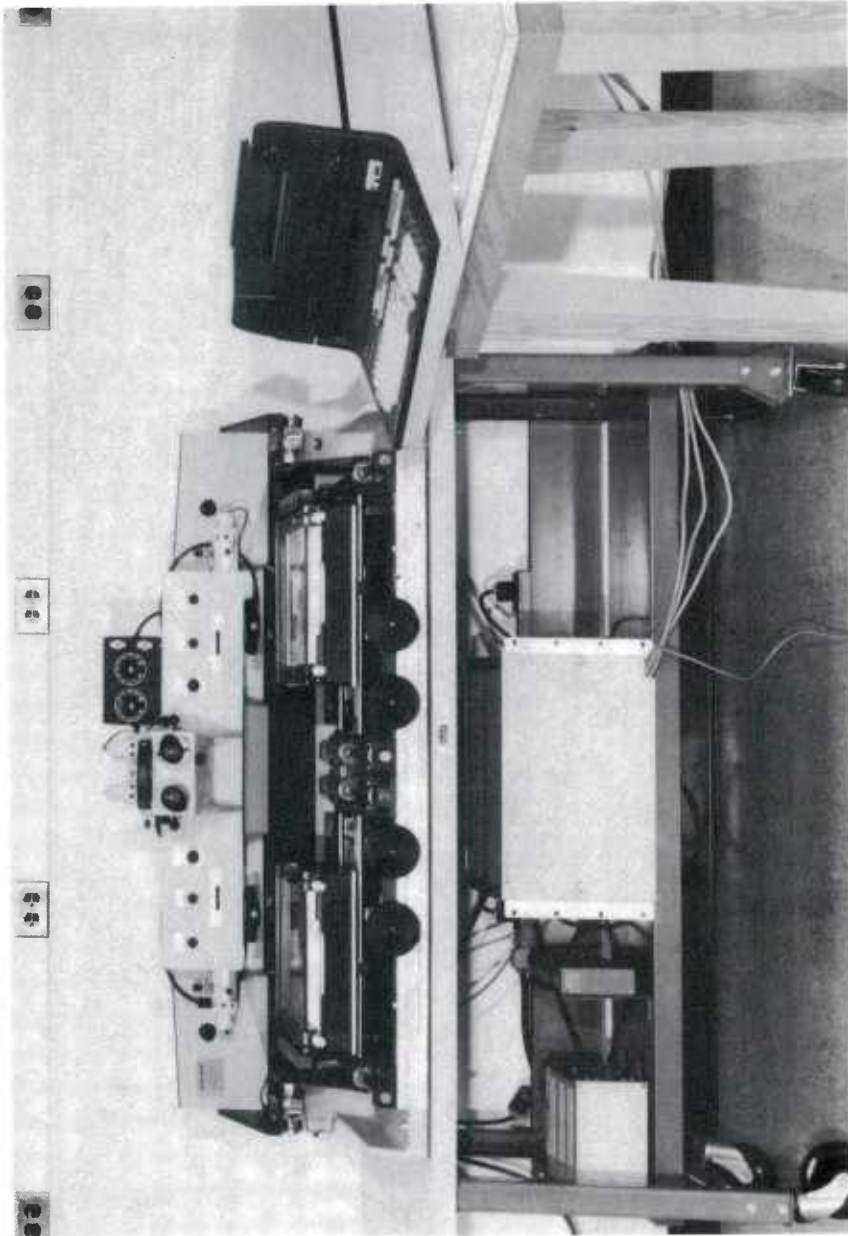
All hardware required for integrating the purchased components onto a functional mensuration system and mounting it on the basic Micromark instrument was designed and fabricated in-house.

Computer/Calculator. If the instrument under discussion were a photogrammetric comparator in the classical sense, a computer/calculator would not be required. The photograph coordinates could be displayed and/or stored by a peripheral device interfaced directly to the measuring system. However, since the ultimate use of this equipment was to compute ground positions of selected image points immediately (in near real time) after their measurement on the photographs, a computing device was required. A computer in the system could also compensate for any consistent and systematic errors by analytical calibration rather than optical or mechanical calibration. This minimized the need for precision mechanical components and adjusting mechanisms, simplified construction of the comparator and reduced its cost.

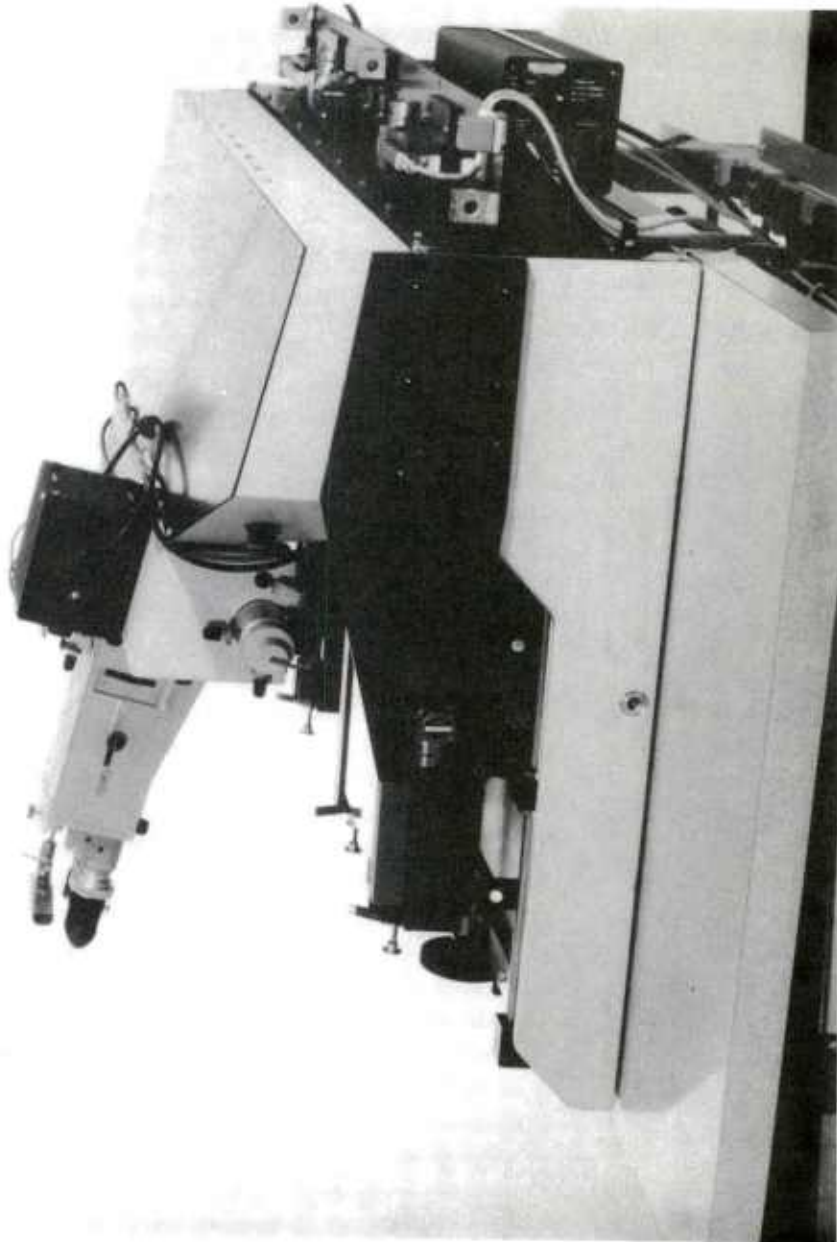
There were several makes and models of programmable calculators and minicomputers with the computing capacity to meet the applicable requirements. The calculator chosen was a Hewlett-Packard Model 9830 with extended memory options. This choice was based primarily upon the fact that the calculator, interface, and mensuration system could all be purchased from the same manufacturer already integrated into a single system; thus saving considerable time, development effort, and money. Some calculator programming was required to enable the printing of coordinates measured with the system.

## RESULTS

The comparator is shown in figures 6 and 7. Figure 6 shows an overall front view of the system. The stereoscopic viewer is the dominant component positioned on the table, with the calculator positioned on its own individual stand on the right side. The electronics associated with the mensuration device are shown on the shelf below the table. Figure 7 shows the laser and some of its associated optics. These components are normally protected by a metal dust cover.



COMPARATOR, FRONT VIEW  
Figure 6



COMPARATOR, REAR VIEW  
Figure 7



## BONDURANT

After the construction of the instrument was completed, the measuring system was analytically calibrated utilizing the following transformation equations:

$$x' = a_1x + a_2y + a_3$$

$$y' = b_1x + b_2y + b_3$$

in which

$x'$ ,  $y'$  are the corrected coordinates

$x$ ,  $y$  are the uncorrected coordinates

$a_1$ ,  $a_2$ ,  $a_3$ ,  $b_1$ ,  $b_2$ , and  $b_3$  are the parameters of the transformation.

The  $a_1$ ,  $a_2$ ,  $b_1$ , and  $b_2$  parameters are recognized as being scalar quantities which correct for scale and nonorthogonality of the measuring axes. The  $a_3$  and  $b_3$  are constants for transforming the origin of the coordinate system.

These parameters were evaluated by measuring a calibrated grid plate, and substituting the known grid values and the measured values into the transformation equations. Since a minimum of 40 grid intersections (producing 80 equations) was used to determine 6 unknowns, a least squares solution was used. Once the parameters were determined, they were stored in the calculator as part of the operating software for application to all subsequent measurements.

The equipment was tested by measuring several calibrated test grids and comparing the measured coordinates with the known coordinates utilizing a least squares technique. Almost without exception, the measuring errors were found to be in the 1- to 2-micrometer (root-mean-square per axis) range. This is the total error which includes operator errors made in positioning the grid intersection at the measuring reference. These accuracies were well within the specified range (10 micrometers max error) and should be sufficient for most photogrammetric applications.

## SUMMARY AND CONCLUSIONS

This paper describes a comparator believed to be unique in many respects. The laser interferometer permits a lightweight, compact design requiring less operating space and making the instrument very portable. The cost of the instrument is relatively low and the

accuracy exceeds that required for most photogrammetric applications. The inclusion of an on-line programmable calculator enables relatively easy calibration of the system and permits near real time computations of the coordinates being measured. With additional programming, the instrument can perform other functions, such as the near real time computation of ground point positions, and any other photogrammetrically related task involving measurements and subsequent computations. The techniques employed in this new instrument represent significant progress in the design of photogrammetric comparators. They also hold great promise for a wide variety of applications in other similar devices.

#### REFERENCES

1. Bender, Lee V., Unpublished lecture notes, Syracuse University, 1966, which references 2 and 3 below.
2. Schwidefsky, D. K. Prof. Dr., "A New Precision Stereocomparator," The South African Journal of Photogrammetry, Vol. 1., No. 3, March 1961.
3. Whitehead, T. N., The Design and Use of Instruments and Accurate Mechanism, Dover Publications, 1954.

REMOTE PORTABLE SOLAR POWERED  
MICROWAVE SYSTEM

MR. ANTHONY G. BOTTONE  
U.S. ARMY YUMA PROVING GROUND  
YUMA, ARIZONA 85364

During the process of testing, development, and evaluation of Army material, data is often required or desired to be transmitted from remote, isolated or rugged locations. Present day methodology regarding communications support of these remote tests and evaluation is limited in flexibility, mobility, bandwidth, and application. In addition, this present day methodology involves reliance on firm-fixed or generator power and presents a drawback of not being able to operate in real-time modes that are essential in support of some missions of the Department of the Army.

To solve the problems mentioned above, a comparatively inexpensive, highly reliable, self contained and simple solution has been devised and successfully tested. A highly efficient microwave transmitter that operates from low voltage D.C. power has been coupled with a photovoltaic solar activated power source (array of solar cells). This combination, using a miniature 8 oz. omnidirectional dish antenna, transmitted a 525 line television presentation of a mission test in real time, over a distance of several miles. The portable solar powered terminal took approximately 15 minutes set up time, and operated successfully for the duration of the test.

A pictorial diagram of this system is shown in Fig 1a. This diagram points out the major (and only) components of the remote terminal. Figure 1b. shows a typical physical concept of the complete remote portable solar powered microwave system.

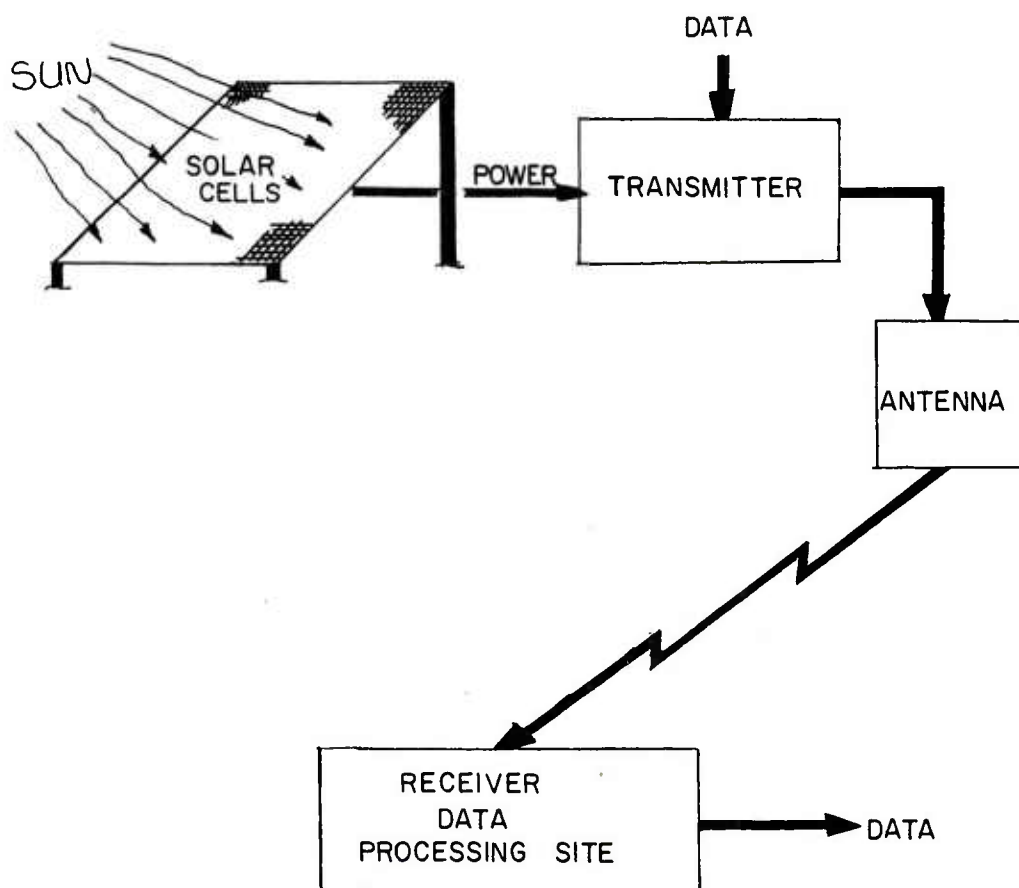


FIG. 1a.  
Pictorial Diagram of Remote Portable Solar  
Powered Microwave System

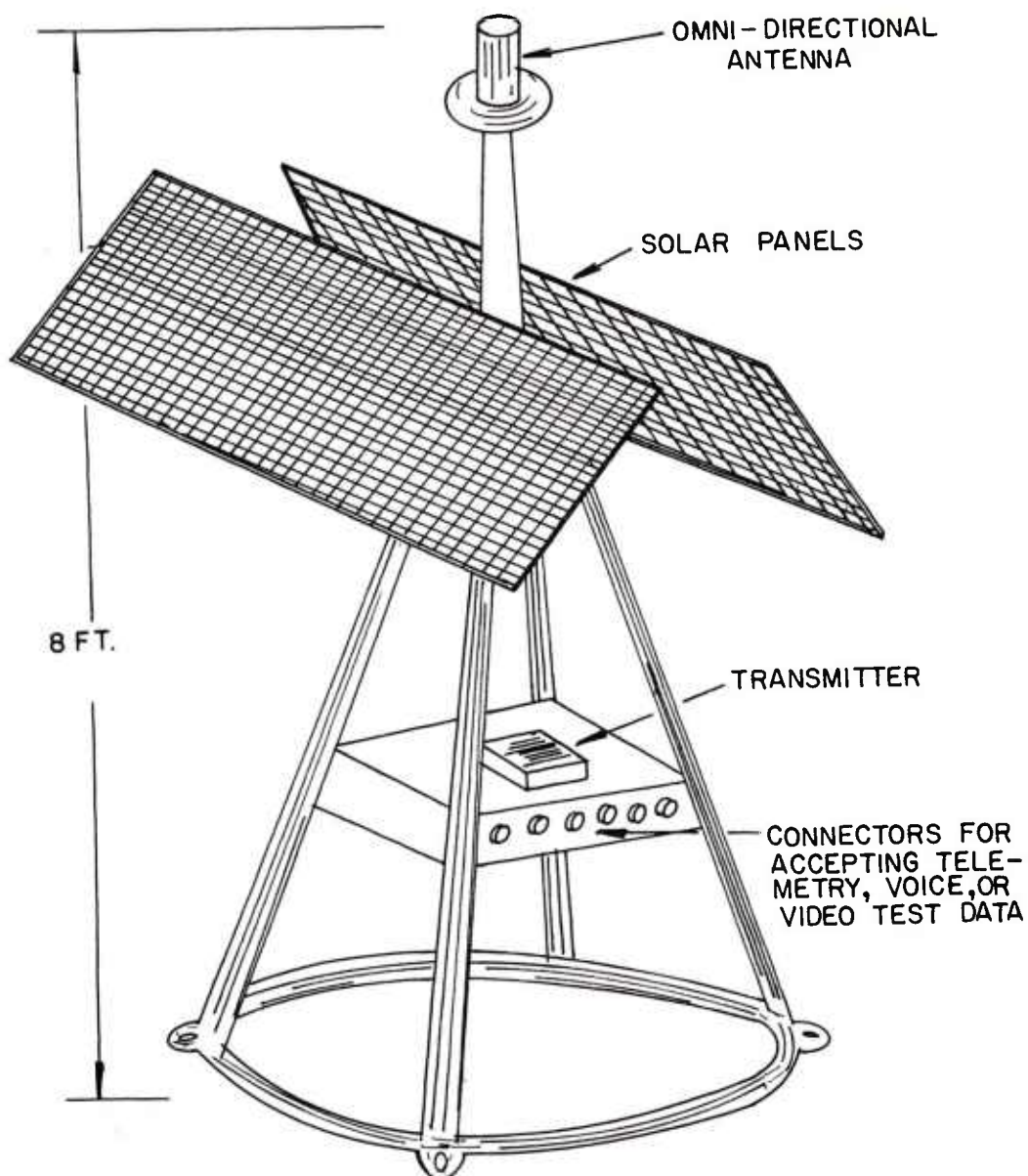


FIG. 1b.  
Typical Physical Concept of Remote-Portable Solar  
Powered Microwave System

To enable a further understanding into the state of the art of photovoltaic energy sources and microwave transmission equipment utilized in the makeup of this system, a summary of present technology is presented below.

#### SOLAR ENERGY POWER SOURCE

Radiated light energy, directly from the sun, diffused by the atmosphere, consists of a stream of energy units called photons. Photons entering solar cells impart energy to the silicon semiconductor material, causing electrons to flow across the semiconductor junction, thereby converting the original light energy to electrical energy.

Using an array concept, practically any voltage and current requirement can be met. The only limitation or constraint would be physical size of the solar array. The number of cells in series determine the module voltage and the number of cells in parallel determine module current capability. The resultant output of a solar array produces ripple-and-noise-free direct current to the load.

To insure that D.C. power is available at all required times (even in darkness, if that is a requirement) and in periods of haze or inclement weather conditions, batteries are used in conjunction with the solar array. This configuration is then nothing more than a solar powered battery charger. The battery stores the current produced in the array and provides energy to the load on demand. A blocking diode insures that the battery doesn't discharge back through the array after dark. Batteries such as the charge retaining, pure lead, lead-antimony and lead-calcium types can be used in this system. These stationary batteries assure very low self-discharge, are easily charged at 95% or more efficiency and can last 15 years or more. They have large electrolyte reserves and require water only once every year or two. A block diagram of a basic power source is shown in Fig. 2.

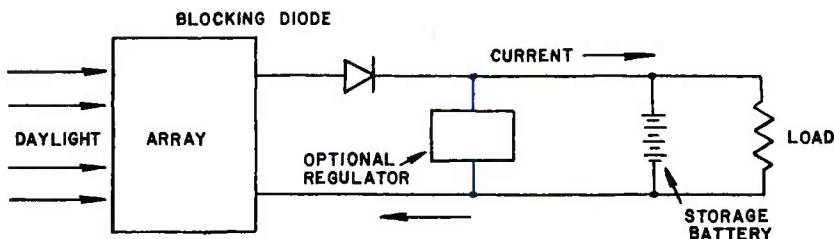


FIG. 2.  
Basic Power System Block Diagram



The solar power source can be utilized in all latitudes of the earth. Any decrease in radiated solar energy in the extreme northern and southern regions can be offset by using a slightly larger array. It is noted that even moderate icing conditions can cause only a small percentage in reduction of output.

#### MICROWAVE TRANSMISSION AND DATA MULTIPLEXING

The present state of the art in microwave transmission equipment coupled with advances in modulation and data multiplexing techniques has greatly enhanced the posture of present day communications technology.

Completely solid state communications transmitters, capable of producing 10-20 watts of R.F. power in the 2000-3000 MHZ carrier frequency range, have been available for the past decade. Their R.F. to D.C. efficiency ratio of typically 25% enables their operation to be powered by a relatively low power D.C. source. It is this characteristic that enables compatibility with a solar power source.

The success of recent efforts to increase the efficiency of photovoltaic conversion, coupled with the comparatively high D.C. to R.F. conversion efficiency of microwave units, permit a communication system to be developed with a wide growth latitude. Such is the case with the remote portable solar powered microwave system. A typical input power requirement for the transmitting component of this system is 28 Volts at 2 Amps. This requirement can easily be accommodated with the solar power system as shown in Fig. 2. The solar array necessary to supply this power would be approximately 8 sq. ft. in size. The compact size of the typical microwave unit itself (sandwich size, 4 lbs. in wt.) in addition to the relatively small size of the solar array makes their combination attractive as a portable system.

Trends in modulation techniques and the electronics of signal processing permit transmission of a significant amount of multiplexed information over a single R.F. carrier. If a requirement is for voice, many hundreds of simultaneous voice conversations can be carried over the modulated output of the portable unit. Similarly, FSK, PCM, FM or other analog or digital data can be transmitted. Even high resolution color video can be relayed. In fact, if the mission so dictates, the complete transmission scheme can be formatted around the particular mission, i.e. a combination of telemetry data and voice, or voice and video, etc.

Solid state signal conditioning equipment, designed to accommodate any chosen and required multiplexing scheme, are powered by a low power D.C. source. In the case of the remote portable terminal, this power is obtained by parallel connection to the solar power unit.

## BOTTONE

Choice of a wide range of R.F. power outputs, multiplexing schemes and data formatting techniques, make the remote solar powered microwave terminal extremely attractive for use as a basic building block in the support of remote tests and evaluation missions.

### SYSTEM CONFIGURATION AND SPECIFICATIONS

Some discussion should be given concerning typical characteristics, both physical and electronic, of the remote portable microwave station. For this typical discussion, assume that T.V. surveillance is needed from a critical remote location, some 8 - 12 miles from a centralized data reduction center or security office. Further, let the surveillance location change, i.e. dictating a mobile requirement.

The configuration for this problem would involve a microwave unit capable of video bandwidth, typically 6.5 MHZ. Depending on the requirement, the unit could operate on a 24 hour basis, or the carrier could be keyed on/off by a separate command link, in which a high efficiency solid state receiver could be in a "listening" mode at all times. This receiver, located at the remote solar powered terminal, would require a very small operating current which can be obtained from the solar source. Once receiving the proper encoded signal the main R.F. video transmitter could be turned on transmitting television on command. This command operation points out an additional feature of this remote unmanned terminal that could be incorporated if the mission so dictates. Similarly, on/off capability could be incorporated for telemetry data.

For purposes of discussion let's assume that a command link is not required, and that transmission of simply a television real-time video presentation is all that is needed. Design calculations such as a classical R.F. path loss, antenna gain, link fade margin are considered routine and hence will not be presented at this point. Once those calculations have been completed, a physical realization of the remote terminal will evolve. This resultant remote terminal configuration, based on the original requirement, would assume the following typical characteristics.

- (1) Transmitter: Input power - 26-32V, 2.0 Amps  
Modulation - FM  
Bandwidth - 6.5 MHZ  
Carrier Frequency - 1700 MHZ - 12.4 GHZ  
Size - 6" x 6" x 1.5  
Wt - 4 Lbs  
Output power - 10 watts

## BOTTONE

- (2) Antenna: Omnidirectional Discone  
Gain 4 dbi  
Wt - 8 oz.  
Size 20 Cubic inches
- (3) Camera: 525 line vidicon  
Input power, 28 volt, 1 Amp  
Output - 4-5 MHZ BW  
Wt - 4 Lbs
- (4) Solar Power Source: 28 Volt nominal  
Output, 6 Amp Capacity Maximum  
Size - approx 8 sq. ft.  
Wt. (with Batteries) - 50 lbs.

The total wt of this sample system is less than 60 lbs. Being light in weight alone makes the self contained system attractive for mission support purposes.

The concept of use of these portable systems in support of Army material and development testing is to keep a pool of these equipments on hand to draw on an as needed basis. This type of arrangement, together with the capability of bandwidth expansion using plug-in modules, enable a wide assortment of tests to be supported using one basic universal communications system.

### COST EFFECTIVENESS

One of the most beneficial aspects of this system, aside from its simplicity, portability and reliability, is its cost effectiveness. To show this, a cost comparison is developed for an approach using direct buried cable and the portable microwave approach to the following problem; transmission of multichannel low speed analog data from an isolated location some 30 miles from a centralized data gathering facility. It is noted that it is presently usual practice to utilize AC powered modems as modulators, and multi pair individually shielded cables as a transmission media. Using this approach, a basic cost estimate and comparison is developed.

#### (1) Cable Approach:

- a. Cost of cable run typically \$6.00 per ft installed is \$950,400.
- b. Today's cost of power line extensions run anywhere from \$10,000 to \$30,000 per mile depending on the terrain. Assuming, for economical or logistical reasons, that a firm fixed power line cannot be installed, the next best choice may be generator sources.

## BOTTONE

c. Cost of generator (typically) is \$3,000. In addition, fuel and maintenance costs can be estimated at \$1,000 per year.

d. Modem cost can be estimated at \$6,000.

Thus for the typical cable/generator/modem approach to this problem, non-recurring costs involved are approximately \$960,000 and recurring costs are \$1000 yearly.

(2) Portable solar powered microwave approach:

(a) Power system - \$6,000

(b) Solid state transmitter/receiver - \$58,000

(c) Signal conditioning, modulators, misc. - \$10,000.

Or, in summary of costing concerning the portable microwave approach, only a non-recurring cost of \$74,000 is involved. Not only would this approach be economically justifiable but intangible benefits of ease of maintenance and reliability could be enjoyed with the remote portable solar powered microwave system approach. Further, this system because of its portability and simplicity, could be moved to another location easily, and the "hard-wired" system could not.

## RELATED CHARACTERISTICS AND CRITERIA

(1) The present methodology of data gathering and analysis that support Army test and evaluation missions in remote areas is limited when real-time operation is required. For example, photography or video taping is commonly used on site, and analyzed later. The remote portable microwave terminal proposed herein relieves this real-time limitation by insuring continuous real-time operation, i.e. transmitting video or data as it happens. This real-time operation becomes especially valuable when some sequence of a test has to be changed (after analyzing data) before the next sequence in testing can be chosen.

(2) The proposed system is self-contained. It depends on no external power sources or mechanical/electrical generating equipment. This feature makes such a system adaptable to the challenging and changing requirements of remote real-time data gathering and communications in support of the testing mission.

(3) No one manufacturer makes this system. The basic system is configured to meet user needs from several components that different manufacturers have "on the shelf".

(4) It was not due to the energy crisis that this system was developed. This system is feasible because of the present design efficiency that is characteristic of the engineering state-of-the-art in microwave equipment and solar energy conversion devices.

(5) Designing a solar power system is essentially a matter of determining the load current requirement in ampere - hours per day (averaged over time), selecting an array that will produce at least that amount of current (averaged over time), in the solar conditions existing at the site and selecting a battery that will carry the load through the periods when little or no energy is produced. A cost effective reliable power design must include evaluation of solar isolation at the site, load analysis, battery selection, temperature and environmental effects, and other considerations.

(6) The variations in solar energy attributable to the earth's rotation (hourly), declination (seasonal) and atmospheric (weather) must all be taken into account in a successful solar power system design. Fortunately, a wealth of excellent solar irradiation data has been recorded daily at hundreds of sites throughout the world for periods ranging up to 40 years. This data (solar isolation) has been measured and recorded in langleys (equal to 1 cal/sq.cm.) falling on a horizontal surface. Because it is actual, recorded data, the daily, seasonal and weather-caused variations are averaged in. To assure reliable performance, the manufacturer of the panels uses computers that store solar history of more than 100 regions of the U.S. and several hundred around the world. Given the site where a system is to be installed, the computer consults the tabulations of solar data to determine the average number of langleys falling in that region each month of the year. It can then select an array large enough to produce the required load current.

(7) During installation, the solar power system is optimized by facing the array directly south and by tilting it to face the sun's path through the sky. Because the historical solar data was collected on a horizontal surface, the computer calculates the corrected langley value for a tilted array.

(8) The current - voltage output from the power source is essentially pure D.C., free of any significant electrical noise and RFI. Because there is no ripple or rectifier noise, no ignition or generator noise, the power system easily meets the requirements of MIL-STD-461. The transmitters, because they are sealed in a metal chassis and operate at very low level currents, also have no difficulty with MIL-STD-461.

(9) Both the transmission equipment and solar power sources are designed to exceed the stringent requirements of MIL-STD-810B for high and low temperatures, temperature shocks, high altitudes, sunshine exposure, explosive atmospheres, rain, blowing sand and dust, high humidity, fungus and salt fog.



## BOTTONE

(10) The portable system is self-contained and is virtually maintenance free. The only maintenance requirement is periodic inspection and infrequent battery checks. There are no engines or generators to overhaul, no battery charges to maintain, no power lines to repair or replace, no fuel burners to adjust or relight and no fuel to haul. Since the unit is microwave, there are no cable pairs to maintain or replace.

(11) The solar powered microwave system is entirely safe to use, presenting no hazards to man or wildlife. There are no hot surfaces, no rotating machinery, no high R.F. power levels, no electrical shock hazards, no fuel or oil spills, no combustible materials, exposed flames or explosive vapors.

## CONCLUSIONS

(1) Present Army methodology of data gathering and transmission (for analysis) that occur in isolated and remote areas can be enhanced and proved more cost effective in several respects.

(2) A remote portable solar powered microwave system, designed to alleviate both logistical and technical problems associated with remote data gathering and transmission, has been developed and successfully tested.

(3) The system appears to have great promise and a wide growth latitude in supporting remote tests of Army material, and other DOD activities.

(4) Substantial cost effectiveness to the government can be realized by using the portable solar powered microwave terminal.

(5) Communications can now be brought to where the test is, rather than to have the test or evaluation constrained to where the communications are.



IN-FLIGHT FAR-FIELD MEASUREMENT OF  
HELICOPTER IMPULSIVE NOISE

DONALD A. BOXWELL  
FREDRIC H. SCHMITZ  
AMES DIRECTORATE  
U.S. ARMY AIR MOBILITY R&D LABORATORY  
MOFFETT FIELD, CA 94035

## INTRODUCTION

Impulsive noise, sometimes called "blade slap," is one of the most annoying and easily detectable sounds a helicopter can generate. Characterized by an intense low frequency and often harsh sounding succession of impulses which radiate efficiently in the direction of forward flight, it has been the subject of much theoretical research (1-7). Unfortunately, the lack of good experimental helicopter impulsive noise data has hindered the verification of existing theories and has probably slowed the development of a clear understanding of the physical events leading to the generation of the noise.

Although impulsive noise can occur in near-hovering flight on some single-rotor helicopters, it usually occurs at high forward velocities and during partial-power descents. Combinations of high advancing-tip Mach numbers, high blade loadings, and blade-wake interaction are prime suspects of its generation. Many researchers believe that two basic and independent mechanisms are responsible for the one phenomenon labeled "impulsive noise." The first is thought to be a direct result of rapid changes in aerodynamic forces on the blade due to blade-tip vortex interaction which is known to exist on many single-rotor helicopters in partial-power descents (8-10) and on tandem helicopters as a function of rotor spacing and trim conditions. The second mechanism, which has been attributed to compressibility effects on the advancing blade of a helicopter in high-speed flight, is often called "high speed" impulsive noise. Although there is presently some controversy about the major sources of this noise (2-5), it is known to occur on helicopters whose advancing-tip Mach numbers approach or exceed 1.

The lack of far-field experimental acoustic data, which can be used to identify the basic noise mechanisms and the radiation patterns of helicopter impulsive noise, can be traced to a variety of measurement difficulties, forcing past investigators to utilize qualitative observations and limited measurements to attempt to judge the extent of the blade slap problem. The most common method of measuring impulsive noise is to station a microphone at a fixed position on or above the ground and to fly the helicopter along nominal trajectories at selected forward flight conditions. Under ideal circumstances, a quantitative assessment of the character of the noise is possible (11,12). However, when one tries to compare in detail the noise produced by the same aircraft under different flight conditions, or to develop directivity patterns of the radiated noise, holding all other pertinent variables, such as distance to the microphone, azimuth angle, and ambient wind effects, constant, the technical problems and statistical uncertainties combine to make the data-gathering task quite difficult. In fact, the

quantification of just one flight condition from ground acoustical measurements can be difficult due to statistical uncertainties in the acoustic transmission path and ground reflection effects.

Wind tunnels have also been used to gather impulsive noise data. For example, several programs have been run in the NASA-Ames 40 X 80-Ft Wind Tunnel on full-scale helicopters. From the noise measurements that were taken, it was often possible to evaluate the relative acoustic merits of competing blade slap configurations or operational conditions, or both. However, the reverberation characteristics of the tunnel, together with its high ambient operational noise levels, make a quantitative evaluation of the blade slap signal difficult.

Another approach currently being used to obtain impulsive noise data due to blade-vortex interaction utilizes microphones mounted on the inside of the helicopter cabin and along chosen exterior surfaces.(8-10) Acoustic signatures taken by this measurement technique have been used to develop subjective "blade slap boundaries" as a function of operating conditions and to attempt to locate, through triangulation methods, the point(s) in space where the noise originates. The blade slap boundary map of references 8 and 9, which was developed utilizing this technique, is reproduced in figure 1 for the

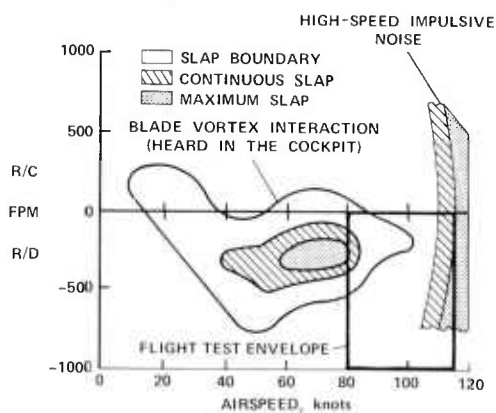


Figure 1.— Impulsive Noise Boundaries for UH-1 Series Helicopters (from ref. 9)

UH-1 series helicopters. One interesting aspect of this figure is that the impulsive noise measured in the cabin was at a maximum level within an enclosed area centered at a rate of descent of 300 ft/min and a forward speed of 75 knots. As airspeed increased, blade slap decreased until it was no longer recorded on the cabin microphone. If this map is indicative of the actual far-field noise radiated by the helicopter, one must then deduce that at some moderately high forward velocities no significant blade-wake interaction exists. It would then be possible to devise high-speed descent profiles to avoid the blade-vortex interaction acoustic radiation — a technique developed in reference 8. However, it will be shown that this is not the case for the UH-1H helicopter. Impulsive noise radiation due to blade-wake interaction, which is apparently not discernible on the cabin microphone, does exist at moderately high forward speeds and moderate rates of descent.

This in-cabin or near-fuselage method of measuring impulsive noise has several limitations. Because either cabin- or fuselage-mounted microphones are in the helicopter's low- to mid-frequency acoustic near field (depending upon their proximity to the rotor disc), it can be difficult to quantitatively evaluate how much of the aerodynamically generated noise actually radiates to the far field. Also, it is not presently feasible to attempt measurements of in-plane acoustic data by this technique. As fuselage-mounted microphones approach the rotor disc, near-field pressures dominate the impulsive acoustic signature. Other factors, such as masking by adjacent noise sources (engine, gearbox, etc.) and reflection and generation of acoustic signals by vibrating fuselage surfaces, can disguise and distort the waveform.

To surmount the difficulties of ground, wind tunnel, and near-field in-flight measurement attempts, an in-flight far-field acoustic measurement technique was developed. This measurement technique utilized a quiet fixed-wing aircraft, instrumented with a microphone, and flown to maintain fixed relative positions with a helicopter. Because impulsive noise was thought to have its maximum intensity radiation patterns in the general direction of forward flight, the microphone was installed on the tail of a monitoring fixed-wing aircraft and flown in front of the helicopter as illustrated in figure 2. Calculated values of microphone wind noise and monitoring aircraft noise levels indicated that with a proper choice

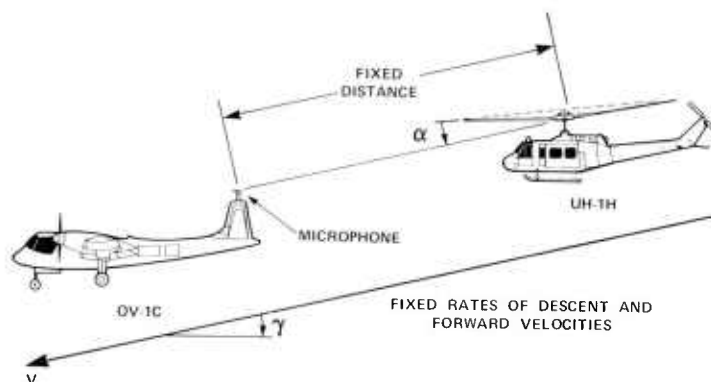


Figure 2.— Schematic of In-Flight Far-Field Measurement Technique

of fixed-wing aircraft, the periodic phenomenon of helicopter blade slap could be measured above or extracted from the potential masking sounds of the testing procedure. By using this testing procedure, quantitative acoustic far-field impulsive noise radiation patterns were easily obtained under a wide range of steady operating conditions.

#### EXPERIMENTAL METHOD

A UH-1H helicopter ("Huey") was chosen as the subject aircraft for the acoustic measurement program because of its known ability to generate blade slap throughout a range of flight conditions and because of its widespread use throughout the U.S. Army. The Huey's general and operational characteristics that are of interest acoustically are given in the appendix.

Many factors entered into the decision to choose the OV-1C ("Mohawk") as the monitoring or lead aircraft for this initial test program. The acoustical characteristics of the Mohawk are of prime importance. Its twin turboprop engines employ a governor system that allows the pilot to specify the rotation rate of both three-bladed propellers. A fixed rotation rate of 1200 rpm, resulting in a propeller tip speed of 628 ft/sec, was predetermined to be the most compatible with the governor system and at the same time served to minimize the amplitude and to position the harmonics of propeller rotational noise to avoid those generated by the main and tail rotor of the UH-1H helicopter.

Relatively good slow-speed flight capability at low rpm settings was another factor in choosing the Mohawk as the monitoring aircraft. Zero to 1000 ft/min rates of descent could be held at 1200 rpm at airspeeds down to 80 knots. These performance limitations are indicated on the forward velocity-rate of descent map for the UH-1H (fig. 1) by the left border of the boxed flight test envelope. As shown in this figure, previously reported regions of intense slap resulting from blade-vortex interaction as well as conditions of high-speed impulsive noise could be investigated with the OV-1C.

A Brüel and Kjaer 1/2-inch condenser microphone, fastened to the center vertical stabilizer of the OV-1C aircraft by a 15-inch aerodynamically shaped strut, was used to record all acoustic data. To minimize wind noise and avoid unnecessary complexity, the microphone was outfitted with a Brüel and Kjaer "nose cone" and oriented to a fixed nominal direction facing the relative wind; the direction was chosen so that the microphone centerline was nearly aligned with the relative wind under all test conditions. (Microphone angles of attack of less than  $10^\circ$  were predicted for trimmed flight throughout the measurement envelope.)

For the test program, normal copilot functions were superseded by acoustic monitoring and recording tasks. This capability was provided for by locating, in the cockpit area, a Brüel and Kjaer microphone preamplifier-power supply unit, a small two-channel oscilloscope, and tape recorder remote controls. Preamplifier gains ( $\pm 20$  dB range) were determined in-flight to maximize signal-to-noise ratios and to avoid peak pressure saturation prior to recording the blade slap signal received from the microphone. This optimized signal was monitored on one oscilloscope channel and recorded on a Honeywell (5600) 14-channel FM tape recorder (DC to 5000-Hz frequency response) that was shock-mounted in the OV-1C instrumentation bay. The recorded signal was then monitored on the second oscilloscope channel for immediate in-flight data confirmation. A one/rev signal, generated by a contactor on the helicopter shaft, was transmitted over a radio channel and served as external trigger input for the oscilloscope display of the acoustic signal. Audio comments of both pilots and the one/rev signal were tape recorded simultaneously with the data. Field calibration signals were provided by a Brüel and Kjaer portable pistonphone.

Spatial orientation of the UH-1H helicopter with respect to the OV-1C aircraft was achieved through visual flight reference. Once the pilot of the Mohawk established a specified flight condition, the UH-1H helicopter pilot utilized predetermined visual cues to fly behind the OV-1C at fixed separation distances, and at relative angular displacements from the direct-in-trail position. Calibrated canopy markings were used by the UH-1H pilot to establish desired separation distances. These canopy markings were established on the ground with the helicopter directly behind the OV-1C. For each measured separation distance, one pair of vertical lines was drawn on the canopy of the UH-1H, spaced so that, to the helicopter pilot, they appeared to intersect the wing tips of the OV-1C aircraft. By simply recreating this same visual image in formation flight, the helicopter pilot maintained fixed separation distances (within an estimated accuracy of  $\pm 5$  ft).

Longitudinal angular directivity ( $\alpha$ ) of microphone position with respect to the helicopter's tip-path (fig. 2) was determined solely by sighting known markings on the OV-1C aircraft. The pilot flew the helicopter so as to position the Mohawk's center vertical stabilizer light in line of sight with preestablished fuselage markings. This determined a fixed angular relationship between the visual sighting line and the Mohawk's reference line. Knowing (by inclinometer measurement) the angle between the Mohawk's reference line and the horizontal, and calculating the UH-1H's tip-path plane angle and hub center position for each flight condition, the longitudinal angular directivity ( $\alpha$ ) of the microphone position could be calculated (within an estimated error of  $\pm 2^\circ$ ).

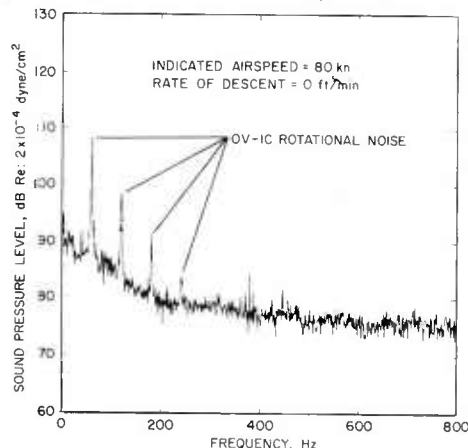


Figure 3.— In-Flight Measurement of Background Noise

Lateral angular directivity ( $\beta$ ) of microphone position with respect to the forward-flight direction of the helicopter was determined in a similar manner. Distinguishable vertical tail features of the Mohawk were placed in line of sight with fuselage and wing markings and noted during flight. Lateral microphone angles ( $\beta$ ) were calculated by constructing these sight lines on scaled drawings of the OV-1C aircraft (within an estimated error of  $\pm 1^\circ$ ).

Before taking acoustic data in formation flight with the UH-1H helicopter, the OV-1C was flown by itself at airspeeds from 80 to 115 knots at rates of descent from 0 to 1000 ft/min in quiescent air. During these initial runs to check out ease of control of the Mohawk during descending flight, background noise levels were recorded. Figure 3 shows a frequency spectrum of the measured background acoustic signature during level flight at an indicated airspeed of 80 knots. The spectrum was



obtained with 1-Hz wide bandwidth resolution and is representative, in character and level, of background noise over the entire flight test envelope. The rotational noise of the OV-1C predominated at higher power settings in the low-frequency range, but fell off rapidly as frequency was increased. Factors contributing to the remainder of the background noise were turboprop engine noise, wind noise over the microphone, and scrubbing noise. Fortunately, the background noise levels were low enough to insure good signal-to-noise ratios when recording the UH-1H impulsive noise.

### EXPERIMENTAL FINDINGS<sup>†</sup>

Forward-flight impulsive noise data were gathered with this in-flight far-field measurement technique with relative ease. By utilizing highly qualified pilots, the entire flight test matrix of about 50 test points was completed in two half days of flying. Acoustic data were recorded over variations in indicated airspeed (IAS) from 80 to 115 knots and rates of descent (R/D) of -200 ft/min to 1000 ft/min. Longitudinal and lateral directivity data were taken at two conditions; 80 knots IAS, 400 ft/min R/D and 115 knots IAS, 0 ft/min R/D. In all cases, signal-to-noise ratios of at least 10 dB, and more commonly 20 dB, were recorded.

It was generally observed from the measured data that the far-field acoustic waveform radiated by each blade was multipulse in nature. Up to three distinct pressure disturbances could be repetitively identified in the acoustic waveform. For identification of this waveform structure and familiarity with data presented in the following sections, an idealized composite drawing of the acoustic waveform showing this multipulse character is presented in figure 4. In this figure, peak pressure amplitude of the acoustic signature is illustrated vs. one-half revolution (one blade passage) in time, with time increasing from left to right. The convention established by early high-tip-speed propeller researchers (14) is adhered to: a pressure decrease (negative pressure) is indicated upward and a pressure increase (positive pressure) is indicated downward. The peak pressure amplitude scale used here and throughout the paper is an absolute scale measured in dynes/cm<sup>2</sup>. On this scale a sinusoidal-shaped waveform with a peak pressure amplitude of 448 dynes/cm<sup>2</sup> would exhibit a root mean square (RMS) sound pressure level of 124 dB (Re: 0.0002 dyne/cm<sup>2</sup> RMS).

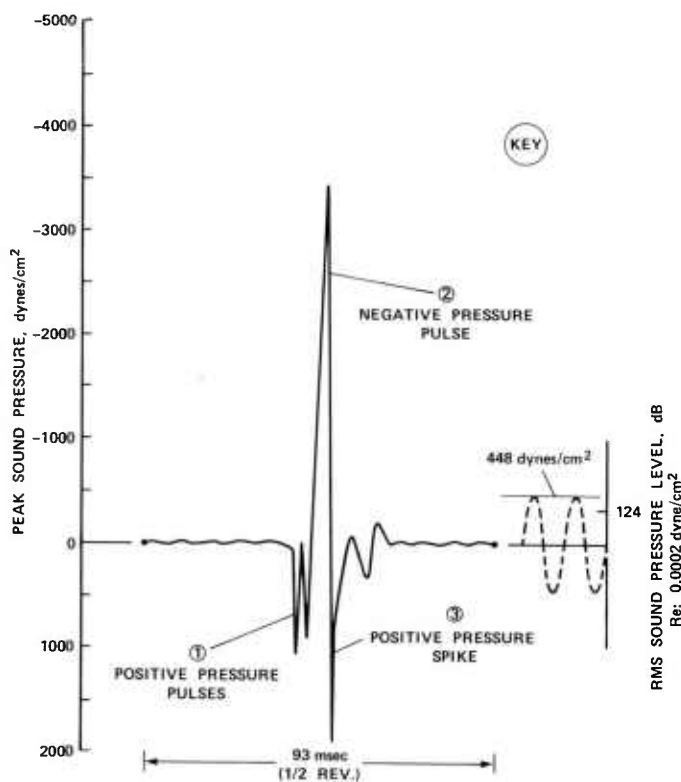


Figure 4.— Composite Illustration Showing Dominant UH-1H Acoustic Waveform Features

<sup>†</sup>See reference 13 for averaged acoustic waveforms and impulsive noise power spectra.

The composite waveform model illustrates three predominant pressure disturbances observed in the data. They are shown in the same relative sequence and approximate pulse width that were characteristic of the measured data. Typically, the sequence began with one or two successive increases in positive pressure of "triangular" pulse shape (fig. 4, no. 1). These positive pressure peaks are followed by a negative pressure rise (fig. 4, no. 2), usually increasing in amplitude slightly slower than its subsequent rapid decrease and represented more by a sawtooth or half-triangular pulse shape. Finally, when it was observed to occur, an extremely narrow positive pressure spike (fig. 4, no. 3) followed immediately after the decrease in negative pressure.

Although it is not the intent of this paper to relate in detail the potential design causes of the radiated noise to the acoustic time history, some discussion and general observations are in order. It is the authors' hypotheses that the initial series of positive pulses (fig. 4, no. 1) is a direct result of blade-tip vortex interaction and that the remainder of the impulsive noise waveform features are associated with high advancing-tip Mach numbers. The large rise in negative pressure (fig. 4, no. 2) is thought to be attributable to "thickness" effects, while the following sharp increase in pressure (fig. 4, no. 3) is related to a radiated shock wave being shed after the position of maximum advancing-tip Mach number. No attempt at theoretical justification of these hypotheses is attempted in this work; the primary intent is to furnish a consistent set of acoustic impulsive noise data. For completeness, each data point is cross-referenced in the appendix, where the acoustically important nondimensional variables are tabulated for each flight condition. The circled number in each of the following figures is the key to this appendix. In the following paragraphs, this composite waveform is shown to be highly dependent on helicopter performance and directivity measurements.

Figure 5 presents a performance matrix of measured acoustic data at flight conditions between 80 and 115 knots IAS and 0 to 800 ft/min R/D. (Reference the boxed flight test envelope in fig. 1.) These unaveraged acoustic waveforms, corresponding to two consecutive blade passages, were recorded at a nominal hub-to-microphone separation distance of 75 ft with the microphone positioned directly ahead of the helicopter ( $\beta = 0$ ) and nearly within the plane of the rotor tips ( $\alpha \cong 0$ ). Each of the acoustic time histories has the same amplitude scale shown, for example, with the upper right waveform in the performance matrix.

Two striking features of the pressure-time histories are present. The first is the multipulse nature that was previously discussed. The second is the presence of a blade-to-blade acoustic variability. This variability was in most cases repetitive, indicating that each blade has a distinct signature — a phenomenon observed by other acoustic researchers. Blade-to-blade variability was most prominent for the positive pressure pulses, tending to indicate a more detailed dependence of these pulses upon the local aerodynamic environment of each main rotor blade.

Several data trends are evident. Peak amplitude of the large negative pressure pulse is strongly dependent on forward speed. Although the width of the negative pulse appears to decrease slightly with increasing speed, no consistent trends in amplitude or pulse width could be deduced with changes in descent rate. It is interesting to note that under level-flight conditions at all airspeeds, no impulsive noise was heard in the cabin, indicating that for all flight conditions tested, the pilot was audibly unaware that the helicopter was radiating that part of the impulsive noise waveform associated with the negative pressure peak.

At the high forward speed conditions of 115 knots, the large negative pressure peak, when measured nearly inplane, was followed by a positive pressure spike which exhibited some variability from blade to blade. These extremely sharp pressure pulses documented here were so intense as to be heard directly in the cockpit of the Mohawk, over and above the aircraft's own internal noise levels. However, no apparent slapping was heard in the cabin of the helicopter at any speed above 100 knots IAS regardless of rate of descent. To the pilot of the helicopter, a moderate increase in vibration level was the only noticeable effect, even though the UH-1H was radiating tremendous amounts of acoustic energy.



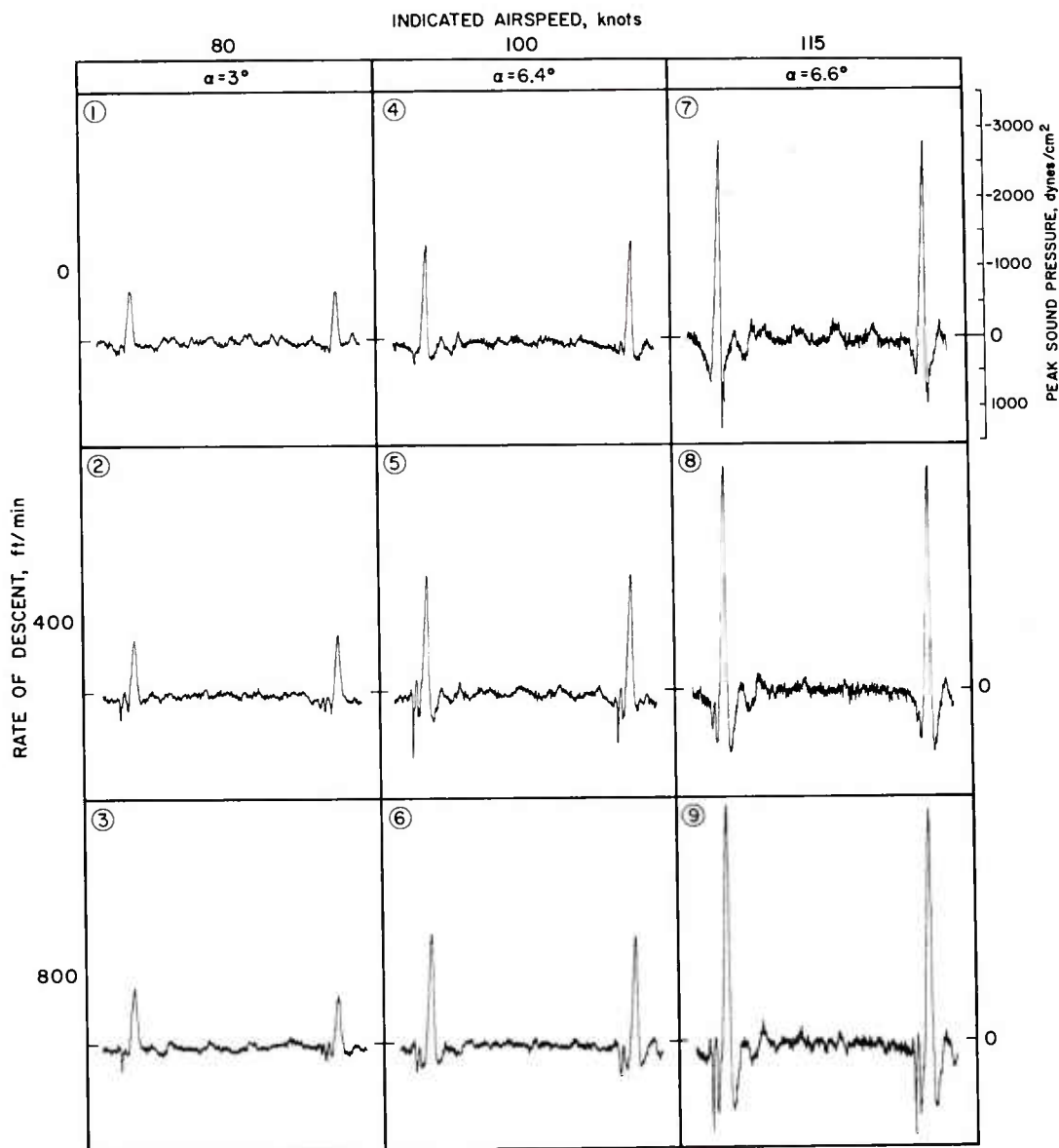


Figure 5.— Unaveraged Acoustic Signature of UH-1H Impulsive Noise Versus Forward Airspeed and Rate of Descent

Blade slap was heard in the cabin under partial-power descents below forward speeds of 100 knots. Similar to the findings of reference 8 (fig. 1), blade slap appeared to be most intense within the helicopter at about 80 knots 1AS at a rate of descent of 400 ft/min. The occurrence of this cabin noise correlates with the positive impulsive pressures which precede the large negative pressure pulse on the acoustic waveforms (fig. 5). Because the occurrence of these positive pressure pulses appears to be very

sensitive to rates of descent and resulting rotor wake geometry, it is thought that these pulses are a direct result of blade-tip vortex interaction. However, contrary to the findings of references 8–10, this blade-vortex interaction noise does not disappear at higher forward velocities. At a given indicated airspeed, the positive pressures were found to increase, maximize, and then decrease again with increasing rate of descent. The point of maximum positive peak pressure occurred at higher descent rates as forward velocity was increased, following a somewhat diagonal path from 80 knots/400 ft/min to 115 knots/800 ft/min conditions.

It is apparent from these findings that the regions of radiated blade slap noise reported in references 8–10 are larger than previously thought. Only the impulsive noise heard in the cabin forms a closed region (fig. 1) when plotted versus forward velocity and rate of descent. The external radiated acoustic signature is quite different and fairly independent of the normal internal noise environment of the UH–1H helicopter at airspeeds above 80 knots. Unfortunately, there appears to be no quiet corridor (8) through which to fly when decelerating for an approach to landing from high forward speeds. The helicopter pilot must descend through regions of measured “severe” blade slap to reach the previously reported less intense regions of blade-vortex interaction at lower forward velocities and high rates of descent.

Directivity profiles of the UH–1H impulsive noise were measured throughout a sweep of angular microphone positions for two operating conditions: 80 knots IAS, 400 ft/min R/D and 115 knots, 0 ft/min R/D. The longitudinal and lateral angles,  $\alpha$  and  $\beta$ , respectively were measured from a line in space drawn between the rotor hub and microphone to the rotor tip-path plane for longitudinal directivity and to the forward velocity vector for lateral directivity. The directivity data were recorded using two different but complementary flying procedures, the primary one being a continuous slow sweep by the helicopter pilot around the Mohawk at a nominal separation distance of 75 ft. The resulting figures present “two-blade passage” snapshots of the continuously changing acoustic waveform at specified angular orientations. The second method of measuring directivity data utilized the stationkeeping procedures outlined in the “experimental method” section. Data gathered by this latter technique are indicated on the directivity figures by an asterisk.

Figures 6 and 7 present the longitudinal and lateral directivity profiles of the UH–1H helicopter in an 80 knot IAS, 400 ft/min rate of descent. As discussed previously, this operating condition produced blade slap noise that was audible to the helicopter pilot.

The longitudinal directivity signatures (fig. 6) contain both positive and negative pressure pulses, the former exhibiting considerable variability from blade to blade. These positive pressure pulses, which are associated with blade-tip vortex interaction, become large for longitudinal angles ( $\alpha$ ) between  $10^\circ$  and  $52^\circ$ . Even at the nearly in-plane or overhead position, some blade-tip vortex interaction radiation is evident, indicating that a wide angular distribution of acoustic energy is radiated to the far field in the longitudinal plane. However, the negative pressure peak exhibits quite different radiation characteristics. It reaches its maximum level near the in-plane positions of the rotor disc but decreases rapidly to half amplitude by the  $23^\circ$  position and continues to decrease uniformly with increasing angle until it is hardly discernible above background noise levels at the  $52^\circ$  angular position.

Lateral directivity, shown in figure 7, for the same operating conditions depicts a rapid decrease in the impulsive nature of the positive pressure pulse for measurements to the advancing blade side of the rotor and a gradual disappearance into background noise by the  $54^\circ$  point. Again, variability between blade signatures is present. The negative pressure pulse is shown to decay less rapidly in-plane than out-of-plane as the directivity angle is increased. It is approximately half amplitude at  $73^\circ$  and still discernible to the side of the helicopter ( $\beta = 94^\circ$ ). Although the helicopter pilot cannot hear any slapping noise associated with the negative pressure pulse, it is clear that near the tip-path plane of the helicopter, large angular distributions of acoustic energy are being radiated.

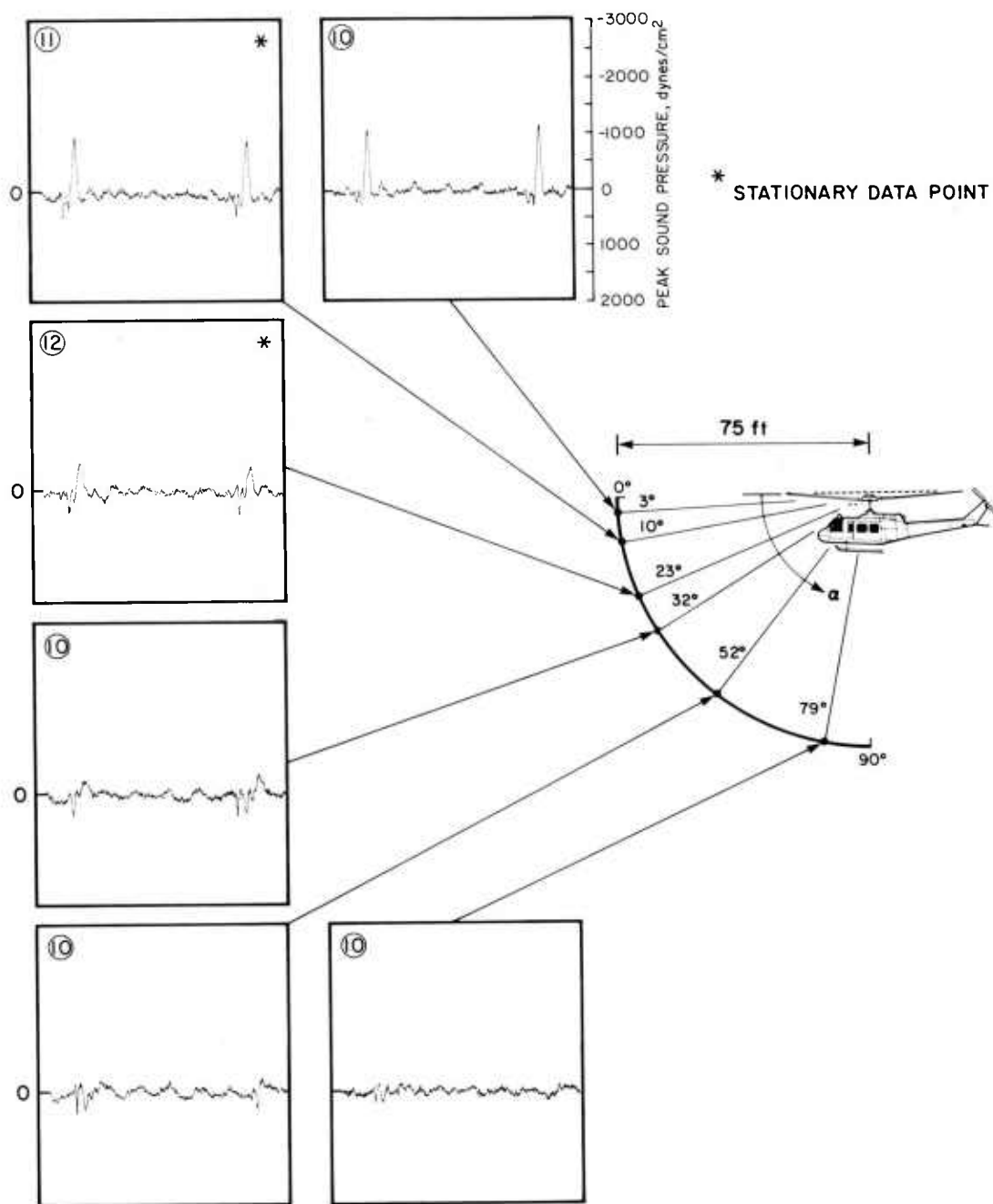


Figure 6.— UH-1H Longitudinal Acoustic Directivity at 80 Knots IAS and 400 Ft/Min R/D ( $\beta = 0^\circ$ )

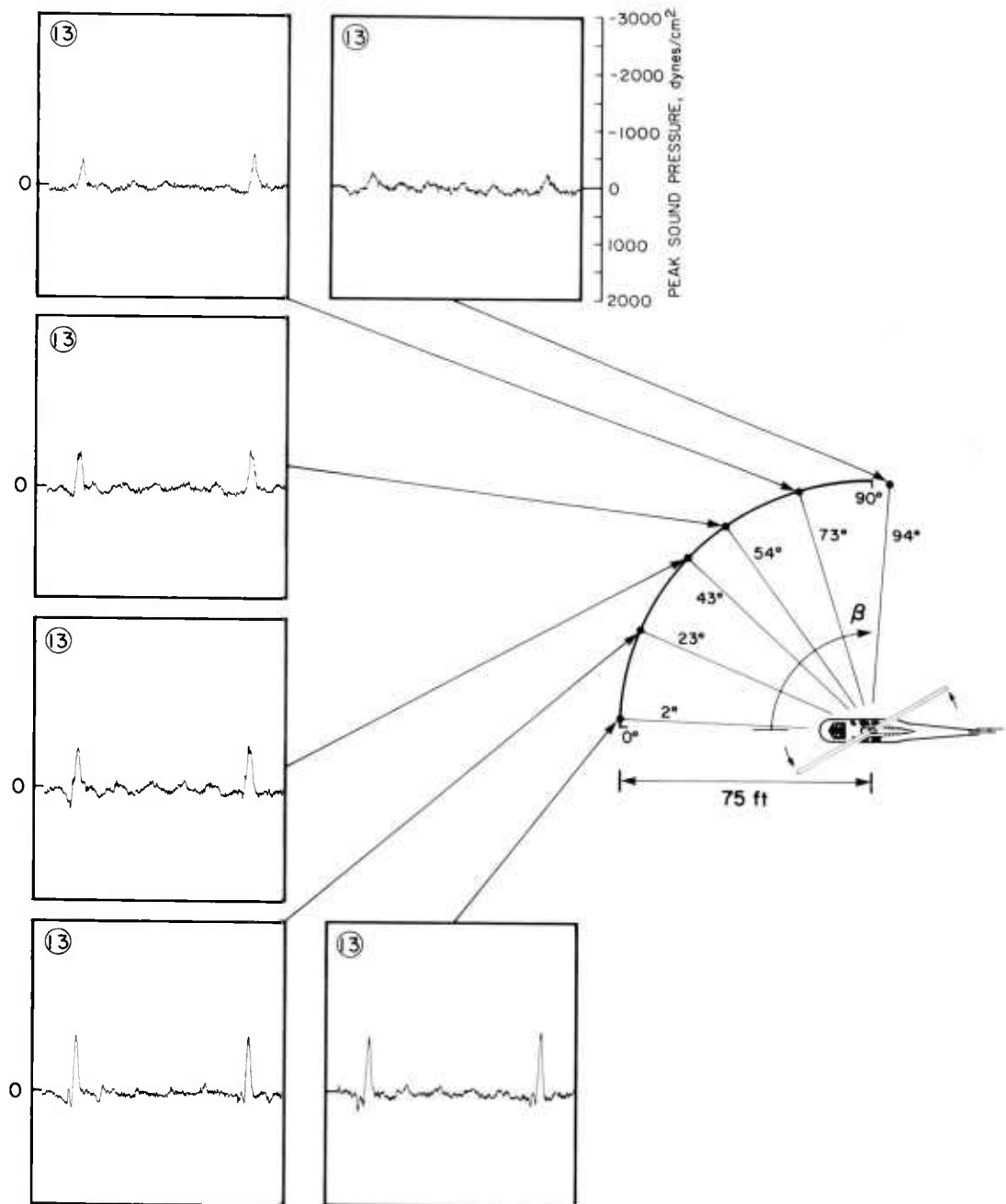


Figure 7.— UH-1H Lateral Acoustic Directivity at 80 Knots IAS and 400 Ft/Min R/D ( $\alpha = 3^\circ$ )

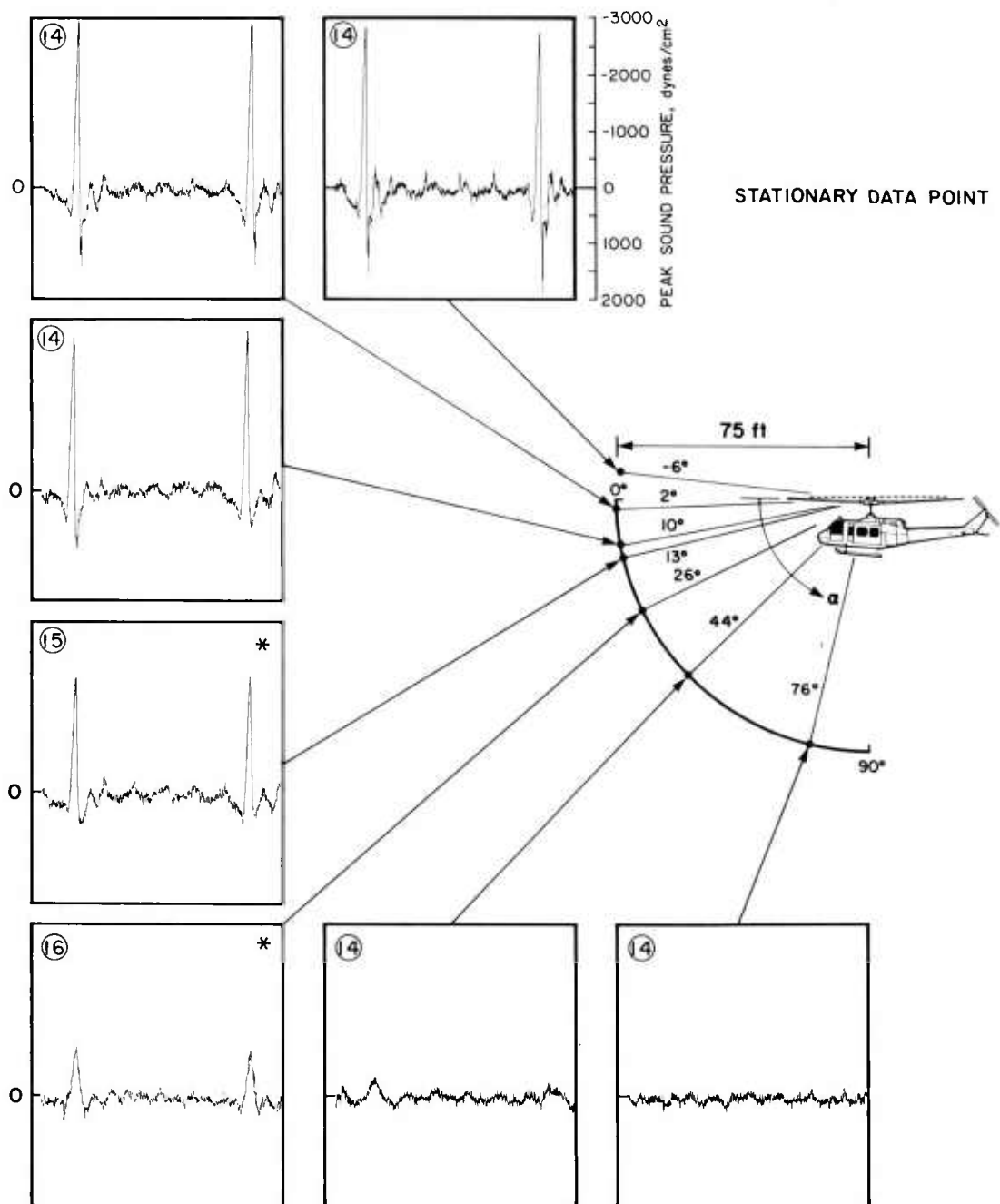


Figure 8.— UH-1H Longitudinal Acoustic Directivity, Level Flight, 115 Knots IAS ( $\beta = 0^\circ$ )

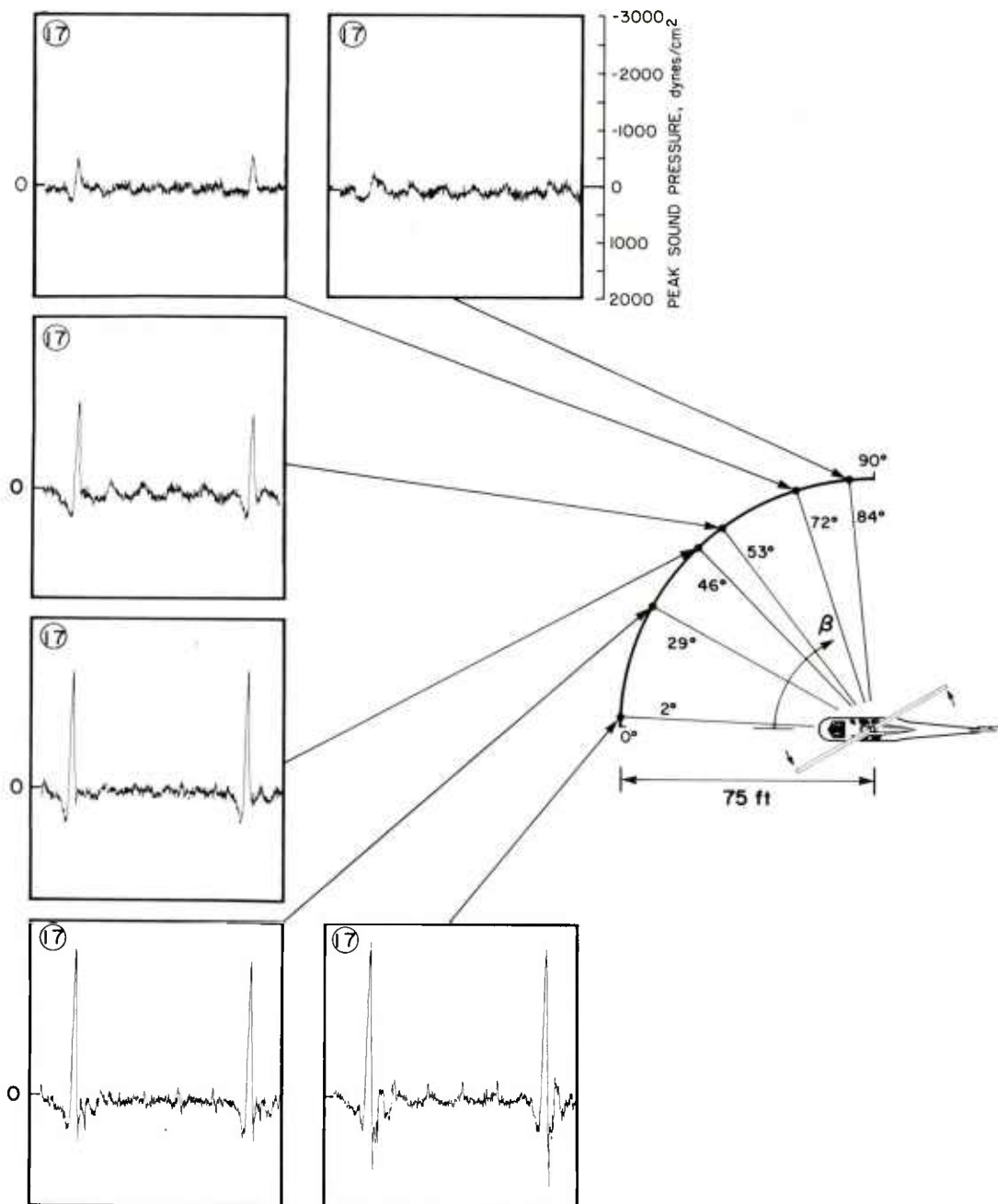


Figure 9.— UH-1H Lateral Acoustic Directivity, Level Flight, 115 Knots IAS ( $\alpha = 7^\circ$ )



The longitudinal and lateral directivity profiles for high-speed level flight are shown in figures 8 and 9. Although the positive pressure pulses associated with blade-tip vortex interaction impulsive noise are noticeably absent for this flight condition, large-amplitude negative and positive pressure pulses do exist.

The negative pressure peak, although much larger in amplitude for this high-speed condition, varies in longitudinal and lateral directivity in much the same fashion as in the low speed case. It is at a maximum near the tip-path plane of the rotor (fig. 8) and falls off uniformly with increasing lateral directivity angles (fig. 9), where, at  $\beta = 84^\circ$ , it is barely noticeable. As indicated previously, the pilot cannot identify this large angular distribution of radiated impulsive noise from inside the helicopter.

The extremely sharp positive pressure rise shown to exist in a narrow angular region near and above the rotor's tip-path plane (fig. 8) and in the direction of forward flight (fig. 9) resulted in very intense radiated noise levels. However, similar to the negative pressure pulse, no impulsive noise radiation could be detected by the helicopter pilot.

### CONCLUSIONS

An in-flight technique for measuring UH-1H helicopter impulsive noise by stationkeeping with a quiet instrumented lead aircraft was found to be highly successful. Far-field quantitative acoustic waveforms and radiation patterns were easily obtained over a wide, continuous range of UH-1H flight conditions, including several areas known to produce annoying acoustic radiation. The data collected using this technique were not (to any significant degree) contaminated by background noise, doppler effects, ground reflections, and other transmission path distortions that have hindered many measurement efforts in the past. Care was exercised, however, in choosing a compatible, quiet fixed-wing aircraft and in accurately recording impulsive noise data. Feasibility of extending this technique for noise measurements of other helicopters appears to be quite promising.

There were two major findings as a result of this initial measurement program:

1. Judging the occurrence and severity of a helicopter's radiated impulsive noise signature from cabin-based noise measurements can be misleading. For the UH-1H helicopter, a reduction in cabin audible impulsive noise levels may constitute a necessary but certainly not a sufficient indication that far-field impulsive noise radiation has been reduced.
2. Three distinct types of impulsive noise are radiated by the UH-1H helicopter while flying between 80 and 115 knots at descent rates from zero to 1000 ft/min.

The first is a series of positive pressure pulses believed to be related to blade-tip vortex interaction. These pulses are responsible for the crisp popping sound of the radiated noise. During blade-vortex interaction, acoustic energy is radiated with relatively large angular directivity in the longitudinal plane, reaching a maximum about  $40^\circ$  below the helicopter's tip-path plane in the direction of forward flight.

The second type of impulsive noise is a negative pressure disturbance that rapidly increases in amplitude with forward velocity, becoming quite intense and sawtoothed in shape at 115 knots IAS. Subjectively, it sounds like a loud thumping and radiates not only near the tip-path plane of the rotor, but over wide azimuthal angles in the general direction of forward flight.

The third is a narrow positive pressure spike that closely follows the sawtooth-shaped negative pressure pulse at high airspeeds (115 knots). The resulting intense impulsive sound dominates all other noises generated by the helicopter and radiates within narrow azimuthal angles in the direction of forward flight near the tip-path plane of the rotor.

## ACKNOWLEDGMENTS

The authors are indebted to: Mr. Richard B. Lewis, who as Deputy Director of AAEFA during the flight test program helped to make this concept of in-flight testing a reality; to Mr. Robert E. George of USAAMRDL, Ames, and Mr. Robert Jeffris of AAEFA for their expert electronic technical guidance; and to Captain M. L. Hanks and Mr. Joseph C. Watts of AAEFA for their excellent piloting ability.

## APPENDIX

## UH-1H OPERATIONAL CHARACTERISTICS



ROTDR SYSTEM DESIGN VARIABLES	MAIN ROTOR	TAIL ROTOR
NUMBER OF BLADES	2	2
ROTDR DIAMETER	48 ft	8.5 ft
ROTDR SOLIDITY	0.0464	0.105
BLADE CHDRD	21 in	8.41 in
BLADE AIRFDIL	NACA 0012	NACA 0015
BLADE TWIST (RDOT TO TIP)	-10.9 deg	0
AIRCRAFT OPERATIONAL LIMITS	MAXIMUM	MINIMUM
MAIN ROTDR TIP SPEEDS [ft/sec]	813.8	740.0
TAIL ROTDR TIP SPEEDS [ft/sec]	736.1	669.0
FORWARD FLIGHT AIRSPEEDS [kn]	115	0
GRDSS WEIGHT [lb]	9500	6600

## INDEX OF FLIGHT CONDITIONS

INDEX KEY	$C_T/\sigma$	ADVANCE RATIO	ADVANCING-TIP MACH No.
1	0.066	0.179	0.857
2	0.062	0.174	0.857
3	0.060	0.172	0.859
4	0.063	0.230	0.893
5	0.059	0.224	0.890
6	0.056	0.219	0.888
7	0.069	0.265	0.918
8	0.066	0.260	0.916
9	0.063	0.255	0.915
10	0.061	0.177	0.862
11	0.064	0.176	0.863
12	0.062	0.174	0.861
13	0.059	0.175	0.860
14	0.063	0.265	0.915
15	0.068	0.266	0.919
16	0.067	0.265	0.920
17	0.063	0.264	0.917

## REFERENCES

1. J. E. Ffowcs-Williams and D. L. Hawkings, Sound generation by turbulence and surfaces in arbitrary motion. *Philosophical Transactions of the Royal Society*, 264, 321–342 (1969).
2. F. Farassat, The acoustic far field of rigid bodies in arbitrary motion. *J. of Sound and Vibration*, 32, 3, 387–405 (1974).
3. M. V. Lowson and R. J. Jupe, Wave forms for a supersonic rotor. *J. of Sound and Vibration*, 37, 4, 475–489 (1974).
4. R. H. Lyon, Radiation of sound by airfoils that accelerate near the speed of sound. *J. of the Acoustical Society of America*, 49, 894–905 (1971).
5. Roger E. Arndt and Dean C. Borgman, Noise radiation from helicopter rotors operating at high tip Mach number. Preprint No. 402, presented at the 26th Annual National Forum of the American Helicopter Society, June 1970.
6. L. T. Filotas, Vortex induced helicopter blade loads and noise. *J. of Sound and Vibration*, 27, 3, 387–398 (1973).
7. S. Widnall, Helicopter noise due to blade-vortex interaction. *J. of the Acoustical Society of America*, 50, 354–365 (1971).
8. Dennis R. Halwes, Flight operations to minimize noise. *Vertiflite*, 17, 2, 4–9 (1971).
9. C. R. Cox, How to operate the medium helicopter more quietly. *U.S. Army Aviation Digest*, 19, 9, 25, 33–38 (1973).
10. Bruce D. Charles, Acoustic effects of rotor-wake interaction during low-power descent. Presented at the United States National Symposium on Helicopter Aerodynamic Efficiency, Hartford, Connecticut, March 1975.
11. Charles L. Munch and R. J. King, Community acceptance of helicopter noise: Criteria and Application. CR-132430, NASA.
12. David Brown, Baseline noise measurements of Army helicopters. TR-71-36, USAAMRDL, March 1972.
13. D. A. Boxwell, F. H. Schmitz and M. L. Hanks, In-flight far-field measurement of helicopter impulsive noise. Presented at the “First European Rotorcraft and Powered Lift Aircraft Forum,” University of Southampton, Southampton, England, September 22–24, 1975.
14. H. H. Hubbard and L. W. Lassiter, Sound from a two bladed propeller at supersonic tip speeds. Report 1079, NACA, 1952.



AN ADAPTIVE PREDICTION FILTER ALGORITHM  
FOR OPTIMIZING SERVO SYSTEM PERFORMANCE

MR. LESTER M. BRADLEY  
INSTRUMENTATION DIRECTORATE  
WHITE SANDS MISSILE RANGE, NEW MEXICO 88002

I. INTRODUCTION

Several approaches have been taken by the Instrumentation Directorate over the past few years to improve the servo performance of various types of optical tracking telescopes such as the one shown in Figure 1. These efforts have concentrated on servo systems having sample rates between 20 and 200 per second where the original approaches centered around using analog techniques to implement lag-lead compensation networks comprised of R-C networks and operational amplifiers. The effects of sample rate on servo performance were generally not accounted for with the result that a significant loss of performance was experienced. In an attempt to remedy this situation, attempts (1) were made to apply sampled-data theory techniques in the design of compensation networks in order to improve the servo performance. Improvements were noted but it was not possible to construct equivalent sample-data networks out of analog components.

Around 1970, efforts were successful (2) in utilizing a special purpose mini-computer to implement a purely digital servo compensation as called for from a sampled-data analysis. Considerable improvements in servo performance were realized but the size of the equipment and the cost involved in using a mini-computer to perform digital compensation effectively prohibited the use of such a system on a typical servo. Both of the approaches thus far mentioned were based on a rather detailed academic technique and required personnel with specialized backgrounds to fully utilize the methods involved. It was recognized that this was not a desirable situation and that a more straightforward approach would be much more valuable.



FIGURE 1. VERSATILE TRACKING MOUNT

In 1974, a compensation method (3) was devised that used a non-linear gain relationship of the servo error signal to control a high performance mirror mount with a system sample rate of 200 per second. A mini-computer was used to implement the compensation and excellent performance results were obtained. This approach suggested that different methods could be used for servo control than had previously been tried and that such techniques could provide satisfactory servo performance.

The experience gained from these earlier approaches coupled with the technique to be described have resulted in the development of an Adaptive Prediction Filter (APF) which allows a simple procedure to be followed in compensating a servo system and yields an optimum performance. Utilizing the recent developments in micro-computer technology, the APF has been constructed on a low cost basis with a unit cost of approximately \$3500.

## II. INITIAL APF CONCEPT

During the period of 1974-1975, a wide field fixed sensor system (4) was in the process of being developed by the Instrumentation Directorate. The system uses sensors whose scan patterns are generated by a mini-computer and generates a small tracking window that is programmed to follow a target as it moves through the sensor's field-of-view as is illustrated by Figure 2.

14° x 14° Sensor Field-Of-View

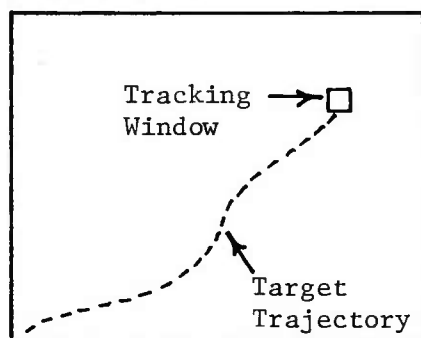


FIGURE 2. TRACK WHILE SCAN SYSTEM

The position of the tracking window is generated by a prediction filter and the position of the target within the window is a measure of the prediction accuracy. This is essentially a servo problem and the prediction filter was evaluated as to how well it could follow a target which is experiencing a constant angular acceleration. After some reflection, it became apparent that this same concept of using a prediction technique could be applied to a conventional servo system for control purposes.

The prediction filter being used (5) is a five point filter based on smoothed position and smoothed velocity with the assumption that over a short time interval an object's trajectory can be adequately represented by a second-order curve. The resulting equation for the output of the filter is given by

$$x_{\text{PRED}} = \frac{(x_4 - x_5) + (x_2 - x_1)}{16} + \frac{2(x_5 - x_2) + (x_5 - x_3)}{4} + x_5 - x_2 + x_1 ,$$



BRADLEY

where

$x_{\text{PRED}}$  = predicted position of target on next sample,

$x_5$  = present target position,

$x_4$  = position of target on previous sample,

etc.

As a servo control element, the filter can be used as shown in Figure 3 and it was this approach that was used to begin the APF development.

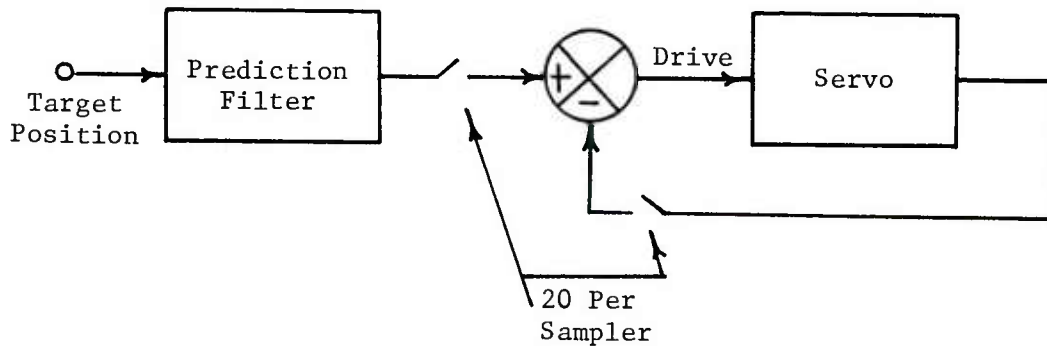


FIGURE 3. BASIC PREDICTION FILTER SERVO

### III. COMPUTER SIMULATION OF THE APF

It is generally more practical and economical to develop a servo compensation through the use of a large scale computer program than to attempt the development on an actual servo system. The APF concept was worked out with such an approach where the servo model was a standard quadratic equation given by

$$G(S) = \frac{\theta_o}{\theta_e} = \frac{7.5}{S(1 + \frac{2 \times 0.47}{18} S + \frac{S^2}{18^2})}$$

This is the azimuth servo transfer function that has been experimentally worked out for the system shown in Figure 1 which was the system

that the APF was primarily developed for. In order to program this transfer function, the technique of numerical integration (6) was used which yields the following equations:

$$\ddot{\theta}_0 = (18)^2(7.5)\theta_e - (18)(2)(.47)\ddot{\theta}_0 - (18)^2\dot{\theta}_0 \quad ,$$

$$\ddot{\theta}_0 = \ddot{\theta}_{-1} + (3\theta_{-1} - \theta_{-2}) \frac{\Delta T}{2} \quad ,$$

$$\dot{\theta}_0 = \dot{\theta}_{-1} + (\ddot{\theta} + \ddot{\theta}_{-1}) \frac{\Delta T}{2} \quad ,$$

$$\theta_0 = \theta_{-1} + (\dot{\theta} + \dot{\theta}_{-1}) \frac{\Delta T}{2} \quad .$$

Using these equations, a simulation program was written (7) that provided the means to analyze the APF concept. Using this simulation, the configuration of Figure 3 was subjected to a step input with the resulting response shown in Figure 4 and then to a constant acceleration forcing function with the response as shown in Figure 5.

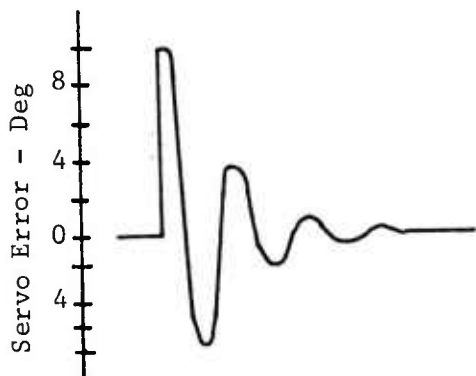


FIGURE 4. STEP RESPONSE

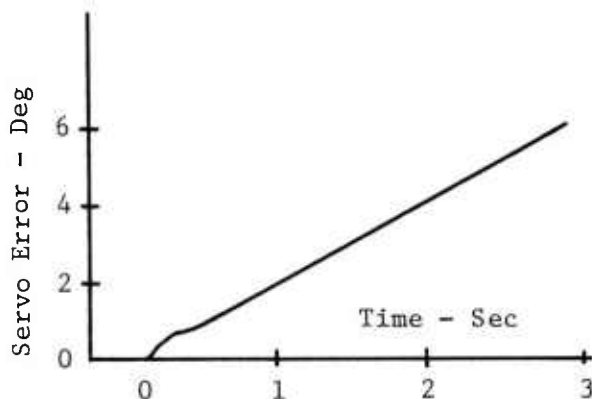


FIGURE 5. ACCELERATION RESPONSE

The results indicated that the system was stable but that the step response had a rather large percentage of overshoot (60 percent) and that it was functioning as a Type I servo since the resulting servo error was increasing as a function of time. This suggested that to reduce the servo error an integration of the error signal added to the

servo drive would be beneficial. To achieve this, the configuration of Figure 6 was used where the APF is represented by the elements inside the dashed lines.

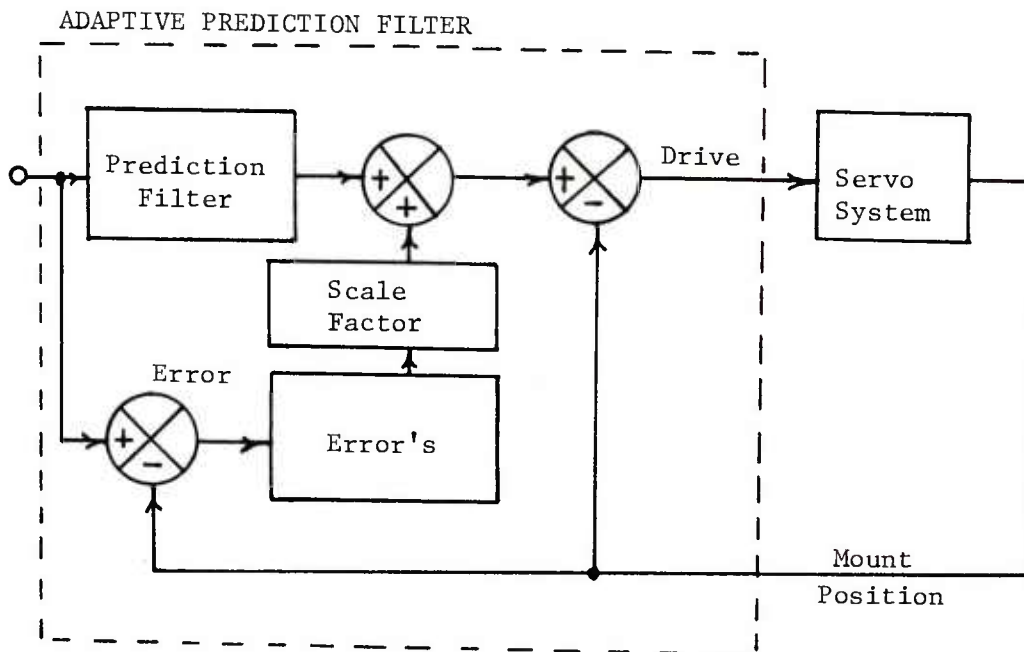


FIGURE 6. MODEL FOR APF

The response of this configuration to a small step input is shown in Figure 7 and the response to a constant acceleration forcing function is shown in Figure 8. The step response still has a very high percentage of overshoot but the addition of the integration term successfully limited the servo error and forced the system into a Type II mode of servo operation. By varying the scale factor shown in Figure 6, the step response can be improved but a loss of performance results in the constant acceleration test. A trade-off between the two parameters is required to arrive at the best overall level of performance.

As seen in Figure 7, the response of the APF to a larger step would cause an undesirable amount of overshoot and require too long for the system to reach the null position. To overcome this, the APF model was adjusted so that when the servo error exceeds a predetermined amount the error summation term in Figure 6 is set to zero and the servo drive is limited to a fixed amount. Under these conditions, the

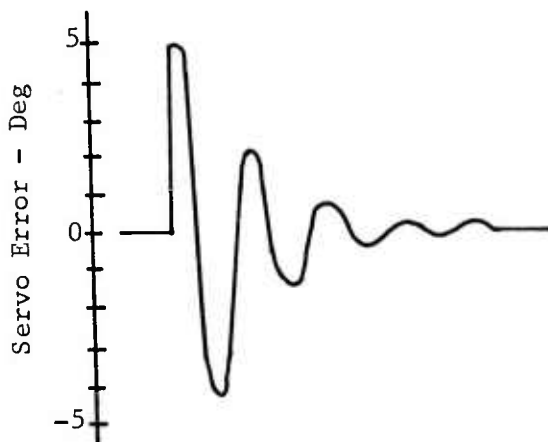


FIGURE 7. STEP RESPONSE

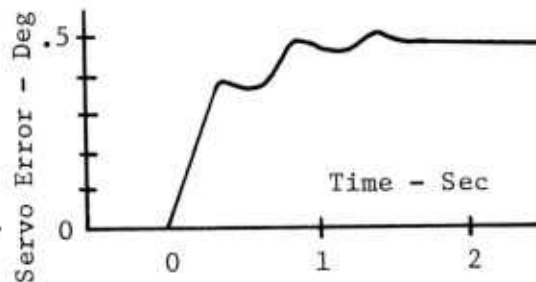


FIGURE 8. ACCELERATION RESPONSE

response of the system to a large step becomes very reasonable as the simulation results of Figure 9 show.

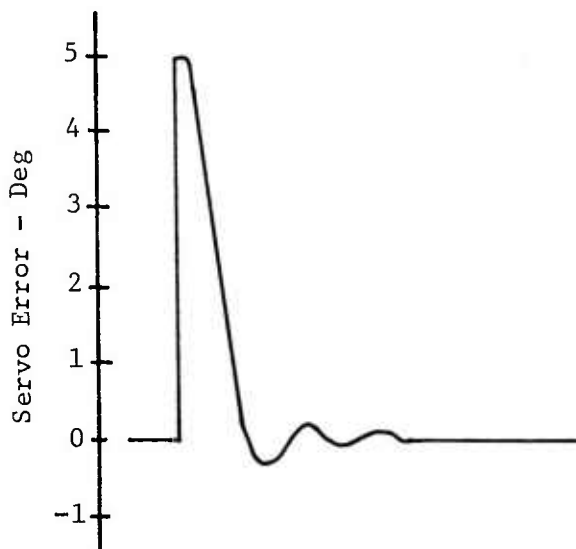


FIGURE 9. STEP RESPONSE

With the inclusion of the provisions to control a large step input, the simulation studies of the APF concept were terminated. A number of significant points were discovered during the simulation study and these are summarized below.

1. The study showed that the APF would provide stable operation at sample rates as low as 20 per second.
2. Type II servo performance can be achieved through applying a cumulative summation of the servo error signals to the drive signal.
3. The final output of the APF will be an analog voltage which can be digitally scaled inside the APF so that noise effects will be minimized.
4. For a fixed input, the cumulative summation of the error signals will collapse to zero which will drop the system into a very low gain Type I servo. The effect will be that the system will selectively switch between Type I and Type II depending on the input requirements. This provides a unique mode of operation.

#### IV. SERVO ANALYSIS OF THE APF

The simulation studies indicated that the APF was producing Type II servo performance since the servo error was constant for a constant acceleration forcing function but it was not immediately obvious why this should be true (8). Figure 10 shows a simplified representation of the APF without the predictive portion.

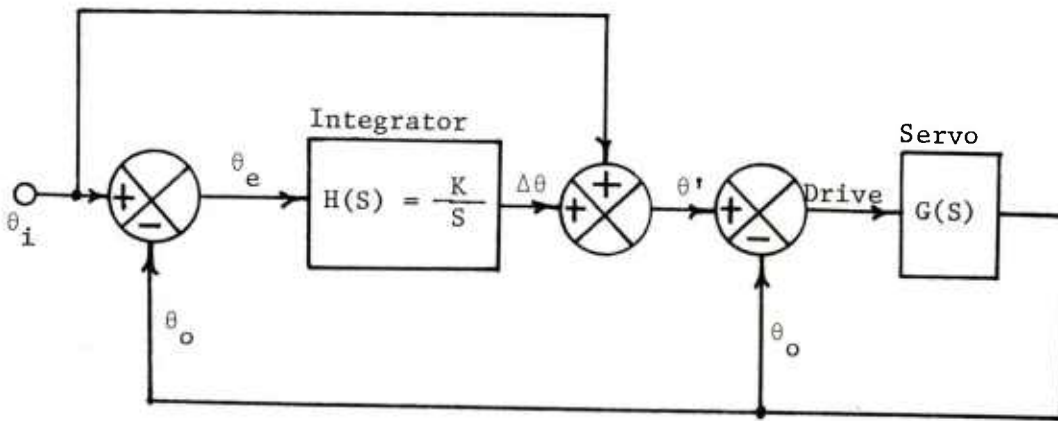


FIGURE 10. SIMPLIFIED APF MODEL

From Figure 10,

BRADLEY

$$\frac{\theta_o}{\theta'} = \frac{G(S)}{1 + G(S)} .$$

But

$$\theta' = \Delta\theta + \theta_i = \frac{K}{S} \theta_e + \theta_i .$$

But

$$\theta_i = \theta_e + \theta_o .$$

Then

$$\theta' = \frac{K}{S} \theta_e + \theta_e + \theta_o = \theta_e \left( \frac{S + K}{S} \right) + \theta_o ,$$

and finally,

$$\frac{\theta_o}{\theta'} = \frac{\theta_o}{\theta_e \left( \frac{S + K}{S} \right) + \theta_o} = \frac{G(S)}{1 + G(S)} .$$

Simplifying,

$$\frac{\theta_o}{\theta_e} = G(S) \left[ \frac{S + K}{S} \right] .$$

This is the form for a Type II servo where the value of K is associated with the system acceleration constant and so it follows that the APF is indeed a Type II servo since it has been shown to be equivalent to this same standard form.

#### V. PROTOTYPE APF

The successful results from the APF simulation indicated that the concept of the APF was valid and so a prototype unit was then built using a micro-processor that was available. The hardware was developed to work from a serial 120 bit modem message of the type generated by the real-time computer system at White Sands and transmitted to various tracking sites at a message rate of 20 per second. Transmitted azimuth and elevation angles are the look angles to the target and are relative to the site receiving the data. The APF takes the azimuth and elevation pointing angles and the mount position in the form of optical encoder data and generates analog drive voltages for the servo. The prototype APF was constructed so that it would function just as the simulation model of Figure 6. The micro-processor



BRADLEY

selected was the National "Imp 16" with a 16-bit word, 4K of volatile memory, and a fairly versatile set of instructions. The prototype APF, shown in Figure 11, includes the micro-processor, interface unit, and a functional test box. The servo system used for prototype testing was the White Sands Versatile Tracking Mount shown in Figure 1.



FIGURE 11. PROTOTYPE APF

Before the testing was begun, the basic servo was set up to accept a simple drive signal. For a 0.7 degree step input, the gain adjustment was set to give the response shown in Figure 12. With adjustment of the gain for a reasonable step response, the servo has had all the adjustments required which makes a very straightforward procedure to follow. It should be noted that the system gain is very low which gives the system a good immunity to noise. With the completion of this step, the APF was configured as shown in Figure 6 and the scale factor was adjusted to give a step response for a 0.35 degree step as shown in Figure 13.

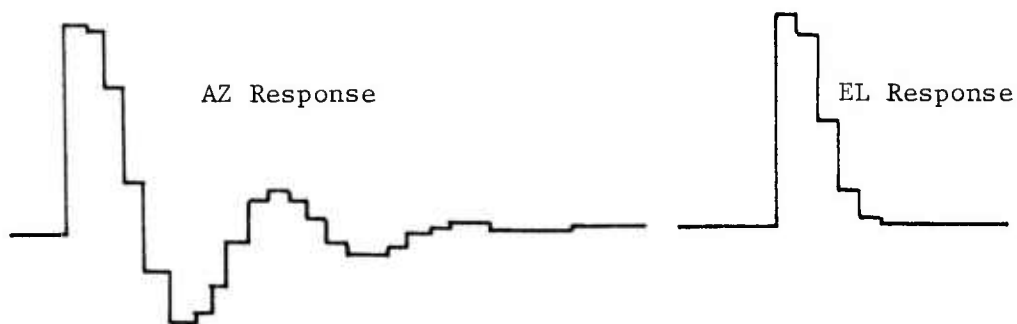


FIGURE 12. UNCOMPENSATED APF STEP RESPONSE

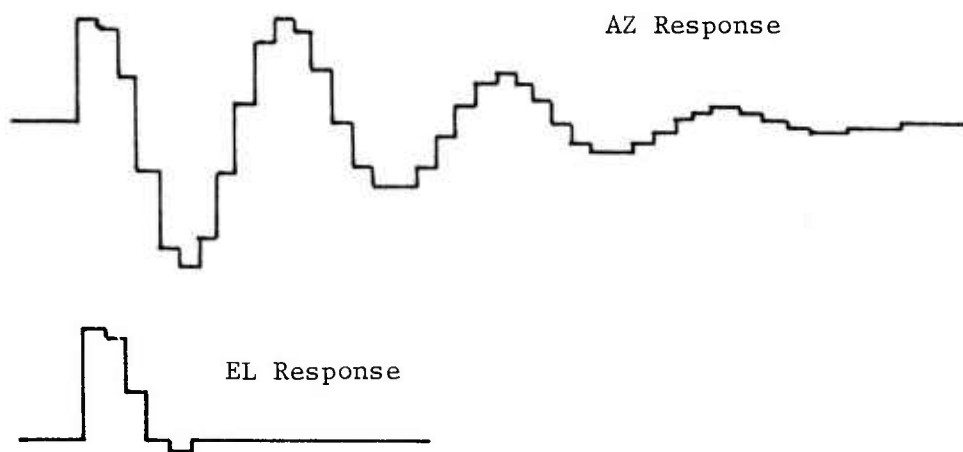


FIGURE 13. APF STEP RESPONSE

One of the primary functions of the APF was to implement a system that would provide a good large scale step response. In the simulation studies, this was done by testing the servo error and applying constant drive for conditions when the servo error exceeded a fixed amount. This same approach was successfully used in the APF prototype and the results of applying a 45 degree step are shown in Figure 14.

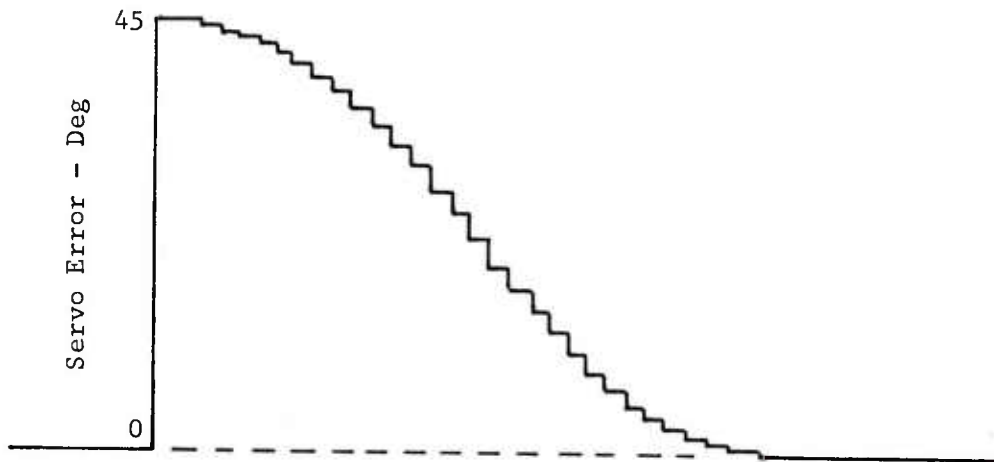


FIGURE 14. APF RESPONSE FOR A LARGE STEP

The final phase of the APF prototype testing was to measure the performance when a constant acceleration forcing function was applied as the input. The scale factor was left at the same value determined by the step response tests as illustrated in Figure 13. The acceleration test results are shown in Figure 15 where the acceleration was 20 degrees per second per second.

As the simulation studies had predicted, the APF does provide Type II servo performance. The test results were satisfactory in every respect and conclusively show that the APF concept is valid and that hardware to implement the concept can be built.

#### VI. PRODUCTION MODEL OF THE APF

Due to the successful results with the APF prototype, a determination was made to build a production version of the APF using Digital Equipment Corporation's LSI-11 Micro-Computer. Working through Lockheed Electronics Company, which serves as the in-house contractor at White Sands, a design for the APF was formulated that has the following features.

1. LSI-11 Micro-Computer with 16-bit word length, 4K of RAM memory, and some 400 programming instructions.
2. 4K of Programmable Read Only Memory (PROM) to insure maximum reliability and protection against loss of operating programs.
3. Serial interface for teletype and serial modem operation.

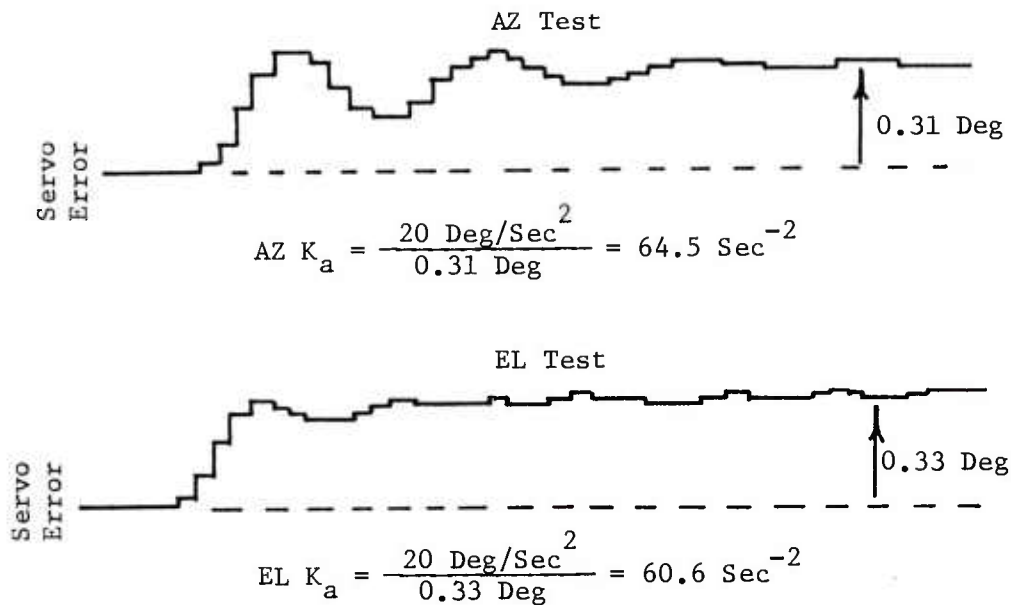


FIGURE 15. APF ACCELERATION RESPONSE

4. Two 16-bit parallel entry data ports serviced as DMA channels.

5. Four 16-bit parallel entry data ports serviced under program control.

6. Four 12-bit D/A output channels providing analog outputs ranging between  $\pm 10$  volts.

The production model APF is shown in Figure 16 and the component cards are shown in Figure 17.

## VII. SUMMARY

The APF concept evolved from several earlier efforts at White Sands to improve the servo performance of various optical tracking systems of the type currently in use at test ranges around the world. These earlier efforts had only a limited success because they required a rather complex analysis to be useable and also because a full sized mini-computer was necessary to implement the approaches. These efforts were not cost effective.

With the advent of small and low cost micro-computers, it became feasible to develop a digital filter for use in servo control

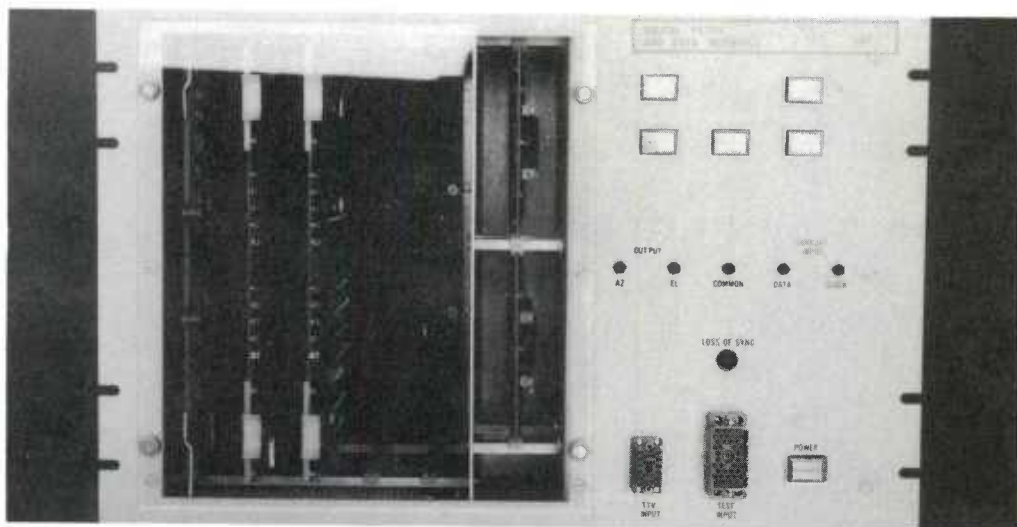


FIGURE 16. PRODUCTION MODEL APF

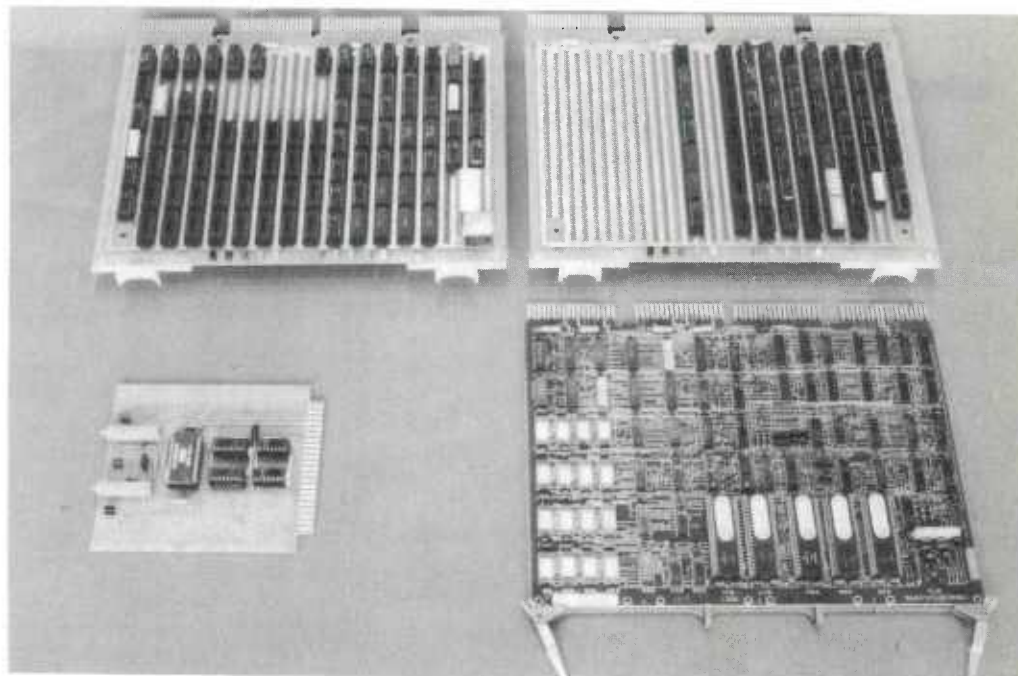


FIGURE 17. APF CIRCUIT CARDS

## BRADLEY

applications. Development of a simple approach to the problem of servo compensation in the form of the APF has made it practical to develop a high performance but low cost system.

The APF concept as outlined in this paper has been verified through the use of a simulation model, a confirming theoretical analysis, and finally a demonstration of a prototype unit. The APF provides a stable Type II servo mode of operation at sample rates as low as 20 per second and offers a proven approach that will yield a high performance system at a low cost.

## BIBLIOGRAPHY

- (1) Bradley, Lester; Compensation of RCT by Sampled-Data Techniques, June 1969; Optics Division Engineering Memorandum 69-2, White Sands Missile Range, New Mexico.
- (2) Bradley, Lester; Servo Compensation With a Digital Computer, April 1972; Optics Branch Technical Memorandum 72-1, White Sands Missile Range, New Mexico.
- (3) Galos, G. E.; Performance of the Dual Servo in the LRTS, April 1975; Optics Division Engineering Memorandum 75-6, White Sands Missile Range, New Mexico.
- (4) Bradley, Lester; Use of Two Electro-Optical Sensors Driven by Computer Generated Scan Patterns to Form a Real-Time Two-Station Tracking System; Proceedings of the IEEE 1975 National Aerospace and Electronics Conference (NAECON '75).
- (5) Dart, John; A Tracking Prediction Routine, November 1974; Optics Division Engineering Memorandum 74-1, White Sands Missile Range, New Mexico.
- (6) Nixon, F. E.; Principles of Automatic Controls, Prentice-Hall, Inc.; 1953, page 263.
- (7) Dart, John and Bradley, Lester; A Servo Simulation Program for the Adaptive Prediction Filter, February 1976; Optics Division Engineering Memorandum 75-3, White Sands Missile Range, New Mexico.
- (8) Stephenson, Henry; Simplified Model of the Adaptive Prediction Filter, February 1976; Data Systems Division Engineering Memorandum 76-10, White Sands Missile Range, New Mexico.





A PROCEDURE FOR THE  
STATISTICAL ANALYSIS OF VEHICULAR  
NOISE EMISSION SPECTRA FOR LIMITED SAMPLES

RICHARD N. BROOKE, JR., Ph.D.  
US ARMY TANK-AUTOMOTIVE DEVELOPMENT CENTER (PROV)  
WARREN, MICHIGAN 48090

INTRODUCTION

Recent emphasis on the reduction of environmental pollution has prompted the legislation of many new standards defining maximum noise limits inside of, and in close proximity to all types of commercial and military automotive vehicles. These standards require the collection of noise emission data on both newly produced and in-service vehicles for determination of conformance. Since every vehicle to be produced or currently in existence that falls within the jurisdiction of the standards cannot be measured individually due to time and cost constraints, a method of accurately predicting the noise profile of a large population of similar type vehicles utilizing data collected from only a limited sample of the population is required. This paper presents such a statistical method, and illustrates its application utilizing data taken on multiple samples of several types of military tactical vehicles. These data were collected at the US Army Aberdeen Proving Ground during April 1973 through March 1974.

It is important to emphasize that the statistical methods presented may be utilized in the prediction of noise profiles on any type of military or commercial equipment under an infinite variety of controlled test conditions. These methods should, therefore, find application in determining conformance to a large and varied number of noise specifications.

With this in mind, the Research Division of the Tank-Automotive Development Center (Prov) has developed an iterative procedure and the associated computer program for the statistical prediction of mean population noise profiles from a limited data sample.

## OBJECTIVES

Develop a statistical method for determining the mean noise spectra of a vehicle type and the variance of that mean from noise spectra data collected on multiple samples of the vehicle type.

Apply this technique in the determination of representative one-third octave band noise spectra for various types of military tactical vehicles.

## VEHICLE NOISE TEST PROCEDURE

Seven different military vehicle types, each with five samples, were withdrawn from depots and used for noise emission tests. The actual vehicle type descriptions are found in a recent report of Brooke and Rees [1]. Each vehicle was basically in new operating condition, and was selected at random from available stock. All vehicles were operated according to MIL-STD-1474 procedures for both interior and exterior noise evaluations [2].

In its exterior noise evaluation section, paragraphs 5.3.1 and 5.3.2, the military standard references two Society of Automotive Engineers' Measurement Procedures for use in the evaluation of noise levels. They are SAE J986a [3] for vehicles having gross weights less than 6,000 pounds, and SAE J366b [4] for vehicles with weights equal to or greater than 6,000 pounds. The 1/4-ton M151A2 was the only vehicle type tested according to the SAE J986a procedure. The gross weights of the remaining vehicles were in excess of 6,000 pounds, and were, therefore, tested utilizing SAE J366b procedures. The vehicles were operated in the gear range that would allow them to accelerate from 2/3 maximum engine RPM to maximum RPM within the prescribed distance while not exceeding the stipulated 35 MPH (56 km/h) maximum within the 40 ft. (12 m) end zone. Tests for different vehicle types were, therefore, not all performed in the same gear range.

For measurement of noise on the vehicle interior, microphones, sound level meters, and associated equipment were calibrated and installed on board the vehicle and noise measurements were accomplished as specified in paragraphs 5.1.3 through 5.1.3.5.6 of MIL-STD-1474. Exterior noise measurements were accomplished utilizing the data collection procedures specified in SAE J986a and SAE J366b. Measurements were made with the vehicle traversing the test course in both directions in order to determine the effect of any noise directionality caused by the exit of the engine exhaust to the left or right of the vehicle.

Analog magnetic type data were recorded of each vehicle test, utilizing a portable instrumentation type recorder and a sound level meter meeting the requirements of MIL-STD-1474. The recorder was connected to the AC output of the sound level meter, and the meter was placed in the flat response mode. Upon return to the laboratory, the magnetic tape data were fed into a real time one-third octave analyzer. This equipment utilizes 34 parallel active filters to store 30 channels of 1/3 octave data as well as the A, B and C weighted, and unweighted total spectrum levels. These data are all updated continuously and simultaneously as the acoustic signal is input to the analyzer, and are available as digital data in the form of a CRT display, a digital print-out, or a paper punch tape.

In the reduction of the exterior drive-by noise data, the analyzer was set to continuously monitor the output of the "A" weighted spectrum filter and automatically stores all 34 channels of data when this filter reached a maximum. By using this technique, the 1/3 octave spectrum that produced the maximum dB(A) level as the vehicle accelerated by the microphone was stored in the analyzer's memory. Similarly, the noise data taken on the interior of the vehicles were also reduced in this manner with the real time 1/3 octave analyzer. Upon completion of each data set, the stored 1/3 octave spectra and the weighted and unweighted total dB values were permanently recorded as digital data on paper punch tape. These data tapes were then interfaced into the computer during the data input portion of the statistical analysis program for each separate vehicle type.

#### DISCUSSION OF STATISTICAL SITUATION

This section discusses several different approaches that may be utilized in reducing drive-by noise spectra data (or any other similar application) and obtaining the required statistical parameters for each vehicle type describing each of thirty 1/3 octave bands. The discussion centers around the analysis of noise data taken on vehicles during the exterior acceleration and drive-by tests stipulated in MIL-STD-1474. The best technique for determination of the maximum exterior noise limit of any particular model of vehicle would be to test as many vehicles of that type as possible. The data derived from these tests could then be statistically analyzed and a standard noise level spectra determined. To execute this task properly, however, would involve testing many vehicles, and huge test costs would result, not to mention the time element involved. It is not economically feasible to test a thousand or even several hundred vehicles of a particular model for determining the standard drive-by noise level spectrum for that model.

This report offers an alternative method for accomplishing the above result utilizing a smaller sample (5 to 25 vehicles) of a certain model type to approximate the total population. First, the small sample of vehicles chosen must be either new or in peak operating condition. With a small sample of vehicles, ideally the same driver should be used for performing the drive-by acceleration tests on every vehicle. This would minimize the human error factor associated with different drivers operating under the same procedure in slightly different manners or interpretations. It may not be physically or financially possible, however, to utilize the same driver for every tested vehicle.

Suppose a certain vehicle (A) is allowed to make repeated (N) drive-by tests (runs) according to the above procedure, and data is acquired in the normal manner for later reduction. When the noise data have been analyzed properly according to its output levels versus frequency, normally it is anticipated that there should be reasonable agreement in the data between the different drive-by tests of the same vehicle. The frequency analysis performed consists of determining the noise level within specified frequency bands, usually octaves or  $1/3$  octaves. The frequency spectra for the "N" pass-by tests can now be statistically analyzed, and the mean and variance for each band calculated in the normal manner to obtain a standard noise spectrum.

But, in reality, regardless of how large the quantity (N) may be, there is a large uncertainty that vehicle "A" is a true representation of that particular vehicle type for determining a standard noise level spectrum. The production of a vehicle incorporates many different items of complex structure assembled together to form the finished product. Each of these complex structures (radiator, muffler, etc.), although similar in design and construction, is not identical to every other one produced. Thus, any two vehicles of the same type would differ enough in physical construction to have slightly different radiated noise levels when measured in identical operation tests. With the many possible noise sources contributing to the total vehicle noise, the tolerances in design of the various major and minor noise components will necessitate slightly different contributions for each vehicle. There are also several variables other than the vehicle that can affect the actual noise measurements. These variables include the test site surface conditions, driver, and instrumentation error to include both human and electronic sources. Changes in the ambient weather conditions will also contribute to the variation of noise levels, even though weather conditions are monitored to insure that wind, temperature, and humidity effects are minimized as much as possible.

In order to determine a noise level standard for a particular vehicle type, it is imperative that multiple vehicles be tested. The test procedure then consists of testing multiple vehicles and subjecting each of these vehicles to many drive-by or similar application tests. Now, with the noise data obtained using the above test procedure or any other method, the problem becomes how to combine all the noise spectra to obtain the best estimate of the true population noise spectrum mean.

In a test procedure such as this, with multiple data runs made on multiple vehicles, one might treat each run (pass-by) of each different vehicle on an equal basis. Thus, if there were  $N$  different vehicles and each vehicle made  $M_i$  runs, the analysis would be made on  $M$  different sets of data to determine the various statistical parameters. This method assumes that each run is a separate and equal component without regard to the actual vehicle. If  $X_{ij}$  is the noise level measurement of the  $j^{\text{th}}$  run for the  $i^{\text{th}}$  vehicle, then the sample mean and variance are:

$$M = \sum_{i=1}^N M_i \quad (1)$$

$$\bar{X} = \sum_{i=1}^N \sum_{j=1}^{M_i} X_{ij} / M \quad \begin{array}{l} i=\text{subscript over} \\ \text{vehicles} \end{array} \quad (2)$$

and,

$$S^2 = \sum_{i=1}^N \sum_{j=1}^{M_i} (X_{ij} - \bar{X})^2 / M - 1 \quad \begin{array}{l} j=\text{subscript over} \\ \text{runs} \end{array} \quad (3)$$

This method would tend to put more emphasis or weight on the vehicles with the greater number of runs, which is reasonable to a certain extent. But the main hypothesis of this paper is that all vehicles are not identical in structure and ultimately in noise emissions. Consequently, treating each run of the different vehicles as a separate and equal component might lead to the case where a vehicle with the greatest number of runs would unfairly distort the means and variances from vehicles with lesser run numbers in determining the standard for this vehicle type. This situation would primarily arise when all vehicles had unequal or varying numbers of drive-by runs.

Another reasonable approach to consider is to treat each vehicle individually, and then average over all vehicles for determining the standard parameters. Data for each vehicle will then have



been determined from the multiple runs performed by that vehicle. This technique would weigh each vehicle equally and would be independent of the number of runs for any one vehicle. In reality, however, the noise data of a vehicle determined from (R) number of runs should be more reliable and have more weight statistically than another vehicle's data determined from only (P) number of runs (where  $R > P$ ). Thus, it would seem reasonable that some technique must be found that incorporates the weighting of various vehicles according to some measure of the number of tests performed on each.

Now the problem reduces to finding the best technique for combining various sample means, where each sample mean has been determined from a varying number of elements. The generalization of this problem to multi-sample means can be solved by utilizing a technique known as the one-way analysis of variance. This approach is applied because there is a variance associated with similar vehicles (groups) which is independent of the variance within each vehicle for all of its different drive-by tests. This technique will provide the correct weightings for vehicles with the greater number of tests. The next section of this paper will briefly describe and outline the application of the one-way analysis of variance to the stated problem.

#### THE ONE-WAY ANALYSIS OF VARIANCE NOISE LEVEL MODEL

The model will assume that the contribution to the total vehicle noise comes from two sources. The first source is directly related to the actual vehicle being tested. One initial assumption is that the means of the different vehicles are not equal, but will differ slightly. Obviously the different runs of each separate vehicle will have the same mean, but the vehicle means are not assumed to be equal in the hypothesis.

The second source to the total noise in this model are the errors in the actual measurements of the noise spectra. These variations will be functions of the multiple runs by the microphone in this case. A block diagram describing the model is contained in Figure 1 below.

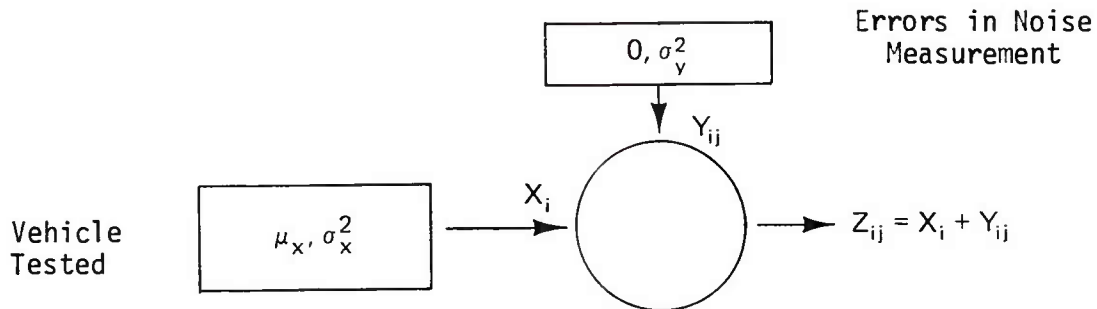


FIGURE 1. Noise Level Model With Two Contributions.

For this model the contribution to the total noise from the actual vehicle being tested is  $X_i$ , which is assumed to be independent normally distributed,  $X_i \sim N(\mu_x, \sigma_x^2)$ . The contribution from the errors in test measurement,  $Y_{ij}$ , is similarly an independent normally distributed variable with zero mean and variance  $\sigma_y^2$ ,  $Y_{ij} \sim N(0, \sigma_y^2)$ . Over the multiple runs for each separate vehicle, it is reasonable to anticipate the mean of this contribution to be zero.

The actual quantity measured experimentally is the sum of the two contributions,  $Z_{ij}$ , where "i" is the index over the vehicle number and "j" is the index for the run number for the  $i$ th vehicle. The contributions from the two sources to the total noise spectrum are totally additive. Thus, the quantities that must be determined in this model are  $\mu_x + (\mu_y = 0) = \mu_x$ , and  $\sigma_x^2 + \sigma_y^2 = \sigma^2$  to obtain the best estimate of the mean and variance respectively for the entire vehicular data set. There are several possible procedures for estimating the above parameters from the literature [5], but the technique employed seems most applicable [6].

The three quantities,  $\mu_x$ ,  $\sigma_x^2$  and  $\sigma_y^2$ , are all estimated by defining various quantities which are dependent on various weighting parameters. These weighting parameters can be solved for by creating various constraints on the resulting relations. The actual derivation of the resulting equations for these three parameters is provided in an earlier paper by this author [1]. From the derived equations, an iterative procedure is utilized for calculating the desired quantities, and this iteration process will be briefly outlined.

THE RECOMMENDED PROCEDURE FOR UTILIZING THIS MODEL

The following outline will briefly describe one technique that can be utilized in solving the model equations through an iteration process for  $\mu_x$ ,  $\sigma_x^2$ , and  $\sigma_y^2$ .

$M$  = total number of vehicles (same type)

$N_i$  = number of runs for  $i^{\text{th}}$  vehicle

STEP 1 - Compute  $S^2$  and equate this quantity to  $\sigma_y^2$

$$S^2 = \sum_{i=1}^M K_i \sum_{j=1}^{N_i} (Z_{ij} - \bar{Z}_i)^2 \quad (4)$$

where:

$$K_i = \frac{1}{M \sum_{i=1}^M (N_i - 1)}; \quad \bar{Z}_i = \frac{1}{N_i} \sum_{j=1}^{N_i} Z_{ij}.$$

$\bar{Z}_i$  is the mean of the  $i^{\text{th}}$  vehicle and  $Z_{ij}$  is the noise level measurement for  $j^{\text{th}}$  run of the  $i^{\text{th}}$  vehicle. The  $K_i$  parameter is actually a constant.

$$\hat{\sigma}_y^2 = S^2 \quad (5)$$

STEP 2 - Compute  $T$  (the Grand Mean):

$$T = \sum_{i=1}^M J_i \bar{Z}_i \quad \text{where } J_i = \frac{1}{M} \quad (6)$$

Likewise, this quantity, which is initially the average of means for all vehicles, is estimated to be  $\mu_x$ . Notice that  $J_i$  is initially a constant also.

$$\hat{\mu}_x = T \quad (7)$$

STEP 3 - Compute  $U^2$  (and then  $\hat{\sigma}_x^2$ ).

$$U^2 = \sum_{i=1}^M M_i (\bar{Z}_i - T)^2 \quad (8)$$

where:

$$M_i = N_i M_0, \text{ and } M_0 = \frac{1}{\sum_{i=1}^M N_i (1 - 2J_i + \sum_{j=1}^M J_j^2)}$$

$$\hat{\sigma}_x^2 = U^2 - \sigma_y^2 \left[ \sum_{i=1}^M M_i \left( (1/N_i) - (2J_i/N_i) + \sum_{j=1}^M J_j^2/N \right) \right] \quad (9)$$

STEP 4 - Recompute  $T$ , using  $\sigma_y^2 = \hat{\sigma}_y^2$ ,  $\sigma_x^2 = \hat{\sigma}_x^2$ , to get another estimate for  $\mu_x$ .

$$T' = \sum_{i=1}^M J_i \bar{Z}_i \quad (10)$$

$$J_i = \frac{\frac{1}{\sigma_x^2 + (\sigma_y^2/N_i)}}{\sum_{i=1}^M (1/(\sigma_x^2 + (\sigma_y^2/N_i)))} \quad (11)$$

and the constraint  $(\sum_{i=1}^M J_i = 1)$  exists. Notice the  $J_i$  values are no longer constants.

$$\mu'_x = T' \quad (12)$$

STEP 5 - Recompute  $U^2$  to get another  $\sigma_x^2$ .

$$U'^2 = \sum_{i=1}^M M_i (\bar{Z}_i - T')^2 \quad (13)$$

$$\hat{\sigma}_x'^2 = U'^2 - \sigma_y^2 \sum_{i=1}^M M_i \left[ (1/N_i) - (2J_i/N_i) + \sum_{j=1}^M J_j^2/N \right] \quad (14)$$

STEP 6 - Compare the latest  $T'$  with the previous one  $T$ , and likewise compare  $\sigma_X'^2$  with previous one ( $\sigma_X^2$ ).

If  $|T-T'| \leq \epsilon$ , then the values have converged to the best estimates for  $\mu_X$  and  $\sigma_X^2$ .

If  $|T-T'| > \epsilon$ , then repeat Steps 4 and 5 until convergence occurs.

### CONCLUSIONS

From the above model procedure,  $\mu_X = T$  gives the best estimate of the true population mean, and similarly  $\sigma^2 = \sigma_X^2 + \sigma_Y^2$  gives the best estimate of the population variance for standardization purposes. Thus, if  $N$  measurements are made on any vehicle, from the above result, one would expect each measurement to have a mean  $\mu_X$  and variance ( $\sigma_X^2 + \sigma_Y^2$ ). Likewise the average  $\bar{Z}_i$  measurement would have a mean  $\mu_X$  and a variance  $\sigma_X^2 + (\sigma_Y^2/N)$ .

This model was applied to each of seven different types of military tactical vehicles, operating in the exterior drive-by procedure. The actual means determined from this model differ only slightly from the means that could be estimated by averaging individual vehicle means or by using a weighted average mean. But the value of using this model is in determining the correct variance that is associated with the computed mean for each center frequency. With the best estimate for the total vehicle variance being the sum of two contributions,  $\sigma_X^2 + \sigma_Y^2$ , one interesting result was that the  $\sigma_X^2$  contribution was larger than the  $\sigma_Y^2$  value in most cases for each center frequency. This should be interpreted to mean that for each vehicle that performs the same test many times, there will be a good correlation and small variance in the results. But when comparing different vehicles that undergo the same test, the results will show greater discrepancies or variations in the noise level spectra. This is basically attributed to the fact that different vehicles (same type) are not identical in physical structure and consequently in their noise spectrum characteristics.

Because different vehicles of the same type (model) have such wide varying noise level spectra, it would seem imperative in setting noise level standards that multiple (>10) vehicles be tested. The tactical vehicles' best estimate spectra are shown in another report [1].

BROOKE

REFERENCES

1. R.N. Brooke, and D.W. Rees, "Procedure for Statistical Analysis of Vehicular Noise Emission Spectra for Limited Samples", USA Tank-Automotive Command Technical Report #82628, July 1975.
2. Military Standard 1474, "Noise Limits for Army Materiel", USA Missile Command (1973).
3. Society of Automotive Engineers Technical Report J986a, "Sound Level for Passenger Cars and Light Trucks", July 1968.
4. Society of Automotive Engineers Technical Report J366b, "Exterior Sound Level for Heavy Trucks and Buses", April 1973.
5. K.A. Brownlee, Statistical Theory and Methodology, Chapter 10, John Wiley & Sons, NY, May 1967.
6. R. Crane, and W. Richardson, private communications.





A NEW CAPABILITY FOR PREDICTING HELICOPTER  
ROTOR NOISE IN HOVER AND IN FLIGHT

THOMAS J. BROWN, MR.  
FEREIDOUN FARASSAT, PH.D.  
USAAMRDL, JIAFS, LANGLEY RESEARCH CENTER  
HAMPTON, VIRGINIA 23665

The problem of noise radiation from helicopter rotors has gained prominence due to its annoyance to the public and detectability. Although the rotor is one of the several noise generating sources of helicopters, it is the most important in the external regions of the present machines. Clearly, the reliable prediction of this noise in the design stage of the rotor is an important step in controlling the level of the noise intensity. There has been a steady advance in the last decade in the prediction of rotor noise (ref. 1). There are still disagreements between the theoretical and experimental results of rotor acoustics. In addition to this shortcoming, the available theories suffer from a combination of the following restrictions:

- a. Compactness of the acoustic sources
- b. Hovering helicopter
- c. Observer in the far field
- d. Limited airfoil shapes
- e. Limited surface pressure distribution models
- f. Singularities in the solution for high rotor tip speeds
- g. Neglect of the thickness noise

It is believed that the removal of these restrictions and the inclusion of the nonlinear propagation effects should result in reliable prediction of the rotor noise.

Traditionally, rotor noise has been divided into several categories such as rotational, vortex and thickness noise. These can be grouped into two broad classes – those depending on the local

pressure and viscous stress distribution on the rotor blades and those due to the normal velocity distribution on the blades. For example, rotational noise belongs to the first class and thickness noise to the second. A theory which incorporates the effects of surface pressure and normal velocity distribution on a moving body is developed in reference 2. The formulation is then specialized for propellers and helicopter rotors. In this work a study of compactness assumption of sources on moving bodies has revealed that in the case of helicopter rotors and propellers, the sources on the blades cannot be considered compact for the observer position in a large region of space around the rotor. If the compactness restriction is removed, then one would like to remove the restrictions of limited airfoil shapes and surface pressure distribution models to improve the prediction technique.

The present paper discusses a new computer program developed by the authors at NASA Langley Research Center based on the results of reference 2. The purpose of developing this program has been to remove the restrictions of the already existing theories and thus achieve a new capability in the prediction of the rotor and propeller noise. The acoustic computation is performed in the time domain and the resulting pressure signature is then Fourier analyzed to get the acoustic pressure spectrum.

Examples are presented in this paper to demonstrate the capabilities of this new program. These examples are selected mainly with regard to the restrictions discussed earlier which are removed by the new formulation.

### THE ACOUSTIC FORMULATION

The formulation derived in reference 2 is briefly discussed here. Consider a moving body whose surface is described by  $f(\vec{y}, \tau) = 0$  where  $\tau$  is the source time. Let  $V_n$  be the local normal velocity of the surface, the acoustic pressure  $p(\vec{x}, t)$  is given by

$$4\pi p(\vec{x}, t) = \frac{\partial}{\partial t} \int_{\tau_1}^{\tau_2} \int_{\Gamma} \frac{\rho_0 c V_n + p \cos \theta}{r \sin \theta} d\Gamma d\tau + c \int_{\tau_1}^{\tau_2} \int_{\Gamma} \frac{p \cot \theta}{r^2} d\Gamma d\tau \quad (1)$$

Where

- $\vec{x}$ ,  $t$ : observer position and time  
 $c$ : speed of sound in undisturbed medium  
 $\rho_0$ : density of the undisturbed medium  
 $r$ :  $|\vec{x} - \vec{y}|$ ,  $\vec{y}$  source location on the body  
 $\theta$ : the angle between radiation direction  $\vec{r} = \vec{x} - \vec{y}$  and the outward normal to the body  
 $p$ : (under the integral) the surface pressure on the body  
 $\Gamma$ : the curve of the intersection of the collapsing sphere  $g = \tau - t + r/c = 0$  and the body  $f(\vec{y}, \tau) = 0$   
 $\tau_1, \tau_2$ : the times when the sphere  $g = 0$  enters and leaves the body, respectively

For application to rotors and propellers, the above equation will be rewritten in the form given below. Let a new frame  $\eta'$  be fixed to each blade such that  $\eta'_1 \eta'_2$ -plane contains the rotor disk and  $\eta'_2$ -axis is along the span of the blade. Let  $\eta'_3 = T(\eta'_1, \eta'_2)$  and  $\eta'_3 = h(\eta'_1, \eta'_2)$  be the equations of the thickness distribution and camber surface, respectively. The components of unit radiation vector  $(\vec{x} - \vec{y})/r$  and the vehicle velocity  $\vec{V}$  in this rotating frame will be denoted by  $(\hat{r}'_1, \hat{r}'_2, \hat{r}'_3)$  and  $(V'_1, V'_2, V'_3)$ , respectively. Equation (1) can be written as follows (ref. 2):

$$p(\vec{x}, t) = \frac{\partial}{\partial t} [I_1 + I_2 + I_3] + I_4 + I_5 \quad (3)$$

The expressions for  $I_1$  to  $I_5$  are

$$I_1 = \frac{\rho_0 c}{2\pi} \int_{\tau_1}^{\tau_2} \int_{\Gamma(Dp)} \frac{T_1 \tilde{V}'_1 + T_2 \tilde{V}'_2}{rD} d\Gamma d\tau \quad (4)$$

$$I_2 = -\frac{1}{4\pi} \int_{\tau_1}^{\tau_2} \int_{\Gamma(Dp)} \frac{\Delta p \cos \theta_h}{rD} d\Gamma d\tau \quad (5)$$

$$I_3 = - \frac{1}{2\pi} \int_{\tau_1}^{\tau_2} \int_{\Gamma(Dp)} \frac{p_T (T_1 \hat{r}_1' + T_2 \hat{r}_2')}{rD} d\Gamma d\tau \quad (6)$$

$$I_3 = - \frac{1}{4\pi} \int_{\tau_1}^{\tau_2} \int_{\Gamma(Dp)} \frac{\Delta p \cos \theta_h}{r^2 D} d\Gamma d\tau \quad (7)$$

$$I_5 = - \frac{1}{2\pi} \int_{\tau_1}^{\tau_2} \int_{\Gamma(Dp)} \frac{p_T (T_1 \hat{r}_1' + T_2 \hat{r}_2')}{r^2 D} d\Gamma d\tau \quad (8)$$

The symbols used in the above expressions have the following meaning:

$Dp$ : disk plane

$T_1, T_2$ :  $\frac{\partial T}{\partial \eta_1}, \frac{\partial T}{\partial \eta_2}$ , respectively

$\tilde{V}_1$ :  $-V_1' + \eta_2' \Omega$

$\tilde{V}_2$ :  $-V_2' - \eta_1' \Omega$

$\Omega$ : rotor angular velocity

$D$ :  $[1 - \hat{r}_3'^2 + T_1'^2 (1 - \hat{r}_1'^2)]^{1/2}$

$\Delta p$ : local pressure differential producing the lift distribution

$p_T$ : pressure distribution on the blade due to the thickness distribution alone

$\theta_h$ : the angle between the upward normal to the camber surface and the radiation direction

Note that in equations (4) to (8), the integrations are carried out once along the arc of intersection of the collapsing sphere  $g = 0$  and the projection of the blade planforms in the disk plane.

## COMPUTATIONAL METHOD

Equations (4) to (6) are evaluated on a computer using a double numerical integration followed by numerical smoothing and differentiation where required. Each of the five terms are integrated separately. The first three are subsequently differentiated and the resulting five pressure contributions are added to obtain the pressure signature and spectrum.

At source  $\tau = \tau_j$  a sphere is constructed with its center at the observer location. Its radius  $R_j$  is selected such that its circle of intersection,  $C'$ , in the plane of the rotor is tangent to the rotor disk. From this initial geometry the initial observer time,  $t_j$ , is calculated from  $t_j = \tau_j + R_j/c$  where  $c$  is the speed of sound in the medium. The sphere is allowed to collapse by an amount  $c\Delta\tau$ , where  $\tau$  is the emission or source time. During this period, the helicopter rotor is allowed to translate and rotate. The resulting arc of intersection between the rotor disk and the new  $C'$  is swept point by point in a counterclockwise direction until an intersection with a blade surface is detected or until the arc passes out of the rotor disk. When a blade is encountered, the integrands of equations (4) to (6) are evaluated and subsequently the line integrals are accumulated point by point using a trapezoidal scheme.

The collapsing process of the sphere  $g = 0$  is repeated, each time yielding a value for the line integrals which are accumulated for the source time integration using Simpson rule. This process is continued until it is detected that the collapsing sphere has passed out of the rotor disk. The integration is thus concluded for the observer time  $t_j$  and the resulting integrals are saved for further processing. Successive points are obtained in like manner.

To facilitate numerical smoothing and differentiation with respect to the observer time  $t$ , it is required that the  $t_j$ 's be equally spaced. Since the relation between the observer time  $t$  and the source time  $\tau$  is in general nonlinear, an iteration technique is used to obtain the initial radius  $R_j$  and the corresponding source time  $\tau_j$  where the sphere  $g = 0$  begins to collapse. The smoothing and numerical differentiation which is used are presented in reference 3. It is based on the theory of finite Fourier series using sigma factors to improve convergence characteristics and to reduce Gibbs phenomenon. As a byproduct of this, the pressure spectrum of the acoustic signature is obtained quite easily using intermediate results of the smoothing and differentiation process.



## EXAMPLES DEMONSTRATING UNIQUE FEATURES

The following examples are selected with realistic data to demonstrate the unique features of the developed program. Rectangular blade planform is used in all examples. This is one of the limitations of the present program which will be removed in future.

In the first two examples, the two-bladed rotor system is 4.58 m in diameter and has a chord of 0.356 m. For the first example, the blade has an NACA four-digit airfoil section of 12 percent thickness ratio. The tip speed is 151.3 m/sec. The pressure distribution  $\Delta p$  corresponding to this tip speed was measured by Rabbott (ref. 4) for various angles of attack. The angle of attack here is  $8.5^\circ$ . The chordwise pressure distribution has a maximum at leading edge and the spanwise loading has the familiar variation of increasing towards tip and reaching a maximum at about 90 percent of the radius. For this example, a function of two variables approximating the pressure distribution in the outer 40 percent of the radius was first obtained and was used as an input to the program. The pressure  $p_T$  due to the symmetric thickness distribution was also obtained analytically using the data given in reference 5 and corrected for compressibility effect by Prandtl-Glauret rule. The observer is 10 m from the center of the rotation and  $45^\circ$  above the rotor plane. The theoretical pressure signature and the pressure spectrum are presented in Figure 1. The shape of the pressure signature is considerably influenced by the thickness noise even for such a high observer elevation. This was found to be true for blades with blunt leading edge. In this and all the examples worked out so far, the contribution of the expression  $\frac{\partial I_3}{\partial t}$  (see eq. (6)), was found to be of the order of 10 percent of the thickness noise due to  $\frac{\partial I_1}{\partial t}$ . This is expected on theoretical basis. The contributions of expressions  $I_4$  and  $I_5$  are very small compared to the other terms except very close to the blades.

The second example has rotor tip speed of 259 m/sec (Tip Mach number = 0.75). To utilize the measured data of reference 4, a similarity rule is applied to the blades of the first example. To obtain the same pressure coefficient  $c_p$  as in the above case, the thickness ratio varies along span by the following rule (ref. 6).

$$\frac{\text{thickness ratio}}{\sqrt{1 - M_2^2}} = \frac{0.12}{\sqrt{1 - M_1^2}}$$

where  $M_2 = \Omega_2 \tilde{r}/c$  and  $M_1 = \Omega_1 \tilde{r}/c$  where  $\Omega_1$  and  $\Omega_2$  are the

angular velocities of the rotors of the first and second example, respectively, and  $\tilde{r}$  is the spanwise distance from the rotor center. The angle of attack  $\alpha$  in this example also varies along the span as follows

$$\frac{\alpha}{\sqrt{1 - M_2^2}} = \frac{8.5}{\sqrt{1 - M_1^2}}$$

where  $\alpha$  is in degrees. Again  $p_T$  from reference 5 was corrected for compressibility effect. The observer is 10 m from the rotor center and in the rotor plane. Figure 2 presents the pressure signature and the spectrum. The signature is again considerably influenced by the thickness noise.

The above two examples demonstrate the use of realistic pressure distributions, airfoils with blunt leading edge, and blade twist.

The third and fourth examples demonstrate that there is no limitation on tip Mach numbers. In these examples a two-bladed rotor of 10-meter diameter and a chord of 0.4 m is used. The blade length is 1 m and a biconvex wedge airfoil section of 6 percent thickness ratio is used. The angle of attack is  $2.5^\circ$ . The tip Mach number is 1.375. Linearized two-dimensional aerodynamic theory was used to calculate  $\Delta p$  and  $p_T$  which vary with spanwise location. Figure 3 gives the pressure signature and spectrum for the observer 50 m from rotor center and in the rotor plane. Figure 4 presents pressure signature and spectrum for the observer 50 m from rotor center but at  $45^\circ$  elevation above rotor plane. The changes in the signatures are striking but expected.

The fifth example demonstrates the forward flight capability of the program. The helicopter speed is 59.2 m/sec (115 kts). The rotor system is that of HU-1H which is 14.64 m in diameter and has a chord of 0.53 m. The rotor rpm is 324. The observer is 22.9 m from rotor center and  $2^\circ$  below the rotor plane. Due to unavailability of reliable surface pressure measurements, only the thickness noise is presented. However, it was found earlier that at high tip speeds and in or near the plane of rotation, thickness noise is dominant (ref. 7). This conclusion is born out by comparing the calculated pressure signature, figure 5, with the measured signature in reference 8. The peaks of the measured signature are higher in magnitude but the deviation is less than 2 db which is considered good agreement in acoustics. The exact effect of the inclusion of the expression involving  $\Delta p$ , which is believed to be important next to the thickness noise, cannot be determined at this stage.

## CONCLUSIONS

The present paper discusses a new theory and a computer program for realistic calculation of acoustic pressure signature and spectrum of rotor and propeller noise. As seen from the examples in this paper, many of the common restrictions of already existing theories are removed using the new theory which is consistent with all previous theories. Only deterministic pressure fluctuations may be used in the program at this stage of development. This will limit the applicability of the program to relatively high tip speeds where it is known that high frequency unsteady pressure fluctuations do not contribute significantly to the sound level. There are very few blade surface pressure measurements and reliable acoustic data available to test the theory in full. Some comparison with experimental measurements has been given in reference 7 (using theoretical thickness noise). Further comparison with the measured acoustic data of a high-speed propeller by Hubbard and Lassiter (ref. 9) using limited aerodynamic data in the blade tip region for acoustic calculations has shown good agreement so far. One important contribution of the new theory is believed to be the removal of the compactness assumption which can introduce errors in acoustic computations. The new capability will be used to study this effect. Already it has been found that in most cases of interest one only needs to keep the two expressions  $I_1$  and  $I_2$ , and in some cases one of these two will give a good estimate of the acoustic pressure of the rotor. More numerical examples and comparison with experimental data are planned.

## REFERENCES

1. Magliozzi, B., et al: A Comprehensive Review of Helicopter Noise Literature. Final Report, U.S. Dept. of Transportation, 1975.
2. Farassat, F.: Theory of Noise Generation From Moving Bodies with an Application to Helicopter Rotors. NASA TR R-451, December 1975.
3. Lanczos, C.: Applied Analysis. Prentice Hall, Inc., Englewood Cliffs, N. J., 1956.
4. Rabbott, J. P.: Static-Thrust Measurements of the Aerodynamic Loading on a Helicopter Rotor Blade. NACA Tech. Note 3688, 1956.

BROWN, FARASSAT

5. Abbott, I. H.; Von Doenhoff, A. E.: Theory of Wing Sections - Including a Summary of Airfoil Data. Dover Publications, Inc., New York, 1959.
6. Liepmann, H. W.; Roshko, A.: Elements of Gasdynamics. John Wiley and Sons, Inc., New York, 1957.
7. Farassat, F.; Pegg, R. J.; Hilton, D. A.: Thickness Noise of Helicopter Rotors at High Tip Speeds. AIAA Paper 75-453, March 1975.
8. Boxwell, D. A.; Schmitz, F. H.; Hanks, M. L.: In-Flight Far Field Measurement of Helicopter Impulsive Noise. Presented at the "First Rotorcraft and Powered Lift Aircraft Forum," University of Southampton, Southampton, England, September 22-24, 1975.
9. Hubbard, H. H.; Lassiter, L. W.: Sound From a Two-Blade Propeller at Supersonic Tip Speeds. NACA Tech. Report 1079, 1952.

#### ACKNOWLEDGEMENTS

The second author acknowledges the support from NASA Grant No. NGR 09-010-085, entitled "Aircraft Noise Reduction." The authors would like to thank Mrs. Christine G. Brown for her kind help in computations.

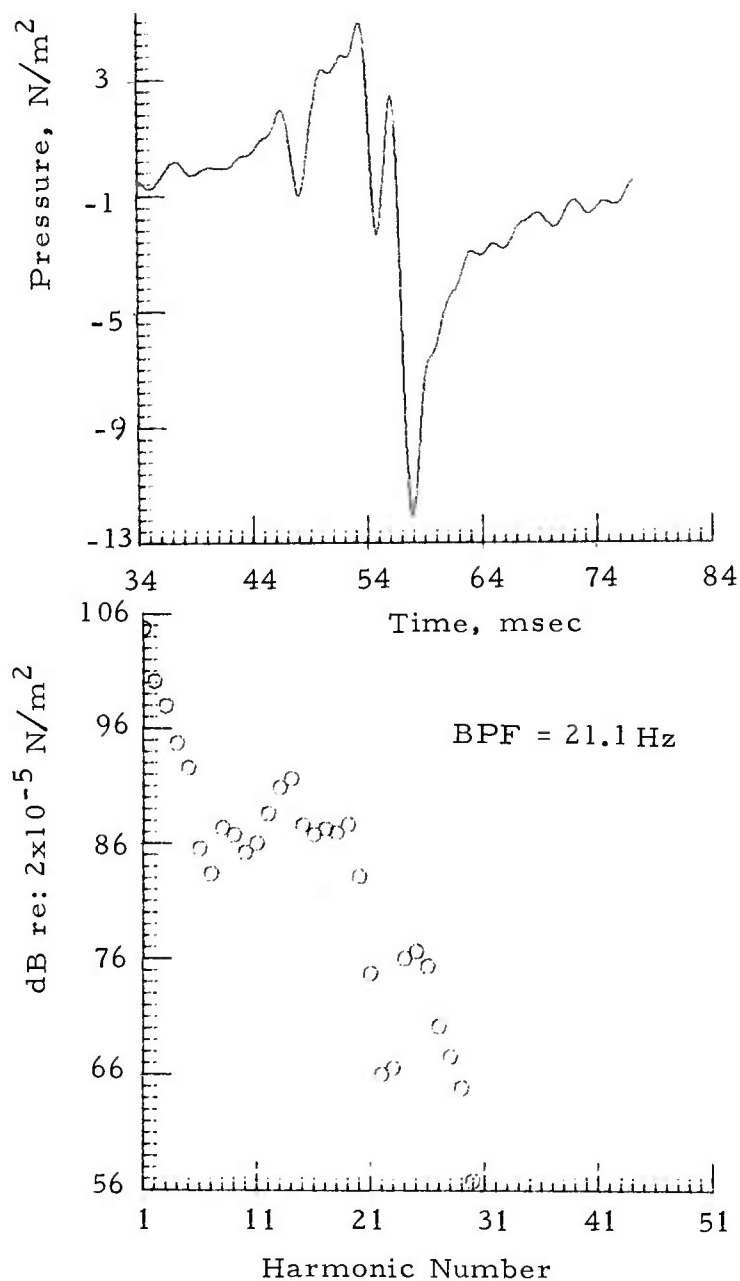


Figure 1. Example 1. - Theoretical acoustic pressure signature and spectrum of a hovering helicopter rotor for an observer at 45° elevation above rotor plane. Tip Mach number = 0.44.

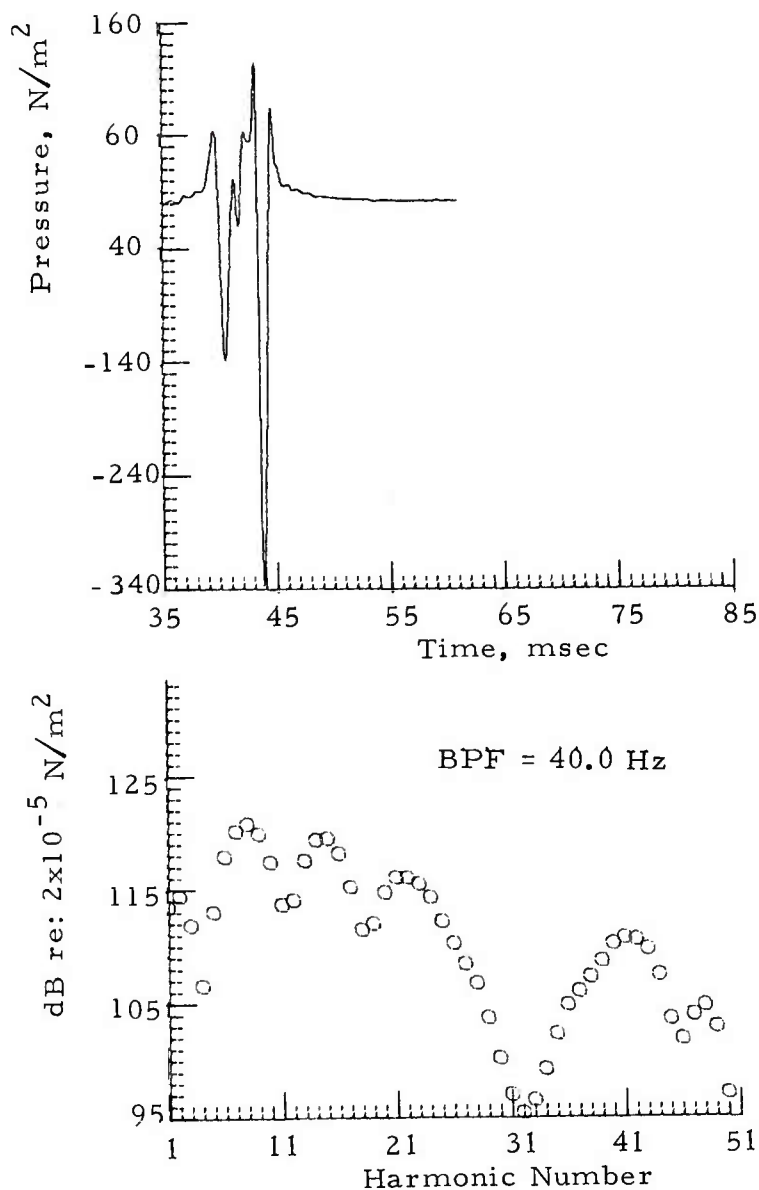


Figure 2. Example 2.- Theoretical acoustic pressure signature and spectrum of a hovering helicopter rotor for an observer in the plane of rotation. Tip Mach number = 0.75.

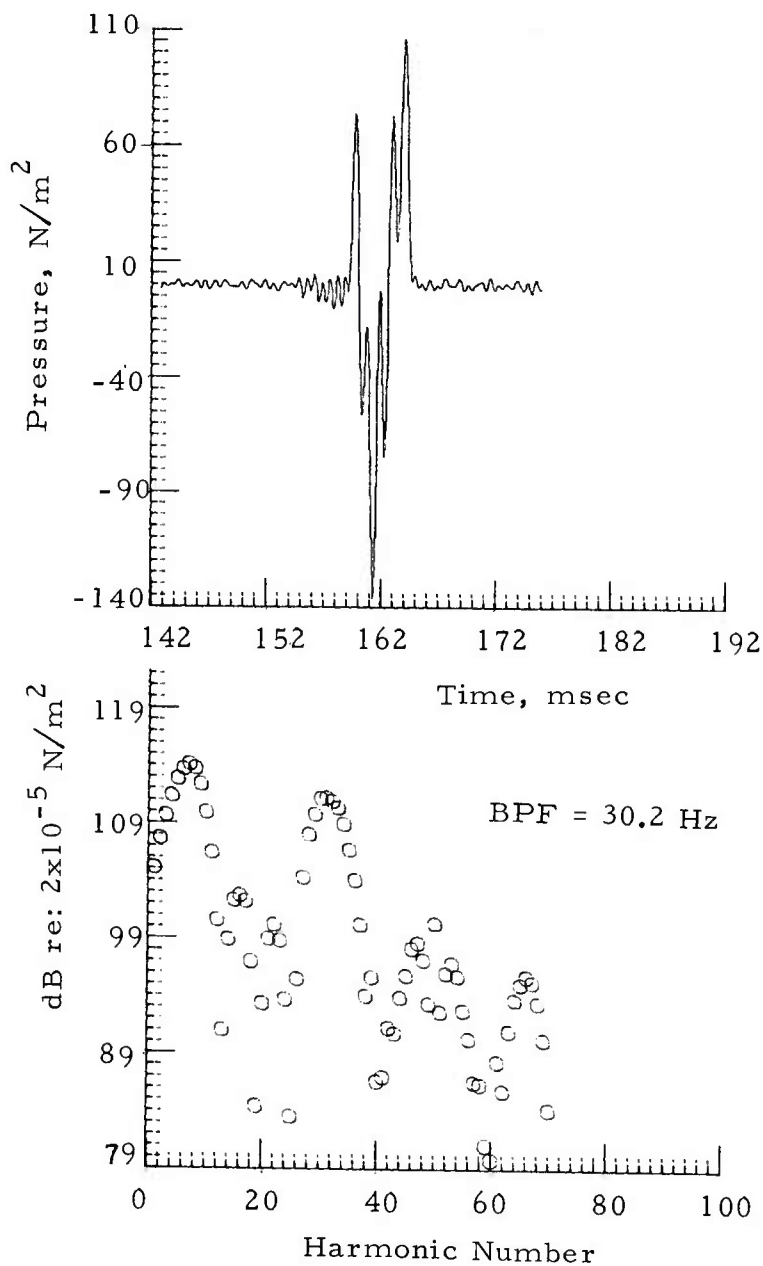


Figure 3. Example 3.- Theoretical acoustic pressure signature and spectrum of a hovering helicopter rotor for an observer in the plane of rotation. Tip Mach number = 1.375.



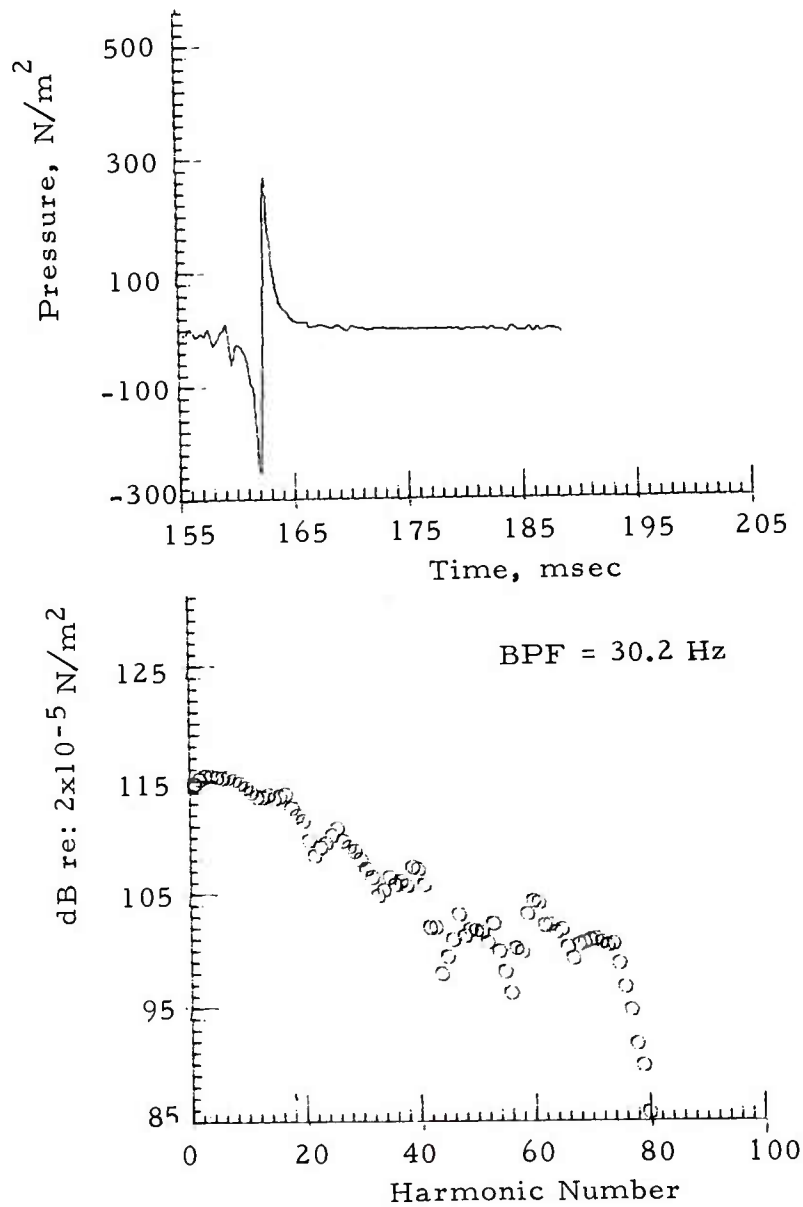


Figure 4. Example 4.- Theoretical acoustic pressure signature and spectrum of a hovering helicopter rotor for an observer at 45° elevation above rotor plane. Tip Mach number 1.375.

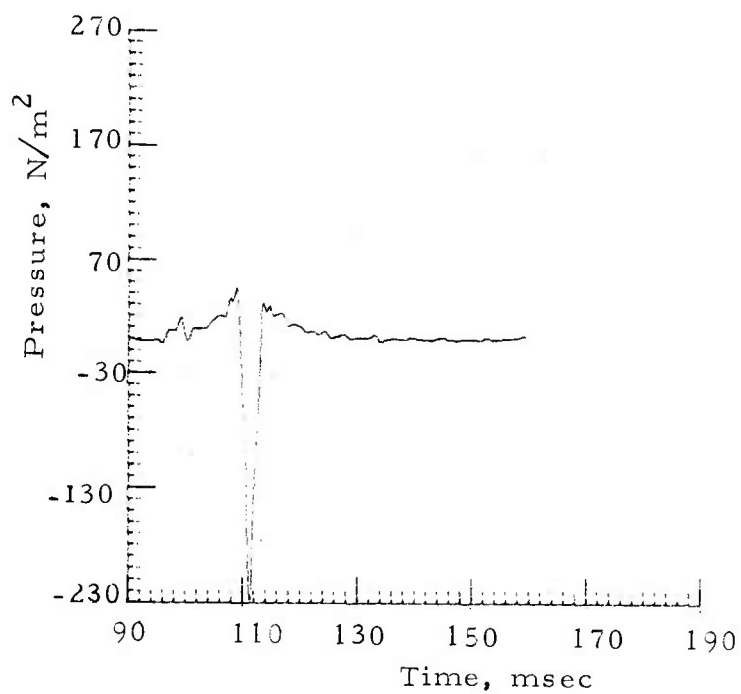


Figure 5. Example 5.- Theoretical acoustic pressure signature (thickness noise only) of a helicopter in forward flight (59.2 m/sec, 115 kts) for an observer  $2^\circ$  below the rotor plane. Advancing tip Mach number = 0.90.

HIGH-VELOCITY FRAGMENT PENETRATION INTO SAND:  
A COMPARISON OF EXPERIMENTAL RESULTS WITH  
THEORETICAL PREDICTIONS

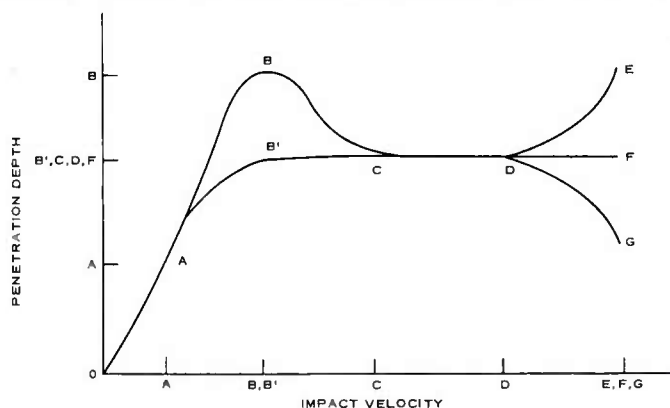
DWAIN K. BUTLER  
USAE WATERWAYS EXPERIMENT STATION  
VICKSBURG, MISS. 39180

INTRODUCTION

Research at the U. S. Army Engineer Waterways Experiment Station (WES) in penetration of high-velocity fragments into earth materials began in 1970 for the purpose of assessing the effectiveness of soil as a fortification material. The effort has consisted of a coupled analytical and experimental approach (1-3). The experimental program has included the construction of a high-velocity powder gun capable of achieving impact velocities up to 0.274 cm/ $\mu$ sec (9000 ft/sec) for nominal 3-g fragments, and penetration tests of fragment-simulating projectiles into controlled soil targets.

Figure 1 illustrates the penetration depth-impact velocity behavior (over the velocity range of interest) for a hypothetical fragment and target material. There has been considerable experimental study in the low impact velocity range OA for penetration into soils, for which an increasing penetration depth with increasing impact velocity is observed. The data presented in Reference 2 cover the velocity range ABB'C. Curve ABC illustrates the

Figure 1. Penetration depth-impact velocity behavior for small fragments into earth media



observed behavior of steel fragments penetrating sand, and curve AB'C illustrates the observed behavior of steel fragments penetrating clay (behavior believed to be due to fragment frontal enlargement). Penetration tests (primarily into sand) in the velocity range CDEFG have been conducted at only a few selected impact velocities with a variety of fragment sizes and shapes, and thus it is not possible to deduce the shape of the curve in this velocity range due to the extremely limited experimental data base. It is clearly important with regard to the design of soil fortifications to define the penetration depth-impact velocity curve in the velocity range CDEFG.

### EXPERIMENTAL PROGRAM

#### Description of Test Program

The experimental program discussed in this report consisted of 25 fragment penetration tests into dense sand targets. Data collected from each test consisted of impact velocity, depth of penetration, initial and final fragment dimensions, initial and final fragment masses, sand target density, and grain-size analyses before and after the penetration event. The high-velocity powder gun used in the tests is documented in Reference 3.

Dense sand targets. A fine sand, known locally as Cook's Bayou sand, was used for the targets. This sand is well documented and was used as a target material, in both loose and dense states, in an extensive series of penetration tests reported in Reference 2. A target preparation procedure was followed which consistently produced targets with densities in the range 1.66 to 1.76 g/cm<sup>3</sup>.

Fragments. Right-circular cylindrical fragments were used in the study. Stress-strain diagrams for the two steels, a "soft" steel (SS) and a "hard" steel (HS), are shown in Figure 2 (static

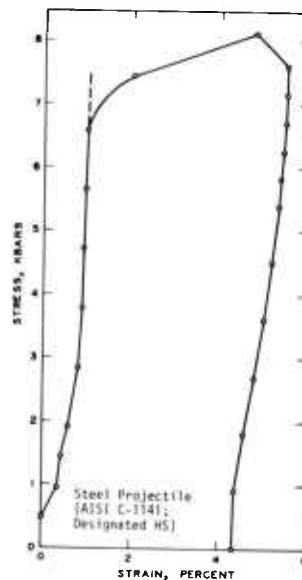
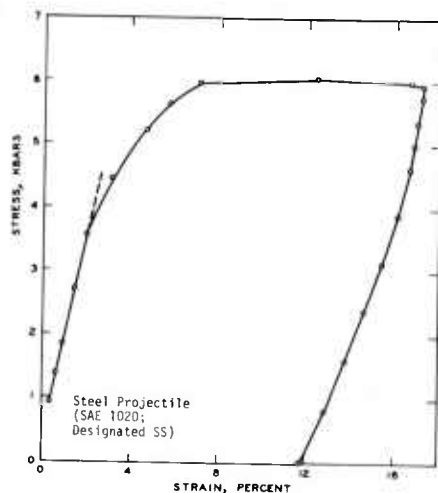


Figure 2. Results of unconfined compression tests of steel fragments used in the test program

unconfined compression tests). Pertinent properties for the two fragment materials used in the study are listed in the tabulation below.

Metal	Length L, cm	Diam D, cm	Mass M, g	Density $\rho$ , g/cm <sup>3</sup>	Yield Strength $\sigma_Y$ , Mbar	Brinell Hardness Number
Steel (SAE 1020)	0.80	0.787	3.00	7.71	0.0035	160
Steel (AISI C-1141)	0.78	0.78	2.87	7.70	0.0068	252

### Test Results

The test results are presented in Figures 3-5 and include penetration depth, frontal area enlargement coefficient  $C_A$ , and reduced mass coefficient  $C_M$  versus impact velocity. The

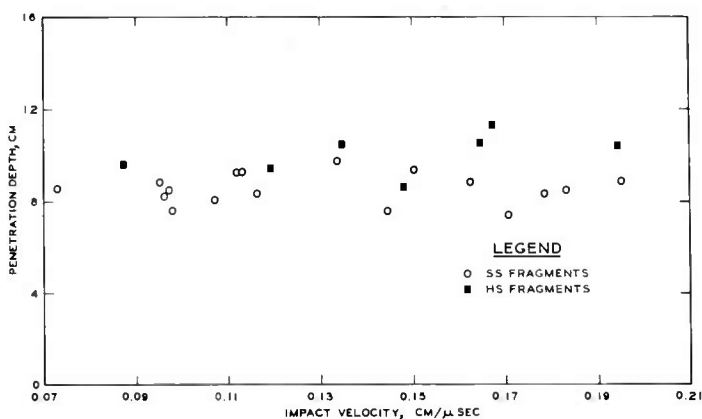


Figure 3. Projectile penetration into dense sand

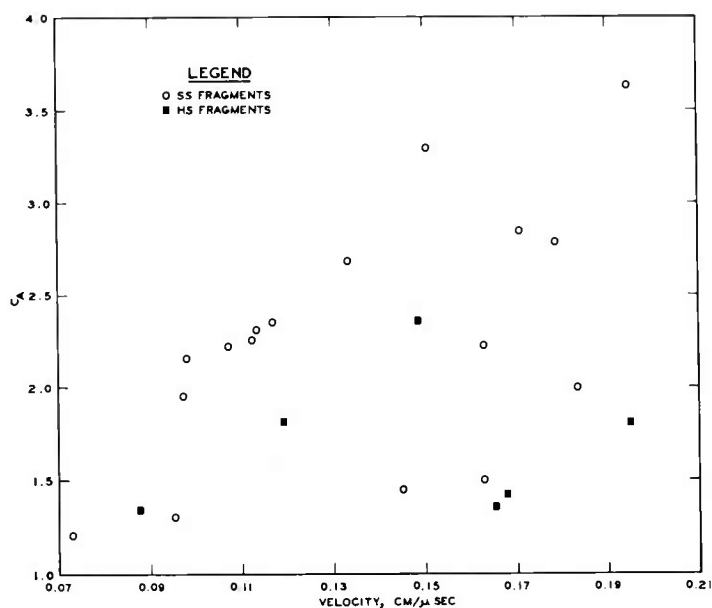


Figure 4. Frontal area enlargement coefficient versus impact velocity

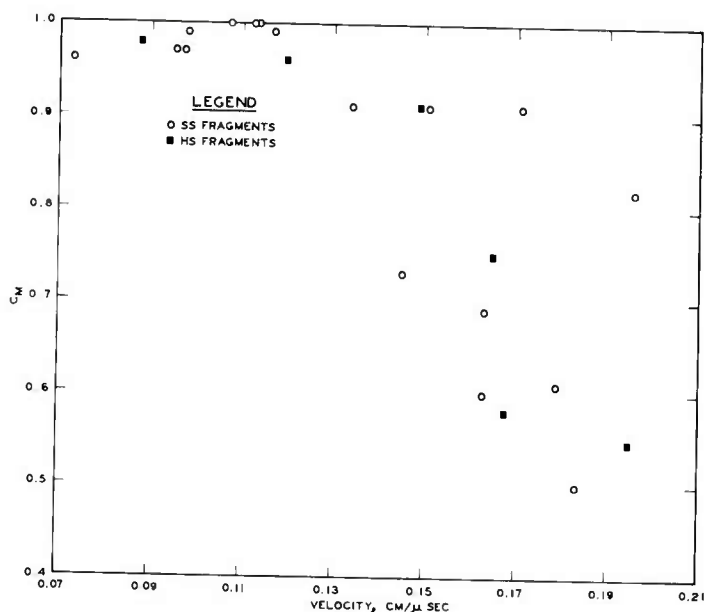


Figure 5. Reduced mass coefficient versus impact velocity

coefficients  $C_A$  and  $C_M$  define the enlargement of the frontal area of the fragment due to plastic deformation and the loss of mass due to erosion, respectively.  $C_A = A_f/A_i$  and  $C_M = M_f/M_i$ , where  $A_f$  = frontal area of fragment after penetration event,  $A_i$  = initial frontal area,  $M_f$  = mass of projectile after penetration event, and  $M_i$  = initial mass.

#### ANALYSIS AND DISCUSSION OF EXPERIMENTAL PROGRAM

##### Projectile Penetration Depth, Deformation, and Mass Loss

Analysis of results. It is evident from Figures 4 and 5 that the fragments did not penetrate as rigid bodies of constant mass in any of the penetration tests conducted. In all cases, the fragments deformed, and in all but three cases, mass was lost during the event. Figure 6 illustrates the typical appearance of the HS fragments following penetration into the dense sand. It was concluded in Reference 2 that, in the rigid penetration range in which the fragments undergo only elastic deformations and no mass loss, the depth of penetration is independent of the yield strength of the material composing the fragment and that penetration depth increases continuously with increasing impact velocity. The data presented in Reference 2 indicate that the rigid penetration range for steel fragments (same material as the HS fragments in the study reported here) terminates at impact velocities of 0.0762 to 0.0914 cm/μsec (2500 to 3000 fps) in dense sand. Thus, the range of impact velocities in this study is above the rigid penetration range.

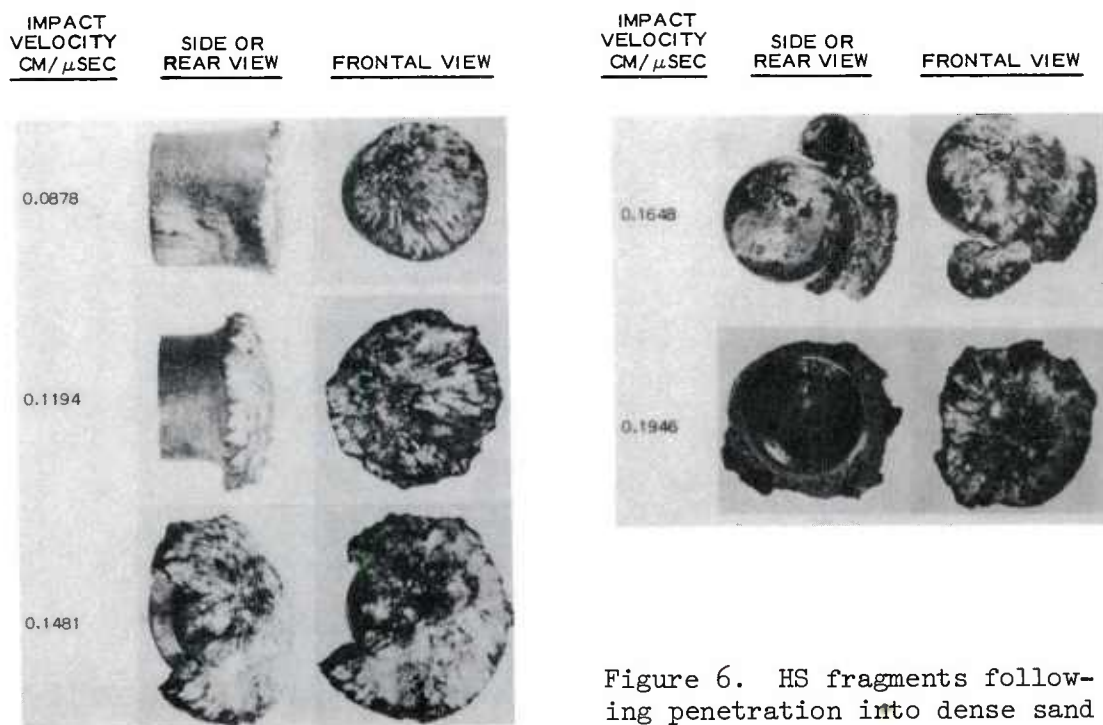


Figure 6. HS fragments following penetration into dense sand

Penetration depths achieved by the SS fragments appear to be slightly smaller over the investigated impact velocity range than those for the HS fragments. The data for the SS fragments are scattered about a constant penetration depth of about 8.6 cm. Figure 7 compares the data from Reference 2 for dense sand penetration with data from the tests in this study for HS fragments. The data from the tests in this study correlate quite well with the higher velocity data from Reference 2 and thus appear to form a logical extension for the dense sand penetration of this type steel (HS) fragment to impact velocities of 0.20 cm/ $\mu$ sec (6500 fps). It is demonstrated in Reference 4 that, for long rod penetration, it is theoretically possible to have a decrease in penetration depth with increasing impact velocity as in Figure 7. It is interesting to note that the general shape of the penetration versus impact velocity curve (say a best-fit curve to the data) of Figure 7 closely resembles the curves of Reference 4 for cases in which the strength of the target is less than the strength of the fragment.

Phenomenological discussion. Following impact, plane shock waves propagate into the target and fragment with magnitudes which depend on the impact velocity and the material properties of the target and fragment. The plane shocks are quickly distorted and



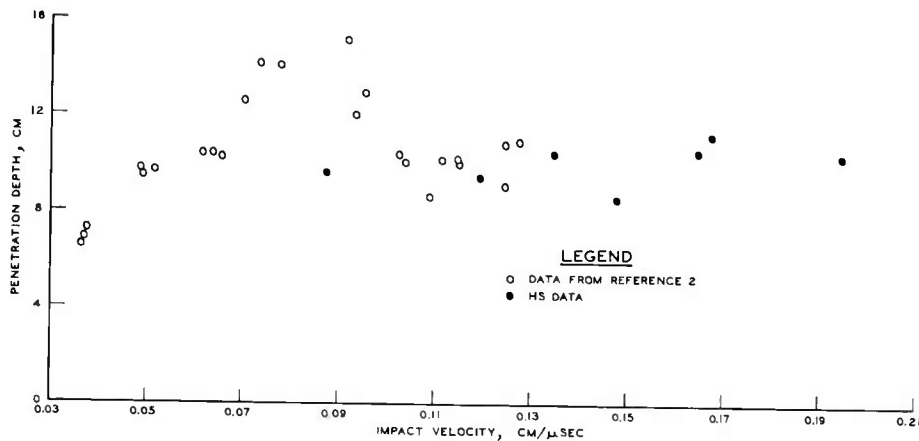


Figure 7. Comparison of data from Reference 2 with data for HS fragments in this study penetrating dense sand

attenuated due to rarefaction waves from lateral and rear surfaces of the fragment and from the "free" surface of the target. The rarefaction waves from the lateral fragment surface will generate tensile stresses in the fragment which, if the dynamic yield strength of the fragment material is exceeded, will tend to cause plastic deformations and lateral material flow (radial flow). It is this mechanism which produces the familiar, characteristic mushroom shapes shown in Figure 6.

Thus, as impact velocity increases above a critical velocity (the impact velocity for which stresses in the fragment exceed the yield stress), plastic flow will occur and continue until stresses fall below the yield stress (which itself may have changed during the event). At high impact velocities, the frontal area will not only increase but the fragment will lose mass as the "mushrooming" material separates. For impact and penetration into sand, mass is also lost due to the abrasive action of the sand grains on the fragment, and this effect should increase in importance as the impact velocity increases and as the yield strength and hardness of the material composing the fragment decrease.

In general, the penetration depth depends directly on the fragment mass and inversely on the presented frontal area (perhaps to some power). The diagrams in Figure 8 illustrate in section view the geometries of the recovered fragments for increasing impact velocity. It is hypothesized that the diagrams can also be considered as a time sequence of events in the penetration process for an impact velocity  $V_6 > V_c$ , where the dashed lines in Figure 8d represent incipient separation of the "mushrooming" material. Figure 9 presents hypothetical plots of  $C_A$  and  $C_M$  versus impact velocity.

Figure 8. Cross-sectional views of fragments following penetration at increasing impact velocities  $V_i$  ( $V_c$  = critical impact velocity for plastic flow)

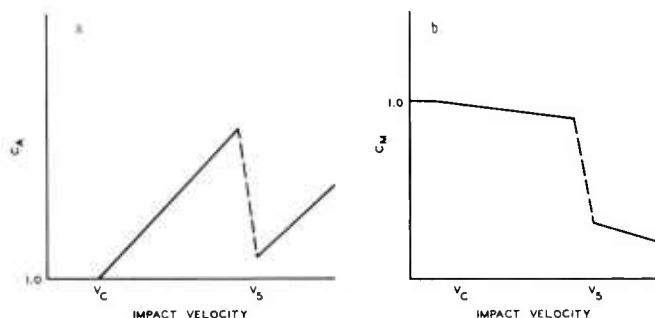
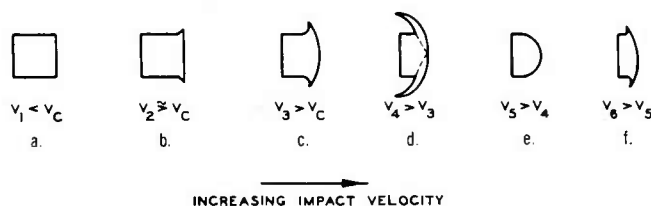


Figure 9. Hypothetical plots of  $C_A$  and  $C_M$  versus impact velocity for the phenomena represented in Figure 8

$C_A$  remains constant at 1.0 until  $V_c$  is exceeded and then increases in some monotonic manner until a velocity  $V_5$  is reached, at which point the separation indicated in Figures 8d and 8e occurs with a sudden drop in  $C_A$ . At some low velocity (not necessarily  $V_c$ ), mass begins to be lost due to erosion and continues throughout the impact velocity range. The sudden drop in  $C_M$  at  $V_5$  again corresponds to the separation indicated in Figures 8d and 8e.

Recovered steel from both type fragments contained rather large curved platelike pieces indicative of the mechanism proposed in Figure 8d. In general, the pieces of the SS fragments were larger than those of the HS fragments, as would be expected due to the lower yield strength and greater ductility of the SS material. Also, the edges of the HS fragments were drawn thinner and had a more jagged, striated appearance (this effect might be indicative of strain hardening; see Figure 2). Very small pieces of the fragments such as might result from the abrasive action of the sand were present following the tests. Evidences of high temperatures during the penetration process were the "charred" appearance of the fragments and a noticeable elevation in temperature of large volumes of the target. Also present in the recovered pieces of the HS fragments were grayish-black spherules ( $<1$  mm in diameter) which could have been formed only by complete melting. An X-ray diffractogram revealed that the spherules contained  $\alpha$ -iron and quartz. Also, the diffractogram contained a broad maximum, characteristic of an amorphous solid, and an intriguing possibility is that the maximum could be an indication of the presence of elemental silicon in an

amorphous form. This possibility is suggested by the presence of iron oxide on some of the steel fragments. Thus, it is possible that the penetration process provided the extreme reducing environment necessary for the reaction  $\text{Fe}_3\text{O}_4 + 2\text{Si} \rightarrow 3\text{Fe} + 2\text{SiO}_2$  to occur in the reverse direction (5).

#### Sand Comminution and Grain-Size Analyses

Comminution (crushing) of sand grains has commonly been observed in standard laboratory testing of sands (6,7). Application of confining pressures (isotropic compression) above a threshold value results in a shift of the grain-size distribution (gradation) curve of a test sample. At a given confining pressure, application of shearing stresses results in a further and relatively larger upward shift in the grain-size distribution curve. Sand comminution has also been observed in fragment penetration tests and considered in analyses of penetration tests into sand (8-11). For a given fragment, a minimum impact velocity exists below which sand comminution does not occur to a significant extent (8,10). Thompson (11, has observed the formation of "sand cones" on the noses of projectiles with blunt, hemispherical, and ogival nose geometries. The sand cone is formed of compacted, comminuted sand which adheres to the fragment and moves through the target media as part of the fragment once it has formed. Some evidence of sand cone formation was present on a few of the recovered fragments, but in none of the cases was a "complete" sand cone observed or recovered as discussed

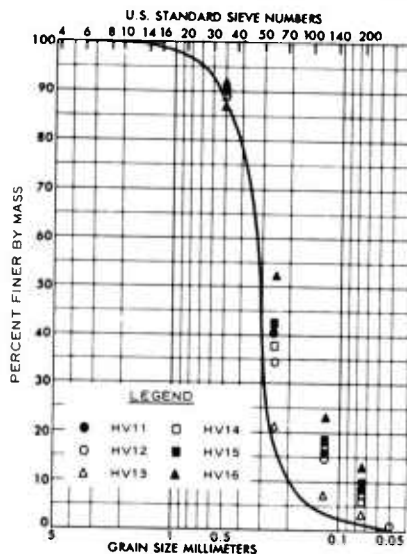


Figure 10. Grain-size data for test Nos. HS-DS-HV11 to -HV16

by Thompson (11) for larger diameter projectiles. It is possible that the complex mass loss and frontal enlargement mechanisms, proposed earlier for the small blunt fragments used in these tests, prevented the formation of other than temporary sand cones. The comminution process is undoubtedly very complex for the fragment penetration case (consisting of comminution caused by the initial shock wave, abrasion between grains caused by shearing motions as the sand is pushed aside, abrasion caused by contact between individual grains and the fragment itself, etc.).

Figure 10 presents typical grain-size analysis results for the comminuted sand material obtained from the fragment tracks following the tests. The figure contains the curve for the parent material, and the data for each test (for

each grain size) are indicated by different symbols. In order to illustrate more explicitly the effect of impact velocity on grain-size distribution, the percent finer by mass data for three selected grain sizes (0.25, 0.125, and 0.074 mm) versus impact velocity are plotted in Figures 11 and 12 for the SS and HS fragment tests, respectively. The points on the percent finer axis for zero impact velocity are for the parent material. A large jump in the percent finer by mass values is evident in Figure 12 at an impact velocity of about 0.10 cm/ $\mu$ sec. It is significant to note that this is about the velocity at which the dramatic decrease in penetration depth occurs in the composite data plot in Figure 7 and also about the velocity at which a significant increase in the frontal enlargement coefficient is observed (Reference 2 and Figure 4). The data in Figures 11 and 12 are consistent with the concept that comminution does not occur below a minimum impact velocity. It is tempting, but would be too much a matter of conjecture at this point, to interpret each of the increases and decreases in the percent finer versus impact velocity data in Figures 11 and 12 in terms of the mechanism proposed in Figures 8 and 9 and the  $C_A$  and  $C_M$  data in Figures 4 and 5. If

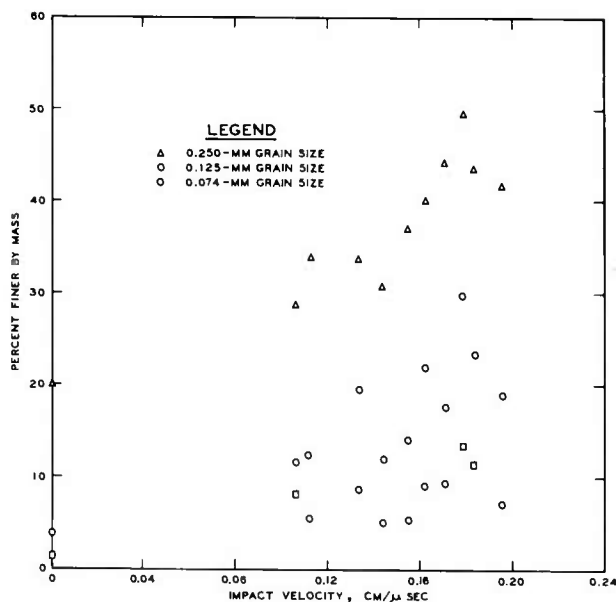


Figure 11. SS fragment tests

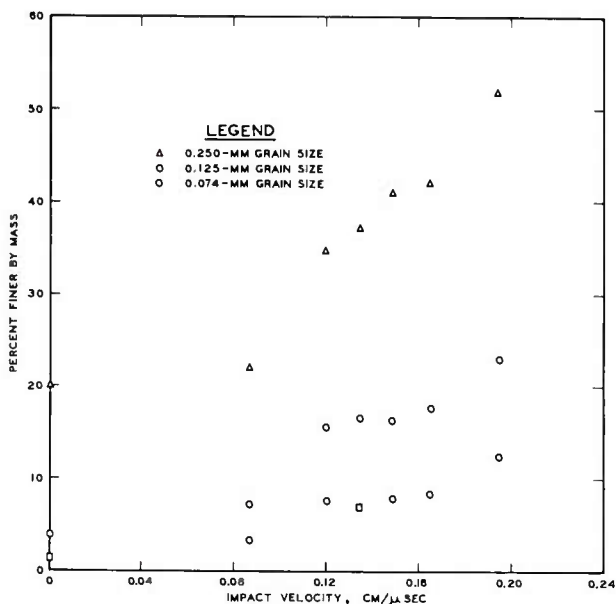


Figure 12. HS fragment tests

such an interpretation can be further substantiated, it will represent a significant advancement in the understanding of the energy exchange mechanisms operating during the impact and penetration process.

#### Dynamic Yield Strengths of Fragment Materials and Energy Partitioning Considerations

Taylor (12) has demonstrated that the profile of a cylindrical rod following impact with a rigid boundary can be related to the dynamic yield strength of the material composing the rod. In a more recent study, Wilkins (13), based on the method proposed by Taylor, simulated the impact of rods, of several material types and length-to-diameter ratios varying from 1 to 15, into a rigid boundary with an elastic-plastic finite difference computer code. He also conducted experimental impact tests and demonstrated that the observed rod profile after impact for a given impact velocity can be duplicated in the code calculations by varying the yield strength parameter; then, using the yield strength parameter for which the profile has been duplicated, the profiles following impact at different impact velocities can also be duplicated. The yield strengths deduced by this procedure agree quite well with previously published values determined by plane shock wave experiments (14,15) and rod penetration tests (16). Butler (17) has demonstrated that measurements of fragment deformations, following penetration into an explosive simulant material, can be used to deduce the dynamic yield strength of a fragment. Using pressure versus relative density relations such as found in References 2, 3, 9, and 18, a computer code based on the method of characteristics was used to solve the one-dimensional analogy of the fragment-target impact to obtain the impact pressure-impact velocity and particle velocity-impact velocity relations shown in Figure 13.

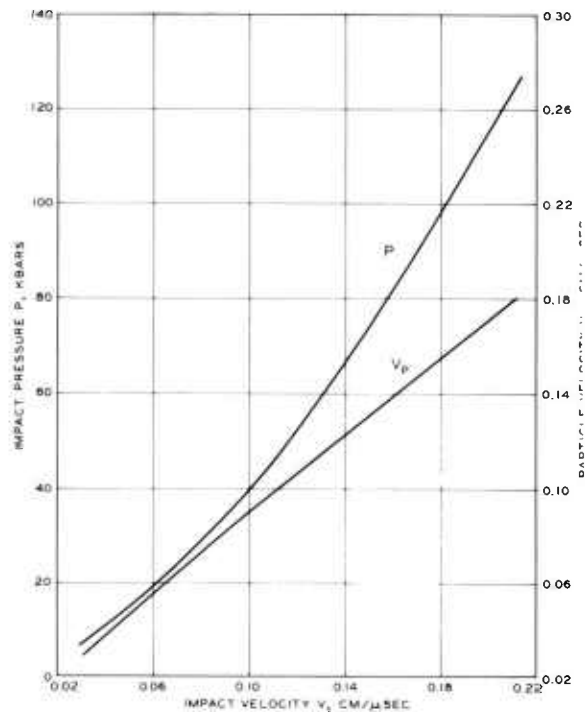


Figure 13. Impact pressure and particle velocity in target versus impact velocity



Based on the data presented in Reference 2 and in Figure 4, critical impact velocities for deformation of the HS and SS fragments were estimated to be 0.07 and 0.042 cm/ $\mu$ sec, respectively. From Figure 13, the code calculations for these impact velocities give 18 and 11 kbars for the dynamic strengths of the HS and SS materials, respectively. The dynamic strength value of 11 kbars for the SS fragment material (SAE 1020 steel) correlates quite well with dynamic yield strength values of 12.8 and 10.4 kbars for two thicknesses of SAE 1020 steel reported in Reference 14. There are no dynamic strength data available for the HS fragment material (AISI C-1141), however it is possible to infer a dynamic strength value for the HS material from published values for SAE 4340 and SAE 1040 steels which is in reasonable agreement with the value determined here (3). Additional credence to the impact pressures computed by the characteristics code using the one-dimensional analogy is given by experimental data such as presented in Reference 19.

With the particle velocities calculated for the fragment and target at impact (see Figure 13), it is possible to calculate the initial energy partitioning at the time when the shock wave reaches the rear of the fragment as a function of impact velocity based on the one-dimensional considerations of Gault and Heitowit (20). The results of this type analysis for the cases presented in this report are given in Reference 3. While the results of such an analysis are valid only for the initial energy partition at impact, they qualitatively confirm many of the phenomenological observations of the experimental program. For example, the predicted increasing percentage of energy transferred to the target as internal energy with increasing impact velocity is consistent with and accounts for the increased sand comminution observed as the impact velocity increases. Also, the observed elevated temperatures in the target at the higher impact velocities are consistent with the increasing percentages of energy transferred to internal energy of the fragment and target. The increasing percentage of energy transferred to internal energy of the fragment raises the temperature and serves as a driving mechanism for the material flow discussed earlier (3).

#### Correlation of Experimental Results with Penetration Model Predictions

Rohani (2) correlated his experimental results with the prediction of an analytical penetration model. The model is based on an analogy with the dynamic expansion of a spherical cavity and has been extended by WES to treat arbitrary fragment nose shapes, to treat layered targets, and to use a complete pressure-density relation for the target (21). He concluded that the WES penetration model could be used to predict or reasonably bound the penetration

depths of high-velocity fragments into soil targets. On this basis, the penetration model was used in an attempt to duplicate the experimental results of Figures 3 and 7 and to investigate the feasibility of bounding the penetration depths.

For the penetration model calculations, the initial target densities, the pressure versus relative density relation for sand (2,3), and the values of Young's modulus, strain-hardening modulus, and yield strength recommended by Rohani (Table 7, Reference 2) for the dense sand targets were used to characterize the targets. The fragments were characterized by their mass, presented frontal area, and a function describing their nose shape. For an upper-bound calculation, it seemed appropriate to use the initial mass  $M_i$  and the initial frontal area  $A_i$ ; for the lower-bound calculation, it was assumed that all deformation and mass loss would occur at the instant of impact, and the final mass  $M_f$  and final frontal area  $A_f$  were used for the calculation. Assuming a hemispherical nose shape results in a higher upper-bound estimate than that obtained by assuming a blunt nose shape. For the lower-bound estimates, the assumption of a hemispherical nose is consistent with the observed deformed shape of the recovered fragments. Correlations of the experimental penetration results for SS and HS fragments with upper- and lower-bound penetration model calculations are presented in Figures 14 and 15, respectively.

In all cases, the experimental penetration depths from these tests are bounded by the penetration model upper- and lower-bound estimates. In fact, in most of the cases the experimental value is approximated by the mean of the upper- and lower-bound estimates. This trend is indicative of the fact that the physical mechanisms actually occurring (perhaps as proposed in Figure 8) are intermediate to the extreme assumptions used to make the upper- and lower-bound estimates. The data from Reference 2 in Figure 15 are not

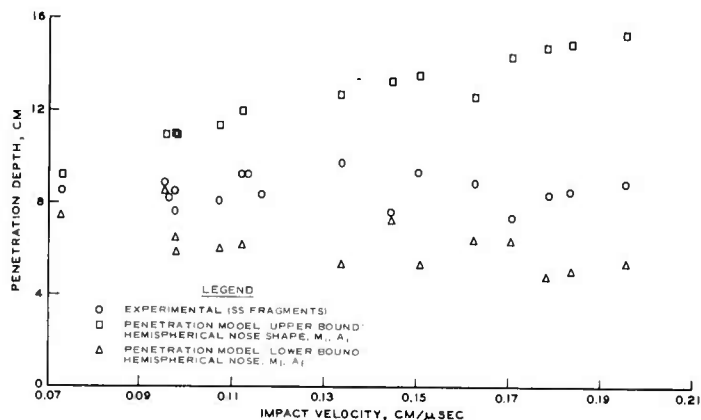


Figure 14. SS fragments



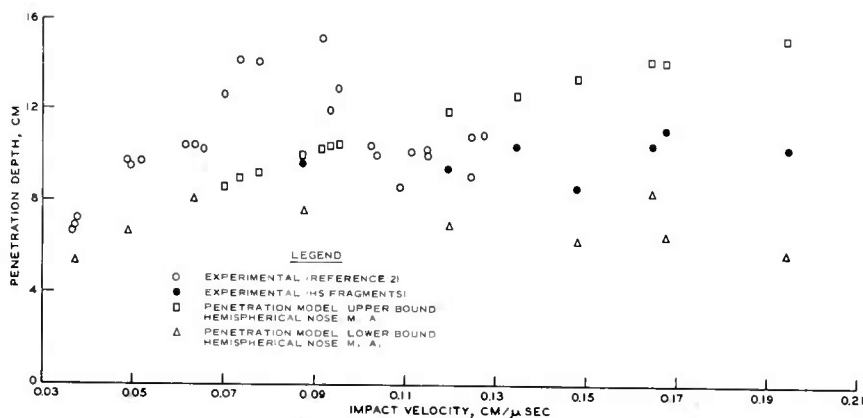


Figure 15. HS fragments

bounded by the upper-bound penetration model calculations. It was demonstrated in a parameter study in Reference 2, however, that the dense sand penetration values could be bounded by a different (and perhaps better) selection of target material properties for use in the model calculations.

### CONCLUSIONS

The results of 25 penetration tests of cylindrical fragments into dense sand targets are presented. The following conclusions and observations are based on these results:

- a. Dense sand is an effective medium for stopping high-velocity projectiles or fragments.
- b. The penetration depth attained by high-velocity projectiles or fragments in dense sand is not a monotonically increasing function of impact velocity but tends to remain constant after a critical impact velocity\* is exceeded. The critical impact velocity increases as the strength of the fragment material increases. The overall shape of the penetration depth versus impact velocity curve depends in a very complex manner on the details of fragment deformation and mass loss during penetration.
- c. With reference to Figure 1, the data of this report and Reference 2 demonstrate that the behavior indicated by curve CDE does not occur for the types of steel fragments tested. Although the desired maximum impact velocity of 0.274 cm/μsec (9000 fps) was not achieved in this study, the observations of penetration depth and fragment mass loss and deformation (at impact velocities up to

---

\* Velocity at which deformation of the fragment is initiated.

0.2 cm/ $\mu$ sec) suggest that the constant penetration depth represented by curve CDF in Figure 1 is an upper bound for the penetration depths which would be observed at higher impact velocities ( $>0.2$  cm/ $\mu$ sec).

d. Sand grain comminution occurring during penetration is reflected in an upward shift of the gradation curves, with increasing impact velocity, relative to the gradation curve of the parent material. The percent finer by mass data for the HS fragments (Figure 12) indicate a jump in value at about the same impact velocity as the critical velocity for the HS material discussed in subparagraph b above. This increase indicates a jump in the energy being transferred to the comminution process at this velocity.

e. A one-dimensional analogy of the fragment penetration process gives reliable values for the impact pressures and particle velocities.

f. The WES penetration model can be used to bound the penetration depths of small projectiles and fragments in dense sand.

#### ACKNOWLEDGMENT

This study was conducted at the U. S. Army Engineer Waterways Experiment Station, Vicksburg, Mississippi, under the sponsorship of the Office, Chief of Engineers, Department of the Army, as part of Project 4A161102B52E, Task 04 Work Unit 013, "Fragment and Projectile Penetration Resistance of Soils." The author gratefully acknowledges the technical consultation and direction provided by Dr. Behzad Rohani.

#### REFERENCES

1. Reeves, G. N., Rohani, B., "Fragment and Projectile Penetration Resistance of Soils; Literature Review and Preliminary Theoretical Study of Soils as a Fortification Material," MP S-71-12, Rpt 1, Jul 1971, USAEWES, Vicksburg, Miss.
2. Rohani, B., "Fragment and Projectile Penetration Resistance of Soils; High-Velocity Fragment Penetration into Laboratory-Prepared Soil Targets," MP S-71-12, Rpt 2, Jun 1973, USAEWES, Vicksburg, Miss.
3. Butler, D. K., "Development of a High-Velocity Powder Gun and Analysis of Fragment Penetration Tests into Sand," MP S-75-27, Oct 1975, USAEWES, Vicksburg, Miss.
4. Tate, A., "Further Results in the Theory of Long Rod Penetration," Jour, Mech and Phys of Solids, Vol 17, 1969.
5. Stacey, F., Physics of the Earth, Wiley, 1969.
6. Clough, G. W., An Investigation of the Shear Strength of Sand at High Pressures, MS Thesis, Ga. Inst of Tech, Oct 1964.

7. Vesic, A. S., Clough, G. W., "Behavior of Granular Materials Under High Stresses," Jour, Soil Mech and Foun Div, ASCE, May 1968.
8. Allen, W. A., Mayfield, E. B., Morrison, H. L., "Dynamics of a Projectile Penetrating Sand," Jour of Appl Phys, Vol 28, No. 3, Mar 1957.
9. Braslau, D., "Partitioning of Energy in Hypervelocity Impact Against Loose Sand Targets," Jour of Geophys Res, Vol 75, No. 20, Jul 1970.
10. Hakala, W. W., Resistance of a Granular Medium to Normal Impact of a Rigid Projectile, PhD Dissertation, Va. Polytech Inst, Jun 1965
11. Thompson, L. J., "Dynamic Penetration of Selected Projectiles into Particulate Media," Development Rpt SC-DR-66-376, 1966, Sandia Corporation, Albuquerque, N. Mex.
12. Taylor, G. I., "The Use of Flat-Ended Projectiles for Determining Dynamic Yield Stress," Proc of the Royal Soc, Vol 194A, Sep 1948.
13. Wilkins, M. L., Guinan, M. W., "Impact of Cylinders on a Rigid Boundary," Jour of Appl Phys, Vol 44, No. 3, Mar 1973.
14. Jones, O. E., Nielson, F. W., Benedict, W. B., "Dynamic Yield Behavior of Explosively Loaded Metals Determined by a Quartz Transducer Technique," Jour of Appl Phys, Vol 33, No. 11, Nov 1962.
15. Duvall, G. E., Response of Metals to High Velocity Deformation, Ed by P. W. Shweman and V. F. Zackay, Interscience, NY, 1961.
16. Tate, A., "A Theory for the Deceleration of Long Rods After Impact," Jour, Mech and Phys of Solids, Vol 15, pp 387-399, 1967.
17. Butler, D. K., "Analysis of Projectile Penetration into Aroclor," U. S. Naval Ordnance Laboratory, NOLTN8916, Jul 1970.
18. Van Thiel, M., Ed, Compendium of Shock Wave Data, Lawrence Radiation Laboratory, UCRL-50108 Vol 1, Supplement 1, Oct 1967.
19. Eichelberger, R. J., "Hypervelocity Impact," Behavior of Materials Under Dynamic Loading, Ed by N. J. Huffington, Jr., ASME, 1965.
20. Gault, D. E., Heitowit, E. C., "The Partition of Energy for Hypervelocity Impact Craters Formed in Rock," Proc of the Sixth Hypervelocity Impact Sym, Cleveland, Ohio, Vol II, Part 2, 1963.
21. Bernard, R. S., Hanagud, S. V., "Development of a Projectile Penetration Theory," TR S-75-9, Rpts 1 and 2, USAEWES, Vicksburg, Miss.



THE DEVELOPMENT OF THIN FILM PHOTODETECTORS FOR THE  
8-14 MICROMETER ATMOSPHERIC WINDOW (U)

MR. ROBERT E. CALLENDER and MR. ROBERT E. FLANNERY  
USAECOM NIGHT VISION LABORATORY  
FORT BELVOIR, VIRGINIA 22060

I. INTRODUCTION

Passive infrared imaging systems have become increasingly important for tactical warfare. The acceptance and growing capabilities of these imaging systems has caused increased demand for even **higher**-performance systems, with a decrease in the cost per detector. The Night Vision Laboratory is working to make a wider region of tradeoff between cost and performance available to the systems designer. A dramatic increase in performance can be achieved by increasing the number of detectors in the focal plane by at least an order of magnitude. However, the cost of these future, very-high-density imaging systems would be prohibitive if they were produced using present-day technology. The cost of the detectors plus their associated electronics can be reduced by developing a detector technology suitable for use with in-focal-plane CCD signal processing. In order to achieve minimum complexity and power dissipation, the signal from the detector must be directly injected into the CCD's. High-impedance detectors are required for direct-injection CCD interfacing. However, the high-performance 8-14 micrometer detectors used in current systems are low-impedance photoconductive devices, requiring buffer amplifiers. The only high-performance 8-14 micrometer detector with sufficiently high impedance at 77°K for direct signal injection into CCD signal processors is photovoltaic PbSnTe.

One of the most promising low-cost approaches for the fabrication of PbSnTe detectors is the use of thin film technology (1, 2, 3, 4). Although high-performance PbSnTe detectors fabricated

by bulk processes have been available for some time, thin film detectors of PbSnTe until recently had quantum efficiencies near 0.1%, compared to quantum efficiencies of around 40% for bulk detectors. At the Night Vision Laboratory thin film detectors of PbSnTe which have quantum efficiencies of 30% and near-BLIP performance have been routinely fabricated. However, these thin film detectors have shown a decrease in quantum efficiency and dynamic impedance upon repeated cycling from room temperature to 80°K. The purpose of this paper is to identify the cause of the decrease in performance and to describe a means of avoiding this degradation.

## II. DESCRIPTION OF THE DETECTOR MATERIAL

The semiconductor studied in this work, for use in the 8 to 14 micrometer atmospheric window, is a complex ternary compound of lead, tin and tellurium. The three elements react to form the pseudobinary semiconductor  $(\text{Pb}_{1-y}\text{Te})_y(\text{Sn}_{1-y}\text{Te})_x$ . For near-stoichiometric cases,  $y \approx 0.5$ , the formula reduces to the simpler formula  $(\text{PbTe})_{1-x}(\text{SnTe})_x$ . Excess metal atoms act as electron donors, while excess tellurium atoms act as acceptors, causing the majority carrier concentration to become  $n$ -type or  $p$ -type, respectively.

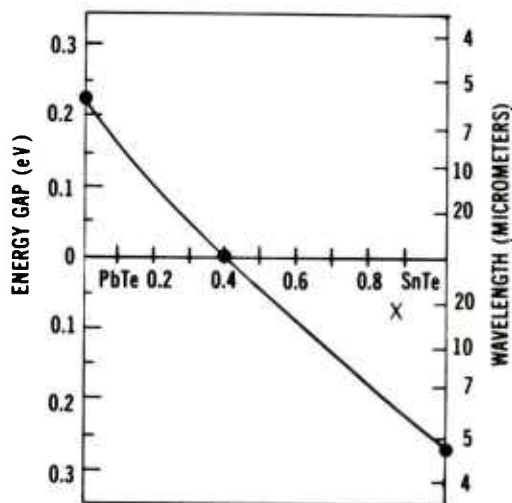


Fig. 1. Energy gap as a function of the mole fraction of SnTe in  $(\text{PbTe})_{1-x}(\text{SnTe})_x$ .

The band gap of a direct transition semiconductor determines the spectral region of photosensitivity. To obtain detectors with a maximum sensitivity in the 8-14 micrometer atmospheric window, a semiconductor with a band gap of approximately 0.1 electron volts is needed. The band gap of  $(\text{PbTe})_{1-x}(\text{SnTe})_x$  is continuously variable from 0.3 eV to 0 eV as a function of the lead-to-tin ratio. Figure 1 shows the relationship between the mole fraction of the tin content and the band gap (5, 6, 7). A band gap of 0.1 eV, corresponding to a maximum sensitivity around 11.0 micrometers, is obtained with a lead-to-tin atomic ratio of 4:1, or  $(\text{PbTe})_{0.8}(\text{SnTe})_{0.2}$ .

### III. EXPERIMENTAL PROCEDURE

The  $(\text{PbTe})_{1-x}(\text{SnTe})_x$  films used in this investigation were grown by a vacuum sublimation technique which is sometimes referred to as Molecular Beam Epitaxy. A polycrystalline alloy of  $(\text{PbTe})_{0.8}(\text{SnTe})_{0.2}$  is heated in a vacuum system to approximately  $640^\circ\text{C}$ . A shutter, which shields the substrate from the evaporant flux, is opened after the material begins to sublime at a predetermined rate. (See Figure 2). A heated, freshly cleaved (111) substrate of  $\text{BaF}_2$  crystal is located in the path of the evaporant flux. This substrate material was chosen because its thermal expansion coefficient and lattice spacing are well suited for the epitaxial growth of  $(\text{PbTe})_{1-x}(\text{SnTe})_x$ . The flux consists of molecules of PbTe, SnTe and a small fraction of the individual elements of Pb, Sn and Te. After striking the  $\text{BaF}_2$  substrate, the molecules align themselves epitaxially, with the (111) plane of the film parallel to the cleaved (111) surface of the  $\text{BaF}_2$ . The process results in a continuous

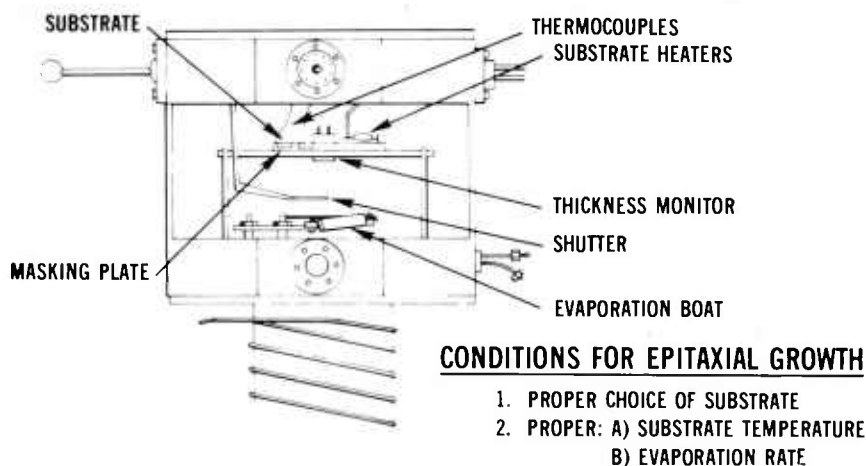


Fig. 2. Vacuum sublimation apparatus.



epitaxial layer of  $(\text{PbTe})_{1-x}(\text{SnTe})_x$  if the substrate temperature is held between 325°C and 400°C and the film growth rate is maintained between one and two micrometers per hour. X-ray analysis of the films indicates that the as-grown crystal quality compares favorably with high-quality  $(\text{PbTe})_{1-x}(\text{SnTe})_x$  crystals grown by bulk techniques. However, good crystal quality is not the only semiconductor material characteristic required for the production of an optimized infrared detector. The carrier concentration and Hall mobility of the semiconductor must be within limits dictated by carrier recombination processes within the material (8). Figure 3 shows the desired mobility and carrier concentration compared to those characteristics for the as-grown crystals. The comparison shows the as-grown films to have a higher p-type carrier concentration and a lower carrier mobility than desired.

TYPE OF FILM	HALL MOBILITY (cm <sup>2</sup> /V-sec)		CARRIER CONC. (cm <sup>-3</sup> )	
	300°K	77°K	300°K	77°K
AS-GROWN	900	7500	$2.5 \times 10^{18}$	$3.9 \times 10^{18}$
OPTIMUM	—	20,000 TO 40,000	—	$\leq 5.0 \times 10^{17}$ $> 1.0 \times 10^{17}$
ANNEALED	400	15,000 TO 20,000	$7.0 \times 10^{17}$	$3.0 \times 10^{17}$

Fig. 3. Hall mobility and carrier concentration of as-grown optimum and annealed films of  $(\text{PbTe})_{0.8}(\text{SnTe})_{0.2}$ .

Published data (9) indicates that the carrier concentration can be reduced by an isothermal anneal of the film with a metal-rich ( $y < 0.5$ ) crush of polycrystalline  $(\text{Pb}_{1-y}\text{Te})_y(\text{Sn}_{1-y}\text{Te})_y$ . If this technique is used, the final carrier concentration is determined by the temperature, rather than the duration, of the anneal. Therefore, by correctly choosing the anneal temperature, the as-grown film characteristics can be modified to closely approach optimum detector parameters. After the film reaches equilibrium with the polycrystalline crush, it must be quickly cooled (quenched) to room temperature. This quenching must be done quickly to "freeze in" the desired carrier concentration. Slow cooling would allow the carrier

concentration to shift as the temperature slowly varied. Figure 3 also compares the carrier concentration and mobility of the as-grown and annealed (15 hours at 525°C) films to the desired optimum values. The anneal results in films with the correct carrier concentration and with a higher mobility than before annealing.

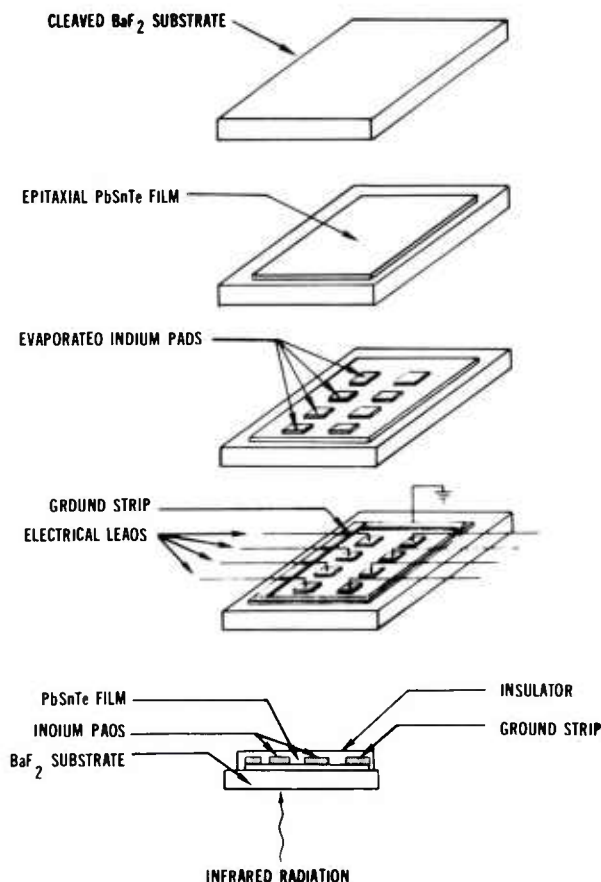
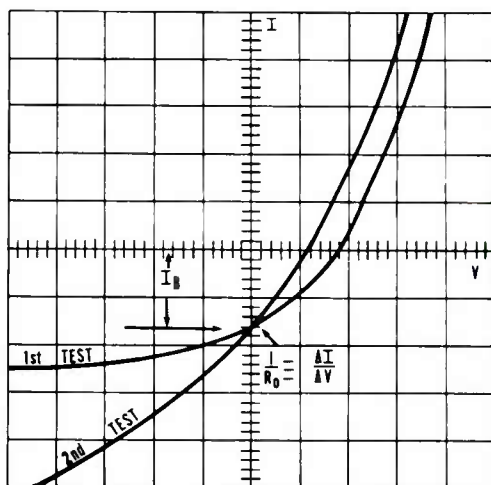


Fig. 4. Fabrication steps and "backside illuminated" feature of  $(\text{PbTe})_{0.8}(\text{SnTe})_{0.2}$  thin film detectors.

After the isothermal anneal the films are processed into photodetectors. A thin layer of a metal (indium) which acts as a donor in  $p$ -type  $(\text{PbTe})_{0.8}(\text{SnTe})_{0.2}$  is evaporated onto the film surface desired as the photosensitive or active area of the photodiode. The film and its indium pads are heated to 110°C for 20 minutes,

allowing the indium to diffuse into the film. This produces an  $n$ -type region in the  $p$ -type film and forms a  $p$ - $n$  junction. Figure 4 shows the fabrication steps and the "backside illuminated" feature of the thin film detectors. Gold is plated on the  $p$ -type film to form an ohmic common connection for the diode array. An insulating layer and lead-out metallization complete the array fabrication procedure. The fan-out metallization has the dual function of enlarging the bonding area of the diodes and protecting the fragile  $p$ - $n$  junction from mechanical damage during the electrical connection of the array to the cryogenic dewar. The finished array is mounted in a vacuum dewar and cooled to approximately 80°K.

Figure 5 shows the current-voltage curves of a typical thin film diode. The resistance-area product ( $2.0 \Omega\text{-cm}^2$ ) and quantum efficiency (31%) calculated from  $R_0$  and  $I_B$ , respectively, indicate that the diode detectivity should be within a factor of two of the theoretical limit. This was confirmed with a measured peak detectivity,  $D^*$ , equal to  $2.2 \times 10^{10} \text{ cmHz}^{1/2}/\text{watt}$  at 180° field-of-view. The peak wavelength of the 77°K detector was 11 micrometers.



Horizontal - 10 mV/div  
 Vertical - 50  $\mu\text{A}/\text{div}$   
 Diode area -  $3.4 \times 10^{-3} \text{ cm}^2$   
 Peak response- 11.0 micrometers

Fig. 5. I-V curves of a typical  $(\text{PbTe})_{0.8}(\text{SnTe})_{0.2}$  diode after the first and second cycle from room temperature to 80°K.

Another requirement for a detector in any infrared imaging application is the long-term stability of the diode. The diodes were found to be unstable as fabricated. Figure 5 also shows typical I-V curves after the first and second test cycles from room temperature to the 80°K operating temperature. After one cycle the diode impedance degrades. After repeated cycling,  $I_B$ , which is directly proportional to the quantum efficiency, decreases. Figure 6 shows the electrical characteristics of an annealed film before and after extensive thermal cycling. The carrier concentration and mobility remained constant, indicating that the cause of the degradation must be something other than impurity contamination or gross crystalline damage. The parameters which did change are the diode quantum efficiency and the dynamic impedance. Both of these parameters are functions of the minority (electron) carrier lifetime.

FILM NO. 154-4B	HALL MOBILITY (cm <sup>2</sup> /V-sec)		CARRIER CONCN.(cm <sup>-3</sup> )	
	300°K	77°K	300°K	77°K
ANNEALED FILM- BEFORE THERMAL CYCLING	590	14,000	4.0 X 10 <sup>17</sup>	4.3 X 10 <sup>17</sup>
AFTER TEN CYCLES	—	13,900	—	4.3 X 10 <sup>17</sup>
AFTER FIFTEEN CYCLES	—	13,900	—	4.3 X 10 <sup>17</sup>

Fig. 6. Hall mobility and carrier concentration of (PbTe)<sub>0.8</sub>(SnTe)<sub>0.2</sub> film No. 154-4B before and after thermal cycling.

In a strongly *p*- or *n*-type material the Hall mobility is independent of lifetime, provided that recombination takes place at lattice dislocations (10). In this case the lifetime depends on the density of dislocations in the crystal lattice. Therefore, as the dislocation density increases, the lifetime decreases. This decrease in lifetime adversely affects the diode dynamic impedance and quantum efficiency. The impedance varies as the square root of the lifetime of carriers generated outside of the depletion region, but it varies directly as the lifetime for carriers generated within the depletion region (11). Thus, the impedance is a function of the lifetime of carriers generated both within and outside of the depletion region. Damage in the crystal lattice on a microscopic scale could give the type of behavior observed. Normal investi-

gative techniques, such as microscopic investigation, did not reveal any damage.

#### IV. X-RAY ANALYSIS

X-ray topography was used as a nondestructive analytical technique for observing the effects of selected processing steps on  $\text{Pb}_{0.8}\text{Sn}_{0.2}\text{Te}$  thin films on  $\text{BaF}_2$  substrates. In this technique the single-crystal sample is oriented so that Bragg diffraction of x-rays occurs for a selected crystallographic plane. A beam of x-rays is scanned across the sample, and the diffracted beam is recorded on a high-resolution photographic plate whose surface is perpendicular to the diffracted beam. The scanning is accomplished by translating the sample and photographic plate together, by means of a motor drive, in a horizontal direction which is parallel to the sample surface, as shown in Figure 7. A commercially available Lang camera for x-ray topography is used for this purpose. Since both the sample and the photographic plate move relative to the stationary x-ray source, a 1:1 correspondence exists between the illuminated area of the sample and the image recorded on the photographic plate. The plate is enclosed within a light-tight cassette so that the image formed on the plate is produced only by x-rays. After sufficient exposure to the diffracted x-ray beam, the high-resolution photographic plate is developed and photographically enlarged. Even higher magnification of topographic features can be achieved by photographing the developed topograph through a microscope. The enlarged photographic print is then examined to determine what defects are present in the sample.

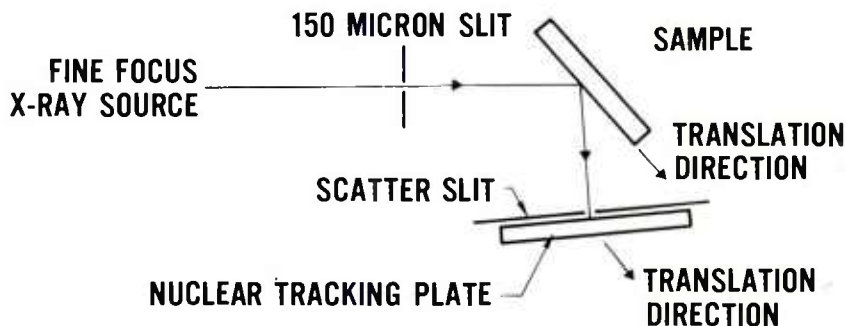


Fig. 7. Schematic diagram of x-ray topographic apparatus.

A perfect single crystal would yield a grey, featureless image of the sample on the photographic plate. Various defects in the crystal can produce contrast effects in the x-ray topographic image. Grain boundaries, elastic and inelastic strain, dislocations, slip, precipitates, polishing scratches, and handling damage are some of the causes of topographic contrast. Very often these features are not visible during microscopic examination of a sample but are clearly delineated in an x-ray topograph.

Figures 8 and 9 show x-ray topographs of thin film  $\text{PbSnTe}$  on a  $\text{BaF}_2$  substrate after two different annealing cycles. Figure 8 is an x-ray topograph of a sample for which the temperature was changed very slowly during the annealing cycle. The results of a second annealing cycle which included an air quench are shown in Figure 9. Low-angle grain boundaries of a few hundredths of a degree and cleavage steps are clearly visible in both topographs. These are formed in the film layer because the epitaxial film is deposited over low-angle boundaries and cleavage steps in the substrate. Figure 9 shows three networks of dislocation lines which are not present in the topograph shown in Figure 8. The vertical lines are very bright, and the two diagonal sets of dislocation lines are relatively dim because of the choice of diffraction vector. The

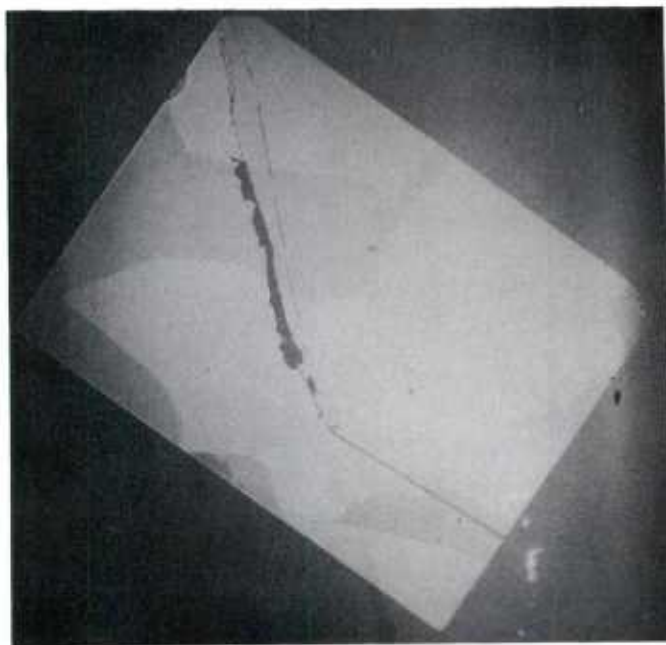


Fig. 8. X-ray topograph of  $(\text{PbTe})_{0.8}(\text{SnTe})_{0.2}$  thin film on  $\text{BaF}_2$  which was cooled very slowly after annealing.



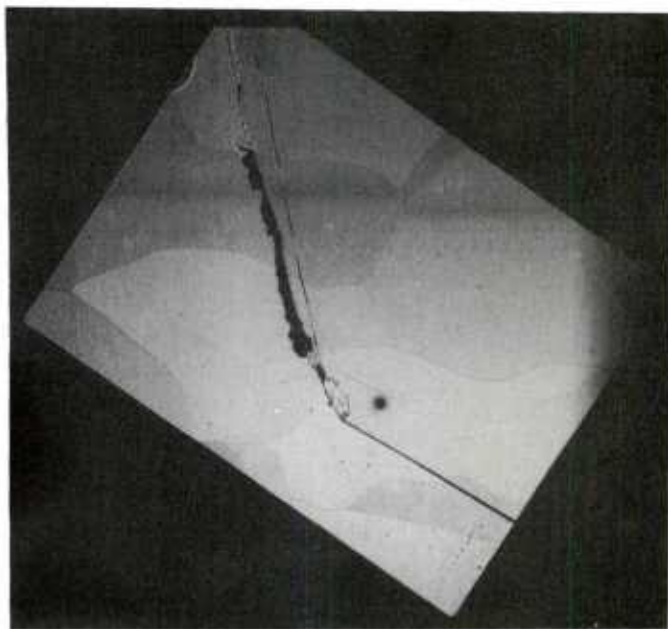


Fig. 9. X-ray topograph of a  $(\text{PbTe})_{0.8}(\text{SnTe})_{0.2}$  thin film on  $\text{BaF}_2$  which was quenched after annealing.

contrast of the dislocation lines gives valuable information which is essential in order to fully characterize the dislocations. The dislocation lines in the sample were not detectable by optical means, but the low-angle grain boundaries and cleavage steps were clearly visible. The x-ray topographic technique is, of course, sensitive to dislocations located beneath the surface of the sample.

After it was determined that the damage was introduced during the anneal, a more thorough examination revealed that the damage was dependent on the rate, rather than on the magnitude, of the temperature change during the anneal. Figure 10 shows the graph of temperature *vs* time of two anneals. The first anneal cycle, which was nondestructive, allowed the temperature to slowly reach its peak value and then slowly descend. The second is a normal anneal cycle with an air quench. The first anneal did not damage the films, but the second anneal resulted in dislocation networks,



as shown by the x-ray topograph in Figure 9.

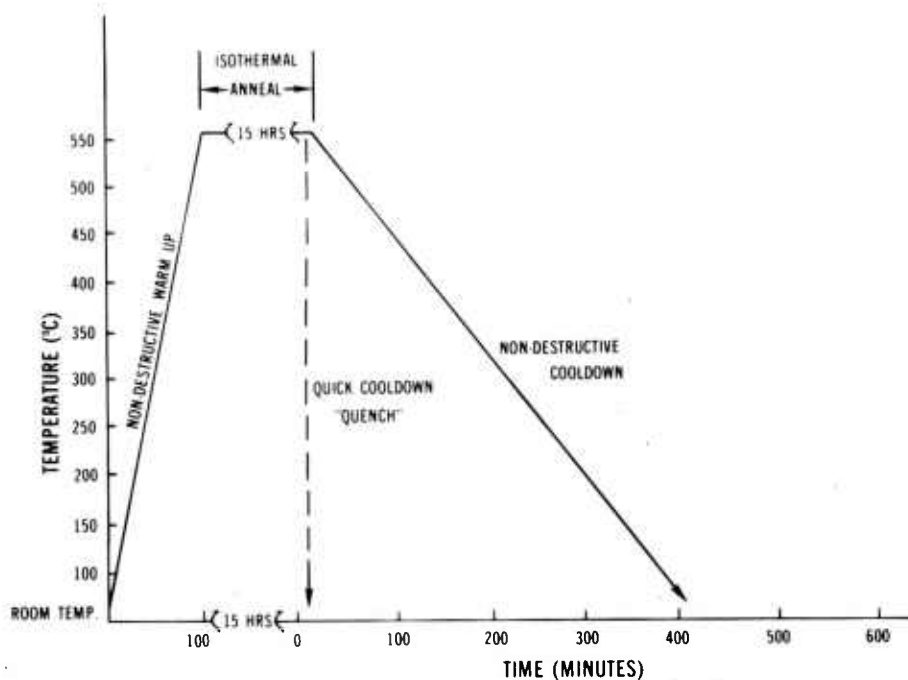


Fig. 10. Temperature *vs* time for the nondestructive and quenched anneal cycles.

There are several possible causes of strain in PbSnTe films on BaF<sub>2</sub> substrates. The lattice spacing and the thermal expansion coefficients of the film are approximately 3% and 10% greater than the corresponding values for the substrate. Because of the difference in lattice spacing, a certain amount of strain is present at the film-substrate interface of as-grown films. Heating the sample increases the difference in lattice spacing, but this difference should not be dependent upon the rate at which the sample temperature is changed. However, the finite thermal conductance of the film and substrate may cause the formation of thermal gradients during rapid cooldown of the sample. This can increase the difference in the lattice spacings of the film and substrate, producing additional mechanical stress at the interface. The strained film

may then form a network of dislocations or slip to relieve the strain.

## V. CONCLUSIONS

Additional experiments revealed that the quench rate required to maintain the desired carrier concentration is faster than the nondestructive cooldown rate. Consequently, an isothermal anneal, with its necessary quick cooling, results in film crystal damage and unstable diode characteristics.

These results do not exclude  $(\text{PbTe})_{1-x}(\text{SnTe})_x$  from consideration as a thin film infrared detector. The results<sup>x</sup> do indicate that some method other than the isothermal anneal must be used to obtain optimum carrier concentration values. The evaporation technique used to grow the films is versatile enough to incorporate a certain amount of control over the as-grown carrier concentration. The addition of a second flux source can be used to add additional metal atoms to the *p*-type films, and thus control the carrier concentration, as the films are grown. The rate at which these excess metal atoms arrive at the growth surface can be controlled by adjusting the temperature of the second source. This two-source technique can yield as-grown thin films with the desired carrier concentration. It remains to be seen whether the Hall mobility and minority carrier lifetime of  $(\text{PbTe})_{1-x}(\text{SnTe})_x$  thin films grown by this method are acceptable for use in infrared detectors.

REFERENCES

1. E. M. Logothetis, H. Holloway, A. J. Varga, and E. Wilkes, "Infrared Detection by Schottky Barriers in Epitaxial Lead Tin Telluride", Applied Physics Letters, Vol. 19, No. 9 (1971).
2. H. Holloway, E. M. Logothetis, and E. Wilkes, "Epitaxial Growth of Lead Tin Telluride", Journal of Applied Physics, Vol. 41, No. 8 pp 3543-3545, July 1970.
3. H. Holloway, "Development of Lead Telluride and Lead Tin Telluride Photovoltaic Detectors by Vacuum Sublimation", Final Report, DAAK02-72-C-0391, AD 917 388L.
4. A. Asch, "Lead Tin Telluride Thin Film Photodiode Detectors", Final Report, DAAK02-74-C-0181, AD B005625L.
5. J. O. Dimmock, I. Melngailis, and A. J. Strauss, Physics Review Letters, 16, 1193 (1966).
6. J. F. Butler, A. R. Calawa, and T. C. Harman, Applied Physics Letters, 9, 427 (1966).
7. J. F. Butler and T. C. Harman, Applied Physics Letters, 12, 347 (1968).
8. M. R. Johnson, R. A. Chapman, J. S. Wrobel, "Detectivity Limits for Diffused Junction Lead Tin Telluride Detectors", Infrared Physics, Vol. 15, No. 4, p. 314, Nov 1975.
9. A. R. Calawa, et al., Transactions of the Metallurgical Society, AIME 242, 374 (1968).
10. W. Shockley, W. T. Read, Jr., Phys. Rev. 87, 835 (1952).
11. M. Johnson, "Intermediate Temperature Photovoltaic Detectors", Final Report, pp. 10-14, DAAK02-72-C-0330, AD 921 432L, May 1974.



## Aerosol Spectroscopy in the Infrared (U)

Mr. Hugh R. Carlon  
Mr. David H. Anderson  
Development and Engineering Directorate  
U. S. Army Edgewood Arsenal  
Aberdeen Proving Ground, Maryland 21010

Many misconceptions exist concerning the spectral properties of liquid droplet aerosols in the infrared. Most are based upon assumptions of aerosol "scatter" but not aerosol "absorption". They have their origins in a time when virtually all infrared instrumentation was confined to wavelengths of less than  $2.5 \mu\text{m}$ . At these shorter wavelengths it is true that the imaginary component of the complex index of refraction, which accounts for droplet absorption, is vanishingly small even for substances like water which have strong absorption at longer infrared wavelengths. The "real" component of refractive index accounts for "scattering" of the type which is well known and understood. Thus, most aerosols are expected to behave like oil droplet smokes, for example, which show progressively better optical transparency as illuminating wavelengths become large compared to droplet size. This can be discussed by reference to Figure 1. This is the infrared spectrum of an aerosol of military fog oil smoke in the infrared wavelength region from  $3.0$  to  $5.0 \mu\text{m}$ . The dashed portions of the curve represent regions of view port window (polyethylene) absorption for the smoke test chamber used in our measurements. The notations specify the aerosol under test. "CL" is the product of aerosol concentration in  $\text{gm}/\text{m}^3$  times optical path length in meters. "Drop conc." refers to the composition of the droplets themselves, in this case 100% oil. "MMD" refers to mass median diameter of the droplets in microns (micrometers will be units of wavelength in this paper, but microns will be used conventionally for droplet diameters).  $\delta$  is the standard deviation of droplet size distribution on either side of the MMD. "RH" refers to relative humidity and is not usually applicable to measurements involving non-hygroscopic aerosols. Alpha,  $\alpha_n$ , is the

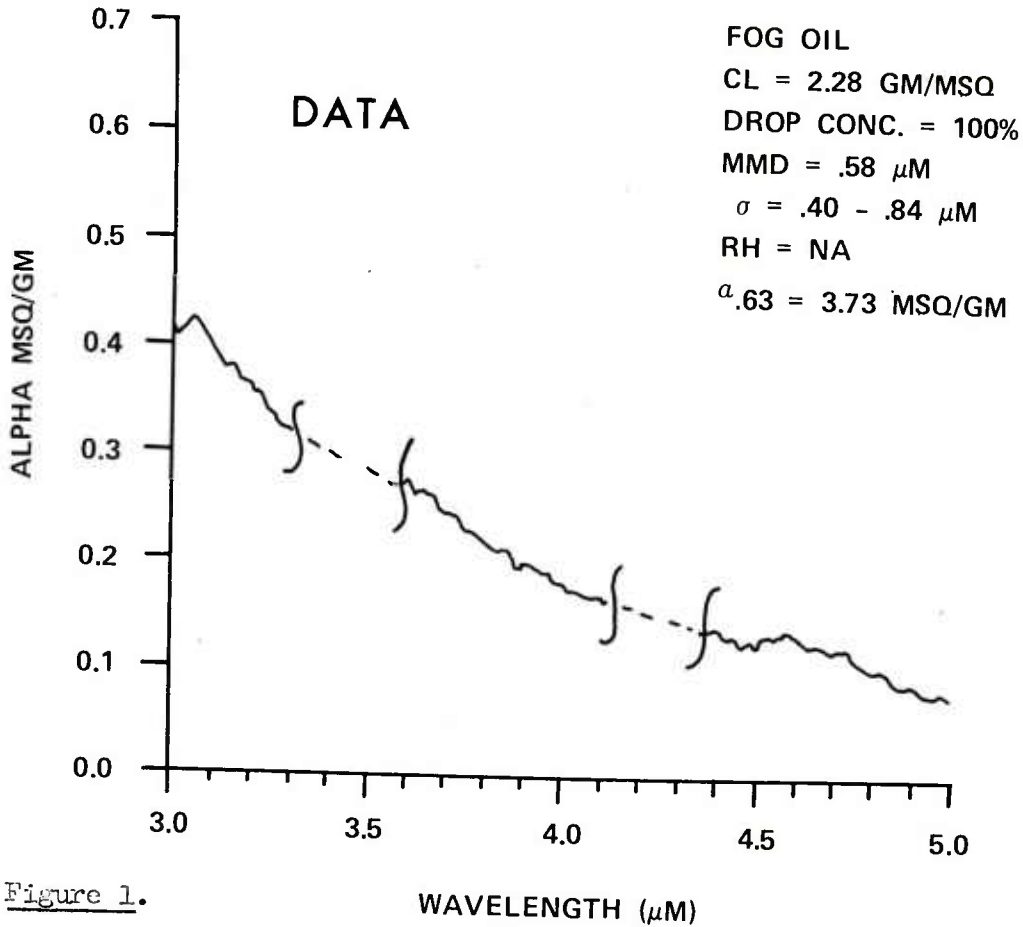


Figure 1.

total extinction coefficient of the aerosol, with the subscript noting the wavelength referred to, in microns. Thus the notation shows that this oil smoke had an  $\alpha_{.63}$  in the visible at .63  $\mu$ m (the Helium-Neon laser wavelength) of 3.73  $\text{m}^2/\text{gm}$ . And, because the droplets are small, extending the wavelength of illumination to the 3-5  $\mu$ m region already has produced a drop of a factor of 10 or more in optical extinction compared to that in the visible. Furthermore, the curve continues to fall uniformly toward longer wavelengths. This is "expected" behavior of an almost purely scattering smoke, such as fog oil smoke is because of its almost total absence of bulk spectral absorption in the infrared. Alpha values are used in the familiar equation:

Equation 1.  $T = I/I_0 = \exp(-\alpha_n CL)$

where  $T$  is fractional optical transmittance,  $I/I_0$  is the ratio of observed to initial energies transmitted at wavelength "n", and other parameters are as already defined.



As we move to still longer infrared wavelengths in Figure 2, the extinction ( $\alpha$ ) has dropped nearly to zero in the 7-13  $\mu\text{m}$  range. The residual extinction is, in fact, partially due to liquid water absorbed in trace quantities in the bulk oil. If we use the term  $D_\mu$  to mean droplet diameter (MMD) in microns and  $n$  for wavelength as  $\mu$  before, we see that an important general case develops when  $D_\mu \ll n$ . "Scattering" arising from the real index of refraction becomes almost negligible in this case, and only the absorption component is seen readily in aerosol spectra. Since a great many natural, atmospheric aerosols occur in diameters very small compared to visible or infrared wavelengths, we see a very important aspect of aerosol spectroscopy developing which we shall now investigate.

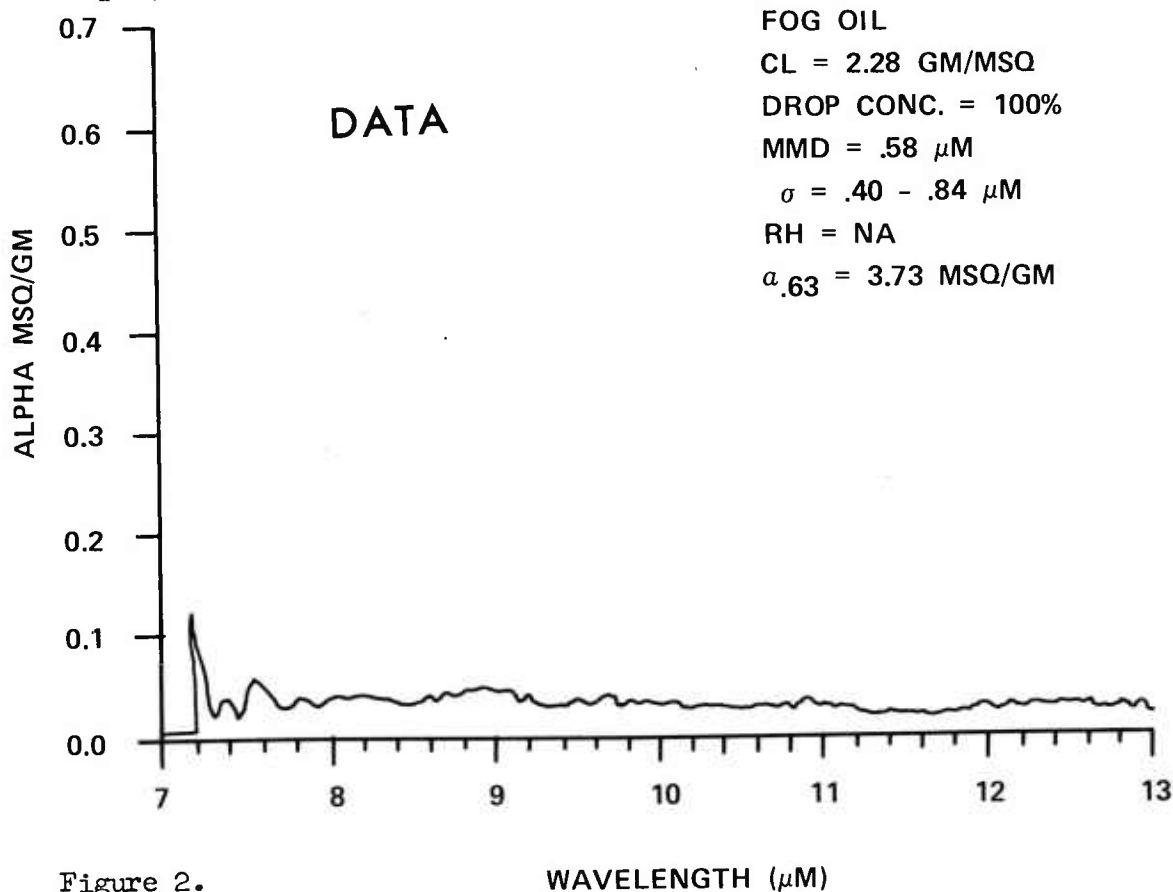


Figure 2.

WAVELENGTH ( $\mu\text{M}$ )

An entire family of approximation equations becomes applicable for the case where  $D_\mu \ll n$ . Such aerosols behave spectrally almost as the vapor, with the important exception that their spectra are those of the liquid comprising their droplets rather than those of the vapor phase. While this is relatively unimportant for materials which show

little difference in absorptivities between physical phases, such as fog oil and other "non-polar" liquids, it is enormously important in the case of "polar" liquids, for example water or its hydrations of atmospheric solutes.

For comparison with Figures 1 and 2, we now consider a highly hygroscopic smoke, that produced by burning phosphorus. In Figure 3 we see the spectrum at 3-5  $\mu\text{m}$  for such a smoke having an MMD of 1.13 $\mu$  and droplets consisting of almost pure  $\text{H}_3\text{PO}_4$ . Alpha at .63  $\mu\text{m}$  is 4-6 times larger than in this region. However, note that the right-hand end of this curve is not dropping with increased wavelength as rapidly as in Figure 1 (for fog oil). This is because 3-5  $\mu\text{m}$  is a transitional region between "real index" scattering at shorter wavelengths, and "imaginary index" droplet absorption toward longer wavelengths. As shown in Figure 4, by the time we reach 7-13  $\mu\text{m}$  we obtain alpha values due to absorption which are vastly different from those for fog oil

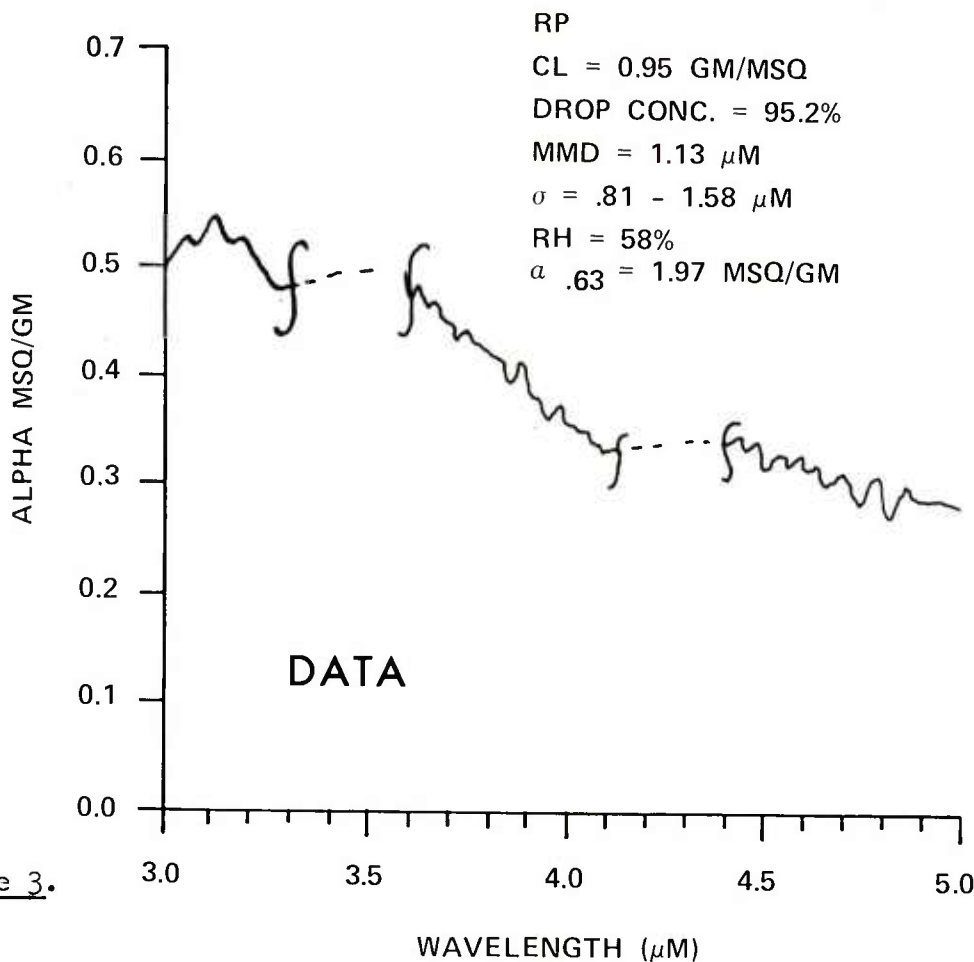


Figure 3.

(Figure 2). Indeed, some alpha values in the 7-13  $\mu\text{m}$  region are larger than some at 3-5  $\mu\text{m}$ . This is completely contrary to "expected" scattering behavior and represents one of those misconceptions addressed in the opening of this paper. In studying aerosol spectra such as in Figure 4, we have found that the peaks are due almost entirely to  $\text{H}_3\text{PO}_4$  liquid absorption, while the longer-wavelength "tail" is due to hydrated water. Later, we shall show how it is possible to study hydration and other reactions as they take place in the air by observations of rapid-scan infrared spectra and data correlation with computer modeling of expected behavior. Potentially, these techniques offer a powerful tool for the study of air pollutants and chamber reaction dynamics.

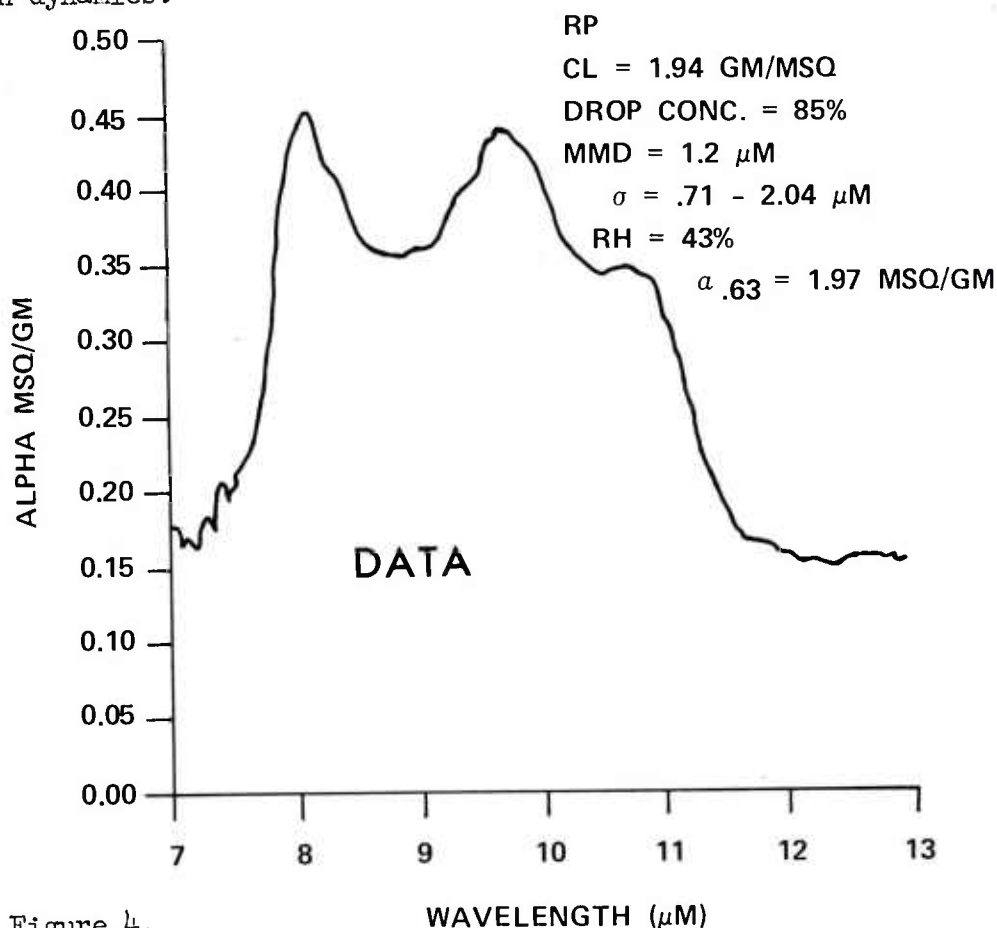


Figure 4.

Two very useful equations are among those developed for our special case where  $D_{\mu} \ll n$ . In these equations,  $\rho$  is the density of the liquid comprising the aerosol droplets,  $k_{L,n}$  is the liquid film absorptivity coefficient at wavelength  $n$ , and  $t$  is the thickness in microns

of the equivalent "precipitable" film of droplet liquid having virtually identical spectral characteristics to the aerosol of specified CL, itself. Because of our choice of units, we cause the equations to produce numerically correct results directly when  $\rho$  is expressed in gm/cm<sup>3</sup>,  $k_{L,n}$  is expressed in  $\mu^{-1}$ ,  $t$  is expressed in precipitable microns, and other parameters are in units already stated:

$$\text{Equation 2.} \quad k_{L,n} \approx \alpha \cdot \rho$$

$$\text{Equation 3.} \quad t \approx (CL)/\rho$$

Both the real and the imaginary components of the complex index of refraction are necessary before one can compute the Mie-model extinction of spherical-droplet aerosols. Thus, when we experimentally observed the behavior of phosphoric acid droplets in the 7-13  $\mu$ m region (Figure 4), we were able to use Equations 2 and 3 to determine the absorptivity coefficients of equivalent liquid films of the acid comprising the droplets by assuming  $D_\mu (1.2\mu) \ll n$  (7-13  $\mu$ m) and obtaining the imaginary indices by standard spectrophotometric and arithmetic techniques. These values were then used with estimated values of the real index to computer-model the expected behavior of the acid aerosol. Reasonable agreement was obtained between measured and computed values in the 7-13  $\mu$ m region. The calculated values for phosphoric acid are presented in a useful way in Figure 5. Here, the center wavelength of the 7-13  $\mu$ m region is specified, and calculated values of alpha are shown versus values of  $D_\mu$  shown on the abscissa. These curves use the subscript "T" to designate total alpha where we have used "n" in Equation 1. Also shown are the components of aerosol absorption (subscript "A") and refractive scattering (subscript "S") which together produce total values of extinction at  $n = 10 \mu$ m. The convergence of the two upper curves is nearly complete as one moves to smaller values of  $D_\mu$  along the abscissa. For  $D_\mu = 1.2\mu$ , the MMD of the aerosol in Figure 4, we see in Figure 5 that the upper curves are nearly coincident. This tells us that our assumption  $D_\mu \ll n$ , and the approximations which it implies, are valid because computed aerosol absorption and total extinction are nearly identical for a wavelength (10  $\mu$ m) at the center of the 7-13  $\mu$ m infrared region. That is, the scattering contribution (arising from the real index of refraction) was negligible for the phosphoric acid aerosol parameters shown in Figure 4. We see, too, from Figure 5 that if our acid droplets had been 10-20  $\mu$ m in diameter, as in typical water fogs for example, scattering and absorption components of optical extinction would have been of similar magnitudes and our approximations would have introduced serious error.

Precision results could not be obtained for phosphoric acid aer-

osols in the manner just described, simply because precise complex index information is not yet available for this material in the infrared. There is one liquid aerosol system for which complex indices are well characterized at least to infrared wavelengths near  $15\text{ }\mu\text{m}$ . That system is sulfuric acid/water. From literature values, and values of the indices interpolated by us using the approximation techniques of Equations 2 and 3, we have compiled both Mie-model "expected" behavior of these aerosols and a large body of experimental data for correlation purposes. We shall now consider some of these correlation procedures.

## SCATTERING EFFECTS WAVELENGTH= $10.0\text{ }\mu\text{m}$ $\text{H}_3\text{PO}_4$

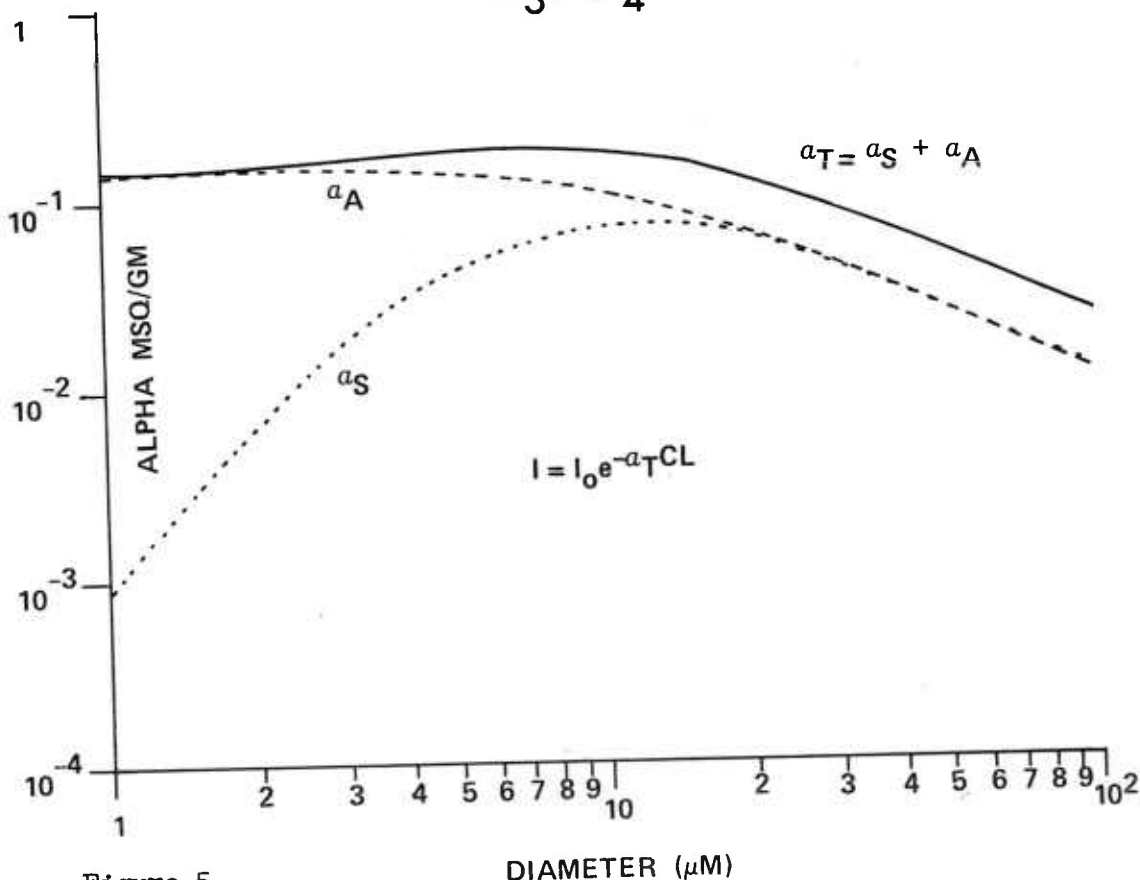


Figure 5.

We may compare Figure 6 for smoke agent "FS" to Figures 1 and 3 for fog oil smoke and phosphoric acid aerosol, respectively. The curve is for droplets of about 44% acid concentration, which have equilibrium diameters (MMD) near  $.78\text{ }\mu\text{m}$ . FS is a material which conven-

iently produces sulfuric acid droplets by spray dissemination. The droplets are then hydrated by natural humidity, or by low-temperature steam introduced in experimental trials for this purpose. We see in

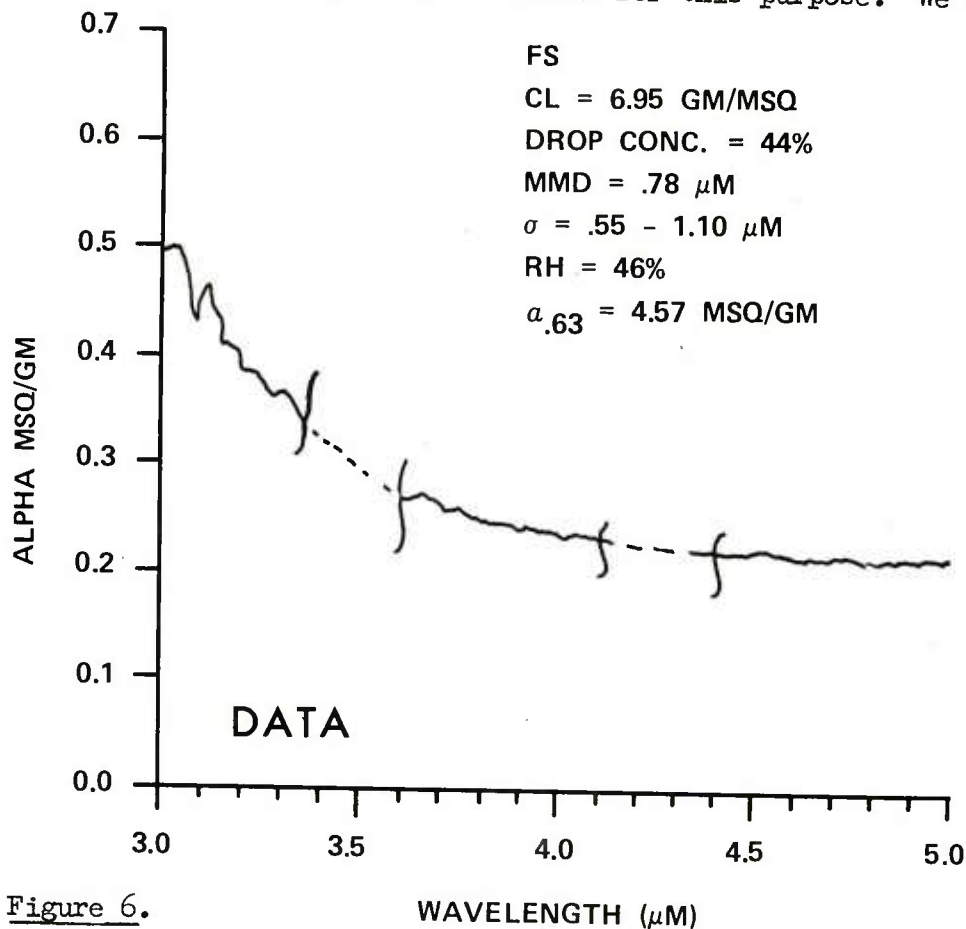


Figure 6.

Figure 6 that the curve flattens toward longer wavelengths because of increasing droplet absorption, and the MMD for such a strongly-absorbing acid will be shown to be small enough for the approximation  $D_p \ll \lambda$  to become valid at the longer infrared wavelengths. In Figure 7, we look at FS aerosol spectrally in the 7-13  $\mu\text{m}$  region as we did earlier for other materials in Figures 2 and 4. Note the absorption peaks due to  $\text{H}_2\text{SO}_4$  at 7-10  $\mu\text{m}$ , and the "tail" due to hydrated water at longer wavelengths. This behavior is not unlike that for phosphoric acid, discussed earlier. The water tail would, in fact, turn up for droplets of higher water content. From this we see that curve shape is a rather sensitive indicator of absorbing aerosol droplet composition. In our hydration studies for application to atmospheric observations, we take advantage of this fact. If we look at the experimental data



of Figure 7, for the wavelength  $\lambda = 10 \mu\text{m}$ , we read an alpha value of about .25 from the ordinate. This value is found to agree rather pre-

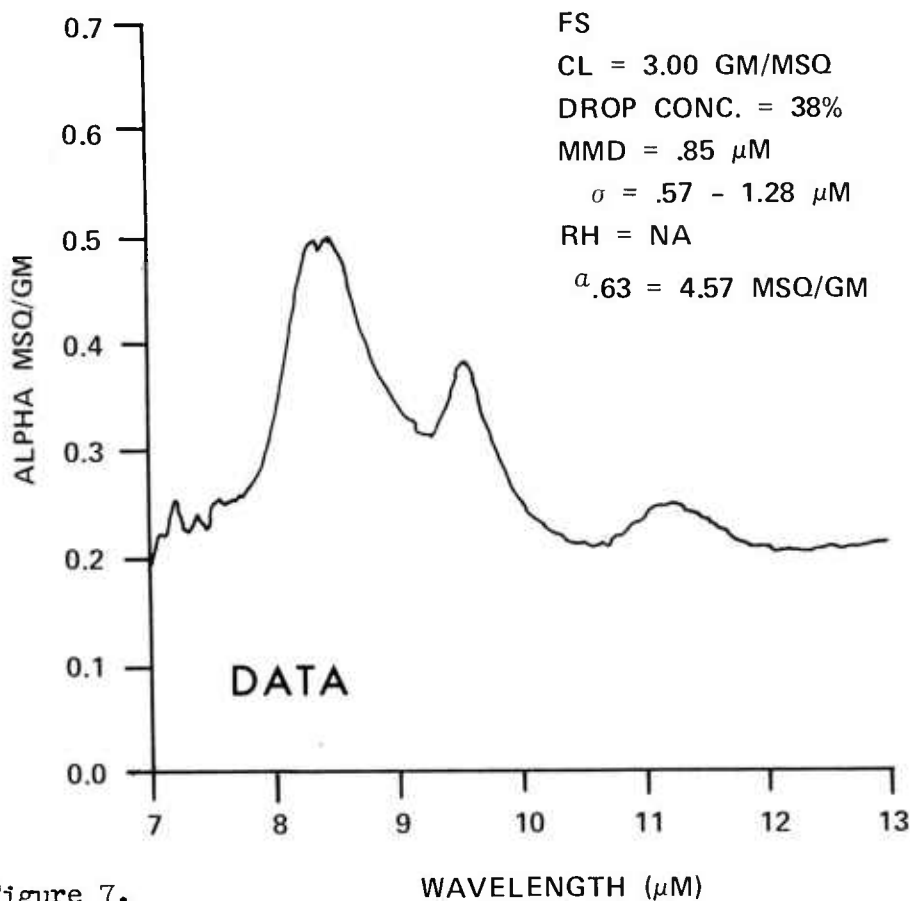


Figure 7.

cisely with the computed values derived from well-known complex indices of refraction for this wavelength. Note the convergence of the upper curves of Figure 8 toward an alpha of about .25 for MMD's well within the range actually measured experimentally for the test conditions of Figure 7. The inherent precision of the approximation and measurement techniques presented here thus would seem to be confirmed. Measurements are now under way for our determination of infrared complex indices of many materials of interest. We note in passing that one planned test series will involve neutralization of acid aerosols with alkaline vapors, in air, and spectroscopic study of the reactions at 7-13  $\mu\text{m}$  using rapid-scan techniques. Later, such quantitative techniques should become applicable to the study of air pollutant reactions in the open atmosphere.



As we approach very dilute  $\text{H}_2\text{SO}_4$  droplet concentrations through extensive hydration, the equilibrium MMD of the aerosol also becomes greater and the transition is made into the realm of water hazes, clouds and fogs. In this sense, it is convenient to think of water aerosols simply as the ultimate dilution case for acid aerosols.

## SCATTERING EFFECTS WAVELENGTH=10.0 $\mu\text{m}$

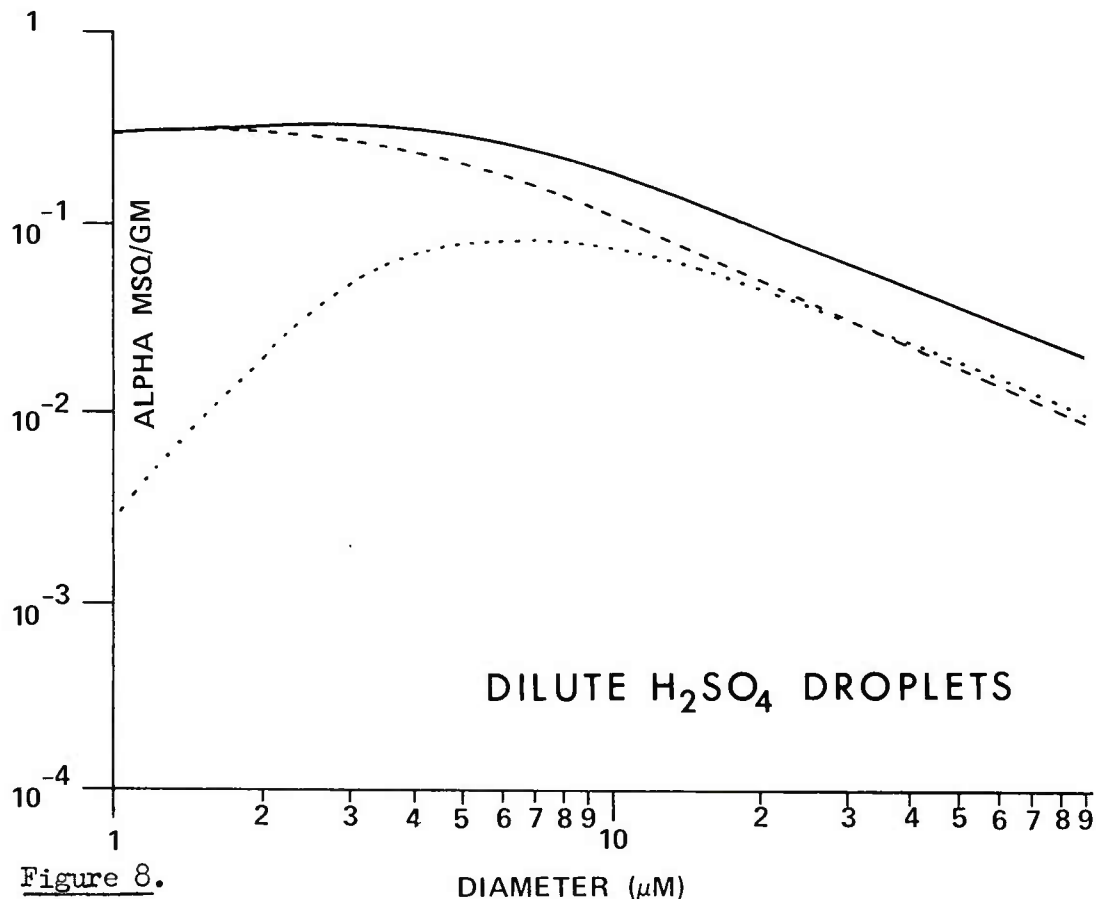


Figure 8.

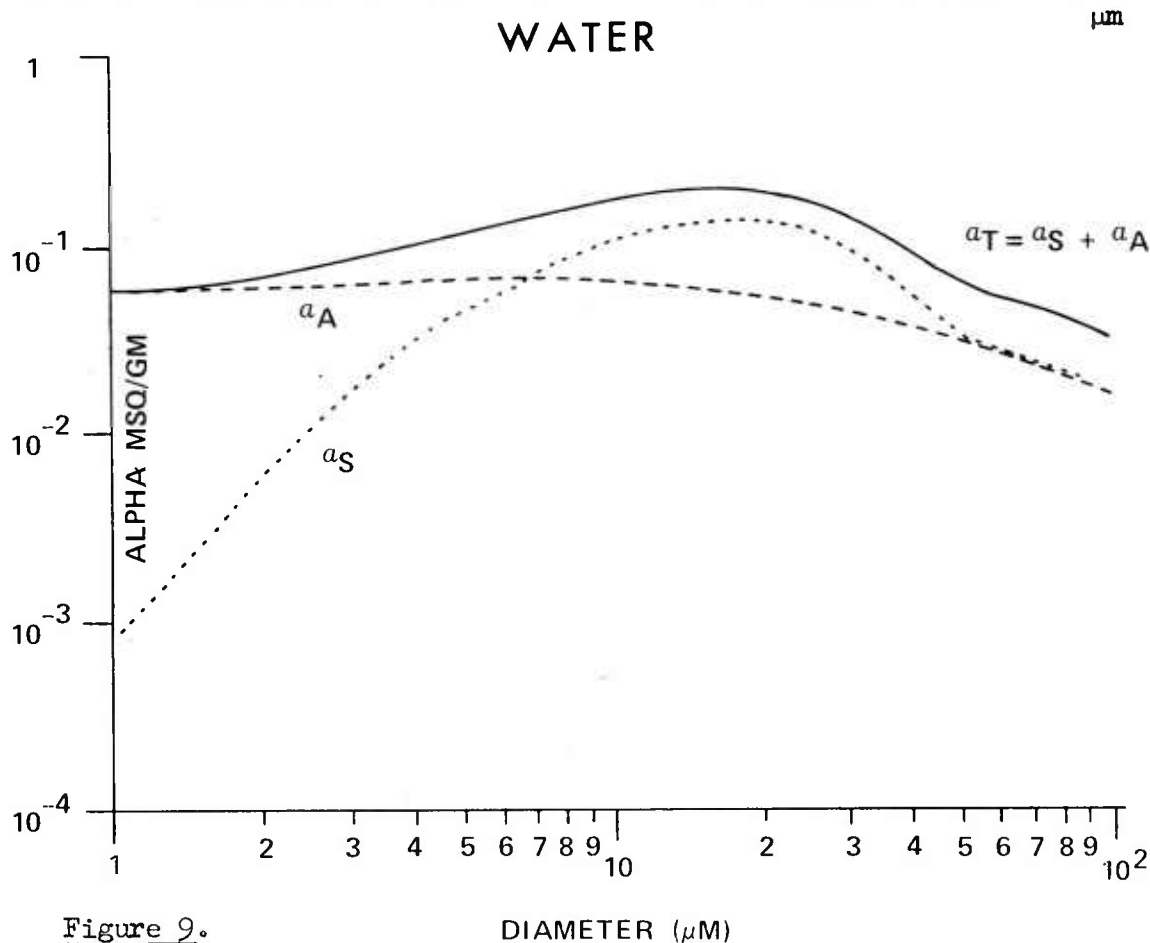
Much has been written in recent years about "e-type" spectral absorption, normally attributed to unusual behavior of atmospheric water vapor. Curves relating anomalous absorption to wavelength in the 7-13  $\mu\text{m}$  region, and attributing the results to water vapor, have been presented in the literature by many authors. Yet our own data taken for dilute sulfuric acid aerosols in this spectral region show that very dilute acid droplets (about 4% by weight) can produce curves identical in shape to those attributed by other workers to water vapor. Furthermore, only a very small quantity of precipitable

aerosol (on the order of a 10 micron liquid film) need be present to account for data attributed by others to much larger quantities of precipitable water as the vapor. Our own interpretation of these data, therefore, favors trace effects of dilute acid aerosols rather than exotic behavior of the vapor.

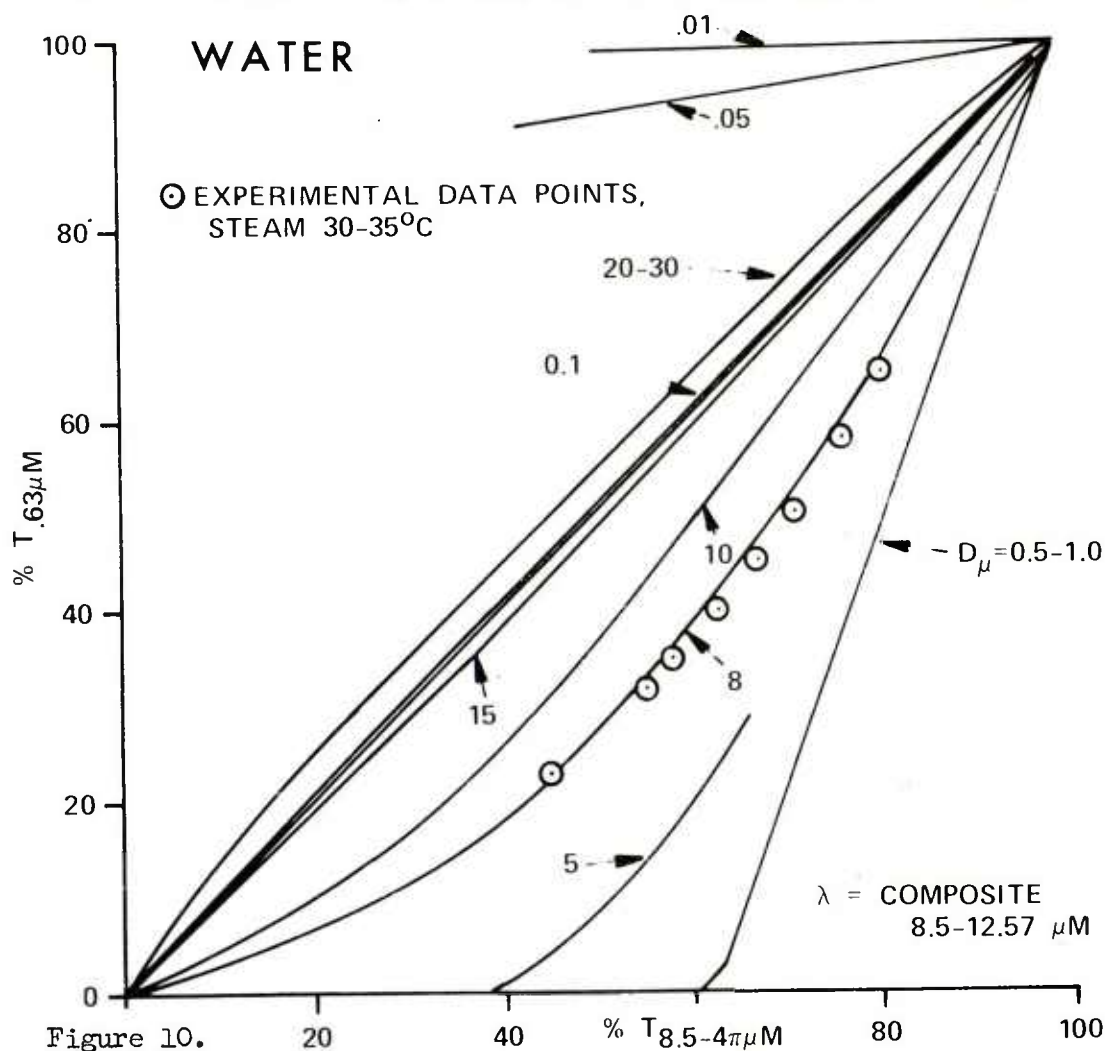
Finally, our discussion brings us to the consideration of water aerosols in the manner of our earlier consideration of other materials. Water droplets comprise what are in all probability the most common and least understood atmospheric aerosols of all. To begin with, most fogs and clouds have optical or mass-median diameters which lie in the  $8\mu$  to  $30\mu$  (or more) range, where "scattering" and "absorption" contributions to optical extinction are comparable as shown in Figure 9. Furthermore, their alpha values are only moderately smaller than those of acid droplets as shown in Figures 5 and 8. Bulk water has

## MIE SCATTERING EFFECTS WAVELENGTH=10.0

### WATER



very strong spectral absorption at 7-13  $\mu\text{m}$ , and virtually none at wavelengths below about 2.5  $\mu\text{m}$ . As a result, we find that what we call "belly curves" give a very sensitive indication of the mean sizes of water drops comprising fogs or clouds. In Figure 10, for example, we show a series of such curves computed from our Mie model for which the complex indices of refraction for water are well known. Here, we compare optical transmission readings taken with the convenient Helium-Neon laser at .63  $\mu\text{m}$  and plotted along the ordinate, with those for a composite of transmission for wavelengths of 8.5-12.57  $\mu\text{m}$ . The composite allows broad-band thermal imagers operating in the 7-13  $\mu\text{m}$  region to be used as transmissometers, for example. These are more commonly available than wavelength-scanning radiometers, and make the curve technique more generally useful to many workers. Curves such



as those in Figure 10 allow us to plot experimental data points on them so that approximations may be made of droplet diameter in the water aerosol being observed. For example, Figure 10 contains many experimental points taken for low-temperature, cooling steam over a wide range of concentrations. These points follow closely the curve for  $D_{\mu} = 8\mu$ , indicating that the effective optical or mass-median diameter was near this value for the observed cloud. Had  $D_{\mu}$  been near  $15\mu$ , the points would have fallen almost on the  $45^{\circ}$  line.<sup>11</sup> This would have indicated that no particular optical transmission advantage lay with the visible or 7-13  $\mu$ m infrared wavelengths for an aerosol of this predominant drop size. In fact, very small or very large droplets would give the transmission advantage to the visible, not the infrared. It is not always true that we have enhanced transmission as we go to longer infrared wavelengths and away from the visible. Yet this notion persists as a fundamental "fact" of scattering by smokes, clouds or fogs. From results such as these, we are developing equations which are valuable in characterizing fog or cloud droplet properties from a few simple measurements. This work will be reported in the open literature as it is completed.

Other interesting aspects of water aerosol behavior are presented in Figure 11. Here, computed curves show expected transmittances at a  $CL = 5 \text{ gm/m}^2$ , with  $D_{\mu}$ , for wavelengths of .63, 8.5, 10.5 and 12.57  $\mu$ m. The curves, reading from top to bottom at their left-hand ends, are in the sequence of wavelengths just related. The flat regions common to all curves correspond to regions where the approximation  $D_{\mu} \ll n$  is valid. The curve for  $n = .63 \mu$ m arises entirely from the real index of refraction at that wavelength, and the extinction mechanism is "scattering" in the sense traditionally considered. The other three curves incorporate the contributions of droplet absorption and real-index scattering in the infrared as we have discussed previously. In typical fog or cloud droplet size ranges (8-30 $\mu$  or more), roughly comparable transmittances are noted for all four wavelengths. This can also be deduced from Figure 10. However, small water droplets of  $D_{\mu} = .1$  or less theoretically would form aerosols with better transmittance in the visible than in the 7-13  $\mu$ m infrared region, because of residual droplet absorption in the latter region. Natural water aerosols do not, however, tend to have droplet sizes in this range. Smaller droplets evaporate rapidly, while larger droplets contribute to the formation of water aerosols with equilibrium diameters determined by parameters such as air temperature and degree of supersaturation. Hydrated acid droplets, on the other hand, do attain equilibrium diameters in this size range, and at even smaller droplet sizes. Thus our hydration studies will also indicate how high  $\text{H}_2\text{SO}_4$  droplet concentrations, for example, must be to obtain such aerosol behavior. Fine acid aerosols would be effective attenuators in the

infrared, while having little effect upon visibility. Such behavior, which we presume already exists in the atmospheres of industrialized areas, would be completely contrary to long-accepted popular concepts of aerosol behavior. Moving to longer wavelengths would actually worsen optical transmission.

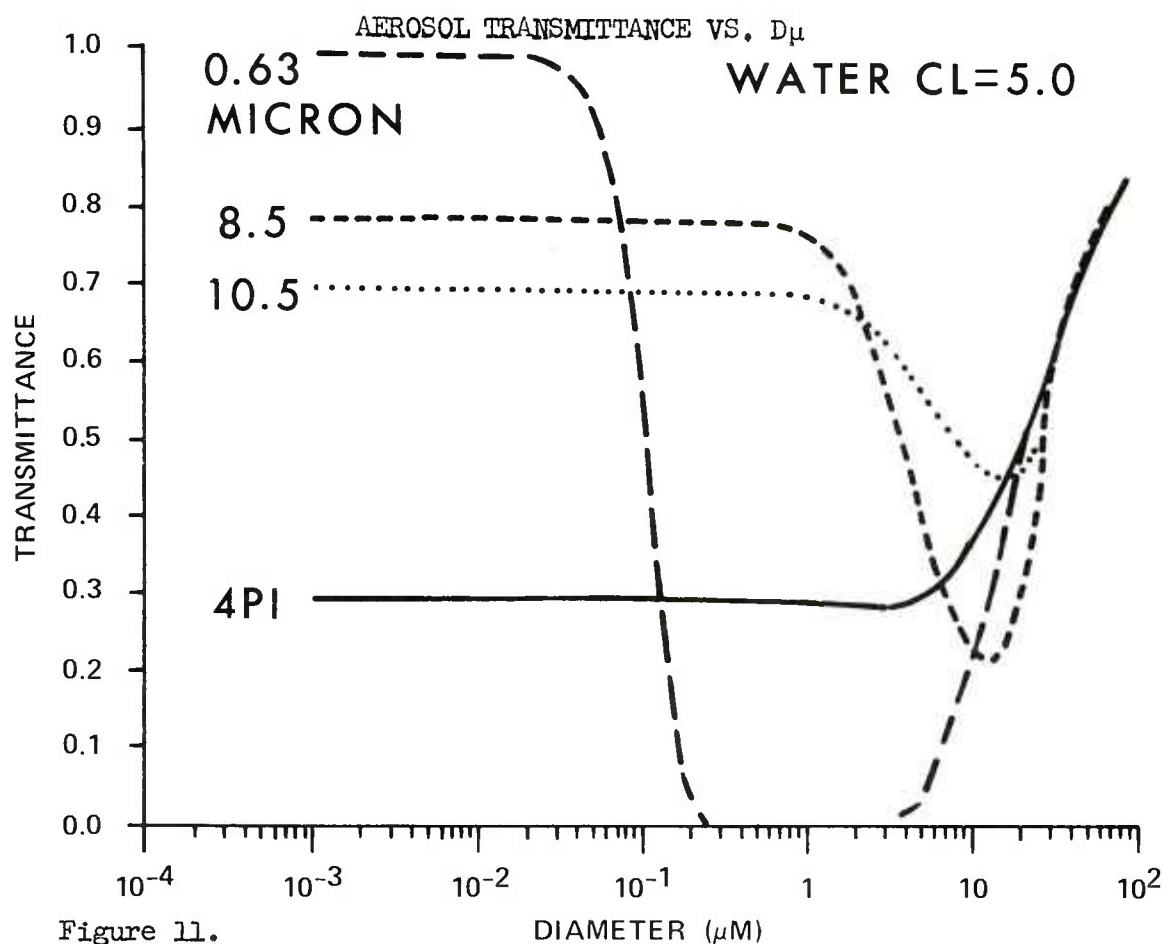


Figure 11.

Because most of our observations reported here were taken using a rapid-scan passive radiometer with 3-5  $\mu\text{m}$  and 7-13  $\mu\text{m}$  wavelength-scanning capability, we have been able to make sensitive thermal emission measurements to supplement more conventional transmittance data. We have discussed the absorption (imaginary component) contribution to total optical extinction in this paper, and shown how for water and hydrated acid aerosol droplets absorption becomes very important at longer infrared wavelengths (7-13  $\mu\text{m}$ ). From classical radiation theory, we would expect this absorption component to produce an equilibrium thermal emission component which could be observed by



a passive radiometer such as our own. Our observations of low-temperature steam, however, have produced apparent emissivities of opaque steam clouds well in excess of unity (the blackbody limit). We had reported some related measurements with this same equipment earlier in the open literature (1,2). Impossible to explain by accepted theory, the observed non-thermal behavior appears to involve luminescence of a type related to that observed by other workers in boiling water experiments at short infrared wavelengths (3). This "phase-transition luminescence" should be almost ideally observed under conditions found in clouds of wet steam. We have been able to measure the apparent luminescence spectrum of wet steam near ambient temperatures under conditions of gradual cloud cooling in a windowless chamber. The spectrum obtained is comparable to that predicted by extrapolation of luminescence magnitudes from reference (3). Our data also tend to confirm those of reference (3) in the finding that the "luminescence spectrum" is not the same as either that for water vapor or for the bulk liquid, but contains spectral features which are "new".

Based upon our experimental data, we have tentatively modeled these infrared luminescence effects and related them to normal aerosol parameters already discussed. Our results give good agreement between luminescence effects predicted by the model and those actually obtained experimentally. A further discussion of luminescence is beyond the scope of this paper, but it is a subject of major and continuing interest to us. For example, numerous literature references to "atmospheric glow" in the 8-13  $\mu\text{m}$  infrared region could involve luminescence effects.

Aerosol spectroscopy is a new field confronted with placing in proper perspective a large body of existing popular "fact" which has its basis primarily in aerosol scattering behavior while it ignores aerosol absorption and emission contributions in the infrared. Effects such as aerosol absorption and probable luminescence must be understood before atmospheric modeling, particularly in and near the 8-13  $\mu\text{m}$  atmospheric "window" through which most of the earth's radiative transfer takes place, can be completed. Many unexplained atmospheric phenomena should become understandable through precise modeling. Many practical aerosol applications should evolve through understanding.

#### REFERENCES:

- (1) Carlon, Hugh R., Applied Optics 10, 2297 (1971)
- (2) Carlon, Hugh R., Applied Optics 9, 2000 (1970)
- (3) Potter, W.R., and J.G. Hoffman, Infrared Physics 8, 265 (1968)





OPTICAL MEASUREMENT OF MISSILE WING DEFORMATIONS  
IN HIGH VELOCITY TESTS

CHARLES R. CHRISTENSEN, J. LYNN SMITH,  
TERRY A. MARTIN, AND JUDSON R. GRIFFIN  
U.S. ARMY MISSILE RESEARCH AND ENGINEERING LABORATORY  
REDSTONE ARSENAL, ALABAMA

INTRODUCTION

Two techniques have been used to measure the behavior of missile components, such as wings or elevons, during high speed rocket sled tests. The missile has been photographed using sled-mounted motion picture cameras or streak cameras at stations along the track. This can produce a large amount of qualitative data on component performance but precise displacement measurements cannot be made from photographs. Strain gauges mounted on the component have been used and precise measurements of deformations can be calculated from the data. However, reduction of the data is tedious and it is not practical to cover a large area such as a wing surface with strain gauges. In order to avoid the deficiencies in these techniques, optical methods capable of measuring displacements over a large area were investigated and applied to the problem of Hawk missile wing deformation during sled tests.

A stereophotographic technique using streak camera photographs made simultaneously from two different angles was considered. Surface contour lines could be mapped using conventional stereoscopic plotting instruments and no major change in the sled track instrumentation would be required. However, a higher precision was desired than could be provided by stereoscopic methods. Moiré topographic methods using optical interference patterns (1) or projected grids (2, 3) can show contour lines directly on the surface but would require a large amount of instrumentation development for measurements during sled tests.

Two optical methods were developed which can measure wing

deformations using the sled track streak cameras and would minimize preparation of the test missile. One method developed involves viewing the reflection of a grid pattern on the surface of a mirror polished test wing. This is similar to that used in previous wind tunnel tests (4) in which the grid was painted on the tunnel wall. For the sled tests the polished test wing reflects a grid pattern painted on one of the missile wings perpendicular to it. The test wing and grid are both moving at the same velocity, therefore the reflection of the grid on the test wing and the test wing itself can be photographed with the sled range streak cameras. The position of the grid reflection on the test wing is used to calculate the tangents to its surface and the spatial deformation or wing profile is found by curve fitting from a point of zero deformation. This technique was used in Hawk missile tests conducted at Holloman Air Force Base, New Mexico and test wing profiles were calculated from streak camera photographs taken at velocities of Mach 1.9 and Mach 2.1.

A Moiré' analysis technique was also developed which requires ruling the wing with a grid pattern and photographing the ruled wing at two different angles both before and after deformation. Phototransparencies for the deformed and undeformed states are superimposed for each angle to form two sets of Moiré' fringes. The wing displacement can be calculated from the distance between rulings on the wing, the angles at which the wing is photographed and the number of Moiré' fringes up to the point of interest at each angle. This method has the advantage of relatively simple data reduction but places more severe requirements on range camera resolution than the mirror wing technique if high accuracy is required. A laboratory demonstration was conducted to demonstrate its feasibility.

#### MIRROR WING TECHNIQUE

##### Optical Considerations

The following analysis (5) for the camera, test wing, and reference grid configuration used in the sled tests is similar to that for the wind tunnel tests (4). The geometric relationships are shown in Fig. 1. For the cross section of interest through the test wing chose a coordinate system with the origin on the missile axis of symmetry. The y-axis is chosen to pass through the center of the undeformed test wing and be perpendicular to the missile axis. The x-axis passes through the center of the wing on which the reference grid is painted. The camera aperture is located at  $y_c, x_c$ . A point at  $x_j, y_j$  on the reference grid is reflected on the test wing at  $x_p, y_p$  and imaged on the film plane. The line connecting  $x_p, y_p$  and  $x_c, y_c$

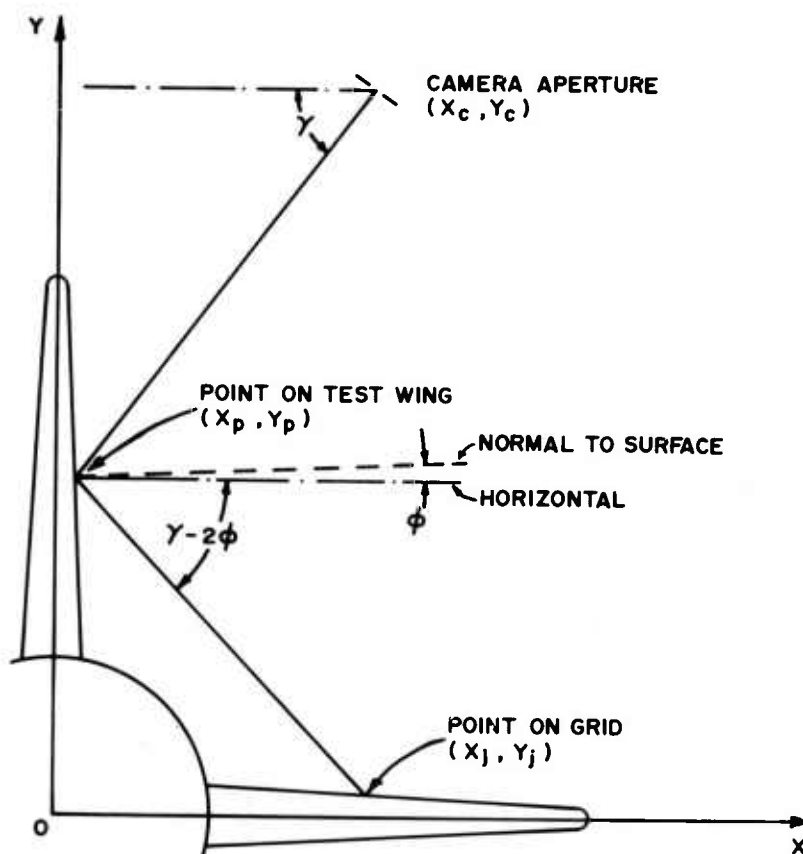


FIG. 1 Mirror wing test geometry.

$y_c$  makes an angle  $\gamma$  with respect to the x-axis. The tangent to the test surface at  $x_p, y_p$  makes an angle  $\phi$  with respect to the y-axis. From Fig. 1

$$\tan \gamma = \frac{y_c - y_p}{x_c - x_p} \quad (1)$$

$$\tan (\gamma - 2 \phi) = \frac{y_p - y_j}{x_j - x_p} \quad (2)$$

and

$$\tan 2\phi = \frac{\tan \gamma - \tan (\gamma - 2\phi)}{1 + \tan \gamma \tan (\gamma - 2\phi)} \quad (3)$$

$$= \frac{(y_c - y_p) x_j (1 - x_p/x_j) - (y_p - y_j) x_c (1 - x_p/x_c)}{x_c (1 - x_p/x_c) x_j (1 - x_p/x_j) + (y_c - y_p) (y_p - y_j)} \quad (4)$$

for test grid points on the horizontal wing  $x_p \ll x_j$  and  $y_j \ll y_p$ . For  $\gamma \approx 30^\circ$ ,  $x_p \ll x_c$ . Under these conditions

$$\tan 2\phi \approx \frac{(y_c - y_p) x_j - y_p x_c}{x_c x_j + (y_c - y_p) y_p} \quad (5)$$

Note that Eq. (5) is independent of  $x_p$  and  $y_j$ . The calculated tangent to the test wing depends therefore on the camera coordinates and the distance of the grid point and the test wing point from the missile center line. The camera coordinates can be accurately located with respect to the sled rails and any sled lateral or vertical motion can be applied as a correction. Deviations from the static values of  $y_p$  and  $x_j$  will be small for any deformations the structures can survive, therefore these values can be used in calculations. Under conditions such that deviations of  $y_j$  from the static values become important, streak camera photographs of the reference grid wing can be used to obtain better values of  $y_j$ .

To measure deformations near the wing root cord a reference grid must also be painted on the missile body. For these points  $x_p \approx x_j$  and  $y_p \approx y_j$ , therefore Eq. (4) must be used in data analysis. Missile body deformations during the tests are small and static values of  $x_j$  and  $y_j$  may be used. An iterative process can be used to calculate test wing deformations. In this case, a static value of  $x_p$  is used in Eq. (4) as a first approximation. Calculated values of  $x_p$  obtained from  $\phi$  are used in subsequent iterations until the  $x_p$  values converge.

In reduction of the data the tangents to the mirror wing surface are obtained at values of  $y_p$  for the section of interest through the test wing. The locations,  $y_p$ , on the test wing are measured from known locations such as the wing root cord, rivets, or identifying marks placed on the wing. The points on the reference grid are identified by color coding or geometrically coding the reference grid. The positions of these reference points on the missile body or wing are determined by calculation or measurement. Accurate measurements can usually be made from large (16" x 20") prints of the streak camera photographs. In this paper a line was drawn on photo-

GRIFFIN

graphs of the test wing surface parallel to the  $y$ -axis and the values of  $y$  chosen where this line intersected the reflected reference grid lines<sup>P</sup>.

The test wing contour is obtained by curve fitting using the set of coordinates,  $y$ , and the slopes,  $\phi$ , at these points. The accuracy of the absolute values of  $x$  is determined by the accuracy of the reference point from which the curve is fitted. The reference point should be a part of the wing rigidly fastened to the missile body or another point of minimum deflection. The principal structural members of the Hawk missile wing are shown in Fig. 2. The wing is

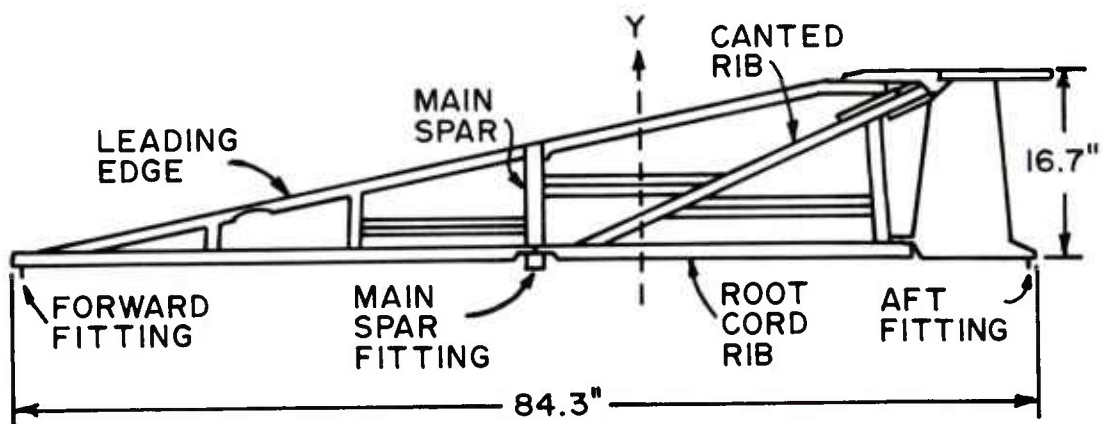


FIG. 2 Hawk wing structure.

rigidly bolted to the missile body at the main spar fitting. The aft and forward fittings hold the wing in alignment perpendicular to the missile body but do not restrict motion away from the body. The best reference point would be near the main spar fitting but the forward or aft fittings also provide points of minimum deflection. Deformation is also expected to be small on the main spar, along the root cord, and on the casting above the aft fitting.

#### High Velocity Test Conditions

Laboratory experiments using deformable model wings demonstrated the feasibility of the mirror wing technique. Only one sled test run was available, therefore a coarse reference grid spacing and broad line width were chosen to ensure that useable data would be obtained to demonstrate the technique. Streak camera photographs taken during previous tests indicated that 0.25 inch resolution could be easily obtained. A grid of 0.25 in. wide lines on 2.25 in. centers



CHRISTENSEN, SMITH, MARTIN and  
GRIFFIN

was painted on one horizontal wing and on the missile body between the horizontal wing and the vertical mirror polished test wing. The reference grid was color coded with a combination of single lines and pairs of lines. Black, red, and green were chosen for color coding. Selected rivets on the test wing were painted blue or yellow to facilitate identification of points on the wing. Greater precision can be obtained in future tests using a less coarse grid spacing. Figure 3 is a static photograph of the missile taken before the test run.

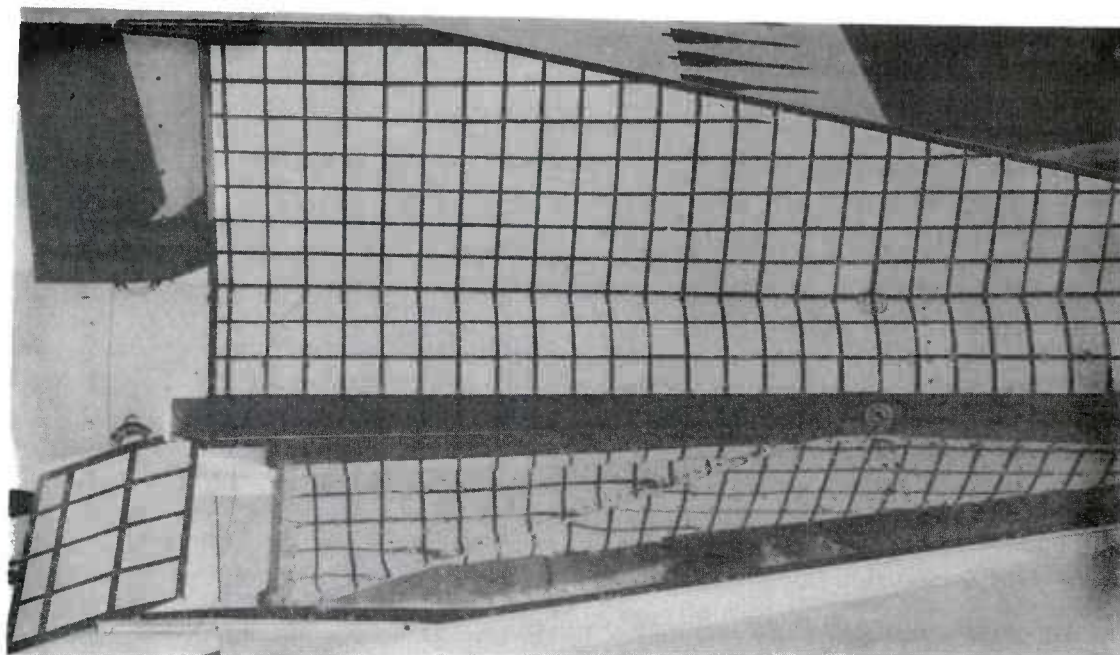


FIG. 3 Mirror wing and missile on sled before test.

The missile was mounted on the test sled with its centerline horizontal and at an angle of  $10^{\circ}$  to the track centerline. The purpose of this series of tests was to measure the test wing deformations at this angle of attack. The two horizontal wings are reenforced and travel parallel to the track, therefore deformation of these wings is small. The function of these wings is to deflect reflected shock waves and ensure that the air flow over the test wing is similar to that under flight conditions.

Streak cameras were placed on three bridges over the test track. One bridge was located at the point of maximum sled velocity, Mach 2.1. The other bridges were located where velocity would be Mach 1.9, one at the point of increasing velocity and the other at the point of decreasing velocity. Camera angles were chosen to show two views of the reflected grid at each bridge. A view in the plane of

CHRISTENSEN, SMITH, MARTIN and  
GRIFFIN

the test wing was also shown to allow a direct measurement of the deformation of the leading edge. The cameras used 70 mm color film and 80 mm, f/5.6 lenses.

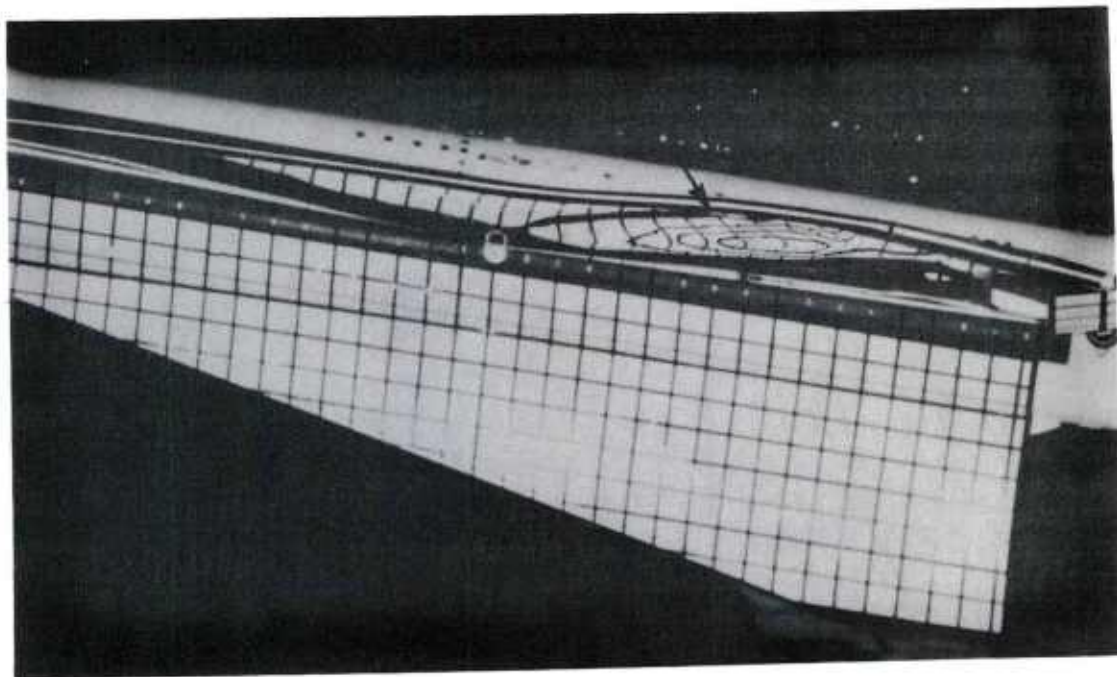


FIG. 4. Missile at Mach 1.9, decreasing velocity, photographed with streak camera mounted above track centerline.

### Results

Figure 4, taken at Mach 1.9 when the velocity was decreasing, demonstrates the amount of qualitative information that can be obtained from this technique. This view was taken with a camera located directly above the track centerline. The missile centerline crosses the track centerline near the trailing edge of the test wing, approximately at the point in Fig. 2 where the arrow points to the canted rib. Deformations in the wing are indicated by the curvature or changes in angle of the reflected grid lines. Three of the lines parallel to the missile centerline on the horizontal wing are reflected twice in this region between the canted rib and the leading edge of the test wing (arrow). One is the red line (numbered 1) nearest the missile body. The other lines are the two black lines (numbered 2 and 3) between this red line and the body. This area must therefore be concave.



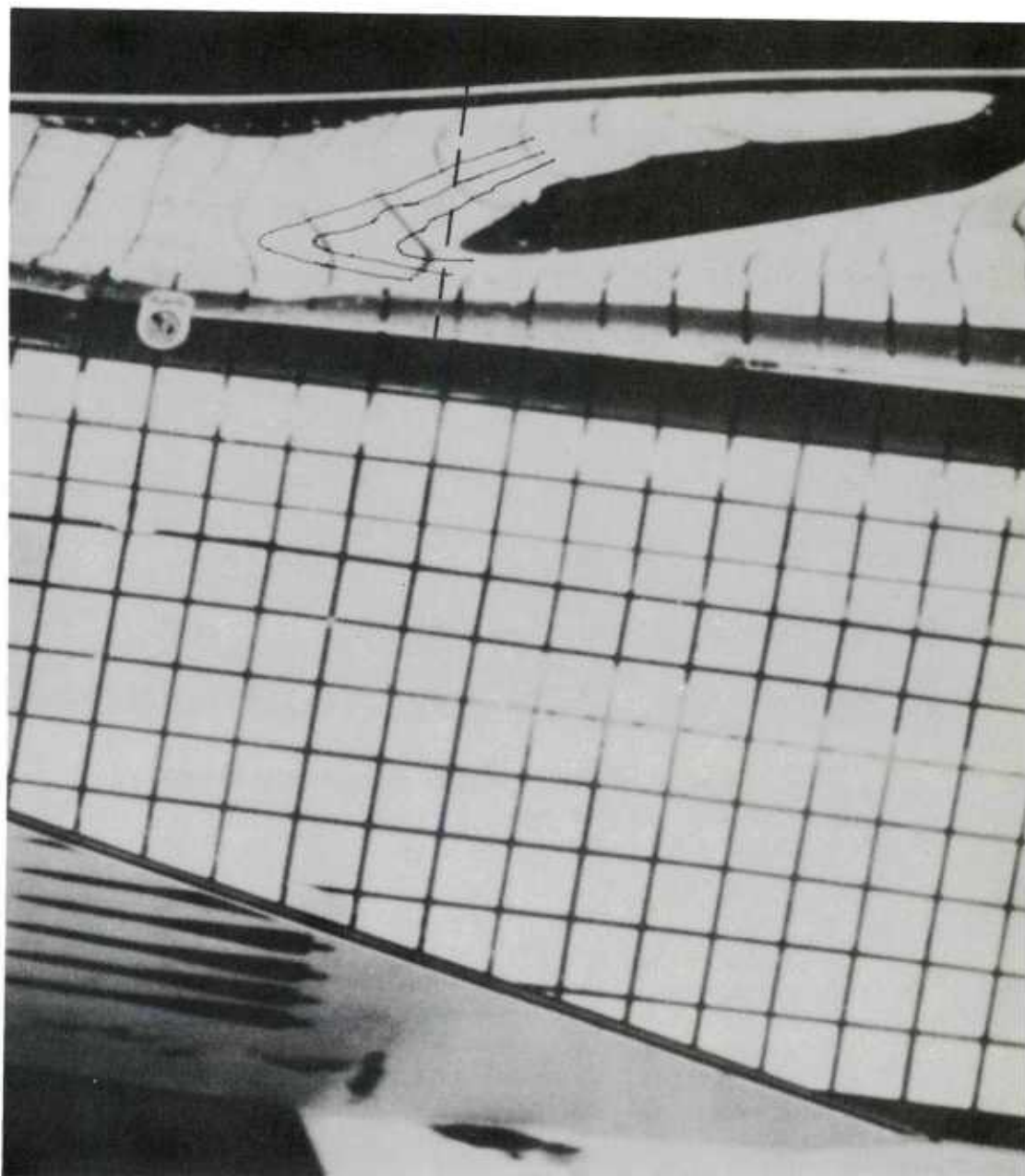


FIG. 5. Missile at Mach 1.9, decreasing velocity,  
photographed with streak camera axis at  $30^{\circ}$  to ver-  
tical.

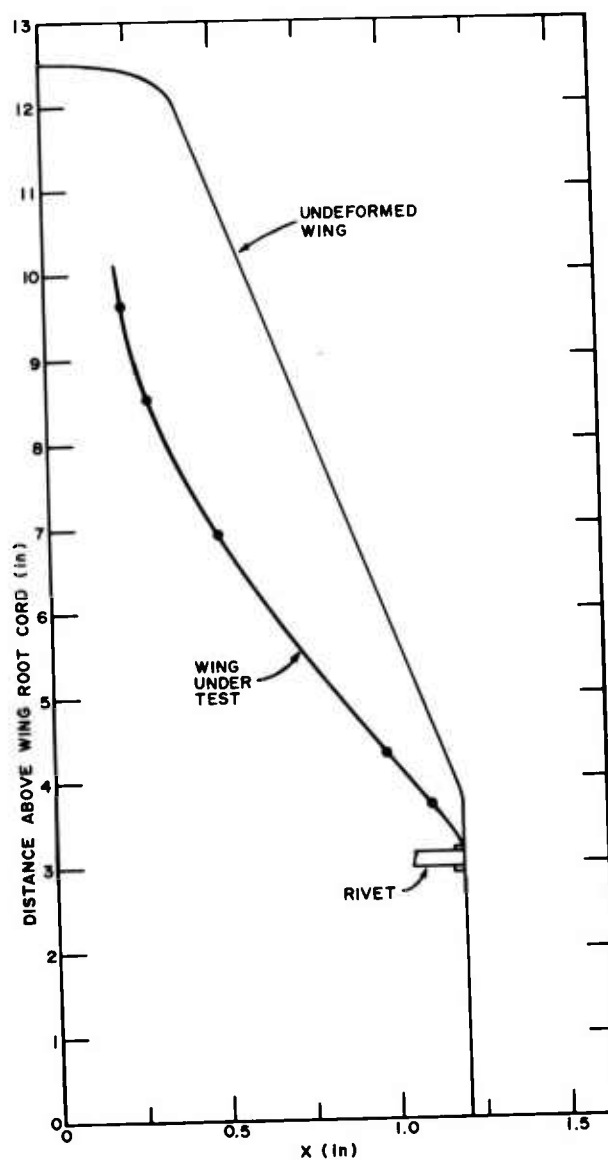


FIG. 6 Test wing profile 19.3 in. aft of main spar fitting. Note expanded scale on x-axis.

The photograph in Fig. 5 was also taken at Mach 1.9, decreasing velocity, but the camera axis made an angle of  $30^\circ$  to the vertical direction. A profile of the wing surface deformation was calculated along a line indicated by the dashed line 19.3 in. aft of the main spar fitting. The location of this profile is also indicated by the dashed line labeled "y" in Fig. 2. The calculated profile is shown in Fig. 6 with the profile for the undeformed wing. The x-axis in Fig. 6 is expanded by a factor of four to show the deformation more clearly. The tangents to the surface were calculated using Eq. (4) with  $x_c = 60.5$  in. and  $y_c = 110$  in. The rivet shown was used as a reference point. Due to the coarse grid spacing used no lines were reflected below the rivet shown in Fig. 6, therefore no values of  $\phi$  could be calculated below this point. This rivet is located on the canted rib near the wing root cord and deformation is expected to be minimal at this point. The concavity indicated in Fig. 4 is shown in the calculated contour. No other data, such as strain gauge measurements reduced to deflections, on similar test wings is available for comparison with the calculated profile.

An indication of the accuracy of this technique can be obtained by a simple calculation. A conservative value of 0.25 in. for the streak camera resolution would lead to an uncertainty of  $0.225^\circ$  in  $\phi$  for the center point of the contour in Fig. 6. If displacement were due to a linear deformation from the wing root cord this would correspond to an uncertainty of 0.028 in. in  $x$  for this point on the contour. Error is also introduced by the uncertainty in the location of the reference point and by extrapolation from this reference point.

#### MOIRE' PATTERN TECHNIQUE

A Moire' pattern technique was devised and tested in the laboratory for possible application to wing deformation analysis. The technique requires ruling a surface with lines, photographing it at some angle in both deformed and undeformed states, and superimposing the resulting photographic transparencies to form a Moire' fringe transparency. The process is repeated for a different viewing angle, and the difference in the number of fringes up to a certain point on each of the Moire' transparencies is proportional to the displacement of the deformed surface.

Fig. (7) shows the geometry appropriate to this analysis. It is assumed that the rulings are normal to the plane of the page. The appendix lists assumptions and derives the expression for the displacement due to deformation:

$$D = \frac{d (N' - N)}{\tan \theta' - \tan \theta} \quad (5)$$

Where  $N$  is the number of fringes from the structure base up to the point of interest,  $\theta$  is the angle between the structure surface normal and the projection plane normal,  $d$  is the distance between rulings, and the primed and unprimed values correspond to the two viewing angles.

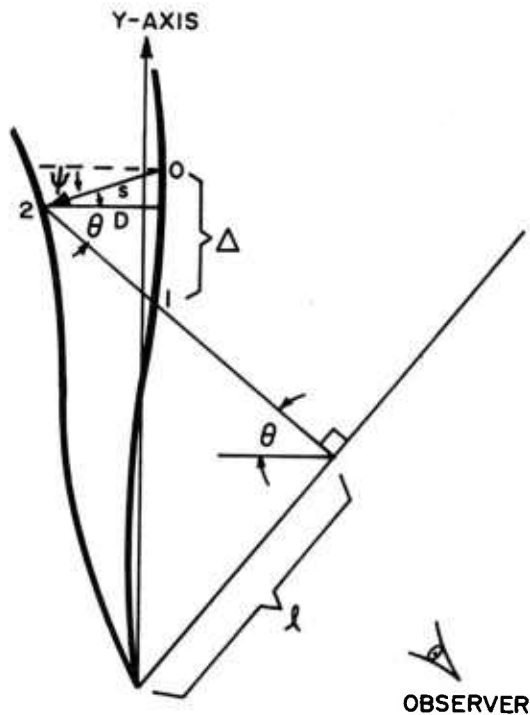


FIG. 7 Geometry for wing deformation. Point 0 moves to point 2 through the distance  $\underline{s}$ . D is taken as the desired displacement.

Fig. 8 shows a Moiré' fringe transparency formed from photographic transparencies of a ruled card in undeformed and deformed states. The fixed edge of the card is at the bottom of the photograph. The analysis indicated a sensitivity of at least 1 mm dis-

displacement in 5 cm for a ruling spacing of 0.85 mm. This corres-

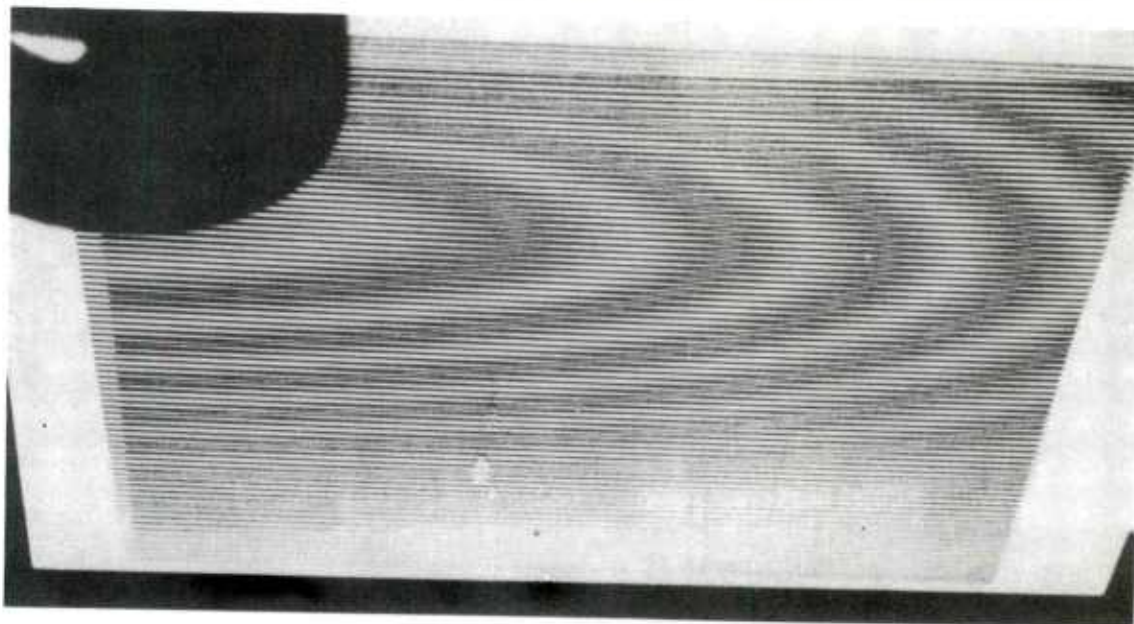


FIG. 8 Moiré fringes formed by superimposing transparencies of a ruled card in deformed and undeformed states. The angle of observation  $\theta$  is  $53^\circ$ . The lower edge of the card is fixed.

ponds to a sensitivity of 0.24 inches over one foot on a wing with approximately 0.2 inches between rulings. The sensitivity could be improved by increasing the number of rulings, but then the streak camera resolution presents a problem in showing such fine lines. The Moiré pattern technique investigated here was not employed in the actual wing deformation sled tests due to the expense of ruling fine lines on the wing and the camera resolution limitations.

#### CONCLUSIONS

In both techniques for deformation measurement the accuracy is limited by the range camera resolution and by the accuracy with which reference points can be located. The cameras used in the sled tests used a relatively short focal length lens selected to obtain photographic coverage of the entire missile. Better resolution could be obtained by using a longer focal length to cover only the test wing or a particular area of interest on the test wing. This should allow the calculation of wing deformation profiles to an accuracy of approximately 0.010 in. using the mirror wing technique. An accuracy of 0.1 in. should be obtainable using the Moiré technique.

CHRISTENSEN, SMITH, MARTIN and

GRIFFIN

We would like to acknowledge helpful technical discussions with Prof. J. G. Castle, Jr. and the able assistance of Mrs. B. R. Williams in laboratory experiments.

#### APPENDIX: DERIVATION OF EQUATION (5)

##### Assumptions:

1. The observation is virtually without perspective, i.e. the observer is far from the wing compared to its dimensions.
2. The wing can deform and wrinkle, but its skin does not stretch.
3. The angle of curvature from the vertical of the undeformed wing is small.
4. The wing displacement at its base is negligible.

The photographic transparency is essentially an isometric projection of the wing structure onto a plane normal to the direction of observation. Let this plane be called the projection plane and coincide with the wing base at the origin. We wish to solve the problem of the number of Moire' fringes  $N$  seen between the wing base and some arbitrary point whenever two transparencies are superimposed, one a photograph of an undeformed, ruled wing and one for a deformed, ruled wing. The ruled lines (or grid) run into the page (see Fig. 7) along the length of the wing.

Let point 0 be displaced to point 2 and  $s$  represent distance  $\overline{02}$ . The observation angle with respect to the wing-plane normal is  $\theta$ .  $D$  is the displacement normal to the  $y$ -axis between the deformed and undeformed surface near the point 0 and is approximately equal to  $s$ .

The number of fringes seen over the distance  $\ell$  in the projection plane is

$$N(y_1) = \frac{S_2}{d} - \frac{S_1}{d} \quad (A1)$$

Where  $S_1$  is the surface distance on the undeformed wing from the base to point 1,  $S_2$  is the distance from the base to point 2 on the deformed wing, and  $d$  is the distance between grid lines. Eq. (A1) is valid for an arbitrary deformation only if  $N$  represents the net fringe number. On photographic Moire' patterns, a certain increment  $\Delta N$  (of  $N$ )



may need an assignment as positive or negative. Eq. (A1) will hold for  $N$  representing the total number of fringes observed if the displacement  $D$  increases monotonically in a given direction.

Note

$$S_1 = S_2 - \Delta \approx S_2 + D (\tan \psi + \tan \theta) \quad (A2)$$

Where the last step in Eq. (A2) employed assumption 3. We define the sign of  $D$  as negative for displacement away from the observer and positive for the opposite direction. The angle  $\psi$  is negative for counterclockwise displacements of  $s$  from the horizontal and positive otherwise. Eq. (A1) becomes

$$N(y_1) = \frac{D}{d} (\tan \psi + \tan \theta) \quad (A3)$$

Hence, by counting fringes, we could determine  $D$  were it not for the term  $\tan(\psi)$  which depends on the fact that a non-stretchable surface cannot simply displace normally in one area if another is anchored.

We may however, view the superposition of deformed and undeformed surfaces from another angle  $\theta'$ . In doing this, we gain new information to use with Eq. (A3) and eliminate  $\tan \psi$ .

$$N' - N = - \frac{D}{d} = (\tan \theta' - \tan \theta).$$

Thus the displacement between undeformed and deformed surfaces is given by

$$D = - \frac{d (N' - N)}{\tan \theta' - \tan \theta} \quad (A4)$$

Recall that  $\Delta N$  may be positive or negative depending on whether the increment of displacement from a certain point is positive or negative. Without skill in interpreting Moiré patterns errors will result. It may well be that certain cases would require additional photographic data for correct interpretation.

#### REFERENCES

1. R. E. Brooks and L. O. Heflinger, "Moiré Gauging Using Optical Interference Patterns". Appl. Opt., 8, 935 (May 1969).
2. J. Wasowski, "Moiré Topographic Maps". Optics Comm., 2, 321 (Dec 1970).
3. Chun Chiang, "Moiré Topography", Appl. Opt., 14, 177 (Jan 1975). also see references contained in this paper.



CHRISTENSEN, SMITH, MARTIN and

GRIFFIN

4. J. G. Castle, Jr. "Automated Analysis of Hawk Wing Responses During Langley Tunnel Test Run 71-20-A. Demonstration of Feasibility", US Army Missile Command, Technical Report RL-75-7, Redstone Arsenal, 4 September, 1974.
5. J. G. Castle, Jr., Private Communication.



## PLASTIC PIEZOIDS FOR FUZE APPLICATIONS

EUGENE L. CHURCH, HOWARD A. JENKINSON and  
ROBERT J. ESPOSITO\*  
PITMAN-DUNN LABORATORY  
FRANKFORD ARSENAL, PHILADELPHIA, PENNSYLVANIA 19137

### INTRODUCTION

Piezoelectric materials generate charge when subject to stress. Their piezoelectric activity is usually characterized by a charge coefficient, which is defined as the charge released per unit force. These materials can be utilized as initiators, impact sensors, and setback generators. The standard piezoelectric material used in fuze systems is the ceramic PZT, which is a mixture of lead zirconate and lead titanate.

In the early 1940s piezoelectricity was demonstrated in polymers but their electrical moduli were generally small and not useful for engineering purposes. Recently, various scientists have shown that certain polymer films, particularly polyvinylidene fluoride, better known as  $PVF_2$ , can exhibit a high degree of piezoelectric activity (1,2).  $PVF_2$  films can be made into sheets as thin as 0.25 mil thickness, and these films can be made piezoelectric by heating and poling them in an electric field. The piezoelectric activity of a  $PVF_2$  film can be as high as 0.2 microcoulombs per ton, which is 0.1 that of PZT. In the unpoled form,  $PVF_2$  is quite similar to plastic sandwich wrap in its physical and chemical properties.

Plastic piezoids have a number of advantages over ceramic fuze elements - they are cheap, lightweight, and flexible, and can be easily fabricated into various shapes. Poled  $PVF_2$  is now commercially available, primarily from Japan, and begins to depole above 100°C. In addition, poled  $PVF_2$  is also a pyroelectric (3), that is, a change in temperature generates electrical charge; and it can be used as an

CHURCH, JENKINSON and

ESPOSITO

infrared detector without requiring cryogenics.

The purpose of this report is to present preliminary results on the piezoelectric activity of PVF<sub>2</sub> devices in both quasi-static and reverse ballistic environments in order to assess their device potential for fuzing circuits. Other military applications will also be discussed.

#### PVF<sub>2</sub> FUZE CONCEPT

One example of a PVF<sub>2</sub> fuze application is shown in Fig. 1 for a dual purpose automatic cannon caliber round (4). The PVF<sub>2</sub> lines the ogive and may have a thin inertial support to produce greater output. In this configuration the output of the piezoid is connected to the detonator located in the base of the projectile. Impact forces on the PVF<sub>2</sub> liner generate electrical charge which sets off the detonator which, in turn, activates the explosive chain for the shaped charge. Two particular advantages of the PVF<sub>2</sub> ogival liner in this fuze concept are that it serves as a graze sensitive initiator for antipersonnel purposes and offers minimum obstruction to the formation of the shaped charge jet for armor penetration. Previous schemes for fabricating ceramic piezoelectric liners within the ogive of a projectile have proven impractical from handling, safety, and reliability criteria.

#### PVF<sub>2</sub> STACKS

One vital question, that arose concerning concept feasibility, was whether PVF<sub>2</sub> could be made sufficiently active to operate this system. From a straightforward estimate of the piezoactivity required in terms of the impact force, the impact time, and the detonator characteristics, the polymer material should have an effective charge coefficient comparable with PZT in order to fire a simple bridge wire detonator. However, the resultant activity of a PVF<sub>2</sub> device can be increased by connecting a number of individually poled layers. Fig. 2 illustrates a polymer stack with the poled PVF<sub>2</sub> sheets bonded in series mechanically, and with their electrical outputs connected in parallel. The stack is comprised of an even number of layers in order that the two outer surfaces are kept at a common ground potential, thus avoiding the need for external insulation and shielding. It should be emphasized that in the fuzing concept given in Fig. 1, the piezopolymer does double duty as both an impact sensor and a power source for the detonator. In other configurations these two functions can be separated, with the PVF<sub>2</sub> acting only as an impact detector. The impact sensing function can be easily performed by a single poled sheet, thus alleviating the energy requirements which necessitate the

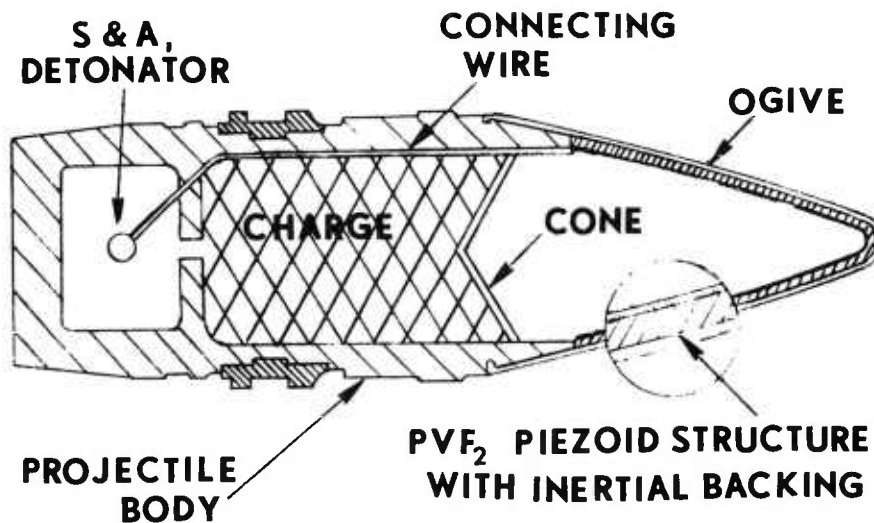


Fig. 1. PVF<sub>2</sub> Fuze Concept for Dual Purpose Automatic Cannon Munition with Improved Graze Sensitivity and Minimum Obstruction to Shaped Charge Cone

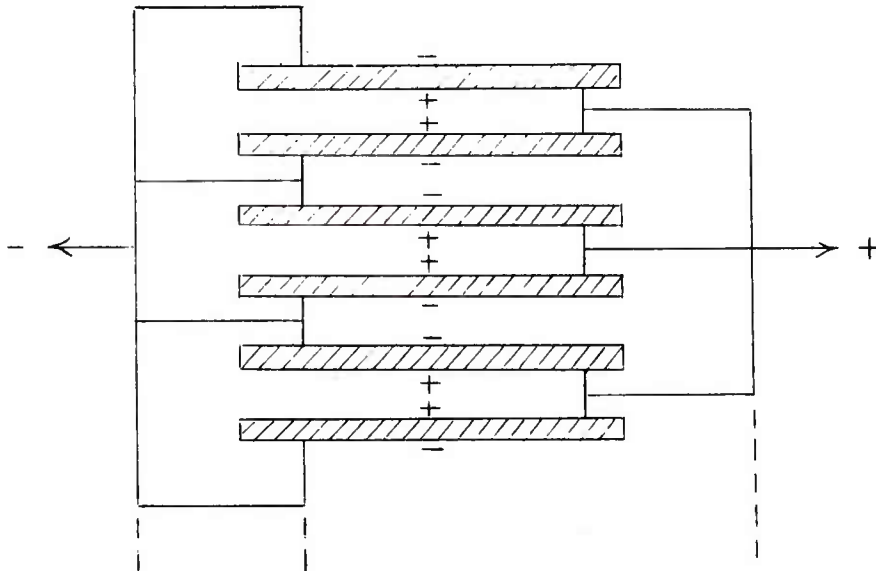


Fig. 2. Schematic Diagram of PVF<sub>2</sub> Stack Configuration

CHURCH, JENKINSON and

#### ESPOSITO

stack configuration. For example, a PVF<sub>2</sub> impact trigger could be placed on the shoulder of the tank-fired M456 HEAT round, immediately behind the stinger nose, or in the howitzer-fired XM622 HEAT round.

Mr. S. Edelman and Dr. P. Bloomfield at the National Bureau of Standards (NBS, Gaithersburg, MD) have fabricated flat PVF<sub>2</sub> stacks for us under contract (5), with the specifications of 2 to 4 microcoulombs per ton total activity and an active area of 30 cm<sup>2</sup> (approximately the ogival area of a 30mm projectile). These stacks consist of 20 to 50 layers of 1 mil material, are approximately 2½ inches in diameter and 25 to 60 mils in thickness, and have the flexibility of a plastic milk bottle.

#### STATIC AND DROP TESTS

Upon receipt of these stacks, we determined their piezoelectric activities by measuring the charge produced by a known force. The force was applied by a Carver hydraulic laboratory press, and the charge output was measured by a coulometer circuit. Typical results for the charge output versus the applied force for stacks #7 and 8 are shown in Fig. 3. The charge output is approximately linear over the range of 0 to 10 tons force; these forces did not damage or depole the samples. The piezoelectric charge coefficients,  $d$ , are the slopes of these lines with the values 4.49 and 3.43 microcoulombs per ton for stacks #7 and 8, respectively. Stack #7 is comprised of 30 sheets (total stack thickness 35 mils), and stack #8 has 24 sheets (total stack thickness 27 mils). A representative activity for PZT discs with 50 mils thickness was measured to be 1.94 microcoulombs per ton.

Further non-destructive tests were then made in a drop test machine at NBS in order to test the stack response in the submillisecond time scale (5). The electrical output from stack #7 was measured across various loads during the impact sequence by a known weight. A calibrated accelerometer was mounted onto the upper surface of the impactor and indicated a maximum force of approximately 2.5 tons during the impact. The measured piezoelectric outputs showed no unexpected or unusual behavior. Figure 4 shows a representative signal generated by the impacted stack (2.5 tons impact) across a 4 ohm resistor, which is characteristic of a bridgewire detonator for automatic cannon caliber ammunition.

#### DESIGN OF REVERSE BALLISTIC EXPERIMENTS

The time and pressure scales involved in the hydraulic press and impact experiments are significantly different from those

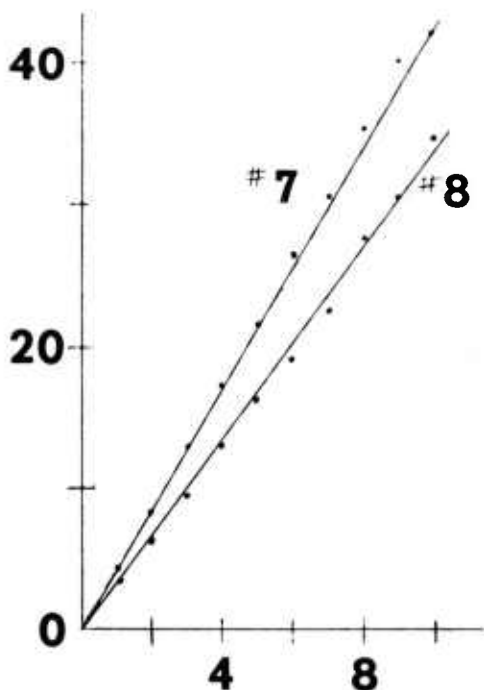


Fig. 3. Charge Output in Microcoulombs Versus Applied Force in Tons for PVF<sub>2</sub> Stacks #7 and 8

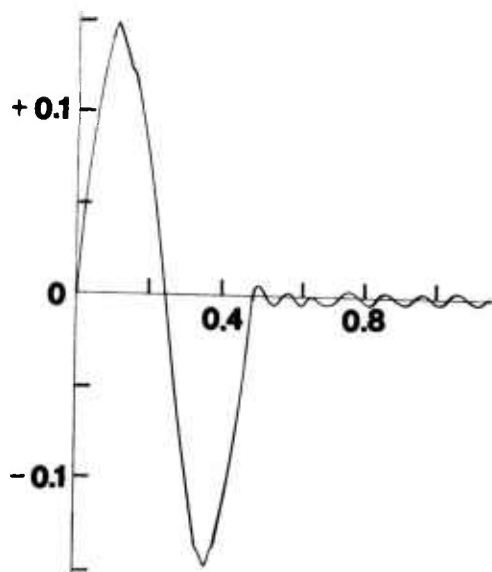


Fig. 4. Volts Generated Across 4 Ohm Load Versus Time in Milliseconds for Drop Test on PVF<sub>2</sub> Stack #7

expected in the ballistic environment. One cannot simply extrapolate the non-destructive test data into the ballistic regime; the static and impact tests are necessary stepping stones to, but not substitutes for, ballistic tests. Some of the characteristic features of the ballistic impact situation which could alter the piezoelectric output include the following: Impact times are the order of a microsecond, which are comparable with shock wave periods through the target structures. Forces are of the order of 50 to 100 tons, and pressures are of the order of  $10^5$  pounds per square inch, which are comparable with and exceed the strength of the material. In this force-time regime the material may behave nonlinearly and is then not describable in terms of a simple linear force-charge relationship. High kinetic energies can lead to local heating of the piezoid. The large stresses and large voltages across the piezoid can induce depolarization. The target stack is subject to severe flexing, stretching, and ultimate tearing. These effects could work singly, or combine



ESPOSITO

synergistically, to produce a net charge output which could be significantly different from the effects estimated from the non-destructive measurements.

We have performed a series of reverse ballistic tests on various polymer stacks in order to test their response under extreme dynamic conditions. Figure 5 is a sketch of the firing geometry. Flat-nosed WECOM-30 projectiles were fired against individual stacks sandwiched between sheets of 0.25 inch mild steel in order to capture a portion of their ballistic response before destruction, and to simulate the crushing of the stack behind the ogival windscreen. The stack output was connected to a 4 ohm resistor to simulate a bridge-wire detonator, and the transient voltage across this load resistor was displayed on calibrated oscilloscopes and recorded photographically. Similar tests were done beforehand on a dummy aluminum disc (to check operation of the electronic circuits and for possible spurious signals/noise) and on PZT discs for comparison of outputs.

The projectile velocity was approximately 2050 ft/sec, chosen to provide an extreme ballistic impact situation within the field velocity of a representative 30mm projectile, and was measured for each firing by standard time of flight techniques. At this velocity the projectile completely penetrated the target assembly in a few tens of microseconds.

Figure 6 illustrates a target assembly before firing. The PVF<sub>2</sub> stack is mounted behind the steel strap, and another stands unmounted in the lower right. Figure 7 is a corresponding photograph taken after firing. A hole about 1½ inch in diameter has been blown through the steel plates and the PVF<sub>2</sub> target. An unfired projectile is shown in the lower right, and a collection of typical penetration fragments is shown in the lower left.

## RESULTS AND DISCUSSION

Figures 8 and 9 show representative voltage outputs measured across the 4 ohm load for the PZT and PVF<sub>2</sub> (stack #7) samples, respectively, during the ballistic tests. (Note the difference in time scales.) Each sample has been connected in the circuit to give a positive signal when in compression. The initial voltage pulses are the same order of magnitude for both families of materials, as is expected. After the initial peaks, both sets of signals eventually become negative and exhibit oscillatory behavior. The PVF<sub>2</sub> trace is remarkably smooth and extends out to almost 50 microseconds. The PZT trace is sharp and spiky with a fine structure (not illustrated) with a period of the order of a microsecond, and its signal terminates

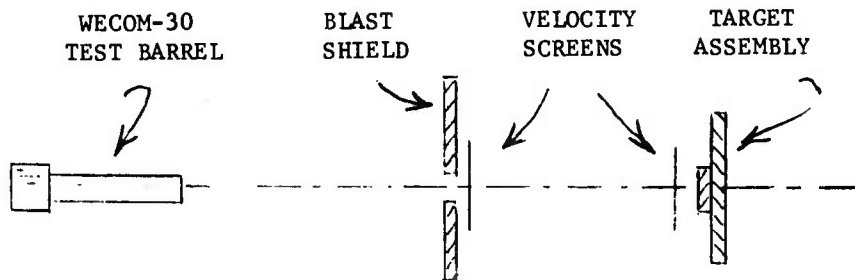


Fig. 5. Sketch of Firing Geometry (Not to Scale)  
Utilized in Reverse Ballistic Tests

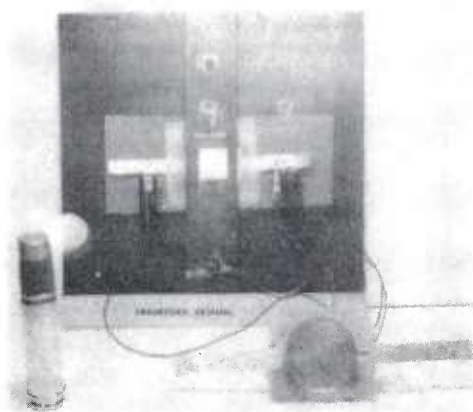


Fig. 6. Target Assembly Containing PVF<sub>2</sub> Stack with Flat-Nosed WECOM-30 Practice Round and Unmounted PVF<sub>2</sub> Stack in Foreground

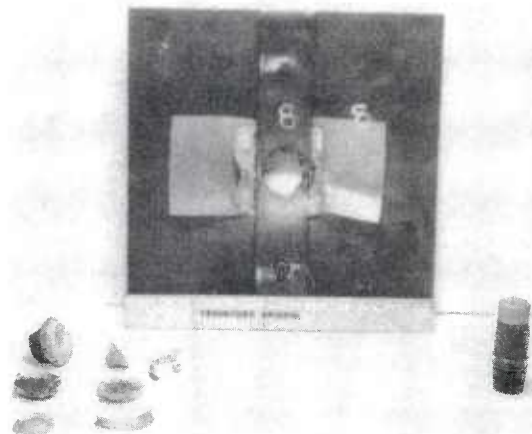


Fig. 7. Target Assembly Containing Remains of PVF<sub>2</sub> Stack After Firing with Penetration Fragments and WECOM-30 Practice Projectile in Foreground

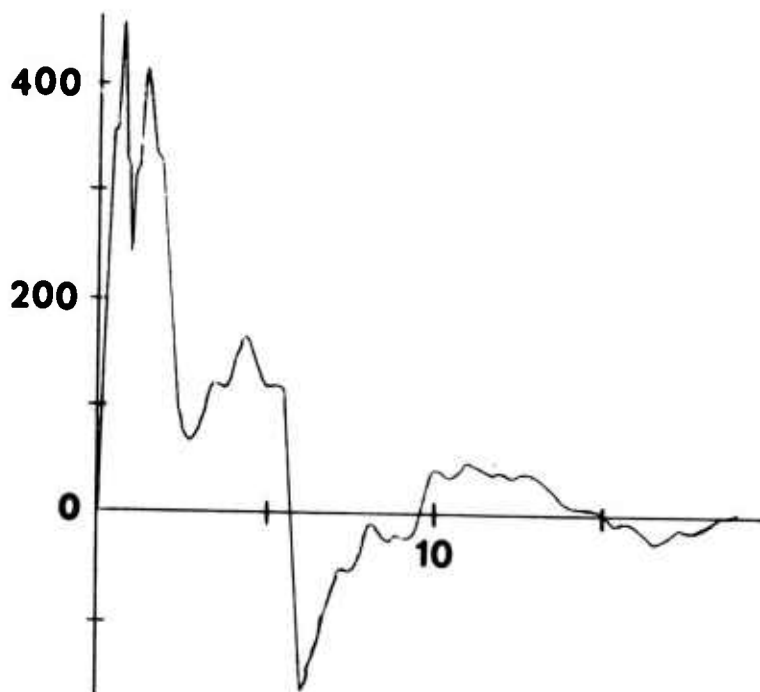


Fig. 8. Volts Generated Across 4 Ohm Load Versus Time in Microseconds for 30MM Reverse Ballistic Test on PZT Sample

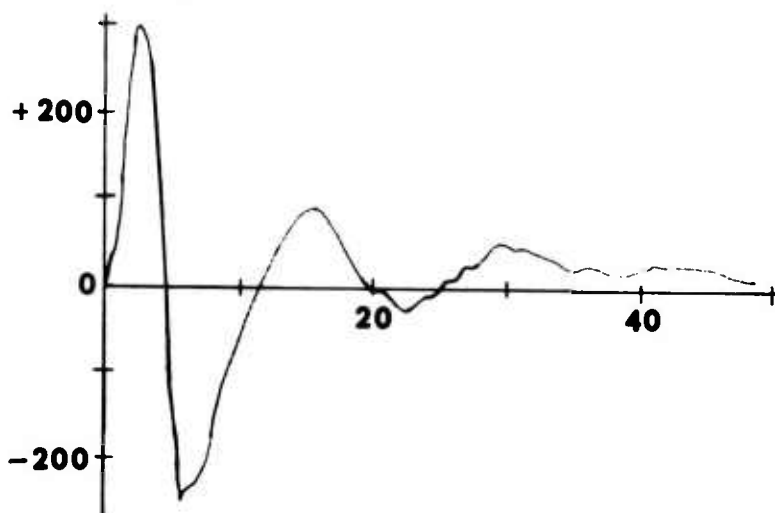


Fig. 9. Volts Generated Across 4 Ohm Load Versus Time in Microseconds for 30MM Reverse Ballistic Test on PVF<sub>2</sub> Stack #7

## ESPOSITO

within 20 microseconds. The time interval of 20 to 50 microseconds corresponds to approximately 0.5 to 1.25 inches of projectile travel, respectively (assuming that the projectile lost little kinetic energy in penetrating the target assembly). We attribute these striking differences in trace lengths and shapes to the very different physical properties of the two materials. PZT is a brittle ceramic which pulverizes shortly after impact, while PVF<sub>2</sub> is a tough flexible plastic which yields rather than shattering.

The energy  $W$  delivered to the load resistance  $R$  in the time  $t$  may be computed immediately from the voltage-time,  $V(t)$ , curves given in Fig. 8 and 9 by

$$W(t) = \frac{1}{R} \int_0^t dt' [V(t')]^2. \quad (1)$$

The resultant energy-time curves for the PZT and PVF<sub>2</sub> samples are given in Fig. 10. Both specimens delivered over  $10^5$  ergs within the first three microseconds after impact. The magnitudes of the output voltage and energy are consistent with order of magnitude design considerations. These tests were purposely designed to test the material properties and to produce much larger forces than might be experienced in the ogive of a projectile. However, our results indicate that a plastic piezoid lining the ogive would deliver, upon a variety of ballistic impacts, more than sufficient energy (250 to 1000 ergs) to fire a 4 ohm bridgewire detonator.

We have utilized the simplified equivalent circuit given in Fig. 11 to determine the charge,  $Q(t)$ , released during the reverse ballistic tests.

$$Q(t) = \frac{1}{R} \int_0^t dt' V(t') + C V(t), \quad (2)$$

where  $C$  is the sample capacitance (0.016 and 0.33 microfarads for PZT and PVF<sub>2</sub>, respectively, both measured at 1 kilohertz), and  $V(t)$  is given in Fig. 8 and 9. The main contribution to  $Q(t)$  comes from the first term on the right hand side of Equation (2). The differences between the charge released from the two samples, shown in Fig. 12, may be explained by their different depolarization mechanisms. Under pressure PZT generates a charge of the same polarity as the original poling potential, while the PVF<sub>2</sub> stack generates a charge of the opposite polarity. The net result is that the depolarization charge adds to the charge release for PZT under pressure, but subtracts for PVF<sub>2</sub>. To provide an independent check on the sign of the depolarization charge of PVF<sub>2</sub>, we deliberately heated a polymer stack and found

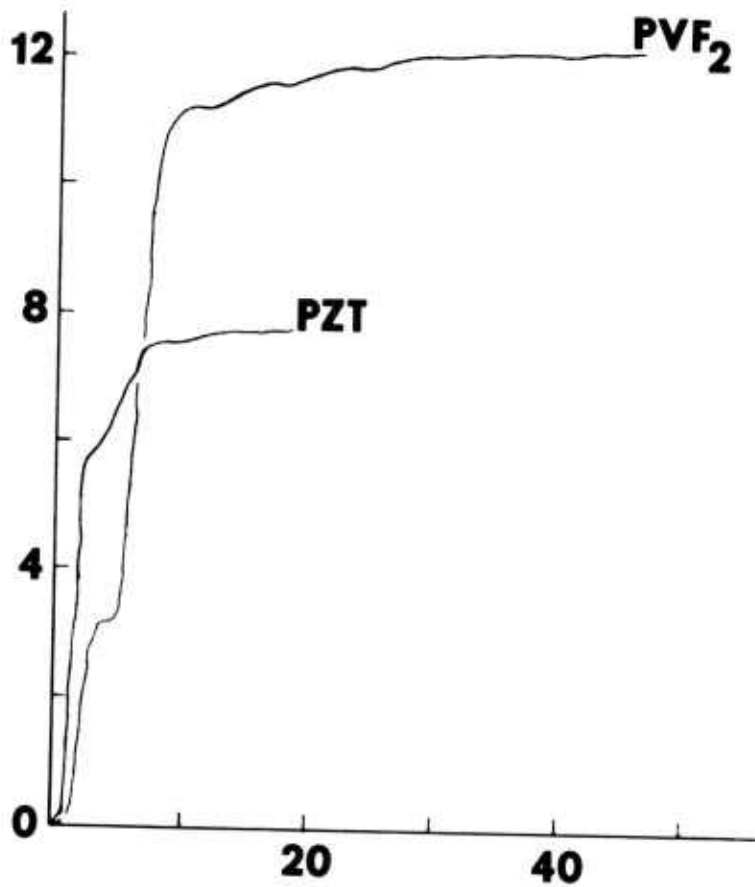


Fig. 10. Energy in  $10^5$  ergs to 4 Ohm Load Versus Time in Microseconds for 30MM Reverse Ballistic Tests on PZT Specimen and PVF<sub>2</sub> Stack #7

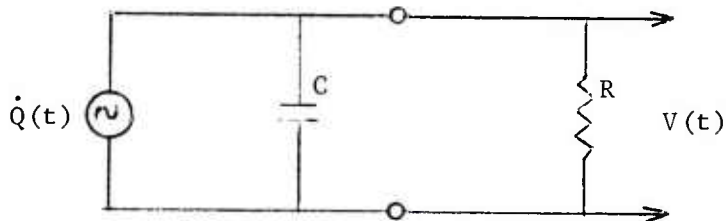


Fig. 11. Current Equivalent Circuit for Piezoid Plus Load Resistor ( $R = 4$  Ohms)

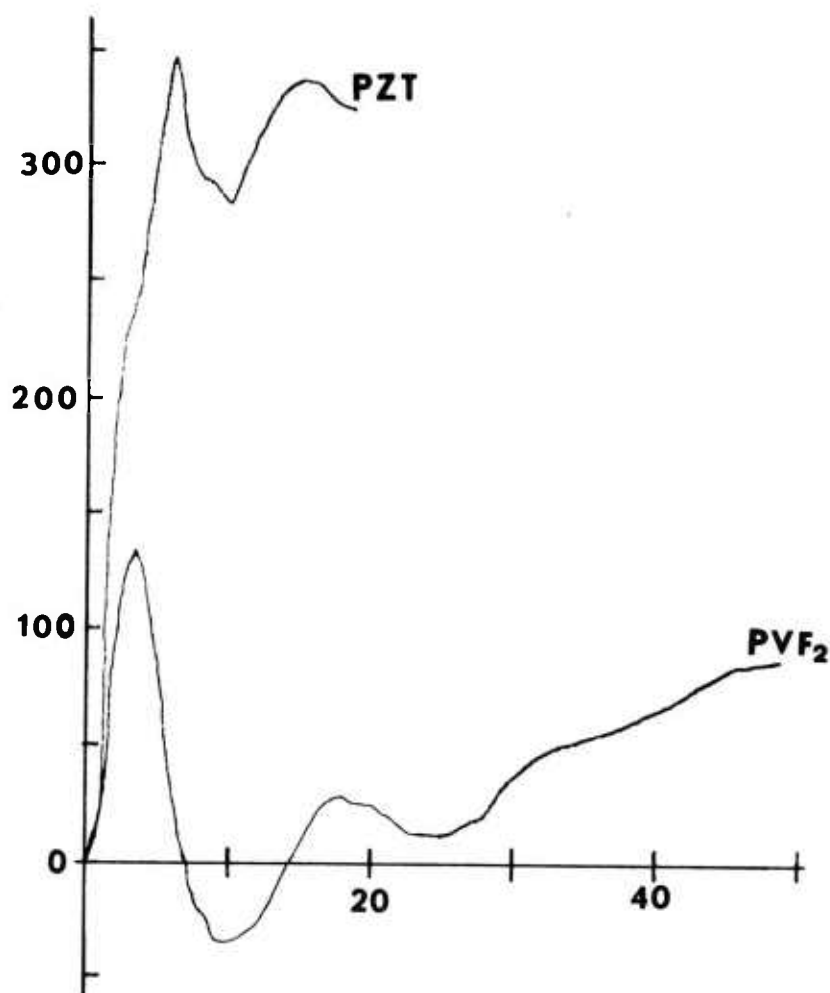


Fig. 12. Charge Output in Microcoulombs Versus Time in Microseconds for 30MM Reverse Ballistic Tests on PZT Specimen and PVF<sub>2</sub> Stack #7

that above 100°C it released copious charge with a sign opposite to that produced by compression.

That the depolarization charge subtracts from the initial piezoelectric charge produced under pressure appears at first sight to make PVF<sub>2</sub> materials less attractive for fuze applications, since it reduces the total charge delivered to the load. However, the energy delivered to the load depends on the square of the rate of



CHURCH, JENKINSON and

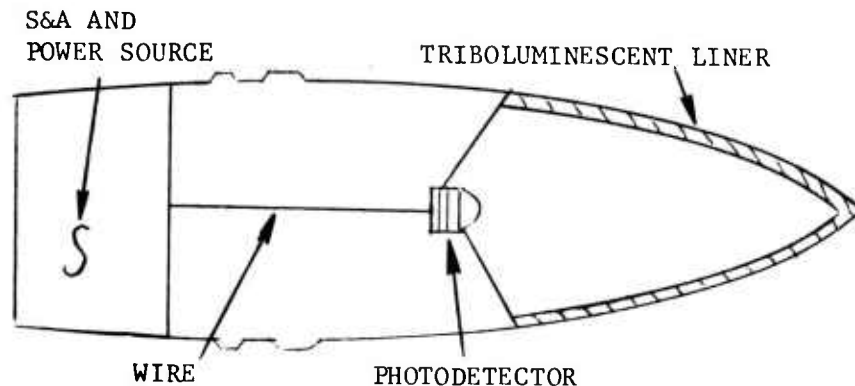
ESPOSITO

charge generation rather than on the charge itself, and that quantity may be increased by having the two charge producing mechanisms operating in opposite directions. This suggests that instead of being a disadvantage, depolarization may provide a useful energy delivering mechanism in PVF<sub>2</sub> in addition to simple piezoactivity.

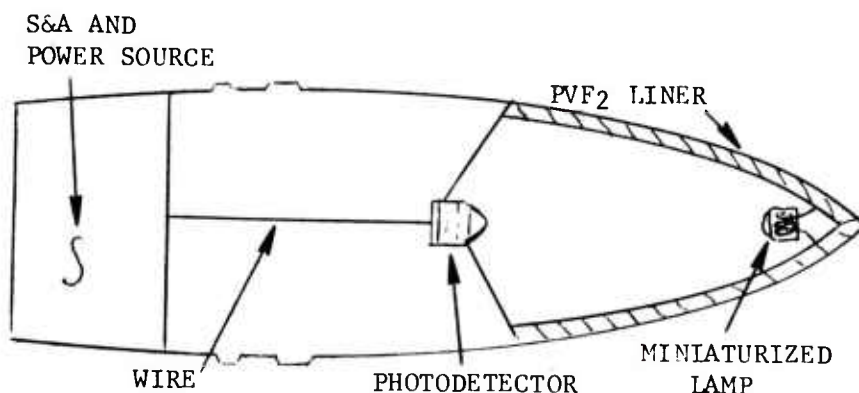
In order to determine the polymer response to a direct impact (that is, the polymer stack not in the metal sandwich), a firing was also carried out in the four inch air gun installation at Harry Diamond Laboratory (5). The front surface of a 20 layered PVF<sub>2</sub> stack was directly struck by a 500 ft/sec projectile (an estimated force of 50 tons). The output voltage rose linearly to its peak value approximately 0.5 microseconds after impact. This test demonstrated that the polymer stack could survive for a sufficiently long time in a direct ballistic impact situation in order to deliver its output signal.

#### ELECTRO-OPTICAL FUZE CONCEPTS

Figure 13 illustrates two recent wireless fuze concepts: (a) the triboluminescent fuze concept proposed by the Ballistics Research Laboratory (BRL) and (b) a PVF<sub>2</sub> modification of the BRL design proposed by Frankford. Both concepts offer improved performance, particularly at graze angles. The BRL design utilizes the emission of light from a triboluminescent coating, when the projectile strikes the target, in order to trigger a photosensitive device which initiates the detonation sequence (6). This concept eliminates possible manufacturing problems arising from a wire connection from the ogive to the detonator in the base of the projectile; however, it requires an onboard power supply such as a thermal battery or setback generator. In the PVF<sub>2</sub> design, given in Fig. 13b, a wire connection to the base detonator (not illustrated) is only necessary if the ogival piezoid is required to do double duty, that is, to act both as an impact sensor and as a power source for the detonator. In actuality, an independent PVF<sub>2</sub> circuit located in the base of the projectile could function as a setback generator. The PVF<sub>2</sub> liner acts as a graze indicator only, and its output is connected to a miniaturized light emitting diode or miniaturized lamp. An electro-phosphorescent coating bonded mechanically and connected electrically to the PVF<sub>2</sub> liner could also function as the light source. The piezo plastic liner plus light emitter could replace the triboluminescent material in the basic BRL design, with the obvious advantage of a controllable, higher intensity spectral output per unit force.



(a) BRL DESIGN



(b) FRANKFORD PVF<sub>2</sub> DESIGN

Fig. 13. Electro-Optical Fuze Concepts

#### OTHER APPLICATIONS

Piezopolymer materials have a number of other ordnance and ordnance testing applications as transducer elements. Their advantages over conventional transducers lie in their flexibility, resistance to damage by mechanical shock, high sensitivity, thinness, large area, low density, low cost, and simplicity of fabrication (in mass production). Such pressure/vibrational sensing applications include high-g accelerometers, instrumented target plates, the testing of composite armor (with polymer sheets interspersed), the determination of forcing levels for wound ballistics, and seismic transducers

CHURCH, JENKINSON and

ESPOSITO

for mine/intrusion systems (due to good impedance coupling with soils).

PVF<sub>2</sub> sheets are transparent in the visible and near infrared spectral regions, including the neodymium laser emission wavelength at 1.06 microns. Hence, PVF<sub>2</sub> can serve as a piezoelectric window for missiles or guided projectiles with active or passive optical/infrared seeker systems. In addition, its pyroelectric behavior can utilize the aerodynamic heating of a projectile in flight as a second arming environment.

There are numerous other applications (7) of these polymers to both the DOD and civilian sectors: thermal imaging systems, underwater transducers, microphones, earphones, band-aid polymer devices to monitor heart beats, non-destructive testing, etc.

Piezoelectric and pyroelectric polymer materials and prototype devices are currently being investigated in a number of university, industrial, and government laboratories. (Other DOD agencies sponsoring work on these materials include the Army Research Office, Army Materials & Mechanics Research Center, Army Night Vision Laboratory, Office of Naval Research, and Naval Underwater Systems Center.) The principal technical barriers being addressed are poling mechanisms, optimum poling and fabrication techniques, reproducibility, and long term electrical stability (2). Potential United States manufacturers and users are carefully investigating polymer device capabilities and market potential in order to determine whether it will be feasible to produce such devices on a commercial scale. In spite of the fact that the aforementioned research questions remain to be answered, a number of commercial products have been recently introduced: polymer earphones and loudspeakers from Japan and pyroelectric radiation detectors from this country.

#### CONCLUSIONS

In summary, we have shown that PVF<sub>2</sub> piezoidal devices offer significant potential for fuzing applications. The encouraging results reported here convincingly show that further development studies and ballistic tests on these materials and stacks should be pursued, as well as a more inclusive study of fuzing circuits tailored to their unique properties.

CHURCH, JENKINSON and

ESPOSITO

REFERENCES

1. For example, see K. Nakamura and Y. Wada, J. Polym. Sci. 9 (A-2), 161, 1971; and also the references contained therein.
2. "Proceedings of Piezoelectric and Pyroelectric Symposium Workshop" coordinated by M. G. Broadhurst, National Bureau of Standards, Report No. NBSIR 75-760, September 1975.
3. J. H. McFee, J. G. Bergman, and G. R. Crane, Ferroelectrics 3, 305, 1972.
4. I. Lefkowitz and C. W. Fleischer, Jr., Frankford Arsenal (private communication).
5. P. E. Bloomfield, "Piezoelectric Polymer Films for Fuze Applications", National Bureau of Standards, Report No. NBSIR 75-724(R), August 1975.
6. C. M. Glass, J. G. Dante, C. M. Cialella, and S. K. Golaski, "An Electro-Optical Fuze System", Ballistics Research Laboratories, Memorandum Report No. 2552, October 1975.
7. For example, see S. Edelman in "Proceedings of Piezoelectric and Pyroelectric Symposium Workshop" coordinated by M. G. Broadhurst, National Bureau of Standards, Report No. NBSIR 75-760, September 1975.



LACTIC ACID DERIVED BIODEGRADABLE IMPLANT MATERIALS

DUANE E. CUTRIGHT, COL, DC, JOHN M. BRADY, COL, DC,  
LEE GETTER, COL, DC, and Mr. ROBERT A. MILLER  
UNITED STATES ARMY INSTITUTE OF DENTAL RESEARCH  
WASHINGTON, D. C. 20012

The requirement for a better method of treating avulsive type maxillofacial wounds has been demonstrated in the common poor esthetic results achieved in the combat wounded soldier up to the present time. The constant search for better techniques of surgical repair and the origination of new biodegradable implant materials led the U.S. Army Institute of Dental Research (USAIDR) to investigate the application of these materials to surgical defects. These materials (polylactic acid in the L<sup>+</sup> and DL forms (PLA) and polyglycollic acid (PGA) were tested in an extensive sequential program, from simple biocompatibility through a multitude of surgical applications subsequently producing an extensive knowledge of their biologic behavior and surgical application. The end result of the program has been a recognition of the wide potential medical use of these materials, including fabrication of copolymers to produce an implant tailor-made for the surgical site for soft tissue as well as bone. In addition the institute's experiments demonstrated a new use of this material as a vehicle for bearing pharmacological agents in the tissue site for long term treatment. The biodegradable materials research program has yielded great rewards and will be a source of many applications not only for the combat wounded but for wider application in surgery and pharmacology. This report will outline the research program which we have accomplished with these materials at USAIDR.

The first phase of the research program involved biocompatibility testing of the materials. The testing began in 1968 using (PLA) in suture form. This early study was designed to show the tissue reaction to the buried material, to characterize the material within soft tissue and gain information concerning the rate of degra-



dation. In the initial experiments sutures were placed in the muscle of white rats. This study demonstrated that (PLA) in suture form is degradable, that degradation is gradual over a period from 42 days to beyond 70 days and the degradation is accompanied by a mild giant cell reaction. These favorable results led to a second study in monkeys again utilizing the (PLA) material in the suture form. However this time it was placed in the mandible and used as a transosseous fixation material. The sutures were hand made and braided to form a large suture approximately 0.20 mm in diameter. The harvesting schedule gave bony samples of 2, 6, 8, 10 and 12 weeks. This study confirmed the previous findings of high tissue tolerance, slow degradation and rapid healing. This was the first report in the literature using these biodegradable materials for fracture fixation. It showed the sutures enlarging during the initial weeks with consequent shortening and then slowly decreasing in cross sectional areas throughout the experiment. A normal vasofibroblastic response with very few inflammatory cells accompanied the degradation (Fig. 1). The bone healed rapidly and normally, demonstrating effective tensile strength over a sufficient period of time to allow bony union.

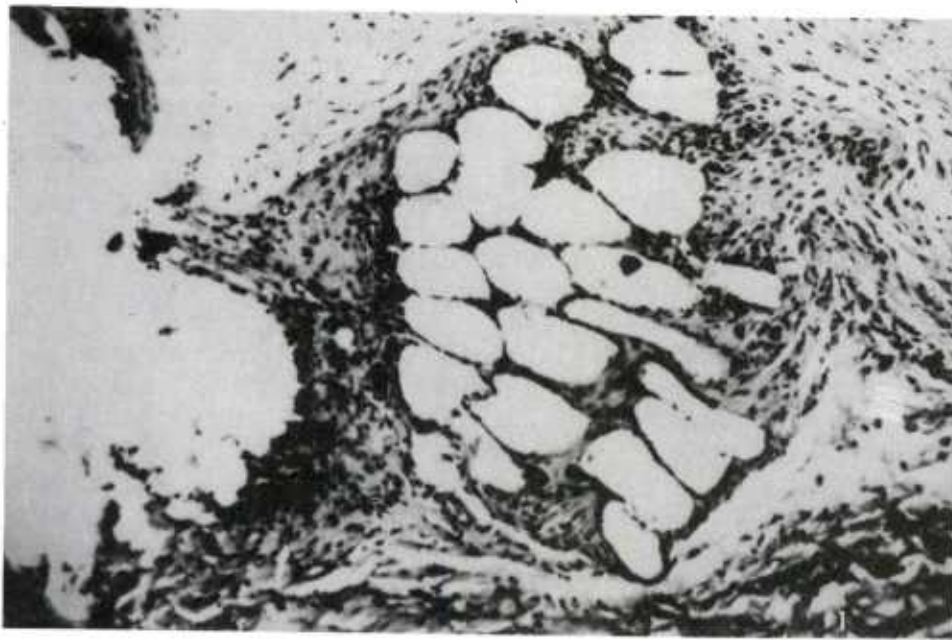


Figure 1. PLA suture site at 12 weeks.

The second phase of the program examined the metabolic fate of the degradable material, duration of the material in the implant site, and the ability to regulate the degradation rate of the material.

Carbon-14 labeled PLA pellets in the abdominal wall of rats exhibited a linear degradation rate, with 63 percent of the implant radioactivity remaining after 168 days (Fig. 2). Total duration of the implant was calculated to be approximately 1 and  $\frac{1}{2}$  years.

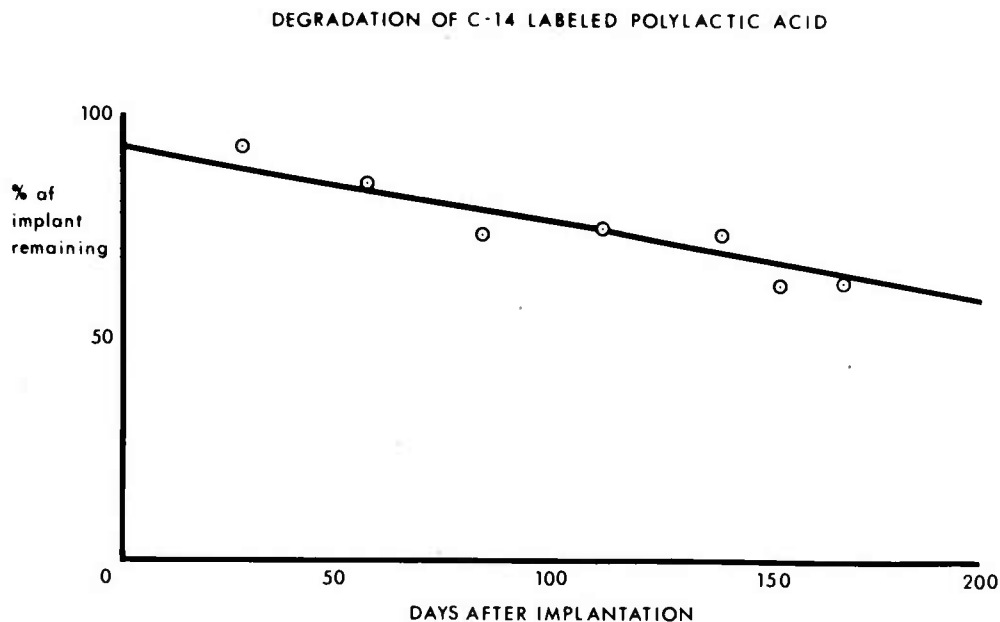


Figure 2. PLA radioactivity in implant site from 7 to 168 days.

Most of the radioactivity was released through respiration. Histologically the implant was invaded rapidly along septal planes of the implant or slowly along broad dense fronts (Fig. 3).



Figure 3. Light micrograph of PLA/tissue interface.

Electron microscopy revealed invading cells with marked mitochondrial accumulations adjacent to the implant surface (Fig. 4).

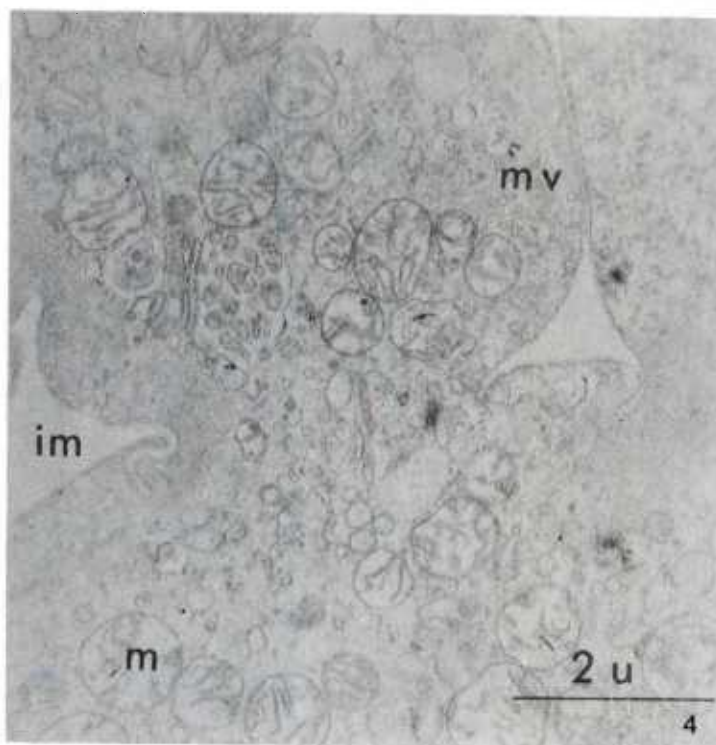


Figure 4. Transmission electron micrograph of PLA resorption.

Implant space (im) is approximated by phagocytic cells filled with mitochondria (m) and microvesicles (mv).

Variation of the composition of the implant material in its PLA and PGA content caused marked changes in the degradation rate of the implant as shown in the following two studies, one histologic, the other, radioisotopic. In the first study degradation rates were histologically determined to occur from 75 days to far in excess of 220 days as shown in the following figures. PLA (100%) shows minimum degradation at the implant margins at 220 days (Fig. 5). A thin ring of connective tissue (A) lies between the material and the bone (B). The bone has remodeled on 3 sides of the implant. In comparison 100% PGA at 220 days is even more slowly degraded (Fig. 6).

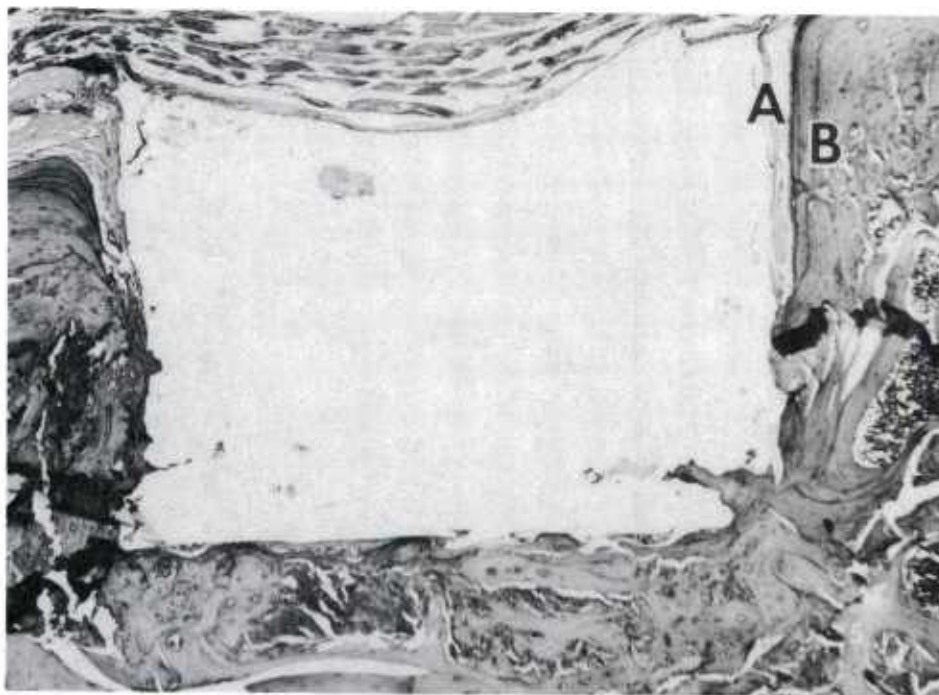


Figure 5. 100% PLA implant site in bone at 220 days.

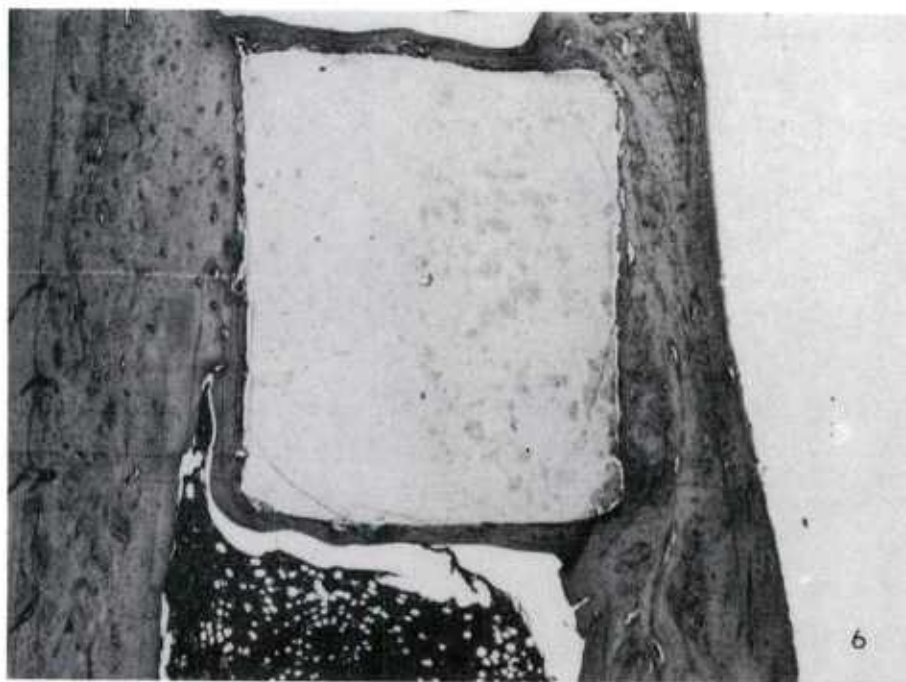


Figure 6. 100% PGA implant site in bone at 220 days.



The only evidence of resorption is the irregular edge of the implant which is closely in contact with surrounding bone.

PGA-PLA (50/50) is the most rapidly degraded copolymer (Fig.

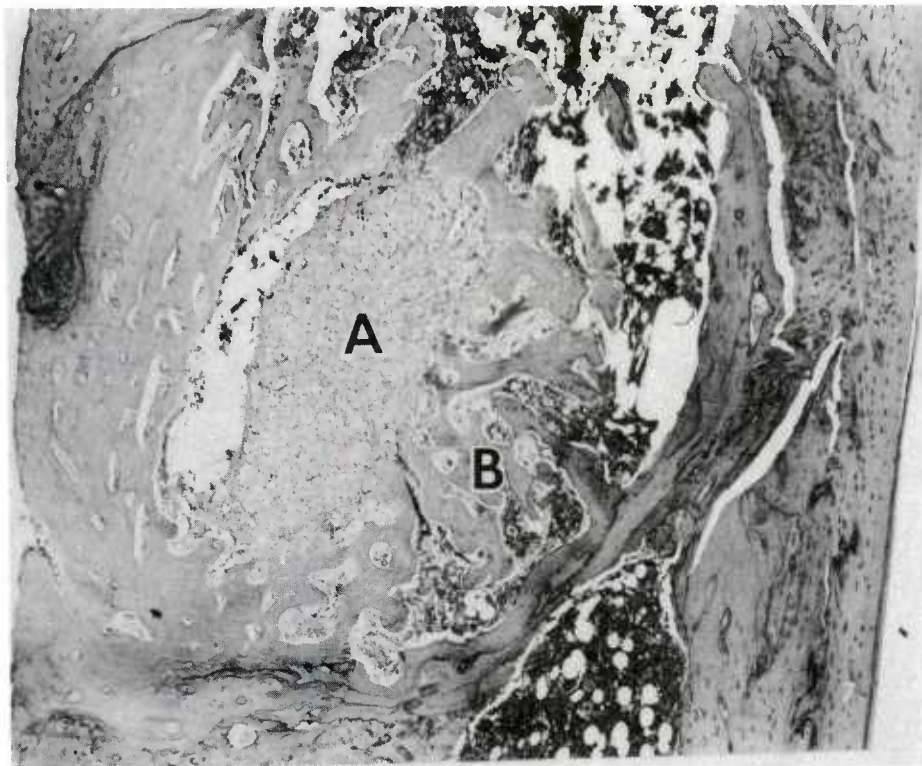


Figure 7. 50/50 PGA/PLA implant site in bone at 80 days.

At 80 days phagocytes are present in the center of the implant (A). The bone has replaced much of the copolymer (B) and connective tissue the remainder. No inflammation is present, with normal remodelling of bone occurring at the wound edge. Intermediate ratios of PLA/PGA showed intermediate degradation rates in examination of light microscope specimens.

PGA/PLA (75/25) is degraded at a rate intermediate to the 100% and 50/50 composites. For example in the 75/25 implant at 80 days. (Fig. 8), the ring of phagocytic and vasofibroblastic tissue response (A) can be seen surrounding the copolymer. The borders of the tissue reaction surrounding the implant exhibit normal new bone and marrow regeneration (B).

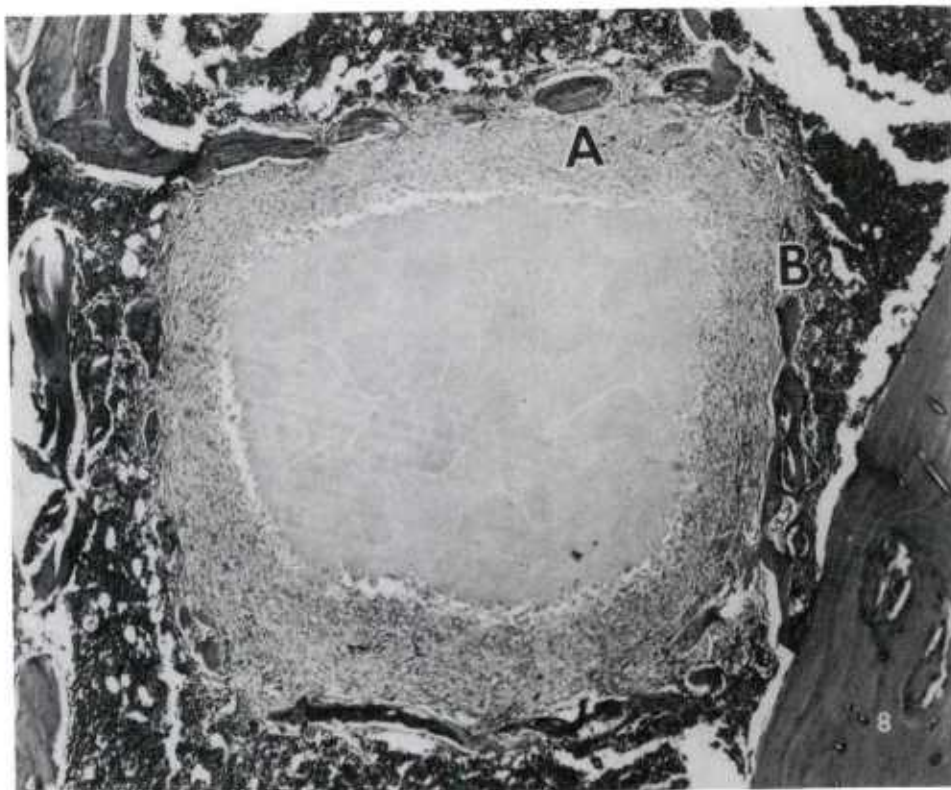


Figure 8. PGA/PLA (75/25) implant site in bone at 80 days.

The second study determined the difference in rate of degradation between pure polymers of lactic acid (PLA), polyglycollic acid (PGA) and various ratios of copolymers of these two substances. Fast-cured and slow-cured polyglycolide was compared with copolymers of glycolide (lactide intermixed in ratios of 75:25, 50:50, 25:75, as well as pure polylactide. A total of 420 rats were implanted with radiolabeled polymers in bone and soft tissue. Half-lives of the different polymers and copolymers decreased from 5 months for 100%



PGA to 1 week with 50:50, PGA; PLA and rapidly increased to 6.1 months for 100% PLA (Fig. 9).

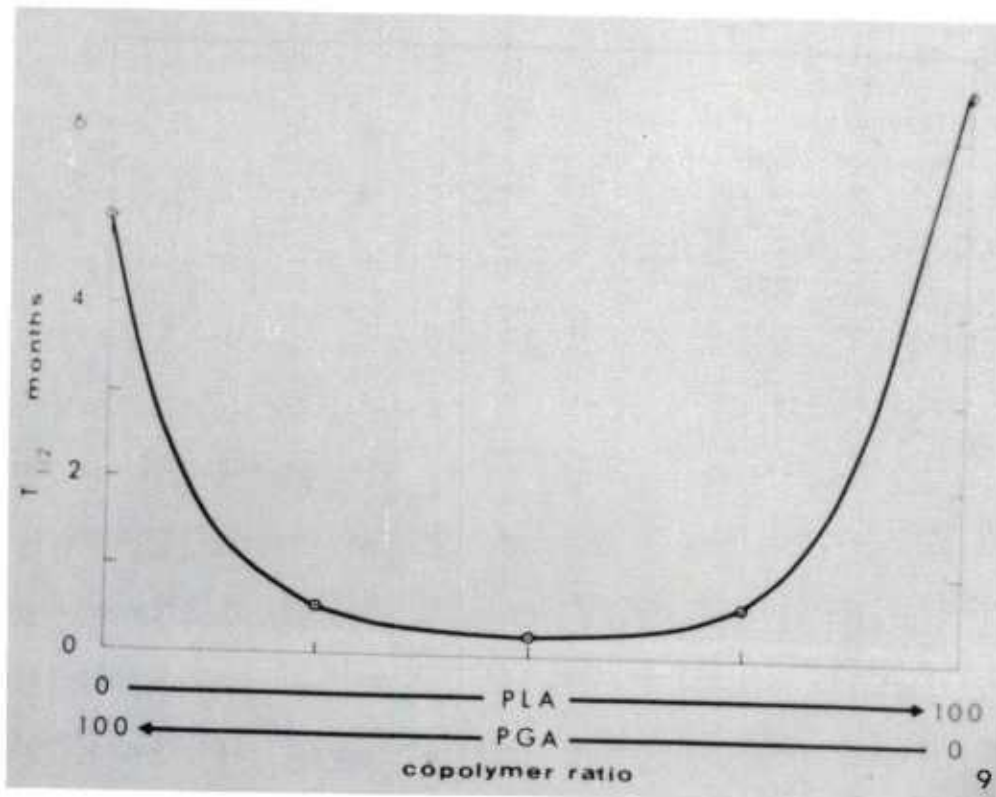


Figure 9. Half-life of PLA/PGA copolymers in tissue as a function of relative composition in the implant.

Fast-cured PGA had a half-life in tissue of 0.85 months. No difference in rate of degradation was seen in soft tissue or bone. We concluded that degradation rate of the implant could best be attained by varying the composition of PLA and PGA between 75% to 100% PLA along with a corresponding 25% to 0% PGA. This would provide a half-life range of the implant of from 2 weeks to 6 months.

The third phase of the testing program was in applications testing.

The very favorable reactions shown in the initial experiments convinced the authors that this material could be used in different forms for various medical and surgical applications.

PLA material was cast into several forms for various surgical applications (Fig. 10).

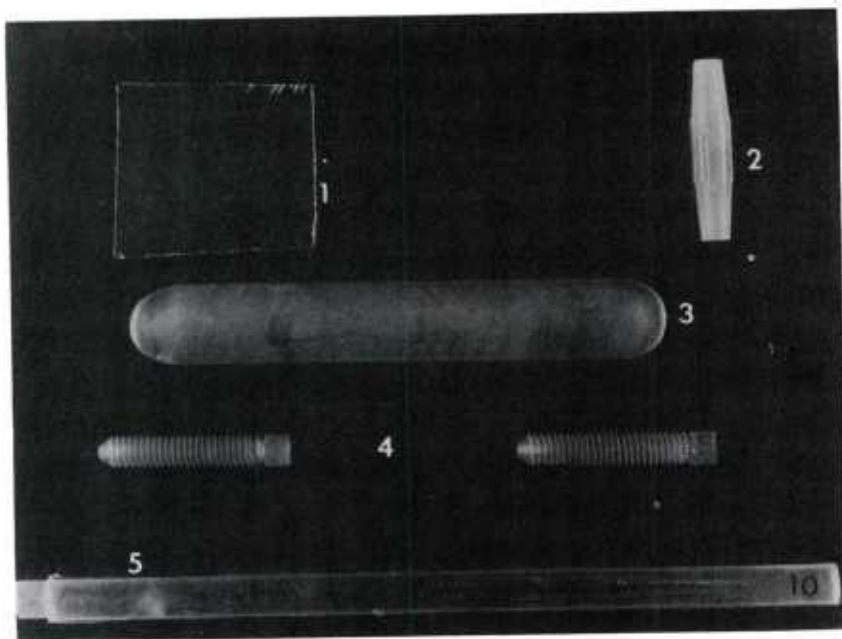


Figure 10. Several shapes to which PLA can be cast for surgical use: Plates (1); Tubes (2); Rods (3); Screws (4); and Cylinders (5).

The first study performed to check the surgical applicability was with the pure PLA in a sheet form approximately 1 mm thick. This sheet was used to repair the orbital floor in blow-out type fractures. This sheet was custom-fitted in the operatory so as to maintain the orbital contents in a normal relationship. Twelve blow-out fractures in *Macacus Rhesus* monkeys were repaired with the custom-fitted PLA in the orbital floors. The orbits were harvested at 4, 8, 12, 18, 24 and 38 weeks and examined histologically. Clinically, eye movement was normal at all time periods, no edema or discoloration of the periorbital tissue occurred after the initial healing. Histologically the

degradation occurred via a vasofibroblastic proliferation which gradually decreased the thickness of the sheet (X) (Fig. 11).

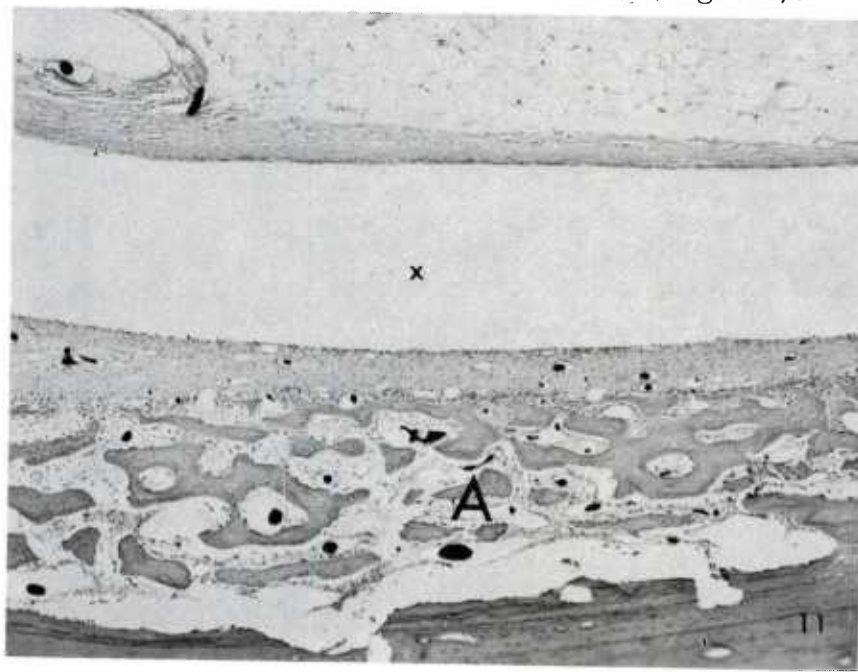


Figure 11. Healing in repair of orbital blow-out fracture at 10 weeks ("X") marks site of implant).

These vasofibroblastic villous processes were accompanied by a very mild inflammatory reaction for the first 8 weeks. The degradation process was intimately associated with the formation of a new bony orbital floor (A). This was the first published study to demonstrate fracture fixation with a biodegradable material other than sutures. This was a very important step because all previous fixation devices either left a foreign body in the tissue or required a second operation for removal. This simultaneously obviated such complications as late appearing foreign body reactions, device migration and paresthesias often associated with nondegradable devices.

In order to demonstrate the feasibility of using the long degrading PLA, an experiment was done utilizing a plate of pure DL PLA to fix mandibular mid-jaw fractures in 6 dogs. The plates were milled to the approximate dimensions of conventionally used steel plates. Screws of DL PLA were also turned on a lathe to be used to fix the plate to the mandible. The previously sterilized plates were

fitted, drilled and tapped. This allowed a strong relatively rigid fixation of bone and plate (Fig. 12a). The animals were sacrificed at intervals up to 40 weeks. The animals showed no sign of rejection, no unusual edema or discoloration and at 24 weeks the plates could no longer be palpated or visualized. Between 32 and 40 weeks when examined grossly and microscopically it was impossible to find the fracture site or any evidence of an increase of collagen formation or scar tissue (Fig. 12b). The degradation was histologically evident around the screws at 6 weeks with nearly complete degradation of both plate and screws by 40 weeks.

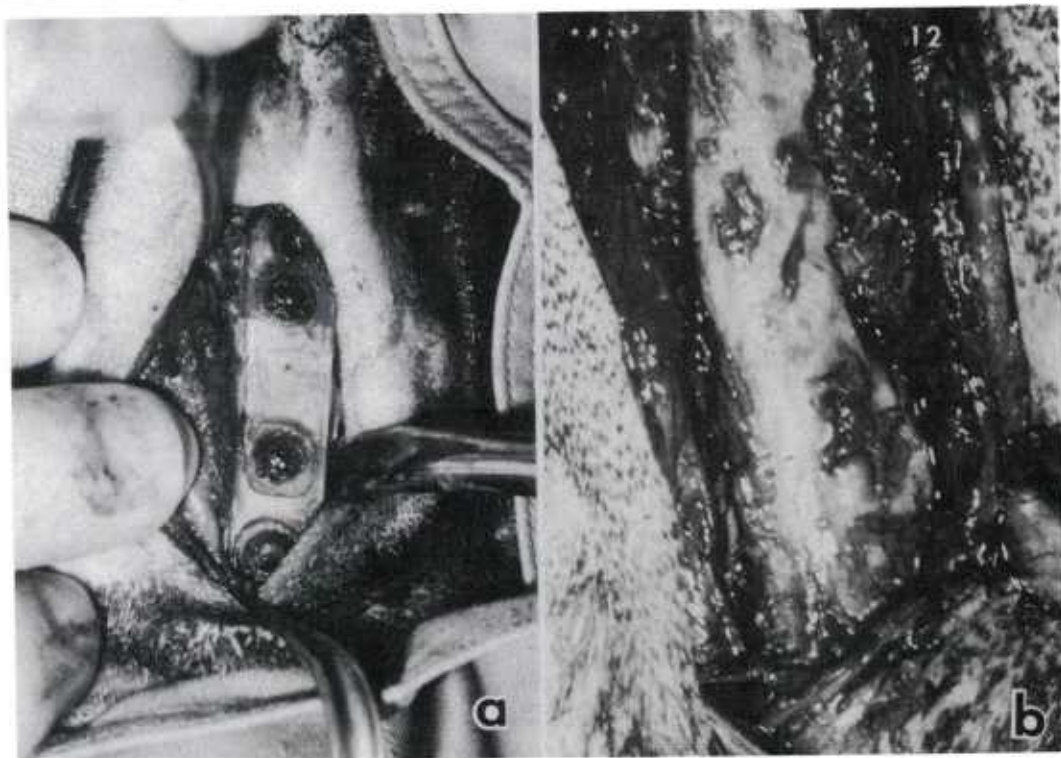


Figure 12. Implantation site in fracture of mandible at time of surgical repair (a) and at 40 weeks after repair (b).

This experiment with PLA plates and screws again demonstrated that mandibular fixation is possible, that the device can be customized, and that degradation is slow and associated with minimal inflammation. The PLA is completely resorbed from the body, therefore a second operation is not required for its removal.

In order to further check the versatility of the copolymers in the practice of surgery a study was done on six monkeys utilizing a ( $\frac{1}{2}$  mm thick) sheet of 50% PLA to 50% PGA. This sheet was placed between the traumatically exposed trabecular bone of the metacarpals and the severely traumatized tendons. The animals were sacrificed to give 12 tissue samples varying from 4 to 25 weeks. The copolymer tissue reaction and degradation followed the process as previously reported. The total disappearance took place in approximately 50 days. The surface softening in this experiment allowed the formation of a slippery surface very reminiscent of that seen in synovial membranes. This film aids the movement of the tendons over the copolymer sheet. A fibrous type synovial cavity formed throughout most of the experimentally traumatized hands, thus allowing healing and free movement of the extensor tendons. This barrier allowed normal healing without the formation of fibrous scar tissue between the bone and the tendon. It was completely successful in blocking ingrowth through the copolymer plate barrier during the initial healing phase.

This was the first reported instance of a biodegradable material being used as a blocking agent to improve healing and tendon gliding after controlled trauma between tendon and bone.

The study proved the following new points about biodegradable PLA/PGA implants.

1. A synovial like cavity formed between the tendons and the implant before the final degradation occurred.
2. The biological degradation process begins as a surface softening of the implant. This allows a glistening lubricated smooth surface to be established between the damaged tendon and bone permitting early extension.
3. The implant reduces or prevents the unwanted fibroblastic reaction between the traumatized tissues but allows healing to occur without loss of function.
4. The use of a biodegradable material in an area with a known marked propensity for scarring reduces unwanted tethering between healing tendon and bone and avoids the necessity of the second operation for removal.

Another study utilized cylinders of 50% PLA and 50% PGA for the repair of severed peripheral nerves. This study which utilized both monkeys and dogs for periods up to 6 months demonstrated again that the material prevents ingrowth of unwanted fibrous connective



tissue during the healing phase and then disappears entirely. These cylinders were made with 3/4 mm thick walls and degraded in approximately 6 weeks with the already described favorable tissue response. The copolymer again blocked the unwanted fibroblastic proliferation between the healing nerve segments allowing better nerve regeneration.

The latest applications of the copolymeric materials was to demonstrate the feasibility of using them as a long term, slow release subcutaneous method of drug administration. This study incorporated vitamin D<sub>3</sub> into the 75% PLA 25% PGA material and checked its release in rats. The findings demonstrated a slow and uniform release of the vitamin D<sub>3</sub> with a half-life of 62.5 days compared to only 21.6 hours when injected in a similar site (Fig. 13).

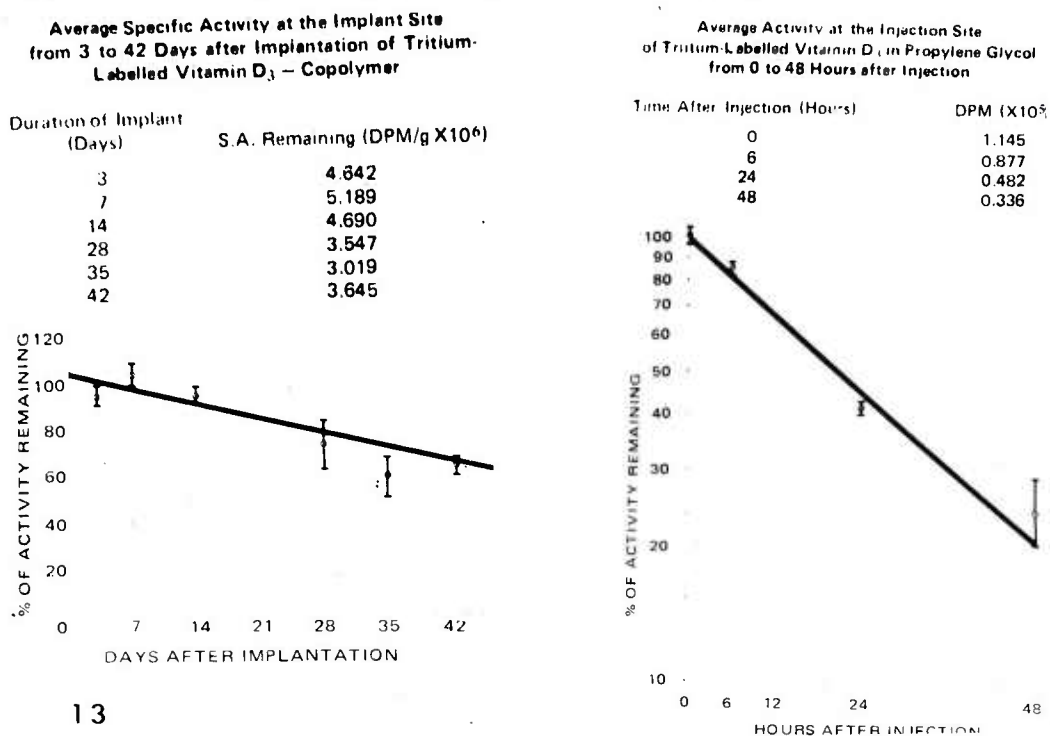


Figure 13. Vitamin D<sub>3</sub> radioactivity at implant site with and without PLA injection vehicle.

In another application the material was used in a semi sponge form for space obliteration. This study showed a rapid ingrowth of vasofibroblastic material and allowed ingrowth of this tissue into the pores and along lines of cleavage with obliteration of the bony defect.

In a planned sequential series of tests characterizing and evaluating the surgical application of biodegradable copolymers of PLA and PGA, the following points have been demonstrated.

1. The material is biodegradable.
2. The reaction is minimal in both bone and soft tissue.
3. By varying proportions of PLA to PGA degradation times can be tailored to fit most any surgical application from a few weeks to 1½ years.
4. The material is strong enough to maintain mandibular fixation.
5. The material is easily fabricated into screws, plates, pins, sponges and cylinders and can be altered in the surgical site.
6. The material can be utilized using the conventional surgical armamentarium.
7. It can be gas sterilized.
8. It requires no second operation for removal as do most conventional devices.
9. It avoids complications due to migration, corrosion or foreign body reaction which occur with conventional implants when left in place for long durations.
10. No tissue toxicity, allergic response, rejection phenomena or migration has been noted.
11. It can be used as a carrier vehicle for long-term drug administration.

An application has been made to the Federal Drug Administration for an Investigative New Drug Number.

In conducting the research described in this manuscript, the investigators adhered to the "Guide for the Care and Use of Laboratory Animals", as promulgated by the Committee on the Guide for Laboratory Animal Facilities and Care of the Institute of Laboratory Animal Resources, National Academy of Sciences - National Research Council.



## A METHOD FOR ANALYZING AIR TARGET FUZES

JOHN F. DAMMANN, JR, Ph.D  
HARRY DIAMOND LABORATORIES  
ADELPHI, MD. 20783

The paper describes a method of analyzing radar fuzes for air targets by using experimental data and the digital computer. Experimental data from velocity scaled tests are very useful for fuze evaluation. Our data come from several sources: an indoor track at Corona, CA; a sled track at China Lake, CA; and a truck track, also at China Lake. In all cases, a full-scale target model is hung over the track, and the fuze is carried past it at a low velocity. The target is placed at different positions and attitudes to simulate different encounter trajectories. Figure 1 shows the indoor Corona track with a MiG-21 target model and a fuze on its cart passing underneath it.

The fuze transmitter and the RF section of its receiver are used in the tests. The target is illuminated, and the backscattered energy from the target is received and mixed with the transmitted signal to obtain a baseband doppler signal. This signal is then recorded on magnetic tape. In the laboratory, the data are sped-up by the appropriate factor to simulate return from a full-speed encounter.

The velocity scaled tests provide a large number of realistic target signatures at a reasonable cost. Full-speed tests of more than a few encounters are prohibitively expensive. On the other hand, the target signature is very complex and, therefore, hard to model on the computer. The missile is passing very close to a large, complex target. The target may also be in the near field of the fuze antenna, further complicating the modeling problem. A wide variety of models to simulate target signatures is presently in use. However,

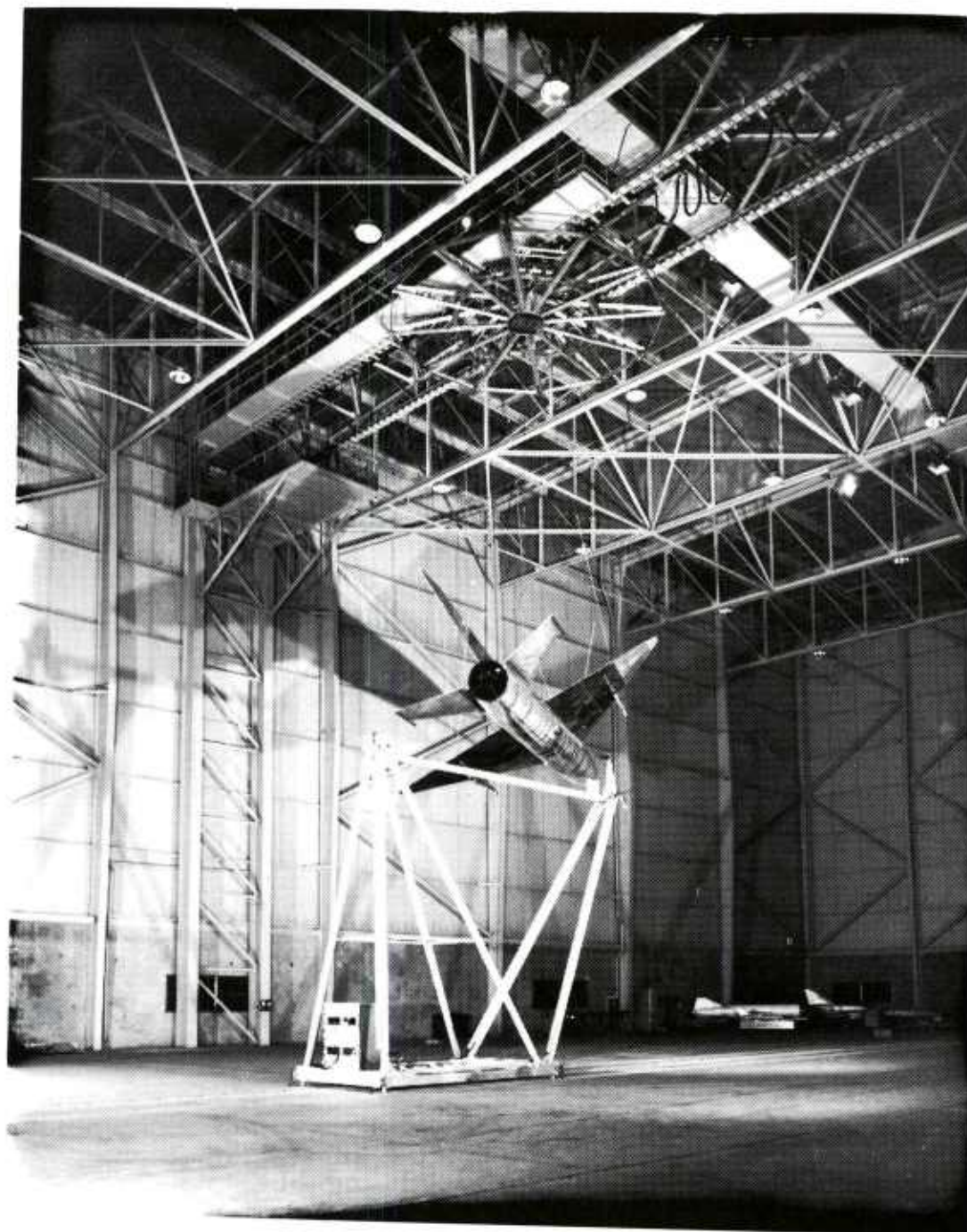


Figure 1. Corona Facility with MiG-21 Target and Fuze on Cart.

we feel we are still a long way from a simulation model we can have complete confidence in.

Until recently, the experimental data have been processed only with analog techniques. The sped-up data are played into the fuze processor hardware, and the fuze output signal is recorded on an oscillograph. This method is rather slow and very limited in scope. Processing the data digitally offers both a time savings and the possibility of a considerably more sophisticated analysis. Computer graphics is especially useful in displaying the large amounts of available data in a meaningful way.

In the computer processing, the doppler signal is first digitized. The doppler return from the target is studied directly by using power spectral analysis. Knowledge of target scattering is useful in developing new fuze designs, and in developing target models so that target return can be synthesized in the computer. The return data are also used as input to computer simulations of fuze doppler processors. Since the processor circuits can easily be changed in the simulation, these circuits can be optimized cheaply and efficiently. Finally, the entire encounter is simulated with an interactive graphics program. The user can see the encounter geometry, including the antenna pattern intersection with the aircraft.

#### THE COMPUTER SYSTEM

Since the nature and success of the research is highly dependent on the advantages or limitations of the computer system, we begin with a description of the system. It is a medium-sized, dedicated system centered around a PRIME 300 minicomputer. This computer is time-shared, presently supporting eight terminals. It has a sophisticated, virtual-memory operating system, 65536 (64K) words of MOS memory, and tape and disk units. Fourteen channels of analog-to-digital and digital-to-analog convertors are attached to the computer. Four of these channels are very fast (up to 1 MHz), enabling the computer to interact real-time with fuze hardware.

The primary terminal is an IMLAC PDS-4 graphics terminal with a refresh screen for display of dynamically changing data. It is a minicomputer in its own right, with its own internal graphics program. Thus, fast moving displays can be shown on it with a minimum of data transmission. A high-resolution Versatec printer-plotter is tied to the terminal for hard-copy output. Three Tektronix graphics terminals with hard-copy are also used. A graphics package, which we wrote in-house, supports both types of terminals. The graphics package is tailored expressly for our needs, and hence is small and efficient—

important considerations on a minicomputer.

There are many advantages to the system. It is relatively inexpensive, requires little overhead to support, and takes relatively little time to become operational. It is configured so that all data processing, including digitizing, can be done on the same machine. Of course, there are time and space limitations on the minicomputer—SPICE, NET or other very large simulation programs cannot be run. However, the system can do most things a large system can. The sophisticated operating system, time-sharing and extensive graphics facilities are particularly useful.

#### TARGET SIGNATURES AND MODELING

Figure 2 is a 3-D spectrum plot of doppler return from a sphere using a fuze with a wide-beam antenna. It shows a sequence of power density spectra, where power in dB is plotted against doppler frequency. The third axis, time or relative position, proceeds from the front to the back of the figure. In the encounter shown, the fuze approaches the sphere at a constant velocity, passing directly beneath it at about a 6-m miss distance.

The first curve is the spectrum of a segment of signal from 0 to 3 ms. The curve immediately behind it is the spectrum of the signal between 1 and 4 ms—a portion of signal that overlaps the first. The next curve is for the signal from 2 to 5 ms, and so forth. This method of presenting the spectrum provides a time history of the entire encounter. The plot shows the doppler frequency of the return decreasing as the fuze approaches, until the frequency is zero when the fuze is directly beneath the sphere. The frequency then increases again as the fuze passes. (The small spectral component near zero frequency is due to experimental noise.)

A 3-D spectrum plot of airplane target return is given in figure 3. The target is a MiG-21, and the fuze has a wide antenna beam with maximum gain normal to the missile axis. The 3 dB beam-width for the two-way pattern is about 30 degrees in the elevation plane, and the gain is symmetric in azimuth. Top and side views of the aircraft, missile and relative velocity vector for the encounter are shown on the following page.

The airplane spectra show many tracks like that from the sphere. The frequency of the return from each point, and the frequency changes with time (position) can be estimated closely from the plot. Also, one can see from the figure several features that realistic target models should have. First, the significant return comes



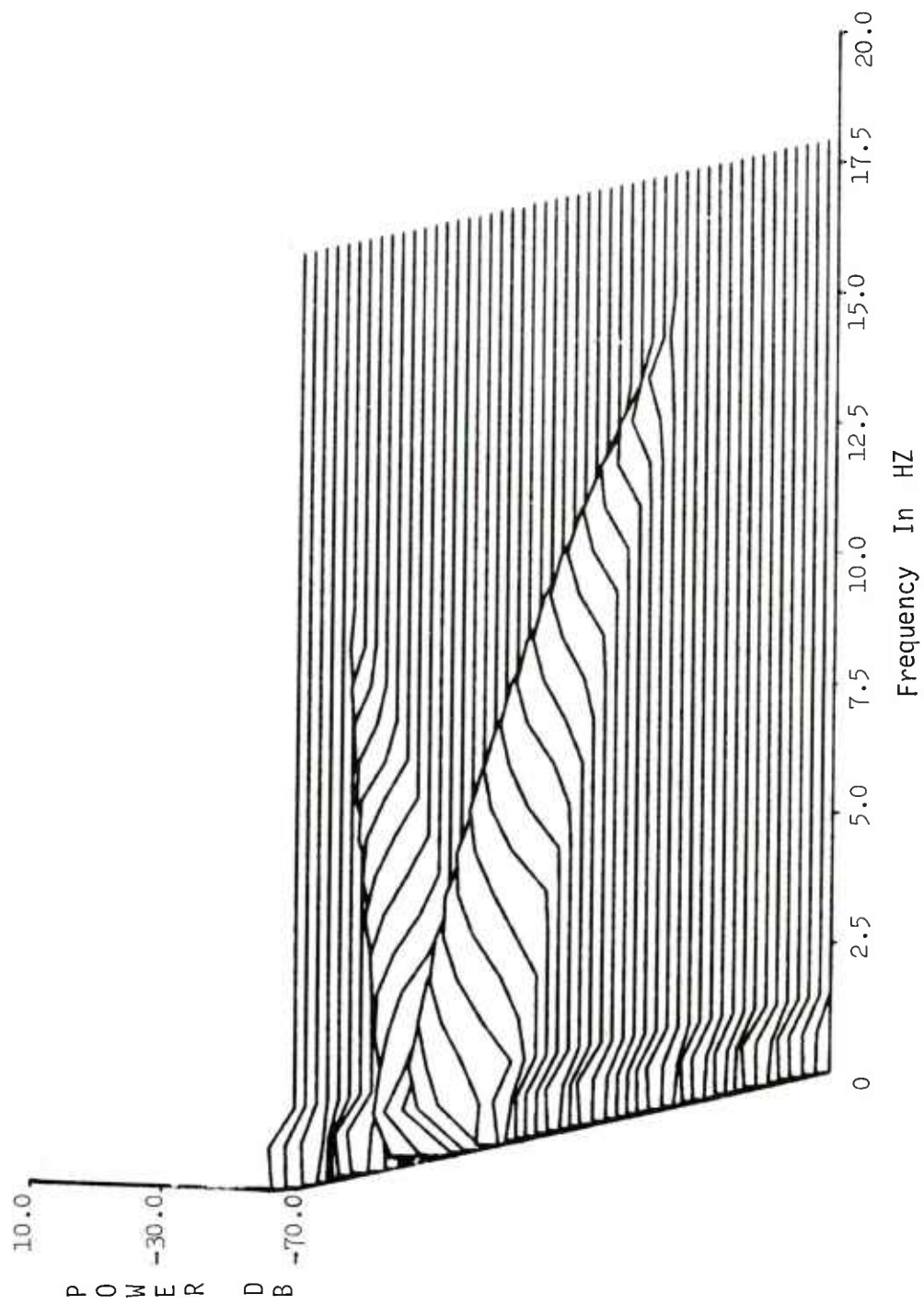


Figure 2. Experimental Sphere Target Doppler Spectra

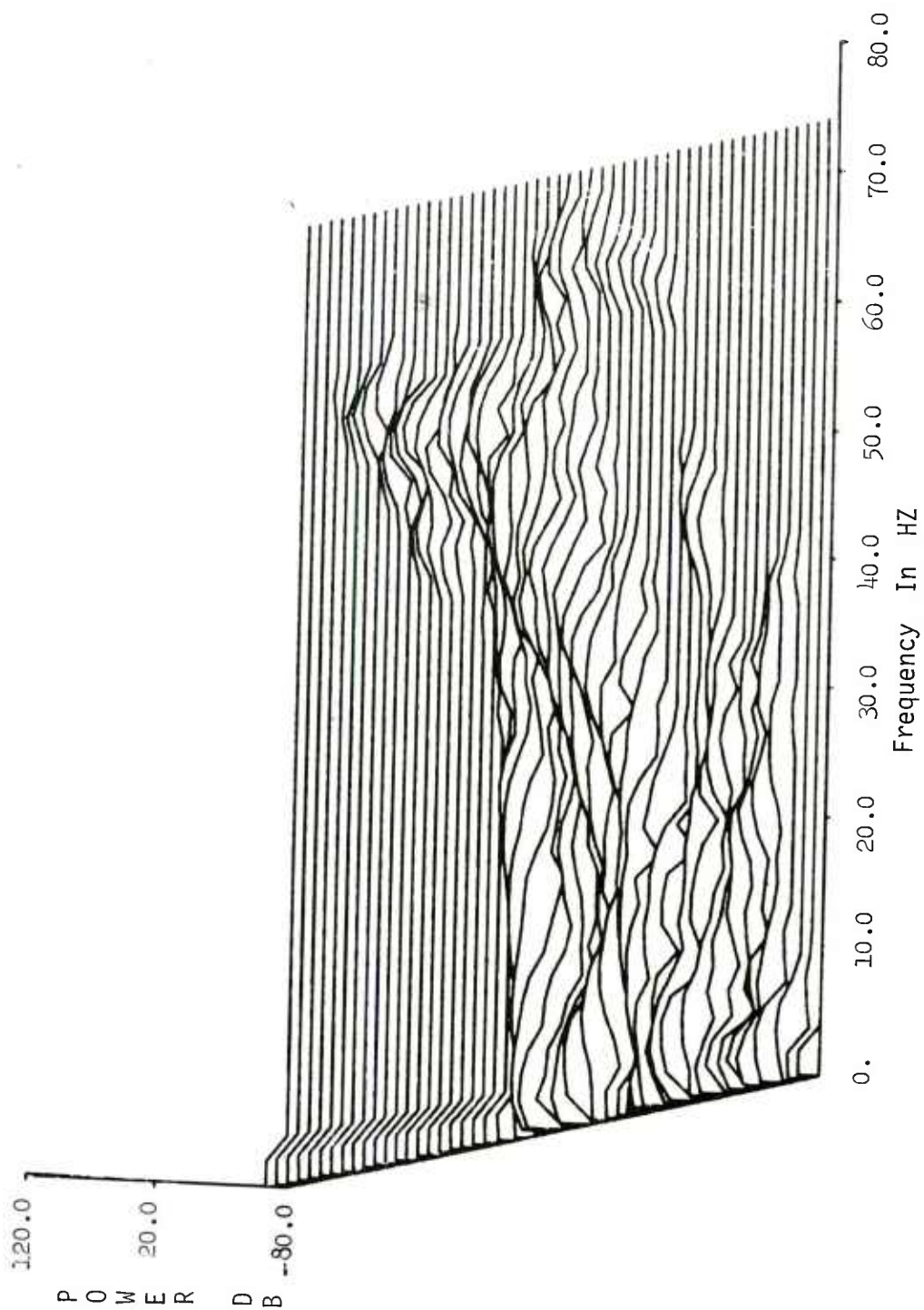
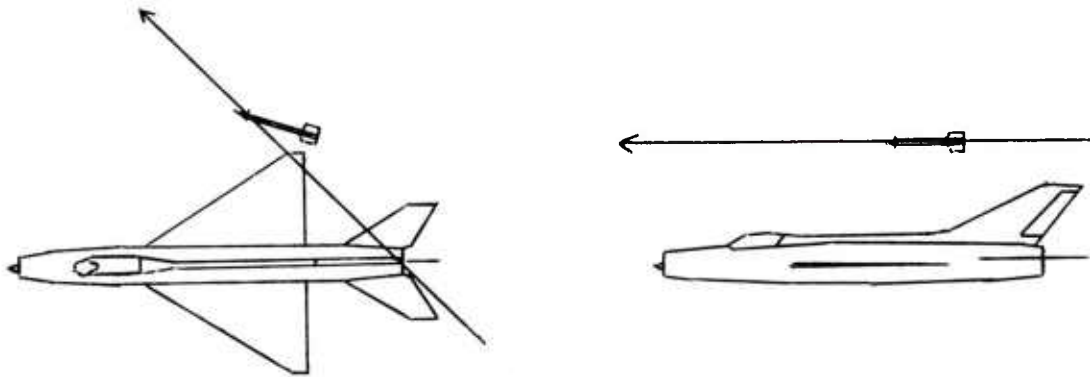


Figure 3. Experimental MiG-21 Target Doppler Spectra



from a small number of discrete scatterers. Second, since the fuze antenna beam is wide and the tracks often appear or disappear abruptly, the intensity of the scatterers must be dependent on aspect angle. Third, since the slopes (changes of frequency with position) of the tracks are very different, some scatterers may move along the aircraft as the fuze passes by. Study of the encounter geometry shows that this is indeed so.



By using the spectra of experimental encounters as a guide, a model of the MiG-21 is now being developed. A simple target model developed at Harry Diamond Laboratories was used as a starting point. The model uses a small number of point scatterers (eight). These points are stationary, and their intensity is independent of angle (except that they are not seen when shadowed by other parts of the aircraft). This model was used to generate the 3-D spectrum given in figure 4a. The same encounter parameters were used as for the previous figure, so the two spectra should match. The agreement is not good, however, with the model predicting significant return before it actually occurs.

A more sophisticated model is now being developed, but has not yet been finalized. Briefly, the model calculates return only from specular points on the aircraft (where the target surface is perpendicular to the incident rays). There are two specular points on the fuselage, one on each wing, one on each tail fin, and one on the vertical stabilizer. The points move along these surfaces as the fuze moves, and their intensity changes with aspect angle. The simulated

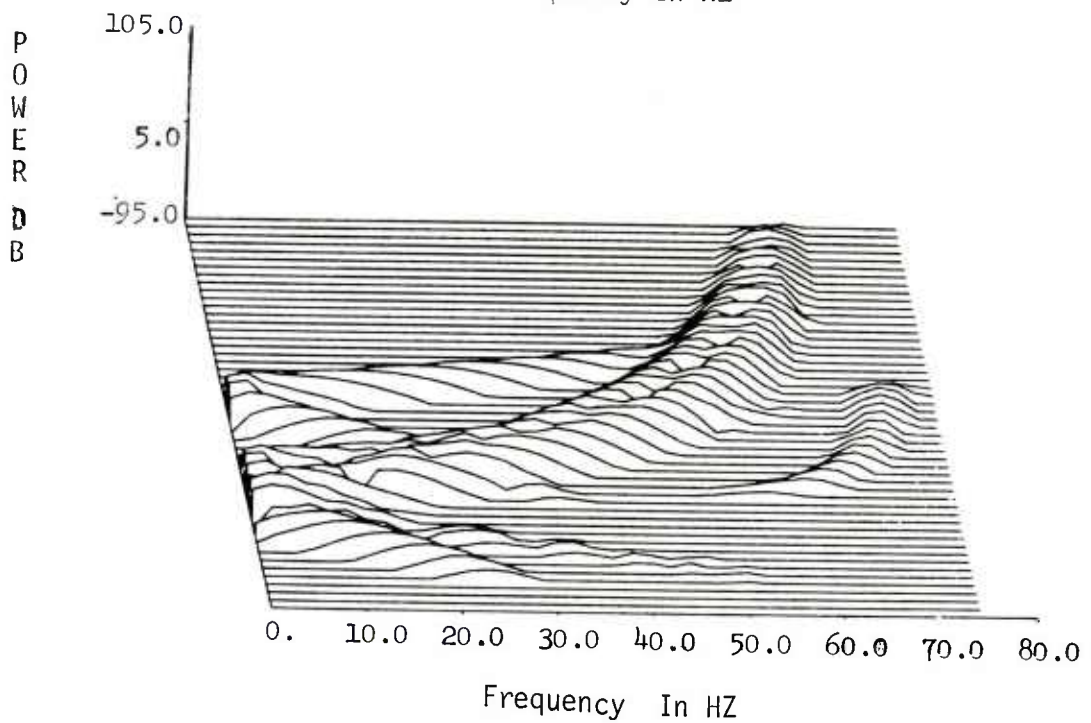
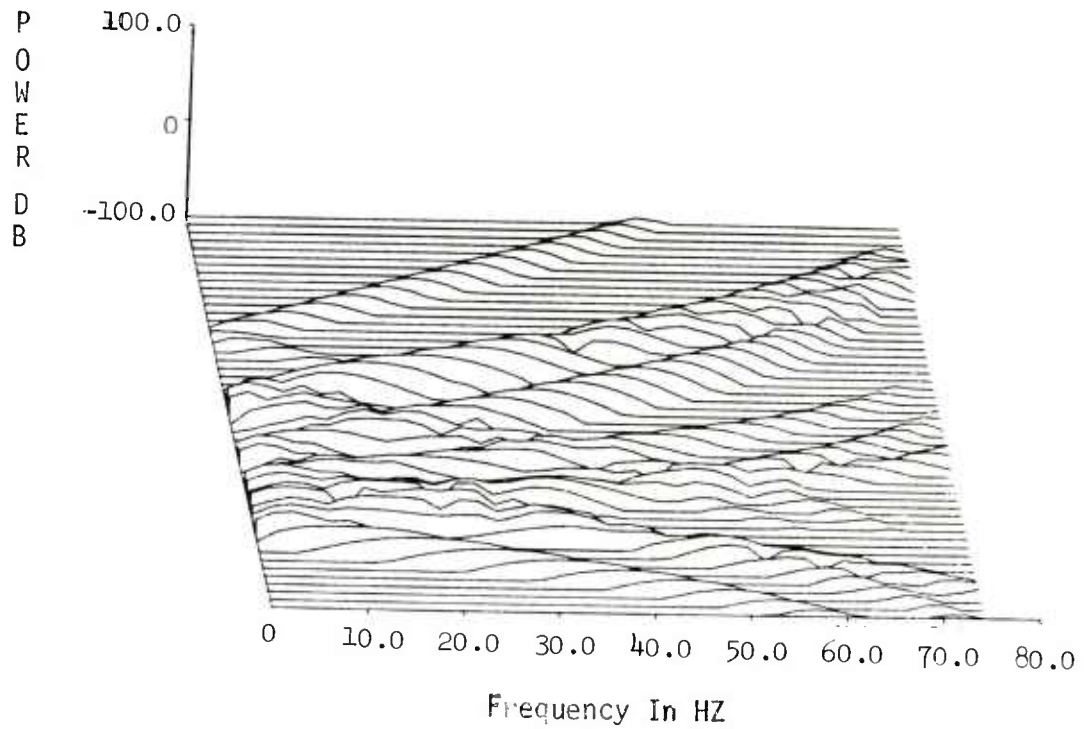


Figure 4. Simulated MiG-21 Target Doppler Spectra  
 a. Simple Model      b. More Complex Model

spectrum generated with this model is given in figure 4b. The more complex model gives a much better match to the real spectrum. Allowing the specular points to move, and their intensities to change makes a significant improvement over the simpler model.

The 3-D spectrum appears to be a very good tool for comparing various fuze models now being used in the fuze community, or for developing new ones. The two models shown give markedly different spectra, and the second model is clearly a better fit to the data. The spectrum contains a lot of information about the return signal. Moreover, it does not depend critically on the exact position of the antennas and scatterers, as does the original doppler signal (voltage vs. time). The original signal contains phase information, and small variations in position may cause large changes in the appearance of the signal.

#### FUZE PROCESSOR SIMULATION

The computer is also useful in simulating fuze processors. All of the components of fuze doppler processors—limiters, amplifiers, bandpass filters, detectors and integrators, etc.—can be simulated on the computer with a high accuracy. In particular, any filter characteristics can be duplicated with recursive digital filters. We have written and tested digital filter programs for low-pass, high-pass, bandpass, and band-stop filters with RC, Butterworth, and Chebyshev characteristics. A nice feature of those digital filters is that their pass-bands and roll-offs can be changed at will by just changing a few parameters in a call to a subroutine. Thus, the job of optimizing fuze parameters is considerably simplified.

The integrator output of a simulated SAM-D fuze processor for a sample encounter is shown in figure 5. The line at 2.6 volts is a firing threshold; when the integrator output exceeds this level, the fuze functions. Exact function positions and maximum integrator output levels can be read from this type of output. Doppler passbands, integrator time constants and other parameters can be changed, and their effects on the output can easily be observed.

#### ENCOUNTER SIMULATION

In studying an encounter, it is useful to be able to see the encounter geometry, especially the intersection of the antenna pattern and the target. For this reason, we have simulated the encounter for viewing on a dynamic graphics display. Figure 6 is a still picture from this interactive program. Shown are three orthogonal views of a MiG-25 target and a missile with its antenna pattern. The

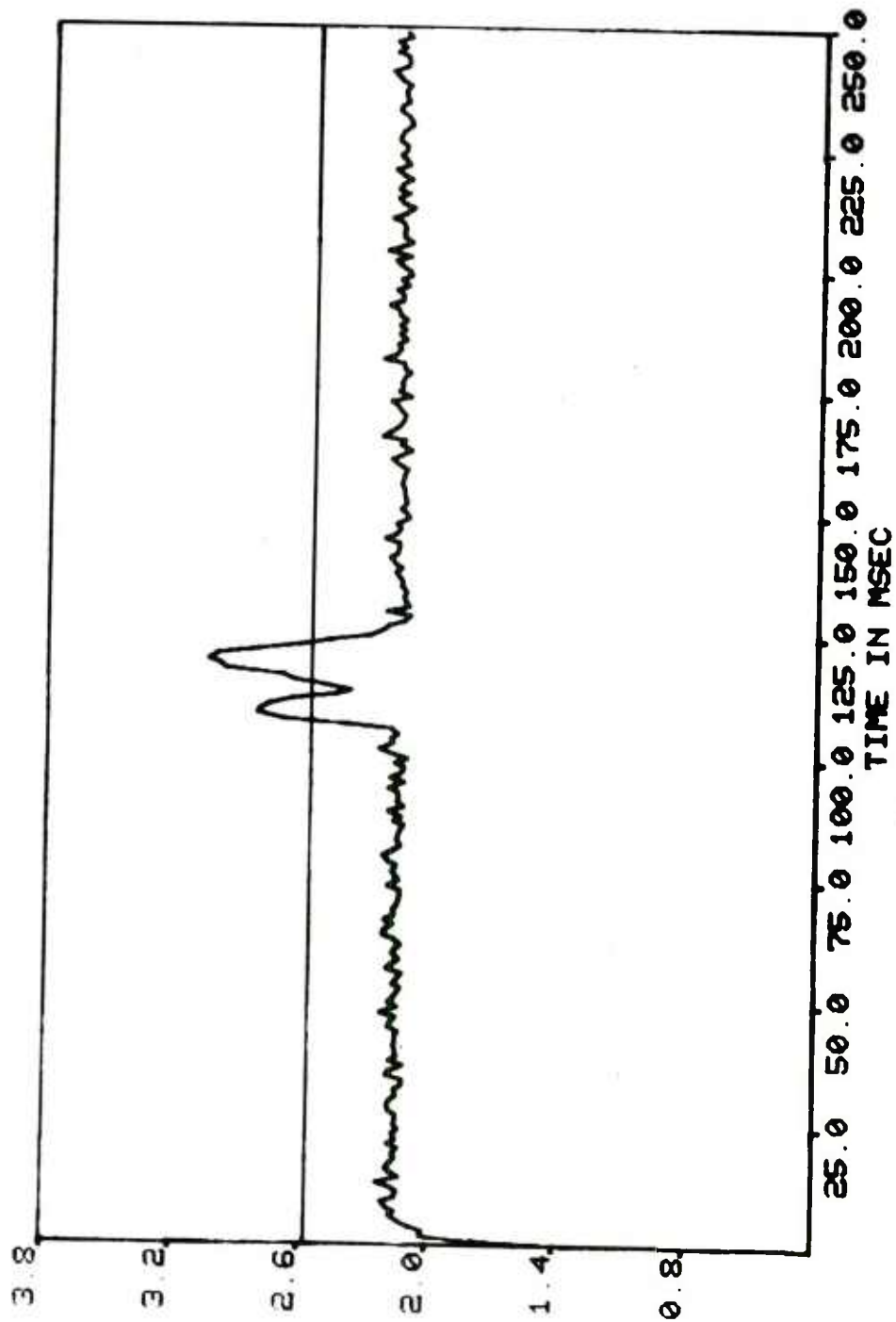


Figure 5. Fuze Integrator Output (Line at 2.6 Volts is Firing Threshold).

Integrator Output in Volts

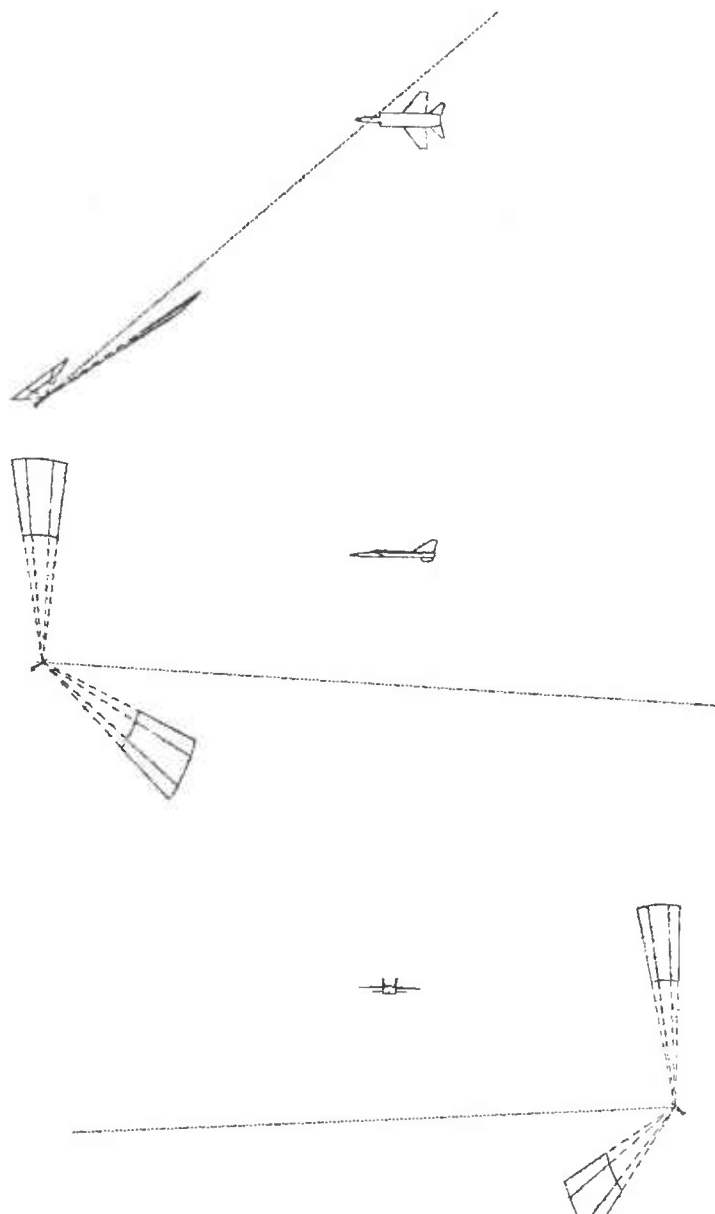


Figure 6. Encounter Simulation Still: MiG-25 Target, Missile and Antenna Pattern

upper portion of the figure is a top view of the target, the middle portion is a side view, and the lower portion is a front view.

The target is stationary on the screen. The missile moves past the target along the relative velocity vector (shown as a dotted line). Although the antenna pattern is a three-dimensional figure, only one plane through it is drawn—the plane that goes through the missile axis and the first point on the target to be intersected. This approach is designed to make the first intersection of antenna pattern and target as clear as possible, since the fuze should function at approximately this point. The inner "box" is the cell formed by the range gate and the -3 dB points of the pattern. The outer box is formed by the range gate and the -10 dB antenna points.

When the operator wishes, he can put on the screen either the instantaneous spectrum of the return signal (like a single curve in figure 3), or the fuze integrator output (as shown in figure 5). Figure 7, another still taken at the time of fuze functioning, shows these options. The upper part of the figure is the side view of the target, the middle part is the instantaneous spectrum, and the lower part is the integrator output. Here the integrator output is plotted from the beginning of the encounter to the instant shown. The output has just risen above the threshold (dotted line), indicating that the fuze has functioned.

Another interest of the fuze design is to optimize the delay time from fuze function to warhead detonation to cause maximum damage to the target. This is a particularly difficult problem when the warhead fragments are focused into the narrow beam. The encounter simulation can be used to gain insight into this problem by seeing how the fragments hit the target. Figure 8 shows a focused fragment pattern at the time when it strikes the target. A simple model for the vulnerable area of the target, two crossed lines in the center of the aircraft, was used. The vulnerable area is shown with a dotted line, and the star indicates where the vulnerable line was hit. Fragment densities and velocities, hit angles, and other pertinent information about the hit are available from the program.

## CONCLUSION

We have described a general technique for analysis of air target encounters. The technique allows a considerably more sophisticated approach to this problem than has heretofore been available. The computer system has the capability of analyzing target signatures, simulating various fuze circuits, and integrating the results



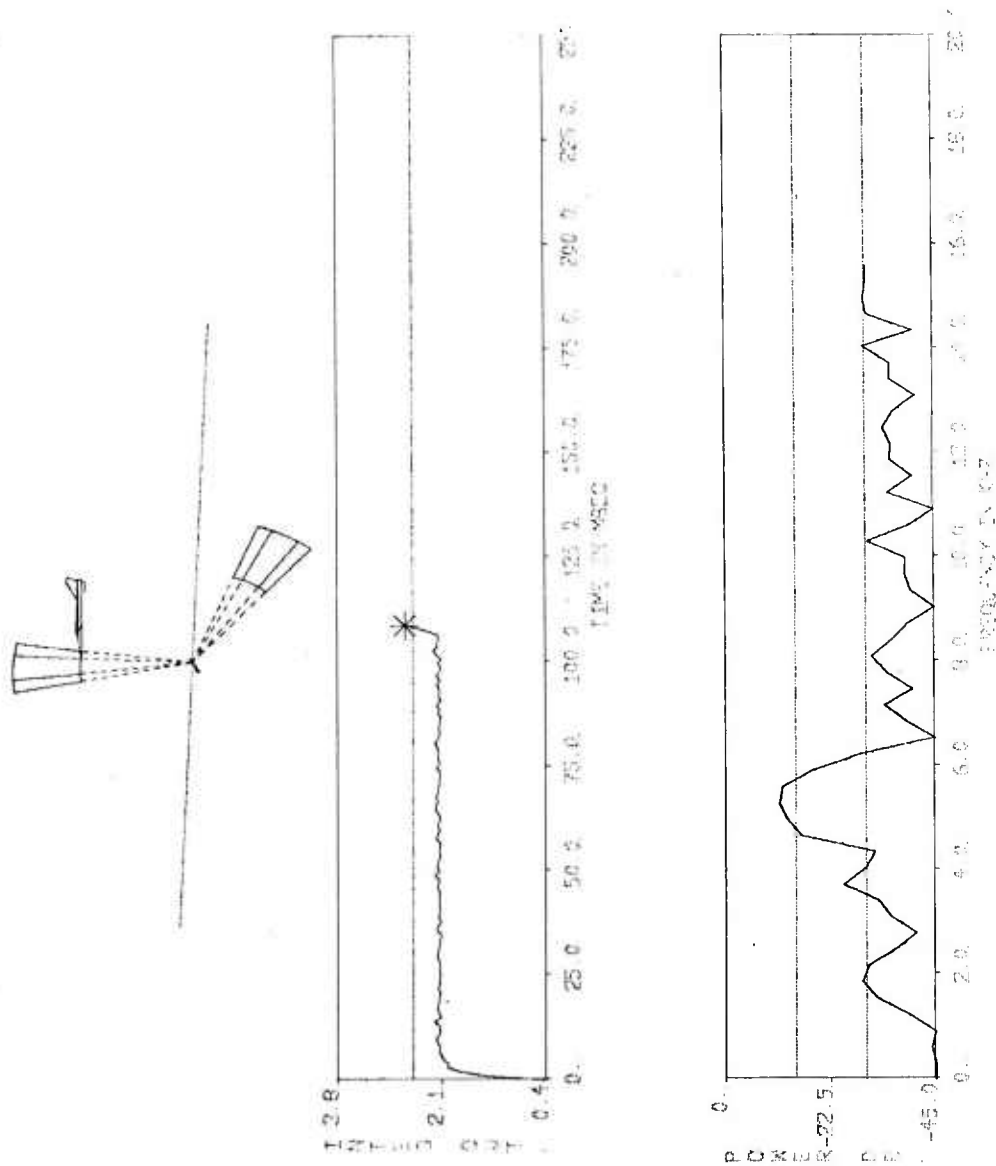


Figure 7. Encounter Simulation Still: Side View of Encounter with  
Fuze Integrator Output and Instantaneous Doppler Spectrum.

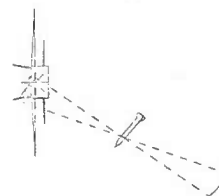
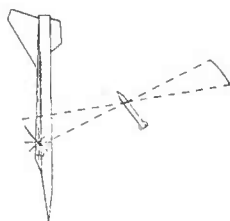
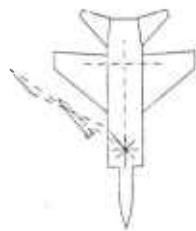


Figure 8. Encounter Simulation Still: Fragment Pattern Fitting Target.

DAMMANN

with a visual display of the encounter geometry. Target spectra are being used to develop a target scattering model for fuzes with wide antenna beams. Fuze doppler processors are also being simulated to test their performance and optimize their circuits. .

#### ACKNOWLEDGEMENT

The author wishes to recognize Dennis Cook, who assembled the computer system, and Steven Choy, who wrote much of the computer graphics package.



UNIQUE MATERIALS AND PROPERTIES IN THE NEW  
HIGH PRESSURE-TEMPERATURE REGIME ABOVE 250 KBARS

THOMAS E. DAVIDSON, PHD, DAVID P. KENDALL, Mr.,  
CLARKE G. HOMAN, Mr., JULIUS FRANKEL, Mr., FREDERICK J. RICH, 1LT  
BENET WEAPONS LABORATORY  
WATERVLIET ARSENAL  
WATERVLIET, NEW YORK 12189

INTRODUCTION

Since the early 1900's high pressure research and technology has been a field of active interest. Starting with the use of high pressure by the geophysicists to reproduce the conditions existing in the earth's crust, it has advanced to formulating the basis for such industries as the synthesis of artificial diamonds, polyethylene, and superhard materials. Over the years much has been learned about materials behavior up to 250 kbars which has been considered the upper limit of attainable static pressure.

Based on the theoretical predictions of new and potentially important pressure induced phenomena, much interest has recently been developed in the pressure regime well above 250 kbars. One example is the metallic state of hydrogen which is predicted to occur in the pressure range of 400-1500 kbar. The technological importance of such a material is that it may be metastable and superconducting to much higher temperatures than attainable through available technology. A high temperature superconducting material would have far reaching impact on military as well as commercial electrical energy generation, distribution and conservation.

To extend the range of attainable high pressure by a factor of 2 to 6, to generate these pressures at cryogenic temperatures, which will be required to study the synthesis of superconducting materials and to perform meaningful experiments and measurements under such

environments, represent formidable technological barriers. This paper describes the overcoming of these barriers and entry into this new high pressure regime.

In order to attain higher pressures and simultaneously accomodate a much larger sample size than possible with prior techniques, a new design concept has been developed by the authors. This new pressure generation system has been tested to in excess of 400 kbars and, with some modification in anvil material and support, has the potential of achieving 1000 kbars. It has been successfully coupled with a cryogenic capability to 10°K.

To gain as much information as possible concerning the properties of materials at these high pressures, new measurement techniques have been developed and combined with resistometric methods. The importance of the new techniques, one of which is ultra-sonic (sound velocity) and the other dielectric measurement, is that they enable the development of equation of state for materials which can be used to enhance the reliability of theoretical predictions of new phenomena.

Exploitation of this new high pressure regime is just beginning. However, important new phenomena have already been discovered. This includes two new phases in bismuth, one of which may be superconducting at high temperature, and new high conductivity phases in NaCl and GaP.

### Pressure Generation

Entry into the pressure regime above 250 kbars required a drastic new concept in pressure generation. The goal established was a system to initially achieve pressures of 400-500 kbars with a capability, through new component materials and staging, of reaching 1000 kbars, and a minimum sample volume of  $1 \times 10^{-2}$  cc as compared to the  $10^{-6}$  in prior systems. The new concept developed is based on the principle of providing variable lateral support to a "Bridgeman anvil" pressure device.<sup>(1)</sup> This system is shown in Figure 1 and incorporates three unique features.

(1) A solid "die ring" is placed in the region between the angled faces of the anvils. This permits more control of the effective compressibility of the anvil support material than can be obtained using pyrophyllite alone, as had been done in the past. It also permits variation of the pressure distribution in this region by shaping the space between the anvil and the die ring.



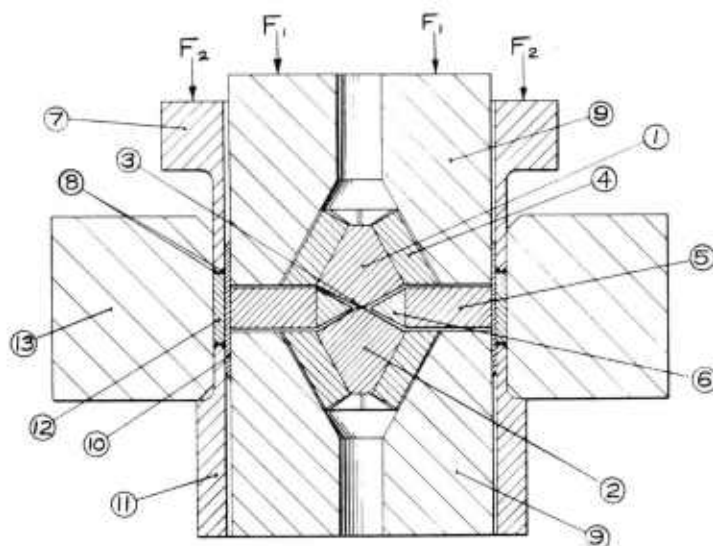


Figure 1. Variable Lateral Support, Bridgeman Anvil Device-Sectional View. 1&2 Anvils, 3-Specimen, 4-Segmented Anvil Supports, 5-Segmented Die Ring Support, 6-Die Ring, 7&11-Support Pressure Pistons, 8-Seal Rings, 9-Anvil Holders, 10-Beryllium Copper Sleeve, 12-Indium Ring, 13-Support Pressure Container.

(2) An independently controlled segmented die ring support system provides for adjustment of the stress state and displacements of the die ring and thus permits adjustment of the anvil support pressure.

(3) A segmented, tapered anvil support system which transmits the applied force to the anvils. This method of force application increases the hydrostatic compressive stress condition in the anvils and permits application of the very large forces required without the need for making the anvils excessively large to prevent their compressive failure. This system also provides direct access to the rear face of the anvils for the attachment of various types of transducers or other instrumentation.

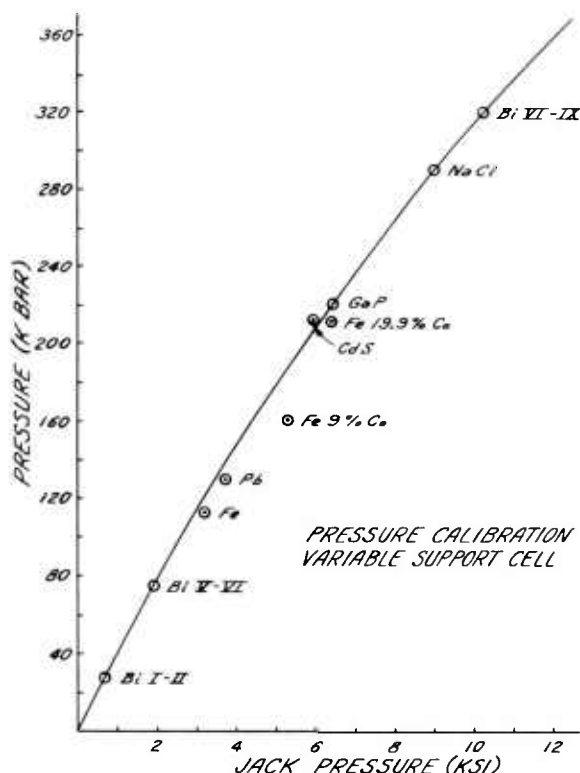
This device is utilized with a tandem hydraulic press. It consists of an upper main jack having a force capacity of 10.7 MN (1200 tons). This provides the force to the anvils through the maraging steel anvil holders and the segmented anvil supports.

A secondary jack of 4.45 MN (500 ton) capacity acts through a sub-press assembly and exerts a force on the annular piston that surrounds the upper anvil holder. This generates an essentially hydrostatic pressure in an indium ring. This pressure which can be as much as 14 kbars (1400 MPa), is contained by the autofrettaged, maraging steel outer ring. It is transmitted through the beryllium copper sleeve to the segmented die ring supports which intensifies the pressure by a factor of 3 and thus provides the variable lateral support of the die ring.

Electrical insulation of the anvils and the die ring is provided by a 0.76mm-thick layer of glass epoxy composite material between the segmented anvil supports and the anvil holders, and between the segmented die ring support and the beryllium copper sleeve.

The anvil pressure face diameter is 0.43 cm. With the sample height of 0.11 cm, the working volume is  $1.5 \times 10^{-2}$  cc.

The calibration of the pressure cell was accomplished using the well established resistance transitions in bismuth, iron and lead. The pressures for these transitions were obtained from Drickamer's<sup>(2)</sup> revised pressure scale published in 1970, i.e. bismuth, 74 kbars; iron, 112 kbars; and lead, 130 kbars. Additional calibration points were obtained from iron-cobalt alloys generously provided by Bundy. The transition pressures for the 10 and 20% cobalt alloys were obtained as follows: The original Bundy data<sup>(3)</sup> were approximated as a linear function of percent cobalt. This gave values of 205 and 280 kbars for the transition pressures of these two alloys according to the old pressure scale. Using the relationship between the old and new scale given by Drickamer,<sup>(2)</sup> these values were adjusted to 160 and 212 kbars, respectively.



Using the above, a calibration curve shown in Figure 2, was established (solid line) based on the least square fit of the data to an equation of the form:

$$Y = A \ln (Bx+1)$$

Extrapolation of this curve to the maximum jack pressure shows that pressures in excess of 400 kbars have been achieved in this pressure system. Also shown on the curve are three new transitions discovered by the

Figure 2. Pressure Calibration Curve Showing Phase Transitions

authors which will be subsequently discussed.

To increase the pressure level, polycrystalline diamond is being substituted for the tungsten carbide anvil material and multiple staging applied. A recent reported result<sup>(4)</sup> is that pressures exceeding 500 kbars have been achieved in a diamond anvil device with a sample volume of  $10^{-6}$  cubic cm. Thus, substitution of the polycrystalline diamond for the tungsten carbide should result in a considerable increase in the pressure limit.

### Cryogenics

In order to investigate the synthesis of new superconducting

phases, one must have the capability of producing ultra-high pressures at very low temperatures, the goal being 10°K. This has been accomplished by placing the pressure cell within a unique, full containment dewar, as shown in Figure 3.

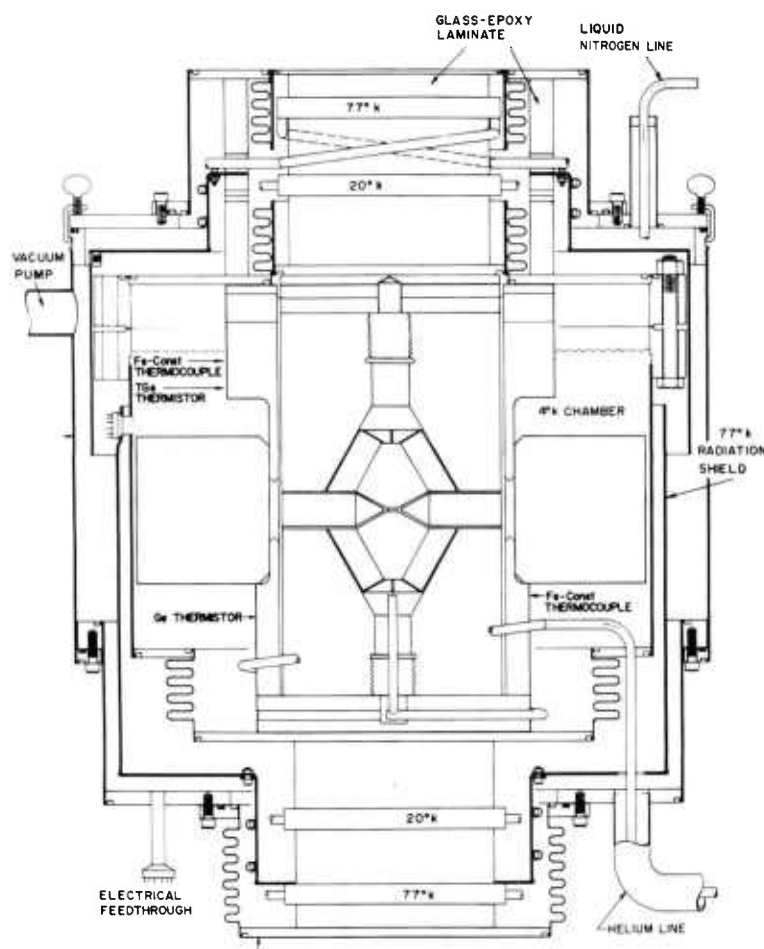


Figure 3. Cryogenic Dewar and Pressure Cell

This dewar was designed to sustain the heat loads due to conduction through the structures which transmit the required forces to the pressure cell and to be compatible with a helium liquifier in a closed loop configuration. This was achieved using liquid nitrogen (LN<sub>2</sub>) shielding, glass fiber laminate insulators,

and a 20°K gaseous He cooling stream from the liquifier, in addition to the 4.2°K liquid main coolant stream. The dewar loss is less than the 50 watts of cooling available at 4.5°K from the refrigerator. The coupled system has been successfully tested to 10°K.

### Measurement Techniques

To gain maximum information concerning the properties of materials under these pressures, three measurement techniques have been developed for use. Resistance measurement has long been used in the high pressure research field but lacks the capability of supplying information other than conductivity. To gain insight into other properties and, in particular, equation of state information, two new techniques consisting of ultrasonics (sound wave) and dielectric measurements have been developed by the authors. Each of these techniques will be discussed separately.

#### Resistance

Specimen resistance is measured by passing a known DC current through the anvil and specimen. The voltage drop across the anvils is measured to determine the total resistance of the anvils and samples. The anvil resistance is then subtracted from the total to obtain the specimen resistance. If one is interested in detecting phase transitions involving a change in electrical conductivity, resistance measurement, as described, is a reliable and relatively simple technique. Those transitions shown in Figure 2 were measured using this technique.

#### Ultrasonics

In many materials, one example being hydrogen, it is important to measure compressibility from which equation of state information can be generated. Such information is of considerable practical interest. First, it can be combined with theoretical analysis as a means of more accurately predicting transition pressures. Second, knowing compressibility as a function of pressure permits predictions of possible new phenomena at some higher defined pressure.

In order to measure compressibility, an ultrasonic interference technique patterned after the earlier approach of Ahrens and Katz<sup>(5)</sup> has been developed for use at ultra-high pressures.

A schematic of this system is shown in Figure 4. High frequency sound waves are produced by the transducers mounted on the outer ends of the anvils. One transducer produces shear waves and the

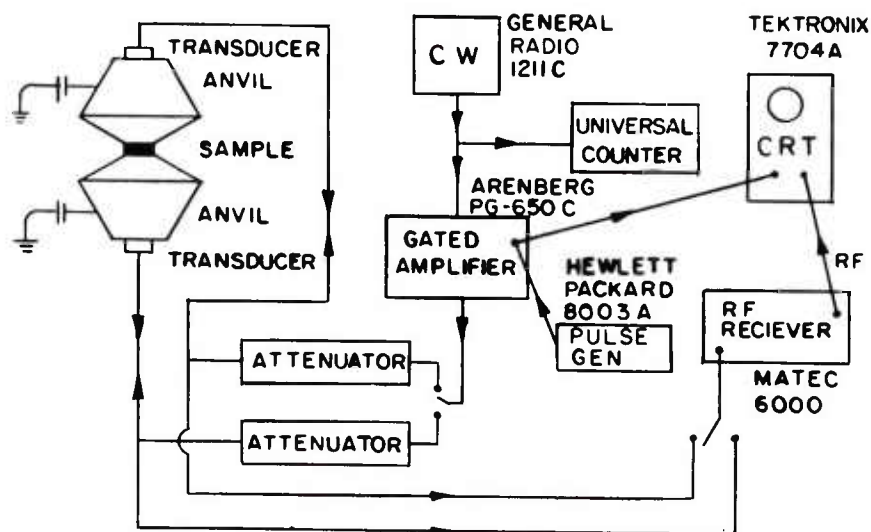


Figure 4. Ultrasonic Interference Measurement System

other longitudinal or compressional waves. A switch is used to alternate between the two acoustic modes. The transducer is excited to produce a short pulse of sound energy. Some of the energy reflects from the surface of the anvil in contact with the sample and some passes through the sample and is reflected from the interface between the sample and the other anvil. Both of these reflected waves are sensed by the original transducer. There are certain frequencies at which these two reflected waves are exactly out of phase which results in destructive interference of the sound energy and thus a minimum amplitude of the transducer output. The interval between the frequencies at which destructive interference is "tuned in" is a constant,  $\Delta f$ . This interval depends on the sample thickness, and elastic properties and the mode of acoustic waves used. The relation is:

$$\Delta f_p = v_p / 2d$$

and

$$\Delta f_s = v_s / 2d$$

"v" is the velocity of sound, "d" is the sample thickness, the subscripts "p" and "s" indicate the compressional and shear acoustic modes respectively. From these data, density ( $\rho$ ) as a function of pressure (P) is obtained from the relationship:



$$\frac{dP}{d\rho} = v_p^2 - \frac{4}{3} v_s^2$$

NaCl has been investigated with the ultrasonic apparatus up to pressures in excess of 300 kbars. Due to scattering of acoustic waves at pressures near the phase transition, the analysis of the ultrasonic data was terminated at 270 kbars. The data is in excellent agreement with other reports up to 100 kbars which is the highest pressure at which velocities in NaCl were previously measured. From 100 to 270 kbars, the velocity data is in good agreement with theoretical predictions of Anderson<sup>(6)</sup> as shown in Figure 5.

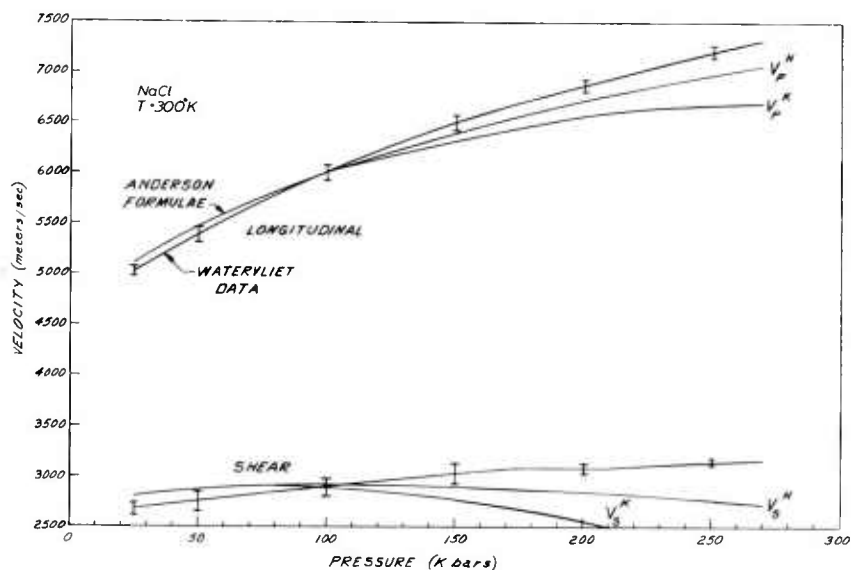


Figure 5. Acoustic Velocities for Longitudinal and Shear Waves as a Function of Pressure

The ultrasonic interference method also provides a direct measure of the Debye temperature of the solid sample through the following relation:

$$\theta_D^3 = 3.8 \cdot E^{-7} \frac{\rho_0 d_0^3}{A_0} \left( \frac{2}{\Delta f_s^3} + \frac{1}{\Delta f_p^3} \right)^{-1}$$

where  $\rho_0$  is the initial density and  $A_0$  is the sample area. This is quite useful in sample identification when the sample is introduced in situ. Good agreement has been found for the Debye temperature measured in this way for NaCl and Ar with reported values at LN<sub>2</sub> temperatures.



Dielectric

A dielectric measurement technique has been developed for sample materials that are essentially non-conductors. This consists of applying a high frequency AC voltage across the anvils in a capacitance bridge circuit. This circuit will provide a measure of the effective capacitance between the anvils. This capacitance includes that of the parallel plate capacitor formed by the two anvil faces and the sample. It also includes a number of stray parallel capacitances for which accurate compensation is difficult. Although this technique is not presently capable of making accurate measurements of dielectric constants, it can be very valuable in detecting certain types of phase transitions and as a means of approximating density ( $\rho$ ) as a function of pressure through the Claussis-Mossotti relationship:

$$\frac{\epsilon-1}{(\epsilon+2)\rho} = K$$

where K is a constant and  $\epsilon = \frac{d}{CA}$  wherein C is the capacitance and d and A the sample thickness and area respectively.

Results

Although entry into this new pressure regime is new, several phenomena have already been discovered that indicate the potential for many new and useful discoveries.

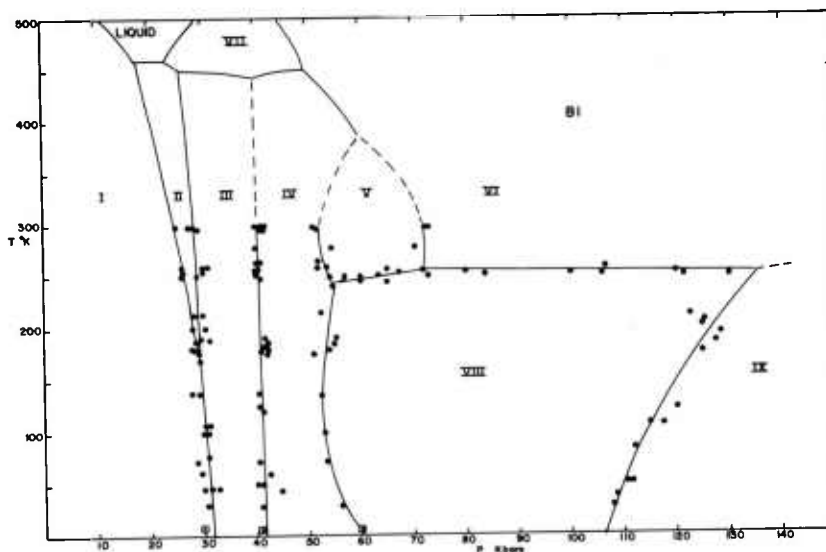


Figure 6. Pressure-Temperature Phase Diagram for Bismuth

Using the cryogenic dewar and cooling system previously described and the resistivity measuring instrumentation, the phase diagram for bismuth has been determined for pressures up to 140 kbars(7) The resultant P-T phase diagram is shown in Figure 6. It shows two previously unknown phases, designated VIII and IX. These both have very low resistance and particularly phase IX may be superconducting up to 200°K. The determination of whether these phases are actually superconducting must be made by Meisner effect measurements. Facilities for making such measurements are presently being developed.

Two additional points are important with respect to the P-T diagram developed. First, it provides several good low temperature pressure calibration points. These are very important for conducting low temperature experiments on condensed gases, wherein room temperature calibration may be greatly in error. Second, phase line extending from the VI-VIII-IX triple point indicates that there should be a transition from phase VI to phase IX at room temperature (300°K) and at a pressure greater than 150 kbars depending upon the slope of the phase line.

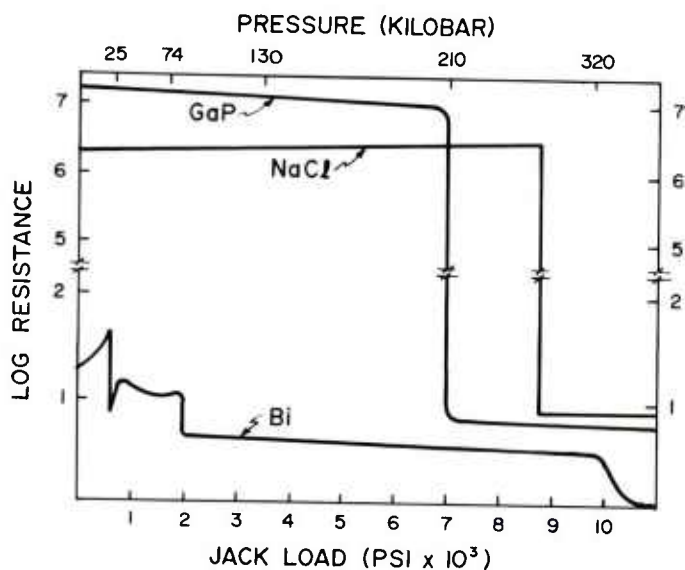


Figure 7. Resistance versus Pressure at 300°K for Gallium Phosphide, Sodium Chloride and Bismuth

Figure 7 shows a plot of resistance as a function of jack load and pressure at ambient temperature. It shows three new high pressure transitions discovered in this current work; a transition being indicated by an abrupt change in resistance over a narrow pressure range. In the case of the three materials studied, all have different electronic properties at atmospheric pressure.

Bismuth is a relatively high resistance semi-metal at atmospheric pressure. At room temperature, it undergoes a number of phase changes as a function of pressure. The transitions up to 72 kbars have been known for many years and commonly used for calibration purposes. The discontinuity at 320 kbars<sup>(8)</sup> is the new VI-IX transition predicted to occur from the phase level of the P-T diagram shown in Figure 6. The transition is quite abrupt; the resistance decreasing to a value less than that of copper at room temperature.

Gallium Phosphide (GaP) is normally a semi-conductor. According to the Van Vechten-Phillips dielectric theory of electronegativity in covalent systems, it was predicted to transform to a metallic phase at 216 kbars.<sup>(9)</sup> As can be seen in Figure 6, a transition was found at a pressure (220 kbars)<sup>(10)</sup> which corresponds quite closely with prediction. The resistance of the high pressure phase indicates that it may actually be a semi-metal.

Sodium Chloride (NaCl) is an ionic conductor at atmospheric pressure. A transition was found in this material at about 290 kbars, wherein it converted to a relatively low resistance phase which may be a superionic conductor or a semi-metal.

These phase transitions measured by the resistance technique were shown in Figure 2. These provide a very useful pressure calibration scale up to 320 kbars, and give credence to having attained pressures in excess of 400 kbars.

Based on the results thus far, particularly in terms of the new transitions, comparison can be made with the work and claims of others. Vereshchagin et al (Russia) and Kawai et al (Japan) have claimed the achievement of pressures in the range of 700-1000 kbars or greater. If one compares the transition pressures used in the calibration of their equipment and, in particular, their recent reproduction of two of the new transitions discussed above (NaCl and GaP) an interesting picture emerges. This can be seen in the following:

	<u>Vereshchagin</u> <sup>(11)</sup>	<u>Kawai et al</u> <sup>(12)</sup>	<u>Present Authors</u>
Claimed max pressure(kbars)	1000	700	450
NaCl transition pressure(kbars)	750		290
GaP transition pressure(kbars)		500	216
Bismuth VI-IX transition pressure(kbars)	-	-	320
Corrected max pressure(kbars)	~400	~250	~450

By factoring the claimed maximum pressure by the ratio of the reported transition pressures to those measured by the authors results in what is likely a better estimate of the maximum pressures achieved. It is important to note that Kawai was not able to observe the Bi VI-IX transition<sup>(13)</sup> which further substantiates the estimate of corrected maximum pressure. Vereshchagin et al have not reported attempts or results to reproduce this transition.

### Conclusions

(1) A new concept for generating static high pressures has resulted in the achievement of pressures exceeding 400 kbars with a sample volume of  $1.5 \times 10^{-2}$  cc. Substitution of diamond for tungsten carbide anvils and multiple staging should increase the attainable pressures to near 1000 kbars.

(2) The developed pressure system has been successfully coupled with a cryogenic capability to 10°K.

(3) An ultrasonic measurement technique has been developed for use at high pressure which by measuring shear and longitudinal velocity, yields density as a function of pressure. Also, a dielectric system has been developed for detecting of transitions and measurement of density.

(4) The P-T diagram for bismuth has been developed to 140 kbars with the discovery of two new phases, one of which may be superconducting to high temperature.

(5) New electronic transitions at room temperature have been discovered in GaP (216 kbars), NaCl (290 kbars), and Bi VI-IX (320 kbars). In the latter, the resistivity is less than that of copper.

References

1. D. P. Kendall, P. V. Dembowski and T. E. Davidson, Rev. Sci Instrm 48, 629 (1975).
2. H. G. Drickamer, Rev. Sci. Instrum, 41, 1667 (1970).
3. F. P. Bundy, J. Appl. Phys. 38, 2446 (1967).
4. G. J. Piermarini and S. Block, Rev. Sci. Instrum, 46, 973 (1975).
5. T. J. Ahrens and S. Katz, J. Geophys. Res. 67, 2935 (1962).
6. O. L. Anderson and H. H. Demarest, J. Geophys. Res. 76, 1349 (1971).
7. C. G. Homan, J. Phys. Chem. Solids, 36, 1249 (1975).
8. C. G. Homan, T. E. Davidson and D. P. Kendall, Appl. Phys. Letters, 26, 615 (1975).
9. J. A. Van Vechten, Phys. Rev. B7, 1479 (1973).
10. C. G. Homan, D. P. Kendall, T. E. Davidson and J. Frankel, Solid State Commun., 17, 831 (1975).
11. L. F. Vereshchagin, E. N. Yakovlev, B. V. Vinogradov, and V. P. Sakun, JETP Letters, 20, 246 (1974).
12. A. A. Onodera, N. Kawai, K. Ishizaki and I. Spain, Solid State Commun. 14, 803 (1974).
13. N. Kawai, The Accurate Characterization of the High Pressure Environment Edited by E. C. Lloyd, p48, NBS Special Publication 326 (1971).





EFFECTS OF LOW-YIELD NUCLEAR WARHEADS  
ON AIRFIELD RUNWAYS (U)

MR. LANDON K. DAVIS  
U. S. ARMY ENGINEER WATERWAYS EXPERIMENT STATION  
VICKSBURG, MISSISSIPPI

Recent changes in the Army's nuclear weapon employment doctrine have placed significant constraints upon the use of such weapons in the tactical theatre. One of the most important of these constraints requires that nuclear strikes against tactical targets be performed in such a manner that undesirable collateral effects, such as casualty-producing fallout, airblast, or thermal effects, be minimized to the greatest possible extent consistent with the mission objectives. The development of an earth-penetrating warhead, together with a missile system capable of delivering such a warhead with extreme accuracy, has been envisioned as a means of meeting these constraints while providing the Army with a new flexibility in the tactical theatre.

A recently-completed study at the Waterways Experiment Station (WES) was designed to evaluate the effectiveness of an earth-penetrating nuclear warhead employed against airfields, which is one of the most important target categories for tactical nuclear attack. The objective of this study was to define damage to airfield runways as a function of warhead yield, burst position, target characteristics, and geological environment. Existing Army manuals stated that damage to runways should extend over a distance equal to 1.5 times the apparent crater diameter. At the onset of this study, it was felt that this estimate was grossly conservative; that effective damage to a runway by a buried nuclear burst might, in fact, be more than twice as extensive.

It was hypothesized that four major zones of damage would be produced in a runway, with the severity of damage decreasing with

distance from the burst location. These damage zones are illustrated in Figure 1. The most obviously severe damage would be represented by the nuclear crater itself. In the second zone of damage would be permanent upheaval and disruption of the pavement around the crater. The third zone of damage was expected to consist of isolated areas of pavement displaced by the intense ground shock, or damaged by the impact of pavement debris thrown out during the crater formation. These three zones would all require reconstruction before resuming flight operations, and therefore represent relatively long-term denial of the runway.

The fourth damage zone is the runway area covered by debris thrown from the crater. Since aircraft operations could be resumed after the debris is removed, this zone represents an area of short-term denial. Basic objectives of the study were to determine how far these damage zones would extend from the burst point, and to determine the relative severity of damage that would control the extent of effort and time required to repair these areas for a resumption of aircraft operations.

The research approach for this program was largely experimental in nature. Three phases of tests were conducted in which modeled sections of runway pavements were subjected to the blast and shock effects of scaled buried explosions. To demonstrate first the potential effectiveness of a deeply buried, tactical-yield, nuclear burst against a runway, the initial test phase involved the construction of an 85-metre long, 6-metre wide model section of a cast-in-place, articulated concrete slab runway adjacent to a previously-planned high-explosive (HE) cratering test. This test, called the 12 MS event, was designed to simulate the effects of a very low-yield nuclear burst at a depth of 12 metres. The test was conducted at Fort Polk, Louisiana, in a clay-sand soil similar to soil types occurring in central Europe. The model runway was built to a scale of 1:3.7 so that the 10-ton (9,090-Kg) HE charge would model a 1-kiloton nuclear yield at a burst depth of about 40 metres.

Figure 2 is a photograph of an early stage in the 12 MS event detonation. As can be seen in the photo, the portion of the test runway overlying the crater was lifted by the explosion, with the pavement slabs near the center of the crater being separated and lofted over a hundred metres through the air. The section of runway lying over the outer portion of the cratered area was simply folded back about a hinge point located just outside the edge of the crater. The actual radius of the apparent crater was 18.5 metres. Records obtained from velocity gages located along the length of the runway

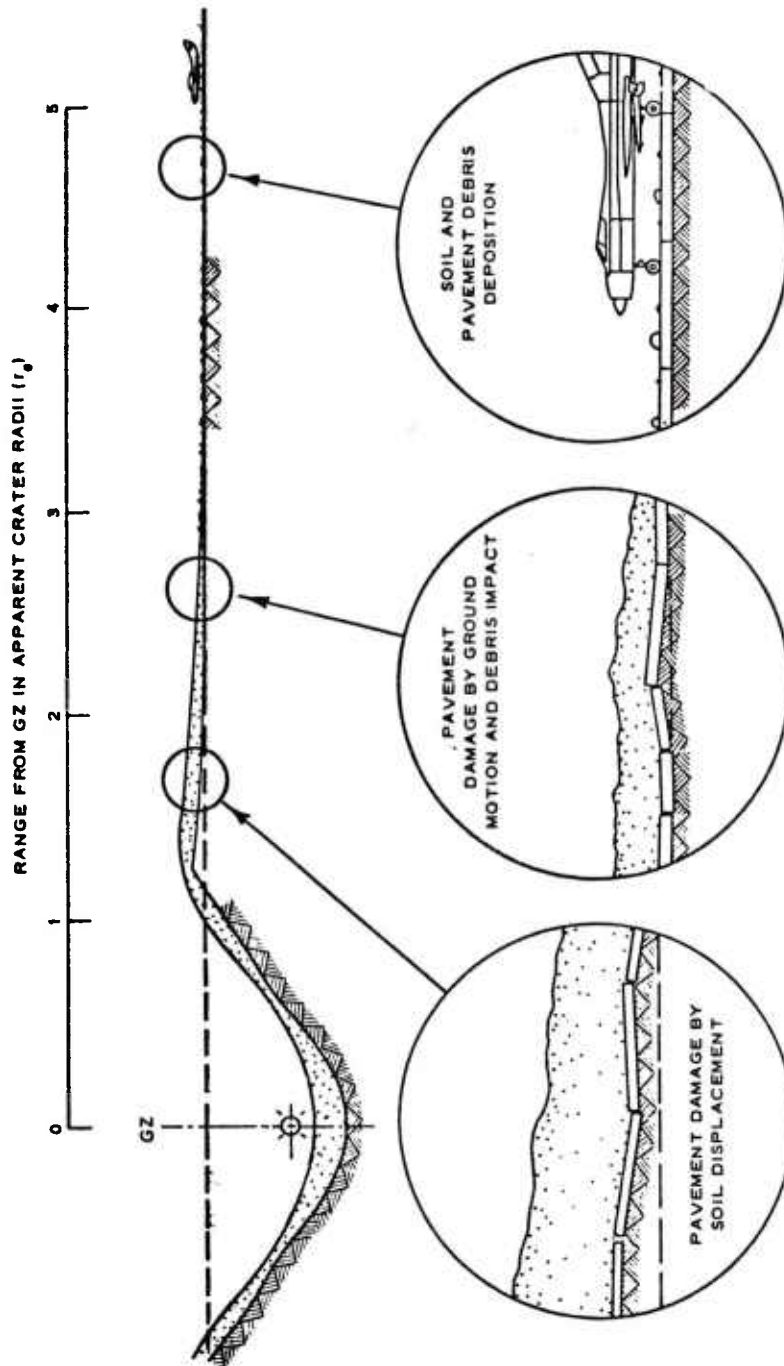


Figure 1. Illustration of zones and mechanisms of damage to a concrete slab runway from a buried nuclear explosion. Ranges and occurrences of zones were originally hypothesized for experiment planning only.

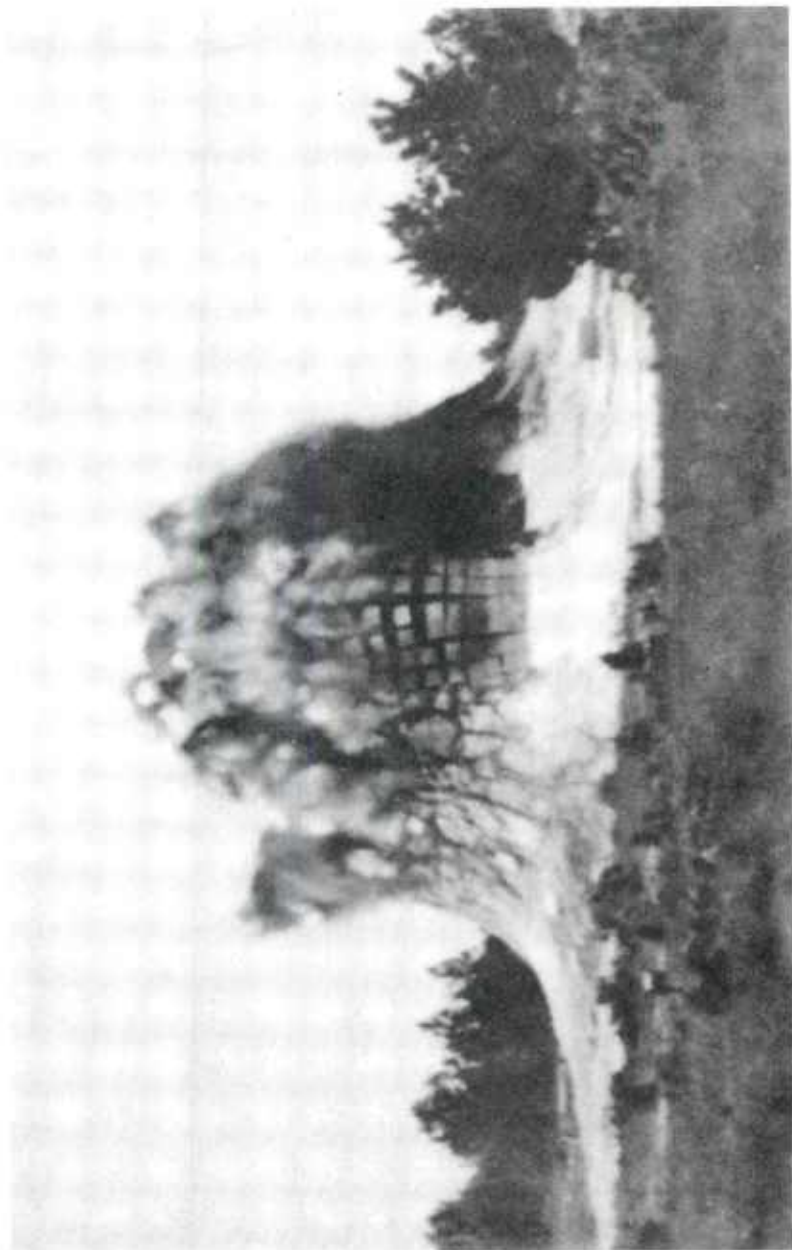


Figure 2. Early stage of venting of 12 MS event detonation, showing separation and lofting of runway pavement over crater area and initial upheaval of runway beyond crater edge.

showed that almost the entire length of the pavement was lifted momentarily to heights that decreased logarithmically from over 2 metres at the edge of the crater to a few centimetres at a range of 50 metres from the crater. The permanent vertical displacement of the runway was only slightly less than the peak transient displacement. Figure 3 shows the postshot profile of the runway beyond the edge of the crater (with an exaggeration in the vertical scale for clarity).

Severe permanent uplift of the runway and accompanying distortion of the pavement profile extended to a range of 50 metres from ground zero (GZ), or 2.7 times the apparent crater radius. The velocity gages installed in and below the model runway showed that the rigid pavement moved independently of the underlying soil, particularly in the horizontal direction. Relative peak displacements of the pavement and the soil base are shown in Figure 4. No evidence was found of damage to the runway from the ground shock.

Beyond the uplifted region, the pavement did sustain moderate to severe damage at isolated points from the impact of whole or large pieces of pavement debris thrown from the crater area. Figure 5(a) shows the location of crack damage in a plan view of the runway strip, and Figure 5(b) shows the areas of the pavement judged to be unusable for aircraft operations due to such debris impact damage.

The second phase of testing was designed to relate the extent of runway damage to runway pavement design and to the nuclear warhead burst depth. Four tests were conducted at Camp Shelby, Mississippi, in which 450-Kg HE charges were detonated at depths ranging from 0 to 7 metres. Four 1/12-scale model runway sections were constructed for each test, representing articulated concrete slab pavements, continuously reinforced concrete (CRC) pavements, asphalt pavements, and an expedient stabilized soil runway. Because of the small scale of these tests, it was felt that the results were not scalable to realistic weapon yields and full-scale runways. However, measurements obtained from the 1/12-scale tests provided a valuable indication of the relative changes in damage levels as a function of the weapon burst position and the pavement design.

The final experimental phase was a second large-scale test at Fort Polk, Louisiana, in which runway sections were again built to the 1:3.7 scale and subjected to the effects of a 10-ton HE detonation. In this test, called the 3 MS event, the charge was buried 3 metres deep, and four pavement designs were tested as in the 1/12-scale tests.

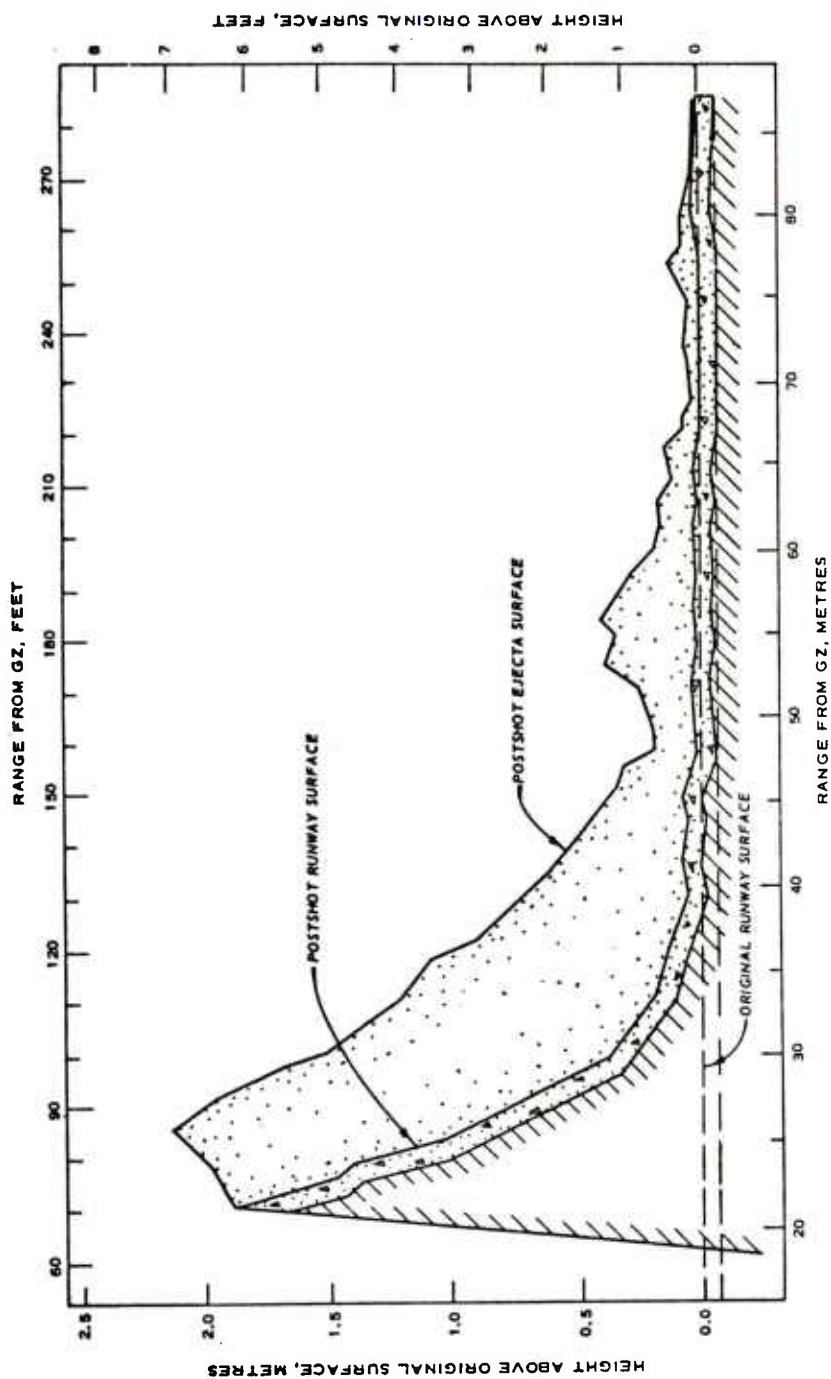


Figure 3. Profile of postshot runway from 12 MS event showing permanent vertical displacement and ejecta coverage depth. Vertical scale is exaggerated for clarity. Profile shown is average of centerline, right edge, and left edge profiles of runway.



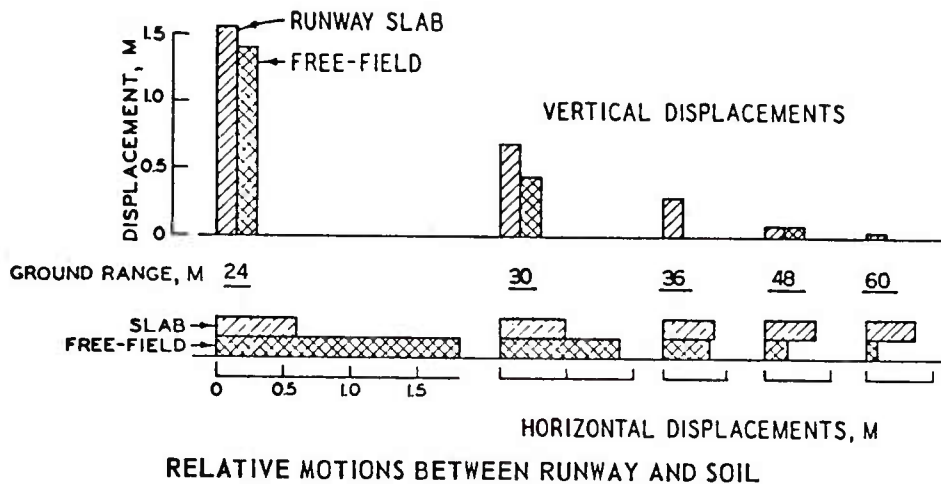


Figure 4. Comparison of relative peak transient displacements of runway versus underlying soil for 12 MS event.

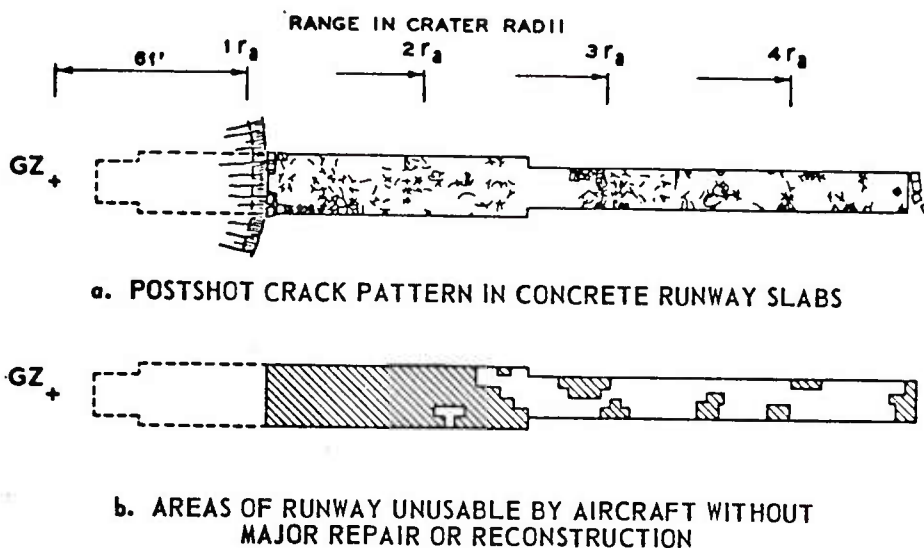


Figure 5. Distribution of crack damage in postshot runway surface, 12 MS event. Damage beyond  $2.7 r_a$  was due to impact of debris thrown from crater.

As predicted from the results of the 1/12-scale tests, damage to the runways from the 3 MS detonation was much less extensive than produced by the deeper 12 MS detonation. On the articulated concrete slab runway, upheaval damage near the crater extended only 16 metres beyond the crater edge, compared to 31.5 metres beyond the 12 MS crater. Damage to the CRC pavement was slightly more extensive. As expected, the asphalt and stabilized soil pavements were disrupted over significantly greater distances than were the concrete pavements.

Because of the shallow burst depth for the 3 MS event, the intense shock from the detonation shattered much more of the pavement overlying the crater area than occurred for the deeper 12 MS event. The pavement debris was also ejected at much higher velocities, so that the wide distribution of debris impact points around the crater resulted in a low areal density of debris impacts. Consequently, there was little impact damage to the pavements.

Figure 6 is a graph relating the radial extent of upheaval damage in the various pavement designs to the explosion depth of burst. All dimensions are normalized by dividing the damage radii, measured from GZ, by the  $1/3.4^{\text{th}}$  power of the explosive charge weight. As mentioned previously, the 1/12-scale data were not intended to scale, but to reveal the relative differences in damage radii for different pavement types and depths of burst. In this respect, the small-scale test data served to better define the slopes of the damage curves for the larger scale test data.

In applying these HE test results to predictions for nuclear bursts, an additional problem stems from the fact that HE/nuclear explosive (NE) equivalence factors change drastically as the burst point approaches the ground surface. For scaled burst depths greater than about 15 metres/ $KT^{1/3.4}$ , an HE detonation produces blast effects equivalent to an NE detonation of roughly twice the yield, i.e., a 20-ton HE detonation would simulate a 40-ton NE detonation. For shallower bursts, the early venting of the explosion results in a loss of radiant energy that would otherwise contribute to cratering and ground shock effects.

An examination of existing NE and large-scale HE test data indicates that the upheaval of the ground surface around a crater is a constant function of the apparent crater size for a given scaled burst depth in a given type of soil. Since the runway damage radii reported here result from such upheaval, an HE/NE damage equivalency was empirically developed from a comparison of HE and NE crater radii and surface displacements (i.e., upheaval) from detonations at

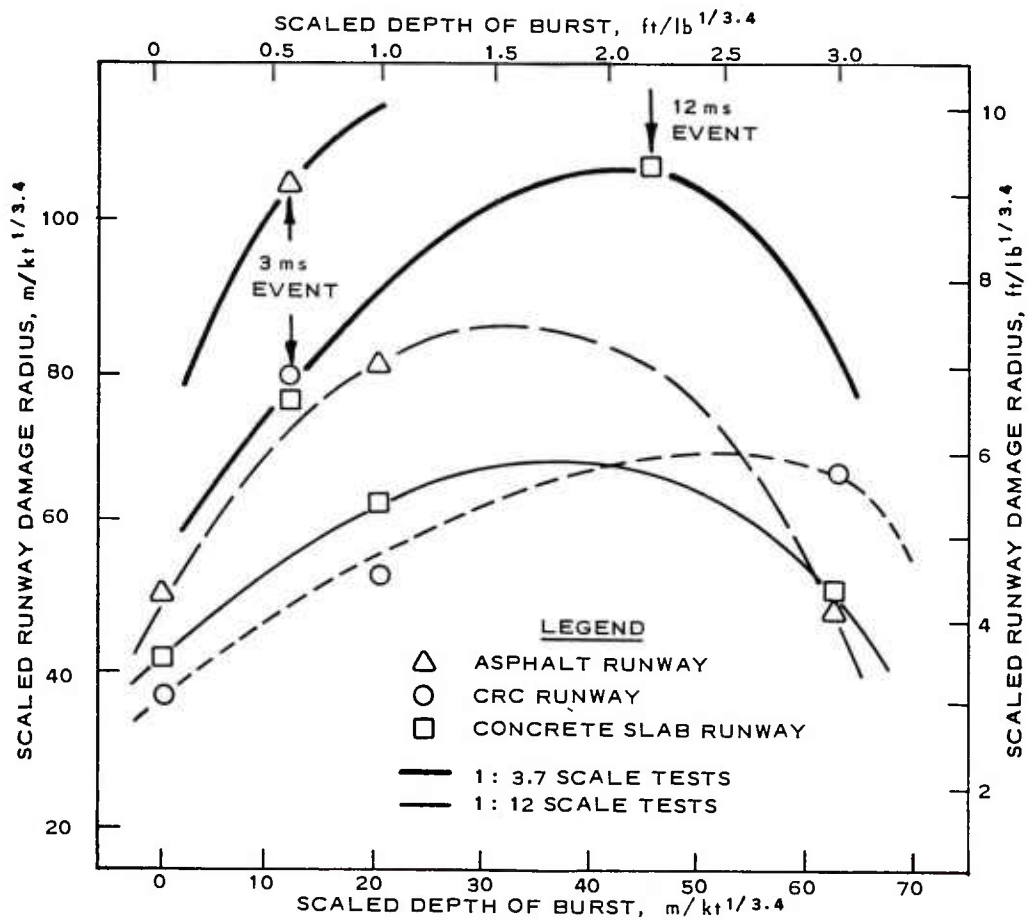


Figure 6. Scaled runway damage radius versus scaled depth of burst, as measured in model runways subjected to high-explosive tests. Radii shown are for pavement damage from upheaval only.

DAVIS

various shallow depths in various geologies.

Using these empirically-derived HE/NE equivalence factors, a final set of damage curves was developed to predict runway damage radii as a function of nuclear yield and burst depth in a sandy-clay geology. Figure 7 shows the scaled damage radii for the concrete slab runway, both in terms of scaled radius from GZ and in multiples of apparent crater radii. The damage radius for a nuclear surface burst is roughly twice the crater radius, compared to almost three times the crater radius for a deep burst. The actual radius of damage for a deeply buried burst is 2.2 times that for a surface burst. This implies that a nuclear surface burst requires 15 times the yield of a deeply buried nuclear burst to produce an equivalent amount of runway damage.

Again, the runway damage discussed here is that resulting solely from upheaval of the ground surface around the crater. A deeply buried burst will also produce additional damage beyond the upheaval region by the ejection and impact of pavement debris. There are not sufficient quantitative data available to state definitely the denial value of such "bonus" damage. However, the impact of a 5- to 20-ton slab of concrete falling on a concrete pavement from a height of a hundred metres or more should produce sufficient damage to prevent an aircraft from taking off across the impact area.

Figure 8 shows the damage areas in a concrete runway from a nominal 1-kiloton nuclear burst. Figure 8(a) shows the damage area from a buried burst, as predicted from Army manuals prior to this study. Figure 8(b) shows the revised predictions for a deeply buried burst based on the results of the study, and Figure 8(c) shows similar predictions of damage for a 1-kiloton surface burst.

In conclusion, the results of this research program have shown that tactical earth-penetrating warheads are, by conservative estimate, almost twice as effective in runway area denial as was previously assumed. If debris impact damage is also considered, the damaged runway length will be three times as great as previous data indicated, and the total airfield damage area, including sod strips adjacent to the runway, will be nine times as great. From a weapons effectiveness standpoint, tactical earth-penetrating warheads appear to offer the Army a viable means of selective destruction or denial of enemy airfields, while greatly reducing the collateral damage associated with the present air-burst warhead system.

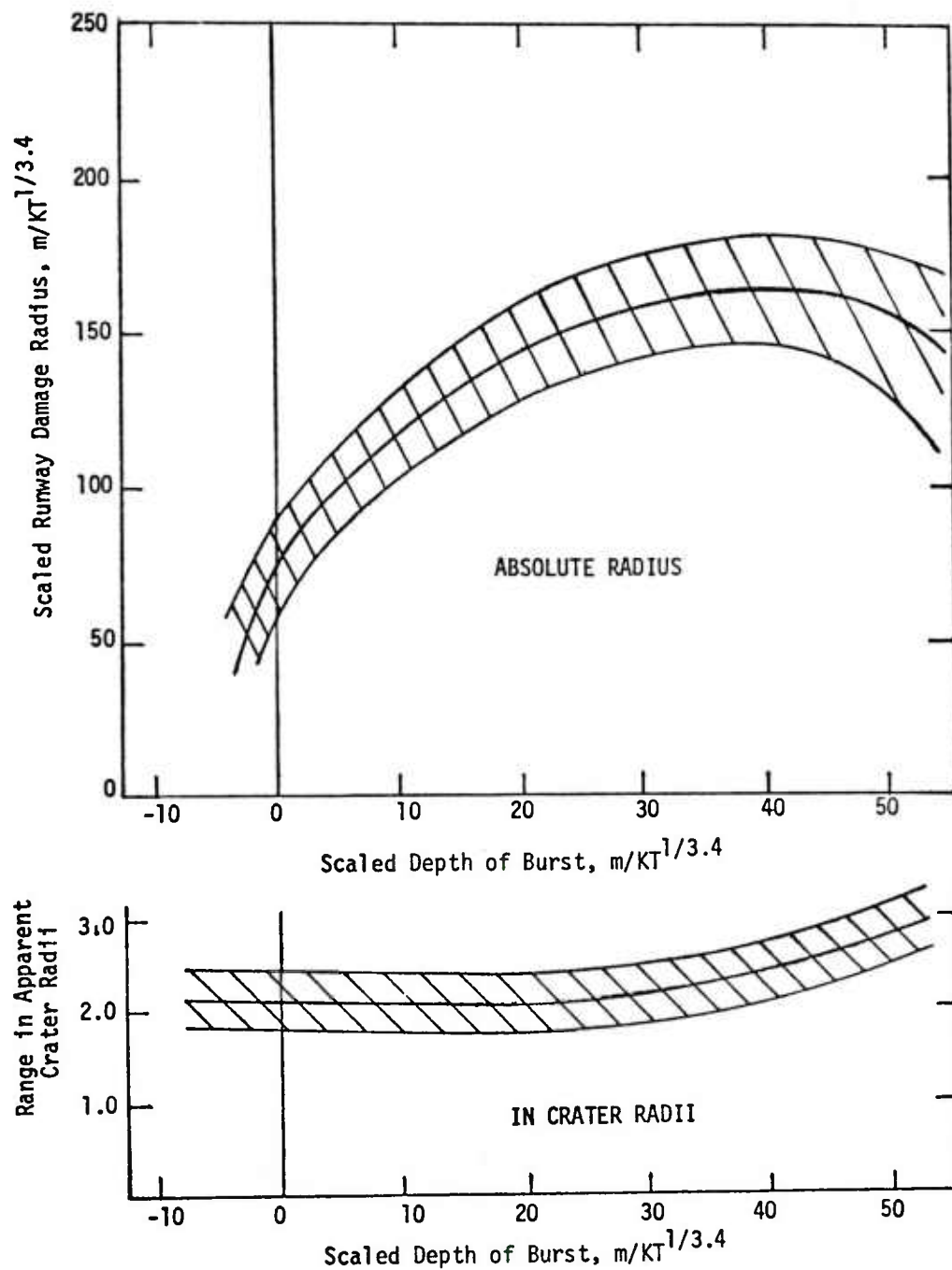


Figure 7. Scaled damage radius in a concrete slab runway pavement for tactical-yield nuclear detonations in moist sandy-clay geologies.

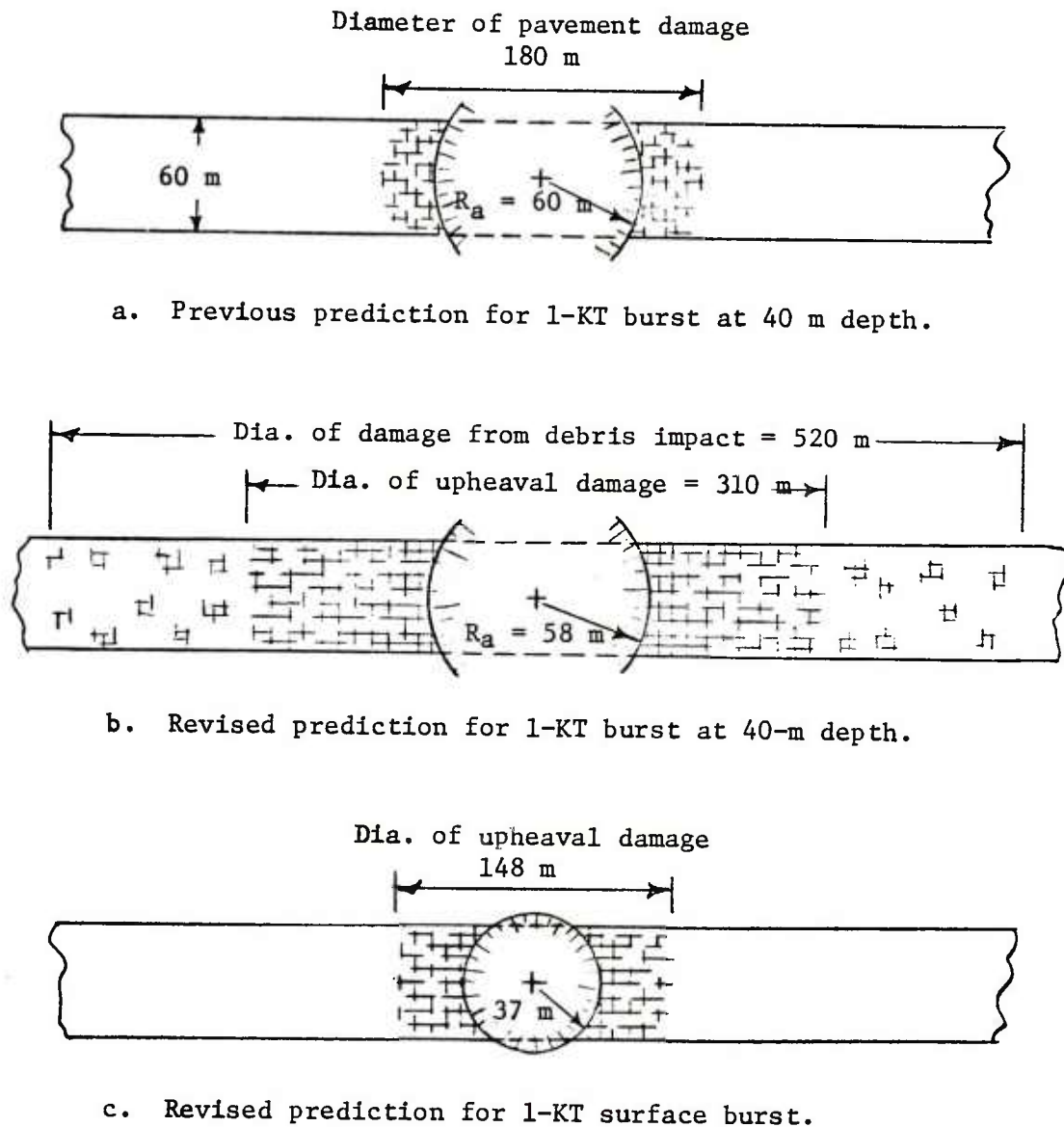


Figure 8. Predicted diameters of damage to concrete slab runway pavements from 1-KT nuclear detonations.  $R_a$  is apparent crater radius.



INCIDENCE OF CORONARY RISK FACTORS AND EVIDENCE OF ISCHEMIC  
HEART DISEASE IN A SELECTED MILITARY POPULATION (U)

JOSEPH C. DENNISTON, MAJ, VC  
MARCOS U. RAMOS, MAJ, MC  
RONALD E. JACKSON, MAJ, MC  
US ARMY RESEARCH INSTITUTE OF ENVIRONMENTAL MEDICINE  
NATICK, MASSACHUSETTS 01760

INTRODUCTION

Ischemic heart disease includes all forms of myocardial damage resulting from the inability of the coronary artery oxygen delivery system to meet myocardial tissue requirements for oxygen. This usually results from occlusive coronary arteriosclerosis where the degree of vessel stenosis restricts the blood supply and hence oxygen available to the myocardium. In more specific terms, ischemic heart disease (coronary artery disease) is classified as angina pectoris, coronary insufficiency, and myocardial infarction.

The exact cause of coronary artery disease (CAD) is unclear. However, the all-inclusive concept of a polygenetic inheritance and multifactorial influence as the basis of the disease is generally accepted. Indeed, various studies have provided evidence that a predictive relationship exists between certain factors (coronary risk factors) and the eventual development of CAD (10,25). Included among these multiple risk factors are: elevated blood cholesterol; arterial hypertension; cigarette smoking; family history of heart disease; abnormal electrocardiogram; emotional stress; lack of exercise; and obesity. It has been suggested that a reduction in the rate of premature mortality from CAD can be achieved by the early detection and management of individuals susceptible to myocardial infarction as well as the identification of predisposing factors (11).

Cardiovascular disease is the major cause of death in individuals over 35 years of age. Impressive is the fact that approximately 61% of the cardiovascular deaths are due to CAD (17). The

high incidence of coronary arteriosclerosis observed during postmortem studies of young men that died in the Korean War has clearly emphasized the early onset of CAD (20). These data and the knowledge that approximately 90% of the American population will develop arteriosclerosis (3) reemphasizes the necessity for the early recognition of ischemic heart disease and the identification of the coronary risk factors if a reduction in the rate of mortality from the disease is to be forthcoming.

The purpose of the present study was to: (1) define the incidence of coronary risk factors (CRF) among noncommissioned officers (NCOs) and officers over 35 years of age in the 2d Infantry Division; (2) define the incidence of ischemic heart disease (IHD) in this population; (3) assess the level of physical fitness in the Division; and (4) determine if the routine assessment of CRF and IHD should be recommended for older personnel undergoing a high intensity physical training program. During the period of this study a high intensity jogging program was a mandatory part of the Division's physical training.

#### MATERIALS AND METHODS

One hundred and eighty-six men (80 officers and 106 NCOs), 35 years of age or older, were randomly selected from a computer printout of personnel in the 2d Infantry Division for participation on a voluntary basis in the study.

A detailed medical and family history of heart disease, hypertension, and obesity was obtained from each participant. Each subject was given a complete physical examination to identify the presence of medical conditions which would preclude his participation in the study. A 12 lead electrocardiogram (ECG) was obtained using disposable ECG electrodes and an electrocardiographic stress test system (Hewlett-Packard).

Systolic and diastolic blood pressure were measured using a mercury sphygmomanometer following a 10-15 minute supine rest period. Blood pressure was categorized as normal ( $<140/90$ ) or abnormal ( $\geq 140/90$ ) for purposes of data analysis. The abnormal group was further divided to include borderline ( $140/90 \leq BP < 160/95$ ) and hypertensive ( $\geq 160/95$ ) categories.

For analysis of smoking data the subjects were grouped as smokers ( $\geq 10$  cigarettes per day) or nonsmokers. Only two of the nonsmokers claimed to have an occasional cigarette.

Overweight indices measured included body fat and Quetelet's index. Body fat (BF) was calculated using the Siri equation (22):

$$BF = [4.95/BD] - 4.50] BW \quad (1)$$

where BW is the body weight (kg) and BD equals the body density calculated from the following equation:

$$BD = 1.71 - 0.706 (\log \Sigma \text{skin folds}) \quad (2)$$

where skin fold thickness (mm) was measured at the subscapular, triceps, and suprailiac sites. Quetelet's index was calculated using the following equation (13):

$$QI = (\text{weight}/\text{height}^2)100 \quad (3)$$

An uninterrupted multistage bicycle stress test (Table 1) was used to elicit electrocardiographic evidence of ischemic heart disease and to assess the physical work capacity of the participants. The exercise was started at a low level (300 kg-m/min) and then increased at specific time intervals until a predetermined submaximal heart rate was achieved. The subject's heart rate was chosen as a guide to the test endpoint in order to apply a standardized stress to the heart which would account for differences in age and physical conditioning. Ninety percent of the predicted maximal heart rate was selected as the test endpoint and calculated using the following equations (21):

$$HR(T) = 0.90 [198 - 0.41A] \quad (4)$$

$$HR(UT) = 0.90 [205 - 0.41A] \quad (5)$$

where HR equals 90% of the predicted maximal heart rate; T and UT refers to trained and untrained subjects, respectively; and A is the age in years. A 12 lead ECG was taken prior to exercise and the precordial leads  $V_4$ ,  $V_5$ , and  $V_6$  were continuously monitored on an oscilloscope and recorded simultaneously on a three-channel recorder. Heart rate was monitored with a heart-rate meter and calculated from the ECG strip recorded at the end of each stage of exercise. A 12 lead ECG was recorded immediately following exercise and at 2, 4, and 6 minutes postexercise. The criterion used for a positive stress test was a ST-segment depression  $\geq 1$  mm that persisted for at least 80 msec after the end of the QRS complex.

TABLE 1. Summary of the uninterrupted multistage stress test

Stage	Work load (kg-m/min)	Duration (min)
1	300	6
2	600	3
3	900	3
4	1100	2
5	1300	2
6	1500	2
7	1700	2

Physical activity was classified by the number of kilometers (km) jogged per week (0-8, 9.6-16, 17.6-32, >32). The total work (TW) achieved (kg-m) during the exercise stress test was calculated using the general equation:

$$TW = \Sigma(t_1W_1 + t_2W_2 \dots + t_nW_n) \quad (6)$$

where t equals the total time (min) for a specific stage and W corresponds to the work load (kg-m/min) for the specific stage.

Plasma cholesterol determinations were made on blood samples from fasting subjects (>12 hr). Cholesterol values were grouped as normal (<200 mg%), borderline (200-249 mg%), or abnormal (>250 mg%).

A psychological questionnaire (POMS, Profile of Mood States) was completed by each subject for analysis of the following mood states (14): tension; depression; anger; vigor; fatigue; and confusion. Perceived exertion (RPE) was graded according to the psychophysical scale developed by Borg (6) at the end of each state of exercise. This scale ranges from 6 to 20 and the odd numbers have verbal anchors (e.g., 7 = very, very light; 9 = very light; 11 = fairly light; 13 = somewhat hard; 15 = hard; 17 = very hard; 19 = very, very hard).

Analysis of variance was used to test the significance of differences between two sample means. Chi-square analysis was used to determine the significance of differences in the frequency of variables between the groups. The level of significance was chosen as  $P < 0.05$ .

## RESULTS

### Anthropometric, Racial and Smoking Data

A small but significant difference was noted between the mean ( $\pm$ SE) age of officers ( $37.8 \pm 0.3$ ) and NCOs ( $39.9 \pm 0.4$ ) studied. Although no significant difference was observed in the percent body fat of officers ( $23.6 \pm 0.4$ ) and NCOs ( $25.1 \pm 0.7$ ) the mean value for Quetelet's index was significantly lower for officers ( $3.6 \pm .05$ ) than for NCOs ( $3.8 \pm 0.1$ ). Analysis of the racial distribution of the population revealed a significantly greater number of Caucasians in the officer group (92.5%) than in the NCO group (70.7%). Smoking data showed a significantly greater percent (66%) of smokers among NCOs than among officers (42.5%).

### Family History

Minimal differences were noted in the subjectively-elicited

incidence of ischemic heart disease, hypertension, and obesity between the families of officers and NCOs. However, significant differences were noted in two categories: there was a greater incidence (13.2%) of overweight among the brothers of NCOs than among the brothers of officers (3.7%); and the incidence (32.5%) of ischemic heart disease was higher among the fathers of officers than those of NCOs (34.6%).

### Cholesterol

Although the mean plasma cholesterol values (mg%) were not different significantly between the two groups, the values tended to be higher for NCOs ( $196.3 \pm 3.6$ ) than for officers ( $186.3 \pm 4.1$ ). Importantly, a greater percentage (65.4%) of the officers had normal cholesterol values than did the NCOs (51.9%). Similarly, more of the NCOs (48.1%) had borderline or abnormal cholesterol values than did the officers (34.6%).

### Blood Pressure

No significant differences were noted in the mean values (mm Hg) of systolic/diastolic blood pressures between officers ( $125 \pm 2/85 \pm 1$ ) and NCOs ( $129 \pm 1/87 \pm 1$ ). However, further analysis of the data revealed differences in the age categories of 40-44 and 45-50 (Table 2): the systolic values in the two categories and the diastolic values of the former category were significantly lower for officers than for NCOs. Additionally, more (71.2%) of the officers had normal blood pressures than did the NCOs (49.1%). In contrast, a significantly higher percentage (50.9%) of NCOs had abnormal blood pressures than did officers (28.8%). These same relationships were evident in the categories of borderline and hypertensive pressures (Fig. 1).

TABLE 2. Mean values ( $\pm$ SE) for blood pressure by age & military group

Age	N	SYSTOLIC (mm Hg)		DIASTOLIC (mm Hg)	
		Officers	NCOs	Officers	NCOs
35-39	(61,61)	125 $\pm$ 2	128 $\pm$ 2	85 $\pm$ 1	87 $\pm$ 1
40-44	(16,27)	125 $\pm$ 3*	134 $\pm$ 3	85 $\pm$ 2*	90 $\pm$ 1
45-50	( 3,18)	114 $\pm$ 8*	130 $\pm$ 2	85 $\pm$ 4	90 $\pm$ 1

\*Significant ( $P < 0.05$ ) difference between officers and NCOs.

A significant difference was observed also in the incidence of abnormal blood pressures between Caucasians (35.6%) and non-Caucasians (62.2%). In general the incidence (47.2%) of abnormal pressures was greater among smokers than nonsmokers (33.7%). Abnormal pressures also occurred with greater frequency (46.8%) among individuals with cholesterol values  $\geq 200$  mg% than among individuals with values  $< 200$



mg% (37.7%). Additionally, a significant difference was noted in the incidence (60%) of abnormal pressures in individuals doing minimal exercise (0-8 km/wk) and those (33%) doing greater work (>8 km/wk).

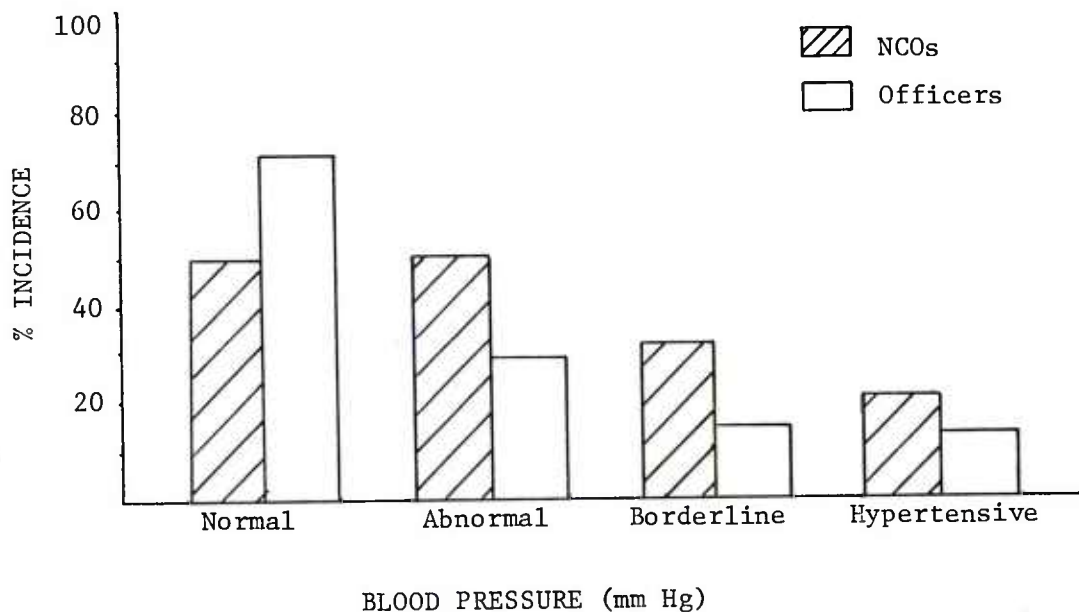


Fig. 1. Distribution of blood pressure values among officers and NCOs.

#### Heart Rate and Resting ECG Data

Officers had significantly lower mean resting heart rates ( $65 \pm 1$ ) than did NCOs ( $70 \pm 1$ ). Officers also had lower heart rates than NCOs at 2 minutes ( $110 \pm 1$  vs.  $116 \pm 1$ ) and at 4 minutes ( $100 \pm 1$  vs.  $106 \pm 1$ ) postexercise. No difference was observed in the mean target heart rates ( $160 \pm 1$ ) achieved by the two groups.

Although there appeared to be more officers (42.5%) who had never had an ECG than NCOs (34%), the difference was not significant. Likewise, no significant difference was noted in the incidence (3.8%) of abnormal resting ECGs for officers and NCOs (10.4%).

#### Physical Activity and Work Capacity

The percent participation of officers and NCOs in the Division's jogging regimen is presented in Fig. 2. A significantly greater number (44.3%) of the NCOs participated in minimal physical activity (0-8 km/wk) than did the officers (10%). In agreement with this finding, a significantly greater percentage (60%) of the officers



participated in a more demanding level of activity (17.6-32 km/wk) than did NCOs (23.6%).

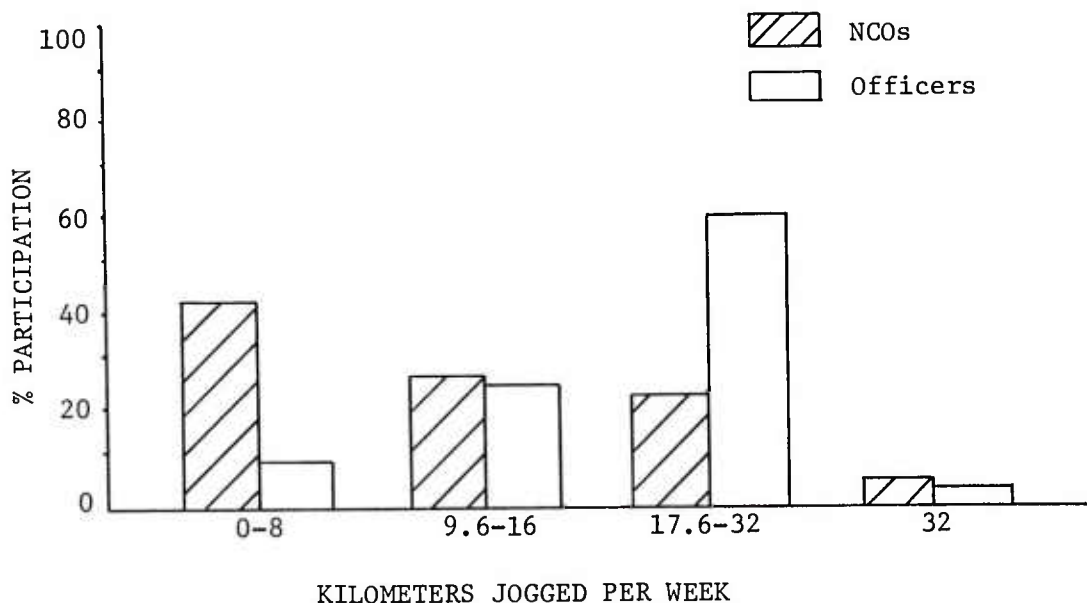


Fig. 2. Percent participation in the Division's jogging regimen.

The mean total work (kg-m) achieved by the two groups in attaining the target heart rate during the multistage stress test was different. Officers worked ( $8329 \pm 360$ ) to a significantly higher level than did NCOs ( $7011 \pm 332$ ). This same relationship was observed in two of three age categories (Fig. 3), indicating that officers achieved more work with increasing age while the work capacity of NCOs decreased with age. Additionally, the work capacity of NCOs decreased with increasing military rank while officers achieved higher work levels with increasing military rank.

The frequency distribution for the two groups at the various work levels (kg-m/min) in achieving their target heart rates is summarized in Table 3. Importantly, significantly more (33.4%) of the NCOs achieved their target heart rates at relatively light work levels ( $\leq 600$  kg-m/min) than did officers (16.5%). Similarly, more (60.8%) of the officers worked at higher work levels ( $\geq 1100$  kg-m/min) in reaching their target heart rates than did NCOs (35.2%).

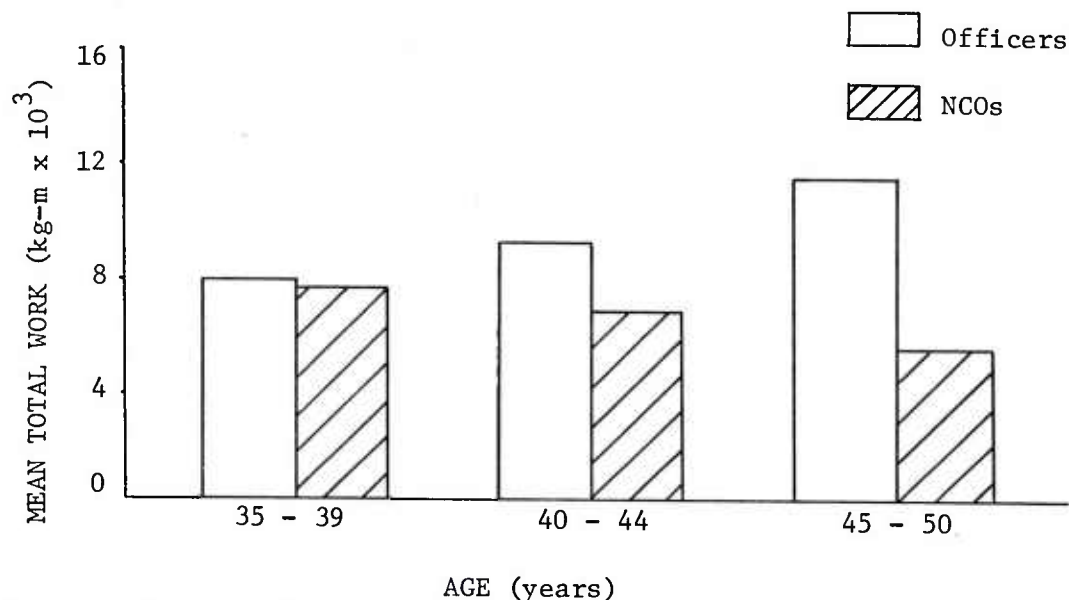


Fig. 3. Mean total work achieved by officers and NCOs by age group.

TABLE 3. Frequency distribution of achieved work levels

Work Load (kg-m/min)	Duration (min)	NCOs (%)	Officers (%)
300	6	6.7	3.8
600	3	26.7	12.7
900	3	31.4	22.8
1100	2	19.0	41.8
1300	2	8.6	11.4
1500	2	5.7	5.1
1700	2	1.9	2.4

#### Psychological Variables

The means ( $\pm$ SE) for each of the mood states measured by the POMS are summarized in Table 4. Analysis of the data revealed that the two groups differed in the level of depression and confusion with the officers having a lower score in each case. In general subjects who have two or more zeros on the POMS also have a high "lie score" as measured by the Eysenck Personality Inventory (15). Subjects answering "all" questions in the socially desirable direction can be assumed to possess distorted profiles. On this basis the incidence of distorted psychological profiles was found to be high in both the officers (24%) and NCOs (26%). The final perceived exertion rating differed for officers ( $14.8 \pm 0.3$ ) and NCOs ( $15.8 \pm 0.3$ ).

TABLE 4. Mean values ( $\pm$ SE) of the mood state variables

Variable	Officers	NCOs
Tension	8.0 $\pm$ 0.6	8.8 $\pm$ 0.6
Depression*	5.2 $\pm$ 0.5	7.1 $\pm$ 0.8
Anger	5.7 $\pm$ 0.9	5.7 $\pm$ 0.2
Vigor	19.1 $\pm$ 0.5	18.9 $\pm$ 0.8
Confusion*	3.2 $\pm$ 0.3	5.2 $\pm$ 0.5
Fatigue	4.8 $\pm$ 0.5	6.1 $\pm$ 0.7

\*Significant difference between officers and NCOs.

#### Positive Stress Test Findings

The incidence of positive stress tests within several categories is depicted in Fig. 4. Although positive stress tests occurred with greater frequency (12.3%) among NCOs than among officers (6.3%) the difference was not significant. Similarly, the incidence of positive tests was higher (15.6%) among non-Caucasians than among Caucasians (8.7%). Positive stress tests occurred with significantly greater frequency (16.9%) in individuals with abnormal blood pressures than in normotensives (6.9%). Although the incidence (14.4%) of positive tests was greater among smokers than nonsmokers (6.1%) the difference was not significant. While individuals with cholesterol values  $<200$  mg% had a lower incidence (8.9%) of positive tests than those individuals (12.7%) with values  $\geq 200$  mg% the difference was not significant.

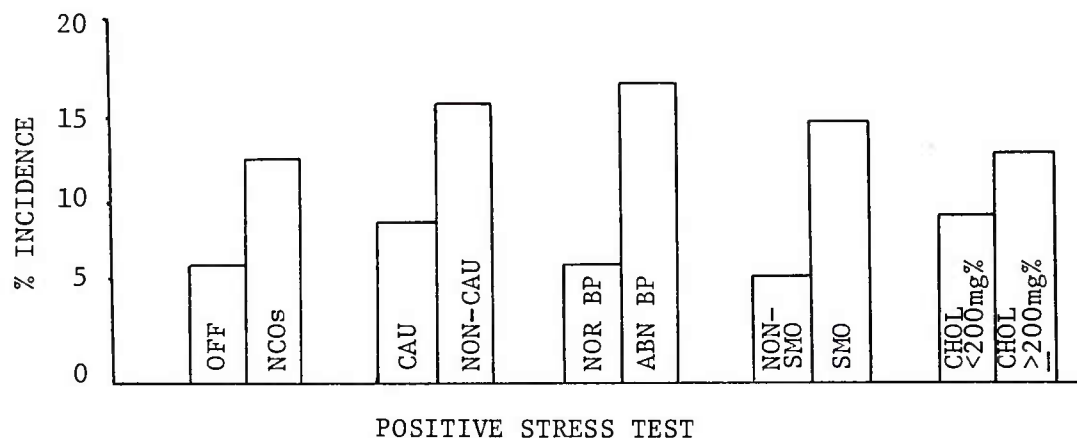


Fig. 4. Incidence of positive stress tests for various categories. OFF = officers; NCOs = noncommissioned officers; CAU = Caucasians; NON-CAU = Non-Caucasians; NOR BP = normal blood pressure; ABN BP = abnormal blood pressure; NONSMO = nonsmoker; SMO = smoker; CHOL = cholesterol.

## DISCUSSION

This study revealed that officers were in better cardiovascular health and physical condition than NCOs. In addition, there was a lower incidence of coronary risk factors and less evidence of ischemic heart disease among officers than NCOs.

There is considerable evidence suggesting that vigorous physical activity reduces the risk of ischemic heart disease and coronary mortality (8,16). Importantly, the risk of sudden death from ischemic heart disease among sedentary men has been reported to be twice that of active men (11). Thus, since officers were more active in the Division's physical fitness program than NCOs one would suspect that they are also at a lower risk of developing ischemic heart disease. The better physical condition of officers was supported by their ability to achieve higher work levels (Table 3) than NCOs during the multistage stress test. The lower perceived exertion ratings of the officers provided further evidence of their better physical conditioning since perceived exertion represents one of the most highly correlated subjective measures of physical fitness (23). The reason why the physical work capacity of the officers increased with age and rank, while correspondingly decreasing for NCOs is speculative. A reasonable explanation would seem to be related to the relatively greater "visibility" of officers in a Division where a rigorous running program was mandatory. The more senior an officer the greater will be his visibility and hence the greater the effort to maintain peak physical conditioning.

Irrespective of the differences in the total work capacity of the two groups it is important to realize that a substantial number (33.4%) of the NCOs and the officers (16.5%), a difference that is also significant, were unable to achieve work loads exceeding 600 kg-m/min during the multistage stress test. This is particularly impressive in terms of equivalent physical activities. Housework or walking at the rate of 5 km/hr are equivalent to a work load of 300 kg-m/min, while 600 kg-m/min is equivalent to walking at the rate of 7 km/hr or doing gardening type work (2). The inability of such a high percentage of both groups not being able to achieve greater work loads in reaching 90% of their maximal heart rates was certainly unexpected in a "physically fit" military population.

Although officers had significantly lower depression and confusion scores (Table 4) than NCOs the mean values for all the mood states fell within normal limits for both groups. The high percentage of distorted psychological profiles among officers (24%) and NCOs

(26%) was somewhat surprising. As anticipated, the distortion was always in the "fake good" direction. Even though an informed consent procedure (voluntary participation) was employed, and confidentiality of the data were emphasized, it is possible that a substantial number of the subjects felt obligated to volunteer for the study. These individuals may have felt that the test results would be placed in their personnel files, and therefore, an attempt to present a good psychological profile followed. These data suggest that an attempt should be made in subsequent investigations to eliminate or minimize "faking" since a loss of 25% of those subjects tested represents both an economical as well as a scientific problem.

The incidence of hypertension in both groups has special significance since ischemic heart disease is the single most important lethal sequela of the disease (9). Hypertensive individuals die at more than twice the rate of normotensives (9). Although NCOs had a higher incidence (20.7%) of hypertension than officers (13.8%) the incidence within the two groups did not differ significantly from that (18%) in the adult male population (9). In considering abnormal elevations of pressures, a range that also has been associated with increased morbidity and mortality (18), the incidence (50.9%) was greater among NCOs than officers (28.8%). The incidence of abnormality using the same criteria is 41% in the adult male population (9). Of additional importance is the fact that hypertension was more common among smokers (47.2%) than nonsmokers (33.7%) since the sequelae of hypertension are more common among smokers than nonsmokers. Our finding of a higher incidence of abnormal elevations in blood pressures among non-Caucasians than Caucasians was expected (24).

The greater incidence (16.9%) of ischemic heart disease among individuals with abnormal blood pressures than among normotensives (6.9%) was not surprising. Hypertension is known to be associated with a higher incidence of positive stress tests (4,27). The risk of all the clinical manifestations of ischemic heart disease is greater among hypertensives than normotensives (9).

The higher incidence (66%) of smoking among NCOs than among officers (42.5%) represents another factor that puts the NCOs at a greater risk of developing ischemic heart disease. The incidence of myocardial infarction and death is three times greater among smokers than nonsmokers (7). In addition, a sparing effect from sudden coronary death has been demonstrated among nonsmokers (11). Although we were not able to show a significant difference in the incidence and degree of ischemic heart disease between smokers (14.4%) and nonsmokers (6.1%), such a relationship is recognized (25). Importantly, the risk of ischemic heart disease decreases in individuals who stop



smoking (26).

Available evidence reveals a gradient of risk for developing ischemic heart disease with increasing levels of serum cholesterol. Individuals with cholesterol values  $\geq 260$  mg% have 4.7 times the incidence of ischemic heart disease as do those with levels below 200 mg% (12). Our observation of a higher incidence (12.7%) of ischemic ST-segment depression in those individuals with cholesterol values  $\geq 200$  mg% than in those individuals (8.9%) with cholesterol values less than 200 mg% is consistent with these facts. Thus the fact that more of the officers (65.4%) had normal cholesterol values than did NCOs (51.9%) suggests that the NCOs are at a greater risk of developing ischemic heart disease.

A postexercise finding of ST-segment depression has been found to be highly predictive of ischemic heart disease (1,5). Individuals with an ST-segment depression of 1.0 to 1.9 mm have 3.7 times the mortality rate of individuals without ST-segment depression (19). The incidence (12.3%) of ST-segment depression for NCOs was approximately that reported (13.5%) in the adult male population (19). In contrast, the incidence of ischemic heart disease was lower among officers (6.3%) than among NCOs or the adult male population.

#### CONCLUSIONS

(1) NCOs had a higher incidence of the factors associated with coronary artery disease than officers.

(2) NCOs had more evidence of ischemic heart disease than officers. Similarly, the incidence was higher among non-Caucasians, smokers, hypertensives, and individuals with elevated plasma cholesterol than their respective counterparts.

(3) Officers were in much better physical condition than NCOs. In addition, the physical work capacity of officers increased with age and rank while the work capacity of NCOs decreased with age and rank. Importantly, a substantial number of NCOs and officers were unable to achieve work loads exceeding 600 kg-m/min (a relatively light work load).

(4) The lower incidence of coronary risk factors and ischemic heart disease and the better physical condition of the officers are probably related to basic differences in motivation and participation in high intensity physical activity.

(5) The data indicate that individuals over 35 years should receive a medical evaluation, to include a multistage stress test when possible, as the basis for participation in a rigorous physical activity program. It seems important that some effort be made to tailor physical fitness programs not only to the needs of the Army, but also



to the medical requirements of the individual. A simple stress test would help predict the risk of disabling manifestations of coronary artery disease in older age personnel.

(6) Greater emphasis is needed in motivating individuals to participate in routine physical activity.

#### ACKNOWLEDGEMENTS

The authors are indebted to the personnel of the 2d Infantry Division for their cooperation in this field study. Our appreciation is also extended to: MAJ Helmut F. Hacker, MSC, for his outstanding performance as the liaison and project officer; CPT John L. Szurek for the ADP support; Mr. Richard Langevin for technical support; and Ms Randy Cherchiglia for the preparation of the manuscript.

A special note of thanks is extended to Dr. James A. Vogel, Director, Exercise Physiology Division, USARIEM, for his scientific direction and support of this study.

#### REFERENCES

1. Aronow, W. S. and J. Cassidy: Five year follow-up of double master's test, maximal treadmill stress test, and resting and post-exercise apexcadiogram in asymptomatic persons. *Circulation* 52: 616-618, 1975.
2. Åstrand, P-O., and K. Rodahl. Textbook of Work Physiology. p.364, New York, McGraw-Hill, Inc., 1970.
3. Berenson, G. S., S. R. Srinivasan, E. R. Dalfreres, F. A. Puyau, L. P. O'Meallie, R. J. Hall, and P. S. Pargaonkar. Serum lipoproteins and coronary heart disease. *Amer. J. Cardiol.* 34:588-593, 1974.
4. Billet, S., and L. Roman. Comparison of the double two-step and the maximal exercise treadmill test. *Studies in coronary prone subjects.* *Circulation* 36:238-244, 1967.
5. Blackburn, H., H. L. Taylor, and A. Keys. XVI. The electrocardiogram in prediction of five-year coronary heart disease incidence among men aged forty through fifty-nine. *Circulation* 41 (Suppl): I-154-I-161, 1970.
6. Borg, G. Perceived exertion as an indicator of somatic stress. *Scand. J. Rehab. Med.* 2-3:92-98, 1970.

7. Doyle, J.T., T. R. Dawber, W. B. Kannel, S. A. Heslin, and H. A. Kahn. Cigarette smoking and coronary heart disease. Combined experience of the Albany and Framingham studies. *New Eng. J. Med.* 266:796-801, 1962.
8. Fox, S. M., and W. L. Haskell. Physical activity and the prevention of coronary heart disease. *Bull. N.Y. Acad. Med.* 44:950-967, 1968.
9. Kannel, W. B. Role of blood pressure in cardiovascular morbidity and mortality. *Prog. Cardiovas. Dis.* 17:5-24, 1974.
10. Kannel, W. B., T. R. Dawber, A. Kagan, N. Revotskie, and J. Stokes. Factors of risk in the development of coronary heart disease--six-year follow-up experience. The Framingham Study. *Ann. Inter. Med.* 55:33-50, 1961.
11. Kannel, W. B., J. T. Doyle, P. M. McNamara, P. Quickenton, and T. Gordon. Precursors of sudden coronary death. Factors related to the incidence of sudden death. *Circulation* 51:606-613, 1975.
12. Keys, A., H. L. Taylor, H. Blackburn, J. Brozek, J. T. Anderson, and E. Simonson. Coronary heart disease among Minnesota business and professional men followed fifteen years. *Circulation* 28:381-395, 1963.
13. Klein, B. E. K., J. C. Cornoni, F. Jones, and E. Boyle. Overweight indices as correlates of coronary heart diseases and blood pressures. *Human Biol.* 45:329-340, 1973.
14. McNair, D. M., M. Lorr, and L. F. Droppleman. Profile of Mood States Manual. Educational and Industrial Testing Service. San Diego, 1971.
15. Morgan, W. P. Personal communication. Director, Ergopsychology Laboratory, University of Wisconsin, Madison, Wisconsin 53706. 1976.
16. Paffenbarger, R. S. and W. E. Hale. Work activity and coronary heart mortality. *New Eng. J. Med.* 292:545-550, 1975.
17. Paul, O. Coronary artery disease: clinical aspects. In: Cardiac and Vascular Diseases. (H. L. Conn and O. Horwitz, eds.). Vol 2. Lea & Febiger: Philadelphia. pp. 1038-1066, 1971.

18. Paul, O., Risks of mild hypertension. A ten-year report. Br. Heart J. 33 (Suppl):116-121, 1971.
19. Robb, G. P., and H. H. Marks. Post-exercise electrocardiogram in arteriosclerotic heart disease. J.A.M.A. 200:918-926, 1967.
20. Rigal, R. D., F. W. Lovell, and F. M. Townsend. Pathologic findings in the cardiovascular systems of military flying personnel. Amer. J. Cardiol. 6:19-26, 1960.
21. Sheffield, L. T., D. Roitman, and T. J. Reeves. Submaximal exercise testing. J. South Carolina Med. Assoc. 65:18-25, 1969.
22. Siri, W. E. Body composition from fluid spaces and density: Analysis of methods. In: Techniques for Measuring Body Composition. (J. Brozek and A. Henschel, eds.). National Academy of Sciences - National Research Council: Washington. pp. 223-244, 1961.
23. Skinner, J. S., G. Borg, and E. R. Buskirk. Physiological and perceptual reactions to exertion of young men differing in activity and body size. In: Exercise and Fitness. (B. D. Franks, ed.). Athletic Institute: Chicago. pp. 282, 1969.
24. Stamler, J., M. Kjelsberg, and Y. Hall. Epidemiologic studies on cardiovascular renal disease. I. Analysis of mortality by age - race - sex - occupation. J. Chronic Dis. 12:440-455, 1960.
25. Tibblin, G., L. Wilhelmsen, and L. Werko. Risk factors for myocardial infarction and death due to ischemic heart disease and other causes. Amer. J. Cardiol. 35:514-522, 1975.
26. U.S. Public Health Service. The Health Consequences of Smoking. U. S. Department of Health, Education, and Welfare Publication No. (HSM) 73-8704: Washington. pp. 249, 1973.
27. Wong, H. O., I. S. Kasser, and R. A. Bruce. Impaired maximal exercise performance with hypertensive cardiovascular disease. Circulation. 39:633-638, 1968.



TRANSFUSIONS WITH HEMOGLOBIN  
PREPARED BY CRYSTALLIZATION

FRANK DEVENUTO, PH.D., ANGELO ZEGNA,  
WILLIAM Y. MOORES, MAJ, MC and THOMAS F. ZUCK, LTC, MC  
LETTERMAN ARMY INSTITUTE OF RESEARCH  
PRESIDIO OF SAN FRANCISCO, CA 94129

The development of plasma expanders and blood substitutes has received the attention of several investigators for many years. Plasma, dextran, albumin and other preparations have been used, and, although they appear to be effective as plasma expanders, they are of limited use as blood substitutes since they do not carry oxygen. As a resuscitating fluid, blood has a limited storage life and requires typing and cross-matching prior to use.

Great advantages can be gained by the development of a solution capable of transporting oxygen, maintaining oncotic pressure, and being readily available when massive clinical transfusions are required. Hemoglobin solution has such potential. Hemoglobin, prepared from outdated human blood, has been evaluated as a blood substitute because of its colloidal osmotic effect and its oxygen carrying capacity (1-11). Hemoglobin can transport and exchange oxygen, does not require typing and cross-matching, has osmotic activity, can be prepared from outdated blood, and can be stored for a long time under sterile conditions. It appears to be the ideal blood substitute in combat situations. In many field situations, logistics make impossible the immediate infusion of blood to the wounded soldiers for several reasons, such as distance from medical treatment centers, lack of blood with proper typing and cross-matching, etc. Death may occur because of delayed treatment.

In most civilian settings in this country, the transfusion requirements associated with massive trauma can be met with conventionally stored blood and its components. However, military needs frequently demand massive fluid support in areas remote from the

supply source, presenting uniquely difficult storage and transportation problems. The inability to predict accurately when modest transfusion requirements may suddenly increase further complicates fluid therapy logistics. The ability to stockpile a stable protein solution capable of carrying oxygen avoids many of these difficulties.

The initial enthusiasm generated by earlier studies has decreased in recent years due to reports that renal damage and methemoglobin formation occur after administration of hemoglobin solution (3,5,12). Furthermore, it has been clearly documented that hemolyzed erythrocytes can initiate blood coagulation (13). The coagulant activity, however, is confined to erythrocyte stroma (14), and it has been postulated that renal damage and other adverse effects observed after the administration of hemoglobin solution are determined by the presence of red cell stromal contaminants. Therefore, it is imperative that if hemoglobin is to be used as a blood substitute it must be as free as possible of any stromal particle, stromal lipid or other soluble and insoluble contaminants which could be carried along during the preparative procedure.

#### PREPARATION OF HEMOGLOBIN BY CRYSTALLIZATION

Recent methods for the preparation of hemoglobin solution (6-9) require high speed centrifugation and filtration through a 0.2  $\mu$  millipore filter to remove stromal particles. With these techniques, however, there remains the possibility of contamination with soluble components of the red cell membrane such as stromal lipids or phospholipids, even if this contamination is minimized by hemolyzing red cells with hypotonic phosphate buffer of controlled osmolarity and pH.

We have developed a rapid, simple and reproducible procedure for the preparation of hemoglobin free of stromal or other soluble and insoluble cellular contaminants. The procedure is based on crystallization of the hemoglobin molecule and repeated washings of crystals prior to solubilization and sterilization. It represents a modification of the technique described by Drabkin (15,16) and it is schematized in Figure 1. Red blood cells, separated by centrifugation from whole outdated blood, are washed three times with 0.9% saline and hemolyzed by addition of one volume of water and 0.4 volumes of toluene. Filtration through a surgical sponge and centrifugation at 4,000 x g yield a hemoglobin solution essentially free of particulate matter. Dialysis against 2.8 M phosphate buffer, pH 6.8, causes crystallization of hemoglobin in the cellulose dialysis tubing. The crystals are removed from the casing, dispersed in 2.8 M phosphate buffer and washed three times with the same buffer



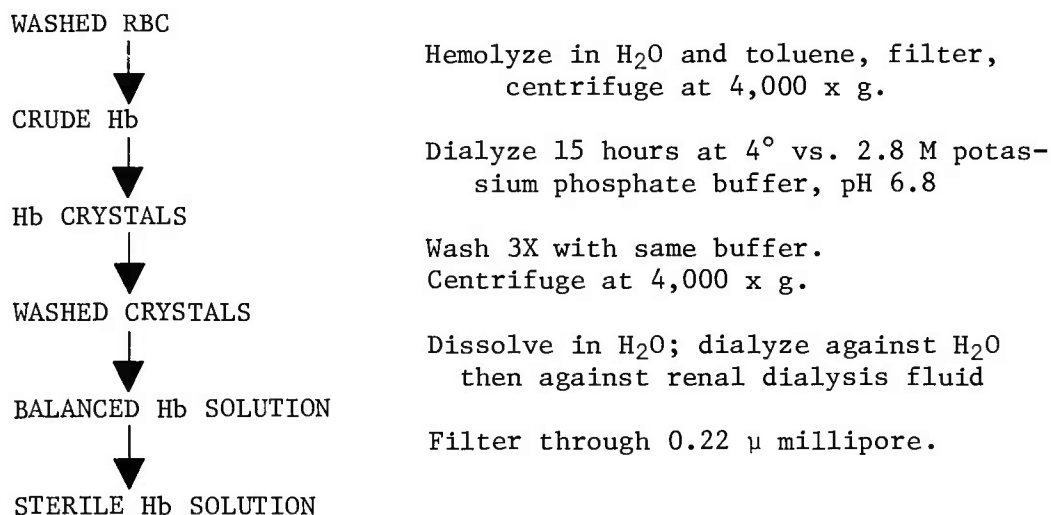


FIGURE 1. Hb CRYSTALLIZATION PROCEDURE

in order to eliminate any particulate or solubilized contaminants which might be adsorbed. The washed crystals are readily dissolved in distilled water and dialyzed, first, against water to eliminate the high potassium and phosphate content and then against standard kidney dialysis fluid to adjust electrolyte concentration and pH. Sterilization is achieved by passing the final solution through a sterile 0.22 μ Millipore filter.

#### ANALYSIS OF CRYSTALLIZED HEMOGLOBIN

An analysis of the final solutions of hemoglobin, prepared by crystallization, is shown in Table 1.

TABLE I  
ANALYSIS OF FINAL SOLUTIONS OF HEMOGLOBIN  
(prepared by crystallization)

		Range	Ave.
Hemoglobin	g/dl	---	7.0
Methemoglobin	g/dl	0.17 - 0.28	0.24
	g/100 g Hb	2.23 - 4.06	3.52
Osmolality	mOs/kg	271 - 310	284
Na	meq/liter	128.6 - 149.5	137.8
K	meq/liter	3.6 - 4.9	4.1
pH	---	7.29 - 7.41	7.35
Sterility	---	---	Sterile

Since the hemoglobin concentration depends on the amount of water used for crystal solubilization, this concentration can be adjusted to a desired value by dilution with kidney dialysis fluid. In all preparations, concentrations of 10-15 g/dl were obtained and the solutions were adjusted to 7.0 g/dl. Methemoglobin values slightly exceed the normal range for whole blood. Other parameters such as osmolality, Na, K and pH had normal serum values. All solutions of hemoglobin were sterile.

The results of the coagulation screening tests are shown in Figure 2. No significant differences (t-test) were observed between the hemoglobin solution and the albumin control on the clotting time of thrombin (TT), diluted prothrombin (DPT) and activated partial thromboplastin (APTT). No aggregation effect was observed either in inhibiting platelet aggregation to added ADP, or in inducing aggregation by addition of the hemoglobin to platelets.

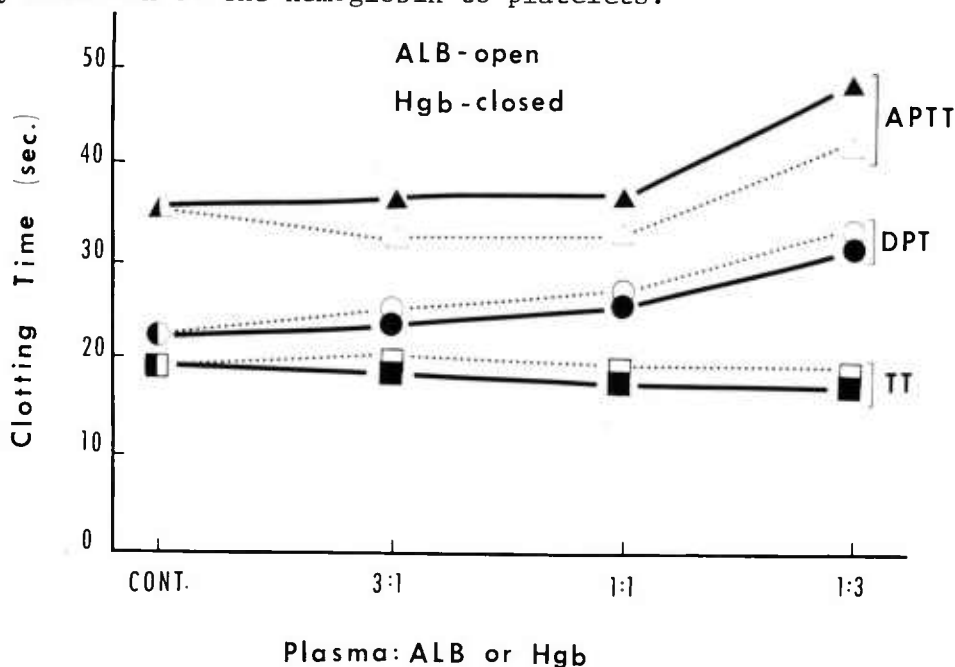


Figure 2. Coagulation activity of hemoglobin solution prepared by crystallization. Diluted prothrombin (DPT), activated partial thromboplastin (APTT), and Thrombin (TT) times with pooled normal plasma and plasma diluted with Albumin (ALB) or hemoglobin (Hgb) solutions.

In hemoglobin preparations from group A, Rh positive blood the crystallized hemoglobin solutions (CHb), assayed for A substance by the hemagglutination inhibition test, gave negative results at all

dilutions. However, solutions of hemoglobin prepared, in our laboratory, by the high speed centrifugation (HsHb) method of Rabiner (6,7) yielded positive reactions at 0, 2 and 4 fold dilutions. The results from one study of each type of preparation are shown in Table II. This table also indicates the positive response, up to 32 fold dilution, by a precipitate obtained when HsHb was further centrifuged at very high speed (214,000 x g for 45 minutes). CHb solution was also centrifuged under the same conditions, but no pellet was obtained.

TABLE II  
ANTIGENIC ACTIVITY OF HEMOGLOBIN SOLUTIONS PREPARED BY  
CRYSTALLIZATION (CHb) AND BY HIGH SPEED CENTRIFUGATION (HsHb)  
Hemagglutination Inhibition for A Substance

	Dilution						
	0	2	4	8	16	32	64
CHb	-	-	-	-	-	-	-
HsHb	+	+	+	-	-	-	-
Precipitate	+	+	+	+	+	+	-

Cellulose acetate electrophoresis of CHb, HsHb and HsHb further purified by centrifugation at 214,000 x g for 45 minutes is shown in Figure 3. Human hemoglobin A was used as a control. The migration of the hemoglobin preparations was the same as that of the control; however, CHb showed a very sharp, well-defined band whereas HsHb resulted in a band with diffused edges, which sharpened following very high speed centrifugation. The minor bands migrated to the expected locations for hemoglobin A<sub>2</sub> and carbonic anhydrase. The resolution of CHb by a sulphoethyl Sephadex column is shown in Figure 4. Five ml fractions were collected and the absorbance determinations at 280 and 540 nm demonstrated a single peak. Figure 5 shows the absorbance curve between 650 and 350 nm of a CHb preparation. The spectrum is identical with that of oxyhemoglobin with absorption maxima at 414, 540 and 576 and absorption minima at 510 and 560 nm.

Oxygen dissociation curves of several CHb preparations showed P<sub>50</sub> values which ranged between 15 and 18 mm of Hg, similar to the values obtained with hemoglobin prepared by high speed centrifugation. Figure 6 illustrates portions of the oxygen dissociation curves for CHb and HsHb. Values of n, slope of the oxygen dissociation curve, ranged between 2.4 and 3.0 for both preparations.

No significant differences were observed in the oxygen dissociation curves, methemoglobin content and chromatographic pattern between hemoglobin preparations obtained from fresh or outdated human blood.

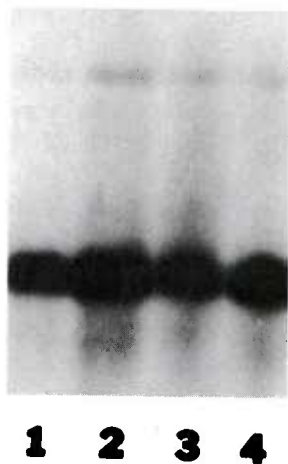


Figure 3. Cellulose acetate electrophoresis 1. Control, human Hb A. 2. Hb prepared by high speed centrifugation (HsHb). 3. HsHb further purified by centrifugation of 214,000  $\times$  g for 45 minutes. 4. Hb prepared by crystallization (CHb).

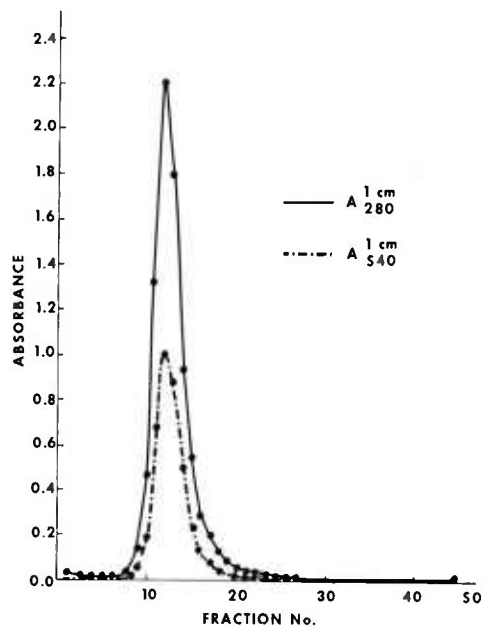


Figure 4. Chromatography of hemoglobin, prepared by crystallization (CHb) on a column of Sulphoethyl Sephadex, C-50, with phosphate buffer, pH 6.46.

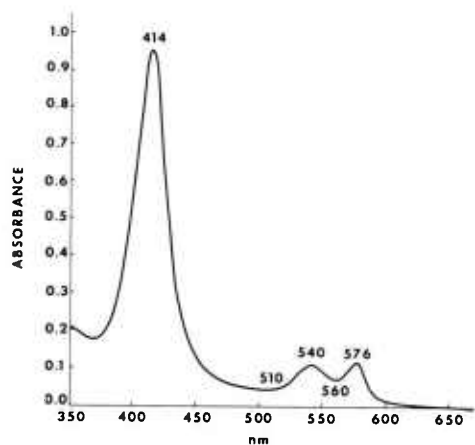


Figure 5. Absorbance of hemoglobin, prepared by crystallization.

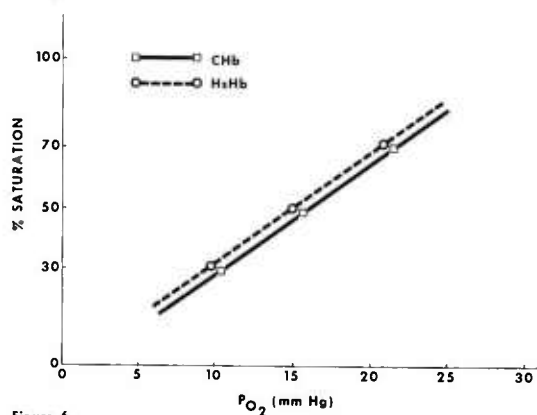


Figure 6. OXYGEN DISSOCIATION OF HEMOGLOBIN SOLUTIONS PREPARED BY CRYSTALLIZATION (CHb) AND BY HIGH SPEED CENTRIFUGATION (HsHb).

## STORAGE STUDIES

Hemoglobin solutions were prepared by crystallization from fresh or outdated human blood and stored in blood bags at refrigerator (4C) or freezer temperature (-20C). Storage of four different hemoglobin preparations for six months at these temperatures did not show any significant change in methemoglobin content, osmolarity, P<sub>50</sub> values, oxygen capacity and slope of the oxygen dissociation curve. Also, the values for pH, K and Na remained the same during the six months for all samples.

## TRANSFUSION STUDIES

Hemoglobin, prepared by crystallization, has been used for transfusion studies (Table III). Two groups of three rats each have been transfused to a total blood replacement of 93-95 percent with the hemoglobin solutions or, in the case of control animals, with albumin solutions. The only difference in the two solutions is the substitution of hemoglobin with albumin, which is a substance unable to carry oxygen.

TABLE III  
EXCHANGE OF RAT BLOOD WITH HEMOGLOBIN (Hb) OR  
ALBUMIN (Alb) SOLUTION, In Vivo

	Ht (%)		Hemoglobin (g/dl)		P <sub>50</sub> (at pH 7.4)		O <sub>2</sub> Capacity (% of normal)	
	Hb	Alb	Hb	Alb	Hb	Alb	Hb	Alb
Pre-Exchange	40	43	12.5	13.6	39.7	42.2	100	100
Post-Exchange	3	3	6.5	1.0	12.3	---	72	16

In this table are data before and after transfusion for hematocrit, hemoglobin concentration, P<sub>50</sub> in mm of Hg and, more important, the oxygen capacity of the circulating fluids. The control rats, transfused with albumin, died at approximately 10 minutes after transfusion; the rats transfused with hemoglobin survived for a period of five hours and normal activity was observed during this time. To obtain an explanation for the inability of the hemoglobin-transfused animals to survive for a period longer than five hours, the plasma disappearance of hemoglobin and the excretion of hemoglobin in the urine were studied. It has been reported that intravascular half-life of infused hemoglobin varies between 1.5 and 3.5 hours. The results, shown in Figure 7, demonstrate that plasma disappearance of hemoglobin is linear with time at a rate of  $0.0152 \pm 0.0011$  mg per 100 ml per minute. Half-disappearance time for the net doses administered in these studies was 3.5 hours. These data were observed in

three rats by determination of plasma hemoglobin concentration or by calculation of the disappearance in percent of initial concentration. By extrapolating the line to five hours, time of death of the animals when 95 percent of their blood is replaced, only about 30 percent of the initial Hb concentration remains in the plasma. An experiment in which a second partial transfusion with a more concentrated Hb solution was done at three and one-half hours after the first infusion resulted in prolonging the survival of the animal to ten hours.

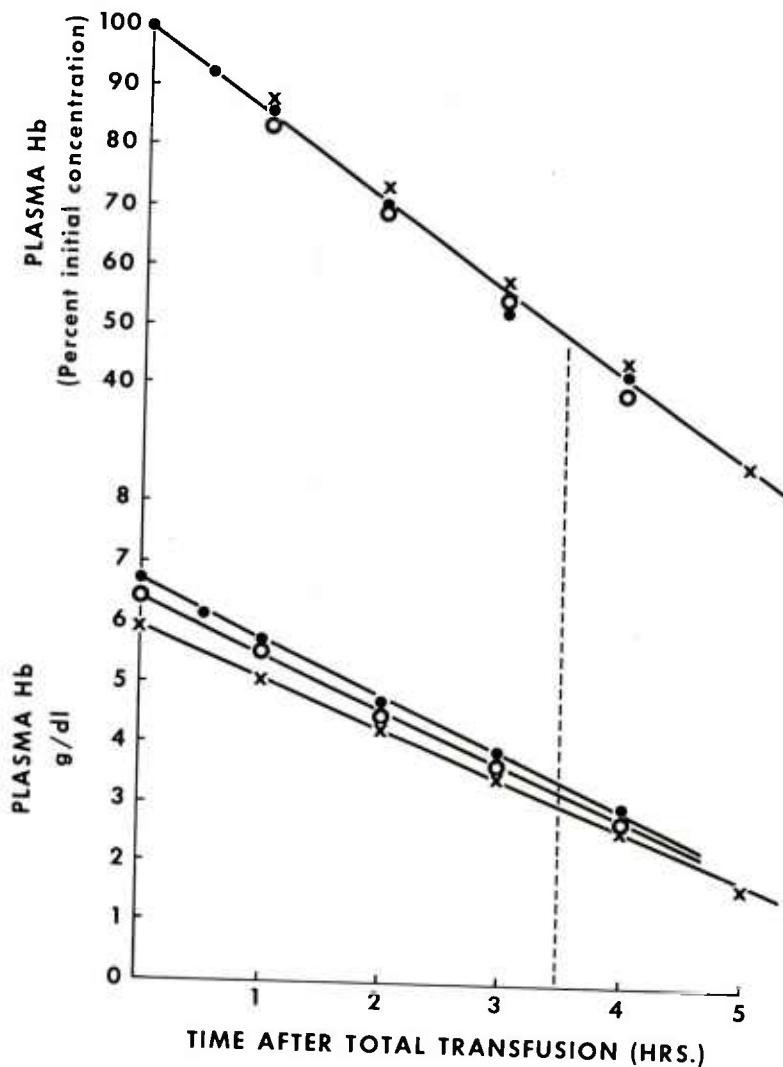


Figure 7. Plasma disappearance of hemoglobin injected in rats to a 95 per cent blood replacement.



In other experiments, two groups of two rats each have been transfused with hemoglobin or albumin solution to a total blood replacement of 70-80 percent, and survival of all animals has been obtained. Several parameters (Ht, total hemoglobin, pH, platelets and P<sub>50</sub>) have been monitored during the post-transfusion period up to two weeks. The results in Table IV show that within five to seven days, these parameters return to normal, pretransfusion levels. However, during the immediate post-transfusion period, the oxygen capacity of the circulating fluid in the hemoglobin transfused animals is greater than that found in the corresponding albumin-infused controls.

TABLE IV  
EXCHANGE OF RAT BLOOD WITH HEMOGLOBIN (Hb) OR  
ALBUMIN (Alb) SOLUTION, In Vivo

	Ht (%)		Hemoglobin g/dl		P <sub>50</sub> (at pH 7.4)		O <sub>2</sub> Capacity (% of normal)	
	Hb	Alb	Hb	Alb	Hb	Alb	Hb	Alb
Pre-Exchange	42	40	14.7	13.4	43.7	39.0	100	100
Post-Exchange	10	11	7.8	3.4	25.5	34.2	61.3	30.3
1 day	19	17	6.4	5.4	40.0	---	51.1	---
2 days	26	---	---	---	41.5	---	62.0	---
5 days	36	27	11.4	7.8	38.7	---	88.2	---
8 days	39	38	11.8	11.7	39.3	39.9	98.8	76.0

In the investigation of plasma disappearance of hemoglobin, urinary excretion was monitored and it was found that, at three hours after transfusion, 13-14 percent of the hemoglobin present in the rat at the end of transfusion was excreted in the urine. Since the hemoglobin content of urine (13-14 percent) and plasma (53-59 percent) at three hours after transfusion did not account for all the hemoglobin infused in the rat, a study of tissue distribution was made using hemoglobin labeled with <sup>51</sup>Cr (specific activity 67,700 cpm per g hemoglobin). Table V shows the results of the distribution of the radiolabeled material in a group of three rats transfused to 91 percent blood replacement and sacrificed at three hours after transfusion. It appears that the radioactive material is present in significant amounts in kidneys, liver, marrow, urine and in the intravascular system.

TABLE V  
DISTRIBUTION OF RADIOACTIVITY IN RATS  
TRANSFUSED WITH  $^{51}\text{Cr}$ -LABELED Hb  
(Percent of initial values)

Rat No.	1	2	3	
Percent exchange	91	91	90	MEAN
Hours after transfusion	3	3	3	
Bladder	0.2	0.1	0.2	0.2
Heart	0.5	0.4	0.4	0.4
Kidneys	5.9	5.2	6.1	5.7
Spleen	0.4	0.2	0.3	0.3
Liver	6.5	5.6	5.3	5.8
Feces	---	0.0	0.0	0.0
Lungs	---	1.1	1.3	1.2
Marrow	10.5	11.2	8.9	10.2
Urine	13.8	14.8	12.9	13.8
Plasma	<u>56.6</u>	<u>53.6</u>	<u>58.5</u>	<u>56.2</u>
Total:	94.4	92.2	93.9	93.8

#### SOURCE OF HEMOGLOBIN

In the preparation of hemoglobin, soluble and insoluble red blood cell components are removed including phosphate compounds, such as 2,3-diphosphoglycerate (2,3-DPG) which have been shown to influence the oxygen binding affinity. Human blood has a  $P_{50}$  of about 27 mm of Hg, whereas hemoglobin, as prepared by the crystallization procedure, demonstrates a  $P_{50}$  of 15-18 mm of Hg. Hemoglobin from other sources (17), however, have been shown to be independent of 2,3-DPG content for their oxygen binding affinity.

It is also realized that with more efficient use of donor human blood and/or new developments in the long term preservation of blood, in liquid or frozen state, there may not be sufficient outdated human blood available for the preparation of hemoglobin for stockpiling in large quantities necessary for massive transfusions. With these considerations in mind, the utilization of bovine hemoglobin has been investigated. Such hemoglobin has been prepared by crystallization, using the same procedure described for human blood, and the solutions analyzed. Preliminary data show that bovine hemoglobin should be considered as a possible blood substitute. Figure 8 illustrates the absorbance, between 650 and 350 nm, of human and bovine hemoglobin. Data on  $P_{50}$ , n-value and  $O_2$  content are presented in Table VI for the two hemoglobin preparations. Since, in contrast

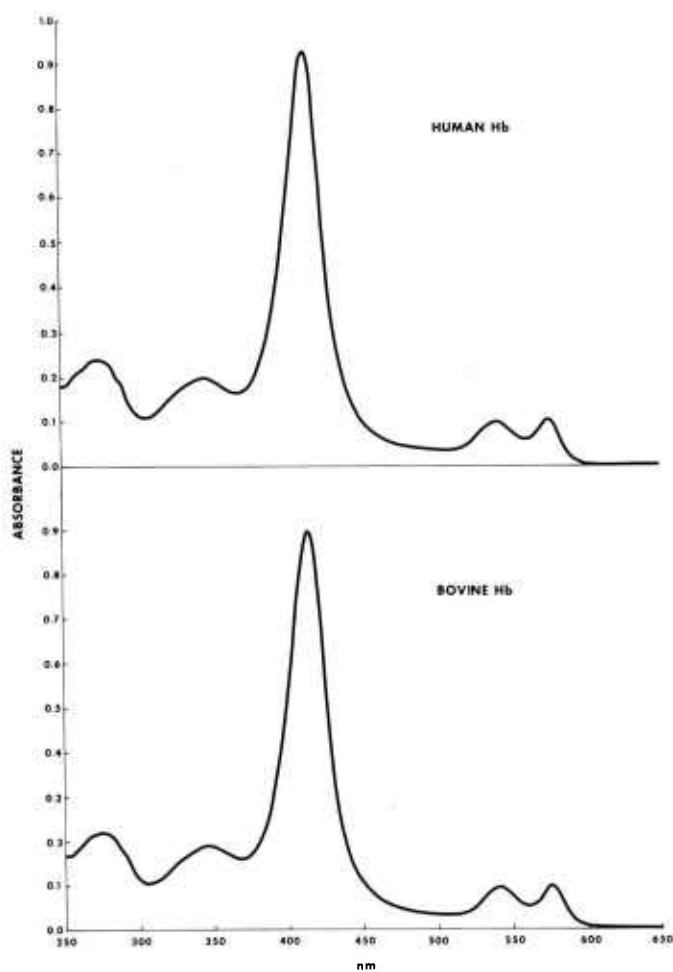


Figure 8. Absorbance of human and bovine hemoglobin, prepared by crystallization.

TABLE VI  
HEMOGLOBIN SOLUTIONS, PREPARED BY CRYSTALLIZATION,  
FROM HUMAN OR BOVINE BLOOD

ASSAYS	HUMAN	BOVINE
Hb g/dl	7.6	7.7
MetHb g/100 g Hb	3.07	3.56
Osmolarity mOs/kg	290	287
pH	7.32	7.35
P <sub>50</sub> at pH 7.4	16.3	28.5
O <sub>2</sub> vol percent	10.5	10.7
n-value	2.44	2.84

to human hemoglobin, bovine hemoglobin does not require diphosphoglycerate as an intermediate for its function (17) the  $P_{50}$  observed for bovine Hb is higher than for human Hb, indicating the possibility of more efficient exchange of oxygen with the tissues upon transfusion.

#### CONCLUSION

The data shown demonstrate that hemoglobin has the potential to become an ideal blood substitute. The method of preparation described in this study uses the crystallization procedure to separate hemoglobin from other cell constituents. High speed centrifugation for sedimentation of small particles is not necessary, as all centrifugations in the procedure are at low speed and adaptable to batch processing. The low volume of medium used for red cell hemolysis presents the advantage of handling small volumes of liquid with considerable savings of time and effort in the centrifugation, dialysis and other operations involved in the preparative procedure. The crystallization method is easily adaptable to large scale preparation to process high volumes of outdated blood to yield quantities of hemoglobin solutions necessary for clinical transfusion.

Hemoglobin obtained by crystallization, except for traces of carbonic anhydrase, is pure as demonstrated by electrophoretic, chromatographic and spectrophotometric analysis; it does not influence coagulant activity and it appears that it does not carry antigenic substances. Furthermore, it is able to reversibly bind oxygen, a very important property of a blood substitute, for which this preparation appears to have great potential.

#### REFERENCES

1. Hamilton AG, Parkins W, Waltzer F: A comparison of ten infusion fluids in the treatment of moderate and severe hemorrhage in animals. *Am J Physiol* 150:461-653, 1947.
2. Farr LE, Hiller A, Van Slyke DD: Preparation of dried hemoglobin without loss of activity. *J Exptl Med* 86:465-475, 1947.
3. Hamilton PB, Hiller A, Van Slyke DD: Renal effects of hemoglobin infusions in dogs in hemorrhagic shock. *J Exptl Med* 86: 477-487, 1947.
4. Hamilton PB, Farr LE, Hiller A, et al: Preparation of hemoglobin solutions for intravenous infusion. *J Exptl Med* 86:455-463, 1947.

5. Thompson WL: Plasma substitutes. J S Carolina Med Assoc 56: 456-460, 1960.
6. Rabiner SF, Helbert SR, Lopas H, et al: Evaluation of stroma-free hemoglobin solution for use as a plasma expander. J Exptl Med 126:1127-1142, 1967.
7. Rabiner SF, O'Brien K, Peskin GW, et al: Further studies with stroma-free hemoglobin solution. Ann Surg 171:615-622, 1970.
8. Rabiner SF: Hemoglobin solution as a plasma expander. Fed Proc 34:1454-1457, 1975.
9. Mock W, Chen D, Mazur A: Cross-linked hemoglobins as potential plasma protein extenders. Fed Proc 34:1458-1460, 1975.
10. Kaplan HR and Murthy VS: Hemoglobin solution: a potential oxygen transporting plasma volume expander. Fed Proc 34: 1461-1465, 1975.
11. Bonhard K: Acute oxygen supply by infusion of hemoglobin solutions. Fed Proc 34:1466-1467, 1975.
12. Baker SB, Dawes RLF: Experimental haemoglobinuric nephrosis. J Pathol Bacteriol 87:49-56, 1964.
13. Rabiner SF, Friedman L: The role of intravascular hemolysis and the reticuloendothelial system in the production of a hypercoagulable state. Brit J Hematol 14:105-118, 1968.
14. Barratt JOW, Yorke W: The production of general symptoms in hemoglobinemia. Brit Med J 1:235-238, 1914.
15. Drabkin DL: Spectrophotometric studies. XIV. The crystallographic and optical properties of the hemoglobin of man in comparison with those of other species. J Biol Chem 164:703-723, 1946.
16. Drabkin DL: A simplified technique for large scale crystallization of human oxyhemoglobin. Isomorphous transformations of hemoglobin and myoglobin in the crystalline state. Arch Biochem 21:224-232, 1949.
17. Bunn HF, Seal US, Scott AF: The role of 2,3-diphosphoglycerate in mediating hemoglobin function of mammalian red cells. Ann N Y Acad Sciences 241:498-512, 1974.





SATFAL - THE APPLICATION OF METEOROLOGICAL  
SATELLITE DATA TO NUCLEAR FALLOUT PREDICTION

LOUIS D. DUNCAN, DR.  
ATMOSPHERIC SCIENCES LABORATORY  
US ARMY ELECTRONICS COMMAND  
WHITE SANDS MISSILE RANGE, NM

## INTRODUCTION

Rapid advances in technology during the space age have provided the Army with many new tools and techniques for observing and understanding the earth's atmosphere and for applying these advances to more efficient solutions of battlefield atmospheric problems. One of the most significant of these technological advances is a family of artificial earth satellites developed for meteorological purposes. Recent advances in satellite sensors which can distinguish the many electromagnetic subtleties of the radiation reflected and emitted from the earth's surface and atmospheric gas point to dramatically increased capabilities for weather measurements.

The Meteorological Satellite Technical Area (MSTA) of the US Army's Atmospheric Sciences Laboratory has conducted an active research program on applications of meteorological satellite data to determination of upper level (above 15 km) wind for nuclear fallout prediction (SATFAL). SATFAL research has advanced to the point where the feasibility of the concept has been established. Meteorological satellite measurements can provide the upper level wind data required for fallout prediction more efficiently than currently operational balloon-sonde systems.

## BACKGROUND

Requirements for the generation of nuclear fallout predictions on the battlefield in support of field Army operations are discussed in several documents.<sup>1, 2, 3</sup> Satisfaction of these requirements presumes a real-time knowledge of atmospheric transportation processes

(in particular the wind field) in the battlefield area in addition to information relative to the nuclear burst time, location and yield, and other important relevant physical parameters. The nuclear fallout prediction capability has been on readiness standby status for the past 30 years and has exerted a distinct impact on Army battlefield meteorological operations as a result of the data collection and analysis necessary for nuclear fallout prediction.

The current procedures for assessing the effects of wind on the distribution of radioactive fallout are described in TM 3-210, "Fallout Prediction".<sup>3</sup> The primary meteorological input is the data obtained by the GMD radio-tracked balloonsonde soundings (frequently referred to as radiosonde or rawinsonde soundings) of the upper atmosphere made by the US Army Artillery Meteorological sections. Soundings to at least 30 km altitude are required at 6-hour intervals<sup>3,4</sup> (minimum acceptable altitude is 24 km).

No other Army battlefield requirement for meteorological data extends above 15 km.

The current nuclear fallout prediction requirement for balloonsonde data in the 15 to 30 km altitude range imposes a substantial increase (over that required for the 0 to 15 km observations) in meteorological equipment, operations, and manhours on the battlefield. In addition, large errors<sup>5</sup> are possible with the current system, partly because of wind measurement errors (especially during strong wind conditions with attendant low elevation angles observed by the tracking systems) and partly because of space and time variability errors inherent in the data. Because of balloon trajectory, measurements at altitudes between 20 and 30 km are frequently taken at distances of 100 to 150 km from the balloon launch site.

## FALLOUT PREDICTION

Complete details for the fallout predictions are given in TM 3-210. Some of the principal factors which are determined from the meteorological data are briefly discussed here. The assessment of wind draft is determined from the effective wind profile which is defined by

$$\vec{v}(z) = \int_0^z \tau(\zeta) \vec{u}(\zeta) d\zeta / \int_0^z \tau(\zeta) d\zeta \quad (1)$$

where  $\vec{u}(\zeta)$  is the actual (measured) wind profile and  $\tau(\zeta)$  is the fall rate for nominal particles. The principal predictands are determined from the effective wind profiles. The predictands are:

a. The downrange distances,  $R$ , to Zone 1 which is related<sup>5</sup> to the nuclear yield,  $Y$ , and the effective wind speed,  $V$ , by the expression

$$R = AY^{2/5} V^{1/2} \quad (2)$$

where A is a proportionality constant.

b. The right and left radial lines which are determined from the effective wind directions at the  $2/3$  stem height and the cloud top height.

The fallout prediction for a specified yield becomes a function of the effective wind speed at the cloud bottom height and the effective wind direction at the cloud top height and the  $2/3$  stem height. These three heights, which are functions of yield, are shown in Figure 1 for yields ranging from 10 kilotons to 10 megatons. (The data for constructing this graph were taken from TM 3-210.) Since only the direction of the effective wind is required for altitudes above the cloud bottom height, it is evident that there is a rather large altitude range through which only the assessment of the direction of the effective wind is required.

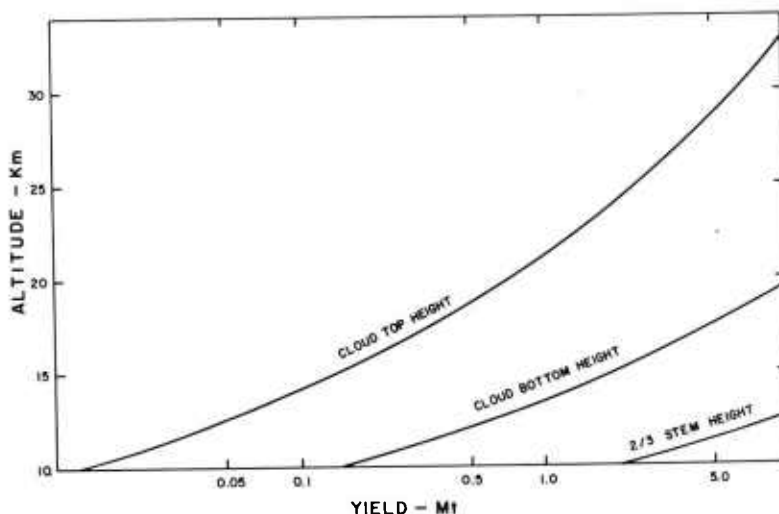


FIGURE 1: Nuclear Cloud Height Parameters

#### SATFAL WIND DETERMINATION THEORY

The advent of vertical temperature soundings from satellites has provided a new tool for atmospheric measurements. The thermal sounder is a passive instrument which senses the outgoing radiances in several wavelength intervals as seen from the top of the atmosphere. These radiances are integrated signatures of the thermal structure in the vertical column of the atmosphere in the field of view of the sounder. The basic physics which connects the radiance

to the temperature structure is provided by the radiative transfer equation. Algorithms have been developed which allow one to "invert" the radiance measurements and obtain the temperature profiles.

Two somewhat similar vertical temperature sounders are in operational use on polar orbiting satellites. These are the SSE instrument currently flown on the DMSP satellites and the VTPR flown on the NOAA satellites. These instruments scan perpendicular to the orbital path in order to obtain data extending approximately 1000 km to either side of subsatellite path. Differences in the scan rate, dwell time, and orbital altitude result in the two distinct observational grid patterns shown in Figures 2 and 3. A temperature profile, if desired, may be determined at each of these grid points.

The use of satellite measured radiance data to calculate a usable approximation of the wind field has been discussed by several authors.<sup>5,6,7</sup> These observations have been based upon well-known relationships between atmospheric thermal and dynamic structures with the wind given by the geostrophic wind through the thermal wind equation. The geostrophic wind,  $\vec{V}_g$ , is given by (cf Holton<sup>8</sup> for derivation of equation)

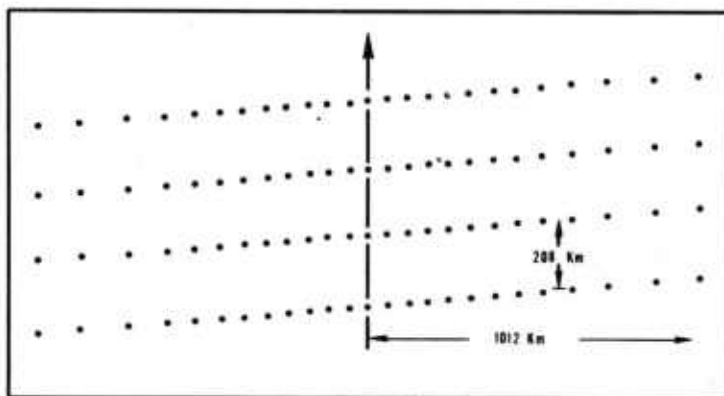


FIGURE 2; Distribution of Earth Scan Scene Stations for the SSE Relative to the Satellite Subtrack.

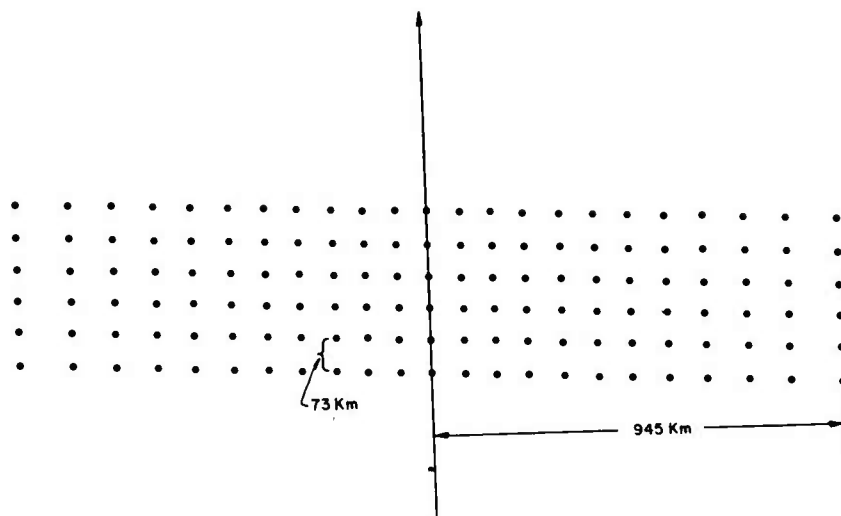


FIGURE 3: Distribution of Earth Scan Scene for the NOAA-4 VTPR.

$$\vec{V}_g = \frac{1}{f\rho} \vec{k} \times \vec{\nabla}_h P$$

where  $\vec{k}$  is a unit vector in the vertical direction,  $\vec{\nabla}_h P$  is the horizontal pressure gradient,  $\rho$  is density, and  $f$  is the Coriolis parameter. The vertical shear (derivative) of the geostrophic wind is given by the thermal wind which may be expressed in finite difference form by

$$\vec{V}_g(P_2) - \vec{V}_g(P_1) = \frac{R}{f} \vec{k} \times \vec{\nabla}_p \bar{T} \ln(P_1/P_2) \quad (4)$$

where  $\bar{T}$  is the average temperature between pressure levels  $P_1$  and  $P_2$  ( $P_2 < P_1$ ),  $R$  is the gas coefficient for dry air, and  $\vec{\nabla}_p \bar{T}$  is the horizontal temperature gradient. (NOTE: Pressure and height are related through the hydrostatic equation.)

Equation (4) shows that determination of the wind at  $P_2$  requires only knowledge of the wind at  $P_1$  and the horizontal temperature gradient  $\vec{\nabla}_p \bar{T}$ . This procedure can be extended through a sequence of pressure levels  $P_1 > P_2 > \dots > P_n$ . This is the basic concept used in SATFAL. A balloonsonde measurement is used to provide the "tie-on" value at the lower level (at or near 15 km altitude).

DUNCAN

The horizontal temperature gradient required by Equation (4) is determined numerically from temperature profiles derived from the satellite observed radiances.

#### SATFAL/RADIOSONDE COMPARISONS

Six radiosonde stations are located on White Sands Missile Range (WSMR), New Mexico. (See Figure 4 for relative locations.) These stations are operated as required for meteorological support of range operations. A special data collection was conducted between February and December 1975 to obtain a data base for SATFAL evaluation. Radiosonde balloons were launched (nearly) simultaneously from the three lower range stations (WSD, SMR and HMN) approximately 1 hour prior to the passover of the NOAA-4 satellite. (The release time was chosen to minimize the time variability of the wind data.) The average of the three measured wind profiles was used as "truth" data for comparative evaluation. Thirty-two sets of comparisons were collected.

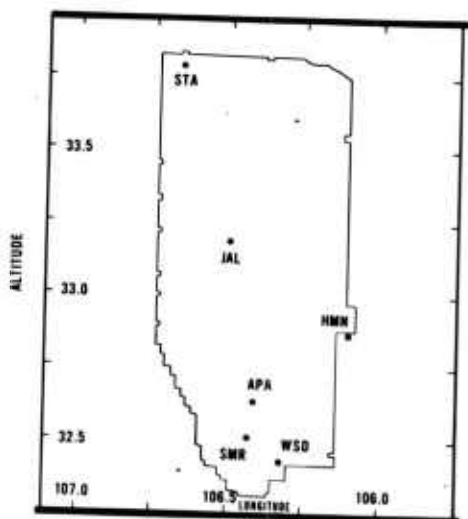


FIGURE 4: WSMR Radiosonde Sites.

Eleven abutting pressure layers extending from 125 to 10 mb (corresponding altitudes are approximately 15 to 31 km) were selected for thermal wind computations employing Equation 4. To determine the horizontal temperature gradients, a 7 by 7 array of



VTPR data centered at WSMR\* was inverted to obtain temperature profiles. The gradients were then estimated by least squares techniques. The average radiosonde measurement at 15 km was used as the "tie-on" value for the thermal winds which were used to construct the SATFAL profile to 30 km. Results for 23 May 75, 14 Oct 75, and 4 Dec 75 are shown in Figures 5, 6 and 7.

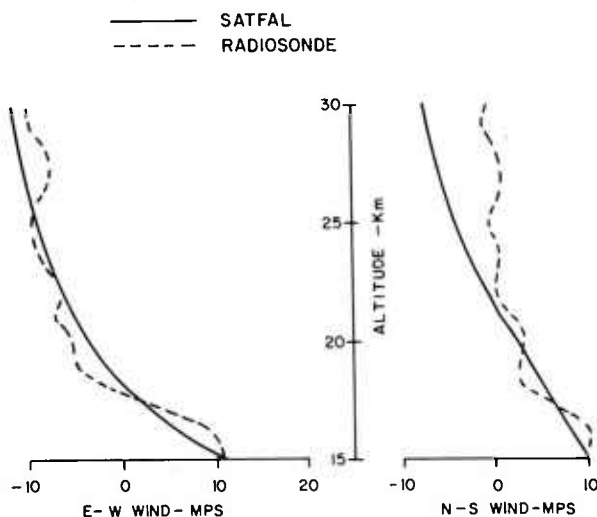


FIGURE 5: SATFAL/Radiosonde Comparison for 23 May 75.

These three cases demonstrate the typical situations which were encountered among the comparisons. The first case shows good agreement between the SATFAL and radiosonde winds throughout the profile. The second example exhibits larger differences at specific altitudes; however, these differences change sign with altitude and tend to cancel each other when the effective wind is computed. For the 4 Dec 75 comparison, the magnitude of the actual wind change was greater than that given by the thermal winds in the altitude range 15 to 18 km. The result was a bias difference throughout the remainder of the profile; however, the two wind profiles agreed well in direction.

---

\*For purpose of this study the location of WSMR was defined to be 32.23N latitude, 106.28W longitude.

DUNCAN

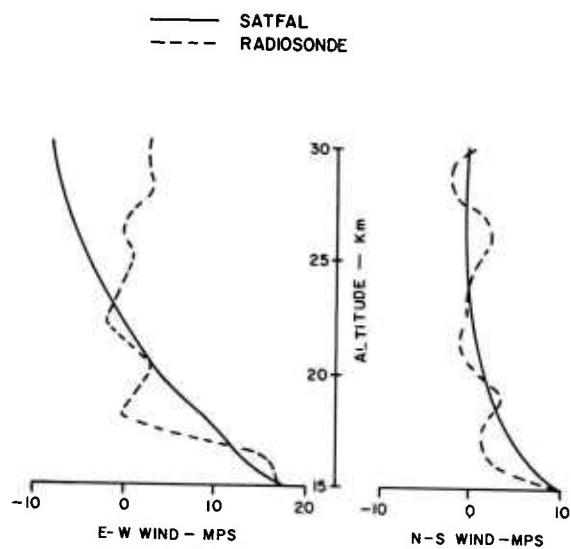


FIGURE 6: SATFAL/Radiosonde Comparison for 14 Oct 75.

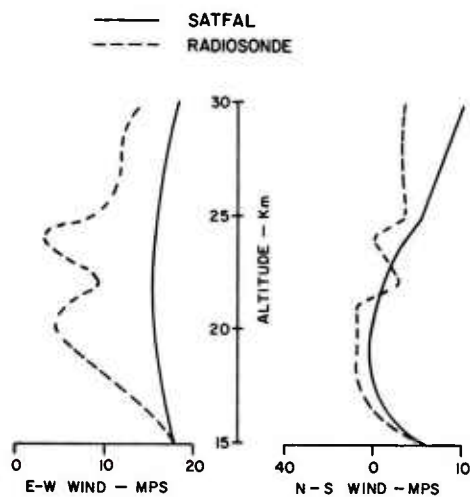


FIGURE 7: SATFAL/Radiosonde Comparison for 4 Dec 75.

Proper assessment of the significance of the difference between the SATFAL wind profile and the radiosonde wind profile must be in terms of the intended application, i.e., the nuclear fallout prediction. Since wind enters the prediction through the effective wind velocity as defined by Equation 1, the first step in this evaluation is the computation of the effective winds. Effective wind profiles for the three cases discussed above were computed by using Equation (1) with the fall rate data given in TM 3-210. These results are shown in Figures 8, 9 and 10.

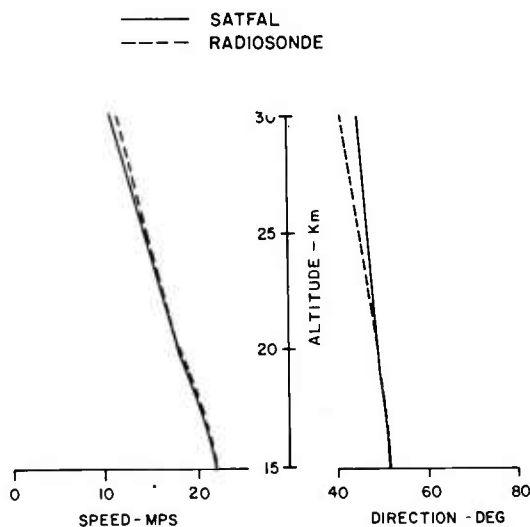


FIGURE 8: Effective Wind Comparison, 23 May 75.

For a fixed yield, Equation (2) shows that the downrange distance to Zone 1 is proportional to the square root of the effective wind speed. Logarithmic differentiation of Equation (2) gives

$$\Delta R/R = 0.5 \Delta V/V \quad (5)$$

Thus the percent change in R resulting from the different methods for determining the effective wind speed is only 1/2 the percent difference in the effective wind speeds. Equation (5) was used to assess the percent difference in R resulting from the two different methods of obtaining the wind profile - SATFAL and radiosonde. Results are shown in Table 1. For the cloud bottom heights shown, the majority of the differences are less than 5 percent with only four observations exceeding 10 percent.

DUNCAN

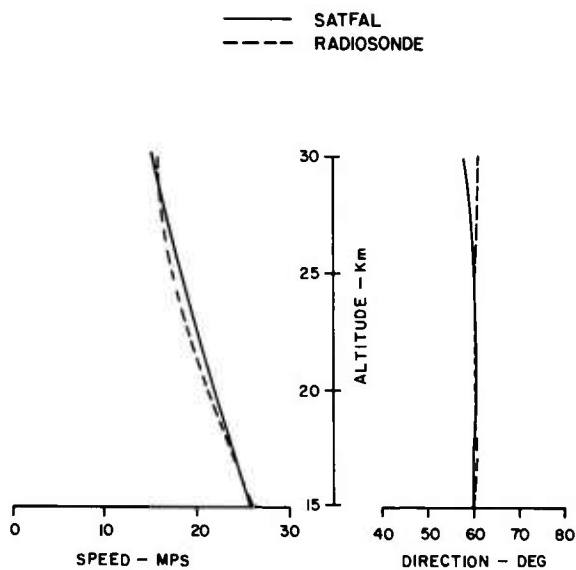


FIGURE 9: Effective wind comparison, 19 Oct 75

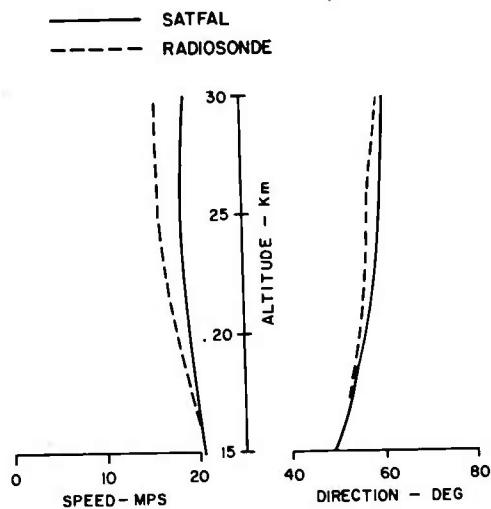


FIGURE 10: Effective wind comparison, 4 Dec 75.

$\Delta R/R$	at 17.5 km	at 20 km
<5%	27	14
5-10%	5	14
10-15%	0	4

TABLE 1: Frequency of occurrence of downrange distances to Zone 1 differences.

$\Delta \theta$	at 20 km	at 25 km	at 30 km
<5°	23	15	14
5°-10°	6	7	6
10°-15°	2	4	3
>15°	1	6	8

TABLE 2: Frequency of occurrence of effective wind direction differences.

Table 2 shows the frequency of occurrence of effective wind direction differences for three different altitudes. Direction differences are quite small, usually less than 10 and frequently less than 5 degrees. Most of the cases where wind differences exceeded 15 degrees were under light wind speed conditions where small changes in the vector wind can result in large direction differences. Very good agreement to 30 km altitude was found in SATFAL/radiosonde comparisons of effective wind direction.

When used in conjunction with Figure 1, the results presented in Tables 1 and 2 show the difference which might be expected between fallout predictions computed from SATFAL and radiosonde winds. As an example, for an assumed yield of 2.5 MT (or smaller), (1) the radial line corresponding to the 2/3 stem height would be the same; (2) the percent difference in downrange distance to Zone 1 would probably be less than 5 percent, and (3) the radial lines corresponding to the cloud top height should agree to within 5 degrees.

#### SATFAL SYSTEM

A block diagram for a proposed SATFAL field system is shown in Figure 11. The principal components are a ground receiver station to obtain and preprocess the satellite data, a minicomputer which will perform the necessary computations, and an output device for display of results. The radiance data from the satellite will be transmitted directly to a battlefield receiving station. Since the data will be transmitted at a low data rate (1000 bits per second), a small omnidirectional quadrifilar antenna will be used to collect the data at the receiver station.

The satellite received radiances and pertinent radiosonde data for the lower levels are input into a minicomputer for determination of the wind profile using the thermal wind relations. The minicomputer will also have the capability for computing the fallout prediction and display of these results in the desired format.

A Letter of Agreement (LOA) for the development of the SATFAL system is currently being negotiated between the Atmospheric Sciences Laboratory and the appropriate elements of the Training and Doctrine Command (TRADOC).

#### CONCLUSIONS

The SATFAL system discussed herein employs the advanced technology provided by meteorological satellites to provide an efficient means for satisfying the Army's requirements for upper altitude wind data. The procedure and theory for determination of the wind profile from radiance measurements obtained by vertical



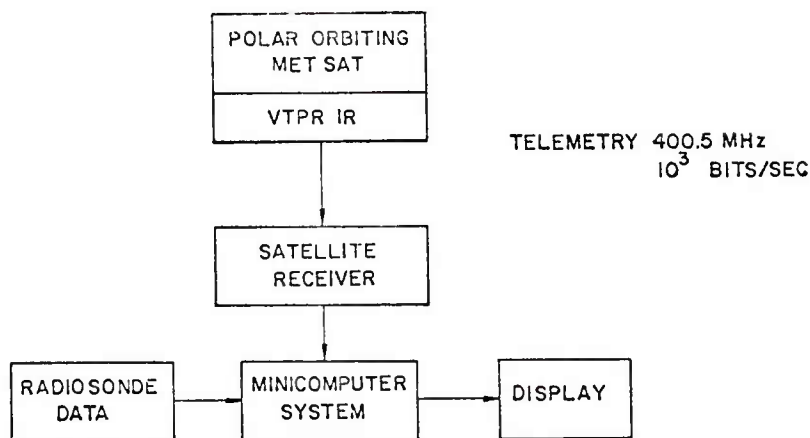


FIGURE 11: Block diagram of SATFAL system.

temperature sounders on polar orbiting meteorological satellites have been presented and discussed.

An analysis of 32 comparisons of SATFAL and conventional radiosonde wind observations shows that there is very little (indeed acceptable) difference between fallout predictions computed from winds obtained by the two procedures. With the current steady improvement of the state of the art in satellite radiometric measurements and technology, steadily increasing SATFAL wind accuracy is expected.

A SATFAL system for tactical use was presented and discussed. Because of its basic simplicity and automated concepts, this system is ideally suited for tactical battlefield applications. Since the SATFAL system will provide all the wind data required by the Army above 15 km, it will obviate the need for high altitude balloonsondes and should, thereby, allow for a reduction in meteorological equipment and personnel required for balloonsonde observations.

REFERENCES

1. "Army Qualitative Research and Requirements for Nuclear Effects Information FY-76 Edition" (U), SECRET, US Army Nuclear Agency, 1974.
2. AR 115-10/AFR 105-3, "Meteorological Support for the Field Army," Department of the Army and the Air Force, Washington, D.C., June 1970.
3. Department of the Army Technical Manual TM 3-210, "Fallout Prediction," Headquarters, Department of the Army, Washington, D.C., December 1967.
4. Shinn, Joseph H., "Optimum Wind Soundings and Army Fallout Prediction Accuracies," US Army Atmospheric Sciences Laboratory, WSMR, NM., 1973.
5. Elsberry, R. L., J.W. Wright, and F.L. Martin, "An Experimental Method of Determining Ballistic Wind Making Direct Use of SIRS Radiances," FAMOS TM 9-71, Naval Postgraduate School, Monterey, CA, 1971.
6. Duncan, L.D. and M.D. Kays, "Determining Nuclear Fallout Winds from Satellite Observed Spectral Radiances," US Army Atmospheric Sciences Laboratory, WSMR, NM, 1974.
7. Alexander, G.D., "Determining Geostrophic Winds Using a Satellite Borne Infrared Radiometer," US Army Atmospheric Sciences Laboratory, WSMR, NM, 1975.
8. Holton, J.R., An Introduction to Theoretical Meteorology, Academic Press, New York, 1972.

## EXPERIMENTAL SCRUB TYPHUS IMMUNOGENS (U)

GEORGE H.G. EISENBERG, JR., MAJ, MSC  
JOSEPH V. OSTERMAN, PH.D.  
WALTER REED ARMY INSTITUTE OF RESEARCH  
WASHINGTON, D.C. 20012

## INTRODUCTION

During World War II, scrub typhus was recognized as a major cause of casualties among troops operating on islands in the Pacific area. The disease was encountered again in Vietnam and its wide geographic distribution suggests that it may be a factor in any future conflict in the Asiatic Pacific region (Figure 1). During World War II, no drugs were available for treatment: men were incapacitated for an average of 60-70 days and case-fatality rates in some areas were as high as 35% (1). Due to lack of an effective vaccine, scrub typhus remained a casualty producer among our troops operating in Vietnam. Fortunately, chloramphenicol and the tetracyclines are now available for treatment and fatality is a rare consequence of infection. However, the availability of antibiotics has not altered the serious reduction in unit combat efficiency resulting from loss of personnel during treatment and recovery from the disease.

Development of a vaccine has been complicated by the considerable number of serologically heterogeneous strains of the causative agent, Rickettsia tsutsugamushi. Repeated attempts to develop a vaccine using conventional methods, such as inactivation with formalin, have been unsuccessful. In animal trials, immunity to challenge with the vaccine strain was relatively low and immunity to heterologous strains was almost nonexistent (2-6). These immunogens were also found to be ineffective in providing protection for man (7,8).

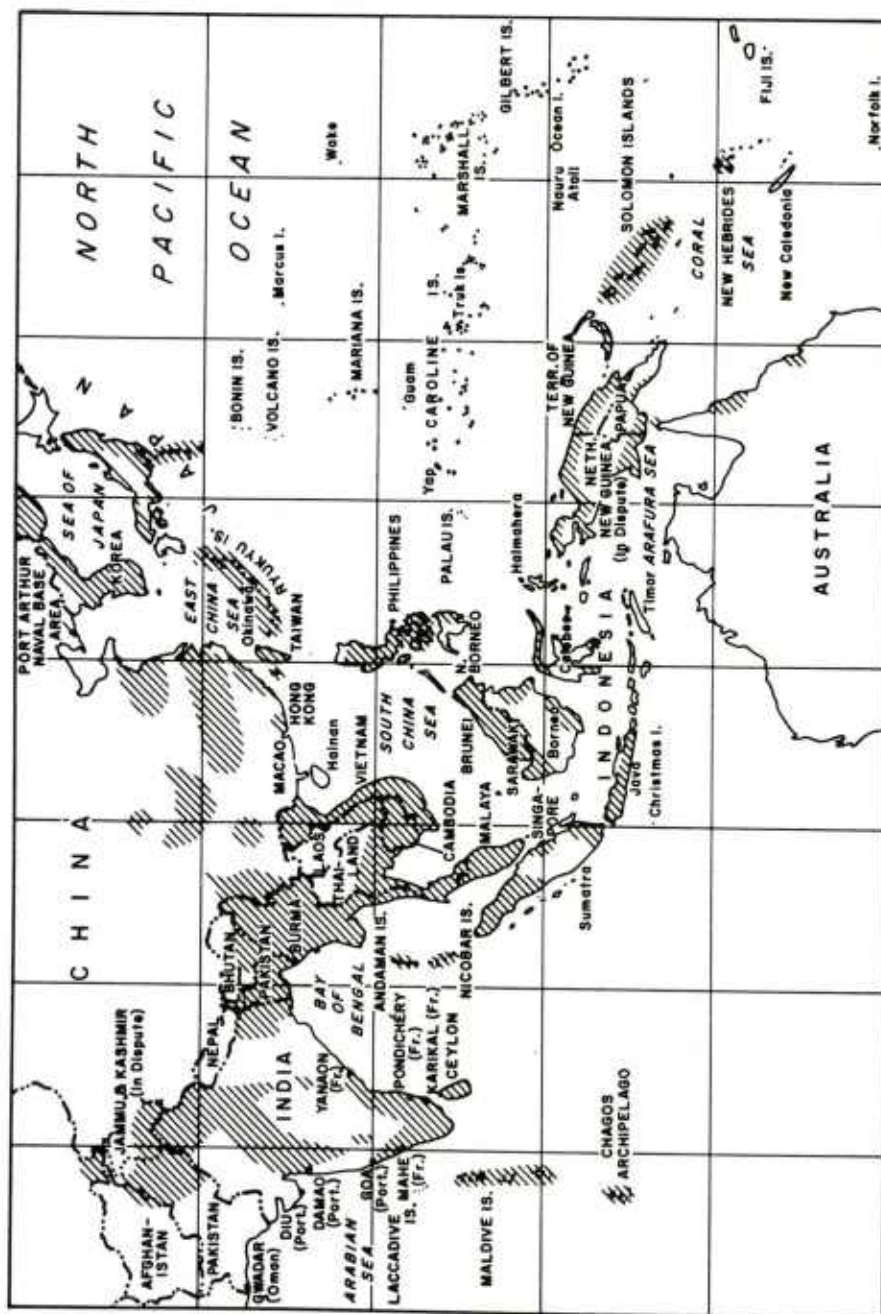


Fig. 1. Geographic distribution of scrub typhus.

This study arose from the conviction that an alternate method of rickettsial inactivation was required. New data suggested that cell-mediated immunity (CMI), rather than antibody, was required for heterologous protection (9). Other investigators had shown that exposure of rickettsiae to ultraviolet light caused a very rapid loss of infectivity, but a much slower decline in metabolic activity (10). Since the penetration of mammalian cells by rickettsiae requires active rickettsial metabolism, it was felt that radiation might be a tool that could be used to produce a non-replicating immunogen capable of infecting at the cellular level and possibly eliciting a cell-mediated immune response. Gamma radiation was chosen because it is more penetrating than ultraviolet radiation, thereby being more suitable for processing large volumes of immunogen.

#### MATERIALS AND METHODS

Suspensions of Karp and Kato strains of R. tsutsugamushi, both of which are highly virulent for mice, were prepared from yolk-sacs of pathogen-free chicken eggs using standard methods (9). At the time of harvest, aliquots were taken for titration in mice (11) and, as appropriate, for preparation of formalin-killed immunogens. The remaining suspensions were rapidly frozen and stored at -80C until required. When titrations were complete, suspensions having titers greater than or equal to  $10^8$  fifty percent mouse-lethal doses (MLD<sub>50</sub>) per gram yolk-sac were used in these studies.

All immunogens were prepared from infected yolk-sac suspensions of the Karp strain. Formalinized immunogens were made by the procedure of Smadel et al (6) and stored at 4C. Radiation-inactivated immunogens were prepared by exposing the frozen suspensions to 300 krad  $\gamma$ -radiation in a <sup>60</sup>Co  $\gamma$ -irradiator. Initial experiments had shown this dose to be well above the level required to completely destroy lethality of the suspensions without seriously affecting immunogenicity. The irradiated immunogens were used on the day of exposure.

Immunogens were evaluated in mice using the outbred ICR strain and the inbred BALB/c strain.\* Vaccination consisted of three

---

\* In conducting the research described in this report, the investigators adhered to AR 70-18 and to the "Guide for Laboratory Animal Facilities and Care," as promulgated by the Committee on the Guide for Laboratory Animal Facilities and Care of the Institute of Laboratory Animal Resources, National Academy of Sciences - National Research Council.

intraperitoneal (i.p.) injections of immunogen administered at five day intervals. The mice were given a graded challenge of virulent Karp or Kato by i.p. injection fourteen days after completion of the vaccination regimen. Deaths occurring from six to twenty-one days post challenge were considered specific. Protection levels were calculated from the difference in  $MLD_{50}$  in vaccinated and normal control mice that had received the graded challenges. Blood specimens were taken from vaccinated animals at time of challenge and from survivors 4-6 weeks post challenge. Serum antibody titers were determined by complement fixation (CF) test (12) using strain-specific antigens (13). The level of cell-mediated immunity at time of challenge was determined by transfer of one mouse-equivalent of spleen cells from vaccinated donor mice to normal recipients. This required the use of the inbred BALB/c strain of mice to allow cell transfer without immune rejection. After enumeration, the washed spleen cells, suspended in cell culture medium, were transferred to normal recipients by i.p. injection. Recipients were given graded challenges of Karp and Kato eight hours after cell transfer. The mice were observed daily and mortality was recorded as previously described.

Studies using the L-929 line of mouse fibroblast cells were performed to determine the penetrative capacity of the immunogens. The rickettsiae were sedimented by high speed centrifugation and resuspended in fresh medium to remove residual traces of formalin or any radiation-induced by-products that could have a potential adverse effect on the recipient animal cells. Equal concentrations of L-cells and rickettsiae were mixed and incubated for two hours at room temperature. The L-cells were washed free of unattached rickettsiae and were used to prepare stained slides, after which 200 cells per slide were examined to determine the total number of rickettsiae that had penetrated the cells. These values were compared with the values obtained in parallel tests using untreated rickettsiae.

## RESULTS AND DISCUSSION

To provide a certain degree of historical continuity to the research and to insure that the comparisons were valid with respect to the capabilities of the formalinized immunogens, the formalinization techniques and the vaccination and challenge schedules used by Smadel and co-workers (6) in their extensive investigations on the efficacy of formalinized vaccines were used for these studies. Mouse protection tests using formalinized immunogens prepared from two different Karp suspensions provided results comparable with those



of Smadel's group (5,6) (Table 1). Approximately 50% of the vaccinated mice were protected against homologous challenge doses in the range of 1,000 MLD<sub>50</sub>, but almost none of the mice were protected against even minute challenge doses of the heterologous Kato strain. In addition, even with homologous challenge, absolute protection was not achieved. Vaccinated mice died at the lowest challenge dose employed and most surviving mice showed signs of distress at some time during the challenge period. The comparison with the results in mice vaccinated with irradiated suspensions is dramatic. Protection against homologous challenge was approximately 100-fold greater, and the protection was absolute in the 1,000-10,000 MLD<sub>50</sub> range. At these doses and lower challenge levels all mice survived with no indication of distress at any time. In addition, there was significant protection against heterologous challenge. The majority of the mice were protected against challenge doses up to 13,000 MLD<sub>50</sub>, a higher level of protection than that achieved against homologous challenge using formalin-killed rickettsiae. However, most of these mice challenged with the heterologous strain did show signs of distress during recovery.

Table 1. Survival of ICR mice vaccinated with Karp immunogens

Inactivating agent	Number of irradiated rickettsiae/injection	Challenge strain	50% protection level (MLD <sub>50</sub> )
Formalin	$3.0 \times 10^7$	Karp	790
	$1.8 \times 10^8$	Karp	3,200
		Kato	$\leq 3$
$\gamma$ -radiation	$1.6 \times 10^7$	Karp	$\geq 79,000$
		Kato	13,000
	$1.3 \times 10^7$	Karp	500,000
		Kato	13,000

The CF test results (Table 2) indicate that neither type of immunogen was a potent stimulator of antibody production, even though the mice were capable of responding to produce high antibody titers when given the appropriate stimulus. The challenged survivors had high titers directed against the challenge strain. Since both the initial response and the response to challenge were essentially the same for both types of immunogens, it is unlikely that antibody played a major role in providing the heightened protection observed with use of the irradiated suspensions. However, spleen cell transfer experiments revealed a profound difference in response of mice after vaccination with the two types of immunogens (Table 3). Little homologous and no heterologous protection was observed among mice that had received cells from donors vaccinated with formalin-killed organisms. On the other hand, of the recipients that had been given cells from donors vaccinated with irradiated immunogens, 80% resisted homologous challenge with 1,000 MLD<sub>50</sub>, 100% survived homologous challenge of 100 MLD<sub>50</sub>, and 20% survived heterologous challenge of 100 MLD<sub>50</sub>. Although protection transferred by spleen cells was lower than that seen in vaccinated donor animals, the relative degree of protection transferred was proportional to the degree of protection observed in the donors. In each case the level of homologous protection was approximately ten-fold greater than the level of heterologous protection. These characteristics appear to be shared by untreated rickettsiae. Shirai *et al* (9) observed that protection after sub-lethal scrub typhus infection was due primarily to induction of CMI. They also noted higher protection levels in donors than in recipients, and proposed that this could be due either to disturbance of normal maturation events by early cell transfer or to a difference in quantities of proper effector cells in the spleen and peritoneal cavity. Therefore, the evidence indicates that both untreated rickettsiae and radiation-inactivated rickettsiae possess capabilities that enable them to trigger a cell-mediated immune response in their host. It is apparent that these capabilities are not shared by organisms killed by treatment with formalin.

Other investigators have shown that *R. tsutsugamushi* infects host cells by active penetration (14) and that the rickettsiae are capable of persisting in an immune host for extended periods of time (15-17). Either of these characteristics could be responsible for induction and maintenance of CMI. Therefore, normal, irradiated, and formalinized rickettsiae were tested to determine their relative capabilities for penetrating mammalian cells (Table 4). The tests, performed by two investigators on separate days, are quite consistent. Both irradiated and untreated

Table 2. Complement fixation titers of ICR mice vaccinated with Karp immunogens

Inactivating agent	Challenge strain	Time of specimen collection			
		Day of challenge		4-6 weeks post challenge	
		CF antigen		CF antigen	
		Karp	Kato	Karp	Kato
Formalin	Karp	10 <sup>a</sup>	<10	640	20
	Kato			80	160
γ-radiation	Karp	<10	<10	320	20
	Kato			20	80

<sup>a</sup> Titers are expressed as the reciprocal of the highest dilution of serum causing  $\leq$  50% hemolysis. Lowest dilution tested was 1:10.

Table 3. Survival of BALB/c mice receiving spleen cells from donors vaccinated with Karp immunogens

Type of Immunogen	Challenge strain	Approximate challenge dose (MLD <sub>50</sub> )			
		10,000	1,000	100	10
Formalinized	Karp	0/5 <sup>a</sup>	0/5	0/5	1/5
	Kato	0/5	0/5	0/5	0/5
Irradiated	Karp	0/5	4/5	5/5	
	Kato	0/5	0/5	1/5	

<sup>a</sup> Ratio of survivors to total number of mice challenged.

Table 4. Penetration of L-929 cells by Karp immunogens

Inactivating agent	Experiment	
	1	2
Formalin	0 <sup>a</sup>	4
$\gamma$ -radiation	68	60
None	94	95

<sup>a</sup> Percentage of cells observed containing intracellular rickettsiae.

organisms were capable of penetration, a property not shared by formalin-killed rickettsiae. Since penetration is an active process requiring metabolic activity by the rickettsiae, the lower values seen with radiation-inactivated immunogens are probably an indication of the extent of total cell damage caused by irradiation. Formalin kills and fixes the rickettsiae. Therefore, the few intracellular formalinized rickettsiae observed provide a base line measurement indicative of the level of phagocytosis by the L-cells. The question of persistence of irradiated rickettsiae after penetration is, as yet, unresolved.

#### CONCLUSIONS

Radiation has been shown to produce an immunogen capable of inducing a high degree of homologous and heterologous protection. Observation of significant heterologous protection is considered particularly important because the existence of a large number of minimally cross-reacting serotypes of *R. tsutsugamushi* make vaccination impractical when protection is monospecific. Considerably greater effort now will be required to purify the immunogen, to test its stability and the duration of immunity it induces, and to determine the most effective vaccination regimen in order to fully develop the vaccine potential. *In vivo* studies have shown that irradiated rickettsiae, like normal rickettsiae, are capable of

triggering a cell-mediated immune response. In vitro studies suggest that the ability to actively penetrate mammalian cells, a property previously observed only in untreated organisms, may be implicated in the triggering mechanism. Therefore, it is felt that further work with irradiated rickettsiae in the mouse model will lead to greater understanding of the mechanism responsible for initiation of cell-mediated immune responses.

#### REFERENCES

1. Maxcy, Kenneth F. 1948. Scrub typhus (tsutsugamushi disease) in the U.S. Army during World War II, p. 39. In F.R. Moulton (ed.), Rickettsial Diseases of Man. Amer. Assoc. for the Adv. of Science, Washington, D.C.
2. Plotz, H., B.L. Bennett, and R.L. Reagan. 1946. Preparation of an inactivated tissue culture scrub typhus vaccine. Proc. Soc. Exp. Biol. Med. 61: 313-317.
3. Fulton, F., and L. Joyner. 1945. Cultivation of Rickettsia tsutsugamushi in lungs of rodents. Lancet 2: 729-734.
4. Bailey, C.A., F.H. Diercks, and J.E. Proffitt. 1948. Preparation of a serological antigen and a vaccine for experimental tsutsugamushi disease (scrub-typhus). J. Immunol. 50: 431-441.
5. Rights, F.L., and J.E. Smadel. 1948. Studies on scrub typhus (tsutsugamushi disease). II. Heterogeneity of strains of R. tsutsugamushi as demonstrated by cross-vaccination studies. J. Exp. Med. 87: 339-351.
6. Smadel, J.E., F.L. Rights, and E.B. Jackson. 1946. Studies on scrub typhus. II. Preparation of formalinized vaccines from tissues of infected mice and rats. Proc. Soc. Exp. Biol. Med. 61: 308-313.
7. Berge, T.O., R.L. Gauld, and M. Kitaoka. 1949. A field trial of a vaccine prepared from the Volner strain of Rickettsia tsutsugamushi. Am. J. Hyg. 50: 337-342.
8. Card, W.I., and J.M. Walker. 1947. Scrub-typhus vaccine; field trial in south-east Asia. Lancet 1: 481-483.

9. Shirai, A., P.J. Catanzaro, S.M. Phillips, and J.V. Osterman. 1976. Host defenses in experimental scrub typhus. II. Role of cellular immunity in heterologous protection. Submitted for publication.
10. Allen, E.G., M.R. Bovarnick, and J.C. Snyder. 1953. The effect of irradiation with ultraviolet light on various properties of typhus rickettsiae. J. Bacteriol. 67: 718-723.
11. Reed, L.J., and H. Muench. 1938. A simple method of estimating fifty per cent endpoints. Amer. J. Hyg. 27: 493-497.
12. Kent, J.F., and E.H. Fife. 1963. Precise standardization of reagents for complement fixation. Am. J. Trop. Med. Hyg. 12: 103-116.
13. Elisberg, B.L., J.M. Campbell, and F.M. Bozeman. 1968. Antigenic diversity of Rickettsia tsutsugamushi: epidemiologic and ecologic significance. J. Hyg. Epidemiol. Microbiol. Immunol. 12: 18-25.
14. Cohn, Z.A., F.M. Bozeman, J.M. Campbell, J.W. Humphries, and T.K. Sawyer. 1959. Study on growth of rickettsiae. V. Penetration into mammalian cells in vitro. J. Exp. Med. 190: 271-292.
15. Fox, J.P. 1947. The long persistence of Rickettsia orientalis in the blood and tissues of infected animals. J. Immunol. 59: 109-114.
16. Smadel, J.E., E.B. Jackson, and A.B. Cruise. 1949. Chloromycetin in experimental rickettsial infections. J. Immunol. 62: 49-65.
17. Smadel, J.E., H.L. Ley, Jr., F.H. Diercks, and J.A.P. Cameron. 1952. Persistence of Rickettsia tsutsugamushi in tissues of patients recovered from scrub typhus. Am. J. Hyg. 56: 294-302.



EFFECTS OF HIGH ALTITUDE AND HEAT ON SIMULATED  
ARTILLERY FIRE DIRECTION CENTER TASKS (U)

BERNARD J. FINE PH.D., JOHN L. KOBRICK, PH.D.  
U. S. ARMY RESEARCH INSTITUTE OF ENVIRONMENTAL MEDICINE  
NATICK, MASSACHUSETTS 01760

This research is concerned with the separate effects of heat and altitude upon the individual performance of a number of tasks analogous to those required of members of artillery fire direction center (FDC) teams.<sup>1</sup>

The FDC is the nerve center of the artillery system, and, as such, is responsible for the collection, integration and processing of a complex body of information which ultimately determines the precision with which the weapons acquire their targets. Errors in target acquisition can have disastrous consequences. The cost of shelling one's own troops, hitting civilian population areas or missing critical tactical or strategic targets is inestimable. While there may be many causes for these occurrences, such as defective materiel and alignment errors at the gun, human errors in calculation and/or judgement by FDC personnel can play a major, if as yet undocumented, role.

Both extreme heat (1,2,3) and high terrestrial elevation<sup>2</sup>

<sup>1</sup>This human research study, in protocol form, was reviewed and approved by the Office of The Surgeon General for The Department of The Army in accordance with Army Regulation 70-25.

<sup>2</sup>"High terrestrial elevation" is used to differentiate the altitude levels involved in land operations from those involved in aviation. For convenience, the term "altitude" will be used throughout this paper, but it is intended that the term refer only to high altitudes encountered on land.

(4,5,6) have been shown to decrease the efficiency and accuracy of certain kinds of mental functions. However, reviews of the literature on the effects of heat and of altitude on human mental performance (7,8,9,10) agree that any generalizations are complicated by differences between separate findings in such factors as the specific tasks or dimensions measured, methods of measurement, severity of conditions, durations of exposure, work schedules, kinds of subjects participating in studies and meaningfulness to the subjects of the work performed.

Insofar as it is possible to extrapolate from this literature, it appears that most performance functions generally deteriorate as temperature increases above 85° effective temperature (ET) or as altitude increases above 4000 meters. These findings have military significance because such limiting conditions will be exceeded in many areas of the world where tactical operations could take place.

There is very little research directly linking the scientific psychological literature to the types of tasks routinely performed in military systems like the artillery FDC. Such a link would have great advantage by allowing real military tasks to be conceptualized in a scientific framework which is more conducive to understanding the nature of decrements or increments occurring in the performance of the tasks, and would aid in the development of techniques by which the decrements could be reduced or the increments enhanced. Understanding the effects of the stressors on performance in terms of scientific concepts can also facilitate generalization of the results to other situations, in contrast to the limited knowledge obtainable from simple observation of performance changes alone.

This study reports an attempt to bridge the gap between the psychological literature and one military system, the artillery FDC. The approach uses an experimental model, firmly rooted in basic science, which has as its dependent variables performance of actual FDC tasks in simulated, but, nevertheless, realistic experimental settings. In this model, the impact of the independent variables, heat and altitude, is assessed by comparison of performance under those conditions with performance under optimum conditions. The real tasks used are conceptualized according to their psychological dimensions, such as analytical thinking, psychomotor performance or short-term memory. The psychological dimensions, in turn, are conceptualized in the light of recent developments in research on brain hemisphere dominance and localization of abilities and functions (11,12,13). In addition, the subjects are broadly characterized according to personality (14,15), cognitive style (16) and

personal demographic information. Assays of biochemical substrates, such as cortisol, dopamine- $\beta$ -hydroxylase and uric acid, which are thought to be correlated with psychological processes, are also included in the model. These intervening psychological and biochemical variables should provide the link between the body of scientific knowledge and the operational military milieu, and should enable the results of specific studies to be generalized to other military systems in which the same psychological dimensions are called into play.

A major difficulty encountered in making conclusions or generalizations about the operational capabilities of professional FDC teams is that the experience and/or training levels of individual members are different. The members also differ in other respects such as those exemplified by the intervening variables noted above.

Consequently, since these sources of variation co-exist and may interact with the environmental stressors, it is virtually impossible to relate the occurrences of errors in performance to their principal predisposing factors with any degree of confidence.

Because of this, it was decided that a more unified and meaningful approach would be to use naive subjects exposed to controlled and standardized training and experience prior to their being tested under stressful conditions. Due to time constraints, training had to be less extensive than that provided in the professional FDC school. To compensate for this, FDC tasks were carefully selected, and in some cases slightly modified, to develop a battery of tasks which were relatively simple to perform but which, nevertheless, appeared to retain the psychological dimensions of their more complex FDC counterparts. Accordingly, it should be emphasized that the model is based on the assumption that naive subjects, highly trained on relatively simple tasks, will react to stress in a manner similar to that of professional FDC personnel, highly trained on similar but more complex tasks. Since this assumption is basic to the entire research program, it is essential that its validity be tested in the course of carrying out the research.

This is the first in a systematic series of studies. It was designed primarily to test the efficacy of the model, the design, the tasks, and the training, and above all, to determine if reasonably large decrements in performance do occur under the environmental conditions involved. Obviously, if decrements in performance of the selected tasks do not appear under the severe environmental conditions used and the fairly heavy work load imposed, the justification for pursuing this line of approach would be seriously weakened.

## METHOD

### SUBJECTS

Thirty male soldiers, ages 18-25, were studied in groups of six. Each group was briefed on the purpose and design of the research and its potential hazards, and received an introductory trial flight at altitude prior to the members signing voluntary consent forms. The groups were sequentially trained and tested as separate units, but otherwise underwent the same test procedures and environmental exposures.

### APPARATUS AND PROCEDURE

All training and testing was conducted in an environmental chamber capable of producing both hypobaric and hot-wet climatic conditions. Subjects were seated at Army field tables grouped together in the center of the chamber, and were provided with individual headphones which could be adjusted separately for preferred loudness. All headphones were connected in common to a tape recorder which played recordings of simulated Army communications. With this arrangement, all subjects heard the same series of messages at the same points in time throughout the study. The messages were designed to simulate actual artillery communications, including typical background noise, a variety of voices and varying levels of distortion. The message content incorporated four different task requirements inherent in the operations of a typical artillery company FDC team. These were: (1) reception and notation in standard artillery fire mission format of the range and elevation of a hypothetical military target, followed by the computation of its associated site value using a regulation artillery graphical site table, a modified slide rule routinely used by an FDC team for this purpose; (2) reception, notation, and decoding of encoded alphanumeric grid coordinates from a standard Army field map by use of a standard Army code wheel device; (3) reception, notation, and decoding of encoded military-type messages using a typical Army code book; (4) reception and notation of meteorological (MET) data in standard format used for transmission to FDC teams for fire mission computations.

The messages were simulated as though coming either from several actual forward observers, or from a MET team in the field. The fire mission messages were designed to approximate eight different levels of difficulty, one-eighth of the messages representing each level, respectively. Each code book message contained from four to eight words. All messages included a call sign identifying

them as either relevant or irrelevant; subjects were trained to discriminate between these categories and to ignore the irrelevant messages.

The subjects recorded each relevant fire mission and coded message on a separate printed card containing standard locations for each item of information, performed the site calculation or decoded the message as appropriate, recorded the answer on the card, and deposited it in a special box located on each table. For an irrelevant message, the subjects checked a certain location on the card and deposited it without completing the remaining message operations. The MET messages were recorded on standard FDC record forms.

The subjects were trained for approximately six hours daily for one week. Training consisted of three phases. In the first phase, the subjects were familiarized with the four tasks and practiced from prepared work booklets containing the elemental steps involved in the eventual tasks. In the second phase, they received undistorted, specially paced tape-recorded messages. In phase three, they received messages identical to those they were to receive under the test conditions. In all, each subject practiced 312 fire mission messages, 210 code wheel messages, 163 code book messages, and 195 MET messages during the course of his training.

After each hour of training, the subjects reviewed their responses for correctness, received extra coaching if necessary, and were encouraged to maintain high quality and accuracy in their performance.

During the training period, a number of personality tests and a background questionnaire also were administered.

Each group then completed four consecutive days of task performance during exposure to the following sequence of environmental conditions: Day 1 - control I (0 elevation, 70°F., 35% RH); Day 2 - altitude (4300 meters/14,107 feet hypobaric equivalent, 70°F., 35% RH); Day 3 - control II (0 elevation, 70°F., 35% RH); Day 4 - heat (0 elevation, 95°F., 90% RH, 92° ET equivalent). Each group completed the entire experimental sequence before the training and testing of another group was begun.

The messages within each testing day were presented in one-hour blocks as follows: Hour 1 - 0830-0930; Hour 2 - 0930-1030; Hour 3 - 1030-1130; rest and lunch - 1130-1230; Hour 5 - 1230-1330; Hour 6 - 1330-1430; Hour 7 - 1430-1530. Hours 1, 3, 5 and 7 each contained 30 messages, spaced by randomly varied intervals. Hours 2



and 6 each contained only four fire mission messages which were irregularly and widely spaced. These were hours intended to simulate periods of inactivity during which boredom and sleepiness would more likely develop, and which the altitude and heat conditions might amplify.

## RESULTS AND DISCUSSION

The answer cards and MET record sheets were scored and then verified for accuracy against a set of response criteria and error priorities established beforehand. These rules were chosen to account for certain conditional relationships among the possible errors which could be committed, such that more important or more tactically serious errors would subsume related errors of lesser importance when both occurred, and would not be counted twice. Errors were classified into two categories, omission and commission. An error of omission involved missing a part of an incoming message or failing to complete its translation. Errors of commission involved incorrect translation or insertion of incorrect information, i.e. number or letter reversals, looking at wrong line in the code book when translating. The total errors for each subject on each task were then collated and form the data base upon which the results were analyzed.

On the basis of preliminary inspection, certain aspects of the data were eliminated from further consideration. The MET transmission for the first hour at altitude was found to have been faulty and caused spuriously high error rates for that message. Therefore, the MET data were deleted from the analysis of variance discussed below. The data of two subjects also were not used, because one subject, by his own admission, failed to follow proper procedures during testing and the second subject had considerable difficulty coping with the intellectual demands of the study. In addition, two subjects were unable to complete the entire heat exposure, and another two subjects could not endure the entire altitude exposure, for physiological reasons. However, since this was likely to occur in real situations, the responses for the periods missed by those four subjects were scored as errors and were included in the analyses described below.

In order to identify the influence of the various test conditions upon performance of the tasks and to assess their general significance, an overall treatments x subjects analysis of variance was first performed based on the individual subject error scores. A summary of the results of this analysis is presented in Table I, in which significance levels are evaluated on the basis of the



respective residual subject mean square interactions.

The main effects of environmental stress (E), duration of exposure (T), and type of performance task (P) were all highly significant ( $P < .001$ ). All simple and second-order interactions were also highly significant ( $P < .001$ ) except the interactions TxP ( $P = .07$ ), and TxPxS ( $P = .05$ ), which were marginal. Thus, the analysis indicates that the environmental stresses of altitude and heat effectively impaired performance of FDC tasks in direct relation to the length of exposure.

TABLE 1

Summary of Analysis of Variance of Performance  
Scores Under The Various Environmental Conditions

Source	DF	Mean Square	F	P
Environment (E)	3	3206.33	12.29	<.001
Exposure Time (T)	3	661.82	6.19	<.001
Performance Task (P)	2	1802.77	16.91	<.001
Subjects (S)	27	1152.62		
Interactions				
ExT	9	287.06	3.52	<.001
ExP	6	292.79	5.82	<.001
TxP	6	63.35	2.08	.07
ExTxP	18	102.52	4.30	<.001
ExTxS	243	81.44	3.42	<.001
ExPxS	162	50.33	2.12	<.001
TxPxS	162	30.51	1.28	.05
ExS	81	260.83		
TxS	81	106.96		
PxS	54	106.60		
ExTxPxS	486	23.79		
Total	1343			

Separate treatments x subjects analyses of variance were then performed on the error data for each task. The results of these analyses clearly confirmed that the environmental conditions and exposure durations were effective in impairing all three tasks, since the main effects and their simple interactions were highly significant in all cases. It is important to note that the subjects main effects were significant in all analyses, indicating a high degree of variability in performance among the subjects.

In order to assess in more detail the nature of the performance impairments which occurred within and between the various tasks and experimental conditions, the actual numbers of errors committed within each task were converted to percent of total possible responses for that task. This was done to allow comparison of proportionate errors between tasks, and to provide a unit index of impairment which would be common to all cells of the design. These group mean percent error values are presented below graphically as Figures 1 through 6.

An overall view of the effects of heat and altitude exposure can be obtained from Figure 1, in which the group mean percent errors averaged across all tasks are shown separately for the altitude, heat and control conditions as a function of hours of exposure. The impairments of overall performance by both altitude and heat were sizable to a degree of practical significance, and increased progressively with exposure duration to a maximum approaching 32% of total responses made. When the altitude and heat conditions are compared, each with its own preceding control condition (altitude with Control I; heat with Control II), these changes represent performance percentage error increases of 78% due to altitude and 88% due to heat at the points of maximum decrement for each (five hours for altitude; seven hours for heat). Performance at altitude was affected sooner than performance in the heat, but both appeared to have been comparably impaired by the fifth hour of exposure. It is interesting to note the moderate facilitation effect due to heat on these primarily cognitive tasks within the first three hours. This corresponds to similar results (7) reported for activities having primarily a motor component such as simple reaction time or tapping.

In contrast, performances in the two control conditions were very similar and showed no evidence of improvement due to practice or of deterioration due to fatigue or lack of motivation.

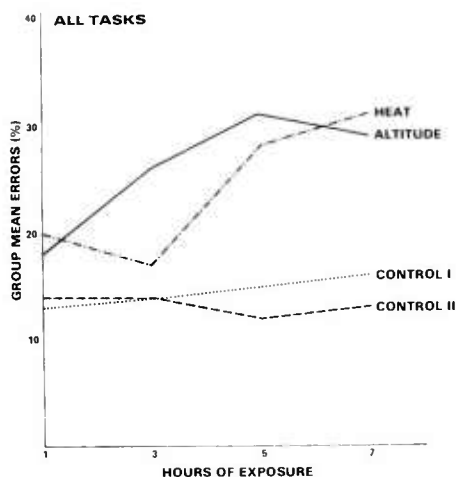


Figure 1 - Group Mean Percent Errors for Combined Tasks by Environmental Conditions and Duration of Exposure

In Figure 2, the group mean percent error values are shown by task for the environmental and control conditions averaged over the entire duration of exposure, along with a combined average across all tasks. A very similar pattern of impairment under altitude and heat can be seen for each task, although the performance levels of the tasks differed from one another. These differences undoubtedly were due to varying levels of inherent task difficulty. However, it should be noted that these differences may be inappropriate for judging artillery skills, since the tasks were selected and modified to evaluate environmental effects on performance rather than to analyze artillery operations.

One should note again the almost complete equality of values for Controls I and II, since this verifies that the subjects were effectively trained initially and showed little change due to practice thereafter.

The altitude MET value in Figure 2 is shown, but it should be remembered that it represents only hours 3, 5 and 7 for reasons mentioned above.

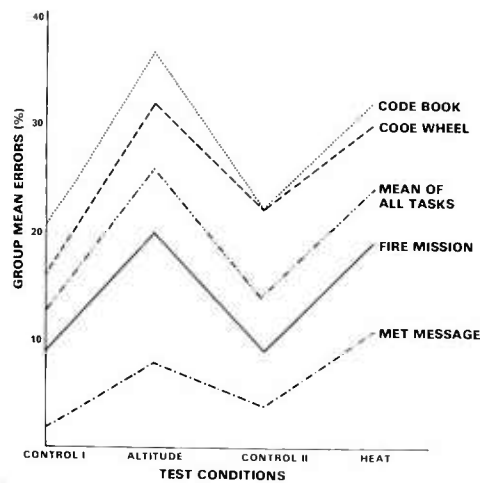


Figure 2 - Group Mean Percent Errors for Each Task by Environmental Condition

Figures 3-6 give a more detailed view of errors in performance of the separate tasks, showing group mean percent errors with respect to hours of exposure.

Figure 3 shows that for the code book task, the effects of altitude developed earlier than those of heat, and followed a negatively accelerated function, while those of heat were positively accelerated. Performances during the two control conditions were clearly equivalent.

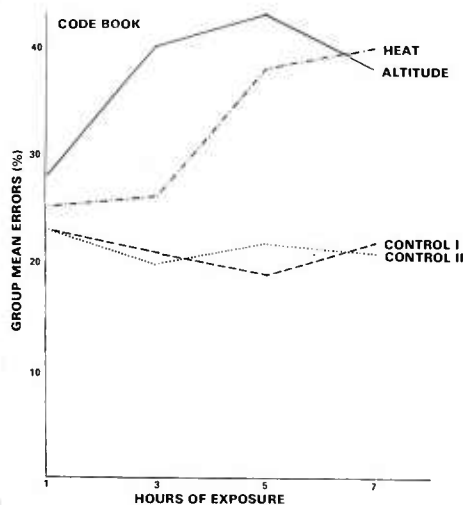


Figure 3 - Code Book Group Mean Percent Errors by Environmental Conditions and Duration of Exposure

Figure 4 presents performance errors in site calculations for fire missions occurring during hours 1, 3, 5 and 7, the hours in which subjects received frequent messages. The shapes of the functions are very similar to those depicted for the code book task (Figure 3).

The error data for infrequent fire missions are shown separately in Figure 5 since it was not considered appropriate to combine the data for different frequencies of message occurrence. The error rates for the sixth hour were considerably higher than those for the second hour. For altitude, the impairment at hour six was higher than at hour five and for heat was less at hour two than at hour 3. However, these differences cannot be attributed to the infrequency of messages, since it is not known what the effect of environment on frequent occurrence of messages would have been in hours two and six.

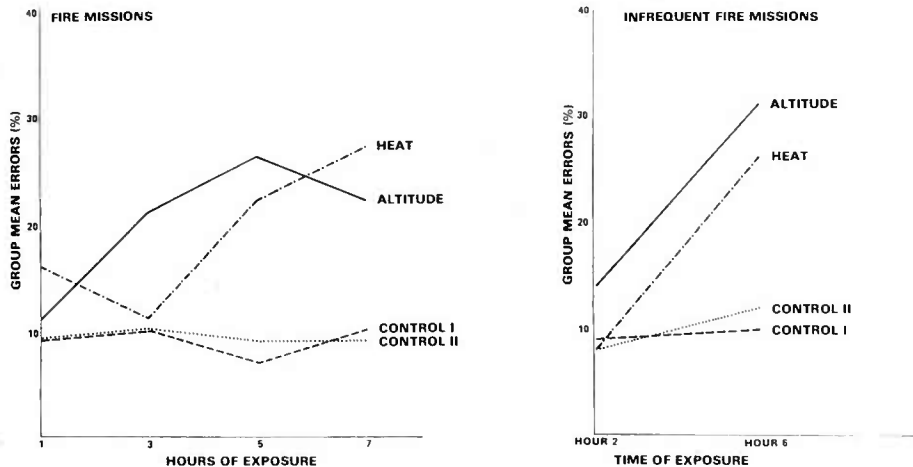


Figure 4 - Fire Mission Group Mean Percent Errors by Environmental Condition and Duration of Exposure

Figure 5 - Infrequent Fire Mission Group Mean Percent Errors by Environmental Condition and Duration of Exposure

The code wheel task errors shown in Figure 6 were positively accelerated in both altitude and heat conditions. However, unlike the other tasks, the control conditions differed considerably from one another. It is impossible to determine the reason for this. It appears unlikely that the differences could be due to poor motivation or lack of training, since the controls for the other tasks indicate that the subjects were performing just as efficiently after seven hours as they were after one hour, even in the second control

condition.

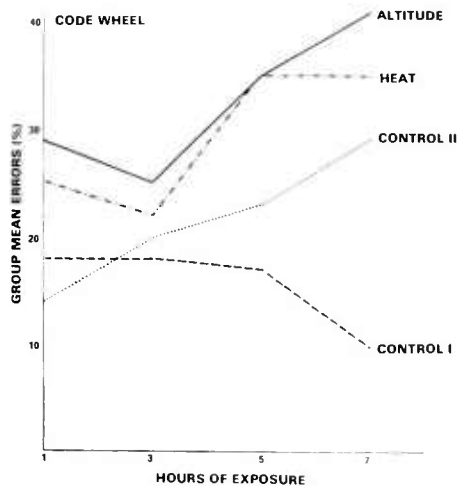


Figure 6 - Code Wheel Group Mean Percent Errors by Environmental Condition and Duration of Exposure

Errors of omission greatly exceeded errors of commission for both the code wheel and the code book tasks under all conditions. However, omission errors increased much more during the stress exposures than did commission errors. For the fire mission task, the frequency of occurrence of both types of errors was approximately equal during the control conditions, but, again, omission errors greatly exceeded commission errors during the stress exposures.

In an attempt to account for the large number of errors of omission under stress, the tape recordings were re-checked to determine whether poor intelligibility could have caused the omissions. However, it was found that subjects had simply missed parts of messages which had been clearly transmitted. Therefore, the increases in both errors of omission and commission apparently are attributable to effects of the environmental conditions.

It was noted previously that the analyses of variance indicated a large amount of variability between subjects. Although the analysis of the differences between subjects has not been completed, it is apparent that the two stress conditions produced similar overall group decrements, but did not affect the performances of all subjects in the same way. The performances of some subjects were strongly affected by altitude and only minimally by heat, while others were affected in the opposite manner. Very few subjects were either unaffected or incapacitated by both stress conditions. This wide range of susceptibility further justifies research aimed



at identifying the types of individuals who are resistant to environmental stress.

With regard to the relevance of messages, Cahoon (17) studied message reception at altitude and found that the ability of subjects to discriminate between relevant and irrelevant messages was unimpaired. The present data support Cahoon's finding and show the same results for heat exposure.

In conclusion, the results of this study have indicated that the environmental stressors used caused dramatic increases of errors in the performance of certain FDC-like tasks. Future studies can now be planned with some degree of confidence that the environment does have a significant impact on performance, and, conversely, that the tasks performed are "sensitive" to the effects of the environment.

Much of the literature on the effects of heat and of altitude on cognitive performance has indicated equivocal results. An analysis of that literature suggests that the equivocality may lie in the fact that most cognitive tasks that have been used were presented in meaningless contexts so that the performers were relatively unmotivated. In the present study, the tasks were perceived by the performers as meaningful components of a functional system of considerable importance. This resulted in the participants becoming highly involved and competitive. By far the majority of the subjects in this study appeared to be operating at the peak of their abilities most of the time.

This high level of motivation on the part of the subjects was no accident, but resulted from a carefully planned attempt by the investigators to instill in the subjects a strong sense of the importance of the FDC mission. Emphasis continually was placed on precision and accuracy and on the extreme cost in human lives of careless errors. To the extent that they became involved in this framework, the subjects became highly motivated. It is this kind of continuous peak performance that most nearly approximates that of professional FDC team functioning in combat and which would be expected to lead to malfunctions in the human elements of the system.

Thus, the major conclusion to be drawn from this research at this time is that there is a likelihood that a highly motivated FDC team, the members of which are functioning at or near the peak of their capacities, may incur serious degradations in performance within the first seven hours of exposure to extreme hot-wet or altitude conditions.

REFERENCES

1. Colquhoun, W. P. Effects of raised ambient temperature and event rate on vigilance performance. Aerospace Medicine, 40:413-417, 1969.
2. Moreland, S. and Barnes, J. A. Exploratory study of pilot performance during high ambient temperature/humidity. U. S. Army, Human Engineering Laboratories, Aberdeen Proving Ground, Md., Technical Memorandum 6-70, 1970.
3. Wilkinson, R. Some factors influencing the effect of environmental stressors upon performance. Psychological Bulletin, 22: 260-272, 1969.
4. Cahoon, R. L. Effect of acute exposure to altitude on time estimation. Journal of Psychology, 66:321-324, 1967.
5. Fine, B. J. and Kobrick, J. L. Note on the relationship between introversion-extraversion, field-dependence-independence and accuracy of visual target detection. Perceptual and Motor Skills, 42:763-766, 1976.
6. Kobrick, J. L. and Appleton, B. Effects of extended hypoxia on visual performance and retinal vascular state. Journal of Applied Physiology, 31:357-362, 1971.
7. Grether, W. F. Human performance at elevated environmental temperatures. Aerospace Medicine, 44:747-755, 1973.
8. Jones, R. D. Effects of thermal stress on human performance: A review and critique of existing methodology. Human Engineering Laboratories, Aberdeen Proving Ground, Md., Technical Memorandum 11-70, May 1970.
9. Tune, G. S. Psychological effects of hypoxia: Review of certain literature from the period 1950 to 1963. Perceptual and Motor Skills, 19:551-562, 1964.
10. Wing, J. F. Upper thermal tolerance limits for unimpaired mental performance. Aerospace Medicine, 36:960-964, 1965.
11. Galin, D. Implications for psychiatry of left and right cerebral specialization. Archives of General Psychiatry, 31:572-583, 1974.

12. Gazzaniga, M. S. The bisected brain. N.Y.: Appleton-Century-Crofts, 1970.
13. Sperry, R. W. Hemisphere disconnection and unity in conscious awareness. American Psychologist, 23:723-733, 1968.
14. Eysenck, H. J. The biological basis of personality. Springfield, Ill.: Thomas, 1967.
15. Fine, B. J. and Danforth, A. V. Field-dependence, extraversion and perception of the vertical: Empirical and theoretical perspectives of the rod-and-frame test. Perceptual and Motor Skills, 40:683-693, 1975.
16. Witkin, H. A., Dyk, R. B., Faterson, H. F., Goodenough, D. R. and Karp, S. A. Psychological differentiation. N.Y.: Wiley, 1962.
17. Cahoon, R. L. Monitoring army radio-communications networks at high altitude. Perceptual and Motor Skills, 37:471-476, 1973.



## CHEMOTHERAPEUTIC AGENTS IN OCULAR METALLOSIS (U)

HORACE B. GARDNER, LTC, MC  
LETTERMAN ARMY INSTITUTE OF RESEARCH  
PRESIDIO OF SAN FRANCISCO, CA 94129

Penetration of the eye by a foreign body is a common form of ocular injury in combat. Large foreign bodies are often so destructive that current treatment is ineffective in salvaging the eye. Smaller foreign bodies may lodge within the eye, doing minimal mechanical damage. Many such foreign bodies are inert--such materials as glass, sand, and several alloys used in military ordnance having been shown to cause little reaction of the ocular tissues (1). With these substances, the major problems are mechanical damage and infection. Modern surgical techniques and antibiotics have greatly reduced visual loss from these causes.

However, two metals commonly found in military ordnance present a markedly different threat. Although iron and copper foreign bodies enter the eye as metallic fragments, once inside they dissolve and produce an insidious chemical toxicity. Delayed retinal damage may thus cause marked visual loss in an otherwise healthy eye.

Ocular toxicity from iron is known as siderosis. Retinal damage, as evidenced by changes in the electroretinogram (ERG), takes from several days to many weeks to develop (2). Masciulli et al (3) have shown this toxicity to be most likely due to the ferrous ionized form, with the ferric ion showing no effect on retinal function. Histological study has shown the iron to remain in the eye in both the ferrous and ferric forms.

Since the onset of siderosis is variable, treatment has been advised in all cases of intraocular iron foreign bodies. Historically, the great percentage of iron foreign bodies has been magnetic

in nature (4), and sophisticated removal techniques using giant magnets have been developed. More recently, however, more nonmagnetic iron containing alloys have been encountered, and problems related to the trauma of the surgical treatment have been noted. Therefore, alternative therapy has been sought.

The use of deferoxamine, a potent ferric chelating agent, in the treatment of siderosis has been the subject of animal study and a few clinical reports (5,6,7). Although represented as promising, deferoxamine has not received adequate evaluation.

Copper toxicity of the eye is known as chalcosis. As in the case of iron, delayed and irregular toxicity have been noted (8). In this case, the nonmagnetic character of the copper has made surgical treatment very difficult. Less is known about the toxic form of copper, although there is histological evidence that it exists in the eye in both the cuprous and cupric forms.

Treatment of chalcosis has received little attention. Intraocular copper deposits associated with systemic copper toxicity (Wilson's disease) have been noted to decrease or disappear when the patient receives penicillamine treatment for his systemic disease (9,10). Three cases of copper intraocular foreign bodies treated with penicillamine for chalcosis are reported in the literature (11,12). Again, evidence of copper removal from the anterior ocular structures was observed, although no evidence for an effect on deeper ocular structures was presented.

Since the onset of chemical damage to the eye from iron and copper foreign bodies is always delayed by at least a few days, and often much longer, detoxification of the foreign body during this period appears feasible. Since avoidance of surgery or, at least, a temporary delay to allow proper medical evaluation and transfer to improved treatment facilities would be a distinct benefit to the treatment of such ocular injuries in a military setting, information on these chemical agents was sought. Both removal of intraocular metal and prevention of retinal damage were investigated in an animal model.

#### MATERIALS AND METHODS

Adult albino rabbits, averaging 2.5 kg, were used throughout the experiment. The procedures were done under IV pentothal anesthesia, supplemented by local anesthetic drops to the conjunctival sac. Intravitreal metal emplacement was via a pars plana approach under direct visualization.



Radioactive iron was obtained from ICN (Fe-59 as  $\text{FeCl}_3$  in 0.5N HCl). For studies involving ferrous excretion, metallic iron was added to the solution and kept under oil for a period of 48 hours. Reaction of the supernatant with ferrocyanide caused formation of a white precipitate, showing that reduction to ferrous chloride had indeed occurred with little or no evidence of a blue precipitate, indicating little remaining ferric ion. Metallic iron foreign bodies were fabricated by electroplating radioactive iron from the solution onto platinum wires. Slow plating produced a hard surface, whereas rapid plating produced a soft, granular surface. Segments of these wires containing 0.25 to 0.35 mg of elemental iron were inserted into the midvitreal via an 18-gauge trochar. Radioactive copper-64 was obtained from New England Nuclear as cupric nitrate in one normal nitrous acid. Radioactive solutions were injected through a pars plana approach in 10-20  $\mu\text{l}$  volumes. Total injected activity was measured both by immediate postoperative counting of the entire animal and by the counting of an aliquot of a dilutional control of the amount injected. Daily total urine and fecal collections were carried out using metabolic cages and radioactivity in these samples assessed by standard well counting procedures.

Ionic solutions were prepared daily for each experiment. Ferrous, ferric and cupric chloride salts were used. The solutions contained 0.1, 0.05, 0.025, 0.013, 0.006, 0.003, 0.0016, and 0.0008 mg of the metallic ion per 10  $\mu\text{l}$ . Ten microliter injection volumes were used, unless greater volumes were necessary to administer larger amounts of metal.

Deferoxamine (Desferal mesylate, CIBA) and penicillamine (Cuprimine, Merck Sharp and Dohme) were obtained in powdered form and prepared in concentrations of 250 mg per cc. Three injection routes were employed. Intramuscular treatment consisted of BID injection of 40 mg of drug per kg. Retrobulbar injections were through a 25-gauge needle into the retrobulbar space in one-cc volumes (250 mg). Intraocular injections were into midvitreal via a pars plana approach under direct visualization in 5-40  $\mu\text{l}$  volumes (1.25-10  $\mu\text{g}$ ).

ERG stimulation was produced by a Ganzfeld, illuminated by a Grass PS-22 photostimulator, giving  $2 \times 10^6$  lumens peak intensity at the corneal surface (approximately one-tenth of the intensity of direct viewing of the flash at 10 inches); amplification by a Hewlett-Packard high-gain preamplifier with band pass 1.5 to 1500 Hz. Responses were recorded at one per second on heat-sensitive paper. ERG criteria of total height (bottom of A wave to peak of B wave) was used, the average of three readings from different days prior to

experimental manipulation determining the preinjection ERG. Post-operative recordings were made at 24, 48, 120 and 168 hours. Pupillary dilatation was induced by cyclogyl 1% and neo-synephrine 10%, two drops each, 15 minutes prior to recording of the ERG.

In conducting the research described in this report, the investigators adhered to the "Guide for Laboratory Animal Facilities and Care," as promulgated by the Committee on the Guide for Laboratory Animal Resources, National Academy of Sciences, National Research Council.

#### EXPERIMENTAL PROCEDURES AND RESULTS

**REMOVAL OF INTRAOCULAR IRON:** Since deferoxamine is known to be a strong chelator of the ferric form (13), its effect on this ion was first investigated. Trace-to-one milligram amounts of ferric chloride injected into individual eyes of five rabbits resulted in no ERG changes or clinical evidence of siderosis over a four-week follow-up period, confirming the results of Masciulli et al (3). Ten animals then received 0.15 mg of iron-59 as the ferric chloride solution in each eye, and urinary and fecal excretion were followed over a one-week period. One week following the intravitreal iron injection, one-half of the animals received 40 mg per kg of deferoxamine BID IM for a one-week period. (This dosage schedule is a moderate increase from the usual therapeutic human doses which range from 15 to 45 mg per kg per day on a BID IM basis.) Irregular excretion of radioactivity in the urine and feces was noted for approximately three days; but, by Day 4, all animals showed stable, low-level excretion (Figure 1). Nontreated animals continued at this low excretion rate; animals treated with deferoxamine showed a 13-fold increase in urinary excretion, while fecal excretion was increased less than twofold (Table I).

TABLE I  
Average daily excretion\* of intravitreal ferric iron (Fe-59)  
BID IM deferoxamine administration\*\*

	Urine		Feces	
	Control	Deferoxamine	Control	Deferoxamine
$\bar{x}$	0.00081	0.01057	0.01431	0.02165
SD	0.00180	0.00631	0.01525	0.01182
n	31	28	31	27
t	8.26		2.08	

\*Percent of administered activity

\*\*One week treatment period

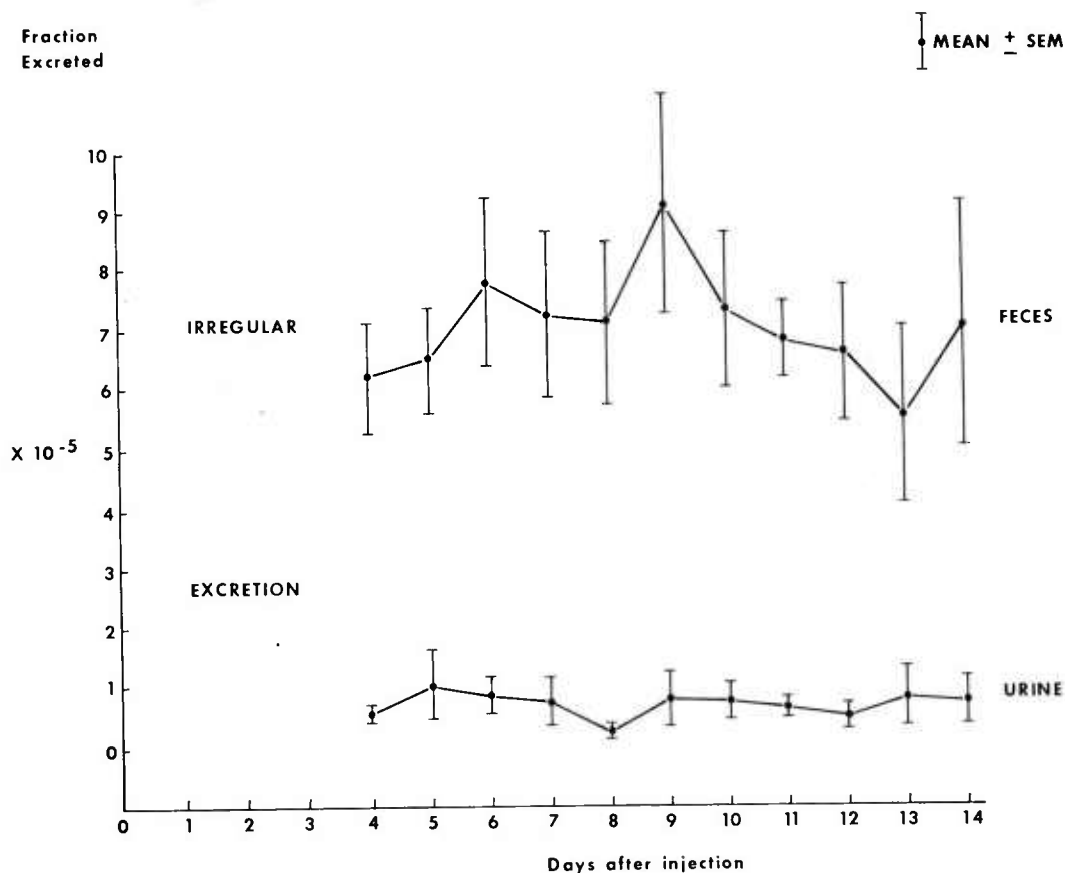


FIGURE 1  
Excretion of intravitreal ferric iron in untreated animals

In order to ascertain whether deferoxamine was also active against the toxic ferrous form, 16 animals were given 0.15 mg of iron-59 as a ferrous chloride solution in each eye. One week later, one-half of these animals received 40 mg per kg of deferoxamine BID IM for a one-week period. The animals receiving intravitreal ferrous chloride all showed ERG extinction within four hours and severe siderotic changes including retinal detachment within the first week. Excretion patterns were similar to those seen with the ferric form. Since Wise (4) reported some success with retrobulbar deferoxamine administration, the excretion induced by this route was assessed in an additional eight animals. These animals received the same intravitreal iron-59 ferrous chloride injections and, one week later, were treated with a single one-cc retrobulbar injection of deferoxamine

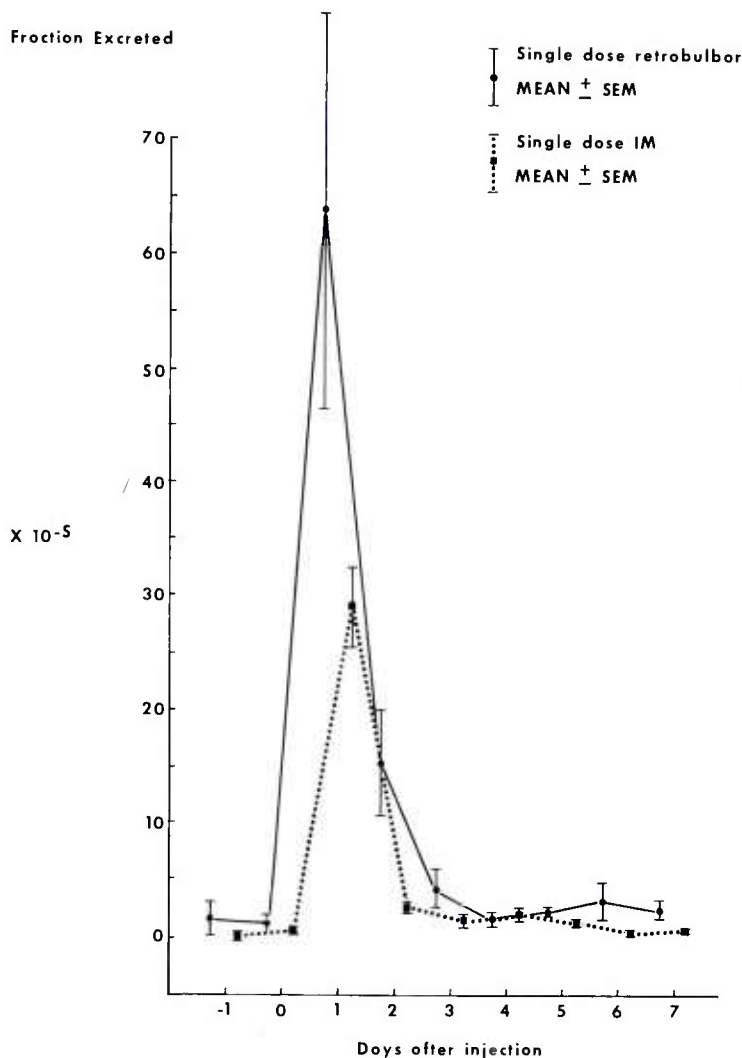


FIGURE 2  
Urinary excretion of intravitreal ferrous iron following single dose retrobulbar or single dose IM deferoxamine

containing 250 mg of the drug. Although the retrobulbar dose gave some enhancement of excretion the day following injection (Figure 2), total iron excretion was not as great as with the seven day BID IM deferoxamine injection schedule (Table II).

TABLE II  
Total excretion of intravitreal ferrous iron\* (Fe-59)  
following single dose retrobulbar or BID IM deferoxamine

	Urine		Feces	
	Retrobulbar	IM (1 wk)	Retrobulbar	IM (1 wk)
$\bar{x}$	0.08396	0.19339	0.07478	0.11862
SD	0.07828	0.16183	0.05142	0.04307
n	8	10	8	10
t	1.75**		1.97**	

\*Percent of administered activity

\*\*Significant at 0.05 level

The most intraocular iron seen in the urine of any animal receiving ferrous chloride was seen the day following retrobulbar deferoxamine and was just under 0.2  $\mu$ g of radioactive iron. To determine if increased iron availability would enhance excretion, five animals received 0.25 mg and five animals 0.50 mg of iron-59 as a ferrous chloride solution in each eye, followed in one week with intramuscular deferoxamine at the above dosages. As seen in Table III, a decreasing fraction of the iron was removed of these increased ferrous loads, resulting in a very similar total amount of iron being removed.

TABLE III  
Urinary excretion of 0.15, 0.25 and 0.50 mg intravitreal  
ferrous iron (Fe-59) loads under deferoxamine use (1 wk BID IM)

Intravitreal iron load (mg Fe++)	Total urinary excretion (% of administered dose)	Total iron excreted ( $\mu$ g in 1 wk)
0.15	0.106	0.15
0.25	0.079	0.20
0.50	0.042	0.21

Iron foreign bodies normally enter the eye as metallic iron, and the action of deferoxamine on this iron form was tested by inserting firm iron platings on platinum wire into both eyes of 15 animals. These platings contain 0.25 to 0.35 mg of metallic iron and produced ERG extinction in approximately one week and siderotic changes of mid-pupillary dilatation, vitreous clouding and, frequently, retinal detachment in three to four weeks. Assay of radioactivity in the urine and feces of these animals, a technique sensitive to less than one part per million of the initial foreign bodies, revealed no detectable excretion of radioactive iron in any of the five control animals, the five IM treated or the five retrobulbar treated animals. To increase iron availability, the procedure was repeated with 15 animals receiving soft platings of iron on platinum wire with 0.25 to 0.35 mg of metallic iron. Although more rapid dissolution occurred, as evidenced by ERG extinction within four hours and siderotic changes within one week, still no detectable urine or fecal radioactivity occurred.

RETINAL TOXICITY DURING SIDEROSIS TREATMENT WITH DEFEROXAMINE: Wise (3) has indicated that deferoxamine may be retinotoxic of and by itself when injected directly into the vitreous. Since the ERG was to be used as a criterion of retinal function, the effect of intravitreal deferoxamine on the ERG was studied. Direct intravitreal injection of 1.0, 0.75, 0.5, and 0.25 mg of deferoxamine was carried out in eight animals, each amount being injected into four eyes. ERGs were recorded three times preoperatively and daily for four days postoperatively in all animals. No detectable change was noted in the ERG during the four day follow-up period in animals receiving 0.25 or 0.5 mg of deferoxamine. However, injections in excess of 0.5 mg resulted in progressive and permanent ERG changes.

The height of the ERG 24, 48, 120, and 168 hours after the injection of intraocular ferrous iron in geometrically increasing doses was determined in relationship to the height of the ERG prior to iron challenge. Twenty animals (40 eyes) received either 0.1, 0.05, 0.025, 0.013, 0.006, 0.003, or 0.0016 mg of ferrous iron as a chloride salt solution or normal saline, five eyes receiving each treatment. An additional group of 20 animals received deferoxamine BID IM at the above doses for a three-day period before receiving the iron injection and for an additional 48-hour period after receiving the iron. Dose-response curves for the treated and nontreated animals are shown in Figure 3. The normal postinjection ERG seen in both treated and control animals receiving no iron indicates the intraocular injection alone does not alter the ERG. Also, treated animals showed no change in the baseline ERGs taken before or during IM deferoxamine administration. At the lowest iron dose, the control animals showed



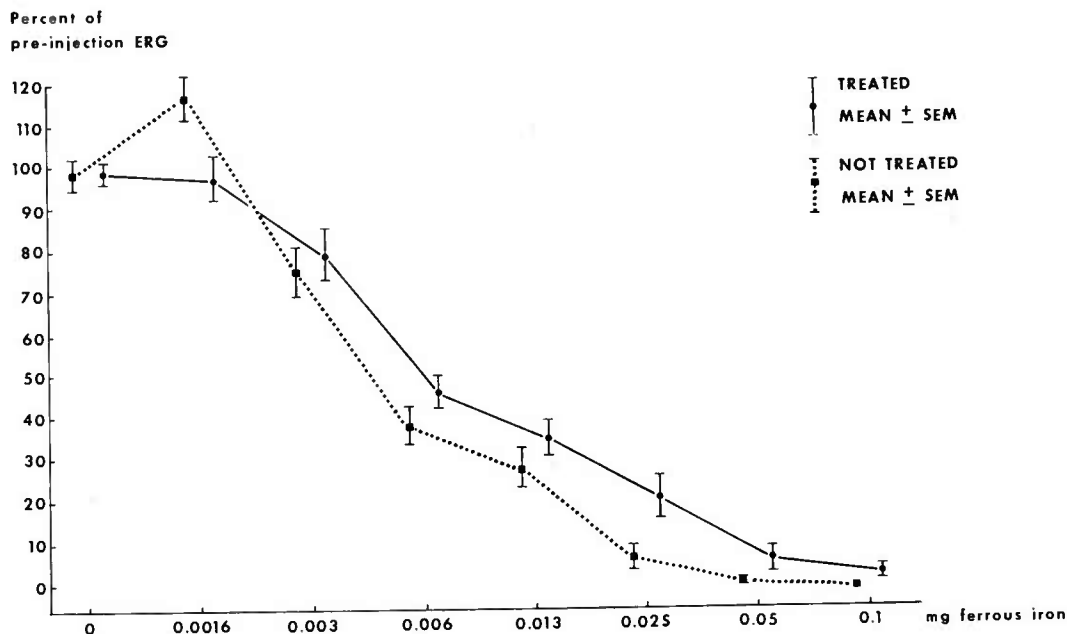


FIGURE 3  
ERG impairment following intravitreal ferrous iron  
injection in treated and control animals

hyperpolarization of the ERG, a finding which has been noted previously (2). No such hyperpolarization was seen in the treated animals. At the remaining iron levels, the treated animals showed improved ERGs when compared to control animals receiving the same iron dose. However, this was not as normal an ERG as seen in control animals receiving half as much iron. Since the ERGs at 24, 48, 120, and 168 hours postoperatively showed a similar height, these four ERGs were averaged to obtain the postinjection ERG. Sixteen additional animals had baseline ERGs recorded, following which one-half of the eyes received intravitreal injections of 10  $\mu$ l of deferoxamine solution containing 0.5 mg of the drug. Twenty-four hours later, two treated and two control eyes received each of these seven dilutions or normal saline. ERGs were again recorded at 24, 48, 120, and 168 hours following the iron injections. Very similar dose-response curves were obtained, still indicating the treated eyes to be resistant to less than a twofold increase in ferrous iron.

REMOVAL OF INTRAOCULAR COPPER: Twenty microliter amounts of radioactive copper-64 as cupric nitrate in one normal nitrous acid were injected into both eyes of eight rabbits. Each injection contained less than one-tenth milligram of copper. Four rabbits received IM penicillamine beginning 24 hours after copper injection. The remaining four animals served as controls. Daily excreted activity was measured until activity levels became too low for significant results (approximately four days). Basal excretion rates of copper showed all animals to secrete approximately 0.22% of the intraocular copper each day in the urine. Fecal excretion was insignificant. The untreated animals continued at this low rate for the four-day period. Urinary excretion in the penicillamine-treated rabbits increased to approximately 1.44% of the intraocular dose each day and stayed at this level over the three-day treatment period. This represents greater than a sixfold increase in intraocular copper excretion (Table IV).

TABLE IV  
Average daily urinary excretion (%) of intravitreal  
cupric ion (Cu-64)

	<u>Control</u>	<u>IM Penicillamine Treatment</u>
$\bar{x}$	0.22	1.44
SD	0.12	0.48
n	15	9
t	7.77*	

\*Significant at 0.025

RETINAL TOXICITY ASSOCIATED WITH CHALCOSIS: Penicillamine toxicity was ascertained by injecting 5-40  $\mu$ l amounts of penicillamine solutions containing 0.5 mg per 10  $\mu$ l into each of three eyes, and, following the ERG for a period of one week, no detectable ERG change occurred from these intraocular injections of 0.25 to 2.0 mg of penicillamine.

Groups of eight rabbits were divided into four treated and four control animals on a random basis. The treated animals received IM penicillamine, 40 mg per kg BID, beginning three days before copper injections. One treated and one control eye then received one of the eight copper challenges, and dose-response curves were determined as above. Four such groups of animals were studied. Figure 4 shows the dose-response curves for treated and control animals. At the lowest administered dose, the treated animals have a hyperpolarized ERG,

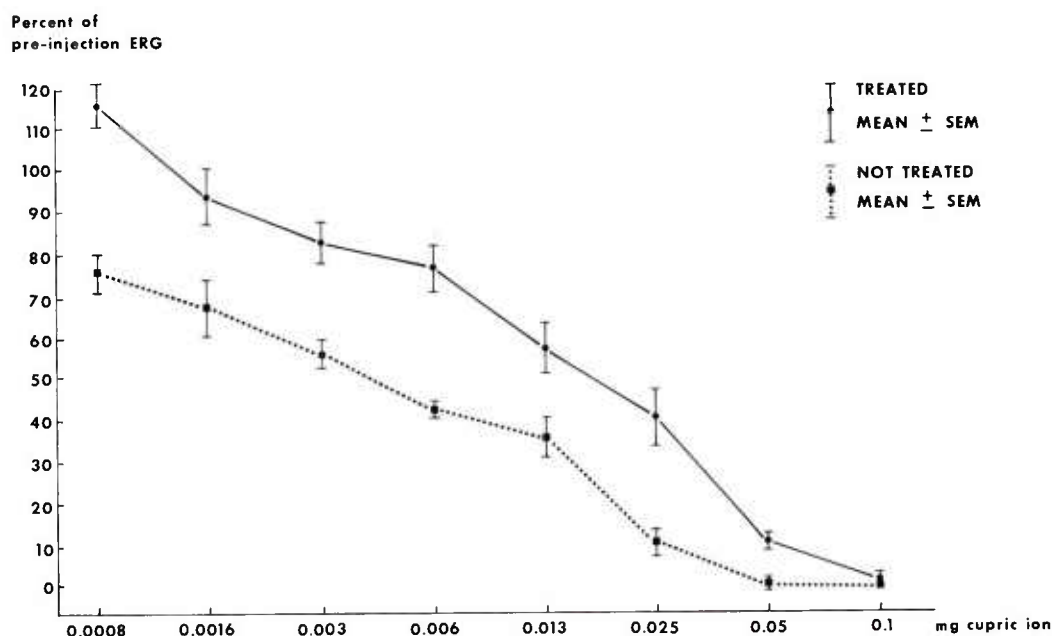


FIGURE 4  
ERG impairment following intravitreal cupric ion  
injection in IM treated and control animals

while the control animals already show impairment. The treated animals show similar ERG impairment at doses four to eight times those giving similar ERG impairment in control animals. Again, postoperative ERGs at 24, 48, 120, and 168 hours were similar and were averaged to obtain the postinjection ERG.

Thirty-six rabbits then received 0.5 mg of penicillamine by intraocular injection in one eye only. At 6, 24, and 48 hours following their penicillamine injection, 12 rabbits were selected on a random basis and received copper challenges to each eye of 0.013, 0.006, and 0.003, or 0.0016 mg of copper. A protective effect was evidenced from intraocular penicillamine at all of the time intervals checked. However, the most protection was seen when the copper challenge occurred 24 hours after the penicillamine injection. This is shown in Figure 5 and is similar to the protection seen with IM penicillamine, being some fourfold to eightfold.

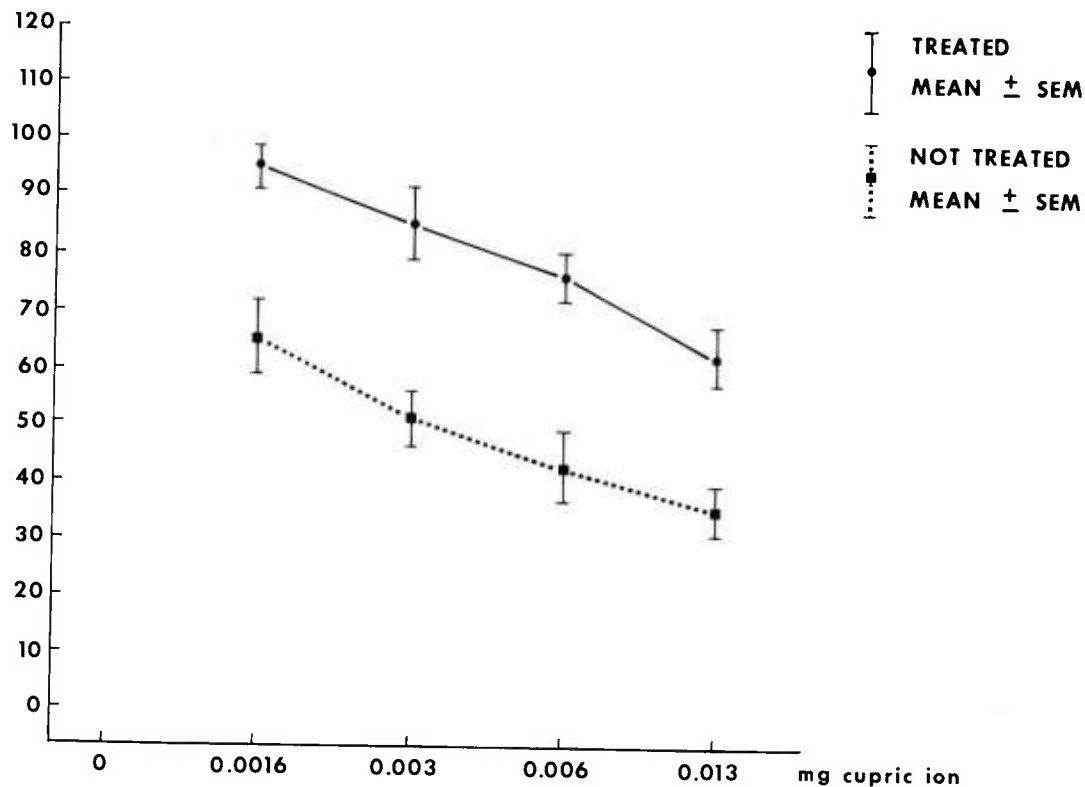


FIGURE 5  
ERG impairment following intravitreal cupric ion injection  
in intraocularly treated and control animals

#### DISCUSSION

Deferoxamine has significant binding capability for ferric iron and results in the excretion of this chelated product in the urine. The fecal excretion of iron during deferoxamine treatment has not been previously noted. The consistency among animals and the marked difference in the effect of deferoxamine on urinary and fecal iron mitigates against this effect being an experimental artifact representing cross-contamination between urine and feces. The increase in total excreted iron during IM deferoxamine treatment may account for the observed change in iris color seen in some human cases of siderosis (6). The iris discoloration may represent minute amounts of ferric iron. Removal of the toxic ferrous form is slow

and could not be increased, even with greater iron load. This suggestion of a possible rate-limiting situation is interesting. Since the deferoxamine doses used are already in excess of those normally used clinically, the possibility of significantly increasing this rate by increasing the deferoxamine dosage is small. The peak excretion rate was increased with retrobulbar administration of the drug, but this administration route is hazardous and cannot be repeatedly used. The total amount of iron removed was greater with repeated IM injection over a one-week period than with the single retrobulbar dose. The iron from solid foreign bodies, the form usually encountered in clinical ophthalmology, was even less available for removal with deferoxamine than the soluble salts, although the production of severe siderotic changes was rapid with the solid form. The reports in the literature indicating some promise for deferoxamine with solid foreign bodies involve extremely prolonged treatment, with deferoxamine being given twice a day for periods of months to years. Even over these periods of time, these studies suggest only a small fraction of an average size foreign body could be removed.

In this experimental model, no significant ERG protection could be shown with deferoxamine. This may indicate irreversible damage having already been done by the iron while in the ferrous form, before its oxidation to the ferric form makes it available to treatment. Even when injected directly intraocularly where it has immediate access to the iron, deferoxamine showed little protection at doses where it was not toxic itself.

The removal of cupric ion from the eye with penicillamine demonstrates activity on intraocular copper at even more posterior ocular structures than previously noted clinically. The maximum removal rate of almost  $1\frac{1}{2}\%$  per day is appreciable, but, since the rate of dissolution of a metallic copper foreign body may be extremely variable, total foreign-body removal with penicillamine might still take a prolonged period. However, for foreign bodies with a dissolution rate presenting copper to the eye at two to eight times the normal toxic rate, penicillamine may well afford retinal protection. Although the animal studies utilized IM treatment, penicillamine achieves significant systemic concentrations by the oral route, also. The oral route would be a much more convenient one for human use. Long-term treatment with this agent is already practiced in humans with systemic copper problems and may be applicable to the eye. If a similar protective effect exists in humans, short-term treatment might at least allow evacuation and better evaluation before surgical intervention becomes necessary.

Since copper showed rapid retinal toxicity when given as the cupric salt, this form would appear to be the toxic one. The cuprous form was not tested, but the solid copper foreign bodies are known to be somewhat delayed in their retinal toxicity. This would indicate that both iron and copper show ERG toxicity in the +2 ionized state. Since they also show ERG toxicity at approximately the same intraocular concentrations by weight, a similar mechanism may be involved. The mechanism of this toxicity, however, remains unknown.

#### CONCLUSIONS

Deferoxamine, a therapeutic agent occasionally used in the treatment of siderosis in humans, has been shown to be of little value in the treatment of animals with retinal toxicity from this problem. Since retinal toxicity is the most important problem for the human from a visual standpoint, this chemotherapeutic agent may have little benefit. Penicillamine, on the other hand, has received prolonged usage in humans for systemic copper poisoning and is easily administered orally. If the protection from retinal toxicity demonstrated in animals also exists in humans, its use as a temporizing method may allow time for improved diagnosis and evacuation to better treatment facilities in the case of intraocular copper injury. Indeed, these results may justify its testing in potential human chalcosis. Prolonged treatment with this drug may even allow avoidance of surgical intervention altogether.

#### REFERENCES

1. Lauring L, Wergeland FL, Jr: Ocular toxicity of newer industrial metals. *Military Medicine* 135:1171-1174, 1970.
2. Knave B: Electroretinography in eyes with retained intraocular metallic foreign bodies. *Acta Ophthalmologica (Kbh)* 100 (suppl): 1-63, 1969.
3. Masciulli L, Anderson D, Charles S: Experimental ocular siderosis in the Squirrel monkey. *Am J Ophthalmol* 74:638-661, 1972.
4. Percival SPB: A decade of intraocular foreign bodies. *Brit J Ophthalmol* 56:454-461, 1972.
5. Wise J: Treatment of experimental siderosis bulbi, vitreous hemorrhage, and corneal bloodstaining with deferoxamine. *Arch Ophthalmol* 75:698-707, 1966.



6. Falbe-Hansen I: Treatment of ocular siderosis and haemochromatosis with desferrioxamine. *Acta Ophthalmologica* 44:95-99, 1966.
7. Luongo E: Trattamento della siderosi oculare con desferrioxamina B. *Ann Ottal* 94:518-530, 1968.
8. Rosenthal AR, Appleton B, Hopkins JL: Intraocular copper foreign bodies. *Am J Ophthalmol* 78:671-678, 1974.
9. Sternlieb I, Scheinberg IH: Penicillamine therapy for hepato-enticular degeneration. *JAMA* 189:748-754, 1964.
10. Goldstein NP, Hollenhorst RW, Randall RV, Gross JB: Possible relationship of optic neuritis, Wilson's disease, and DL-penicillamine therapy. *JAMA* 196:734-735, 1966.
11. Delbecq P, Sourdille J, Delthil S: Traitement de la chalcose oculaire d'origine traumatique par la penicillamine. *Bull Mem Soc Fr Optalmol* 77:275-282, 1966.
12. Haut J, Legras M, Desvignes P: Cryo-extraction d'eclats de cuivre intra-vitreens. *Bulletin des Societes D'Ophtalmologie*, 69:143-146, 1969.
13. Moeschlin S, Schnider U: Treatment of primary and secondary hemochromatosis and acute iron poisoning with a new, potent iron-eliminating agent (desferrioxamine-B). *New Eng J Med* 269:57-66, 1963.



## SILICON NITRIDE/YTTRIA: A POTENTIAL GAS TURBINE MATERIAL (U)

GEORGE E. GAZZA, MR.

ARMY MATERIALS AND MECHANICS RESEARCH CENTER  
WATERTOWN, MASSACHUSETTS 02172

## INTRODUCTION

Propulsion and power generation continues to be the most promising area for the application of ceramic materials. High strength, thermal shock resistant ceramic materials, such as silicon nitride and silicon carbide, offer the materials capability required to raise the operating temperature of various heat engines (such as gas turbines, Stirling, or diesel), with the resultant advantages of lower specific fuel consumption and higher power density. As the gas turbine engine has the highest power density of any known power source, and hence the greatest Army potential, this work is directed towards the development of silicon nitride ceramics for gas turbine engines.

A small gas turbine operating at 2500°F turbine inlet temperature, uncooled, would yield the same power as a diesel engine but with less weight (approximately 40%), and a 10-20% decrease in specific fuel consumption. The operation of large power-generating turbines, with only the vanes uncooled, at 2500°F turbine inlet temperatures, without cooling, in engines of Army interest, means that ceramic materials will have to be employed in the engines' hot flow path (combustors, nozzles, vanes, rotors, shrouds, and ducting).

Previous work on hot pressing of  $\text{Si}_3\text{N}_4$  using various additions, principally  $\text{MgO}$ , and subsequent analyses of such systems have been well documented<sup>1-6</sup>. Due to viscous creep problems and degradation of strength at temperatures above approximately 1250°C which are associated with impurity effects in  $\text{MgO}$  doped  $\text{Si}_3\text{N}_4$ , considerable experimental effort has been devoted to improving the properties of the

hot pressed product by synthesizing higher purity alpha phase  $\text{Si}_3\text{N}_4$  powders for use as starting materials and by modifying processing techniques to improve product homogeneity. As suggested by Richerson,<sup>7</sup> the use of higher purity  $\text{Si}_3\text{N}_4$  powder improves the high temperature properties by increasing the refractoriness of the grain boundary phase. However, the high temperature properties, although improved, are limited by the properties of the reaction products produced by the particular additive being used to promote sinterability. Thus, the effects of additives which would increase the refractoriness of the boundary phase by producing a more refractory reaction product were studied. An effective additive found was  $\text{Y}_2\text{O}_3$ .<sup>8</sup>

#### EXPERIMENTAL PROCEDURE

Silicon nitride powders of various purity and alpha/beta phase ratios were used as starting materials. Specific impurity content as well as oxygen level and percent alpha phase are shown for each powder in Table I. Percent oxygen shown was determined by neutron analysis.\* Percent alpha phase was determined by x-ray diffraction analysis.<sup>9</sup> Powder G is high beta phase material while the others are all high alpha phase. The Ca impurity level ranges from 100 ppm in high purity powder to approximately 2000 ppm in commercial purity grades. This impurity is reported<sup>10</sup> to be significant in degrading high temperature properties of  $\text{Si}_3\text{N}_4$ . Cation impurity content and Y content in hot pressed material were obtained by emission spectroscopy.<sup>11</sup>

Additions of  $\text{Y}_2\text{O}_3$  up to 20 wt. % were made to each powder. The mixtures were milled with ethanol in plastic jars with WC balls for 16-17 hours. After milling, the powder was dried and loaded into a graphite die coated with BN and lined with grafoil to separate the BN coating from the  $\text{Si}_3\text{N}_4$  powder. A pressure of 6500 psi was applied at 1550°C and the temperature was raised to 1750-1800°C and held for 2 hours. A  $\text{N}_2$  atmosphere was used.

Some  $\text{Si}_3\text{N}_4$ - $\text{Y}_2\text{O}_3$  additive materials were studied by monitoring densification through the hot pressing sequence and extracting specimens for analysis by stopping hot pressing at various stages of densification.

Specimens for modulus of rupture (MOR) and stress-rupture testing were machined at a 4-5 rms finish and tested at room temperature and high temperatures (1300-1485°C) using four point loading.

\*F. Burns, G. Priest, and H.F. Priest, Army Materials and Mechanics Research Center, Watertown, MA.

TABLE I  
Composition of  $\text{Si}_3\text{N}_4$  Powders (wt%)

<u>Powder Ident.</u>	<u>Ca</u>	<u>Fe</u>	<u>Al</u>	<u>Other</u>	<u>O</u>	<u>%<math>\alpha</math></u>
A	<0.01		<0.03	<0.03	1.3	94
B	<0.02	<0.06	0.08	<0.02	1.22	93
C	0.04	0.25	0.10	<0.07	1.80	86
D	0.06	0.32	0.24	<0.10	1.36	91
E	0.20	0.45	0.51	<0.10	0.94	95
G	0.17	0.53	0.55	<0.14	1.81	35

Hot pressed specimens were subjected to crystallographic analysis.\*\* Studies involved determination of lattice parameters and structure type.

#### RESULTS AND DISCUSSION

All powders reported in this study could be fully densified with  $\text{Y}_2\text{O}_3$  additions ranging from 5-20 wt%. The density of each sample was determined by the liquid immersion technique and varied approximately linearly with percent  $\text{Y}_2\text{O}_3$  addition. Mean bulk density values for 5, 10, and 20 wt%  $\text{Y}_2\text{O}_3$  additions were 3.25, 3.31, and 3.44 g/cc, respectively. The density increase appears primarily due to the formation of increasing amounts of secondary phase formed at the grain boundaries. As will be discussed later, the phase was identified as a yttrium-silicon oxynitride.

A comparison of modulus of rupture (MOR) for a high purity silicon nitride hot pressed with 10 wt%  $\text{Y}_2\text{O}_3$  and high purity HSL30 silicon nitride hot pressed with  $\text{MgO}$  is shown in Figure 1 as a function of test temperature. On a comparative strength basis, the temperature has been extended 200-300F for the  $\text{Y}_2\text{O}_3$  containing material.

However, high temperature MOR values also appear to be dependent on other starting powder characteristics in addition to recognized impurity effects. This is illustrated in Figure 2 where MOR is plotted as a function of testing temperature for specimens hot pressed from  $\text{Si}_3\text{N}_4$  powders with a 10 wt%  $\text{Y}_2\text{O}_3$  added.

---

\*\*University of Newcastle Upon Tyne, Metallurgy Dept. Newcastle Upon Tyne, England.

Specimens prepared from high purity powder, A, show excellent strength retention of ~80,000 psi MOR at 1485°C. Specimens fabricated with commercially pure powder E have MOR values, at 1315°C, only slightly lower than obtained with high purity material B. Hot-pressed commercially pure, high beta phase powder G produces MOR values considerably lower than those obtained for the high alpha phase powders.

Room temperature MOR values for hot-pressed materials fabricated by starting with high alpha phase powders fell generally between 98,000-138,000 psi. Hot-pressed specimens produced with high beta phase starting powder G, however, yielded room temperature MOR values of only 70,000-80,000 psi.

The amount of  $Y_2O_3$  addition was varied to determine whether certain minimum amounts of additive were required to complete grain boundary reactions to produce a refractory boundary phase and enhance high temperature properties. Figure 3 shows the high temperature (1315°C) MOR's obtained with the various grades of  $Si_3N_4$  using  $Y_2O_3$  additions up to 20 wt%. In general, a minimum of 5-10 wt%  $Y_2O_3$  addition is required to approach maximum properties. As expected, material prepared from the high purity powder shows the highest strength values of 110,000-115,000 psi at a 10 wt%  $Y_2O_3$  level, while the high beta phase powder specimens show the lowest strengths and highest scatter of data for each addition level.

Structural analyses of the phases produced in hot-pressed specimens of  $Si_3N_4$  with  $Y_2O_3$  additions up to 20 wt% were carried out by Rae, et al.<sup>12</sup> In addition, they synthesized various  $Y_2O_3$ - $SiO_2$  and  $Y_2O_3$ - $Si_3N_4$  compositions for study. They concluded that the effectiveness of  $Y_2O_3$  as an additive is primarily due to the formation of  $Y_2Si_3O_3N_4$  with tetragonal cell dimensions a, 7.597 and c, 4.098 Å. A complete structure determination showed that this oxynitride is isostructural with the melilite silicates akermanite  $Ca_2Mg[Si_2O_7]$  and gehlenite  $Ca_2Al[SiAlO_7]$  with which it forms a complete series of solid solutions. It can therefore accommodate Ca, Mg and other impurities which would otherwise form a low melting glass. Two yttria-rich intermediate phases H and J were also produced by  $Y_2O_3$ - $Si_3N_4$  or  $Y_2O_3$ - $Si_3N_4$ - $SiO_2$  reactions at lower temperatures (<1500°C). Both melt in the 1650°-1720°C range but react below 1700°C with more  $Si_3N_4$  to give the refractory oxynitride  $Y_2O_3$ - $Si_3N_4$ . Further work at Newcastle Upon Tyne<sup>13</sup> identifies H as a nitrogen-apatite  $Y_5(SiO_4)_3N$  with hexagonal cell dimensions a, 9.42 and c, 6.76 Å; it is isostructural with fluorapatite  $Ca_5(PO_4)_3F$  and with the mineral spencite  $Y_4Ca(SiO_4)_3O$ . The phase J has a composition of  $2Y_2O_3 \cdot Si_2N_2O$ . H and J phases could be produced at lower temperatures (<1500°C) by  $Y_2O_3$ - $Si_3N_4$  reactions. Wills<sup>14</sup> recently substantiated the existence of the  $Si_3N_4 \cdot 3Y_2O_3$



composition which is closely equivalent to J phase. Such phases depend on the  $Y_2O_3$  concentration and distribution. It has been suggested<sup>12,14</sup> that the lower melting characteristics of these phases enhance densification; further reaction at higher temperatures results in the formation of  $Si_3N_4 \cdot Y_2O_3$ .

Initial densification studies conducted in this work where shrinkage was monitored through the hot pressing cycle using the various grades of  $Si_3N_4$  shown in Table I, indicated that a high linear shrinkage rate occurs to 70-80% of full density in a relatively short time, 10-15 min, at between 1450°-1650°C. Since the temperature at which rapid densification begins varies with the grade of starting powder being used, this suggests that the amount of surface  $SiO_2$  and/or specific residual impurities may alter additive reaction rates with the  $Si_3N_4$  starting powder producing variations in the temperature and time dependence of formation of grain boundary  $xY_2O_3 \cdot ySi_3N_4$  compounds.

Changing material characteristics occurring during the hot pressing sequence were determined by stopping the hot pressing cycle at various stages of densification. Specimens produced at each stage were examined by scanning electron microscopy (SEM) to observe microstructural changes and by x-ray diffraction to determine the percent transformation of alpha to beta phase. Diffraction data was obtained on specimen surfaces both parallel and perpendicular to the hot pressing direction and correction factors were applied in the data analysis program<sup>9</sup> to minimize preferred orientation effects. The extent of transformation to beta phase at various stages of hot pressing, as determined by diffraction analysis, is shown in Figure 4 for various starting powders with 10 wt%  $Y_2O_3$ . The rate of beta phase formation varies with each grade of starting powder but the initiation of the phase transformation appears to correspond approximately with the onset of rapid shrinkage during hot pressing.

SEM fractographs of hot pressed specimens fabricated from a commercially pure, high alpha phase powder and high beta phase powder with 10 wt%  $Y_2O_3$  additive are shown in Figures 5 and 6. The development of a fibrous or prismatic grain morphology is apparent, for the high alpha phase starting material, as the hot pressing sequence is interrupted at temperatures just prior to the onset of rapid shrinkage (Figure 5a) and subsequent to rapid shrinkage (Figure 5b). The changing grain morphology produces a significant increase in the degree of preferred orientation. Further heating to the highest hot pressing temperature, 1780°C, produces some increase in grain size and preferred orientation. Specimens produced from high beta phase starting material (Figure 6) showed that a more equiaxed structure

develops. It has been suggested that these morphological differences are the primary reason for higher strengths being produced in hot pressed bodies when high alpha phase starting powders are used.

Stress-rupture properties obtained using  $Y_2O_3$  additions to  $Si_3N_4$  have been equally as impressive as results found for high temperature MOR. Specimens produced by hot pressing powder C with 10 wt%  $Y_2O_3$  addition, sustained a 37,000 psi stress, applied by four-point loading, for greater than 100 h without failure at 1400°C. Lange<sup>15</sup> reported testing a  $Si_3N_4$ -20 wt%  $Y_2O_3$  additive composition by incrementally increasing the stress level from 15,000 to 60,000 psi during creep-rupture testing at 1400°C in air. The specimen survived 450 h before the test was stopped; the final 100 h under a 60,000 psi stress. Visual examination indicated that oxidation resistance of the specimen was good.

The best data obtained for stress-rupture of commercially pure, high alpha powder hot pressed with 15 wt%  $Y_2O_3$  was specimen survival of >300 h under 10,000 psi flexure stress at 1320°C.

The determination of thermal expansion and thermal conductivity data is vital for this system if potential turbine applications are to be realized. A sample of high purity, high alpha powder C hot pressed with ~10 wt%  $Y_2O_3$  was used to determine coefficient of thermal expansion and thermal conductivity values. Lange<sup>16</sup> determined a thermal conductivity value of  $0.673 \text{ cm}^{-1}\text{K}^{-1}$  for this sample as compared with values of ~0.4 for HS 130  $Si_3N_4$  and 0.8 for hot-pressed SiC. The increase in thermal conductivity for the  $Si_3N_4/Y_2O_3$  additive material over that of  $Si_3N_4$  hot pressed with MgO is apparently due to the higher thermal conductivity of the yttrium-silicon oxynitride boundary phase as compared with the boundary phase produced with the MgO addition.

The average value of coefficient of thermal expansion found for the  $Si_3N_4/10 \text{ wt}\% Y_2O_3$  sample was 3.37 in./in./°C from room temperature to 1000°C. This is slightly higher than values of 2.8-3.0 in./in./°C obtained for HS 130  $Si_3N_4$ .

## CONCLUSIONS

Yttria is an effective densification aid to silicon nitride due to the formation of  $xSi_3N_4 \cdot yY_2O_3 \cdot zSiO_2$  reaction product compounds which liquify at intermediate temperatures to promote sintering and then further react with  $Si_3N_4$  to produce more refractory compounds. Significant increases in strength and stress-rupture properties have been demonstrated for the  $Si_3N_4-Y_2O_3$  system in comparison with

current  $\text{Si}_3\text{N}_4$ -MgO hot pressed materials, at temperatures exceeding 2400-2500°F. These are projected turbine inlet temperatures desired for high efficiency operation of gas turbines.

Further studies on oxidation resistance, thermal shock, etc. are required to fully assess the overall capabilities of the  $\text{Si}_3\text{N}_4$ - $\text{Y}_2\text{O}_3$  materials system for operation in high temperature gas turbine environments.

## REFERENCES

1. G.G. Deeley, J.M. Herbert, and N.C. Moore, "Dense Silicon Nitride", Powder Met., 8, 145-15, (1961).
2. Y. Oyama and O. Kamigaito, "Solid Solution of Some Oxides in  $\text{Si}_3\text{N}_4$ ", Japan Jour. of Applied Phys., 10, 1637, (1971).
3. S. Wild, P. Grieveson, K.H. Jack, and M.J. Latimer, "The Role of Magnesia in Hot Pressed Silicon Nitride", Special Ceramics, Vol. 5, P. Popper, Ed., Stoke-on-Trent, British Ceramic Res. Assn., 377-384, (1970).
4. K.H. Jack and W.I. Wilson, "Ceramics Based on the Si-Al-O-N and Related Systems", Nature, 238, 28-29, (1972).
5. I.C. Huseby and G. Petzow, "Influence of Various Densifying Additives on Hot-Pressed  $\text{Si}_3\text{N}_4$ ", Powder Met. Int., 6, No. 1, 17-19, (1974).
6. W.J. Croft and I.B. Cutler, "Review of Silicon Nitride", E.R.O. Report No. 2-73, ONR Report No. R-16-73, July 1973.
7. D.W. Richerson, "Effect of Impurities on the High Temperature Properties of Hot-Pressed Silicon Nitride", Bull. Amer. Cera. Soc., 52, 560-569, (1973).
8. G.E. Gazza, "Hot-Pressed  $\text{Si}_3\text{N}_4$ ", Jour. Amer. Cera. Soc., 56, 662, (1973) (See Also U.S. Patent No. 3,830,652).
9. C.P. Gazzara and D.R. Messier, "Quantitative Determination of Phase Content of  $\text{Si}_3\text{N}_4$  by X-Ray Diffraction Analysis", AMMRC Tech Report 75-4, February 1975.
10. R. Kossowsky, "Cyclic Fatigue of Hot-Pressed  $\text{Si}_3\text{N}_4$ ", Jour. Amer. Ceram. Soc., 56, No. 10, 531-535, (1973).

11. T.A. Ferraro and B.H. Strauss, "Emission Spectrographic Determination of Metallic Impurities in Silicon Nitride by a Solution Method", AMMRC PTR 73-5, April 1973.
12. A.W.J.M. Rae, D.P. Thompson, N.J. Pipkin, and K.H. Jack, "The Structure of Yttrium Silicon Oxynitride and its Role in the Hot-Pressing of Silicon Nitride with Yttria Additions", presented at the Sixth Symposium on Special Ceramics, B.C.R.A., Stoke-on-Trent, July 9-11, 1974; published in "Special Ceramics 6", 1975, pp 347-360.
13. K.H. Jack, "Sialons and Related Nitrogen Ceramics", Wolfson Research Group for High Strength Materials, University of Newcastle Upon Tyne, England.
14. R.R. Wills, "Silicon Yttrium Oxynitrides", Jour. Amer. Ceram. Soc., 57, No. 10, 459, (1974).
15. F.F. Lange, "Recent Developments in Gas Turbine Ceramic Materials", presented at the Third Materials Conference Turbine Applications, Univ. of Michigan, Oct. 30 - Nov. 1, 1974.
16. F.F. Lange, personal communication.

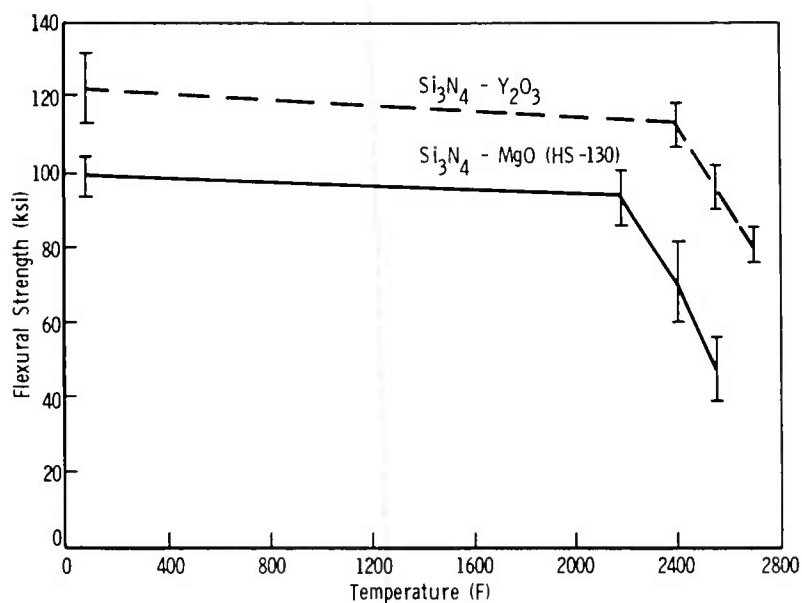


Figure 1. Strength Versus Temperature For  $\text{Si}_3\text{N}_4 + \text{Y}_2\text{O}_3$  Versus  $\text{Si}_3\text{N}_4 + \text{MgO}$

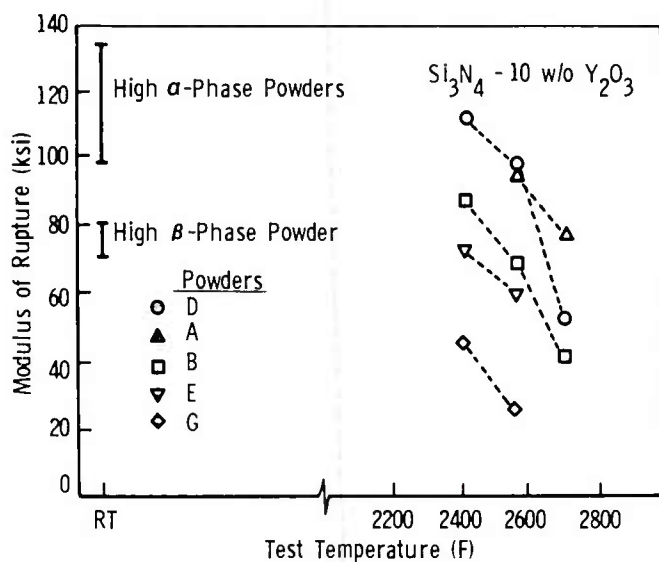


Figure 2. Effect of Starting Powder on the High-Temperature Strength of Hot-Pressed Silicon Nitride

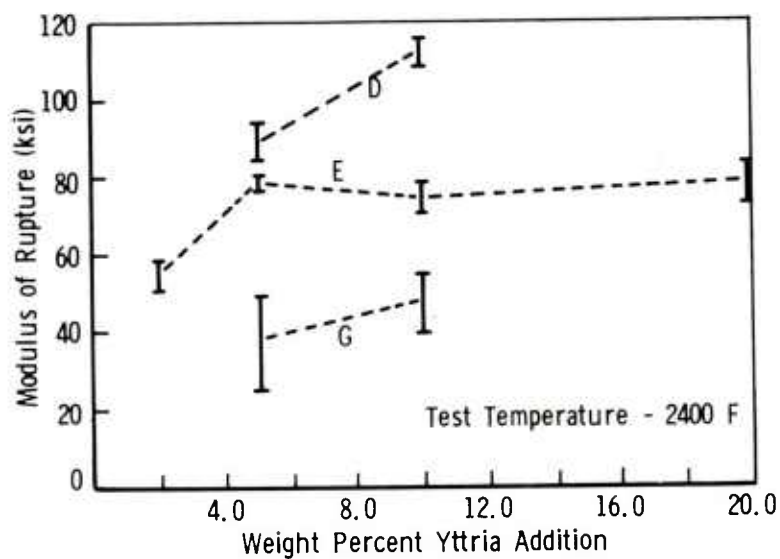


Figure 3. Effect of Yttria Addition Level on High-Temperature Strength of Hot-Pressed Silicon Nitride Formed from Various Powders

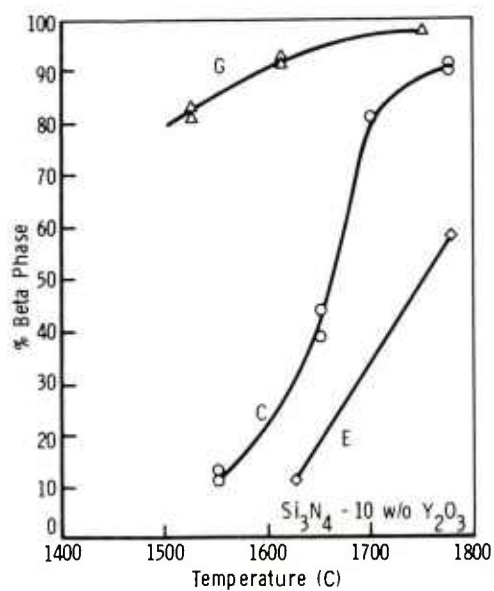


Figure 4. Percent Beta Phase Formation of Various Starting Powders During Hot-Pressing



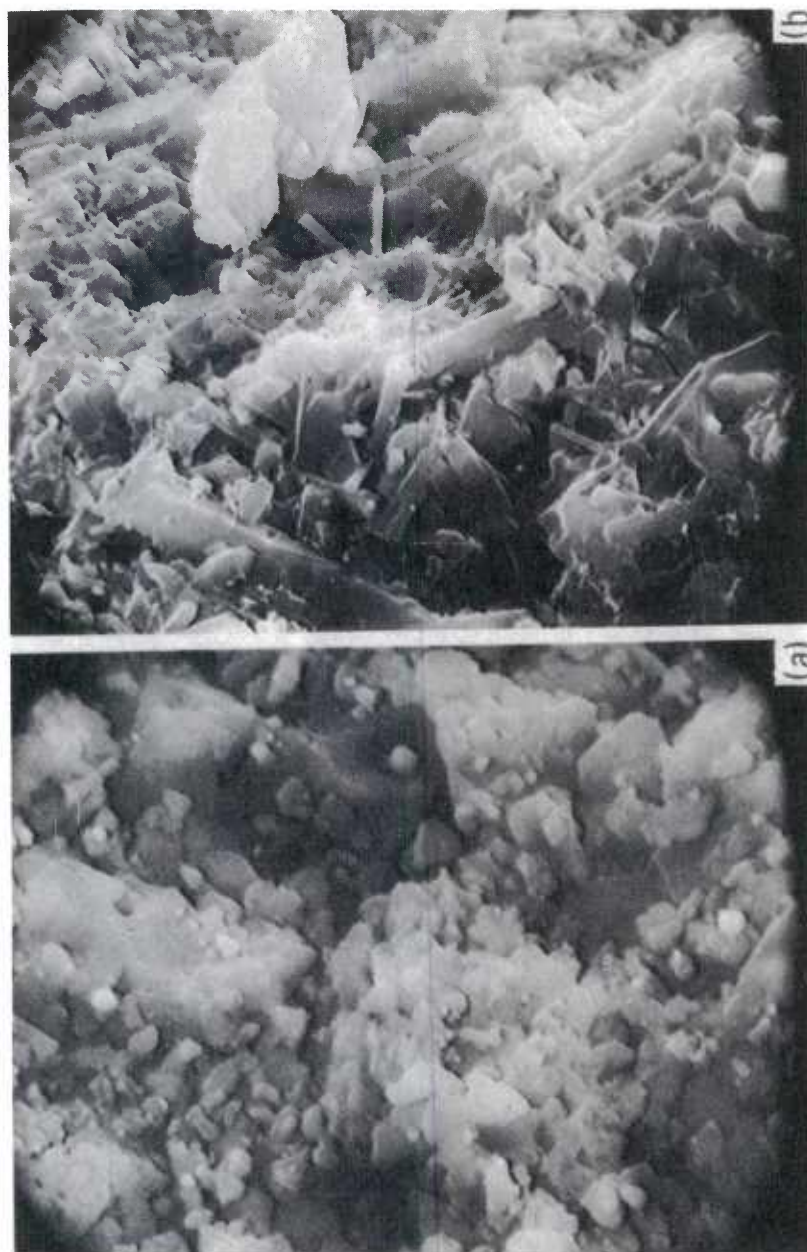


Figure 5. HIGH ALPHA PHASE STARTING POWDER - HOT  
PRESSED (a) 1625C, (b) 1780C  
Mag. 5000X

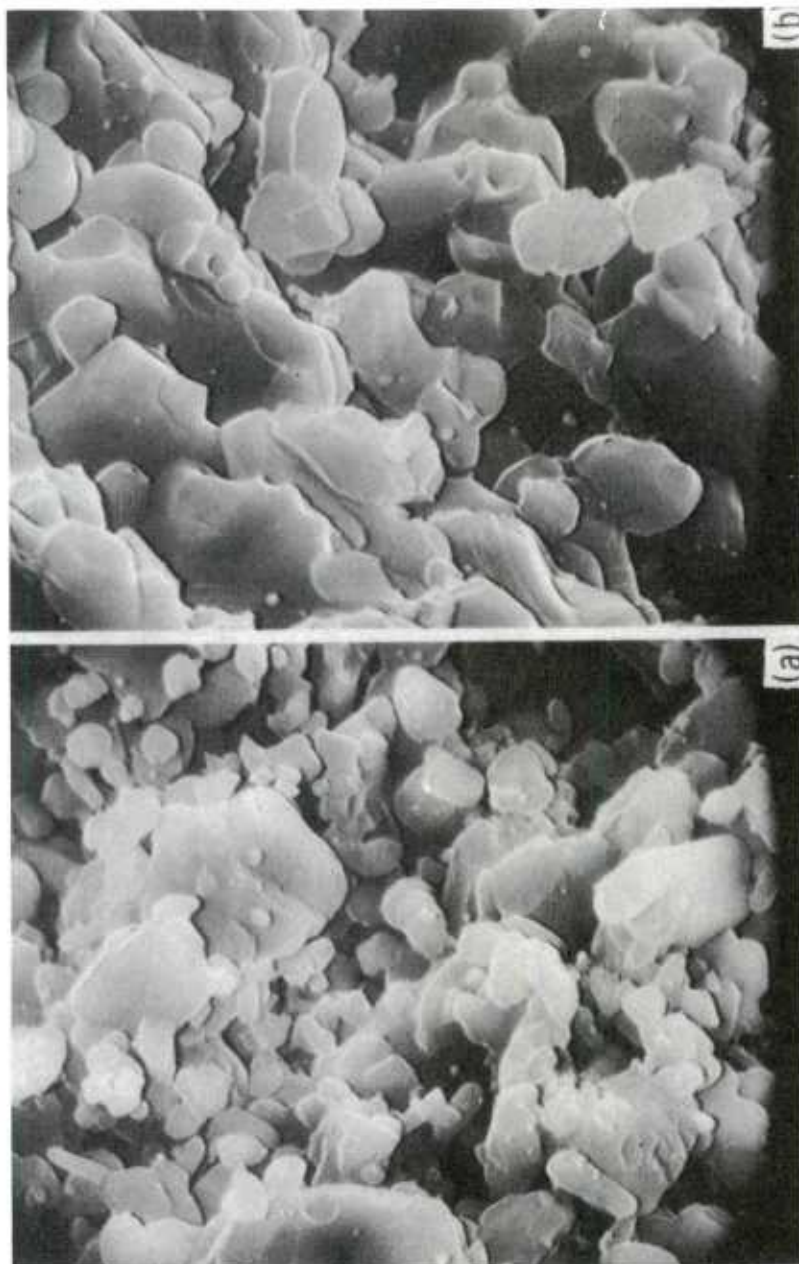


Figure 6. HIGH BETA PHASE STARTING POWDER - HOT  
PRESSED (a) 1640C, (b) 1780C Mag. 5000X

A NEW EXPERIMENTAL TECHNIQUE FOR STUDYING  
THE EXPLOSIVE COMMINATION OF LIQUIDS (U)

BERNARD V. GERBER, MSChE  
\*ARTHUR K. STUEMPFLE, MS  
EDGEWOOD ARSENAL  
ABERDEEN PROVING GROUND, MD 21010

I. INTRODUCTION

Persistent and non-persistent liquid chemical warfare agents are typically delivered to the target as a consolidated mass which is then disseminated by some energetic mechanism to form an initial cloud whose dimensions are large compared with those of the delivery container. Agent persistency is a function of volatility but, regardless of volatility, the effectiveness of dissemination is controlled by the particle size distribution initially formed. With non-persistent agents, the initial particle size distribution controls the mass rate of evaporation and thus the rate of formation and maintenance of the vapor cloud. In the case of persistent agents, the particle size distribution controls the subsequent atmospheric dispersion and fallout mechanisms. Further, casualty production mechanisms are usually functions of particle size as well. Particle size control is, therefore, of primary importance to the weapons systems designer and estimation of particle size is a primary knowledge requirement for the vulnerability analyst.

The ban on open air testing of chemical agents imposed in 1969 dictated reliance on simulation methods in the development of the XM687 155mm shell designed to explosively disseminate the non-persistent nerve agent GB (manufactured in flight by a binary chemical reaction). A dissemination/dispersion simulant was required having a volatility equal or close to that of GB and producing a similar initial particle size distribution. The accepted diffusion model for chemical agent weapons systems considers the source cloud to be a trivariate Gaussian distribution surrounding its centroid. The initially disseminated mass is some fraction of the fill weight (iden-

tified as percent return) since usually losses are involved. The necessary and sufficient empirical information which was obtained from agent field tests in the past and which must now be obtained from simulant field tests includes percent return, location of the source cloud centroid and estimates of the time zero standard deviations of mass with radial distance in each of the three coordinate directions. Due to the complexity and costliness of field tests which is further compounded by the uncertainties due to the use of simulants as opposed to the actual agent, it is imperative to obtain as much information as possible in the laboratory and chamber. However, the mechanisms of explosive dissemination are inadequately understood and scaling laws have not been completely developed. Further, the rapid vaporization of volatile liquids has precluded measurement of the critically important and controlling particle size distribution in the laboratory, chamber, and field. Another complicating factor is the spatial non-uniformity and lack of symmetry of the explosively formed cloud from actual munitions which then requires an extensive sampling array to achieve an adequate description of the spatial distribution of mass. Chamber testing specifically has presented formidable complexity in the past and the interpretation of the results has often been debatable. The most acceptable information from chamber testing of volatile compounds has been high speed motion pictures of the dissemination event in the 0-2 millisecond time frame and the average vapor dosage return in the minutes time frame made uniform and reproducible by mixing. Particle size information has not been previously obtained in the case of volatile liquids.

The method to be described in the following sections appears to have overcome some of the previous difficulties. An indirect measure of the particle size distribution is obtained. The method gives surprisingly reproducible results and has uncovered differences in the behavior of various liquids explosively disseminated which had not been previously known or predicted. Useful empirical results have already been obtained and additional ones are anticipated, but a theoretical basis explaining the liquid behavior has yet to be established.

## II. METHODS

### A. Basic Experimental Concept

The basic experimental concept is to direct the explosive dissemination along a preferred axis to achieve control over the spatial distribution of mass. The resulting cloud is contained in a relatively small sampling space. The projected droplets are sampled by an array of interception/impaction devices. A non-volatile tracer material added to the liquid allows subsequent quantitative assessment even if the liquid evaporates totally, or in part, following



impaction. The following sections describe the implementation of these concepts in more detail.

#### B. Explosive Projector System

A reuseable, vertical, high explosive projector has been developed that is essentially shrapnel-free (shrapnel produces anomalous results) in two versions; one for non-reacting simulants and one for in situ binary GB production. The general components of the device are shown in Figure 1. The steel hold-down fixture (1.375" I.D. x 2" length bore) is followed by an aluminum retainer ring designed to enable the rupture disk to fold open during the detonation process while preventing shearing of the petals and formation of metallic shrapnel. The next component is a 1/8" thick scored steel rupture disk which is employed to cause pressures on the liquid fill as would occur during the casing rupture of an actual bursting munition. Figure 2 is a close-up of the rupture disk before, during and after detonation. The next component in line is a shock transmitting disk whose purpose is to retain the ampule sleeve in the projector and to protect the retainer ring and hold-down fixture during the explosive event.

Seven steel ampule sleeves of varying lengths were constructed in order to accommodate the disparity in liquid densities of the simulants under study. The distances from the bottom of the rupture disk to the top of the liquid fill and from the bottom of the liquid fill to the top of the burster train have been held nearly constant for all liquids by use of appropriately sized spacers. Hemispherical glass end caps (total mass of 5.6 gms) have been bonded to the steel ampule sleeves to contain the liquid. A constant fill weight of 35.3 gms was used. The ampules are filled, frozen and the glass end sealed under vacuum. The glass-to-metal bond maintained a complete vacuum seal over the extreme temperature range of -76°C to +135°C.

An approximate 5/1 agent-to-burster (A/B) ratio was used in the projector system as in the XM687 binary-product GB projectile and the burster consisted of 7.6 gms of Composition C-4 high explosive. As shown in Figure 1, the explosive is packed into a cylindrical nitrocellulose sleeve. Electrical functioning of the system is performed from outside the test chamber.

As shown in Figure 3, provisions have been made for heating the high explosive projector and the simulant/agent fill as appropriate prior to detonation in order to simulate the effects of exothermic binary reactions.

The binary GB in-situ reaction version of the explosive projector is more sophisticated than the neat simulant version in that the binary ingredients are contained in separately filled ampules with provisions for causing mixing by remote control.

### C. Sampling Array

The sampling array consists of a tower sixteen feet high and six feet square as shown in Figure 4. There are nine horizontal sampling planes (levels) consisting of an array of rectangular steel bars. A continuous length of 3mm diameter cotton rope ("pipe-cleaner") is tautly threaded through equally spaced retaining rings welded to the bar. The sampling material between two rings is referred to as a segment. The location of each segment is identifiable. The sampling surface itself faces downward so that the projected liquid drops are intercepted by the absorptive rope through the impaction and interception mechanisms.

The bars in each successive level of sampling are oriented  $90^\circ$  from those in the previous level. The number of sampling bars per level ranges from 7 to 11 as established by experience. The experiments are conducted in a large toxic agent test chamber capable of confining the explosive shock.

### D. Sampler Assessment

At the conclusion of a test, the chamber is purged and the sampling surfaces surveyed to determine the extent of the cloud signature left behind by the visible dye tracer. Individual sampler segments are placed in labeled bottles identified as to sampler segment location in the array.

The sampler segments are then analyzed in the analytical laboratory to assess the quantity of fluorescent tracer dye.

### E. Cloud Development

An appreciation of the cloud development from a typical shot is shown by the time sequence montage in Figure 5. Clouds from various liquids will differ in the total distance projected and in the degree of radial dissemination.

### F. Data Reduction and Analysis

The mathematical technique for calculating the liquid mass passing through each level of the sampling array had been suggested by Monsanto Research Corporation<sup>(1)</sup> and makes use of cubic spline functions. Spline functions are defined as piecewise polynomials of degree  $k$  that are joined together at points termed knots so as to have  $k-1$  continuous derivatives. The Fortran program given by Greville<sup>(2)</sup> has been adapted to the Univac 1108 digital computer to obtain the cubic spline function that interpolates a given number of data points and calculates the integral of the spline function over the given interval.

A simplified procedure has been used to approximate the liquid mass passing through each level of sampling. The three dimensional



position coordinates of each sampling station on each rod for each level of sampling are known relative to the origin (the projector bore). A total of 623 discrete sampler segments are taken from the various levels and are analyzed for each experiment. The liquid mass associated with each segment is multiplied by a factor of 1.25 to account for the sampling area covered by the retainer rings. Corresponding sampling stations on each rod define the knots for the cubic spline function approximation such that a "ribbon" is generated across the rods of the plane. The function is evaluated every 1/8" and the liquid mass of the "ribbon" is obtained by integration over the interval from -36" to +36" relative to the center of the "ribbon". Empirically, this interval encompasses the entire cloud throughout its projection pattern. An estimate of the total liquid mass passing through a particular level of sampling is made by summing the masses obtained for each "ribbon" in that plane. Figure 6 is a paper reconstruction of typical data associated with each sampling plane as obtained by cubic spline analysis. The integrals under the mathematically described surfaces are very reproducible numbers in replicate trials in spite of the non-uniform distributions of each "ribbon".

The cumulative mass fraction lost with height above the projector has been found to exhibit a two parameter Weibull type distribution expressed by Nelson<sup>(3)</sup> in cumulative distribution form (CDF) as:

$$F(z) = 1 - e^{-\left(\frac{z}{\eta}\right)^{\beta}}$$

where:  $z$  = height (feet)

$\eta$  = scale parameter of distribution (feet) ( $\eta > 0$ )

$\beta$  = shape parameter of distribution ( $\beta > 0$ )

Typical digital computer fits to the data for two differently behaving compounds are shown in Figure 7. The reproducibility in replicate trials is also shown. Substantial differences among liquids have been observed in the mass median height ( $\bar{Z}_{50}$ ) and the mean height ( $\bar{Y}$ ) which are calculable measures of central tendency related to the first moment of the distribution. The distribution of mass with height is clearly a function of particle size distribution. The probability density function (PDF - first derivative of the CDF) is an alternative representation of the data which can be more clearly interpreted in terms of particle size implications. Additional information is contained in measures of dispersion calculable for the distribution; i.e., the second moment (variance) and the third moment (skewness).<sup>(4)</sup>

#### G. Remarks

An estimate of the cloud front velocity was obtained from a frame-by-frame inspection of high-speed motion pictures. Four milli-

seconds following detonation, the leading edge of the cloud extends to a height of approximately four feet above the projector for all liquids studied. Above four feet, the cloud fronts for various liquids decelerate at different rates. Sampling efficiency is a function of drop size and velocity. Given the velocity, the minimum size of drop that should be collected at a particular impaction efficiency can be computed.<sup>(5,6)</sup> At the lower levels of the sampling array, where the drops experience velocities near sonic conditions, all particles greater than  $\sim 8\mu\text{m}$  in diameter should be collected with a greater than 90% efficiency. At higher levels of the sampling array, e.g. ten feet above the projector, where the cloud front velocity has decreased to a speed ranging between 52 and 103 ft/sec depending on the liquid under study, the inertial samplers are 90% effective in capturing drops larger than  $15\mu\text{m}$  in diameter. It can be concluded that the inertial samplers are effective for capturing the liquid component of the projected aerosol/vapor cloud. The inhalable "vapor" portion of the cloud is considered to consist of all particles less than  $\sim 5\mu\text{m}$  in diameter. For some liquids a large fraction of the fill is comminuted to "inhalable vapor" within the first two milliseconds. Evaporation cannot account for the effect according to theory unless the drops are initially very small.<sup>(7)</sup>

### III. GB SIMULANT STUDY

The prototype experimental techniques had been conceived and demonstrated prior to the urgent requirement to develop a binary GB dissemination simulant for the XM687 shell. The urgency compelled an accelerated effort and contractual support was obtained from Monsanto Research Corporation (MRC).<sup>(1)</sup> The contractual scope of work specified by the present authors directed that simulants be sought that bracket the performance of the binary shell in operation (defined as the "compositive" simulation approach). MRC reviewed previous studies to determine the possible explosive dissemination mechanisms and the probable controlling liquid physical properties. They suggested cavitation, evaporation, divergent flow and aerodynamic shear as the possible mechanisms of breakup. The probable liquid properties of relevance included compressibility, heat of vaporization, tensile strength, surface tension, viscosity, volatility and density. Consequently, MRC suggested a set of liquids of varying properties to be tested in the chamber to verify the choice of properties and the feasibility of the "compositive" simulation approach. MRC accepted the authors' recommendation that the basic experimental concepts previously described be used in the chamber test program to be conducted by Edgewood Arsenal. As the program progressed, the hardware and techniques were refined to the presently reported state. The results for a subset of the liquids tested, for which all of the physical properties were available or estimable, are shown in Figure 8 (CDF form) and in Figure 9 (PDF

form). Unanticipated differences in disseminated liquid behavior are observed. Figure 8 shows clearly, for example, that the major portion of the water cloud projects quite far whereas only a small portion of the 1,1,2,2-tetrachloroethane cloud projects as far. The curves in Figure 9 imply that the mean drop size in the water cloud is much larger than the mean drop size in the 1,1,2,2-tetrachloroethane cloud. A further implication is that the drop size distribution for water is fairly symmetrical whereas that for 1,1,2,2-tetrachloroethane is dramatically skewed to the right (biased toward small particles). GB behaves similarly to water. Tetrachloroethylene behavior is even more extreme than that of 1,1,2,2-tetrachloroethane and could not be conveniently plotted on Figure 9. Trichloropropane, previously used to simulate GB in field testing due to similar volatility, is clearly seen to be different than GB in comminution behavior.

MRC attempted to correlate a measure of central tendency (their choice was the Weibull mean) with measured and/or estimated liquid properties. The best correlation was obtained considering only solubility parameter, surface tension and volatility. The correlation and supporting data base is given in Figure 10. The correlation accounts for approximately 95% of the variation for the selected data base.

Postulation of mechanisms and controlling liquid properties was incidental to the main objective of the contract effort which was to recommend better simulants for binary GB. In this latter respect the contract was unequivocally successful.

#### IV. PROBATIVE EXPERIMENTS

The MRC equation was developed on a relatively small data base. Consequently, analysis and additional testing has continued at Edgewood Arsenal. The MRC equation is obviously sensitive to volatility which does vary by many orders of magnitude among liquids. Carbon tetrachloride was chosen as a convenient liquid for test whose volatility was about 5 times greater than other liquids tested. Experimentally it was shown to be close in comminution behavior to 1,1,2,2-tetrachloroethane. The MRC correlative equation, however, breaks down and gives a high negative value for the Weibull mean which is impossible to interpret physically.

A compound was then chosen for test which lay within the range of property values used in deriving the MRC correlation. The experimental data for 1,2-dibromo-1,1-dichloroethane shows it to behave also very similarly to 1,1,2,2-tetrachloroethane but the MRC correlations would predict its cloud to project twice as far as observed.

It can be concluded that the MRC correlation is not general. Further, it can be concluded that the most likely way of obtaining a

predictive model would be through clarification of the physical mechanisms involved in explosive dissemination of liquids. Not only is there a scientific impetus to further investigation, but a practical one since the possibility exists that additives can be found for GB that promote comminution and thus increase operational effectiveness.

#### V. ADDITIONAL EXPLORATORY EXPERIMENTS

The mechanism easiest to alter (if it occurs) is cavitation. It is known that suspended particles and dissolved gases can act as sites to increase cavitation. A test run with water containing a small percentage of fumed silica dust (cabosil) did show a 22% decrease in projected height. Adding cabosil to trichloropropane appeared to also decrease projected height but was within the range that could be due to experimental error. Propanol-water mixtures gassed with carbon dioxide and GB gassed with propylene showed no significant changes. Overall these results are inconclusive but further experimentation is certainly warranted since trends are apparent.

#### VI. CONCLUDING REMARKS

The innovative chamber test technique employing a unique reusable high explosive projector and a three dimensional array of impact samplers developed to study explosive dissemination in the 0-1 second time frame has uncovered previously unobserved behavior of volatile liquids.

The experimental data are very reproducible and yield indirect measures of the particle size distribution. It can be inferred that the particle size distribution formed by the dissemination process can be considerably different between liquids and can result in different cloud formations in space and time.

Efforts to explain the liquid comminution mechanisms in terms of known physical properties have so far been unsuccessful. Further experimentation with this technique is highly warranted and may lead to a clearer understanding of the physical mechanisms and the physical properties controlling explosive comminution of liquids.

Various speculations and hypotheses can be proposed as a basis for further work. The properties of liquids measured at or near normal ambient conditions may not be appropriate for the liquid under the stresses of the shock and transient pressure waves caused by the detonation product gases and casing rupture. It is proposed that the liquid might exhibit non-Newtonian characteristics under high transient stress and that the time history of recovery to the normal ambient state would be important. Non-Newtonian behavior could extend through viscoelasticity and under sufficiently severe stress could end in a glassy or crystalline solid state. It is, therefore, recommended that



the properties of liquids be studied under high stress to determine if non-Newtonian characteristics are exhibited.

REFERENCES

1. Hedley, W. H. et al, Feasibility Study of Compositive Simulation Applied to Field Testing of a Specific Dissemination System (U), Final Report, Contract DAAA15-72-C-0281, Apr 76. Confidential Report.
2. Ralston, A. and Wilf, H. S. Mathematical Methods for Digital Computers, Vol II, pg 156. John Wiley and Sons, Inc., NY, 1967.
3. Nelson, L. S. Weibull Probability Paper. Industrial Quality Control 23, 452, 1967.
4. Stuempfle, A. K. and Pellegrino, C. R. EC-TM-74007. Weibull Distribution Parameter Estimation by Digital Techniques and Application to Particle Size Distributions, June 1974. Unclassified Report.
5. Stuempfle, A. K. EATR 4705. Impaction Efficiency of Cylindrical Collectors in Laminar and Turbulent Fluid Flow. Part I. Inertial Impaction Theory, March 1973. Unclassified Report.
6. Stuempfle, A. K. and Pellegrino, C. R. EC-TR-74050. Inertial Impaction Efficiency of Cylindrical Collectors by Digital Techniques and Effects of Particle Size Distributions, October 1974. Unclassified Report.
7. Stuempfle, A. K. EATR 4353. Theoretical Analysis of the Evaporation of Liquid Droplets of Agents VX, GD, GB and EA 1356 (U), April 1970. Confidential Report.

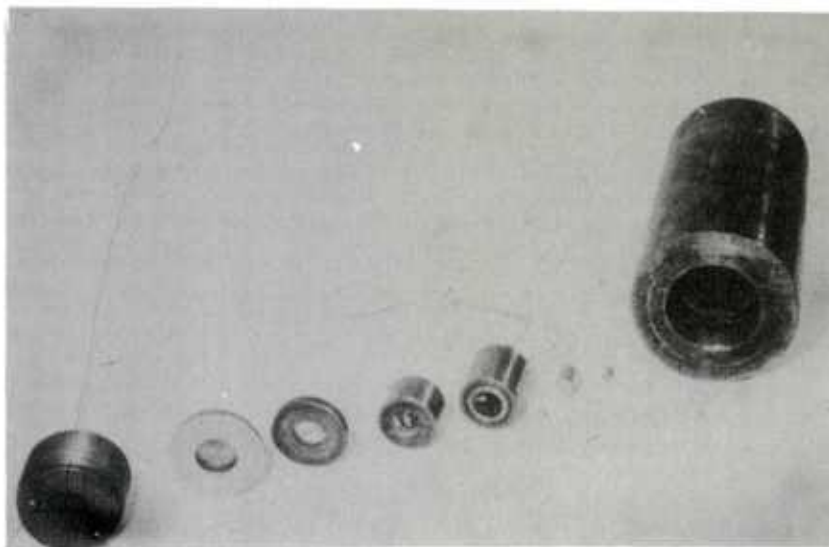


FIGURE 1 PROJECTOR COMPONENTS

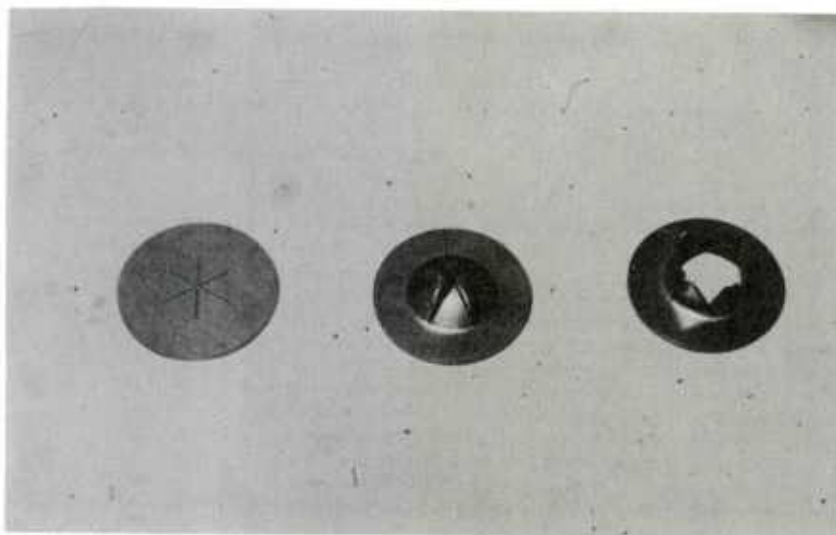


FIGURE 2 RUPTURE DISK OPENING SEQUENCE



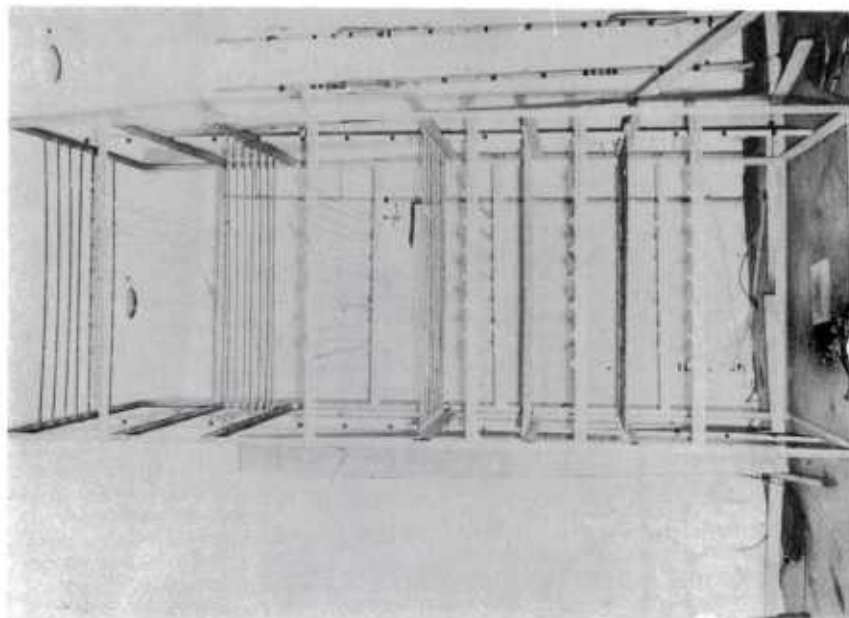


FIGURE 4 SAMPLING ARRAY

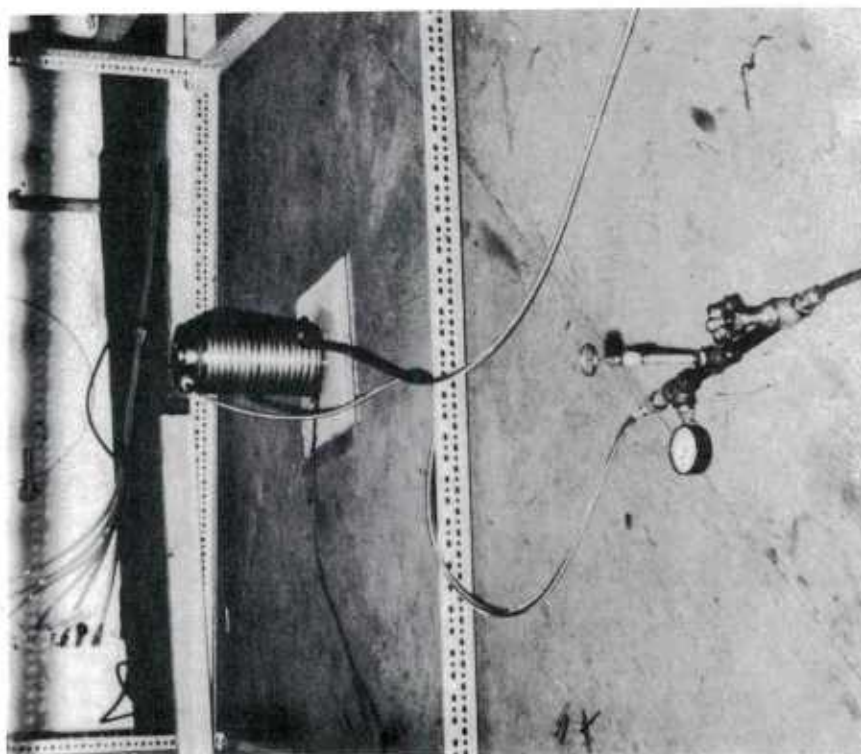


FIGURE 3 HEATING MECHANISM

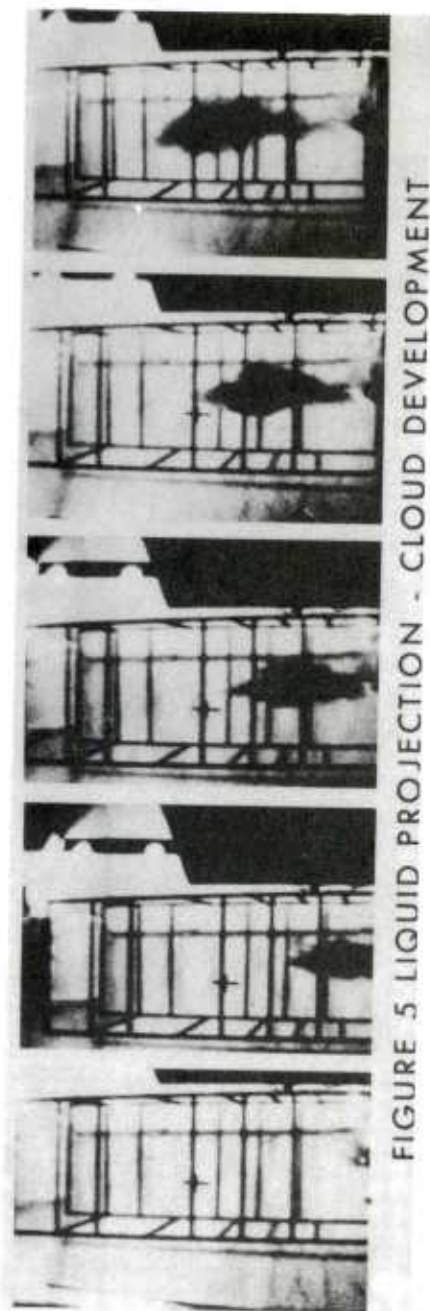


FIGURE 5 LIQUID PROJECTION - CLOUD DEVELOPMENT

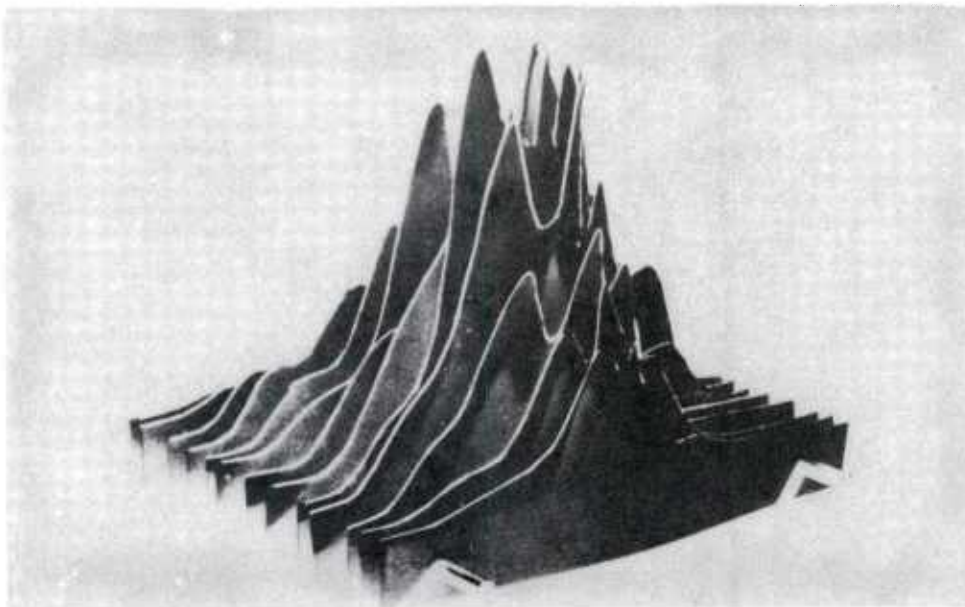


FIGURE 6 CUBIC SPLINE FIT TO SAMPLER RESULTS IN A PLANE

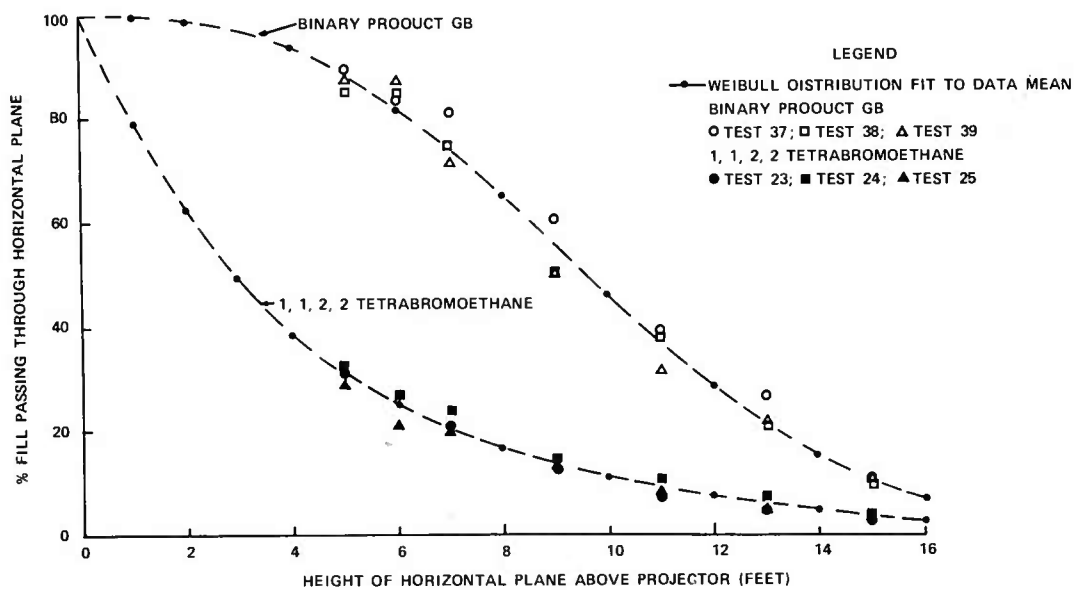


FIGURE 7 LIQUID MASS DECAY CURVE

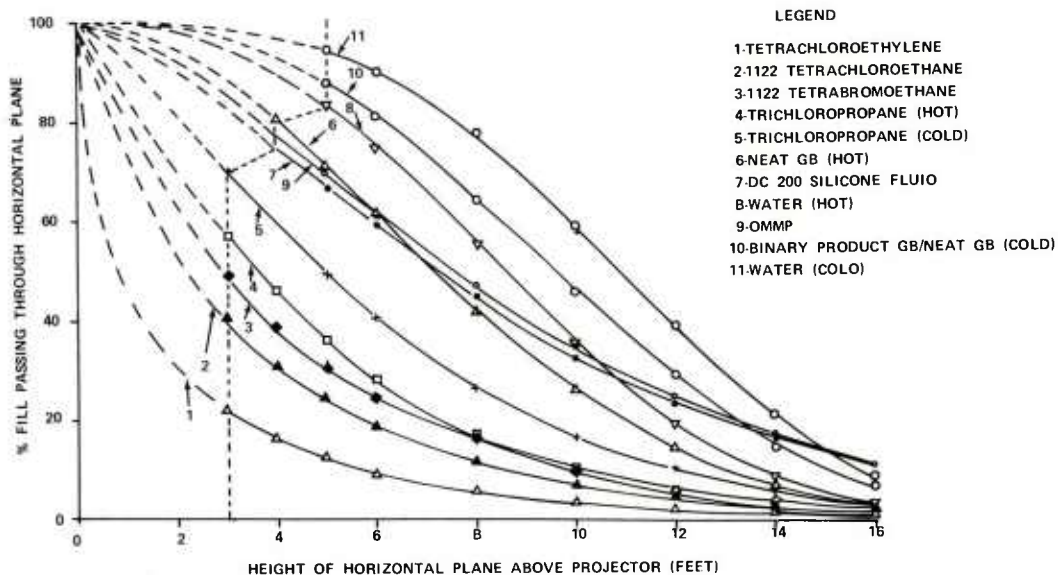


FIGURE 8 LIQUID MASS DECAY CURVE

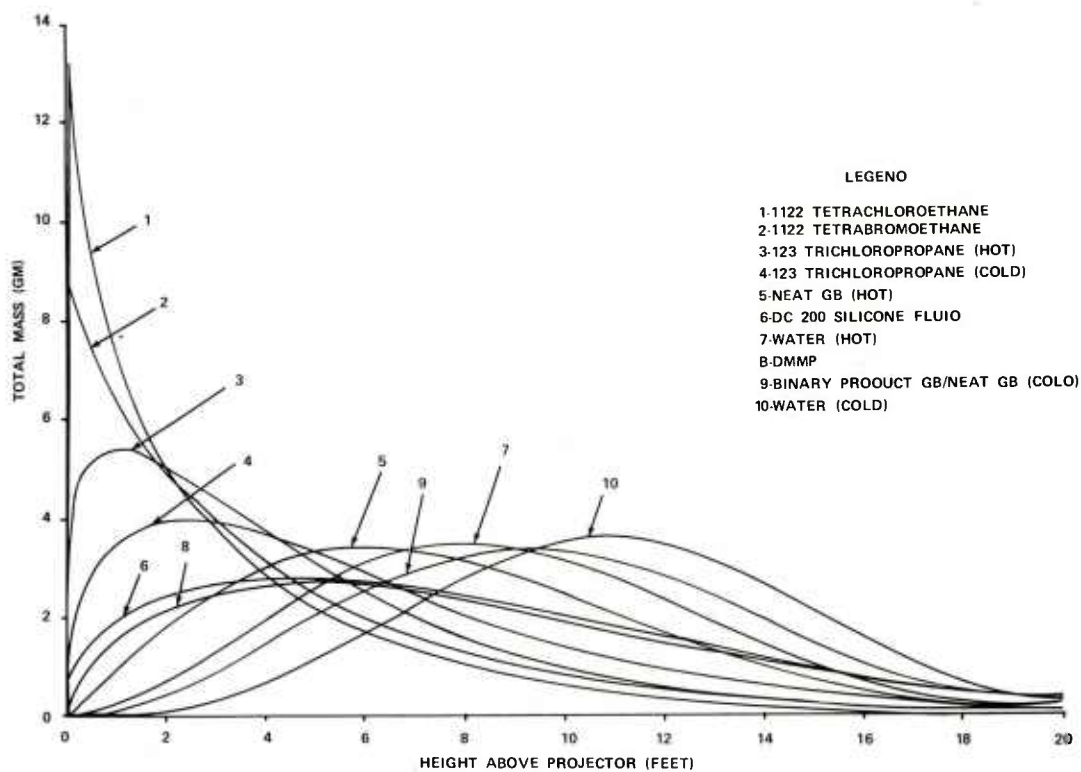


FIGURE 9 LIQUID MASS DISTRIBUTION FUNCTION

## CORRELATION ①

$$\bar{V} \text{ (cm)} = 29.75 \delta - 8.10 \sigma - 0.90V + 214.9$$

## DATA BASE ②

SIMULANT/AGENT ③	WEIBULL MEAN $\bar{V}$ (cm)	SOLUBILITY PARAMETER $\delta$ (cal/ml) <sup>1/2</sup>	SURFACE TENSION $\sigma$ (dynes/cm)	VOLATILITY $V$ (gm/m <sup>3</sup> )
TETRACHLOROETHYLENE (HOT)	66.0	8.20	30.6	165
1, 1, 2, 2 - TETRACHLOROETHANE (HOT)	107.4	8.54	35.0	54
1, 1, 2, 2 - TETRABROMOETHANE (HOT)	135.6	10.10	47.0	0.37
1, 2, 3, - TRICHLOROPROPANE (HOT)	147.6	8.77	37.0	29
1, 2, 3, - TRICHLOROPROPANE (COLD)	197.9	9.94	37.0	29
NEAT GB (HOT)	241.1	8.25	25.9	21
DC 200 SILICONE FLUID (HOT)	259.2	7.00	20.0	0.01
WATER (HOT)	273.0	22.01	72.0	23
DIMETHYLMETHYLPHOSPHONATE (HOT)	281.7	13.60	36.0	11
BINARY PRODUCT GB/NEAT GB (COLD)	295.1	9.26	25.9	21
WATER (COLD)	314.6	23.54	72.0	23

① CORRELATION. DERIVED BY MONSANTO RESEARCH CORPORATION

② SELECTED PHYSICAL PROPERTIES ESTIMATED BY MONSANTO RESEARCH CORPORATION

③ HOT = 130° C ; COLD = 20° C

FIGURE 10 INITIAL SELECTED COMPOUNDS





THE MEASUREMENT OF THE  
THIRD-ORDER ELASTIC CONSTANTS IN A SLIGHTLY  
ANISOTROPIC SOLID USING ULTRASONIC SURFACE WAVES

GRANT R. GERHART, PhD.  
U.S. ARMY TANK-AUTOMOTIVE DEVELOPMENT CENTER (PROV)  
WARREN, MICHIGAN 48090

INTRODUCTION

A solution of the Rayleigh Wave (RW) equation cannot be obtained for surface wave (SW) propagation on a general, anisotropic solid except for special symmetry conditions. In particular, for single crystal materials, the anisotropy is quite large and the wave equations cannot be solved in closed form except for planes of special symmetry. Amorphous and certain poly-crystalline materials have nearly isotropic mechanical properties in the unstressed state because of the random nature of the atom or grain orientations. The latter class of solids are very nearly isotropic for ultrasonic SW propagation provided that the wavelength is much longer than the diameter of the single crystal grain sizes. The mechanical properties of these materials in the stressed state can be adequately described by specifying the two independent second-order and the three independent third-order elastic constants for small stress levels. Changes in the SW velocity are caused by externally stressing the sample. The measurement of the velocity changes and the external stress uniquely determines the third-order elastic constants.

The medium for the propagation of surface waves is a homogeneous, isotropic half-space which becomes elastically anisotropic under small deformations. Plane, parallel Rayleigh Waves are assumed to propagate on the surface along some arbitrary direction. The transverse and longitudinal wave equations are written for displacement in an elastic anisotropic medium, and solutions are sought which decay exponentially into the medium, normal to the surface. The SW particle displacement is obtained by substituting these solutions into the boundary

conditions for a traction-free surface. The SW velocity is determined by solving the determinant of the coefficient matrix for these boundary conditions, and yielding the SW velocity changes as a function of the third-order elastic constants for a known applied stress.

The experimental procedure for measuring the small velocity changes to one part in  $10^5$  is also described in this paper. The pulse overlap velocity measurement technique, as applied to SW velocity measurements, is described in some detail. The main object of this procedure is to measure very accurately the SW velocity directly in terms of a frequency parameter by overlapping two echoes of an incident SW pulse on an oscilloscope. This measurement provides a precise determination of the transit time difference between the two reflected echoes. Each echo is a reflection from a pair of shallow grooves which are scribed a known distance apart.

#### THEORETICAL DETERMINATION OF THE SURFACE WAVE VELOCITY

The equation of motion for a displacement in an elastic, homogeneous, anisotropic medium is<sup>1</sup>:

$$\rho \partial^2 U_j / \partial t^2 = 1/2 C_{ijkl} (\partial / \partial x_i) (\partial U_k / \partial x_l + \partial U_l / \partial x_k). \quad (1)$$

The displacement component  $U_j$  is measured along the cartesian axis  $x_j$ , and  $C_{ijkl}$  is the elastic stiffness tensor which is referred to the  $x_j$  coordinate system. The total displacement components for the surface wave problem are assumed to be of the form:

$$U_i = \sum_{n=1}^3 C_n \alpha_{ni} \exp(iK l_{n3} x_3) \exp\{iK(l_1 x_1 + l_2 x_2 - Vt)\}. \quad (2)$$

where  $l_1$  and  $l_2$  are the direction cosines for the propagation vector on the surface, and  $l_{n3}$  is one of three complex, lower-half plane roots of the secular equation<sup>1</sup>. Each  $\alpha_{ni}$  is the  $i$ th component of the normalized eigenvector corresponding to the  $n$ th root. The coordinate system is chosen so that the  $x_3$ -axis is the outward normal to the traction free surface, and the medium occupies the half space  $x_3 \leq 0$ . The total displacement is substituted into the boundary condition where the normal and tangential components of stress vanish on the surface  $x_3 = 0$

$$0 = T_{3j} = C_{3jkl} \partial U_k / \partial x_l. \quad (3)$$

The complex determinant of these three homogeneous equations is also zero. The individual components in this matrix are:

$$d_{mn} = C_{m3kl} \alpha_{nk} l_{nl} \quad (4)$$

where:  $l_{n1} = l_1$ ,  $l_{n2} = l_2$ .

The stiffness tensor components <sup>2</sup> using abbreviated notation are assumed to have the following form:

$$C_{ij} = C_{ij}^0 + C_{ij}^1. \quad (5)$$

The quantity  $C_{ij}^0$  is an elastic stiffness tensor component for the isotropic, unperturbed medium, and  $C_{ij}^1$  is the anisotropic term which is a linear combination of the third-order elastic constants. The correction factors have the most general form which is consistent with the symmetry relations among the third-order elastic constants in an isotropic medium.

The approximate equation after substituting Eq. 5 into the boundary condition is:

$$\sum_{n=1}^3 (C_{3jkl}^0 + C_{3jkl}^1) \alpha_{nk} l_{nl} = 0. \quad (6)$$

The quantities  $C_{ijkl}$  depend explicitly upon the third-order elastic constants while  $\alpha_{nk}$  and  $l_{nl}$  depend implicitly upon  $C_{ijkl}$  through the transverse and longitudinal wave velocities  $V_t$  and  $V_l$ . The first-order correction factors<sup>1</sup> to the eigenvalues,  $\rho V_t^2$  and  $\rho V_l^2$  are:

$$\lambda_1 = C_{66}^1 \quad \lambda_2 = C_{55}^1 \quad \lambda_3 = C_{11}^1 \quad (7)$$

where  $\lambda_2$  corresponds to a transverse displacement which is normal to the plane  $x_3=0$ , and  $\lambda_3$  to a longitudinal displacement which is parallel to the  $x_1$ -axis.

The determinant of the coefficient matrix, Eq. 4, yields an approximate equation for the Rayleigh Velocity

$$C_{55} (1 - l_{32}^2) (C_{31} + C_{33} l_{33}^2) = \{ 2 C_{55} l_{32} l_{33} - C_{53} l_{32} (1 + l_{33}^2) \} (C_{33} - C_{31}) \quad (8)$$

where each term is first-order and linear in  $C_{ij}^1$ . The quantities  $l_{32}$  and  $l_{33}$  are:

$$l_{32}=l_{31}=-i(1-\eta^2)^{1/2} \quad l_{33}=-i(1-\xi^2\eta^2)^{1/2} \quad (9)$$

$$\eta=V/V_t, \quad \xi=V_t/V_l.$$

The substitution of  $l_{n3}$  into Eq. 8 and squaring yields:

$$(2-\eta^2)^2(1-\xi^2\eta^2A)^2=4(1-\eta^2)(1-\eta^2\xi^2)(1-\eta^2\xi^2\beta)$$

$$A=C_{33}^0/(C_{33}^0-C_{31}^0)+\alpha \quad \beta=C_{53}^1/l_{33}^0C_{55}^0 \quad (10)$$

$$\alpha=\{(2\xi_0^2-1)C_{33}^1+C_{31}^1\}/4\xi_0^4C_{33}^0.$$

The quantity  $\eta$  can be expressed to first-order as:

$$\eta=\eta_0+\Delta\eta_0 \quad \Delta\eta=\eta_0(\Delta V/V_0-\Delta V_t/V_{t0}) \quad (11)$$

where all subscript zero variables have isotropic values<sup>3</sup> and  $\Delta\eta$  is small for a slightly anisotropic material. The substitution of  $\eta$ ,  $\xi$  and  $l_{n3}$  into Eq. 10, which is solved for  $\Delta V/V_0$ , yields:

$$\Delta V/V_0=JC_{33}^1/C_{33}^0+KC_{31}^1/C_{33}^0+LC_{53}^1/C_{55}^0+(M+0.5)C_{55}^1/C_{55}^0$$

$$+NC_{11}^1/C_{11}^0-0.5\Delta\rho/\rho_0 \quad (12)$$

where J, K, L, M and N are given by:

$$J=(2\xi_0^2-1)S/4\eta_0\xi_0^4$$

$$K=S/4\eta_0\xi_0^4$$

$$L=16\xi_0^2\{\eta_0^2(1+\xi_0^2-\xi_0^2\eta_0^2)-1\}/\eta_0l_{33}^0r_0$$

$$M=-N=16\xi_0^2(\eta_0^2-1)/\eta_0r_0$$

$$S=-8\xi_0^2\{\eta_0^4+2(\eta_0^2-1)(4\xi_0^2-3)-2\}/r_0$$

$$l_{33}^0=-i(1-\eta_0^2\xi_0^2)^{1/2}.$$

The Rayleigh velocity change  $\Delta V$  is determined by the isotropic parameters  $\xi_0$ ,  $\eta_0$ , and the third-order elastic constants  $C_{ijk}$  where:

$$C_{ij}^1 = C_{ijk} S_k$$

and  $S_k$  is the strain tensor in abbreviated notation. The quantity  $\Delta V$  in Eq. 11 is a complex number. The imaginary part is the  $C_{53}^1$  term which contains  $1_{33}^0$ , and it produces an exponential attenuation of the surface wave. The remaining terms are real, and they change the propagation velocity.

### EXPERIMENTAL CONFIGURATION

The measurement of bulk transverse and longitudinal wave velocities using the pulse overlap technique is well established. Two distinct methods have been developed using ultrasonic pulse technology. The first<sup>4</sup> involves gating two out of a number of multiple reflections of an incident ultrasonic pulse and displaying the gated pulses on an oscilloscope. The horizontal axis of the oscilloscope is driven at a precise frequency with an external oscillator. The two pulses will appear overlapped when the frequency of the horizontal drive voltage is the reciprocal of the transit time difference between the two echoes. The velocity of the ultrasonic waves is the ratio of the transit path difference of the two echoes to the transit time difference. The second method<sup>5</sup> is similar to the first except the reflected echoes are not gated, but are enhanced by pulsing the z-axis modulation input on the oscilloscope with two delayed pulses. These pulses are synchronous in time with the desired two echo pulses. The oscilloscope will display just the intensified portion of the trace that contains the pulses of interest. The advantage of using these pulse selection processes is that otherwise unwanted reflections and noise clutter the oscilloscope trace making the determination of pulse overlap very difficult.

The pulse overlap velocity technique using image intensification was adapted for velocity measurements on surface waves. A block diagram describing the pulse circuitry is contained in Figure 1.

The basic component of this system is the pulsed r.f. oscillator. The frequency synthesizer (FS) feeds a 2.25 mhz. signal into the gated amplifier input. In this mode the r.f. oscillator amplifies and gates the 2.25 mhz carrier signal. The gating is accomplished by pulsing the external modulation input with a pulse of sufficient delay and width. The r.f. output is a 2.25 mhz sine wave which is modulated into a pulse shape with the same width as the modulation input.

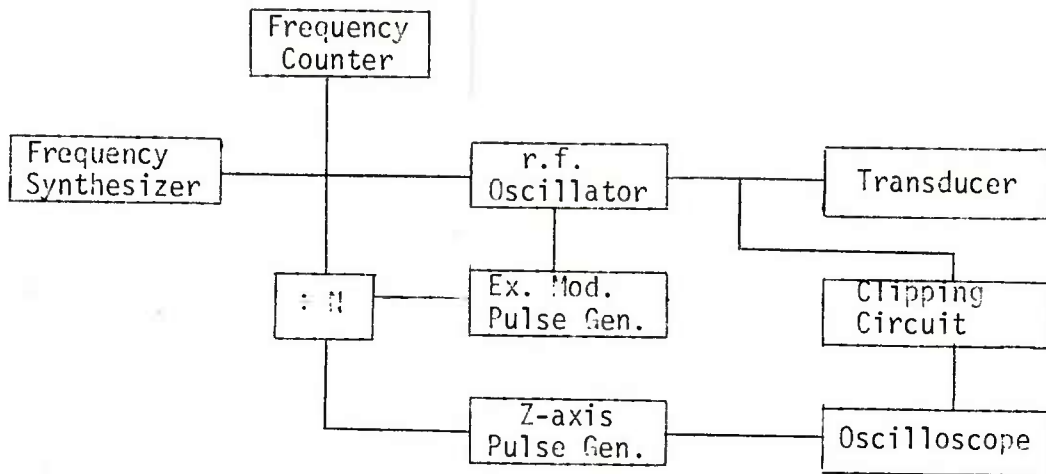


Figure 1

The carrier frequency is divided by a digital counting circuit. This signal is synchronous with the carrier and triggers the pulse generator output to the external modulation input. The divide by N output signal frequency is adjusted to a few khz. This signal is also used to trigger the delay double pulse generator which intensifies the oscilloscope trace.

The r.f. pulsed oscillator output goes directly to the ultrasonic surface wave transducer. The transducer is both a transmitter of the incident pulse and a receiver of the two reflected echoes. The output from the transducer contains a 700V pulse in addition to the 100 millivolt amplitude echo pulses. The main pulse is clipped to a few volts by a Zener diode clipping circuit and the two echo pulses pass on into the oscilloscope input terminal. The clipped main pulse is still an order of magnitude larger than the echo pulses and must be eliminated from the oscilloscope trace using z-axis illumination techniques.

The z-axis pulse generator consists of four one-shot chips which are sequentially triggered to produce a dual pulse output where each pulse has a variable width and delay time. These four variables can each be changed by adjusting the one-shot RC time constants. Commercial dual pulse generators are also available for the same purpose. The output from this one-shot circuit is amplified by means of a power operational amplifier to produce a 30V to 50V amplitude pulsed input into the z-axis oscilloscope terminal.



A Lithium Niobate wedge type SW transducer was used to generate and detect the ultrasonic surface waves. Two small grooves were machined on the surface as in Figure 2 to produce the two reflected echoes which are overlapped on the oscilloscope.

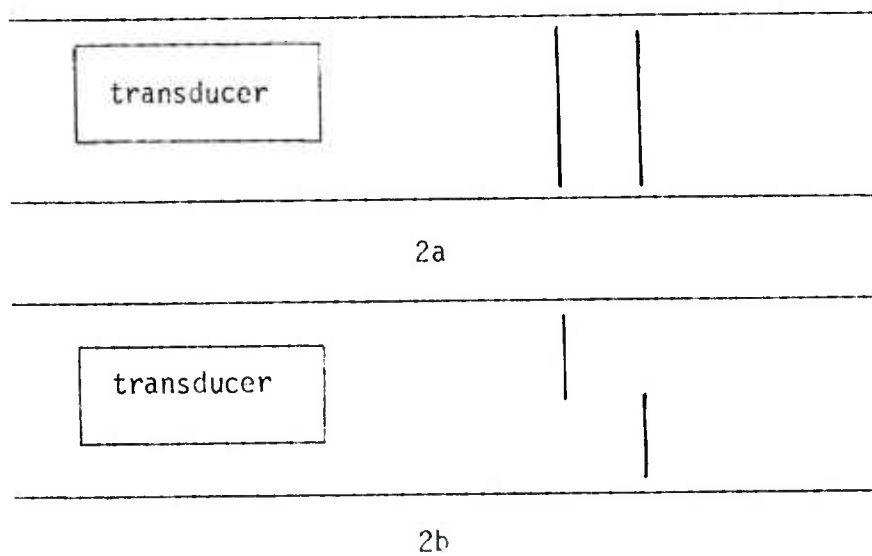


Figure 2

In Figure 2a the groove closest to the transducer is about one-third the depth of the second or one percent of the wavelength  $\lambda$ . The second groove is deeper to compensate for the partial reflections from the first. The two grooves in Figure 2b are the same depth, but they are slightly deeper to compensate for their shorter lengths.

The advantage of using a single transducer to generate and detect the SW echoes is in avoiding coupling problems between the transducer and the sample. The sample is a flat tensile bar which is 1-1/2" x 1/4" in cross-sectional area. When a tensile stress is applied to the sample, the adhesive or coupling agent stretches to produce large changes in the position and amplitude of the detected waves. Since the two echoes are affected equally by the coupling changes, the difference in their transit times is relatively independent of these problems. The large coupling changes which were induced by external tensile stresses made this velocity technique mandatory for obtaining reproducible data.

Strain gages were placed on the tensile bars to monitor the induced strain. The velocity measurements were corrected for changes in the separation distance of the two grooves caused by the strain. Differential strain measurements were made on gages that were located between the two grooves. These measurements insured that no plastic straining was being induced by the presence of the grooves for stress levels below the yield point.

#### EXPERIMENTAL DATA

Three velocity measurements in conjunction with three independent stress configurations are needed to uniquely determine the independent third-order elastic constants. Two measurements are made by recording the SW velocity parallel and perpendicular to the direction of an uniaxial tensile stress. The third measurement could be made by applying a pure shear stress to the sample; however, this procedure proved to be extremely difficult experimentally. Instead, a longitudinal velocity measurement was performed in conjunction with an uniaxial tensile stress.

Figure 3 illustrates the configuration of the sample for the three velocity measurements:

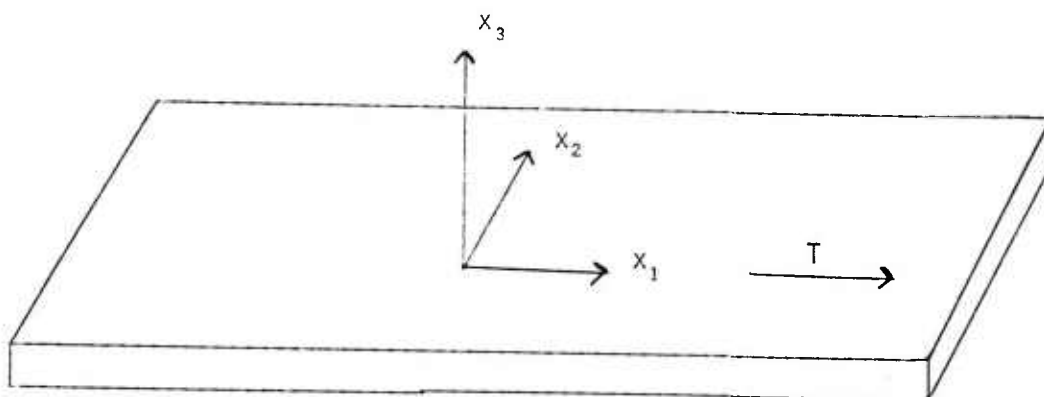


Figure 3

A flat 1/4" x 1-1/2" x 15" tensile bar of 5086-H32 aluminum was tensile stressed along the  $x_1$ -axis while SW velocity measurements were made for waves propagating along the  $x_1$  and  $x_2$  directions. Similar velocity measurements were made for longitudinal waves which were propagating parallel to the  $x_3$ -axis. A quartz x-cut transducer was mounted on the sample and longitudinal waves propagated along the  $x_3$  direction. The velocity was measured by overlapping two of several

multiple reflections on the oscilloscope and measuring the transit time interval in a fashion similar to the SH velocity measurements. The fractional change in the longitudinal velocity is related to the fractional changes in the elastic constants and the density  $\rho$  by:

$$\Delta V/V_0 = 1/2(C_{11}^1/C_{11}^0 - \Delta\rho/\rho_0) \quad (14)$$

The slope of the curve  $\Delta V/V_0$  as a function of the tensile stress  $T$  is tabulated in Table 1 for each of the three types of velocity measurements. In addition, the calculated values of the second and third order elastic constants are also tabulated in Table 1.

	$(\Delta V/V_0)_1$	$(\Delta V/V_0)_2$	$(\Delta V_L/V_{L0})_3$	Units
Slope	6.02	<b>1.75</b>	3.0	$\times 10^{-12} \frac{\text{m}^2}{\text{nt}}$
2nd Order Stiffness $\times 10^{10}$	$C_{11}^0$ 9.67	$C_{12}^0$ <b>4.22</b>	$C_{44}^0$ 2.72	$\times 10^{10} \frac{\text{nt}}{\text{m}^2}$
2nd Order Compliance	$S_{11}^0$ 14.1	$S_{12}^0$ -4.9	$S_{44}^0$ 36.7	$\times 10^{-12} \frac{\text{m}^2}{\text{nt}}$
3rd Order Constants	$C_{111}^0$ -14.6	$C_{112}^0$ -1.92	$C_{244}^0$ -3.17	$\times 10^{11} \frac{\text{nt}}{\text{m}^2}$

Table 1

The values in Table 1 correspond very well to other experimental data for similar aluminum samples.<sup>6,7</sup>

### CONCLUSIONS

The change in the Rayleigh Wave (RW) velocity is desired to first-order in the third-order elastic constants for a stress anisotropy in an otherwise isotropic solid. The fractional changes in the RW velocity are, in fact, proportional to the fractional changes in the third-order elastic constants  $C_{ijk}$ . The largest contribution comes from the  $C_{111}^1$  term which for aluminum accounts for about 50% of the total change in RW velocity. This result is reasonable since

$V_{to}^2 = \rho C_{55}^0$  is the major factor in determining the RW velocity for an isotropic solid. Density variations caused by the term  $\Delta\rho/\rho_0$  account for only a few percent of the total RW velocity change and essentially can be neglected.

The pulse overlap technique successfully eliminated large coupling errors in the determination of the RW velocity. In particular, differential strain measurements revealed that the surface grooves had no observable effect on the elastic behavior of the sample below the limit of proportionality. The depth of the grooves will even be smaller for higher frequency Rayleigh Waves. In principle, three relatively simple stress configurations will determine the three independent, third-order elastic constants for a slightly anisotropic material.

#### BIBLIOGRAPHY

1. C.W. Farnell, Ch. 3, "Properties of Elastic Surface Waves", Physical Acoustics, edited by W.P. Mason and R.W. Thurston, Vol. 3, Academic Press, 1970.
2. R.F.S. Hearman, Advanced in Physics, 5, 323 (1956).
3. I.A. Viktorov, Rayleigh and Lamb Waves, Plenum Press, 1967.
4. McSkimin, H.J., J. Acoust, Soc. Am., 33, 12 (1961).
5. E.P. Papadakis, J. Acoust, Soc. Am., 42, 1045 (1967).
6. J.F. Thomas, Phys. Rev. 175, 3, 955 (1968).
7. D.I. Crecraft, J. Sound Vib., 5, 173 (1967).

POROSITY AND SPALL FRACTURE OF SHOCK LOADED METALS

COY M. GLASS, PhD  
VICTOR A. GREENHUT, PhD<sup>+</sup>  
PRISCILLA W. KINGMAN, Ms.  
US ARMY BALLISTIC RESEARCH LABORATORIES  
ABERDEEN PROVING GROUND, MARYLAND  
<sup>+</sup>RUTGERS UNIVERSITY, NEW BRUNSWICK, NEW JERSEY

The impact of a warhead against an armored target produces plastic deformation and failure (fracture) of the armor as the penetrating part of the warhead is consumed through the same processes. The most common examples coupling these events are shaped charge jets or kinetic energy penetrators defeating vehicle armor. Fragments and small arms projectiles attacking body armor and thin structures made of hard materials produce the same phenomena.

The total extent of flow and failure is a function of the strength and ductility of the materials involved in impactive events. At one extreme a ductile shaped charge jet flows as a virtual liquid introducing plasticity in impacted rolled homogeneous armor (RHA). Deformed fragments are ejected from the front of the armor while spall from the rear surface produces damage to equipment and personnel behind the plate. At the other extreme a strong, brittle tungsten carbide penetrator deforms only slightly before breaking in an impact with ceramic armor. The ceramic armor exhibits only microscopic flow as stresses build beyond its failure strength.

Common to encounters between warhead and armor at extremes of strength and ductility is an interplay between plastic flow and fracture (failure) of the interacting materials. The optimum effectiveness of either a penetrating device or armor is dictated by controlling this interplay.

A fundamental understanding of flow and fracture of solids during dynamic loading is required in order to define the desirable properties materials should have to be effective penetrators or armors.

At velocities of impact where shock waves are created and sustained in the penetrator and target the process has historically been viewed as a hydrodynamic one: that is, the strength of the shock is generally several times greater than the strength of the solid and the solids are considered to flow like a fluid. Material "strength", as viewed in the usual sense of mechanics, played no part in the material reactions.

The first published demonstration that crystal anisotropy influences the reaction of metals to shocks was Reinhart's experiment using a single crystal of aluminum internally loaded with explosive (1). The thin-walled specimen fractured into sections as a function of the orientation of the crystal planes in the metal.

A conclusive demonstration that crystalline structure affects the reaction of metals to shock loading was given by Glass and Gainer in studies begun in 1956 at the US Army Ballistic Research Laboratories, (BRL) (2,3). Preferred orientation of crystal planes introduced in the walls of shaped charge liners during fabrication by shear forming were shown to result in effective spin compensation of the shaped charge jet. These basic research results were used to establish x-ray diffraction inspection techniques and parametric orientation control for producing liners. (The production line inspection techniques have subsequently been computerized and automated by workers at Frankford Arsenal).

This initial success in introducing material anisotropies and properties into the flow of explosively loaded solids led to an extensive program at BRL to establish the extent of control exercised by microstructural and submicrostructural material properties on the flow and fracture of metals subjected to shock loading. It was shown that a metal will react according to its strength and structure under shock stresses two orders of magnitude greater than its static ultimate strength. A number of papers have been published giving results of this work including analysis of hypervelocity impact from a material standpoint (4). Some of the results led to a proposed mechanism for spall and fracture under shock loading which rejected the then current concept that there existed a unique "critical" stress at which a given metal fractures when subjected to a tensile shock (5).



The research reported here has been continued in an effort to completely define the mechanisms involved in shock failure of crystalline solids based on imperfections formed by shock waves. The two objectives of this work were: (a) complete the study of the imperfections formed during shock loading and failure of metals; (b) relate the substructures created by the shocks to the macroscopic reactions of metals subject to shocks. This paper presents the results obtained.

## RESULTS

Studies conducted on metal deformation and failure caused by explosively generated shocks were carried out using cylindrical specimens surrounded by metal of the same type and buffer plates for attenuation of the shock, permitting controlled loading of specimens at desired pressures. Spall plates (momentum traps) were placed on the end of the experimental arrangement to carry the compressive shock away after it passed through the specimen when only the effects of compression on the specimen were to be studied. Absence of momentum traps permitted the shock to reflect back into the specimen as a tensile shock. This experimental procedure has been described in detail elsewhere (5).

Results from previous work delineated macroscopic, microscopic and some sub-microscopic reactions of metals to compressive shocks only and compressive shocks followed by reflected tensile shocks (6,7,8,9). For purposes of understanding the current studies a brief summary of prior results is presented.

A macroscopic tensile shock fracture stress was obtained for specimens that fractured with no decrease in specimen diameter from the original. These data are plotted in Figure 1. As the specimen diameter is decreased the shock stress required to produce fracture with no neck-down increases and as the specimen diameter approaches zero the stress required for fracture approaches the theoretical strength of the metal (Young's Modulus divided by  $2\pi$ ). This result strongly implies that the role of imperfections in shock failure is critical since as the area over which the stress can operate decreases below a given size of imperfection the stress required to cause failure increases. That is, as the specimen diameter approaches zero, the imperfections become uninvolved in the fracture process, requiring the "theoretical" stress for failure.

X-ray topographical studies showed that net long range lattice rotation in shock loaded specimens is negligible except in

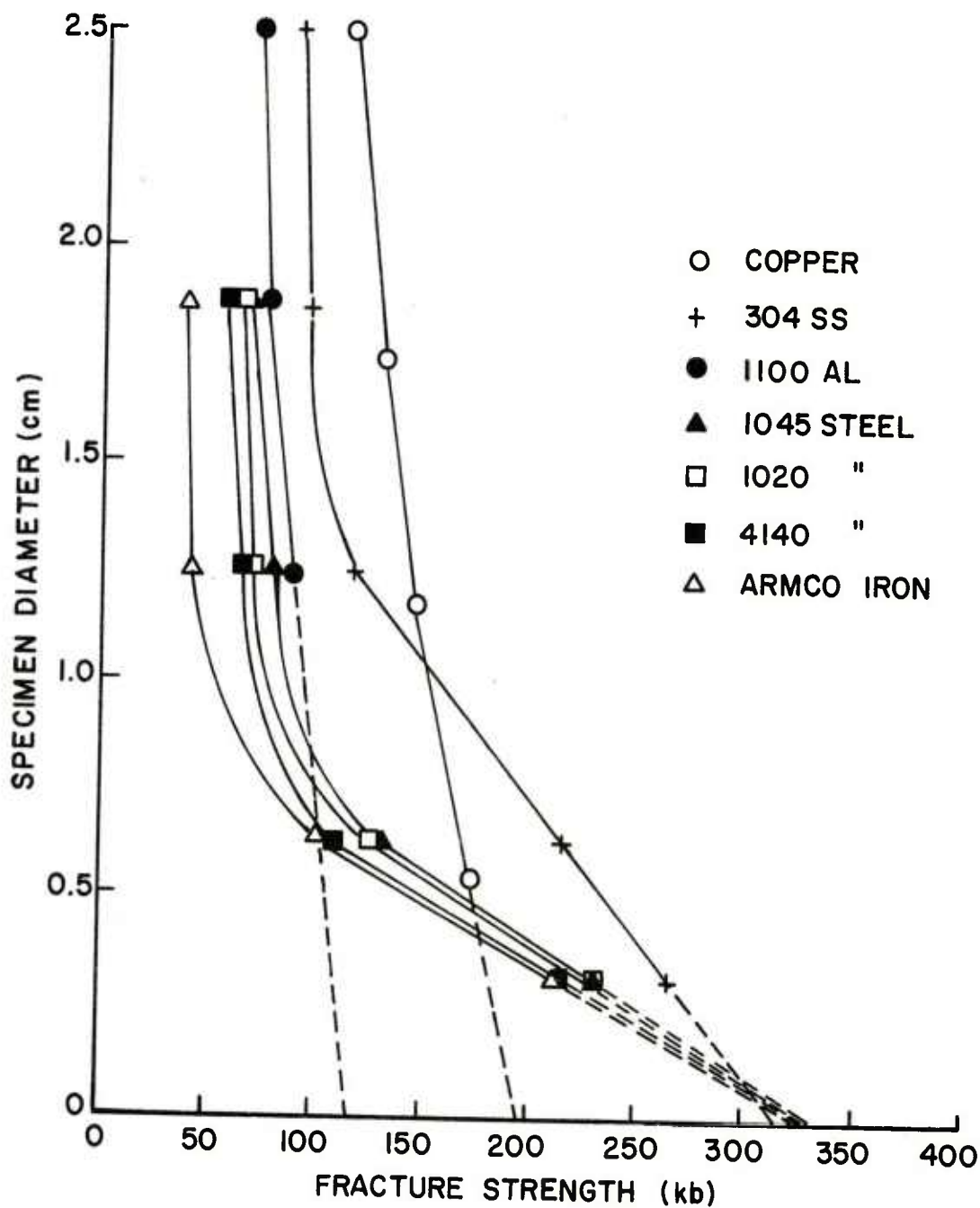


Figure 1. Stress Required for Shock Fracture vs. the Specimen Diameter for Various Metals.  $\left(\frac{D_F}{D_0} = 1\right)$

the vicinity of the fracture. Figure 2 is a typical topograph from copper, showing a series of homogeneously distributed striations with a spacing of about  $100\mu$ , indicating short range misorientations created by the shock, but no continuous long range connective changes. Transmission electron microscopy (TEM) delineated this short range effect showing that the substructure was composed of narrow zones of micro-twinning separated by approximately  $100\mu$ , surrounded by dense dislocation networks. Because of the synergistic nature of the experimental techniques and because care was taken to obtain orthogonal views of the samples, it was possible to deduce the three-dimensional structure arising from passage of compressive and tensile waves. This is illustrated in Figure 3. The dislocations formed the walls of sub-micron-size cells. Figure 4 is a composite TEM photograph showing the micro-twins and dislocation cells.

X-ray rocking curves showed that the distribution of the deformation substructure remains very uniform down the specimen not changing as the compressive shock strength decreases. The only change in the dislocation cells produced by the compressive shock is in size; as the shock stress decreases the cell size increases in an approximate 1:1 relationship. A two-fold decrease in shock pressure produces a two-fold increase in cell size. Stored energy measurements confirm the above observations.

Of primary importance is the fact that the reflected tensile shock alters the dislocation network surrounding the cells. The compressive wave forms cell walls which are loose dislocation tangles: the reflected tensile wave moves the dislocations together producing a tight network of dislocations as cell-walls. The movement of the dislocations is critical in forming vacancies.

The x-ray, TEM and stored energy measurements show that a uniform substructure is formed during passage of the compressive wave. This substructure pre-conditions the material for changes created by the passage of the tensile wave. Material failure is then dictated by tensile-shock-induced micro-mechanisms acting upon the compressive-shock-created substructure.

The interaction of the tensile shock with the existing substructure creates pores, or voids, in the metal lattice. A shock tensile stress favors the lowering of the bulk density and the formation of porosity, which arise from the condensation of vacancies. The vacancies come from two sources: the initial compressive wave creates vacancies during formation of twins and dislocations; tightening by the tensile shock of the dislocations surrounding the cells causes the dislocations to interact and form vacancies.

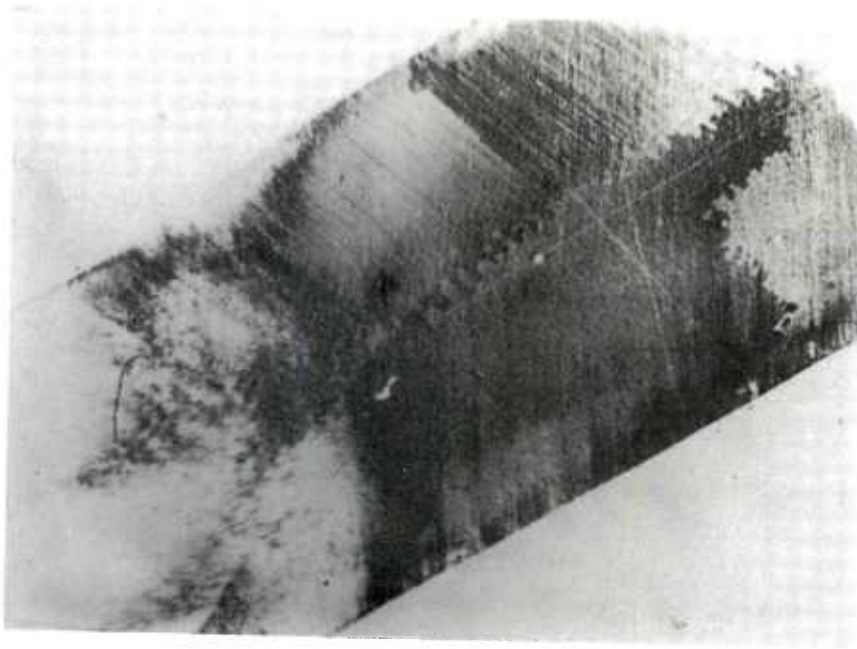


Figure 2. X-ray Topograph of Shock-Fractured Copper Specimen Showing  $100\mu$  Spaced Deformation Markings.

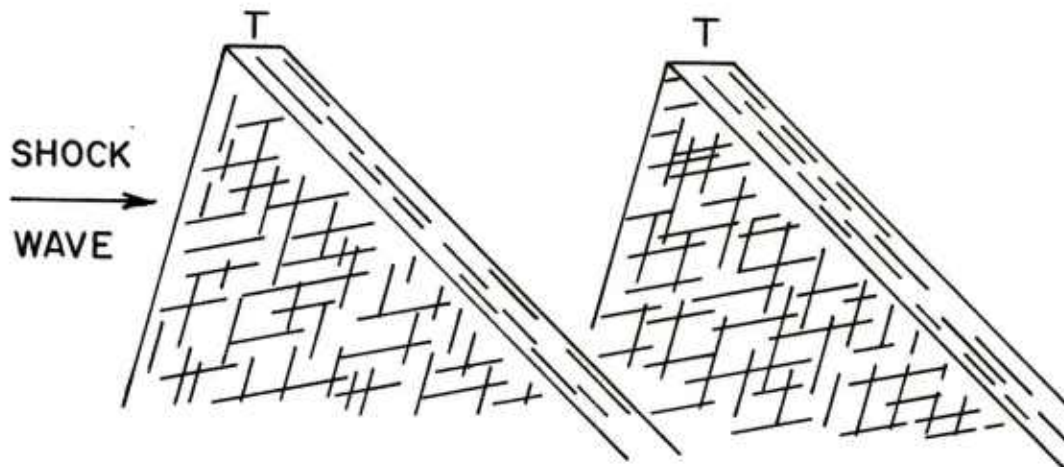


Figure 3. Drawing of the Three Dimensionality of the Micro-Twin Concentration in Shock-Fractured Copper. The Platelets are Spaced  $100\mu$ 's Apart.

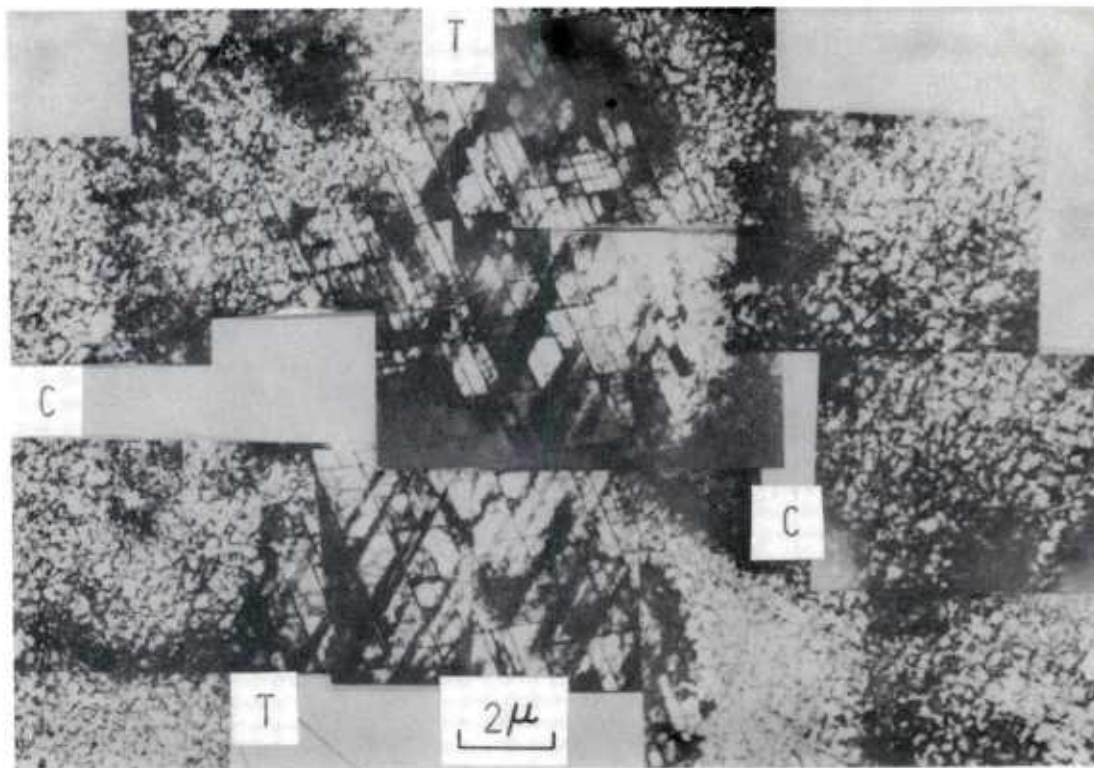


Figure 4. A composite TEM micrograph of a shock loaded copper single crystal, taken parallel to  $[100]$  shock propagation direction. A band of extensive micro-twinning, T, is seen at the center of the picture surrounded by a fine sub-micron size dislocation cell structure, C.



A very high density of pores were observed in the vicinity of the fracture surface, decreasing in number as a function of distance from the fracture.

The pores have crystallographic octahedral shapes with faces corresponding to close-packed (111) planes. (Figure 5a shows a large pore). Twin clusters are often associated with the pores which form by interaction of the tensile pulse with the substructure. The crystallographic growth shape of the pores indicates that the vacancies producing the pores arise by a mechanism of intersection of jogged dislocations. This mechanism is operative during creation of the dislocation walls by the compressive wave, and continued at an accelerated pace during the tightening of the dislocation walls by the reflected tensile wave.

The pores function as stress risers for creating failure. The metal between large pores is observed to fail by shear. Cracks are formed in the metal, linking pores, away from the fracture plane. These are incomplete fractures.

At the 1974 US Army Science Conference it was reported that vacancies formed by the shock waves would produce precipitate growth in a series of Al-Cu alloys (9). By controlling the precipitate distribution the vacancies were "used" to transport copper atoms to precipitates of Al-Cu. Vacancies thus engaged were not active in pore formation. Large, stable precipitates spaced widely apart were not as effective in reducing pore formation as were small, underaged precipitates closely spaced. These results required further work to show the role of vacancy formation and coalescence in pore formation. Direct evidence was required to prove that pores develop a continuous (or quasi-continuous) network and to delineate when and where vacancies form during shock loading.

Recent studies using TEM to examine shock fractured aluminum-copper alloy specimens show that individual pores exist on the sub-micron size level in octahedral or tetrahedral crystallographic form. They have (111) faces, supporting the hypothesis developed from observations of large pores. To obtain these results extremely delicate specimen preparation techniques were required to prevent attack on the pores. Slow electro-chemical thinning at  $-100^{\circ}\text{C}$  of sections taken near the fracture surface of spalled specimens of aluminum-copper alloy were used to prepare samples for TEM studies. Sample tilting and examination revealed no change in contrast from the areas identified as micro-pores. Figure 5 shows typical areas from a sample. These sub-micron size pores form an almost continuous network within shock loaded Al-4.5% Cu alloy samples.



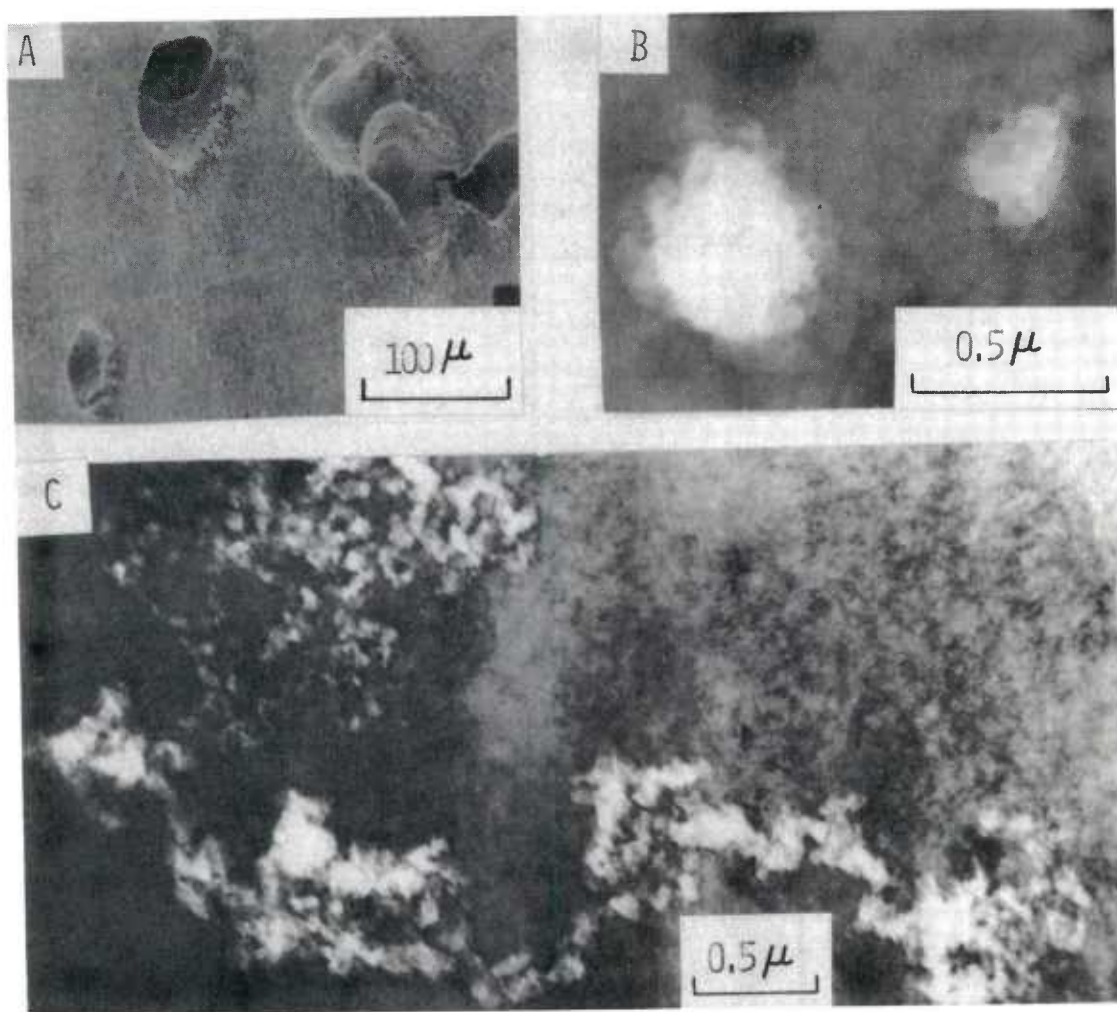


Figure 5. a. SEM micrograph showing several large octahedral-shaped pores in shock fractured copper.

b. TEM micrograph of sub-micron size pores in Al-Cu alloys. A tetrahedral pore is on the right; a truncated octahedral pore with (111) facets is on the left.

c. TEM micrograph of continuous network of sub-micron size pores in the fracture region of Al-Cu alloy specimens.

Alloy precipitate studies were extended to determine the role vacancies played in the shock-induced changes in the metal. Aluminum-copper alloys were used and data obtained on the frequency of occurrence of various precipitate sizes in the specimens. Figure 6 summarizes the results obtained using Al-4.5% Cu alloy. Three sets of specimens were studied in which the precipitate size was varied by the heat treatment. Some specimens had underaged precipitates which were very fine and closely spaced; some samples contained critically aged precipitates, larger and more widely spaced than the first set. The third group were overaged and contained large precipitates widely spaced. Material from each set were subjected to compressive shock loading only, while identical specimens were subjected to a compressive pulse and a reflected tensile shock which produced spall fracture.

The precipitate size and frequency of occurrence of each size was determined for each of the three types of precipitates. These data show a distinct broadening of the frequency-of-occurrence peak for the underaged when subjected to only the compressive pulse. The peak is the most populous precipitate size at a given plane in the sample and is plotted vs position on the specimen in Figure 6. The change in precipitate size is indicative of the efficiency of the vacancy transport mechanism in transporting copper atoms to the precipitate to promote growth. The size of the underaged precipitates change near the spall fracture by 180%. This coupled with the frequency - distribution data reveals the presences and activity of vacancies during both the compressive and tensile shock cycles.

The underaged material proved most effective in controlling pore formation. Enhancement of this mechanism for the prevention of pore formation should be achieved by incorporating a larger fraction of an atom species which would have a more rapid diffusion rate than copper. Zinc atoms substituted into the lattice instead of copper fits this concept. Experiments (as above) were carried out on Al-10% Zn alloy. Complete suppression of porosity within the grains of the specimens was obtained. (Porosity near the grain boundaries where the precipitate size was larger was not prevented).

#### ANALYSIS OF RESULTS AND CONCLUSIONS

The experimental results fall into three categories: sub-microscopic, microscopic and macroscopic. The inter-relations between these three scales of reaction have been delineated by this study.

The experimental data from studies of sub-microscopic structures and the changes in precipitates as a function of shock

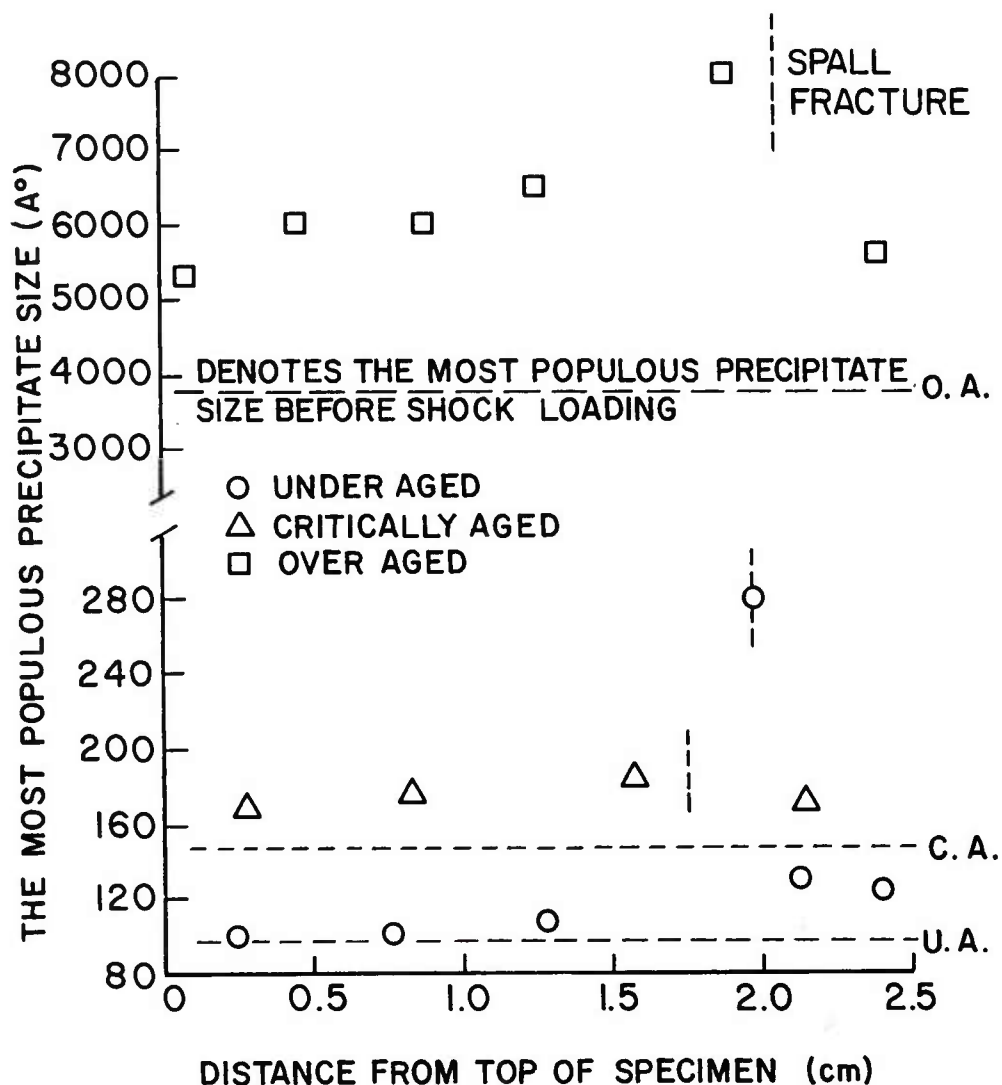


Figure 6. Precipitate size Al-4.5% Cu alloy before and after shock fracture. Each point is the peak of the frequency - precipitate size curve obtained at the indicated distance. The vertical dashed lines locate the fracture surfaces for each type of specimen.

loading indicates how shock fracture depends on imperfection creation and interaction at all size levels. Vacancies are formed by the intersection of dislocations and motion of jogged dislocations over small distances. Such vacancies may then migrate over long distances in the lattice. Also, vacancies condense to form pores on particular crystallographic planes.

In the underaged Al-4.5% Cu alloy the passage of a compressive pulse does little to change the "average" precipitate size. However, the migrating vacancies are absorbed by the very fine precipitates and the frequency-size-distribution broadens. The presence of large numbers of underaged precipitates prevents an accumulation of vacancies in the specimen. The precipitate size increases dramatically near the spall plane when the tensile shock creates vacancies as it reflects back into the specimen to produce fracture.

Specimens containing critically aged precipitates exhibit broad changes in precipitate size after the tensile shock is reflected back into the specimen. Vacancies created by the compressive pulse have not been annihilated by the presence of precipitates. These vacancies, and vacancies created by the tensile shock cause precipitate growth throughout the specimen. Overaged Al-Cu specimens react in a manner analogous to those critically aged. In all cases, the vacancies appear to migrate towards the spall plane. This phenomenon results in the accumulation of vacancies during fracture causing precipitate growth. In addition, the tensile shock is seen to create large pores by condensing vacancies.

Specimens of Al-10% Zn exhibit greater control of porosity than the Al-4.5% Cu alloy because of the more rapid diffusion rate of zinc substitutional atoms and the higher proportion of the substitutional species, zinc.

On the microscopic scale the compressive pulse conditions the metal for the fracture process performed by the reflected tensile pulse. Long range migration of vacancies occurs during the passage of the compressive pulse. The dislocation cell size becomes larger as the peak pressure and total impulse decreases with distance of travel of the compressive shock.

The long range structure of deformation bands and twin formation is a direct function of the sub-microscopic phenomena occurring in the metal. The short range changes are combined to produce long range effects, conditioning the metal to fail under a variety of stress-time loading conditions.

The tensile shock causes the loose dislocation boundaries present from the compressive shock to tighten-up. The dislocations move over very short distances, intersecting each other and forming vacancies which are then free to migrate.

The macroscopic fracture stress observed for metals fractured by a reflected shock is a function of the specimen size. Figure 1 shows that above a given specimen size the stress value defined by extending the shock travel distance becomes approximately constant. Above a given size (diameter) specimen the fracture occurs on localized sites which "link-up" across the fracture surface. As the specimen diameter decreases and approaches the dimension of the microscopic area over which migration of vacancies to form voids occurs, the stress required for fracture increases.

The macroscopic observations may be interpreted in terms of the microscopic and sub-microscopic results. At low stress levels large voids are given time to form. (The decremental particle velocity acting to separate the metal at low stresses is less than the decremental particle velocity at high stresses). Vacancy migration and condensation can occur over longer times thereby forming more and larger voids. Fracture occurs at lower stresses since the voids are closer together and less metal must be sheared by the tensile pulse.

Continued decrease in the diameter of the specimen being fractured brings the fracture plane dimension down to the size of the dislocation cell network that is the prime vacancy generator in the tensile fracture process. When the diameter is the same dimension as the dislocation cell, or a small set of dislocation cells, there are few vacancies available for forming voids, and the metal must be sheared between the vacancy clusters formed by the compressive shock. These are insufficient to produce a fracture at a low stress. The shock tensile stress required for fracture rises still further for shearing the increased amount of undamaged metal in the fracture plane. By "increased amount of undamaged metal" is meant the metal containing only the vacancies present due to the compressive shock.

Further decrease in diameter of the specimen causes the macroscopic fracture stress to equal the theoretical strength of the metal since it is implicit in the theoretical strength value the no imperfections take place in the fracture process. At this dimension fracture is occurring essentially in between vacancy clusters. The vacancies formed by the compressive pulse have all been annihilated in the specimen-surround interface or at grain boundaries. The metal is being pulled apart in tension with no assistance from imperfections.



In conclusion:

A mechanism for shock fracture has been delineated covering the material reactions from the sub-microscopic to the macroscopic scale, showing how the various observed phenomena are related.

A simple shock stress criterion is not sufficient to describe fracture.

Combinations of stress and time are required for creation, migration and condensation of vacancies to produce pores which produce fracture nucleation sites. Vacancies are created during the compressive cycle but more are required for producing fracture. These come from the interaction of dislocations in the micro-cell walls during the tensile shock phase of the cycle.

It is now possible to calculate energies required to produce failure, migration speeds of vacancies and to arrive at a quantitative description of the process based on cell-sizes, vacancy energetics and effective stress results. This is being done to provide shock fracture criteria.

The average size of spall fragments should be predictable based on studies of dislocation cells in metals subjected to compressive shocks and basic data on vacancy migration in the metal.

#### ACKNOWLEDGEMENTS

This brief paper summarizes the extensive work of many excellent scientists. The authors gratefully acknowledge: the work of Mr. Stanley K. Golaski at BRL on shock fracture; the optical microscopy carried out on specimens by Mr. Jeffery Sakai at BRL; the early studies of energy absorption and helpful discussions of Dr. Andrew W. Dietrich; the original studies of Dr. Gerald L. Moss at BRL on shear between pores was very stimulating; the many helpful discussions, particularly concerning the concept of precipitate absorption of vacancies, by Dr. Sigmond Weissmann at Rutgers University; and the excellent experimental assistances of Mr. Ming-Guang Chan at Rutgers University.



REFERENCES

1. Rinehart, J. S., J. Appl. Phys., Vol. 26, 1955, p. 1315.
2. Glass, C. M., Gainer, M. K. and Moss, G. L., "Effects of Anisotropics in Rotary Extruded Liners," BRL Report #1084, November, 1959.
3. Gainer, M. K. and Glass, C. M., "A Study of Metallurgical Effects in High Velocity Deformation of Copper Using Rotary Extruded Liners (U)," BRL Report #1167, May, 1962.
4. Pond, R. B. and Glass, C. M., "Metallurgical Observations and Energy Partitioning," High Velocity Impact Phenomena, Ray Kinslow ed., pp. 420-459, Academic Press, Inc., New York, 1970
5. Glass, C. M. and Golaski, S. K., "Fracture of Metals by Shocks," Proceedings of the Army Symposium on Solid Mechanics, 1972, pp. 379-394. AMMRC MS 73-2.
6. Greenhut, V. A., Kingman, P. W. and Weissmann, S., "The Response of Copper to High-Strain Rate Deformation as Disclosed by Electron-Optical and X-ray Methods," Microstructural Science, 3, 475-490, 1975.
7. Kingman, P. W., "X-ray Topography of Shock Loaded Copper Crystals," Metallurgical Effects at High Strain Rates, AIME, 659-668, 1973.
8. Dietrich, A. M. and Greenhut, V. A., "Energy Absorption and Substructure in Shock Loaded Copper Single Crystals," Metallurgical Effects at High Strain Rates, AIME, 645-658, 1973.
9. Dietrich, A. M., Greenhut, V. A. and Golaski, S. K., "A Method of Controlling Shock-Induced Damage in Aluminum Alloys," Proc. US Army Science Conference, 247-262, 1974.



LASER TERMINAL HOMING ENGAGEMENT SIMULATOR (EYE-SAFE) (U)

Thomas James Gleason, PhD, Mr. Melvin Ernest Sword  
US Army Harry Diamond Laboratories  
Adelphi, MD 20783

1. INTRODUCTION

The Laser Terminal Homing Engagement Simulator (LATHES) was developed for the US Army Operational Test and Evaluation Agency by the Harry Diamond Laboratories (Army Materiel Development and Readiness Command) for use in test and training exercises involving laser terminal homing systems. In the US Army these systems include the Cannon Launched Guided Projectile (CLGP), Helicopter Laser Fire and Forget Missile (HELLFIRE), Ground Laser Locator/Designator (GLLD), Airborne Target Acquisition and fire control systems (ATAFCS), Light Weight Laser Designator (LWLD), and Airborne Laser Tracker (ALT). The most important feature of LATHES is that it makes it possible to conduct a realistic field simulation of a tactical laser terminal homing engagement without using any components that pose a hazard to the eyes of user or bystander personnel. All LATHES components are eyesafe at zero range.

The basic concept of the LATHES system is to provide eye-safe equipment capable of realistically simulating the tactical characteristics of a laser terminal homing engagement. As such, the LATHES system allows test or training of tactical proficiency (command and control, tactical fire control, selection and utilization of tactical position, etc.) as opposed to technical proficiency (operator tracking capability, operation of the GLLD controls for ranging, etc.). Integration of both tactical and technical training on one system is possible if desired. The elements of the engagement that are simulated with LATHES are target acquisition and identification, selection of target to be engaged, call for fire of close air support, coordination of laser code, initiation of designation,

acquisition of coded target by the laser tracker or weapon seeker, and termination of designation. The LATHES hardware is designed to allow simulation of the elements of the engagement that involve active interactions between the designator, target, and seeker (from initiation of designation to the end of the engagement). The LATHES designator simulator provides a visible light beam to cue the target when designation is initiated and to confirm the existence of a clear optical line of sight from the designator to the target. The LATHES target simulator, turned on upon the cue provided by the designator simulator, generates a coded laser target signature fully compatible with tactical seekers and search-track systems. The LATHES receiver provides a low-cost simulation of a seeker or search-track system with full DoD standard decoding capability.

## 2. LATHES SUBSYSTEMS

The LATHES system consists of three major subsystems, (Figure 1).

a. Designator Simulator: (Figures 2 and 3) The Designator simulator takes the place of a ground laser designator in the tactical engagement. It is primarily intended to simulate a precision designator such as the GLLD. The Designator Simulator consists of a color-coded, narrow-beam, visible light source provided with a tracking sight, telemetry interface, instrumentation camera mount, and battery power-pack. The Designator Simulator mounts on a TOW traversing unit to provide full viscous damped manual target tracking. It is compatible with TOW tracking optics, including the TOW night-sight.

b. Target Pallet: (Figures 4 and 5) The Target Pallet is designed for mounting on 1/4-ton trucks or Armored Personnel Carriers. It provides physical protection and shock-mounting for a laser target simulator (International Laser Systems NC-10) that is capable of producing a valid laser-designated-target signature. The laser target simulator is a pulsed laser whose output is spread through somewhat more than a hemisphere. It is eye-safe at zero range and operates on vehicle power. In addition, a remote control unit is provided that allows a controller to set codes on the laser target simulator and to turn it on and off. A telemetry interface is provided and a spare, manually operated telemetry input is available on the remote control console.

c. Receiver: (Figure 6) The LATHES receiver performs the target acquisition functions of a laser terminal homing seeker. It is configured as a "box camera" with a simple viewfinder and may be used hand-held, on a tripod, or mounted on a vehicle. The receiver detects the laser designated target signature from the laser target

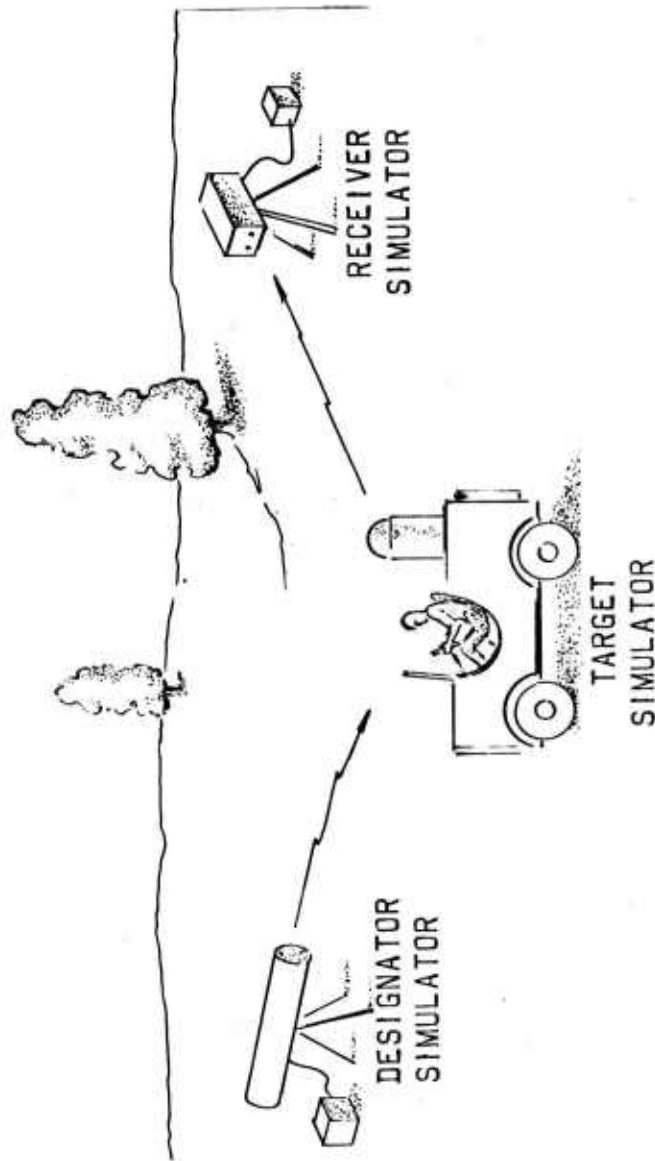


FIGURE 1 LATHES COMPONENTS



FIGURE 2 DESIGNATOR SIMULATOR

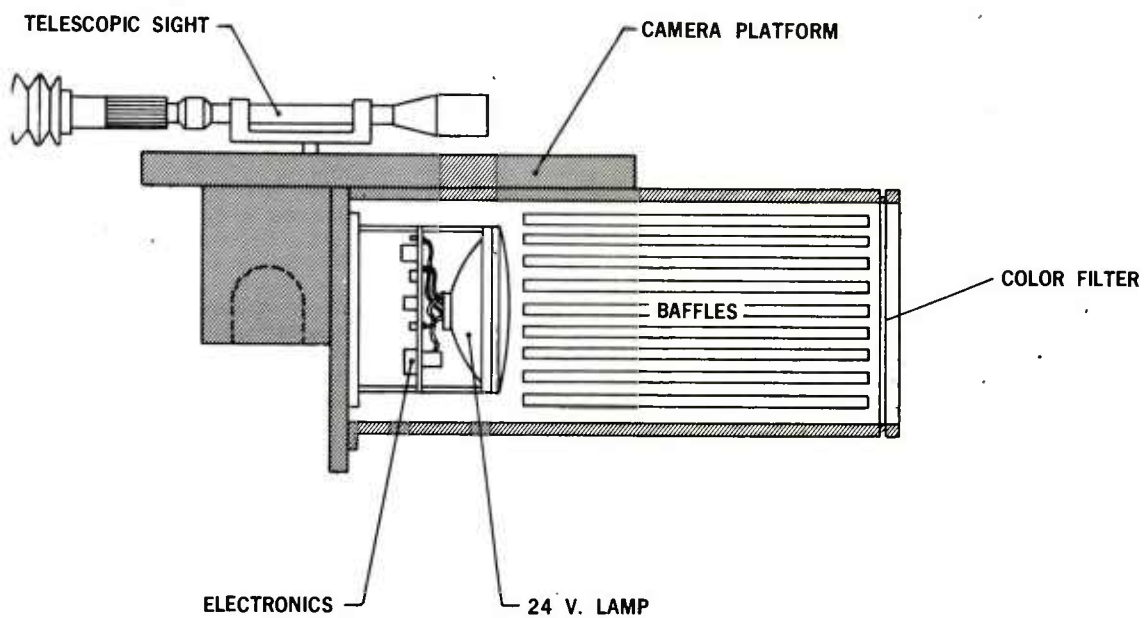


FIGURE 3 DESIGNATOR SIMULATOR CUTAWAY VIEW





FIGURE 4 TARGET PALLET ON 1/4 TON TRUCK

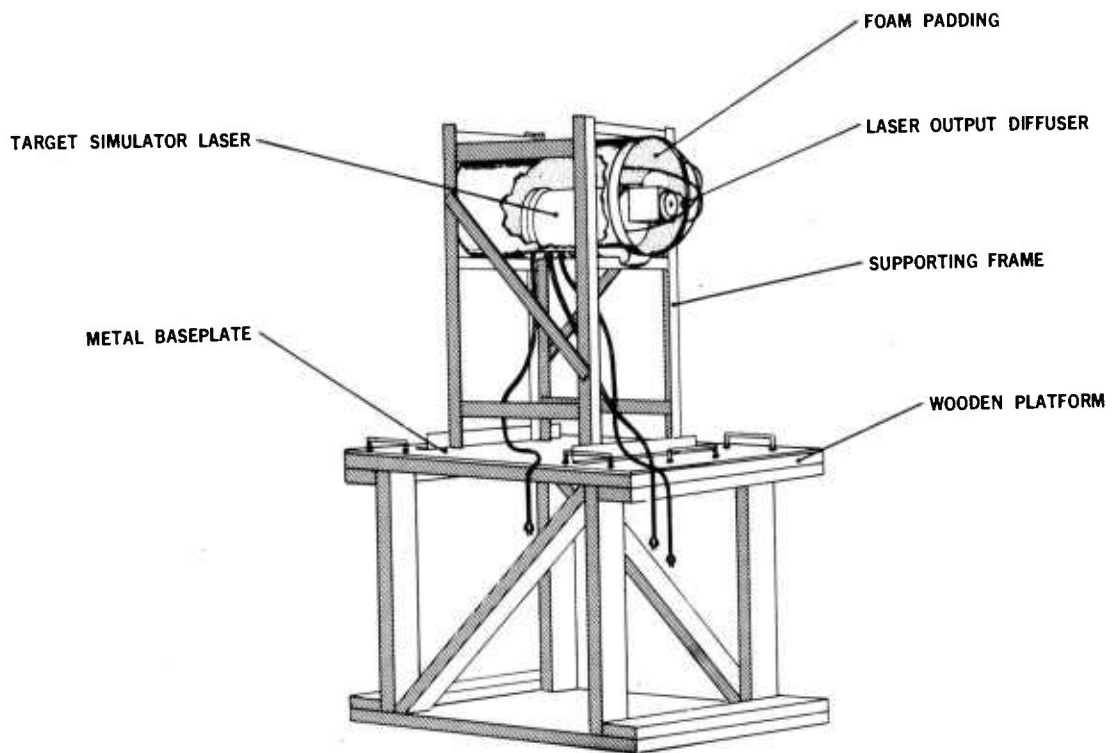


FIGURE 5 TARGET PALLET DESIGN



FIGURE 6 LATHES RECEIVER IN USE AT FT. HOOD, TX

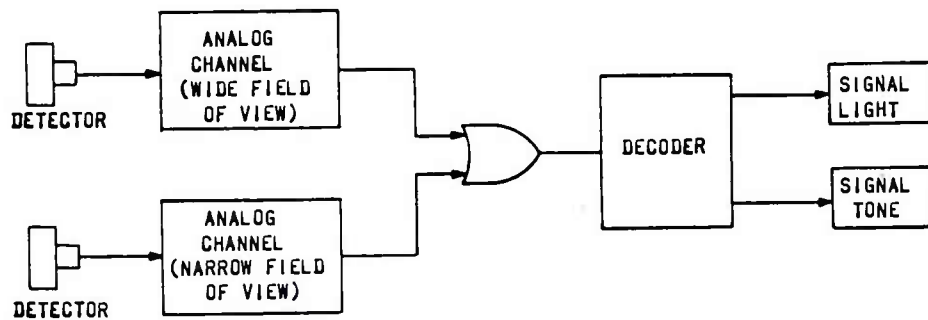


FIGURE 7 BLOCK DIAGRAM OF LATHES RECEIVER

simulator or a real designated target. It has a decoder that is compatible with all standard (DoD) laser designators. When a properly coded target is present within the receiver field of view (FOV), visual and audible acquisition alarms are activated. The target acquisition criteria and "missing-pulse" logic capabilities of the receiver are identical to typical laser-guided weapons seekers. The receiver has two simultaneous FOVs, a wide FOV of 15 degrees and a narrow FOV of 2 degrees centered in the wide FOV. A distinct narrow-FOV acquisition indication permits the operator to determine when he has centered the receiver on the target being "designated." The receiver has no automatic direction finding or tracking capability. A remote acquisition indicator can be located at the observer position when the receiver is vehicle or aircraft mounted.

### 3. LATHES OPERATIONAL CONCEPT

In operation, the designator simulator is used to cue the observer on the target vehicle when to turn on the target simulator, and also to confirm the existence of designator-to-target line of sight. Color coding of the designator simulator can be used to indicate which code to set into the target simulator. The receiver can be operated either at a ground position (perhaps a hilltop to simulate a helicopter just breaking mask) or on an aircraft. If the proper code has been set into the receiver and the target is in its field of view with unobstructed line of sight, the receiver will signal acquisition of the target. All elements of the system are useable at ranges of at least two kilometers and will significantly exceed this range under most conditions.

a. CLGP Engagement: The Forward Observer team equipped with the LATHES designator simulator occupies a tactical Observation Post and performs its assigned role in target acquisition and fire command from the FDC the designator operator initiates designation using the color indicated by the code coordination procedure in use. A controller on the target vehicle, cued by the timing and color of the designator beam, sets the target's code and turns it on. He continuously monitors designator-to-target intervisibility by watching for obscuration of the designator beam. A controller on an overwatching position sets the LATHES receiver to the code specified by the firing unit and reports acquisition of a properly coded target, thus confirming that the code coordination between the FO and firing unit has been successfully accomplished.

b. Close Air Support (all Services): The ground unit occupies a tactical position and performs its target acquisition function. Close air support is requested, and target and code information

processed through the command and control system. Upon command, the designator operator initiates designation and the target is turned on (coded). If all functions have been successfully performed, the tactical laser acquisition devices of the aircraft acquire a properly coded target within their search pattern and weapons release is simulated.

#### 4. DESIGNATOR SIMULATOR DESIGN

The designator simulator, shown in a cutaway view in figure 3, is designed to project a bright visible light beam for several kilometers. It utilizes a 24-V aircraft landing lamp with a 5-in. diameter sealed-beam reflector. The landing lamp output is baffled to about 2 deg total beam spread by passing it through 10 in. of aluminum honeycomb. Interchangeable plastic color filters provide red, green, amber, and white beams.

The lamp is turned on and off by a push-button trigger in a pistol grip handle that attaches to the right-hand elevating knob of the TOW traversing unit. A switch-closure telemetry output from the designator simulator indicates when the lamp is turned on and off.

A mounting platform is provided for an instrumentation camera. Camera on-off control is provided by a relay in the designator simulator that switches the camera power on and off. Normally the camera is switched on when the lamp is turned on. However, a camera override switch located on the pistol grip allows independent operation of the camera.

A flasher circuit in the designator simulator can be activated to cause the lamp to blink with a period of 2 seconds. This optional mode of operation can be used either to expand the code set provided by the color filters or to increase the subjective visibility of the light beam.

The designator simulator is powered by two 12-V motorcycle batteries that are packaged in a separate aluminum battery case. They provide about 1 hr on-time between recharging. A battery charging console capable of charging up to five battery packs simultaneously is part of the LATHES support equipment.

#### 5. TARGET PALLET DESIGN

The LATHES target pallet provides a mount for the target simulator laser on a 1/4-ton truck or armored personnel carrier (APC). It provides shock-mounting and enough physical protection for the

laser to allow off-road movement with reasonable care. The target simulator laser, an ILS NC-10 provided by the Precision Laser Designator Product Office of U. S. Army Missile Command has at its output a diffuser that spreads the laser pulse energy out into approximately a hemisphere. The resultant diffused output is eye-safe at zero range. The laser is powered directly from 28 VDC vehicle power and controlled remotely by the the LATHES remote control console.

Figure 5 shows the target pallet design, while figure 4 shows the target pallet installed on a 1/4-ton truck. The wooden platform, when installed on the truck, raises the laser output diffuser above the driver's head. For APC installation, the wooden platform is omitted and the metal base-plate is mounted directly on the top surface of the crew compartment hatch. In this configuration the diffuser height is designed to be just above the head of a crew member exposed from the thorax up out of the driver's or vehicle commander's hatch.

The remote control console is mounted on a clipboard to facilitate use by a data recorder or test controller. It provides a remote on-off and code setting for the NC-10 by use of an extender cable harness. The remote control module is visible in the passenger seat of the 1/4-ton truck in figure 4.

The target pallet is lashed to the vehicle with nylon tie-down straps. In the field, the pallet is left on the vehicle during overnight breaks in the test while the laser, in its cylindrical housing, is removed and placed in covered storage. Removing or replacing the laser takes less than 5 min and is performed by the vehicle crew.

## 6. RECEIVER DESIGN

The LATHES receiver consists of two component parts, the power supply and the receiver, joined by an interconnecting cable. The power supply contains two PRC 77 field radio batteries wired in series and center tapped to provide + 14 VDC, a + 45 VDC battery to provide bias voltage for the photodiodes, and a switch and meter for checking all of the batteries.

The receiver has two analog channels, one for the wide-field-of-view detector the other for the narrow-field-of-view detector, a decoder, and aural and visual acquisition indicators. A block diagram of the receiver is shown in figure 7.



A schematic diagram of an analog channel is shown in figure 9. The detector used in both analog channels is a Schottky barrier silicon PIN photodiode with an active area of  $1.0 \text{ cm}^2$  and an average responsivity of  $0.3 \text{ mA/mW}$  at  $8500 \text{ \AA}$ . Light energy entering the receiver passes through an optical filter with a spectral bandwidth of  $250 \text{ \AA}$  centered at  $10.7 \text{ micrometers}$  before striking the photodiode. The photodiode is reverse biased at  $45 \text{ VDC}$ , which produces an average junction capacity of  $45 \text{ pF}$ . Each photodiode is followed by an analog channel having a voltage gain of  $58 \text{ dB}$  and bandwidth of  $35 \text{ MHz}$ . The first stage of the analog channel is a transimpedance amplifier to convert the low level output current of the photodiode to a manageable voltage level. The gain of this stage is  $34 \text{ dB}$ . The following two stages provide the bandpass characteristics of the channel and an additional voltage gain of  $24 \text{ dB}$ . The three stages combine to provide a signal-to-noise ratio of 8 at the input to the SN52106 comparator under worst case conditions (with the receiver looking directly into the sun and the minimum calculated signal being received).

The SN52106 has two threshold settings which are switch selectable. One threshold setting, designated as "normal," is for use when the receiver is being operated in a normal bright background environment. The other threshold, designated as "solar blind" is for use when the receiver is being operated with the sun directly in the field of view.

The outputs from the analog channels are fed to the decoder, which is shown schematically in figure 10, where they pass through a NAND-gate and set a 20-msec one-shot. The Pulse Repetition Frequency code that the decoder is to accept is entered by setting a count-down circuit driven by the  $10.250\text{-MHz}$  clock, and it produces output pulses that are properly spaced in time for the code selected. The output pulses from the count-down circuit shift the two shift registers providing the inputs to the SN74H52, which is composed of four AND gates and an OR gate. When three successive pulses with the proper interpulse spacings have been received, the SN74H52 produces an output pulse which, at the end of another interpulse interval, produces a signal to drive the acquisition light and the Sonalert aural signal, and provides a TM output signal. After acquisition of a properly coded signal the decoder will continue to produce an output signal as long as no more than three successive properly spaced received pulses are missing. This feature constitutes the so called "missing pulse" logic of the decoder. If the received signals arrive in the wide field of view analog channel only, the acquisition light will be on continuously and the Sonalert will produce a solid sound. If the received signals are in both the wide field of view



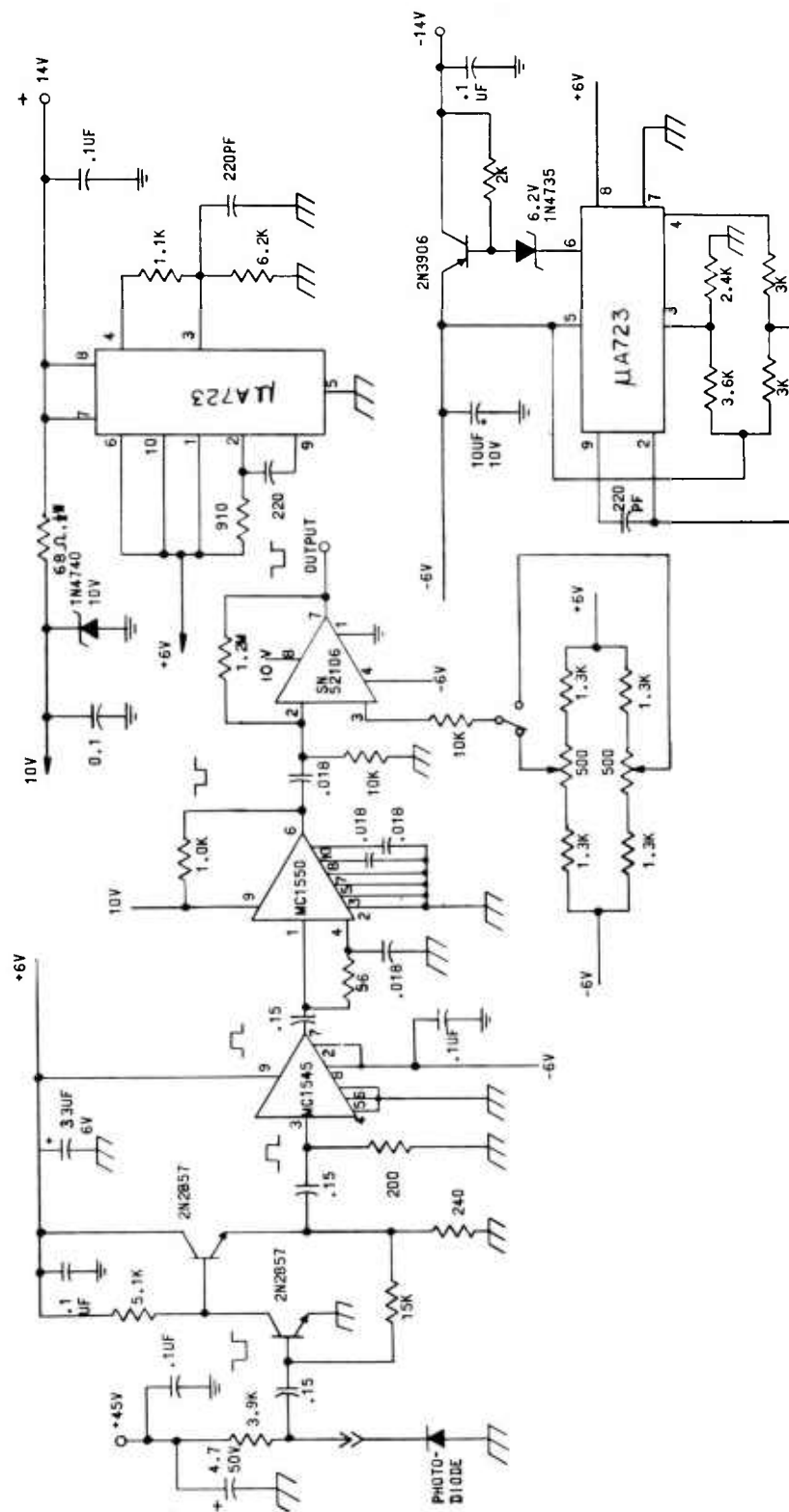


FIGURE 9 RECEIVER ANALOG CHANNEL SCHEMATIC DIAGRAM

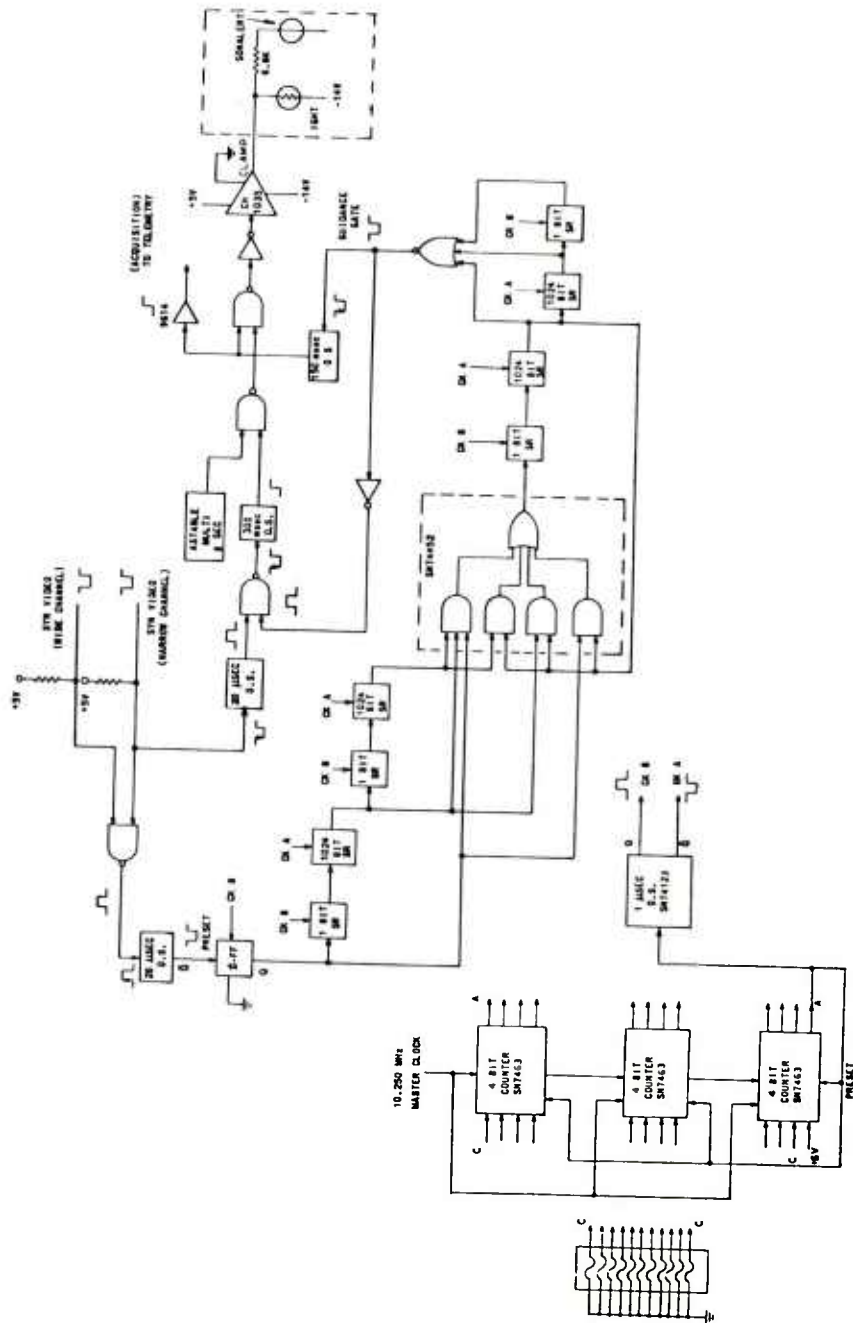


FIGURE 10 DECODER SCHEMATIC DIAGRAM

and the narrow field of view, or from the narrow only, the acquisition light operates in a blinking mode and the Sonalert produces a beeping sound. Provisions are incorporated in the receiver to switch the Sonalert off if desired. However, to preclude the possibility of the receiver detecting a properly coded signal but producing no indication of its presence, the acquisition light cannot be disabled.

## 7. PERFORMANCE OF LATHES IN THE FIELD

The LATHES system was delivered to Fort Hood, Texas on 2 March 1975 for use in the Joint Service Test of Laser Guided Weapons in Close Air Support. The system met all specifications, with a demonstrated receiver acquisition range of 2 km when the target simulator was used on the LATHES target pallet and up to 4 km when real targets were designated. As a side benefit, the LATHES receiver proved extremely valuable as a test and diagnostic tool for checking the performance of the many laser designators being used in the test. No maintenance problems were encountered with LATHES hardware during a total of about five weeks in the field, and routine preventive maintenance was sufficient to ensure a nearly 100 percent availability record for the laser target simulators.<sup>2</sup> A total of six designator simulators, four target pallets, and four receivers (plus one spare) were deployed.

## 8. LATHES MODIFICATIONS

### a. Increased Target Output Energy

Based on experience gained during the initial phases of the Joint Service Test at Fort Hood, it was decided to modify the LATHES target pallet to provide increased output energy and thus increased detection range. This was accomplished by replacing the NC10 target simulator lasers with MPT Laser Designators, provided by the Precision Laser Designator Product Office.

The MPT designator is larger than the NC-10, has a 100- to 120mj output pulse (compared with 6- to 10-mj for the NC-10), and has a highly collimated output beam about a 10 cm diam. The size and output beam characteristics of the MPT laser required changes in the mounting arrangements on the pallet and in the diffuser.

In the MPT diffuser a plane mirror changes the beam direction 90 deg and is adjustable to permit alignment of the beam uniformly over the inside of the diffuser. The effective diffuser area is 265 cm<sup>2</sup> and the resulting output is eye-safe.<sup>3</sup> With this target the LATHES receiver has demonstrated target acquisition at ranges greater than

7km under clear atmospheric conditions.

b. Additonal Signal Outputs from Receiver

The fringe-benefit usefulness of the LATHES receiver for test and monitoring of laser designator performance at the Joint Service Test was sufficient to create a demand for additional receivers to be used in this role. As a first step in this direction a LATHES receiver has been prepared with additional signal output suited to laser monitoring. The amplified video signal at the output of the MC-1550 amplifier (see figure 9) and the synthetic video at the output of the SN52106 comparator (through a "one-shot" buffer) are available at coaxial connectors on the modified receiver. The amplified video can be used to monitor pulse amplitude. The synthetic video can be used to trigger timers that monitor the pulse-to-pulse timing of the laser being tested. The modified receiver has been delivered to the Precision Laser Designator Product Office for use in development tests.

9. FUTURE LATHES CONFIGURATIONS

The LATHES system has demonstrated its ability to simulate the operational aspects of a laser terminal homing engagement from the standpoint of troop procedures and command and control. Future use of the system may include troop training as well as further operational tests. The existing system was built in a very short time to support a specific test. There are several areas in which major improvements might be made.

The visible beam from the designator simulator can be made narrower by the use of an imaging optical system, probably utilizing inexpensive Fresnel lenses. This would increase the selectivity of the designator in specifying a target, particularly at long range.

A more significant improvement would be to replace the visible designator simulator beam with a coded infrared beam, at eye-safe levels, that could be detected at the target and automatically turn on the laser on the target pallet. Elimination of the manual link in the system, represented by the observer/operator at the target, should increase the realism of the simulator. This upgrading is feasible with a gallium-arsenide injection laser, appropriate optics at the designator simulator, and simple detectors at the target.

In the future, the LATHES receiver might be equipped with a four-quadrant detector system to more nearly simulate operational receivers. In a future training system, the LATHES receiver might be

replaced by operational search/track sets.

The physical packaging of the LATHES designator simulator was dictated by availability of TOW traversing units and the non-availability of GLLD traversing units. Once the GLLD enters the inventory, the LATHES designator simulator should be repackaged to match its form and use its traversing unit.

#### 10. SUMMARY

The Laser Terminal Homing Engagement Simulator system allows field simulation of a tactical laser terminal homing engagement without introducing any eye-safety hazards. It allows test of tactical proficiency or training without the extensive range safety requirements associated with the use of laser designators. LATHES has demonstrated its potential as a training system that is associated with the generation of laser terminal homing systems now under development.

#### ACKNOWLEDGEMENTS

T. F. Geiger, C. Boykin, R. N. Curnutt, D. L. Chambers, D. G. Green, O. Edwards, and N. Disario all made important contributions to the design and fabrication of the LATHES hardware described in this report. Their ingenuity in using available components and diligence in completing fabrication of the hardware were critical in completing the LATHES system on schedule and to its successful performance in the field.

#### REFERENCES

1. "Radiation Protection Special Study 42-143-75," US Army Environmental Hygiene Agency, February 1975.
2. With the Exception of one laser that was inoperable, awaiting repair parts for the first three weeks of the test.
3. "Radiation Protection Special Study 42-161-75", US Army Environmental Hygiene Agency, May 1975.
4. A limited demonstration of this capability was performed at China Lake NWC using a GaAs laser transmitter and receiver borrowed from the Multiple Integrated Laser Engagement Simulator Program (MILES) managed by Project Manager, Training Devices, Fort Benning, GA.





CURRENT APPROACHES TO RESOLVING THE PHYSIOLOGICAL HEAT STRESS  
PROBLEMS IMPOSED BY CHEMICAL PROTECTIVE CLOTHING SYSTEMS (U)

RALPH F. GOLDMAN, Ph.D.  
JOHN R. BRECKENRIDGE  
US ARMY RESEARCH INSTITUTE OF ENVIRONMENTAL MEDICINE  
NATICK, MASSACHUSETTS 01760

INTRODUCTION:

There is a long history of Army research addressing the question of the limitations of men wearing chemical protective clothing in the heat. The results, beginning with a study carried out by the Harvard Fatigue Lab at Camp Sibert, AL in the early 1940's (1), have been extremely consistent in indicating that men encapsulated in chemical protective clothing cannot work for extended periods in the heat.

The relationship between ambient temperature and tolerance time for totally impermeable systems for men at moderate work levels can be clearly delineated. Safe work times, wearing a completely impermeable garment with all apertures closed (gas mask, hood and gloves worn), range downward from 8 hours at an ambient temperature of 30°F, as shown in Table I, (2-7).

Table I. Safe "Closed" Suit Times for Moderate Work  
(250 kcal/hr); data from ref (2-7) as presented by Custance (8)

Environmental Temperature (°F.)	Wearing Time (Closed Down)
30° or less	8 hours
30° - 50°	5 "
50° - 60°	3 "
60° - 70°	2 "
70° - 80°	90 mins.
80° - 85°	60 "
85° - 90°	30 "
90° or more	15 "

Less impermeable clothing, particularly when worn with open apertures (i.e., without gloves, hood or mask) give somewhat longer unit tolerance times, as a function of work rate, as shown in Fig. 1 (9).

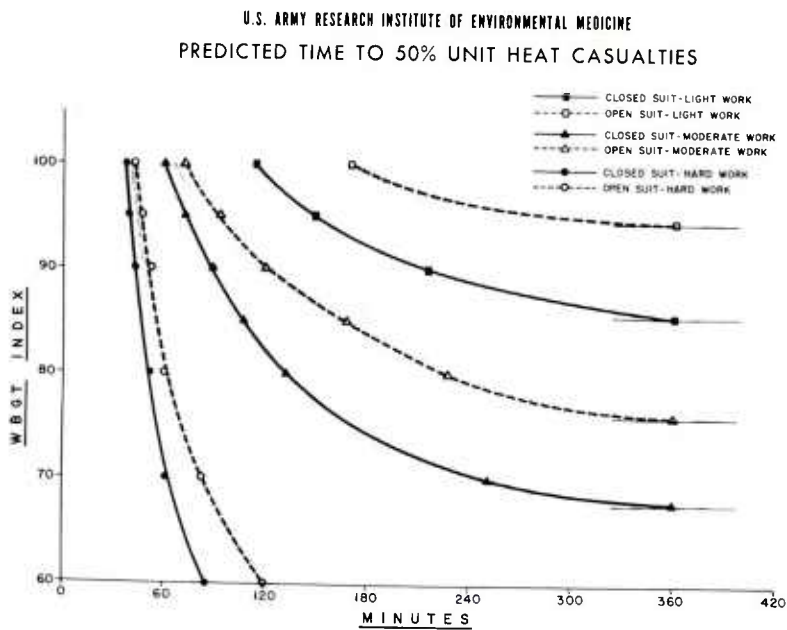


Fig. 1 Prediction graph for 50 per cent unit survival time for CB protective uniforms with reduced water vapor permeability. "Light work" is 200 kcal/hr., and "hard work" is 300 kcal/hr.

There are only 4 possible solutions to the problem; the first 3 involve modifications of the impermeable nature of the clothing, or adjustments in its ability to eliminate heat, while the fourth involves complete redesign of tactical operations to permit adequate recovery time between short work periods. Methods for accomplishing the latter were detailed in a presentation at the 1970 West Point Army Science Conference (10, 11). Possible modifications of chemical protective clothing include the use of more permeable garments incorporating a charcoal layer for adsorption of agent, after wicking it across as much clothing surface as possible to minimize the dose presented at a given spot on the surface of the garment. This approach, as incorporated in the current US Army Standard A Chemical Protective Suit has been evaluated extensively (12).

A second approach is to provide ventilating filtered air within a totally impermeable clothing system, as currently done in the new Engineer Ordnance Demolition (EOD) Suit (13, 14). The final clothing approach is to use a wettable cover over a totally impermeable garment. This approach was originally used in the Toxicological Agent Protective (TAP) Uniform in the 1950's and 60's, and is currently the approach used in the Israeli Defense Forces.

The extension of tolerance time allowed by the first approach, i.e., the current US Standard A charcoal-in-foam protective overgarments, can be assessed by comparing the 50% tolerance values for moderate work presented in Fig. 1, with the values presented for the totally impermeable system in Table I, which also represent moderate work levels. With the second approach, viz, the air ventilating EOD garment, tolerance is essentially unlimited as a function of ambient temperature, per se, but becomes simply a function of the ambient humidity and the extent to which the body can produce sweat. In essence, the soldier wearing such a garment is no worse off than he would be working in the ambient environment in conventional clothing and, in most cases, is substantially better off because of the great amount of air ventilation afforded over the body and the associated increase in the man's ability to evaporate sweat.

The third approach, use of a wettable cover over an impermeable garment, is less well defined with regard to its range of applicability. The remainder of this brief presentation will be concerned with clarifying the range of environmental conditions, and other factors under which such an approach can significantly reduce heat stress.

The amount of body cooling which can be derived from a wetted cover depends on the rate of water evaporation and its effec-

tiveness in removing heat at skin level. Approximately 0.6 kcal of heat is absorbed in evaporating one gram of water, but part of this heat of vaporization is supplied by the air in contact with the cover, thus reducing the amount extracted from the body. Rate of evaporation from the cover depends on air movement and the difference between the vapor pressures at the cover surface and the environment. The most rapid evaporation takes place with high air movement and low humidity. Little evaporation will occur under calm conditions with humidity near 100%, especially if air temperature is above 90°F(31°C). However, studies at our Institute using an electrically-heated manikin show that, in only a slightly less severe environment (80°F, 90% relative humidity and normal room air movement) up to 100 grams of water per hour can be evaporated from a cover worn over a moderately heavy impermeable garment. At 80°F, 25% humidity this figure increases to almost 400 grams per hour, representing an evaporative heat removal of 230 kcal/hr.

The effectiveness of this surface evaporative cooling in extracting heat from the man (i.e., from the skin rather than from the air) is a function of air movement and the insulation value, or thickness, of the protective ensemble. Efficiency for a typical single-layer garment plus cover ranges from 30 to 40% in calm air, to about 15% for winds above 10 mph. For any given air temperature and humidity, maximal body cooling will be obtained at some intermediate wind speed, where the rate of evaporation from the cover is high enough to compensate for the loss in cooling efficiency caused by the air motion.

Based on this analysis and copper manikin results, plus experience in the field with a wettable cover ensemble, it appears that important reductions in heat stress on the totally encapsulated soldier may be realized using this approach. In a typical tropical environment increased heat dissipation of 70-100 kcal/hr, or up to 25% of an active soldier's average heat production, may be expected. The benefit would be much higher in a desert environment with its low humidity. In most cases, the added heat removal here would be sufficient to compensate for solar heat load on the man, in addition to removing some of his metabolic heat. However, the problem of availability of water for wetting the cover, may act as a deterrent for successful application of this approach. Under typical field conditions with moderate humidities (50%) and air movement, upwards of 1 liter per hour will be evaporated if the ensemble surface is completely wet. This figure could easily double in a desert environment. It is apparent that the logistics associated with supply of enough water to maintain cover wetness over an extended period would be quite formidable for even a moderate size combat force.

SUMMARY:

Possible improvements over totally impermeable chemical protective clothing for use in toxic environments have been characterized along three approaches: partially permeable garments impregnated with detoxifying or adsorbing substances; impermeable systems supplied with filtered ambient air ventilation; impermeable systems with wettable covers. Although the latter approach has much to recommend it, logistics of required water is a distinct problem. The only other alternatives, short of air conditioned clothing ensembles, is by intelligent, informed command control of work-rest ratios, or actual replacement of units as they approach tolerance limits, during operations in environments above 75°F WBGT.

REFERENCES

1. Darling, R.C., R.E. Johnson, M. Moreira and W.H. Forbes. Physiological Tests of Impermeable Suits (Part I Field Tests at Camp Sibert, AL; Part II Improvements in Performance by Wetting the Outside of Impermeable Protective Suits. Harvard Fatigue Laboratory Report No. 89, October 1943 (OSRD No. 21).
2. US Army TM3-290. Miscellaneous Gas Protective Equipment, pg. 22, March 1944.
3. US Army Research Institute of Environmental Medicine. Guidance for Safe "time-in suit" Limits for USATECOM Project 8-3-6610-05-K, Part III, pg. 102, July 1963.
4. Robinson, S. and H.S. Belding. Advances in Military Medicine, Vol 2, pg. 576, Little Brown and Co., Boston 1948.
5. Craig, F.N. Ventilation Requirements in Impermeable Protective Suits. Med. Div. Report No. 5, Army Chemical Center, MD, April 1950.
6. Goldman, R.F. Tolerance Time for Work in the Heat when Wearing CBR Protective Clothing. Mil. Med. 128:776, 1963.
7. Alkhazvo, V.A. and Tkachev, A.P. Individual Means of Protection Against Chemicals and Radiation. USSR Translation by US Dept. of Commerce, Joint Publ. Res. Service, Washington, D.C. pp42-43, September 1964.
8. Custance, A.C. Stress-Strain Relationships of Man in the Heat. Med. Serv. J. Canada. 23:721, 1967.
9. Joy, R.J.T. and R.F. Goldman. A Method of Relating Physiology and Military Performance: A Study of Some Effects of Vapor Barrier Clothing in a Hot Climate. Mil. Med. 133:458, 1968.
10. Goldman, R.F. Tactical Implications of the Physiological Stress Imposed by Chemical Protective Clothing Systems. Proc. 1970 West Point Army Science Conference.
11. Doctrinal Guidance for the Wearing of Individual CW Protective Clothing. Draft Proposal for TTCP Working Panel E-1. June 1971.
12. Yarger, W.E., P.L. Schwartz and R.F. Goldman. An Assessment of CBR Protective Uniforms During An Amphibious Assault in a Tropical



GOLDMAN & BRECKENRIDGE

Environment. U.S.N. Medical Field Res. Lab. Camp LeJeune, 19(#17), November 1969.

13. Pandolf, K.B. and R.F. Goldman. Convergence of Skin and Rectal Temperatures as a Criterion for Heat Tolerance. Physiologist. 18:343, 1975 (abstr.) and MS in preparation.

14. US Army Dugway Proving Ground. Development Test II, Integrated, Engineering and Service Phases of the CB Protective Clothing Ensemble for EOD Personnel. DPG Rpt No. FR-72-201 on TECOM Project 5-EI-825-000-002.



CONTACT AND SURFACE EFFECTS IN THE ELECTRIC  
FIELD INITIATION OF EXPLOSIVES (U)

THADDEUS GORA, PhD; JAGADISH SHARMA, PhD; DONALD A. WIEGAND, PhD;  
WAYNE L. GARRETT, PhD; DAVID S. DOWNS, PhD.  
EXPLOSIVES DIVISION, FELTMAN RESEARCH LABORATORY  
PICATINNY ARSENAL, DOVER, NEW JERSEY 07801

INTRODUCTION

A number of explosive azides, including lead azide, can be initiated by the application of sufficient voltage *via* conducting electrical contacts. This occurs for both single crystal (1-4) and pressed pellet (5,6) samples. The effect is normally referred to as electric field initiation and we shall adopt that terminology here. The related problem of the sensitivity of azide compounds to static electric charging and electric discharge has also received considerable attention (7). These phenomena are relevant to safety in the storage and handling of munitions items (lead azide is the Army's prevalent primary explosive), and to novel initiation mechanisms for potential fuzing applications (1,2).

A great deal of work has been done to characterize field initiation effects in explosives (3,5,6) and to understand them on the basis of the fundamental electronic, decomposition and conductivity properties (1,2) of the materials. But it has been difficult to relate experiments using single crystals (easiest to reproduce and understand) to experiments on pressed pellets and powders. Our recent results and analysis, reported here, indicate that contact and surface effects are central to understanding the electric field initiation of explosives and to relating the results of experiments performed under different conditions and on different sample forms.

A. Background

An experiment which measures the threshold voltage for electric

field initiation of an explosive is basically straightforward. A sample is placed between two electrical contacts and a voltage applied in some prescribed manner until initiation is observed. On the other hand the analysis of the experiment is not at all straightforward; the effects of several parameters (such as the dielectric and conductivity properties of the explosive, the nature of the electrical contact and the particular sample-electrode geometry) must be taken into account. Only by considering these parameters can the electric field intensity, in the sample, be determined as a function of position. As we will show, it is a detailed knowledge of the field distribution which leads to an understanding of electric field initiation.

Our previous experiments (1,2,3) on lead azide  $[Pb(N_3)_2]$  using gold contacts and a sandwich geometry showed the following: Single crystals initiate upon the application of a voltage corresponding to an average threshold electric field (voltage/sample thickness) of  $3.5 \times 10^4$  V/cm. Gold forms a blocking (non-injecting) contact to  $Pb(N_3)_2$  under the conditions of the experiments. The voltage drop across the sample is relatively uniform near threshold voltages, i.e., the bulk of the sample experiences an electric field near the average field. The pressed pellet threshold average field approximates the single crystal value. Simultaneous application of low-intensity band gap radiation decreases the single crystal (but not the pressed pellet) threshold average field by a factor of two; this was explained qualitatively in terms of free charge motion and a consequent field redistribution resulting in higher electric field at the metal-explosive surface. Finally, the conductivity of  $Pb(N_3)_2$  is very low,  $\sim 10^{-12}$  (ohm-cm)<sup>-1</sup>, while photoconductivity is up to four orders of magnitude higher.

Russian experiments (6) on cupric azide  $[Cu(N_3)_2]$  and thallous azide  $[TlN_3]$  pressed pellets found that threshold field values depend on the electronic work function of the metal contacts. This was interpreted to be evidence for the injection of charge. Experiments by Leopold (5) on  $Pb(N_3)_2$  pressed pellets showed that no initiation occurs, even at much higher fields, if either or both of the electrodes were separated from the sample by thin mylar sheets.

In the analysis of experiments the dielectric constant of lead azide was generally taken to be  $\sim 5$ , based on pressed pellet data (8). The stoichiometry and impurity content of the lead azide powders were not characterized.

## B. Approach

Our theoretical aims were twofold: to understand and model the Russian field initiation experiments (6) (the proposed explanation

appears neither reasonable nor useful in understanding other field initiation experiments); and to form a quantitative basis for understanding internal field distributions in azide explosives. The average threshold field value (voltage/sample thickness) simply does not provide sufficient information for comparative purposes.

Three areas of experimental work were indicated by the theoretical results and preliminary analysis. Leopold's experiments (5) were extended to single crystals and pellets of  $\text{Pb}(\text{N}_3)_2$  at higher fields, and the effects of simultaneous irradiation examined.  $\text{Pb}(\text{N}_3)_2$  single crystal dielectric constants were measured as a function of crystallographic direction. And the gross surface properties of explosive azides were examined by x-ray photoelectron spectroscopy.

The individual results are described in the next Sections, and are assembled into a general picture in the DISCUSSION Section.

## THEORETICAL RESULTS

### A. Initiation by Carrier Emission from Schottky Barrier Contacts

Recent Russian work on the initiation of  $\text{Cu}(\text{N}_3)_2$  and  $\text{TlN}_3$  by the application of a voltage to metal electrodes contacting high-density pressed pellets (0.02 cm thick) has revealed that the threshold field  $E_t$  for initiation depends on the electrode material (6). Three metals were examined. In order of increasing work function, they were Zn, Cu and W. With  $\text{Cu}(\text{N}_3)_2$ , it was found that  $E_t$  increases with increasing work function of the anode metal; and with  $\text{TlN}_3$ , that  $E_t$  decreases with increasing work function of the cathode metal (there is also a weaker dependence on anode metal).  $E_t$  values (using applied voltage/sample thickness) corresponding to 50% initiation probability fell between  $1.1\text{--}6.8 \times 10^4$  V/cm, with changes of 10–80% when the contact metals were varied.

This effect was associated with hole injection into the valence band in the case of  $\text{Cu}(\text{N}_3)_2$ , and with double injection into the valence and conduction bands in the case of  $\text{TlN}_3$ , in both cases followed by impact ionization (6). However, it is difficult to understand how the work function can play any significant role in a model based on current injection, for then (with the ohmic contacts that injection explicitly requires) current limitation is a bulk or volume phenomenon; and the electrodes should play no part other than to provide current carriers as the volume field conditions demand (9). In a later publication (10) the Russian group also qualitatively attributes the effect to the emission of carriers into the bulk at a Schottky-type barrier

contact (11) but offers no quantitative accounting of the electrode material-dependent initiation data (6). Such an accounting, together with a discussion of the limitations of the emission model, is provided by our theoretical model (12).

Considering  $\text{Cu}(\text{N}_3)_2$  first, we demonstrate that an increase of  $E_t$  with anode metal work function is consistent with a model based on the emission of holes into the valence band at a Schottky barrier contact. The metal- $\text{Cu}(\text{N}_3)_2$  contact is viewed as that between a metal and a p-type semiconductor, as shown in Figure 1. Our detailed analysis

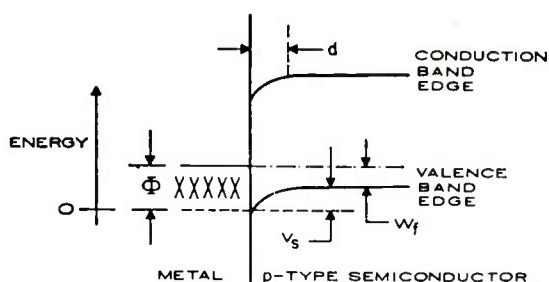


Figure 1. Energy band diagram for a p-type semiconductor-metal Schottky barrier contact with thickness  $d$ , barrier height  $\Phi$ , surface potential  $V_s$  and Fermi energy  $W_f$ .

shows that when a back-bias voltage is applied to a Schottky barrier contact, the nonequilibrium electric field  $E_s$  at the interface in the presence of an applied voltage  $V$  is

$$E_s = A [V - W_m + \Gamma]^{1/2}; \quad (1)$$

where  $A$  and  $\Gamma$  are related to material properties of the semiconductor only, and  $W_m$  is the metal work function. This shows that there can be a trade-off between  $W_m$  and a threshold applied voltage  $V_t$  (equivalent to an average applied electric field when scaled by the sample thickness) if initiation is associated with a critical interface field  $E_{s, \text{crit}}$ . The observation with  $\text{Cu}(\text{N}_3)_2$  can then be understood qualitatively, for as the electrode work function increases  $V_t$  must also increase to have the right-hand side of Eq. 1 remain equal to a given constant  $E_{s, \text{crit}}$  value.

For semi-quantitative agreement,  $V_t$  must be comparable to (or smaller than)  $\Gamma - W_m$ . In the Russian experiments  $V_t$  was approximately 400 volts, much larger than reasonable values for  $\Gamma$  (a few volts at most). Thus it would appear that our model does not apply. However, the samples were pressed pellets comprising individual powder grains that are most likely separated by potential barriers (13). In that event, the voltage drop across each grain, including those in contact with the electrodes, is  $V/n$  where  $n$  is the number of grains in the specimen thickness; and



further, the potential drop within each grain is predominantly across the surface barriers. Thus, if the grain diameter is about a micron ( $10^{-4}$  cm),  $n \approx 200$  and  $V_t$  is about 2 volts. Then  $V_t$  and  $\Gamma$  are of the same order and the model becomes plausible. Using reasonable values for semiconductor material properties and letting  $V_t = \Gamma = 2$  volts yields (from Equation (1))  $E_{s,crit} = 2.2 \times 10^5$  volts/cm, a plausible value. Fields of  $10^5$  -  $10^6$  volts/cm frequently cause destructive breakdown in other materials owing to carrier emission into the bulk.

Similar analysis shows the plausibility of viewing the metal-TlN<sub>3</sub> contact as that between a metal and an n-type semiconductor, with initiation associated with electron emission from the contact into the conduction band at a threshold  $E_{s,crit}$ :

#### B. Interface Electric Field Distributions in a Sandwich Geometry

The one-dimensional sample-electrode configuration considered is shown in Figure 2. The sample is a slab with parallel sides and thickness  $d$ , located symmetrically a distance  $\ell/2$  away from two parallel capacitively coupled electrodes (electrode spacing is  $L$ ). The static dielectric of the sample is  $\epsilon$ , and that of the spacing material  $\epsilon'$  ( $\epsilon_0$  for free space). Complete field distributions were determined for three assumptions as to the nature of the specimen: perfect insulator, intrinsic semiconductor, and extrinsic semiconductor (uniform photo-excitation can be included in the last two cases) (14). For all non-uniform fields the maximum field value in the sample occurs at the surface, and so results for only the surface field are presented.

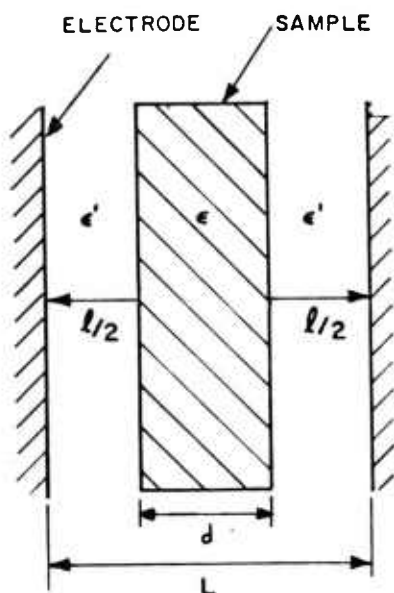


Figure 2. Sample of thickness  $d$  and dielectric constant  $\epsilon$  between two electrodes separated by the distance  $L$ . The spacing material has the dielectric constant  $\epsilon'$ .

In the perfect dielectric case, the field is uniform throughout the sample and so is equal to the surface field  $E_s$ , which is simply

$$E_s = \frac{V}{\kappa_r \ell + d}, \quad (2)$$

where  $\kappa_r = \epsilon/\epsilon'$ , the dielectric constant of the sample relative to that of the spacing medium. Equation (2) implies the following: For the case where the sample is directly contacted ( $\ell=0$ ),  $E_s = V/L$ . If the sample is thin ( $d \ll L$ ),  $E_s = V/\kappa_r L$ . For given  $\ell$  and  $d$ , increasing  $\kappa_r$  leads to a decreasing  $E_s$ .

In the intrinsic semiconductor case, mobile carriers of both signs accumulate on the surfaces and screen out the applied field. It is assumed that overall charge neutrality is maintained, and that no immobile free charge is present. If the uniform free charge density is  $\rho$  and the surface free charge per unit area  $\sigma$  is induced upon application of a voltage,  $\sigma = \rho d$  up to the limit  $\sigma_{\max} = \epsilon' V/\ell$  (in which case the field is totally screened from the sample). Then

$$E_s = \frac{V - \sigma \ell / \epsilon'}{\kappa_r \ell + d}. \quad (3)$$

It is clear from Equation (3) that the presence of a uniform mobile free charge distribution can only lower the value of  $E_s$  from its perfect dielectric value (for constant  $V$ ). This conclusion holds equally well for uniformly generated photo-carriers if both carrier types are mobile. The presence of free carriers of both types has the effect of changing the relative dielectric constant of Equation (2) by

$$\kappa_r \rightarrow \frac{\kappa_r V + \sigma d / \epsilon'}{V - \sigma \ell / \epsilon'}. \quad (4)$$

The extrinsic semiconductor case assumes that only one carrier type is mobile, and the compensating volume charge is present in the form of immobile charged impurities or trapped carriers. The analysis and results are more complicated, as two separate cases must be considered: complete sweep-out and partial sweep-out (of the mobile charge). In the former, the volume charge density  $\rho$  is insufficient to provide complete screening of the applied field anywhere in the sample. In the latter, a portion of the sample is completely screened. The complete sweep-out case occurs when  $\rho$  is less than a critical charge density  $\rho_{cr}$  (which depends on the voltage), and the partial sweep-out case when  $\rho$  exceeds  $\rho_{cr}$ , where

$$\rho_{cr} = \frac{2 \epsilon V}{d (2 \kappa_r \ell + d)}. \quad (5)$$

The field at the surface is then

$$E_s = \frac{V + \rho d^2/2\epsilon}{\kappa_r \ell + d} \quad \text{for } \rho < \rho_{cr} , \quad (6)$$

$$\text{and } E_s = \frac{\rho \ell}{\epsilon'} \{ [1 + \frac{2\epsilon' V}{\kappa_r \rho \ell^2}]^{1/2} - 1 \} \quad \text{for } \rho > \rho_{cr} .$$

Both expressions in Equation (6) lead to larger values of  $E_s$  than do either of Equations (2) and (3).  $E_s$  increases monotonically with  $\rho$ , and its maximum change can be seen to be

$$\frac{E_s(\rho \rightarrow \infty)}{E_s(\rho=0)} = \frac{\kappa_r + d/\ell}{\kappa_r} \quad (7)$$

(note that this ratio approaches infinity as  $\ell$  approaches zero).

Equations (2), (3) and (6) will be used in the following Sections to aid in the interpretation of experiments.

## EXPERIMENTAL RESULTS

### A. Threshold Initiation Fields in $Pb(N_3)_2$

All experiments were performed in the sandwich geometry of Figure 2. Prior results with direct explosive-metal contact were summarized above, and only the non-contacted experiments ( $\ell \neq 0$  in Figure 2) are discussed here. The importance of using single crystal as well as pressed pellet samples is evident from the fact that the Schottky barrier model presented earlier explicitly requires the presence of intergrain barriers (for semiquantitative agreement with the Russian experiments). In the analysis of experiments with single crystals, only the barriers at the azide metal contacts are considered.

Samples were mounted between mylar insulators in a vacuum chamber at  $2 \times 10^{-5}$  torr. (The high voltage experiments reported by Leopold (5) were performed with the samples immersed in oil). Care was taken to avoid discharges from the high voltage points of the sample holder to ground. The voltage was increased in steps of 500 volts to a maximum of 5 kV, and was held constant for 30 sec at each step.

The expression appropriate to calculating the average electric field in the sample  $\bar{E}$  is Equation (2), which is also the expression for the surface field if the field is uniform throughout the sample. Lead

azide's dielectric constant ( $\epsilon/\epsilon_0$ ) was taken to be 5 for the values quoted in this Section.

No initiation occurred in the pressed pellet samples ( $\sim 3.5$  gm/cm<sup>3</sup> density,  $1-3 \times 10^{-2}$  cm thick), using the insulated electrodes, up to the highest  $\bar{E}$  - values applied,  $1.4 \times 10^5$  V/cm. This corresponds to the upper limit (5 kV) of the power supply for the sample dimensions used. It is a factor of four greater than the  $\bar{E}$  - values that lead to initiation in contacted samples (1-3), and a factor of two greater than the highest  $\bar{E}$  - value reported by Leopold (5). The same result (no initiation) held for single crystal samples (grown by the method of Garrett (15), and cut and polished to provide parallel flat surfaces), with the highest  $\bar{E}$  - value attained being  $1.02 \times 10^5$  V/cm. The highest  $\bar{E}$  - values were maintained on the sample for about a half-hour. Some samples were subjected to combinations of 400.0 nm irradiation (strongly absorbed by  $\text{Pb}(\text{N}_3)_2$ ) and a strong field, for both polarities, again with no initiation.

The results lead us to conclude that electrode interface effects dominate the field initiation of  $\text{Pb}(\text{N}_3)_2$  single crystals and pressed pellets, with or without simultaneous low-level, strongly absorbed radiation, when the samples are directly contacted with the electrodes. Samples not directly contacted can sustain rather higher fields without initiation. It will be clear from the results below that only relative values of  $\bar{E}$  are reliable from these experiments; they were performed without determining crystallographic orientation, and the dielectric constant will be seen to be strongly anisotropic.

### 3. Dielectric Constant Measurements on $\text{Pb}(\text{N}_3)_2$

Measurements were performed using both the GR-1615-A and GR-716-C capacitance bridges. The technique, and expressions used to deduce dielectric constants, are described elsewhere (16). The single crystal samples were grown by the method of Garrett (15), crystallographically oriented, and cut and polished into plates ( $\sim 0.05$  cm thick, and  $0.1$  cm<sup>2</sup> surface area).

The dielectric constants ( $\epsilon/\epsilon_0$ ), measured along the unit cell axes, were found to be highly anisotropic:  $\kappa_{\langle 100 \rangle} = 17$ ;  $\kappa_{\langle 010 \rangle} = 120$ ; and  $\kappa_{\langle 001 \rangle} = 40$ . The experimental inaccuracy was  $\pm 10\%$ , and is a consequence of the difficulty of measuring the small evaporated electrode surface areas, the lack of perfectly parallel sample surfaces, and unaccounted edge capacitances. The values are frequency-independent at room temperature over the range  $10^2$  to  $10^6$  Hz. At a fixed frequency of  $10^3$  Hz, the dielectric constant varies slightly with temperature

(it has a positive slope), changing by 2% over the temperature range  $-100^{\circ}\text{C}$  to  $+100^{\circ}\text{C}$ . The dissipation factor is small for each orientation ( $<10^{-3}$ ), indicating negligible loss over the frequency range investigated.

The dielectric constant of  $\text{Pb}(\text{N}_3)_2$  is thus both highly anisotropic and large compared to most other materials. The value determined for pressed pellets depends on the density and is lower than the lowest crystalline value because of averages over direction and voids. In any case, it is clear that the threshold initiation field experiments discussed earlier have to be done on oriented crystals in order to use Equation (12) to obtain reliable absolute values of  $\bar{E}$ ; and that true average threshold field values for crystals are lower than those quoted earlier and in the literature.

### C. Elemental Surface Composition Studies of Explosive Azides

The x-ray photoelectron spectroscopy (XPS) technique, and its application to the study of explosives, were described at a previous Army Science Conference (17). The technique determines the binding energies of electronic states by measuring the kinetic energies of x-ray-induced photoelectrons (using a monochromatic x-ray source). This allows elemental analysis, and yields information on the chemical states of observed elements. The signal from the first few surface layers makes the dominant contribution to the total XPS signal.

The XPS spectra were obtained with a Varian IEE-15 Spectrometer. The samples were either mounted as powders on Scotch Tape, sprayed onto a gold substrate from a methanol solution, or prepared by exposing the metal to  $\text{HN}_3$  vapor. The powdered samples of alkali halides, alkali azides, thallous azide, and laboratory grade lead azide were freshly ground before mounting and insertion into the instrument. Silver azide, copper azide and commercial grade  $\text{Pb}(\text{N}_3)_2$  were not ground. Light-sensitive samples were handled in weak sodium light. Details of the methods and approximations used to analyze the results are available elsewhere (18).

All samples showed significant surface contamination. Carbon is generally the dominant element detected, the amount being greater by a factor of three to ten over the constituents of the sample (taking relative cross-sections into account). The position of the  $\text{C } 1s_{1/2}$  peak indicates that the carbon is present in hydrocarbon form. Less oxygen contaminant is detected, but the amount is comparable to that of the host cation.

The degree of surface stoichiometry was examined by comparing intensity ratios of the sample's constituent elements (again taking relative cross sections into account). The results indicate that the



surface layers sampled were approximately stoichiometric for the following compounds (examined as a basis for comparison): NaCl, KBr, AgCl, TlCl,  $\text{KN}_3$  and  $\text{RbN}_3$ . In contrast, surface layers of the explosive azides  $\text{Pb}(\text{N}_3)_2$ ,  $\text{AgN}_3$ ,  $\text{TlN}_3$ , and  $\text{Cu}(\text{N}_3)_2$  were generally deficient in azide content. In the cases of  $\text{AgN}_3$ ,  $\text{TlN}_3$ , and  $\text{Pb}(\text{N}_3)_2$ , the degree of surface stoichiometry depends on the chemical preparation of the sample and also on its history. Freshly prepared samples of  $\text{AgN}_3$  gave stoichiometric ratios between 0.6 and 0.9 (ratio of anion to cation concentration, normalized to unity for correct stoichiometry). Samples 2-3 years old gave values ranging from 0.2 to 0.4. When an old sample was exposed to aqueous vapors of  $\text{HN}_3$  overnight, the stoichiometric ratio improved somewhat, but not to unity.

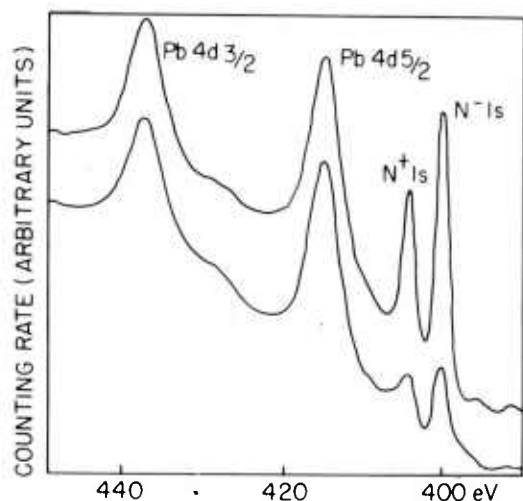


Figure 3. XPS spectra of  $\text{Pb}(\text{N}_3)_2$ , in a binding energy range having both Pb and N signals, for unirradiated (upper) and photo-decomposed (lower) samples.

The highest ratio (0.73) obtained for  $\text{Pb}(\text{N}_3)_2$  was on samples freshly prepared and exposed to  $\text{HN}_3$  vapor. The value for the upper curve of Figure 3 is 0.68. Samples which had been kept in the laboratory for a few months in the dark, and not freshly ground, gave values of  $\sim 0.44$ . Commercial grade  $\text{Pb}(\text{N}_3)_2$  had stoichiometric ratios ranging from 0.22 to 0.38. Samples subjected to sub-initiation level shocks showed an increase in the ratio. This is probably due to particle break-up and consequent exposure of fresh surfaces, assuming that the bulk of the material has a higher stoichiometry than the old surfaces.

Thallous azide exhibited behavior similar to that of lead azide. Aged samples showed a lack of stoichiometry on the surface, which could be increased to a value of unity by exposure to  $\text{HN}_3$  vapors overnight.



All of the explosive azides investigated decompose when irradiated. This is illustrated in the lower curve of Figure 3, where the ratio of azide nitrogen to lead was considerably reduced by irradiation. In many samples of  $\text{Pb}(\text{N}_3)_2$  and  $\text{TlN}_3$ , all nitrogen can be removed from the sample surface layers by irradiation. Irradiation of silver and copper azides removes all azide nitrogen signal, and the results suggest the formation of stable nitrides. In normal handling, azides are exposed to room light (irradiation). Thus non-stoichiometry and the presence of other compounds at the surfaces which will influence electrical contact properties can be expected.

It appears that surface layers on lead azide form a protective coating, preventing further decomposition with aging (otherwise, a twenty-year-old sample would not give any azide signal). This is consistent with the fact that shock waves improve stoichiometry due to cracking and exposing of new surfaces. In addition, twenty-year-old samples can be detonated, indicating appreciable azide content in the bulk although the surface stoichiometry is poor.

#### DISCUSSION

Our results have been discussed individually in earlier Sections. A more general discussion is performed here relating them to each other and to prior results. The most important conclusion is that contact and surface effects dominate the electric field initiation properties of explosive azides, and that this can explain apparent discrepancies when comparing experiments performed under dissimilar conditions. The detailed mechanisms involved are not fully understood, but the nature of the crucial experiments and calculations are now clear.

The Russian field initiation experiments (6) provided an important clue to the role of interface contacts. Our theoretical model shows that the experiments using non-ohmic metal contacts can be explained if initiation is the result of a critical threshold field  $E_{s,crit}$  at the metal-explosive interface. A different value of  $E_{s,crit}$  would then be associated with each explosive azide, and be independent of the nature of the non-ohmic metal contact (so long as a contact is available); its magnitude is of the order of  $10^5$  V/cm in  $\text{Cu}(\text{N}_3)_2$  and  $\text{TlN}_3$ . Recall that our model cannot explain these experimental results without explicitly taking the pressed pellet nature of the samples into account. The field initiation experiments on contacted  $\text{Pb}(\text{N}_3)_2$  samples appear also to require a critical interface field.

These conclusions point to an initiation model involving carrier emission from a barrier contact. Two alternative mechanisms are suggested for this emission model based on field breakdown mechanisms in the literature. Both rely on high local internal fields to generate

hot electrons, which can then cause impact ionization. The first, due to O'Dwyer (19), assumes that the impact ionization leads to avalanche multiplication with eventual breakdown at the exit electrode, where most of the energy of impact-generated carriers is dissipated. The second mechanism, due to DiStefano and Shatzkes (20), suggests that impact ionization generates a space charge in the volume of the sample which concentrates the internal field at the emitting electrode; this in turn produces an increase in the emission current, with eventual catastrophic power dissipation at the entrance electrode. The choice between the two mechanisms (for a given explosive azide) can thus be made on the basis of experiments that determine whether initiation occurs near the entrance or exit electrode.

The experiments of Leopold (5), and their extensions reported here, showed that no initiation occurs without direct metallic contact up to the limits of the experimental apparatus. This is consistent with the emission model just presented. Values for the interface fields  $E_s$  attained can be calculated from Equation (2) by using the appropriate dielectric constant  $\kappa_r$ . Lead azide's dielectric constant was found to be large and highly anisotropic. Thus single crystal experiments on oriented samples must be performed to establish reliable values of the highest  $E_s$  attained in the samples; and other experiments testing at what value of  $E_s$  initiation occurs, without direct contact, would be valuable.

Our previous model for the photo-electronic initiation effect (decrease in average threshold field for initiation when strongly absorbed light is applied simultaneously) involved a redistribution of the electric field as a consequence of the illumination. The analysis of the field initiation experiments provides a more quantitative basis for this model. We assume that  $Pb(N_3)_2$  is highly insulating (a perfect dielectric), and acts as an extrinsic semiconductor upon irradiation. Equations (6) and (7) then describe the increase in  $E_s$  that can result from a uniformly absorbed radiation pulse. The analysis must be expanded to include non-uniformly absorbed irradiation (which is straightforward), and also the direct ( $\ell=0$ ) metallic contact situation (as in the Schottky barrier analysis).

Finally, our surface studies of explosive azides give the first unambiguous picture of the topmost several layers of these materials. The presence of contamination and absence of stoichiometry in even laboratory quality sample surfaces apparently results from the highly reactive nature of the surfaces. This may explain why attempts to find injecting contacts have not been successful, and also how to overcome this problem. The relation between prior treatment of azide surfaces and the sensitivity of explosive azide powders bears closer scrutiny.

### CONCLUSIONS

An integrated experimental and theoretical program to understand the field initiation properties of explosive azides has resulted in an important broad conclusion. Contact and surface effects dominate the electric field initiation properties of these materials. This realization has been successfully used to relate the results of experiments performed under different conditions on different sample forms.

The results and understanding are directly relevant to a number of novel fuzing device applications (e.g., fuzes that require more than one stimulus to fire), and to safety against electrical and electrostatic hazards in the storage and handling of munitions.

### ACKNOWLEDGEMENTS

We are most grateful to Professor Peter Mark of Princeton University for his considerable contributions to all phases of this work, to Dr. Harry D. Fair, Jr. for his direction and comments, and to Dr. R. F. Walker for his support.

### REFERENCES

1. H.D. Fair, Jr, D.S. Downs, A.C. Forsyth, W. Garrett, M. Blais, T. Gora and F.E. Williams, Picatinny Arsenal Technical Report 4607, December 1973.
2. D.S. Downs, W. Garrett, D.A. Wiegand, T. Gora, M. Blais, A.C. Forsyth and H.D. Fair, Jr., Picatinny Arsenal Technical Report 4711, September 1974.
3. D.S. Downs, T. Gora, M. Blais and W.L. Garrett, Picatinny Arsenal Technical Report 4874, November 1975.
4. F.P. Bowden and A.C. McLaren, Proc. Roy. Soc. A246, 197 (1958).
5. H.S. Leopold, Naval Ordnance Laboratory Technical Report 73-125 (1973).
6. Y.A. Zakharov and Y.N. Sukhushin, Izv. Tomsk Politeckh. Inst. 251, 213 (1970).
7. M.S. Kirshenbaum, Picatinny Arsenal Technical Report 4559 (1973).
8. J.E. Schiviner, Sandia Laboratories, Report No. 73-5001 (1973).
9. M.A. Lampert and P. Mark, "Current Injection in Solids", Chap. 1, Academic Press, New York (1970).
10. Y.N. Sukhushin, Y.A. Zakharov, and F.I. Ivanov, Khim. Vys. Energiy 7, 261 (1973).
11. S.M. Sze, "Physics of Semiconductor Devices", Chap. 8, John Wiley and Sons, New York (1969).
12. P. Mark and T. Gora, J. Solid State Chem. 15, 79 (1975).
13. R.H. Bube, J. Appl. Phys. 31, 2239 (1960); P. Mark and B.W. Lee, J. Phys. Chem. Solids 35, 865 (1974).
14. T. Gora and P. Mark (unpublished calculations).

GORA, SHARMA, WIEGAND, GARRETT, DOWNS

15. W.L. Garrett, Mat. Res. Bull. 7, 949 (1972).
16. W.L. Garrett, Mat. Res. Bull. (to be submitted).
17. J. Sharma, T. Gora, S. Bulusu and D.A. Wiegand, Proceedings of the Army Science Conference, West Point, N.Y. (1974).
18. P. DiBona, D.A. Wiegand and J. Sharma, J. Vac. Sci. Tech. (in press).
19. J.J. O'Dwyer, J. Appl. Phys. 40, 3887 (1969).
20. T.H. DiStefano and M. Shatzkes, Appl. Phys. Lett. 25, 685 (1974); J. Vac. Sci. Tech. 12, 493 (1975).

PHOTOELECTRON NOISE LIMITATIONS IN HIGH  
PERFORMANCE IMAGING SENSORSRONALD, D. GRAFT, PhD  
U. S. ARMY NIGHT VISION LABORATORY  
FORT BELVOIR, VA 22060

## INTRODUCTION

In the conventional signal-to-noise ratio analysis (1) of image forming sensors, the imaged area is broken into fictional "resolution elements" and the noise calculated as the square root of the total number of counts or events,  $n$ , falling within a single element. Since the signal is proportional to the total number of counts within the element, the signal-to-noise ratio is  $n^{1/2}$ . By postulating a minimum required, or threshold, signal-to-noise ratio, these calculations have led to expressions (2) for the limiting resolution of the device as a function of incident light level. The effects of a finite aperture have been considered by Schade (3) and more recently by Rosell (4). Schade's analysis led him to define the noise equivalent sampling area as the reciprocal of the noise equivalent passband. The concept of a noise equivalent sampling area has been used by Rosell to calculate the display signal-to-noise ratio and limiting resolution of a variety of television camera tubes. Analyses of this type have been extensively used to calculate the performance of military television systems.

In the following analysis some of the ambiguities of the Rosell-Schade approach are resolved. The apriori assumption of the existence of fictitious resolution elements is eliminated and reintroduced only after considerable development. Two equivalent square sampling apertures or areas are defined: a signal sampling aperture,  $x_s$ , and a noise sampling aperture,  $x_n$ . It will be shown that the noise equivalent sampling area of Schade is given by  $x^* \equiv 1/N_e = x_s^2/x_n$ ; the proper interpretation of  $x^*$  is thus as an equivalent aperture that weights both signal and noise, not noise alone.

The theoretical development is in the language of television or raster scan type sensors. This is not essential and with minor modification can be applied to other imaging sensors such as direct view intensifiers and discrete solid state arrays.

## THEORY

### General

For convenience and brevity of notation, a one dimensional imaging system is assumed. With certain simplifying assumptions, the extension to two dimensions is straightforward and will be indicated later. The input and output of a linear, spatially invariant system are related by (5)

$$g_o(x) = \int_{-\infty}^{\infty} h(x-x') g_i(x') dx' \quad (1)$$

where  $g_i$  and  $g_o$  are the input and output respectively and  $h(x-x')$  is the impulse or point response of the system. That is, if  $g_i(x') = \delta(x'-x'_0)$ , then  $g_o(x) = h(x-x'_0)$ . It is assumed that the system has some characteristic integration time  $\tau$  such that during the time interval  $t, t + \tau$ ,  $K$  photoelectrons are emitted at positions  $x'_1, x'_2, \dots, x'_K$ . The input is thus  $g_i(x') = \sum \delta(x'-x'_i)$  and the output image at time  $t + \tau$  is  $g_o(x) = \sum h(x-x'_i)$ . In general, the  $K$  emission positions and the value of  $K$  itself form a set of  $K + 1$  independent random variables so that the average output,  $E[g_o(x)]$ , is given by (6):

$$E[g_o(x)] = \int_{-\infty}^{\infty} \dots \int_{-\infty}^{\infty} \sum_{i=1}^K h(x-x'_i) p(x'_1, \dots, x'_K) p(K) dx'_1 \dots dx'_K dK \quad (2)$$

where  $p(x'_1 \dots x'_K) dx'_1 \dots dx'_K$  is the probability that the  $K$  electrons are emitted at positions  $x'_1, \dots, x'_K$  and  $p(K)dK$  is the probability that  $K$  electrons are emitted during the time interval. To evaluate the output noise, the following expression for the variance is required:

$$\begin{aligned} \sigma^2 &\equiv E[|g_o(x) - E[g_o(x)]|^2] \\ &= \int_{-\infty}^{\infty} \dots \int_{-\infty}^{\infty} \sum_{i,j=1}^K h(x-x'_i) h(x-x'_j) p(x'_1, \dots, x'_K) \\ &\quad p(K) dx'_1 \dots dx'_K dK - E^2[g_o(x)] \end{aligned} \quad (3)$$

The signal-to-noise ratio is defined as  $S/N = E[g_o(x)]/\sigma$  and, in general, is a function of position. Equations (2) and (3) will be evaluated for four cases of special interest.



Uniform Background

For a uniformly illuminated background, the photoelectrons are emitted at purely random positions (Poisson process) so that

$$p(x'_1, x'_2, \dots, x'_K) dx'_1 \cdot dx'_K = \frac{1}{w^K} \prod_{i=1}^K dx'_i; -\frac{w}{2} \leq x'_i \leq \frac{w}{2} \quad (4)$$

$$= 0, \quad |x'_i| > w/2$$

where  $w$  is the width of the photocathode. Furthermore,  $p(K)dK$  is given by

$$p(K)dK = \frac{\bar{K}^K}{K!} e^{-\bar{K}} dK \quad (5)$$

where  $\bar{K}$  is the average number of photoelectrons emitted during the time interval. Substitution of Equation (4) into (2) gives

$$E[g_o(x)] = \int_0^\infty p(K)dK \left[ \sum_{i=1}^K \frac{1}{w} \int_{-w/2}^{w/2} h(x-x'_i) dx'_i \right] \quad (6)$$

Neglecting edge effects, the expression in brackets can be written as

$$\sum_{i=1}^K \frac{1}{w} \int_{-w/2}^{w/2} h(x-x'_i) dx'_i \approx \sum_{i=1}^K \frac{1}{w} \int_{-\infty}^{\infty} h(x-x'_i) dx'_i = \frac{K}{w} \int_{-\infty}^{\infty} h(x) dx \quad (7)$$

Then Equation (6) becomes

$$E[g_o(x)] = v_B \int_{-\infty}^{\infty} h(x) dx \quad (8)$$

where  $v_B = \bar{K}/w$  is the average number of photoelectrons per unit distance emitted from the photocathode during the time interval. A similar calculation for the variance gives

$$\sigma^2 = v_B \int_{-\infty}^{\infty} h^2(x) dx \quad (9)$$

so that the signal-to-noise ratio is

$$\frac{S}{N} = \frac{v_B \int_{-\infty}^{\infty} h(x) dx}{[\int_{-\infty}^{\infty} h^2(x) dx]^{1/2}} \quad (10)$$

and is independent of  $x$ .

### Isolated Point Source

Consider a small but finite "point" source of photoelectrons centered at  $x' = x'_0$  with width  $a$ . Then

$$p(x'_1, \dots, x'_K) dx'_1 \dots dx'_K = \begin{cases} \frac{1}{a} \prod_{i=1}^K dx'_i; & x'_0 - \frac{a}{2} < x'_i < x'_0 + \frac{a}{2} \\ = 0 & \text{otherwise} \end{cases} \quad (11)$$

With this substitution Equation (2) becomes

$$E[g_0(x)] = \int_{-\infty}^{\infty} p(K) dK \left[ \sum_{i=1}^K \frac{1}{a} \int_{x'_0 - a/2}^{x'_0 + a/2} h(x - x'_i) dx'_i \right] \quad (12)$$

Since  $a$  is small,

$$\frac{1}{a} \int_{x'_0 - a/2}^{x'_0 + a/2} h(x - x'_i) dx'_i \approx h(x - x'_0)$$

and

$$\begin{aligned} E[g_0(x)] &= \int_{-\infty}^{\infty} K p(K) dK h(x - x'_0) \\ &\equiv \bar{K} h(x - x'_0) \end{aligned} \quad (13)$$

A similar calculation for the variance gives

$$\sigma^2 = \bar{K} h^2(x - x'_0) \quad (14)$$

and the signal-to-noise ratio is

$$S/N = \bar{K}^{1/2}, \quad (15)$$

an easily anticipated result.

#### Point Source in a Uniform Background

The signal-to-noise ratio can be calculated using the same methods as before but a simpler procedure is to use system linearity and superimpose the previous results. It is found that

$$E [g_0(x)] = v_B \int_{-\infty}^{\infty} h(x) dx + \bar{K} h(x-x'_0) \quad (16)$$

and

$$\sigma^2 = v_B \int_{-\infty}^{\infty} h^2(x) dx + \bar{K} h^2(x-x'_0) \quad (17)$$

The signal-to-noise ratio is then

$$\frac{S}{N} = \frac{v_B \int_{-\infty}^{\infty} h(x) dx + \bar{K} h(x-x'_0)}{[v_B \int_{-\infty}^{\infty} h^2(x) dx + \bar{K} h^2(x-x'_0)]^{1/2}} \quad (18)$$

In Equations 16 - 18,  $\bar{K}$  is the average number of emitted photoelectrons due to the point source alone and  $v_B$  the average density of emitted photoelectrons due to background alone.

#### Periodic Input

A case of interest, particularly in the laboratory evaluation procedure, is the case of a periodic input for which the average brightness is  $B(x') = B(0) [1 + c (2-c)^{-1} \cos \omega x']$ . The quantity  $B(0)$  is the maximum brightness and  $c$  is the contrast. The probability density function is found to be

$$\begin{aligned} p(x'_1, \dots, x'_K) dx'_1 \dots dx'_K &= w^{-K} \left(1 + \frac{c}{2-c} \operatorname{sinc} \omega w\right)_{i=1}^K \left(1 + \frac{c}{2-c} \cos \omega x'_1\right) dx'_1; \\ &\quad - \frac{w}{2} \leq x'_1 \leq w/2 \\ &= 0, \quad |x'_1| > w/2 \end{aligned} \quad (19)$$

After straightforward but tedious calculation,

$$E [g_o(x)] = v_p \left[ \int_{-\infty}^{\infty} h(x) dx + \frac{c}{2-c} \cos \omega x \int_{-\infty}^{\infty} h(x') \cos \omega x' dx' \right] \quad (20)$$

$$\sigma^2 = v_p \left[ \int_{-\infty}^{\infty} h^2(x) dx + \frac{c}{2-c} \cos \omega x \int_{-\infty}^{\infty} h^2(x') \cos \omega x' dx' \right] \quad (21)$$

where  $v_p$  is the peak photoelectron density given by

$$v_p \equiv \frac{\bar{K}}{w} \left( 1 + \frac{c}{2-c} \operatorname{sinc} \frac{\omega w}{2} \right)^{-1}$$

From Equations 20 and 21, the signal-to-noise ratio is

$$\frac{S}{N} = \frac{v_p \int_{-\infty}^{\infty} h(x) dx + \frac{c}{2-c} \cos \omega x \int_{-\infty}^{\infty} h(x') \cos \omega x' dx'}{\left[ \int_{-\infty}^{\infty} h^2(x) dx + \frac{c}{2-c} \cos \omega x \int_{-\infty}^{\infty} h^2(x') \cos \omega x' dx' \right]^{1/2}} \quad (22)$$

#### Definition of Averaging Distances

Equations 10, 15, 18 and 22 are expressions for the signal-to-noise ratio in terms of various integrals (or averages) over the point response function. Although not essential, it is convenient to rewrite these equations in terms of averaging distances or apertures so that a simple "resolution element" analysis can be used. Two such sampling distances are defined: the signal sampling distance,  $x_s$ , is defined as

$$h(o) x_s = \int_{-\infty}^{\infty} h(x) dx$$

and the noise sampling distance,  $x_n$ , as

$$h^2(o) x_n = \int_{-\infty}^{\infty} h^2(x) dx$$

The signal-to-noise ratio for a point source on a uniform background (Equation 18) can then be rewritten as

$$\frac{S}{N} = \frac{v_B h(o) x_s + \bar{K} h(x-x'_0)}{[v_B h^2(o) x_n + \bar{K} h^2(x-x'_0)]^{1/2}} \quad (23)$$

and at the peak of the point source,  $x = x'_0$ ,

$$\frac{S}{N} = \frac{v_B x_s + \bar{K}}{[v_B x_n + \bar{K}]^{1/2}} \quad (24)$$

Equation 24 has the desired form of a ratio of signal counts to noise counts. For  $\bar{K} = 0$  (background alone), Equation 24 becomes

$$\frac{S}{N} = (\nu_B x^*)^{1/2} \quad (25)$$

where  $x^* \equiv x_s^2 / x_n$ . It is a straightforward matter to show that  $x^* = 1/Ne$  and that  $Ne$  is the noise equivalent passband of Schade. Thus for a uniform background, a single averaging distance is sufficient to calculate the signal-to-noise ratio. However, when considering a point source and a background, a two parameter description is required. It is concluded that both signal and noise averaging distances are required and that the noise averaging distance of Schade is actually a combination of signal and noise averaging distances.

The signal-to-noise ratio for a periodic input, Equation 22, can be rewritten as

$$\frac{S}{N} = \nu_p^{1/2} \frac{(x_s + \frac{c}{2-c} \cos \omega x \mathcal{F}\{f(x)\})}{[x_n + \frac{c}{2-c} \cos \omega x \mathcal{F}\{f^2(x)\}]^{1/2}} \quad (26)$$

where  $f(x) \equiv h(x)/h(0)$  is the normalized impulse response and  $\mathcal{F}$  implies a Fourier transform.

#### Extension to Two Dimensions

If the system is spatially invariant in both dimensions so that  $h(x, x'; y, y') = h(x-x'; y-y')$ , the calculation proceeds along the lines of the one dimensional model. One obtains the following modifications:

$$x_s \rightarrow a_s = \frac{1}{h(0,0)} \int_{-\infty}^{\infty} \int_{-\infty}^{\infty} h(x,y) dx dy$$

$$x_n \rightarrow a = \frac{1}{h^2(0,0)} \int_{-\infty}^{\infty} \int_{-\infty}^{\infty} h^2(x,y) dx dy$$

$$\nu_B \rightarrow \text{average area density of emitted photoelectrons}$$

Although in general a raster scan system is spatially variant in the direction perpendicular to the scan direction, the data of a following sections shows that SIT or EBS type television tubes closely approximate a continuous scan system for scan line densities in excess of about 40 scan lines per mm of raster height.

## GRAFT

### Some Useful Results

(1) The MTF and impulse response are Fourier transform pairs so that

$$h(x) = \frac{1}{2\pi} \int_{-\infty}^{\infty} H(\omega) e^{i\omega x} d\omega$$

and

$$H(\omega) = \int_{-\infty}^{\infty} h(x) e^{-i\omega x} dx$$

If the MTF is normalized at zero spatial frequency, then  $\int_{-\infty}^{\infty} h(x) dx = 1$  and  $x_s = h^{-1}(0)$ . Therefore

$$x_s = 2\pi / \int_{-\infty}^{\infty} H(\omega) d\omega$$

Using Parseval's theorem, it can be shown that

$$x_n = \frac{2\pi \int_{-\infty}^{\infty} |H(\omega)|^2 d\omega}{[\int_{-\infty}^{\infty} H(\omega) d\omega]^2}$$

Thus if the MTF is known the signal and noise sampling distances can be calculated. Analogous results can be derived for a two dimensional system.

(2) A commonly observed impulse response is the Gaussian for which

$$h(x, x'; y, y') = (2\pi\sigma_x\sigma_y)^{-1} e^{-\frac{(x-x')^2}{2\sigma_x^2}} e^{-\frac{(y-y')^2}{2\sigma_y^2}}$$

then

$$a_s = 2\pi\sigma_x\sigma_y$$

$$a_n = \pi\sigma_x\sigma_y$$



GRAFT

and

$$a_n = a_s/2$$

Thus the noise sampling area is half as large as the signal sampling area for a Gaussian impulse response.

(3) The signal-to-noise ratio for a periodic input and Gaussian impulse response is found to be

$$\frac{S}{N} = (v_p a^*)^{1/2} \frac{1 + \frac{c}{2-c} \cos \omega x e^{-\sigma_x^2 \omega^2 / 2}}{(1 + \frac{c}{2-c} \cos \omega x e^{-\sigma_x^2 \omega^2 / 4})^{1/2}} \quad (27)$$

Equation 27 can be used to derive an expression for the sensor limiting resolution by redefining the signal to be the peak-to-peak signal and averaging the spatially dependent noise over the photocathode area. Then

$$\frac{S}{N} = (v_p a^*)^{1/2} \frac{2c}{2-c} e^{-\sigma_x^2 \omega^2 / 2} \quad (28)$$

if  $\omega w \gg 1$ . Assuming that the limiting resolution,  $\omega_\ell$ , occurs at some threshold signal-to-noise ratio  $k$ , then

$$\omega_\ell = \frac{\sqrt{2}}{\sigma_x} \left\{ \ln \frac{2c (v_p a^*)^{1/2}}{(2-c)k} \right\}^{1/2} \quad (29)$$

Up to this point only photoelectron noise has been considered. In the likely event that an internal noise source contributes an effective noise count  $n_p$ , it can be added in quadrature with the photoelectron noise. For example, Equation 29 would be modified to read as

$$\omega_\ell = \frac{\sqrt{2}}{\sigma_x} \left\{ \ln \frac{2c v_p a_s}{(2-c)k(v_p a_n + n_p)} \right\}^{1/2} \quad (30)$$

## EXPERIMENTAL

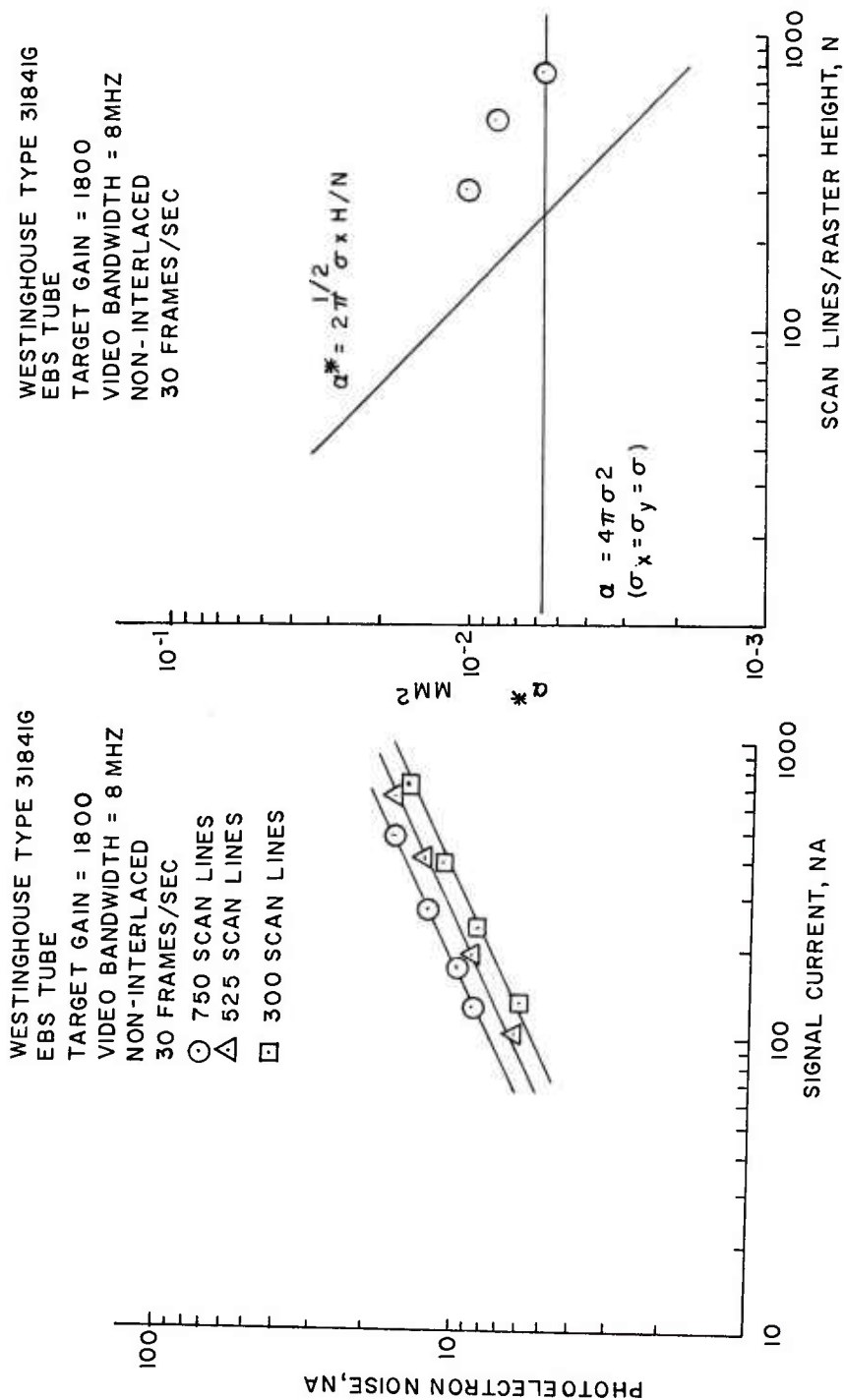
Measurement Technique

All uniform background data were taken using the US Army Night Vision Laboratory Television Test Set. This extremely flexible system permits a wide range of measurements under non-standard conditions. For example, line and frame rates are variable from 100-2000 lines/frame and from 1-60 frames/sec. An on-line Varian 620i minicomputer and a Computer Lab Model 615 A/D converter are used for real time data collection and processing. Video is digitized into 6 bit brightness words at a 15 MHz sampling rate. A buffer memory accepts up to 2048 words which are then clocked into the computer at a 200 KHz rate. Thus up to 2048 points in a single frame of video can be sampled and fed to the computer. The sampled points can be adjacent points on a single line or selected segments of successive lines. The same points can be sampled over successive frames for a multi-frame average. The photoelectron noise is measured by calculating the standard deviation of the collected data and correcting for preamplifier noise.

Experimental Results

The photoelectron noise due to a uniform background is shown in Figure 1. These data were taken at 750, 525, and 300 scan lines per frame on a Westinghouse 31841G EBS tubes. This tubes has a 40 mm S-20 photocathode, a 25 mm deep-etched metal cap silicon array target, and a target gain of 1800 at 10 KV acceleration potential. Values of  $a^* = a_s / a_n$  calculated from the data of Figure 1 are plotted in Figure 2 as a function of scan line density. The horizontal line is the expected  $a^*$  value for a symmetrical, continuous sampling system as calculated from measured MTF data. The sloping line is the expected value for a purely discrete sampler in the y direction and a continuous sampler in the x direction. The  $\sigma_x$  value is determined from horizontal MTF measurements. It is seen that the data approach a continuous sampling model for scan line densities in excess of approximately 700 scan lines/frame.

Figure 3 is a plot of photoelectron noise current versus signal current for a point source and a uniform background taken separately. These data were taken on an RCA SIT Tube Type 4826. This tube has a 25 mm photocathode, an 18 mm diode array target, and a target gain of 700 at 6 KV. Assuming a symmetrical, continuous scan model and using measured measured MTF data, the calculated value of  $a^*$  is  $2.4 \times 10^{-3} \text{ mm}^2$ . The measured value from Figure 3 is  $2.3 \times 10^{-3} \text{ mm}^2$ . It thus appears that 525 scan lines on an 18 mm target are sufficient for an

FIG. 1 PHOTOELECTRON NOISE,  
UNIFORM BACKGROUNDFIG. 2 SAMPLING AREA AS A FUNCTION  
OF SCAN LINE DENSITY

RCA TYPE 4826 SIT TUBE  
 TARGET GAIN = 700  
 525 SCAN LINES  
 30 FRAMES/SEC  
 NON-INTERLACED  
 VIDEO BANDWIDTH = 4MHZ

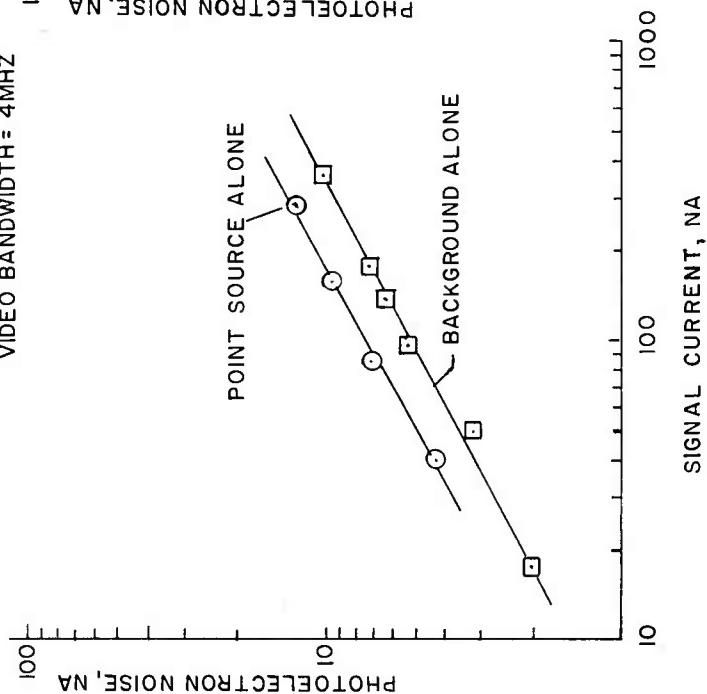


FIG. 3 PHOTOELECTRON NOISE, POINT SOURCE & UNIFORM BACKGROUND

RCA TYPE 4826 SIT TUBE  
 TARGET GAIN = 700  
 525 SCAN LINES  
 30 FRAMES/SEC  
 NON-INTERLACED  
 VIDEO BANDWIDTH = 4MHZ  
 FIXED BACKGROUND  
 CURRENT = 108 NA

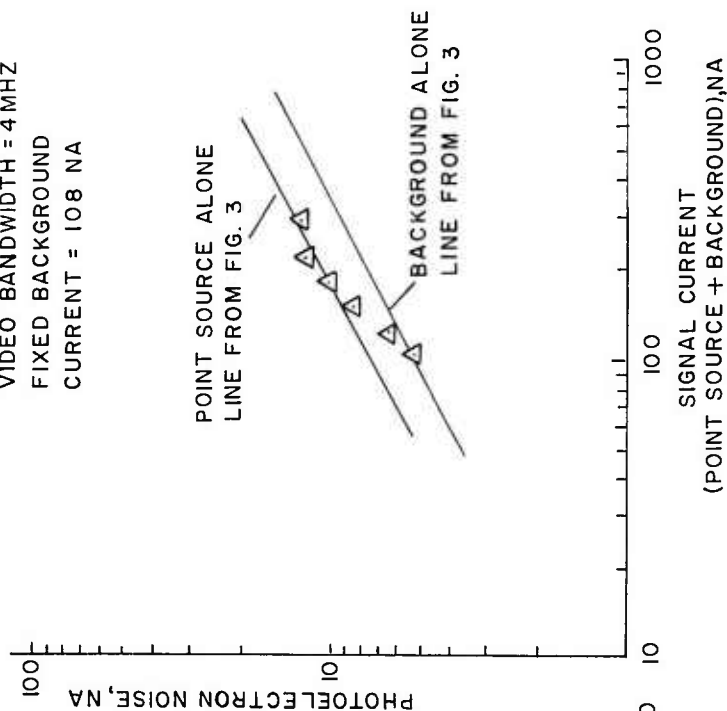


FIG. 4 PHOTOELECTRON NOISE, VARIABLE POINT SOURCE ON A FIXED BACKGROUND

## GRAFT

effective continuous scan in the y direction. Since the larger format (25 mm) Westinghouse tube requires 700 scan lines approximately 40 scan lines per mm of raster height is required in each instance.

It is noted that the noise current at the peak of a point source is larger than for a uniform background of equal signal current. It is easily shown that the expected noise currents should differ by  $(a_s/a_n)^{1/2}$ . For a Gaussian impulse response,  $(a_s/a_n)^{1/2} = \sqrt{2}$ . Reference to Figure 3 shows that the experimental noise measurements do indeed differ by  $\sqrt{2}$ .

Figure 4 is a plot of photoelectron noise measured at the peak of a point source immersed in a constant uniform background of 108 nanoamperes. The noise is plotted as a function of total signal current (point source current plus background current). At large signal currents when the point source current is large compared to the background, the data approach the point source alone data of Figure 3. The single point at 108 na corresponding to zero point source current falls on the curve of background alone in Figure 3. Thus for any combination of point source and background current, the measured noise current will be on or between the two straight lines of Figure 3.

## SUMMARY AND CONCLUSIONS

The effect of a finite aperture on photoelectron noise has been described in some detail. Two equivalent sampling areas or apertures,  $a_s$  and  $a_n$ , were defined which permit a rapid calculation of signal-to-noise ratio when viewing a uniform scene, a point source immersed in a uniform scene, or a periodic pattern. The averaging areas may be visualized as fictitious areas on the photocathode over which photoelectrons are effectively averaged by the imaging device. The necessity for two sampling areas was demonstrated by calculating the signal-to-noise ratio for a point source in a uniform background. When considering background alone, Schade's  $N_e$  parameter is sufficient and was shown to be related to the averaging areas by  $N_e^{-2} = (a_s^2/a_n)$  =  $a^*$ .

Data from two intensifier silicon type television tubes shows that  $a_s$  and  $a_n$  can be calculated from measured MTF data and the assumption of continuous sampling in the y direction. The latter assumption is valid for scan line densities equal to or greater than about 40 scan lines per mm of raster height.

#### ACKNOWLEDGEMENTS

The author wishes to thank Dr. D.W. Tufts and Mr. W.V. McCollough of the University of Rhode Island for the point source measurements and to acknowledge the assistance of Mr. R.L. Brooks and Mr. R.E. Franseen of the Night Vision Laboratory

#### REFERENCES

1. A. Rose, J. Optical Soc. Am. 38 (2), 196 (1948).
2. F.A. Rosell, "The Limiting Resolution of Low Light Level Imaging Sensors," in Photoelectronic Imaging Devices, Vol I, Plenum Press, 1971.
3. O.H. Schade, RCA Review 9, 1948.
4. F.A. Rosell and R.H. Willson, "Recent Psychophysical Experiments and the Display Signal-to-Noise Ratio Concept," in Perception of Displayed Information, Plenum Press, 1973.
5. J.W. Goodman, Introduction to Fourier Optics, McGraw Hill, 1968.
6. W.B. Davenport and W.L. Root, Random Signals and Noise, McGraw Hill, 1958.